Building a software tool for simulating the multi-physics of thermal protection systems.

Fields, Shaun

Building a Software Tool for Simulating the Multi-Physics of Thermal Protection Systems

Shaun Fields

Swansea University

A thesis to be submitted in partial fulfilment of the requirements of the degree of

Doctor of Philosophy

August 2014

ProQuest LLC.
789 East Eisenhower Parkway
P.O. Box 1346
Ann Arbor, MI 48106 – 1346

THESIS SUMMARY

Full title of thesis: **Building a Software Tool for Simulating the Multi-Physics of Thermal Protection Systems**

Candidate's Surname: **Fields**

Candidate's Forenames: **Shaun**

Candidate for the Degree of: **PhD**

The motivation for this research is to overcome the costs of using the current wind tunnels which replicate the high speed, temperatures and Reynolds numbers of new concept vehicles such as Hyper-Sonic passenger jets. The idea is that by employing accurate computational methods, costs can be reduced and more scenarios can be investigated. It will be argued that the characteristic based split scheme is a modified central difference temporal scheme, and can be utilized to capture the flow regimes of interest to the European Space Agency (ESA). The hypothesis of this thesis is that it is possible to model Hyper-Sonic applications with shock capturing reliably in a collocated, unstructured polyhedral, Finite Volume (FV) software framework. The reason for this hypothesis is a desire to develop an alternative approach for accurate, non-oscillatory solutions to the conservation laws for high speed flows that does away with calculating the upwind flow direction, donor nodes, Riemann solvers and can avoid Jacobian evaluations.

The finite volume method is generally preferred for industrial Computational Fluid Dynamics (CFD) because it is relatively inexpensive and lends itself well to the solution of large sets of equations associated with complex flows according to Greenshields et al. [1]. Usually physical variables such as velocity, temperature, density and pressure are co-located, which means that the values at the centroid of a control volume are chosen to represent these physical variables in the enclosed control volume. Co-location is popular in industrial CFD, because it allows greater freedom in mesh structure for complex 3D geometries and for refinement of boundary layers as mentioned in Greenshields et al. [1]. It is no coincidence that collocated, polyhedral, FV numerical methods are adopted by several of the best known industrial CFD software packages, including FLUENT, STAR CCM+ and CFD-ACE+. There is a current preference for unstructured meshes of polyhedral cells with six faces (hexahedra) or more, rather than tetrahedral cells that are prone to numerical inaccuracy and other problems. For example, Ferguson and Peric [2] mention that they are unsuitable for features such as boundary layers.
Discontinuities, such as shocks, in Hyper-Sonic compressible computations require numerical schemes that can accurately capture these features while avoiding spurious numerical oscillations. Current methods that are effective in producing accurate non-oscillating solutions are first of all monotone upstream-centred schemes for conservation laws- by Van Leer [3]; secondly the non-oscillatory (ENO) schemes by Harten A, Engquist B, Osher S [4], and lastly the weighted ENO schemes known as WENO schemes by Liu, X. D., Osher, and Chan [5]. Unfortunately these methods typically involve Riemann solvers and Jacobian evaluation, making them complex and difficult to implement in a collocated, 3D unstructured framework. This work seeks to find a method which overcomes these disadvantages.

Declaration

This work has not previously been accepted in substance for any degree and is not being concurrently submitted in candidature for any degree.

Signed.....(candidate)

Date...14/11/2014.....

Statement 1

This thesis is the result of my own investigations, except where otherwise stated. Where correction services have been used, the extent and nature of the correction is clearly marked in the footnote

Signed.....(candidate)

Date.....14/11/2014.....

Statement 2

I hereby give consent for my thesis, if accepted, to be available for photocopying and for inter-library loan, and for the title and summary to be made available to outside organisations

Signed.....(candidate)

Date.....14/11/2014.....

Acknowledgments

Completion of such a project would not have been possible without the help and assistance of a number of people. The author would like to thank his Supervisors, Prof. M. Cross and Dr N. Croft for their continued feedback, support and encouragement throughout the project and for introducing the author to Computational Fluid Dynamics.

The author would also like to acknowledge the help of the industrial supervisor Johan Steelant at the European Space Agency for his feedback and suggestions on the research efforts. Thanks are also due to Mr. Healy and Mr. Beer at Swansea University for helping to iron out any problems related to software issues. Mr. Beer managed to save a backup of copy of my hard-drive when the computer I was using at the time had a computer virus. I am indebted to his help. Discussions with Prof. Nithiarasu on the technicalities of CFD schemes also proved helpful. His and Prof. Zienkiewicz provided a major contribution to the project in their studies on CFD.

Special thanks need to go to the ESA and Swansea University for making the funds available so I could complete this research.

Contents

List of Figures

List of Tables

1. INTRODUCTION TO THE THESIS: MOTIVATION AND INITIAL CONSIDERATIONS

The European Space Agency (ESA) has performed feasibility and parametric studies on initial configurations of prospective Hypersonic cruise air-breathing vehicles (CAVS), and within the same agency the Computational Fluid Dynamics (CFD) programs have indicated poor lift/drag performance and high heat loads at the intended operating velocity range. The result of these tests is that ESA has seen a need to pursue simulations involving complex physical thermo-viscous interactions —an area in which the Multi-physics Research Group at Swansea University has considerable experience [1]–[3]. As a consequence ESA, has co-sponsored this PhD programme at Swansea University to tackle the problem described below.

1.1 Introduction to the Research Problem

The ***Research Problem*** to be addressed in this PhD programme may be summarised as: to simulate thermo-viscous interactions that will enable the analysis of thermal protection systems of cruise air-breathing vehicles (CAVS) subject to the Hypersonic flow regime. The CFD solver will require input data on the geometrical configuration and the operating velocity of the CAVs, and it will then capture the characteristics of Hypersonic flow such as the oblique shock layer, viscous boundary layer, far field viscous-inviscid interactions and transpiration cooled thermal protection systems so as to make inferences on the aerodynamic and heating performance of CAVs.

To identify the most appropriate method for an integrated approach to the ***Research Problem*** mentioned above, this literature review focuses on the vast number of computational methods and strategies used by the aerospace and scientific community. After identifying the numerical scheme most suited to the problem in question, careful implementation of this candidate scheme into the existing computational framework at Swansea University for CFD will then be described.

The literature review focuses on computational strategies in engineering because an informed decision is needed to successfully identify a strategy that best models the thermal protection systems for CAVs. This literature review has been broken up in such a way as to highlight the decision making process so when choosing the final strategy it becomes straightforward for the reader to understand the rationale.

The case for CFD

Few wind tunnels exist that can simultaneously simulate the high Mach speeds, Reynolds numbers and high flow field temperatures that would be encountered by Hypersonic trans-atmospheric vehicles. Those available are located in the USA and Europe but are extremely expensive to use. Anderson [4] has speculated that widespread access to these wind tunnels at a low economic cost is unlikely, and that when the development of CFD has reached the point where the complete three dimensional flow field over the external surface and the engines can be computed in an accurate and efficient manner, CFD will propel the optimized geometries of Hypersonic trans-atmospheric vehicles to become a reality.

There are three methodologies for studying systems that are effected by fluid flow; experiments, pure theory and CFD. It has to be argued that finding closed form theoretical solutions for the system of partial differential equations of mixed mathematical nature becomes fruitless, as no general mathematical theorem exists to guarantee existence and uniqueness[1]. Experiments are difficult, dangerous and expensive, and certain analyses become impossible in a laboratory. CFD however, represents an attractive alternative to experiments and theory. This is due to the advent of high speed digital computers combined with algorithmic development from the 1950s. Arguably, this revolutionized the way fluids are being studied today Hirschel and Weiland [5].

By the late 1970s, the use of supercomputers to solve aerodynamic problems was beginning to pay off. A relatively early success story was the NASA built experimental aircraft, the Highly Manoeuvrable Aircraft Technology (HiMAT). The wind tunnel tests of the preliminary design showed that, if built, it would possess unacceptable drag at transonic speeds, and the financial cost of redesigning it in further wind tunnel tests would have been around the $150,000 mark, which would have caused lengthy delays. Instead of wind tunnel tests, the wing was redesigned by CFD simulation at a cost of $6,000 as stated by Ceruzzi [6], 4% of the projected wind tunnel costs. In addition CFD simulation, as Lyra [7] states, has already made a large impact in design of many areas such as meteorology, the nuclear industry and petroleum exploration.

Despite the relative maturity reached by CFD, in which the basic methodologies that underpin its application areas remain well established, computer simulation still does not have quite the same status as physical experiments inside industry. The dearth of numerical results concerning complex practical applications and the remaining doubt about the accuracy of the available techniques for various problems still persist according to Lyra [7]. For example according to Hirschel and Weiland [5], to make computer simulations widely accepted and reliable, intricate flow phenomena such as transition to turbulence and re-laminarisation must be addressed.

According to Hirschel and Weiland [5] the next century will witness the emergence of CFD simulation as the critical software tool for designing new aerodynamic concepts and vehicles. This will contribute to a dramatic shortening of the design process, which will enhance and enable concurrent engineering. However, this will demand significant advances in algorithm research and CFD code development, of the kind which drives this research.

1.2 Properties of a CFD Code

The exact prediction of a physical system cannot be obtained even with the adoption of the most refined mathematical model. Therefore, the key step in scientific analysis is the choice of a suitable mathematical model, the knowledge of its limitations and the physical approximations in its derivation. The continuously expanding application of numerical methods in dealing with engineering and scientific flows of interest means it is important to utilize novel algorithmic developments to improve the quality of the present solutions and to enable the solution of previously intractable problems. The success of designing a computational procedure requires, as Lyra [7] states, at the very minimum that the computer code should have a combination of the following properties:

- Efficiency

The required response must provide sufficient accuracy, at least cost and within reasonable time, to allow an impact on design. This implies the utilisation of appropriate data structures, the exploitation of the currently available high performance computer configurations, the use of techniques for

[1] Uniqueness is the mathematical property of obtaining only one solution to the initial and boundary conditions of the

enhancement of stability and the convergence rate. Foremost efficiency endeavours to have an impact on design.

- Reliability

The adopted methods and models must rest on a solid mathematical basis and reasonable physical approximations in such a way that the predicted response is known to be within a selected level of accuracy. The success of designing a computational method requires methodologies to assess the solution's accuracy, such as, benchmarks with known analytical or experimental solutions.

- Robustness

The adopted method should exhibit stability for comprehensive classes of applications with few user defined parameters.

- Versatility

The final computational code must be able to deal with complex geometries and boundary conditions, different types of loads, and domain discretisation.

Lyra [7] states that the effort involved in accomplishing the requirements for finding a solution to practical fluid dynamic and heat transfer problems is enormous, as many difficulties arise in the process. The importance of improvements in these related areas drives most of the present research in CFD.

The different physical phenomena intrinsic in the system of the partial differential equations, such as coupled convection and diffusion problem leads in general to Elliptic-Parabolic-Hyperbolic mixed nature types of mathematical models. The development of multi-purpose CFD codes is perceived as very difficult, or even impossible, as the success either in terms of accuracy, robustness or efficiency is directly connected to the exploitation of the particular characteristics of each class of mathematical model.

1.3 Gas Modelling Methods for Hypersonic Air Flow

At present numerically modelling the physics of Hypersonic flight of cruise air-breathing vehicles (CAVs) cannot currently be overcome by a single effort. The main challenges as the scientific community understands them are illustrated in Figure 1-1. The next stage of this literature review focuses on the different continuum gas models used in studies carried out on Hypersonic CAV applications.

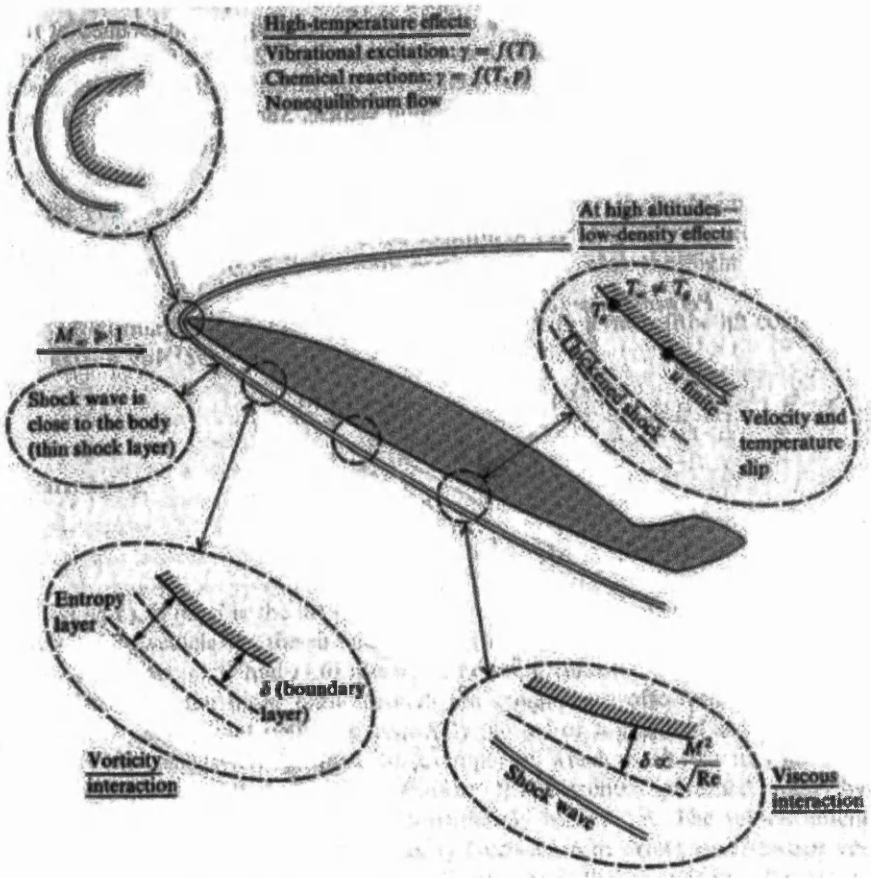

Figure 1-1 Complexities of the coupled physics at Hypersonic air flow [8].

Numerically modelling Hypersonic flows is fraught with challenges to infer adequate information on the aerodynamic and heat transfer performance of the vehicle. As the flow regime changes from Subsonic to Hypersonic, compressibility effects dominate.[2] Oblique shock waves form at the leading edges of the body, where large velocity and temperature gradients arise, and this makes it difficult to accurately predict energy dissipation and boundary layer shapes. Anderson [4] states that a highly curved shock wave and flow with a low Reynolds number in certain situations means the shock wave merges with the boundary layer, producing a viscous shock layer that drastically changes the heating properties of the fluid. This will have serious implications on the coefficient of friction and

[2] In contrast to modelling Sub-Sonic speed flows which statistically can be assumed to be incompressible thereby simplifying the problem enough to infer adequate information on the aerodynamic and heat transfer performance of the vehicle

coefficient of heat. These parameters will ultimately define the fuel economy and safety of such vehicles.

In high speed Supersonic and Hypersonic- applications, velocity, as Anderson [9] states, is measured as a Mach number which is a measure of the vehicle's kinetic energy relative to the kinetic energy of the surrounding air molecules. At high enough speeds the energy absorbed by the surrounding air is enough to chemically change the state of the air[3]. Appropriate chemical models are needed to capture the physics at work, and approximate the thermal and chemical properties of the gases involved. There are four basic physical models of a gas that are used by aeronautical engineers who design heat shields, where each model used is dependent on the state of the gas under review and each level of refinement in the model requires higher computational cost [5].

1. Perfect gas model
2. Frozen Gas Model
3. Equilibrium
4. Non Equilibrium

The perfect gas model is used in this research and the reason is three fold. Firstly for the engineering benchmarks and final application pursued, the perfect gas model is sufficient at approximating the actual physics, when temperatures will be below 2000K. Secondly the perfect gas model still poses a substantial and focused effort when trying to capture the flow using CFD, and thirdly as the temperatures for all the benchmarks in this study are below 2000K the perfect gas model in the CFD solver will be used throughout this work. A more detailed discussion of Equilibrium and Non Equilibrium models can be found in the appendices.

The perfect gas theory is both basic and useful for designing aircraft, but its limitations are that it takes the gas to be chemically inert. The perfect gas theory begins to break down at 800 K and is not usable at temperatures greater than 2000 K. For temperatures greater than 2000 K, a heat shield designer must use a *real gas model.*

For the perfect gas model the fluid is treated as a perfect gas and hence no chemistry is taken into account. From a physical standpoint, the simulations are typical of cold gas flows which are usually achieved in experimental facilities such as gun tunnels [10]. This is certainly not representative of actual flight conditions in which dissociation and vibrational relaxation are important phenomena especially for the higher Mach number cases[4]. However, it is necessary to construct a robust code to deal with the complete environment encountered in actual flight.

1.3.1 Continuum Mechanics: The Knudsen Number

The majority of the phenomena encountered in fluid mechanics falls well within the realm of the continuum postulate, and the physical description of our world can neglect the phenomena occurring at a microscopic level [4].

The continuum assumption requires that the mean free path of individual elements must be very small when compared with the physical-length of the system under consideration, i.e. the density of elements is high enough so that the mutual interaction dominates over the individual behaviour.

[3] Assumptions about the properties of air used in standard mathematical models are no longer valid because the physical properties of the fluid change.

[4] Mach 12-16

Where the microscopic-length scale approaches macroscopic dimension, such as when a rocket passes through the edge of the atmosphere, where rarefied gas exists, the interaction between particles becomes significant and the particles behave essentially as individual elements. These limited situations are outside the field of this research.

The Knudsen number is useful for determining whether the statistical mechanics model or the continuum mechanics model of fluid dynamics should be used:

$$Kn = \frac{\lambda}{L}$$

λ-mean free path
L-Length scale of the body

When the dimensionless Knudsen number >0.1, the mean free path of a molecule is comparable to a length scale of the problem, and the continuum assumption of fluid mechanics is no longer an adequate approximation. In this case statistical methods must be used, such as the Lattice Boltzmann equations. Statistical mechanics strategies such as the Lattice Boltzmann equations are employed in the research carried out by Succi [11] and more recently by Schaefer and Yuan [12].

However, the benchmarks pursued in this research are all in the continuum regime, because the associated Knudsen numbers are far smaller than 0.1. For the case studied in Chapter 8, the Supersonic viscous flow over a plate length of 10 micron-meters (10^{-5}m) has a Knudsen number of 6.1×10^{-3} and a mean free path of 6.1×10^{-8}m. This case possesses the greatest Knudsen number in this thesis, but it can be remarked that it still behaves as a continuum. More information on the continuum model can be found in [4], [13], [14].

1.4 CFD Discretisation of Conservation Laws

This section will look at the basic aspects of discretisation and how to replace the spatial partial differential i.e. the integrals in the governing equations of motion with discrete numbers. Discretisation of the partial differential equations is called finite differences, and discretisation of the integral form of the partial differential equations is called finite volumes. Anderson [15] states that:

"[essentially] discretisation is the process by which a closed-form mathematical expression, such as a differential or an integral equation involving functions, all of which are viewed as having an infinite continuum of values throughout some domain, is approximated by analogous expressions which prescribe values at only a finite number of discrete points in the domain"

In fluid mechanics the basic conservation laws can be derived in a Eulerian framework by considering the fluid which passes at a time through an arbitrary fixed control volume, V, with surface, S, in relation to a fixed Cartesian system see reference [16], [17]. The governing equations are then approximated at discrete locations on either structured or unstructured meshes.

1.4.1 Fundamental Definitions: Consistency, Stability, Convergence

The objective here is to give a short review of some important concepts required for numerical schemes used to spatially discretise and solve partial differential equations. More detailed and formal discussions can be found in the research of [17]–[20].

Consistency

It is necessary to define the truncation error ϵ_T of a given discrete equation, which represents the difference between the partial differential equation, and the corresponding discrete equations as built up by the algebraic difference quotients. This allows the definition of consistency, which states that the discrete equation should tend to the corresponding exact solution under refinement of the spatial and time lengths.

$$\lim_{\Delta x, \Delta t \to 0} \varepsilon_T = 0 \tag{1.1}$$

The utilization of the Taylor series allows the verification of consistency for a given scheme and the determination of the order of accuracy, or the rate at which the discrete equation tends to the differential equation as Δx, Δt tend to zero.
The truncation error is generically expressed in the form-

$$\varepsilon_T = \left(\Delta x^r, \Delta t^t\right) \tag{1.2}$$

With r, s being the order of spatial and temporal accuracy respectively, and for the finite difference expression to follow in equation (1.6), it can be seen that $r = 1$.

Stability

A second requirement of a numerical technique, concerns the stability of the scheme and establishes a relationship between the computed and the exact solutions of the discretised equation. As introduced by Lax and Richtmyer, [21] the stability criterion states that any component of the initial solution should not be amplified without bound. Following the procedure given by Hirsch , consider a marching solution in which at a certain time level n the variable u^n is known.

$$u^{n+1} = \Re u^n \tag{1.3}$$

Where $\Re$ is a discrete operator when applied to u^n returns a value for the unknown u^{n+1} at the time level n+1. The stability condition for the scheme represented by operator $\Re$ can be achieved if a constant K exists.

$$\left\|\Re^n\right\| < K \quad \text{for} \quad \begin{matrix} 0 < \Delta t < \tau \\ 0 < n\Delta t < T \end{matrix} \tag{1.4}$$

For fixed values of τ, T and for all n, with $\|\bullet\|$ denoting an appropriate norm.

The analysis of stability can be accomplished by various methods, such as the von-Neumann method, the equivalent differential equation and the matrix method as seen in the book by Hirsch [18]. Each method has its own merits, but all result from linear theory and represents only a rational support and guideline for non-linear problems, for which the last word will be given to numerical experiments.

Convergence

The primary requirement of a scheme is that the numerical solution must approach the exact solution of the differential equation at any point and at any time when Δx, Δt tend to zero. This condition is called convergence and despite being very difficult to establish directly, it is automatically achieved once consistency and stability are verified as a result of the fundamental Lax's equivalence theorem. It is argued by Richtmyer and Morton [22] that "*For a well-posed linear initial value problem and a consistent discretisation, stability is necessary and sufficient condition for convergence*"

A solver will partition a flow domain with a mesh otherwise known as a grid before applying the numerical algorithms: Meshes divide the solution domain utilizing a number of discrete points, control volumes or elements. Meshes employed can be constructed of a variety of elements; triangles and quadrilaterals in two-dimensional domains, tetrahedrals, wedges and hexahedrals in three dimensions. A description of the three main approaches a solver can employ to discretise spatially the governing equations now follows.

1.4.2 The Finite Difference Method

The discretisation is accomplished by employing discrete points in the domain to the solution of the partial differential equations under investigation. It was originally developed for structured orthogonal 1 & 2 dimensional problems and ultimately is not suitable for unstructured non-orthogonal multidimensional grids. Richardson [23] presented a paper on the first finite difference method (FDM). Many papers on FDM in CFD have followed, such as Lewy, Courant, and Friedrichs [24]; Evans and Harlow [26]; Godunov [27]; Lax and Wendroff [28]; MacCormack [29]; van Leer [30], amongst many others. Historically, FDMs dominated the earliest CFD codes because of their simplicity in formulation and their computational procedure. As mentioned they are not suitable for multidimensional problems with complex geometries that require unstructured grids and so can be omitted for this research.

Imagine a two-dimensional flow field which is governed by the Navier-Stokes equations, or as the case may be by the Euler equations. The analytical solutions of these partial differential equations would provide in principle a closed form expression of u,v,p,ρ as functions of x and y. Which would theoretically state values of the flow-field variables at any of the infinite points in the flow domain. If the partial derivatives in the governing equations are replaced by approximate algebraic difference quotients, where these quotients are expressed in terms of the flow field variables at two or more of the discrete points shown in fig 4.1, then the partial differential equations are totally replaced by a system of algebraic equations, which can only be solved by the values of the flow field variables at the discrete points. In this sense the partial differential equations have been discretized with this, the method of finite differences.

Most common finite difference representations of derivatives are based on the Taylor Series expansions. For example if $u_{i,j}$ denotes the x component of velocity at point (i ,j) then the velocity $u_{i+1,j}$ can be expressed in terms of a Taylor series expanded about point (i,j) as follows-

$$u_{i+1,j} = u_{i,j} + \Delta x\left(\frac{\partial u}{\partial x}\right)_{i,j} + \frac{\Delta x^2}{2}\left(\frac{\partial^2 u}{\partial x^2}\right)_{i,j} + \frac{\Delta x^3}{6}\left(\frac{\partial^3 u}{\partial x^3}\right)_{i,j} + O(\Delta x^4) \qquad (1.5)$$

Equation (1.5) is mathematically an exact expression for $u_{i+1,j}$ and the series converges if-

(1) the number of terms is infinite.
(2) $\Delta x \rightarrow 0$.

Re-arranging equation (1.5)

$$\left(\frac{\partial u}{\partial x}\right)_{i,j} = \underbrace{\frac{u_{i+1,j} - u_{i,j}}{\Delta x}}_{\substack{\text{Finite-}\\ \text{Difference}\\ \text{representation}}} \underbrace{- \frac{\Delta x}{2}\left(\frac{\partial^2 u}{\partial x^2}\right)_{i,j} - \frac{\Delta x^2}{6}\left(\frac{\partial^3 u}{\partial x^3}\right)_{i,j} + \ldots}_{\substack{\text{Truncation}\\ \text{error}}} \qquad (1.6)$$

The first term on the right hand side is a finite difference representation of the partial derivative. The remaining terms on the right hand side constitute the truncation error. If we wish to approximate the partial derivative with the following algebraic finite difference quotient-

$$\left(\frac{\partial u}{\partial x}\right)_{i,j} \approx \frac{u_{i+1,j} - u_{i,j}}{\Delta x} \qquad (1.7)$$

Then the truncation error in equation (1.6) tells us what is being neglected in this approximation. In equation (1.6) the lowest ordered term in the truncation error involves Δx to the first power; hence this finite difference expression is called first order accurate.

$$\left(\frac{\partial u}{\partial x}\right)_{i,j} = \frac{u_{i+1,j} - u_{i,j}}{\Delta x} + O(\Delta x) \qquad (1.8)$$

In (1.8) , the symbol $O(\Delta x)$ is a formal mathematical notation which represents " the numerical order for Δx".

1.4.3 The Finite Volume Method

The Finite Volume Method (FVM) was originally developed as a special class of the finite difference formulation, but has since become the most common and preferred approach in CFD analysis. The FVM was first introduced by McDonald in 1971 [31], for the solution of the two dimensional time dependent Euler equations, and was subsequently extended to three-dimensional flows by Spalding and Patankar [32].

In the finite volume method the solution domain is divided into a number of contiguous control volumes. The conservation equations are integrated in physical space over these control volumes and a solution sought which makes each of these integrals equal to zero. The resulting expression maintains exact conservation of the relevant properties at each cell volume. The finite volume method can be applied to cell centres, cell vertex or vertex-centred control volumes. According to McBride, [33] because of their simple data structure, and the fact that the governing fluid flow equations, are actually applied to structures akin to control volumes, means that the finite volume method, has become the most popular of the three approaches stated. The finite volume method is central to five of the main computational fluid dynamic tools such as FLUENT, CFX , FLOW3D, CFD-ACE+ and STAR-CD and the host CFD tool used in this research, PHYSICA.

Using simple finite difference type approximations to discretise the various terms in the governing equations, combined with comparatively low storage requirements, have made this approach favoured by the commercial codes referred to above. The earliest finite volume approach to incompressible problems used fully orthogonal Cartesian meshes and employed a staggered grid for the velocity components. When Spalding and Patankar [32] applied staggered grid arrangements it was introduced as a means of overcoming spurious oscillations in the pressure and velocity fields that can be encountered when employing equal order co-located methods. Difficulties were encountered as a consequence of the fact that only gradients of pressure appear in the momentum equations. Instead of evaluating primitive variables, i.e. pressure, temperature, on the ordinary Cartesian mesh, the idea is to evaluate the momentum components on the control volume faces. By the 1970s the FVM was being successfully applied to complex flow phenomena, but was limited to fully orthogonal structured meshes [34]–[37]. Although these methods were fast and efficient, but lacked the ability to model physically realistic domains.

The CFD community then began researching methods to cope with realistic flows and small degrees of non-orthogonality in a structured mesh environment. For a more comprehensive study of the ideas and strategies needed to cope with non-orthogonality for the finite volume approach, review Croft [38]. More background information for finite volume methods on unstructured grids in CFD can be found in the literature [39]–[41].

1.4.4 The Finite Element Method

Both the Finite Element Method (FEM) and Finite Volume Method (FVM) can be viewed as sub-sets of the method of weighted residuals, and the main differences between these methods are the finite space over which the equations are integrated and the weighting functions used in the FVM. For FVMs the weighting functions can be regarded as equal to 1 [42].

In FEM's a variety of weighted residual methods have been studied, and the optimal method is generally accepted as being the Bubnov-Galerkin weighted residual approach. In this method the governing equations are multiplied by a set of weighting functions, integrated and residuals minimised. The issue is the choice of element type and associated basis function best suited for minimizing the integrated errors. The solution domain is meshed using any type of element for which a shape function exits. This gives the advantages of allowing complex geometries to be meshed using fully unstructured grids. FEM, however, is known to be more complicated in its formulation and more time consuming in computations than FVM for flows according to [43].

The first FEM work was published in the Aeronautical Science Journal in 1956, and dealt with applications to aircraft stress analysis. This research was a result of a collaboration between Turner, Clough, Martin, and Topp. Since then, FEM have been developed extensively in fluid dynamics, solid mechanics, and related areas [44]. Research papers on the FEM in CFD includes; Generalized Petrov-Galerkin Methods [45]; Taylor Galerkin methods [46]; Characteristic Galerkin methods [47]; Discontinuous Galerkin methods [48] and Incompressible flows [49]

For the finite element method simple piecewise shape functions valid on local elements are used to describe the local behaviour of a variable within an element. The shape functions approximating ϕ are then substituted into the governing equations. These approximate functions to the governing equations will not hold exactly and a residual is defined to measure the errors. The residuals are only required to be zero in some weighted sense, which means that the conservation principle is not enforced locally.

The advantage of the finite element approach is a high degree of accuracy for arbitrary meshes, allowing complex geometries to be modelled. This advantage of handling distorted meshes, when compared to structured meshes, comes at a cost as it requires extensive storage of topological information [33].

1.5 Mesh Type

The accuracy of computational fluid dynamics (CFD) analysis not only depends upon a CFD code that accurately models the physical process, but also the ability to solve on a mesh that matches the true geometry of the physical domain. Significant advances have been made in the development of numerical methods designed to yield accurate solutions on structured and unstructured meshes.

Meshes govern the amount of detail in the solution, and an example is the complex geometrical features with significant localized physics, especially with regard to the boundary layer and stagnation region for viscous applications. A decision on the grid type used to discretize each application needs to be made on the grounds of efficiency, versatility and reliability. This part of the literature review will focus on the pros and cons of the two choices for constructing a grid.

1.5.1 Structured Grids

The extensive development of structured grid algorithms to a large class of non-linear problems using a large stencil of grid points means enhanced accuracy and stability behaviour when compared with unstructured grid algorithms [50]. An attempt to fit structured meshes to real life geometries has been practised by a number of researchers. A wide range of strategies have been employed; cell blocking, curvilinear grids, multi-block techniques and mesh embedding amongst others.

- Cell blocking: To sculpt structured meshes to the physical geometry, elements can be fully or partially blocked. An example of a partially blocked solution strategy can be found in [51]. This however can only handle a relatively small amount of curvature of the physical geometry.
- Curvilinear grids: The use of body fitted co-ordinates otherwise known as curvilinear grids, can enable solutions when a strict Cartesian mesh is unsuitable as seen in Gordon & Hall [52] and Shyy and Vu [53]. The solution grid and associated transport equations are mapped onto their topologically equivalent Cartesian mesh. As stated by Demirdžić & Perić [54] this approach considerably increases the storage requirements and adds to the complexity of the discretisation process. Errors accumulate during the mapping process and become increasingly significant if the physical domain is substantially different from the body fitted mesh.
- Multi-block techniques. Solving realistic geometries on a Cartesian mesh can be further improved by the use of multi-block techniques. An example of multi-blocks can be found in the references [55] and [56]. The solution domain is divided into a number of blocks, each block being mapped onto its equivalent Cartesian mesh. Multi-block techniques allow quite complex geometries to be modelled, external surfaces can be represented accurately but internal complexity still presents problems due to the lack of flexibility when using different element types. Another major problem, as stated by Anderson [15] in page 209, encountered in the use of multi block grids is the proper interfacing across regions where two blocks are joined together. Here large differences between the aspect ratios of neighbouring elements can occur causing numerical errors which can lead to divergence.

As referred to previously, structured mesh methodologies have been developed since the early days of CFD and still persist to the present day [57]. The main reason for this arises from the fact that the CFD practitioner can chose an appropriate solution method from among the large number of algorithms which are available. These algorithms can be implemented in a fairly straightforward manner to produce computer codes for multidimensional analysis (Lyra [7]). The straightforward concept of upwind directionality, the small bandwidth of the geometrical Jacobian matrix and the possibility to use implicit methods based on sparse matrix technology make structured grids effective at solving problems with structured geometrical domains. However the large elapsed time necessary to produce structured grids for extremely complex domains, the difficult control on the quality of elements and the unstructured type overhead which arises when strategies such as curvilinear and multi-block are implemented represent the main disadvantage when using the structured approach.

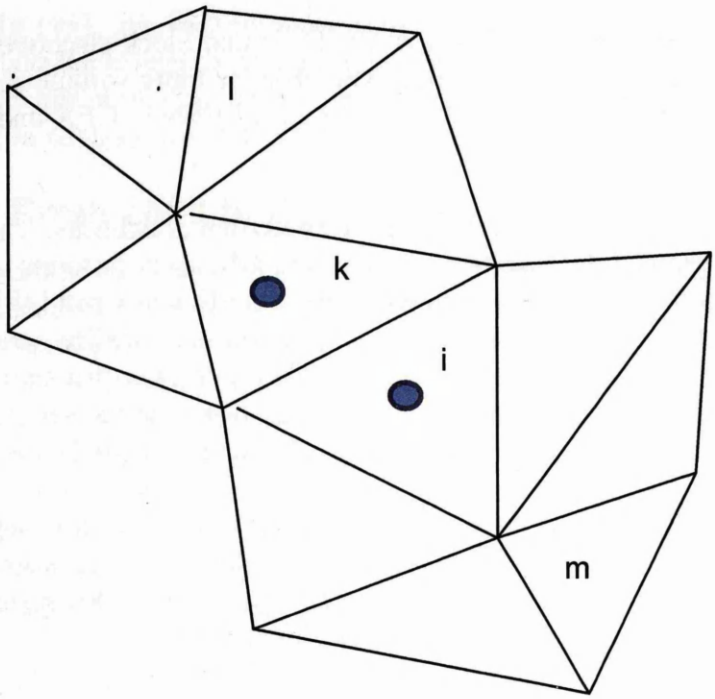

Figure 1-2 Graphical representation of an unstructured co-located grid.

1.5.2 Unstructured Grids

For complicated geometries, attention has shifted to unstructured grids that can be easier to generate than structured grids as argued by Powell and Coirier [59] because unstructured techniques permit any mixed element types to be employed allowing complex internal and external domains to be represented accurately. The solution of the Euler equations on arbitrary unstructured grids generated by Jameson and Mavripilis [60], lead to impressive results using cell-centred approximations.

Since the finite volume and finite element methods do not demand a uniform, rectangular grid for computations, as opposed to finite difference, then such calculations can be made directly to the physical plane. No transformation between a physical and a computational plane is necessary as seen in [54, 55] the case of finite differences to curvilinear grids. Finite volume methods (FVM) in the early 1980s were extended to unstructured meshes for the solution of the Navier-Stokes equations, where cell-centered FVM were employed by Pan, Lu, and Cheng [39] to solve laminar flow problems using an unstructured mesh of triangular elements. Thomadakis [61] and Chow [40] employed polygonal elements, including triangles, squares, and octagons to solve simple flow and heat transfer problems. More complex swirling, turbulent, reacting flows have been solved by Croft [38].

The research community focused on non-staggered techniques as staggered grid arrangements do not easily extend to unstructured meshes because staggering also requires a large increase in storage of geometry information. Many ideas have been developed for structured mesh solvers and are can now adopted within the unstructured context. After modifications they imply more complexity and less efficiency, yet, a lot work has to be done to remove any scepticism that still remains in the industrial community.

For unstructured grids, the grid generation is fairly straightforward and automatic as it was originally developed for finite element methods. Ultimately unstructured grids allows for maximum flexibility in matching mesh cells with the boundary surfaces and placing cells where the modeller wants them. Thereby constructing unstructured grids, around complex geometrical features, does not require large

time overheads as is the case with curvilinear grids (Shyy and Vu, [53]) and block structured grids (Powell and Coirier [59]). These grid generators are now widely available for finite volume methods. Unstructured grids are now the norm in commercial CFD software i.e FLUENT, CFX and CFD-ACE+.

Unfortunately the unstructured approach is accompanied by some well known drawbacks. The main concern at present centre upon the accuracy of the results computed, the efficiency in terms of CPU time and storage requirements. Another drawback of unstructured grids according to Croft [38] is that numerical errors in the quantities due to distorted meshes, non-conjunctionality and non-orthogonality can arise. Substantial progress has been made on the development of unstructured mesh methodologies with significant achievements in areas such as mesh generation, and the efficiency of unstructured mesh solution algorithms, see for example the following references [60], [62]–[64].

Refinement procedures for unstructured meshes at localized regions is less time consuming to implement than structured multi-block procedures, and since the final modelling application will involve, components which with a high degree of curvature. Therefore because of this reason, the computational strategy will choose unstructured grids to discretize the domain.

In addition to the considerations above, advances in CFD, i.e. scaling up problems of increasing complexity to vector and parallel processors, are coupled to the state of the art in computer hardware. The following section provides a brief background to this active research area.

1.6 Parallelisation

. CFD solvers repeatedly manipulate millions of numbers, a task which is tedious without the aid of super-computers, particularly in regard to storage and execution speed. One of the strongest drivers for developing new supercomputers is coming from the CFD community. This has been manifested in the development of large mainframe computers.

1.6.1 From 1970s - 1990s

In the 1970s high speed digital computers were serial machines, capable of one computational operation at a time, which meant that all computations had to get in line before execution. The speed of electrons, limited the speed of such serial computers Simon and Kowalik, [65]. To bypass this physical limit, two new configurations of computer architecture were being investigated;

1. Vector Processors, a configuration that allowed a string of identical operations on an array of numbers simultaneously, thus saving time and memory.
2. Parallel processors, a configuration that has two or more fully functioning central processing units (CPUs). Each of which can handle different instruction and data streams; executing separate parts of the program simultaneously.

However in the 1990's CFD reached a critical juncture, since it became more and more apparent that future growth in computational speed would result from parallel processing technology. A wide variety of parallel machines became available for exploring the issues of using parallelism in scientific computing in general and CFD in particular. Most of the early parallel machines were experimental in nature and served mainly as research investigations in areas such as algorithmic development, languages and operating systems. Then several members of a first generation of parallel supercomputers became available. Unfortunately limitations arose as it became clear that these machines were deficient in their systems aspects, such as their ability to handle a large number of

users. In 1991, the second generation of parallel supercomputers arrived, which offered an order of magnitude improvement in computational power over the previous generation as well as an improved software and user environment as noted by Simon and Kowalik, [65]. Therefore researchers who wanted to advance the state of the art in CFD had to consider parallel processing.

1.6.2 From 2000 to the Present Day

An important innovation in high-performance parallel computing is the recent use of hardware known as graphic processing units (GPUs), which was originally designed for graphics and game consoles to solve general purpose computing problems. From the web Nvidia-Coe [66] state that the GPUs have enormous peak performance for arithmetically intensive computations, and at relatively low cost when compared to their counterparts with similar performance levels. The multi-core processors or GPUs are no longer the future of computing, they now host present applications. As stated by Simon and Kowalik, [65], a typical mass-produced CPU will have several processor cores, whereas a GPU may have hundreds or even thousands of cores meaning technology trends are driving all microprocessors towards multiple core designs. To summarize the motivation and initial considerations of the thesis;

1. The use of structured discretisation techniques represents an advantage in terms of the efficient implementation of all classes of schemes and techniques to enhance convergence. On the other hand, algorithms for unstructured grids suited to parallel computations, which represent the possibility to perform certain numerical analysis within an affordable time, have a faster and hence bigger impact on industrial design. For example parallelization strategies based on forced and natural domain partitioning techniques require the use of overlapping mesh partitions to keep the parallelization work simple. Fortunately, many of the tools needed to create overlapping partitions give good results [3] and [67].

2. Algorithms that perform well in parallel include the explicit and implicit FVM employed by the CFD group at Swansea in the in house code PHYSICA [68]–[70]. Due to the efforts of these researchers unstructured mesh FV discretisation framework, topological solvers, and partitioning tools for parallel operation are already embedded in the host code PHYSICA. They are therefore ready to be accessed, when modelling the 3-D non-linear geometry, the final industrial goal.

1.7 Structure of Thesis

This PhD thesis documents the challenges and novel strategies employed when simulating Hypersonic flows on vehicles containing porous materials specifically the new generation of CAVs. The thesis details many sub-categories that were needed and built on to enable a strategy to accomplish the final goal. These chapters include:

Chapter 1. The first part of the literature review. The Chapter opens with the Research Problem mentioned in Section 1.1, this is the primary reason for conducting this thesis. In addition, Chapter 1 also lists and detail the many essential properties of numerical techniques required for a stable and accurate solution, and, covers the three main approaches for spatially discretising the solution domain.

Chapter 2. The second Chapter is the Mathematical Basis listing the governing equations that will be solved and detailing the mathematical character of the equations for different speed regimes and the difficulties associated with their solution.

Chapter 3 The second part of the literature review, will list and detail the many numerical techniques that have gained popularity in CFD. The reason for breaking the literature review into two chapters is due to the importance of establishing a red line going from the various numerical techniques to the choice of the final candidate technique for the research problem.

Chapter 4 The fourth chapter contains the results for inviscid 1-D Supersonic flow through a De Laval nozzle modelled with the judicious use of artificial viscosity.

Chapter 5 The fifth chapter contains the Numerical Implementation for the CBS algorithm in Multi dimensions.

Chapter 6 The sixth chapter contains the results for inviscid 2-D Supersonic flow over a wedge and a mesh sensitivity study for the NACA aerofoil.

Chapter 7 Incompressible flows are detailed and solved in Chapter 7.

Chapter 8 Compressible viscous flows are modelled for the Flat plate example in [15].

Chapter 9 Modelling compressible and incompressible flow through a porous structure using an appropriate source term is tackled.

Chapter 10 Modelling the real world application - the winged Hypersonic vehicle employing transpiration cooled components.

Chapter 11 Conlusion and Discussion, evaluates the performance of the CBS algorithm to scientific benchmarks. Discusses the pertinent issues raised during the calculations and reccommends future work.

The code was implemented and compared against several benchmarks where the physical complexity of each problem increases for every new problem. The following table details these benchmarks, culminating in the scheme being finally applied to the target application.

Table 1-1- **Table of cases computed and now displayed in this Thesis**

1-D Invisicd Benchmark:	**Speed**	**Shock Capturing**		**Comments**
De Laval Nozzle	Transition from Subsonic to Super Sonic flow	No		Speed Ranges from Mach 0.1 at the inlet to Mach 3 at the exit
De Laval Nozzle	Choked Nozzle: Subsonic to Supersonic Values	Yes		Shock was captured with the JST AVT
2-D Invisicd Benchmark	**Mach Speed**	**Shock Capturing**		
2-D Wedge	Mach 2	Yes		Mesh sensitivity
2-D Wedge	Mach 3	Yes		Comparison with analytical solution and FLUENT CFD solver

NACA Aerofoil	Mach 1.2	Yes		
2-D Viscous Benchmark	**Speed / Regime**	**Length**	**Thermal Boundary**	
Flat Plate Case 1	10m/s (M=0.01) Incompressible	1m	Cold Wall	Investigating whether the modified AC CBS algorithm is reliable at capturing the Blasius boundary layer
Flat Plate Case 2	694m/s (M=2), Compressible		Cold Wall	
Flat Plate Case 3	1300m/s(M=4), Compressible		Cold Wall	
Flat Plate Case 4	1300m/s(M=4) Compressible		Adiabatic	
Porous Media	**Speed / Regime**	**Length**	**Isothermal**	
Case 1: 1-D Plug Flow	8m/s-90m/s Incompressible		Yes	Ergun source term
Case 2: 1-D Plug Flow	90m/s, Compressible		No	Ergun Source term
Case 3: 2-D Flat Plate with porous membrane	M=2.06, Compressible		No	Utilized Langener [71] Boundary condition approach
Novel Application	**Mach Speed**	**Length**	**Isothermal**	
Supersonic Flow over porous components with transpiration cooling	M=2.06, Compressible		No	Utilized Langener [71] Boundary condition approach

Where Red signifies a compressible Supersonic problem.
Green signifies incompressible Subsonic problem.

2 MATHEMATICAL BASIS

2.1 Initial Considerations and Preliminaries

The conservation laws for compressible applications are expressed in terms of Hyperbolic partial differential equations. Hyperbolic partial differential equations possess mathematical properties that need to be understood before developing a CFD numerical method for their solution. For example the physical nature of, Hyperbolic equations are more complicated than Parabolic equation, because the Hyperbolic equations exhibit discontinuities [16]. CFD solvers for compressible applications need to permit the possible existence of these discontinuities. Elements of the theory of Hyperbolic equations are, in some way, incorporated into many numerical schemes. For instance the propagation of information, is finite and equal to the wave speed. The propagation of information is otherwise known as Characteristics. A detailed presentation of the basic theory of Hyperbolic partial differential equations can be found in the literature [18], [72]–[74].

As discussed by Patankar [36] total conservation of a generic flow variable ϕ i.e. the density or x-momentum component, within a finite control volume can be expressed as a balance between, various processes tending to increase or decrease the density or x-momentum.

$$\begin{bmatrix}\textit{Rate of change}\\ \textit{of } \phi\\ \textit{in the}\\ \textit{control volume}\\ \textit{with respect to}\\ \textit{time}\end{bmatrix} = \begin{bmatrix}\textit{Net Rate of}\\ \textit{increase of } \phi\\ \textit{due to}\\ \textit{convection}\\ \text{into the}\\ \textit{control volume}\end{bmatrix} + \begin{bmatrix}\textit{Net Rate of}\\ \textit{increase of } \phi\\ \textit{due to}\\ \textit{diffusion}\\ \text{into the}\\ \textit{control volume}\end{bmatrix} + \begin{bmatrix}\textit{Net Rate of}\\ \textit{creation}\\ \textit{of } \phi\\ \textit{inside} \text{ the}\\ \textit{control volume}\\ \textit{from sources}\end{bmatrix} \tag{2.1}$$

Equation (2.1) is taken from [36] and expresses the conservation of a generic flow variable, ϕ , for a coupled convection-diffusion problem in one dimension:

$$\frac{\partial(\phi)}{\partial t} = -\frac{\partial(u\phi)}{\partial x} + \frac{\partial}{\partial x}\left(\Gamma\frac{\partial\phi}{\partial x}\right) + S_{\phi} \tag{2.2}$$

Where u -velocity component (m/s)
ϕ - general flow variable
Γ - Coefficient of diffusion (kg/(ms))

The central differencing finite volume approach to diffusion only problems has been scrutinized in detail by Spalding & Patankar [32] and Patankar [36] who showed the central differencing to be both accurate and robust. It would seem obvious then to extend the central differencing practice to the more challenging coupled convection-diffusion problems. Unfortunately it is well known in the CFD community that central schemes become unstable when solving highly convective flows with an ill-conceived grid as, confirmed by Courant, Isaacon & Rees [75]. This manifests itself in a stringent upper limit on the grid size for stable calculations. This can be inferred from the technical detail that follows.

$$CFL = c\frac{\Delta x}{\Delta t} < 1 \qquad (2.3)$$

As a consequence, the time step is less than a certain value for explicit time-marching computer simulations, otherwise the calculations will become unstable. For a second order wave equation there is a connection between the characteristic lines associated with the stability condition, a connection which helps to elucidate the physical significance of the CFL condition. Let us pursue this connection because the final result is informative for, the governing equations that have to be numerically solved:

$$\frac{\partial^2 u}{\partial t^2} = c^2 \frac{\partial^2 u}{\partial x^2} \qquad (2.4)$$

The characteristic lines for equation are given by:

$$x = \begin{cases} ct \\ -ct \end{cases} \qquad (2.5)$$

The characteristic lines are given by the full black lines sketched in Figure 2-1 and Figure 2-2.

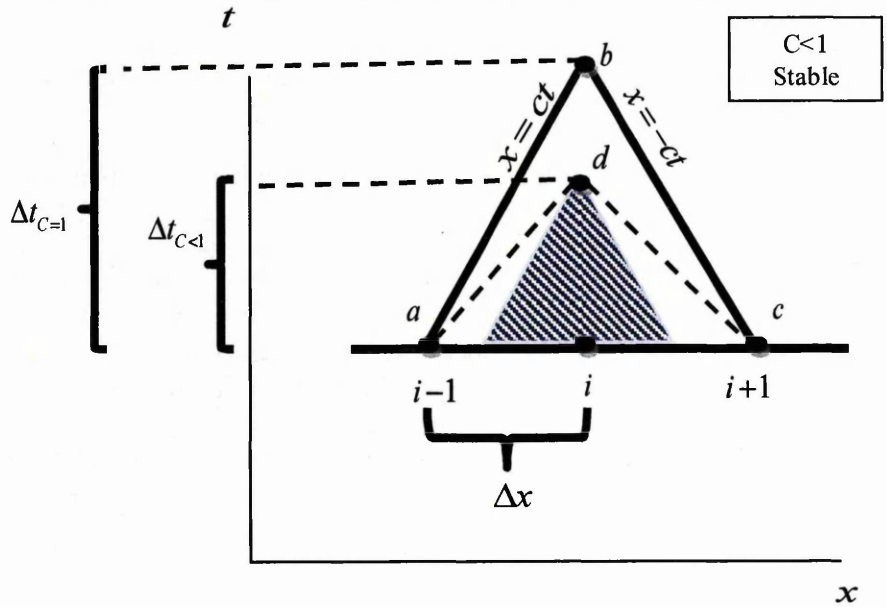

Figure 2-1-Illustration of a stable case. The numerical domain includes all the analytical domain.

The shaded triangle is the analytical domain. The analytical domain is defined by the characteristics passing through point d. These characteristics are parallel to those that pass through point b. The numerical domain is a,d,c, the broken line triangle. Note that the numerical domain of point d, the broken lines, includes the analytical domain i.e. the shaded triangle. In contrast, consider the case shown in Figure 2-2.

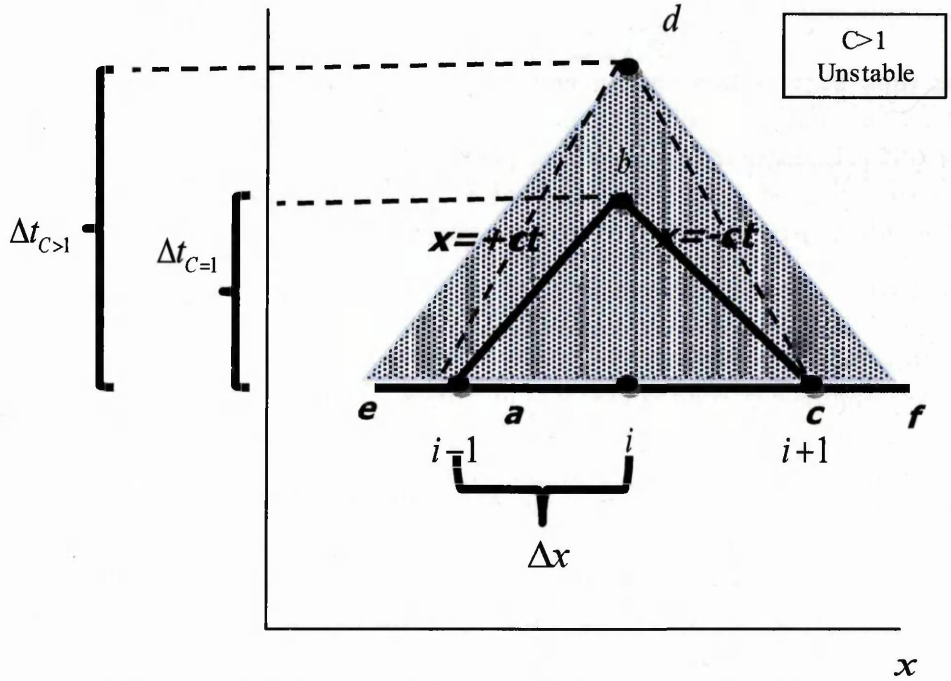

Figure 2-2- Illustration of an unstable case. The numerical domain does not include all the analytical domain.

Point d lies on node i and is at a time level of $t+\Delta t_{C>1}$. Since properties at point d are calculated numerically from the partial difference equation (PDE) using information from point i+1 and i-1 then the numerical domain is a,d, c shown in Figure 2-2. The shaded triangle is the analytical domain points e,d,f. Point b, is determined by the intersection of the characteristic line through grid point i-1 and i+1. Note that the numerical domain does not contain the analytical domain, e,d,f,. This has a theoretical and practical significance –which states that, the Courant number should be CFL<1, otherwise the numerical solution to the PDE will be unstable. Therefore, the following physical interpretation of the CFL condition is proposed:

"For stability the numerical domain must include the all the analytical domains".

The above constraint essentially deals with stability. The question of accuracy, which is something quite different as Anderson states, can also be examined from the point of view of Figure 2-1. The physical properties at point d depend only on those points within the shaded triangle. However notice that the numerical points i+1 and i-1 are outside the triangle-the domain of dependence for point d- and hence *theoretically* should not influence the properties at point d. The numerical calculation of properties for the PDE seen in equation (2.6) at point d however takes information from grid points i-1 and i+1. This is exacerbated when $t+\Delta t_{C<1}$ is chosen to be very small. In this case even if the calculations are stable, the results may, according to Anderson, be inaccurate due to the mismatch of the domain of dependence of point d and the location of the actual numerical data used to calculate properties at point d. In light of the above discussion, Anderson [15] concludes that the Courant number must be less than unity for the stability and have C as close to unity as possible for accuracy.

An issue that has a close comparison to the CFL number for viscous fluid flows is the Peclet number and is discussed in the following section. For the one-dimensional steady state convection-diffusion problem without a source where the grid is given in Figure 2-3 we have:

$$\frac{d}{dx}(\rho u A\phi) = \frac{d}{dx}\left(\Gamma A \frac{d\phi}{dx}\right) \qquad (2.7)$$

$$(\rho uA\phi)_{i+1/2} - (\rho uA\phi)_{i-1/2} = \left(\Gamma A \frac{d\phi}{dx}\right)_{i+1/2} - \left(\Gamma A \frac{d\phi}{dx}\right)_{i-1/2} \quad (2.8)$$

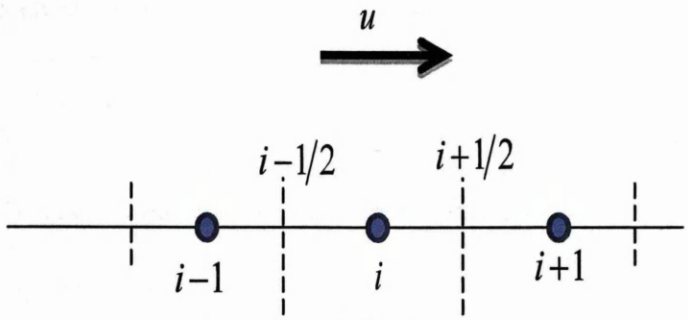

Figure 2-3 Schematic illustration of 1-D grid in which the conservation equation are applied. Circle indicates grid point.

Using central differencing for example gives the following template after re-arrangement.

$$F_{i+1/2}\frac{(\phi_{i+1}+\phi_i)}{2} - F_{i-1/2}\frac{(\phi_{i-1}+\phi_i)}{2} = D_{i+1/2}(\phi_{i+1}-\phi_i) - D_{i-1/2}(\phi_i - \phi_{i-1}) \quad (2.9)$$

For central differencing, the scalar or coefficient of diffusion at the face i+1/2 is evaluated as an average of the two nodal values straddling i+1/2. For this case the nodes are equidistant.

$$\left(\frac{F_{i+1/2}}{2} - D_{i+1/2}\right)\phi_{i+1} + \left(\frac{F_{i+1/2}}{2} + D_{i+1/2} - \frac{F_{i-1/2}}{2} + D_{i-1/2}\right)\phi_i - \left(\frac{F_{i-1/2}}{2} + D_{i-1/2}\right)\phi_{i-1} = 0 \quad (2.10)$$

Where

$$F_{i-1/2} = (\rho u)_{i-1/2} \qquad F_{i+1/2} = (\rho u)_{i+1/2}$$

$$D_{i-1/2} = \frac{\Gamma_{i-1/2}}{\delta x_{i-1,i}} \qquad D_{i+1/2} = \frac{\Gamma_{i+1/2}}{\delta x_{i,i+1}}$$

$$a_i\phi_i = a_{i-1}\phi_{i-1} + a_{i+1}\phi_{i+1} \quad (2.11)$$

where

a_{i-1}	a_{i+1}	a_i
$D_{i-1/2} + \frac{F_{i-1/2}}{2}$	$D_{i+1/2} - \frac{F_{i+1/2}}{2}$	$a_{i+1} + a_{i-1} + (F_{i+1/2} - F_{i-1/2})$

Re-writing (2.11) so the updated value for the conserved variable is ϕ^{n+1} and the previous values for the conserved variables are ϕ^n.

$$\Rightarrow a_i\phi_i^{n+1} = \sum_{j=i-1}^{N=i+1} a_j\phi_j^n \quad (2.12)$$

For a converged solution $\phi^{n+1} = \phi^n$ everywhere therefore (2.12) becomes.

$$a_i = \sum_{j=i-1}^{N=i+1} |a_j| \qquad (2.13)$$

For a bounded solution the left hand side must be greater than the right hand side of (2.13).

$$\Rightarrow a_i \geq \sum_{j=i-1}^{N=i+1} |a_j| \qquad (2.14)$$

Dividing both sides by (a_i) diagonal dominance states that in the absence of sources the internal nodal values of the property ϕ should be bounded by its boundary values. For diagonal dominance, we need large values of net coefficient (a_i).

$$\therefore 1 > \frac{\sum_{1=i-1}^{N=j+1} |a_j|}{a_i} \qquad (2.15)$$

Equation (2.15) is also known as the Scarborough condition which was presented by Scarborough in [76].

In general central schemes become unstable when solving highly convective flows. This manifests itself in a stringent upper limit on the grid size for stable calculations. This is known as the transportiveness property of a numerical scheme. For the unidirectional flow case seen in Figure 2-3, $a_{i+1} = D_{i+1/2} - F_{i+1/2}/2$, given that $F_{i-1/2} > 0$ and $F_{i+1/2} > 0$. Now for a_{i+1} to be positive: then $F_{i+1/2}/D_{i+1/2} < 2$ has to be satisfied.

The second 1-D example in Versteeg & Malalasekera [17] with Pe = 5 shows incorrect and unbounded results, for a simple convection diffusion problem, while cases 1 and 3, where Pe<2, both gave bounded and accurate answers. Therefore Roache [77] stated for the simplest case of central differencing, the cell Peclet number should be less than 2 .

$$Pe = \frac{\rho u}{\Gamma / dx} \leq 2 \qquad (2.16)$$

The non-dimensional cell Peclet number is a measure of the strength of convection relative to diffusion, where dx is the cell width. This is an essential requirement for boundedness, all coefficients of the discretised equations should be positive. Physically this implies that an increase in the variable ϕ at one node should result in an increase in ϕ at neighbouring nodes.

From this generic convection-diffusion equation, we have seen that the numerical difficulties when solving the equation iteratively are far from straightforward. Now we have to keep this in mind when solving physically realistic problems in the field of fluid dynamics.

2.2 Fluid Mechanics

The purpose of this chapter is not to cover the whole area of fluid mechanics but to develop computational methods that solve the equations of fluid motion for the benchmark cases presented later in this thesis.

In obtaining the basic equations of fluid motion, the following philosophy is always followed:

1. Choosing the appropriate fundamental physical principles from the law of physics, for example.
   i. Mass Conservation, for more detail on step 1 review Currie, [78].
   ii. Momentum Conservation.
   iii. Energy Conservation.
2. Apply the physical principle from above to a suitable model of the flow either:
   a. Eulerian description- a finite control volume fixed in space with fluid moving through it
   b. Lagrangian description- a control volume moving with the fluid such that the same fluid particles are always surrounded by the control volume review Gurtin, [14].
3. From this application extract the mathematical equations which embody the physical principles.

The Eulerian description in continuum regime was chosen in 2 for this research. Alternatively for more detail on methods for the Lagrangian method review the literature. The following section deals with step 3 above, namely the extraction of the mathematical equations.

2.3 Conservation Laws

The basic Conservation Laws in Fluid Mechanics can be derived in the Eulerian framework by considering the fluid which passes at time, t, through an infinitesimal fixed control volume with surface, S, in relation to a fixed Cartesian system of a reference. From this, equations in differential form are obtained. For more information on how these equations are extracted from the physical principles review [14], [79], [80]. The equations presented in this section are derived assuming a single-phase, homogenous fluid in which no chemical reactions take place. An indicial notation is adopted ,i,j, with the indices i=x,y,z and j=x,y,z the Einstein summation convention is used [81].

2.3.1 Mass Conservation

Mass is conserved within the control volume resulting in the following partial differential equation i.e. Continuity Equation:

$$\frac{\partial \rho}{\partial t} + \frac{\partial (\rho u_i)}{\partial x_i} = 0 \qquad (2.17)$$

where ρ - density (kg/m^3)
u_i - velocity component (m/s)
$\partial/\partial t$ - temporal derivative
$\partial/\partial x$ - spatial derivative

2.3.2 Momentum Conservation

Within the control volume momentum is conserved and Newton's Second Law results in the following partial differential equation.

$$\frac{\partial (\rho u_i)}{\partial t} + \frac{\partial (\rho u_i u_j)}{\partial x_i} + \frac{\partial P}{\partial x_i} - \frac{\partial \tau_{ij}}{\partial x_i} = 0 \qquad (2.18)$$

where μ - dynamic viscosity (kg/(m s))
P - Pressure (N/m^2)
τ_{ij} - is the viscous stress tensor (N/m^2)

2.3.3 Energy Conservation

Energy is conserved (First Law of Thermodynamics) within the control volume resulting in the following partial differential equation. i.e. the energy equation

$$\frac{\partial(\rho\varepsilon)}{\partial t}+\frac{\partial}{\partial x_i}(\rho u_i\varepsilon)+\frac{\partial(Pu_i)}{\partial x_i}-\frac{\partial}{\partial x_i}\left(k\frac{\partial T}{\partial x_i}\right)-\frac{\partial(u_i\tau_{ij})}{\partial x_i}=0 \qquad (2.19)$$

where k - Coefficient of thermal conductivity (W/(m °K))
C_v - specific heat and constant volume (J/(Kg °K))
T - Temperature (°K)
and the total specific energy, ε, is defined as:

$$\varepsilon = e+\frac{1}{2}u_iu_i \qquad (2.20)$$

where ρe is the internal energy per unit volume (J/(m^3))
and e is the internal energy per unit mass

$$e=\frac{\rho e}{\rho}=\frac{Jm^{-3}}{kgm^{-3}}=\frac{J}{kg}=\frac{Nm}{kg}=\frac{kgms^{-2}m}{kg}$$

$$\Rightarrow e=\frac{m^2}{s^2}$$

$\frac{1}{2}\rho u_iu_i$ is the kinetic energy per unit volume (kg/(m s^2))

To close the system of equations, consider an ideal gas, where no real gas effects or chemical reactions occur, the fundamental gas relationship, derived from kinetic theory [82], relates pressure with density and temperature according to.

$$P=\rho RT \qquad (2.21)$$

where R is called the universal gas constant (J/(Kg °K))

The pressure is calculated from the ideal gas law and the temperature is calculated from equation (2.20) and a constitutive relationship relating temperature to the internal heat per unit mass. Further axioms must be stated to fully define a constitutive equation for a specific material or class of materials.

2.3.4 Constitutive Equations

The conservation laws, the Navier-Stokes equations, described previously, represent a mathematical formulation of the physical principles of conservation and therefore apply to all fluids. To complete the specifications of the mechanical properties of a fluid some additional equations, which are denoted the constitutive equations, are required. It is thereby unlikely that any real fluid will conform exactly to any mathematical model, however they are models which form an excellent approximation to the behaviour of the real fluid. The constitutive equations must satisfy fundamental principles, such as the principle of material-frame independence, the principle of determinism, the principle of local action and also be dimensionally consistent. For more information on these principles review [14], [79], [83].

In fluid mechanics, axioms which allow us to determine the relations between stress and rate of strain, heat flux and temperature are required. The first constitutive relation relating the stress tensor σ_{ij} and the rate of strain tensor ϵ_{ij} can be deduced with the assumption of the following four postulates [79], [80]:

1) The stress tensor is linearly dependent on the deformation-rate tensor ϵ_{kl}. This behaviour is characteristic of a Newtonian viscous fluid and is mathematically expressed by

$$\sigma_{ij} = \mathbf{a}_{ij} + \mathbf{b}_{ijkl}\varepsilon_{kl} \tag{2.22}$$

Where **a**, **b** represent second and fourth-ordered tensors and are independent of the rate of strain components

2) In a fluid at rest, the stress is hydrostatic and the pressure exerted by the fluid is the static pressure. This condition requires that the stress tensor defined in equation (2.22) must have the form

$$\sigma_{ij} = -P\delta_{ij} + \tau_{ij} \tag{2.23}$$

where the shear stress tensor τ_{ij} depends on the motion of the fluid;

3) The shear stresses τ_{ij} will not be effected by rigid body motion of the fluid

4) The fluid is isotropic, i.e. there are no preferred directions for the fluids motion

After all possible simplifications using these assumptions, the constitutive equations for the stress tensor reduces to

$$\sigma_{ij} = -P\delta_{ij} + \lambda\delta_{ij}\varepsilon_{kk} + \mu\varepsilon_{ij} \tag{2.24}$$

where p,$\boldsymbol{\lambda}$ and $\boldsymbol{\mu}$ are independent of ϵ_{ij}. The rate of strain tensor is described in terms of velocity variations according to

$$\varepsilon_{ij} = \frac{\partial u_i}{\partial x_j} + \frac{\partial u_j}{\partial x_i} \tag{2.25}$$

The parameters $\boldsymbol{\lambda}$ and $\boldsymbol{\mu}$ must be determined experimentally and represent the dynamic viscosity and second viscosity coefficients, respectively. These two viscosity coefficients are related through the bulk viscosity χ [19], [80], and for monotonic gases, χ is negligible ($\chi \approx 0$), leading to the requirement that

$$\lambda = -\frac{2}{3}\mu \tag{2.26}$$

Which represents the so-called Stokes relation. In practice, according to Lyra [7] it is found that the model given by equations (2.24) to (2.26), despite the fact that it can be regarded as describing an ideal material, simulates extremely well the mechanical behaviour of many fluids, including air. From equation (2.23) the shear stress tensor becomes.

$$\tau_{ij} = \mu\left(\frac{\partial u_i}{\partial x_j} + \frac{\partial u_j}{\partial x_i}\right) - \frac{2}{3}\mu\frac{\partial u_k}{\partial x_k}\delta_{ij} \tag{2.27}$$

The second constitutive relation involves a relation between the conductive heat-flux , $\dot{\mathbf{q}}_j$, and the temperature gradients. A simple, but accurate, constitutive equation is given by Fourier's law for heat transfer by conduction, which can be expressed as

$$\dot{\mathbf{q}}_j = -k\frac{\partial T}{\partial x_j} \tag{2.28}$$

Where $k = k(T)$ is referred to as the thermal conductivity of the medium, and T is the temperature. For heat conduction to a solid wall the following expression is employed.

$$\dot{\mathbf{q}}_w = \left(-k\frac{\partial T}{\partial n_j}\right) \text{ at } \Gamma_w \tag{2.29}$$

where $n_j = [n_x, n_y, n_y]$ denotes the direction normal to the wall and where Γ_w denotes the wall boundary location.

2.4 The Gas Equations

When the application of the governing laws involves flow speeds comparable or in excess of the speed of sound, this is generally accompanied by large pressure gradients leading to substantial changes in density. This is what is meant by compressibility effects [84]. These effects are of practical importance for aerodynamics application. Let us consider the governing laws for fluid flow without body forces and without external or internal heat sources as described by equation (2.17) to equation (2.21) . In order to close the system of equations it is necessary to set up the relations between the thermodynamic variables through the state equations and to relate the coefficients of viscosity and the thermal conductivity k to the thermodynamics variables.

It is convenient to introduce the thermodynamic variable called the enthalpy h, which is defined as

$$h = e + \frac{p}{\rho} \tag{2.30}$$

Where e is the specific internal energy.

Assuming further that the gas is calorifically perfect, where the specific internal energy e and the enthalpy h are functions of temperature alone and the specific heats are constant, then.

$$e = C_V T$$
$$h = C_p T \tag{2.31}$$

$$\gamma = C_p / C_V$$
$$C_V = R/(\gamma - 1) \tag{2.32}$$

where C_p and C_v are the specific heats of the fluid at constant pressure and at constant volume respectively.

To obtain the temperature from the Enthalpy equation by employing (2.31) we re-arrange (2.20) and get.

$$T = \frac{1}{C_V}\left(\rho\varepsilon - \rho\frac{1}{2}u_i u_i\right) \tag{2.33}$$

Sutherland's experimental law relates the dynamic coefficient of viscosity μ, to the temperature accordingly

$$\mu_i = \mu_\infty \left(\frac{T_i}{T_\infty}\right)^{3/2} \frac{T_\infty + S_0}{T_i + S_0} \tag{2.34}$$

where μ_i has the units (kg/(m s)) and the subscript ∞ denotes the free-stream values and S_0 is a constant for a given gas [18]. The coefficient of thermal conductivity can be related to the coefficient of viscosity through the dimensionless quantity

$$\mathrm{Pr} = \frac{\mu_i C_P}{k_i} \tag{2.35}$$

This is known as the Prandtl number, which is assumed constant for ideal gases at moderate temperature [82]. For an isentropic process, i.e. adiabatic reversible process in a perfect gas , the speed of sound c is given by [82].

$$c^2 = \left(\frac{\partial P}{\partial \rho}\right)_s = \frac{\gamma P}{\rho} = RT\gamma \tag{2.36}$$

where s is the entropy and c represents the speed at which the small disturbances (waves) are propagated through a compressible fluid. The effects of compressibility in a moving fluid can then be analysed, by the value of the dimensionless parameter.

$$M = \frac{(u_i u_i)^{1/2}}{c} \tag{2.37}$$

which is called the Mach number, and its variation significantly alters the characteristic of the flow. Finally, another important dimensionless relation is given by the Reynolds number.

$$\mathrm{Re} = \frac{\rho |\mathbf{u}| L}{\mu} \tag{2.38}$$

where L is the characteristic length of the problem, such as the length of an aerofoil, and $|\mathbf{u}|$ is the modulus of the velocity. The Reynolds number represents the ratio of the inertial terms and the viscous terms, with the flow remaining laminar up to a certain critical value of the Reynolds number and above this value the flow becomes turbulent.

In applications associated with Hypersonic flows, where temperatures can be extremely high, the perfect gas assumption of a gas, meaning no chemical reactions and the calorically perfect assumption, no longer applies. Furthermore the assumption of constant Prandtl number and Sutherland's law do not hold either. In this regime, more complex state equations and relations with the transport coefficients have to be adopted [85], [86].

2.5 The Navier-Stokes Equations

The Navier-Stokes equations describe combined viscous-convection flow problems which are non-linear, multidimensional and at larger Reynolds numbers solutions contain turbulent flow structures. To model them numerically requires a considerable amount of effort to capture the localised physics and alleviate the numerical instabilities. The last two decades have seen a marked progress in creating "Navier-Stokes numerical solvers'' but three dimensional complex geometry flows currently remains a challenge The Navier-Stokes equations are obtained by simultaneously taking the Euler equations and augment with the 2nd order diffusion terms. The 2nd order diffusion terms have the effect of distributing the physical properties, velocity and temperature, along gradients in all directions. The Navier-Stokes equations may be summarised as follows as presented in [17], [18], [80]:

$$\frac{\partial \mathbf{U}}{\partial t} + \frac{\partial \mathbf{F}^j}{\partial x_j} = \frac{\partial \mathbf{G}^j}{\partial x_j} \quad \text{for } i=1,\ldots N_d \tag{2.39}$$

where N_d indicates the number of spatial dimensions to be considered in each problem, **U** represents the vector of conservative variables and F and G are the relevant inviscid flux and the viscous flux terms, respectively. Taking the two dimensional counterpart of equation (2.39) these vectors can be written as:

$$\mathbf{U} = \begin{bmatrix} \rho \\ \rho u_1 \\ \rho u_2 \\ \rho \varepsilon \end{bmatrix} \mathbf{F}^j = \begin{bmatrix} \rho u_j \\ \rho u_1 u_j + P\delta_{1j} \\ \rho u_2 u_j + P\delta_{2j} \\ (\rho \varepsilon + P) u_j \end{bmatrix} \mathbf{G}^j = \begin{bmatrix} 0 \\ \tau_{1j} \\ \tau_{2j} \\ \tau_{ij} u_i - q_j \end{bmatrix} \tag{2.40}$$

where ρ - density(kg/ m^3)
P - Static pressure(N/m^2)
u_1 - velocity component in x direction (m/ s)
u_2 - velocity component in y direction (m/ s)

ε- Specific total energy per unit mass (J/ (Kg))
and the Kronecker delta term is determined by.

$$\delta_{ij} = \begin{cases} 0 & i \neq j \\ 1 \mapsto & i = j \end{cases} \tag{2.41}$$

and finally τ_{ji} and q_i are defined by the two constitutive equations (2.27) and (2.28).

These equations are valid for any Newtonian compressible fluid and can also be used to deduce the particular equations for different dynamic levels of approximation analysed in this thesis.

2.6 The Euler Equations

The Euler equations describe flows where diffusion of any kind whether viscosity or thermal conduction are ignored. These flows are non-linear and multidimensional. Since the dissipation terms in the momentum and enthalpy equations are neglected the Euler equations are an approximation of the physical reality. However interest in solving the Euler equations from the 1960s onwards in the aerospace sector began for applications where viscous interactions can be assumed to be negligible, meaning the inviscid assumption leads to good approximations for the pressure field for non-separated flows [84], [87]. Because according to Prandtl's boundary layer analysis, flow at high Reynolds numbers with no separation, confines the viscous effects to very narrow regions close to the walls [86]. Outside these layers the flow behaves as inviscid. The inviscid approach is motivated by the advantages with regards to the reduced requirements for the computational task at hand when compared to those for the viscous model. Examples include the large regions of flow over wings and bodies outside the thin boundary layer, flow through rocket engine nozzles and the flow over compressor and turbine blades for jet engines. Surface pressure distributions, as well as aerodynamic lift and moments on some bodies can be accurately predicted by means of the assumptions of inviscid flow. These examples include flow over a 2D wedge [84] and the transonic flow over a NACA aerofoil [88] . The Euler equations may be summarised as seen in the work [17], [18], [80], [84].

$$\frac{\partial \mathbf{U}}{\partial t} + \frac{\partial \mathbf{F}^j}{\partial x_j} = 0 \quad \text{for i=1,...N}_\text{d} \tag{2.42}$$

$$\mathbf{U} = \begin{bmatrix} \rho \\ \rho u_1 \\ \rho u_2 \\ \rho \varepsilon \end{bmatrix} \quad \mathbf{F}^j = \begin{bmatrix} \rho u_j \\ \rho u_1 u_j + P\delta_{1j} \\ \rho u_2 u_j + P\delta_{2j} \\ (\rho \varepsilon + P) u_j \end{bmatrix} \tag{2.43}$$

where the physical quantities are the same for the Navier-Stokes formulation (2.40). Additional information is required for well posed problems before the numerical code can be run for the catalogue of benchmarks. This additional information includes physical constants such as the gas constants as well initial conditions and the boundary values. These are dealt with in detail in the next section.

2.7 Initial and Boundary Conditions

The progress of a solution to all categories of PDEs depends on the initial and boundary conditions. The initial conditions are specified throughout the computational domain. For external flow applications in aerodynamic applications these values are taken as the free-stream values. In practical CFD calculations there are two important criteria for the selection of initial conditions: Firstly efficiency in generating results, the closer the initial conditions are to the final answer, the faster the

time marching procedure will converge and secondly and most importantly, enhancing the stability of the calculations. If the initial conditions are too far from the analytical results, the initial time wise gradients will be very large potentially causing instability.

Once we have the initial conditions and governing flow equations as described in section 3.4 and 3.5, then the driver for any particular solution are the physical boundary conditions. This has a particular importance in CFD as stated by Anderson [15] any numerical solution of the governing flow equations must be structured so as to see a strong numerical representation of the physical boundaries.

As mentioned by Lyra [7] the Navier-Stokes equations, represents a hybrid system, being Parabolic-Hyperbolic in time and space, but becoming Elliptic-Hyperbolic in space for steady state problems. No general mathematical theorems concerning the proper boundary conditions are available that ensures existence and uniqueness of the solution, [89], [90]. In this way the approach normally adopted consists of the physical analysis of the problems to provide a guideline for the choice of number and type of boundary conditions, followed by a posterior numerical validation.

In practical applications, the solution of a system of PDEs is realized in an enclosed limited domain where physical and artificial boundary conditions must be imposed to produce a realistic solution. In general, the boundaries can be grouped into two, either solid body surfaces, or free surfaces, such as far-field boundaries in external flows. First let us review the proper physical boundary conditions for viscous flow. At a solid body surface experimentally no relative velocity between the fluid and a solid boundary at the interface is observed.[5] Since the no slip condition is assumed to hold it can be stated as:

$$u_1 = u_2 = u_3 = 0 \text{ at } \Gamma_w \tag{2.44}$$

where Γ_w denotes the wall boundary location. In addition to (2.44), there is an analogous "no-slip" condition associated with the temperature at the surface i.e. an isothermal wall. The temperature of the surface material is denoted by T_w, hence the temperature of the fluid layer immediately in contact with the surface is also T_w, hence:

$$T = T_w \text{ at } \Gamma_w \tag{2.45}$$

On the other hand, if the wall temperature is not known, or if it is changing as a function of time due to aerodynamic heating to the surface, then the Fourier law of heat conduction provides the boundary condition at the surface. The Fourier law, if we let $\dot{\mathbf{q}}_w$ denote the instantaneous wall heat flux is given previously in (2.29). For this case, the surface material is responding to the heat transfer to the wall, $\dot{\mathbf{q}}_w$, hence changing T_w, which then affects $\dot{\mathbf{q}}_w$ resulting in an unsteady coupling between $\dot{\mathbf{q}}_w$ and T_w. This, unsteady heat transfer problem must be solved by treating the viscous flow and the thermal response of the surface material simultaneously. This type of boundary condition, as far as the flow is concerned, is a temperature gradient at the wall, in contrast to stipulating the wall temperature itself as the boundary condition. That is, from (2.29) the temperature conduction at the wall is:

$$\left(\frac{\partial T}{\partial n_j}\right)_w = -\frac{\dot{\mathbf{q}}_w}{k} \text{ at } \Gamma_w \tag{2.46}$$

where k is the thermal conductivity (W/(mK))

Γ_w denotes the wall boundary location n_j is the vector normal to the wall

When the wall temperature becomes such that there is approximately zero heat transfer to the wall surface, the resulting wall temperature is the adiabatic wall temperature T_{aw}. This condition comes

[5] On a microscopic level slippage is possible [78], but this is out of the domain of continuum mechanics.

from (2.46) with $\dot{\mathbf{q}}_w = 0$. Hence, for an adiabatic wall, equation (2.46) reduces to $\left(\partial T/\partial n_j\right)_w = 0$ at Γ_w . Then the mathematical challenge is the calculation of the the adiabatic wall temperature T_{aw}, that satisfies $\dot{\mathbf{q}}_w = 0$.

The most common wall boundary condition is, an isothermal wall, where T_w is constant irrespective of the temperature of the flow. The next most popular is the adiabatic wall, where T_{aw} falls out of the numerical solution when $\left(\partial T/\partial n_j\right)_w = 0$. For the more complicated case as seen in equation (2.46), where the coupled simultaneous relationship between the flow field with the thermal response of the surface material, k, through an additional physical relationship is by far the most difficult to set up mathematically.

For inviscid flow there is no viscosity to promote it sticking to the surface. Hence, the flow velocity at the wall is a finite value. Moreover, for a non-porous wall, there is no mass flow into or out of the domain through the wall; this means that the velocity vector immediately adjacent to the wall must be at a tangent to the wall. If n_j is a unit vector on the surface and is perpendicular to the wall, the wall boundary condition can be given as.

$$u_j \bullet n_j = 0 \text{ at } \Gamma_w \qquad (2.47)$$

Equation (2.47) is a statement that the velocity component perpendicular to the wall is zero; for example the flow at the surface is tangent to the wall. This is the only surface boundary condition for an inviscid flow. The magnitude of the velocity as well as the values of the fluid temperature, pressure and density of the wall, falls out as part of the solution.

As stated above the only physical boundary conditions along a wall for a viscous flow problem are the no slip condition associated with the temperature and velocity. The pressure and density at the wall fall out as part of the solution according to [15].

It should be noted that the simplified cases represented by the Euler equations or the heat conduction equation are mathematically fully determined. These boundary conditions when used to solve the Navier-Stokes equations have to be compatible with the simplified cases, otherwise, non-physical behaviour may appear in the solution [87]. Furthermore, since the benchmark problems considered in the work each have a distinct mathematical nature, the adopted boundary conditions for each specific case will be presented in detail when dealing with each problem.

When defining the free surface boundary conditions, it is also useful to distinguish between internal and external flows. For external flow computations, a possible approach provided that the far field boundary is placed far from the body, so that viscous effects can be assumed to be negligible. For internal flows the approach is to determine the boundary conditions through the analysis of the incoming and outgoing characteristics [87]. A detailed discussion about this essential subject can be found in [87], [89], [91], [92].

The complexity and importance of the boundary condition theme cannot be underestimated, and one has to be aware of the influence of the selected boundary conditions on the final stability, convergence rate and accuracy of the numerical solution. Finally it should be noted in the solution of partial differential equations it is sometimes easy to attempt a solution using incorrect boundary and initial conditions. Whether the solution is being attempted analytically or numerically, such an "ill posed problem" will lead to spurious oscillations at best and no solution at worst [15].

A well posed problem is defined as follows: if the solution to a partial differential equation exists and it is unique and if the solution depends continuously on the initial and boundary conditions then the problem is "well-posed". It is important to establish that a CFD problem is well posed before carrying out a solution.

2.8 Further Considerations

A summary of the issues concerning the difficulties faced, when designing a computational procedure in CFD are now discussed.

A lack of mathematical foundations establishing consistency, stability and convergence for non-linear problems according to Lyra [7], leaves only the well based linear theory to give necessary, but not completely sufficient conditions on the behavior of the chosen numerical scheme. It is also far from an easy task to establish the degree to which the boundary conditions are "well-posed", especially for systems of partial differential equations of mixed nature, where there is no general mathematical theorem to guarantee existence of a solution [7]. In general, an under-prescription of boundary conditions leads to non-uniqueness and an over prescription leads to unphysical solutions in the proximity of the boundary layer according to Fletcher [93]. There are also some occasions where multiple physically meaningful solutions may be possible and the "well posed" concept fails. An example of this, according to Fletcher [93], is when flow undergoes transition from laminar to turbulent motion.

When solutions to a Hyperbolic equations are considered another mathematical difficulty arises from the appearance of discontinuities. The fact that the CFD solutions to the Euler system of equations allow spurious solutions is in general a result of ignoring some physical effects in the determination of the model[6]. Although viscous effects may be negligible throughout most of the flow, near discontinuities the effect is always strong, and the apparent discontinuities are in reality thin regions with very steep gradients. Some conditions must be imposed in order to pick up the correct physical solution and to guarantee uniqueness [18], [73]. In fluid dynamics the second law of thermodynamics, which states that the entropy should increase, is invoked, and turns out to be a sufficient condition to determine a physically correct and unique solution. This consideration is normally referred as the entropy condition [18].

[6] the viscous effects have been neglected

3. LITERATURE REVIEW FOR CFD TECHNIQUES

3.1 Introduction

This chapter is the second part of the literature review. It is intended to be an overview for the numerical techniques currently available in Computational Fluid Dynamics (CFD). The reason for breaking the literature review into two chapters, is that it was deemed important for presentation purposes to establish a line of reasoning that is inferred going from the numerous numerical techniques employed to the final candidate scheme, in this thesis. That scheme finally attempts to tackle the research problem referred to in Chapter 1 Section 1.1.

Partial differential equations (PDE) are at the heart of many simulations of physical systems of engineering interest, such as fluid dynamics, heat conduction and, solid mechanics. As a result, a broad class of methods has been developed to solve PDE, such as separation of variables, integral transforms and numerical methods. All of these have their own importance and achievements in the solution of PDE, but none of them is as flexible and general as numerical methods, which allow complex geometry configurations, non-linearities and a number of coupled systems of partial differential equations to be tackled [7].

Modern CFD is awash with different numerical methods – some old, some new, some quite simple and straight forward, and some very sophisticated and elaborate [15]. They all possess strengths and weaknesses. A particular numerical method will not be appropriate for all problems, because the diverse mathematical nature of PDE means that some schemes will be effective for elliptic equations while the same scheme may not be suited to Hyperbolic problems [16].

3.2 Continuity Solvers

Numerical CFD methods pre 1980 were initially divided into two major classes; "pressure-based" methods originally devised for solving incompressible flows with primitive variables such as SIMPLE scheme by Spalding & Patankar, [32] and "density-based" methods as developed by Chorin [94], which was formulated to solve the compressible flow equations for gas dynamic applications. This part of the literature review will briefly review both approaches.

3.2.1 Pressure Based Schemes

The origins of most pressure based CFD methods lie in the Semi-Implicit Method for Pressure Linked Equations (SIMPLE) scheme by Spalding & Patankar, [32]. A thorough description of SIMPLE is given in Versteeg & Malalasekera, [16], and a discussion can also be found in the appendices of this thesis. In its basic form for solving pressure and velocity this algorithm is applicable to incompressible constant density flows. The coupling between pressure and velocity is done by interpreting the mass conservation equation as a constraint equation for the pressure, leading to a guess and correct algorithm for establishing the pressure field. For this reason these schemes are often denoted as pressure-correction methods [16].

It must be noted that the pressure based schemes make theoretical assumptions that allow a solution to a flow problem to be attempted. When the free-stream speed becomes compressible (Mach>0.3)

these assumptions need to be re-assessed, i.e. such as dρ/dp being assumed to be negligible. Which has consequences for applying the pressure based schemes.

3.2.2 Density Based Schemes

The density based formulation is more suited to compressible flows than the pressure based schemes, because it solves the conservation variables (ρu, ρE or ρv) at the cell centres and then closes the system of equations, with the perfect gas law. For compressible flow problems this has resulted in a robust, accurate and versatile procedure as described in [15], [35], [95]. However, density based schemes (DBS) for incompressible problems are problematic, as density will be constant throughout the flow domain. A fix or relationship is needed to couple the pressure and velocity, and this can be done in a number of ways. The main route for this is the standard scheme.

The industrial sponsor wants a solver applicable to all flow regimes from incompressible Subsonic flow through to Hypersonic highly compressible flow, and this caused the author to look at strategies to capture incompressible flows when using the density based schemes. It was concluded that the DBS provided the best scheme of the two because it can be easily extendable to compressible flows later on in the research program Malan, Lewis, and Nithiarasu [96].

3.3 Methods for Resolving the Convection Term

The co-located discretisation of the governing equations assumes that the density, velocity and enthalpy field has been resolved at control volume centres. Then the transported property, whether it be ρu, ρE or ρv for shorthand, one replaces with ϕ. These transported properties are all estimated on the control volume faces. Methods employed to do this are discussed in the following section. The relative strength and weaknesses of each of the following methods such as- central differencing, simple 1st order upwind, 2nd order upwind and hybrid differencing of the convection terms will be outlined. As will be discussed in the following sections the type of differencing used will often be more suited to solving a certain types of problem over others.

3.3.1 Central Differencing Schemes

The cell-centred central differencing approach is a two point scheme which employs a linear fit of values in the elements on either side of the face under inspection. In discretising the convection terms ϕ over a control volume, only surrounding nodal values of ϕ appear in the system matrix, because the contributions at control volume i, will cancel out. The system matrix will possess diagonal coefficients of zero, meaning, therefore no steady state solution is established for convection only problems with no diffusion, using iterative solution methods. However since diffusion always occurs alongside convection in nature, the problem of zero leading coefficients is overcome by coupling convection with diffusion terms, providing diffusion is of the same order as the convection term. This method produces stable and accurate solutions when the strength of convection relative to diffusion is low. However for cases when convection dominates the neighbouring coefficients can become negative. For example Patankar, [36], noted that in this instance the boundedness criteria is violated and the solution fails to converge, producing physically unrealistic oscillating results.

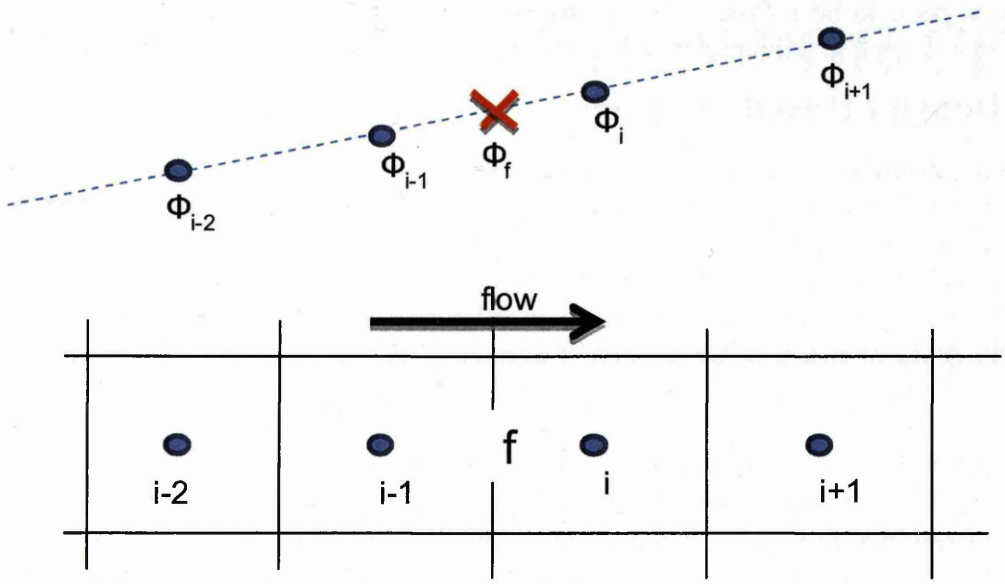

Figure 3-1-Depication of central differencing for a scalar field ϕ.

Central differencing schemes, such as, Hughes's, [97], Sub Grid Scale methods (SGS) and MacCormack's predictor-corrector scheme, [29], are easy to understand, however, they will not always track the proper flow of information throughout the flow field. The numerical scheme can draw information from outside the node's domain of dependence, as discussed in Versteeg & Malalasekera [16]. This compromises the accuracy of the final solution. Flow fields that involve low convection speeds, otherwise known as low Peclet number, do not appear to cause solution instability. Because of this, central difference schemes work suitably well for solving elliptic and Parabolic equations. Parabolic problems include the Coeutte flow between non-porous boundaries or shock free compressible solutions through a de Laval nozzle as seen, for example, in Anderson [15]. Courant, Isaacon, and Rees, [75], noted that central difference schemes become unstable when solving highly convective flows. This manifests itself in a stringent upper limit (CFL limit) on the grid size and time step for stability when solving certain partial differential equations (usually Hyperbolic PDEs) numerically by central differencing. The main challenge occurs when discontinuities exist in the flow for Hyperbolic problems, meaning a central differencing schemes will not effectively capture the shock or discontinuity. For example, it is possible to see in the research of Kuruvila, [98], the undesirable severe oscillations around the shock wave when a central differencing finite differencing scheme has been used. Even with the addition of artificial viscosity the results shown in Kuruvila, [98], exhibit oscillations albeit much smaller than those results garnered with no artificial viscosity.

3.3.2 Upwind Differencing Schemes

Upwind differencing schemes in contrast to central differencing methods are designed to factor the directionality of the flow into the calculations. Using an upwind formulation the direction of flow is ascertained on each cell face. This means the value on the face is taken as the upstream control volume value. Upwind methods a system of equations containing non-zero leading coefficients, giving stable and converging solutions for both convection-diffusion problems, and, convection only problems. Unfortunately the upwind discretisation however, as stated by Raithby, [99], is only first order accurate which makes it prone to numerical diffusion. The diffusive nature of first order schemes means that they cannot be used to produce accurate results with affordable mesh spacing for real scientific problems. As seen in Versteeg & Malalasekera, [16], is that first ordered upwind methods, are also highly diffusive when the flow is not aligned with the grid lines.

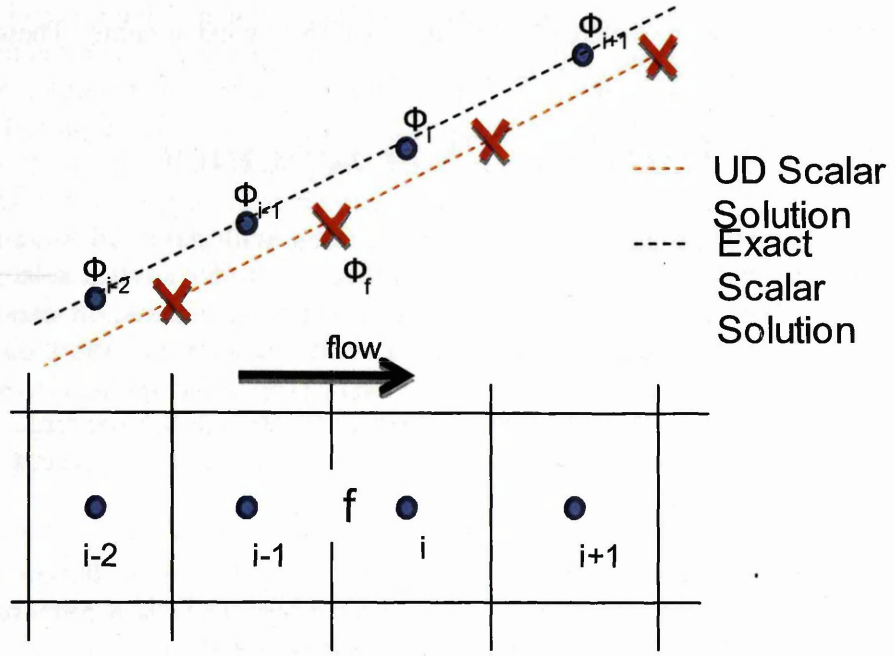

Figure 3-2-**Depication of upwind differencing for a scalar field ϕ .**

For discontinuous solutions, the central differencing schemes, which have second order accuracy, lead to spurious oscillations, as seen in the work of Spalding & Patankar, [32]. The use of upwinding, however, ensures that the schemes are very stable, yet, the first order accuracy of these schemes makes them prone to numerical diffusion errors. This can be remedied at a penalty of complexity by either employing hybrid differencing or higher order upwind schemes.

3.3.3 Hybrid Differencing

Spalding [100] developed the hybrid-differencing scheme for finite-difference formulations, which is based on a combination of central and upwind differencing schemes. It is applied here using a combination of linear shape function interpolation and upwind formulations. The hybrid formulation exploits the beneficial aspects of both upwind and central differencing methods.

The hybrid scheme has become the default differencing scheme in many CFD codes due to its stability and robustness. It gives good approximations to exact solutions when the flow aligns closely with the grid lines and the sources are small. Numerical accuracy is degraded due to the introduction of numerical diffusion whenever flow stream lines are at an angle to grid lines. Solutions can also suffer from a jump at points where the local Peclet number, $|Pe| = 2$ which is due to the suppression of physical diffusion.

3.3.4 Classical Higher Order Upwind Schemes

Classical higher order upwind (HOU) schemes involve more neighbour points and reduce the discretisation errors by bringing in a wider stencil with more information. One of the oldest higher order schemes is Leonard's, [101], Quadratic Upwind differencing scheme (QUICK). The drawbacks of QUICK is that it is not suited for unstructured grids as presented by Cross et al, [3], and is therefore not bounded by the boundary values and requires more bandwidth than CDM when solving in parallel. Versteeg and Malalasekera, [17], argues that in addition to these problems QUICK schemes are plagued by undershoots and overshoots around discontinuities. Advanced second ordered accurate spatial upwind methods have been designed to eliminate this undesirable property

while at the same time retaining the inherent advantages of an upwind scheme. These methods are termed Total Variation Diminishing (TVD) schemes.

3.4 2nd Ordered Upwind TVD schemes

The fact that central differencing and hybrid schemes, even with artificial viscosity can give undershoots and overshoots, has led to the development of second order upwind schemes that avoid these numerical problems [20]. The idea for any higher order upwind scheme, classical or advanced, is to produce high resolution methods by modifying upwind methods to cure their deficiencies. Initially von-Neumann & Richtmyer, [102], introduced the concept of artificial viscosity. This was also suggested by Lax & Wendroff, [28], who further developed this concept. The idea of introducing the artificial viscosity which resembles the physical viscosity, represents a conceptual breakthrough towards the development of high resolution schemes.

Another class of schemes has been specially formulated to achieve oscillation-free solutions otherwise known as Total Variation Diminishing (TVD) schemes. TVD is a property used in the discretisation of the time-dependent fluid dynamic governing equations.

The tendency towards oscillations is counteracted by adding an artificial diffusion fragment. In the literature see [103] early schemes based on these ideas were called flux corrected transport schemes. However concerns persisted on the computational efficiency and the complexity in implementing these schemes, which can be crucial when dealing with a large set of equations, such as modelling turbulent or non-equilibrium flows. Thus, there still remains a need for maximising accuracy, efficiency and robustness for a wide variety of problems. The search for the most functional and accurate numerical scheme continues to be the research of Quirk [104].

3.4.1 Classical Shock-Capturing Schemes

The diffusive nature of the 1st order upwind schemes means that they cannot be used to produce accurate results, with affordable mesh spacing, for all problems, and the use of higher-order schemes leads to spurious oscillations in the results when solving shocks. The idea for classical shock capturing is to produce high-resolution methods without the deficiencies, i.e. spurious oscillations around shocks. To achieve this, von-Neumann & Richtmyer, [102], introduced the concept of artificial viscosity, which was further developed by Lax & Wendroff, [28]. This idea of introducing an artificial dissipation, which resembles the physical viscosity, represented a conceptual breakthrough in the development of high resolution schemes. In classical schemes, such numerical dissipation terms are linear so that the same amount of diffusion is applied to all grid points, or contain empirically adjustable parameters [86]. As a consequence, classical shock capturing schemes can only address problems with smooth or weak shock solutions. This is an important point and needs to be kept at the forefront of the readers mind. As mentioned by Lyra, [7], most numerical schemes and the limiters employed are frequently problem dependent, which makes their use difficult for applications for which the analyst has no previous knowledge.

3.4.2 Advanced Shock-Capturing schemes

Advanced shock capturing schemes utilize more elaborate non-linear devices, than classical shock capturing. Whether this is artificial viscosity or limiters, it allows an adaptive control of the numerical dissipation which is added to stabilize the solution. These advanced shock capturing methods can be generically classified as advanced artificial viscosity, algebraic or geometric schemes. Methods of the first type rely on the explicit addition of an artificial dissipation consisting of a blend of fourth and second - order terms, which are activated non-linearly by the use of a switch that is normally based

upon pressure [105]. Such schemes have been extensively applied, with significant success, to Trans-Sonic flow simulations. Importantly for this research, with certain modifications, initially suggested by Turkel [106], success for Supersonic and Hypersonic applications has been reported [107], [108]. The division into algebraic and geometrical approaches was originally suggested by Goodman and Le-Veque, [110], and refers to the method used to compute the interface fluxes. In both approaches, the incorporation of concepts from the theory of characteristics plays a major role. For a theory of characteristics review Hirsch, [18] . When comparing the classical and advanced shock capturing approach, the main difference is the implicit inclusion of the numerical diffusion in the discrete equation, resulting in the elimination, or the reduction, in the number of free parameters needed to be tuned. These algebraic schemes fall into a number of sub categories including flux vector splitting, flux difference splitting and a hybrid of the two called flux splitting. The strategy behind these higher order upwind schemes i.e. flux vector splitting and flux difference splitting, is splitting the convection terms into two parts.

Flux vector splitting has a positive and a negative part to the convective flux depending on the local Mach speed. The local Mach speed determines the weighting of these two parts to the final convection flux, which can be seen in van Leer, [111]. Flux difference splitting such as the splitting, seen in [95], has been shown to be one of the most accurate explicit techniques available today. However, Liou and Steffen, [112], noted this accuracy, comes at a huge setup cost where differentiation of the Jacobian matrix is required to linearise the implicit scheme to yield a tractable explicit scheme. The setup cost of this method, as Quirk [104], describes, requires the order of n^2 operations per grid point for each iteration - where n is the number of equations - 4 for 2D Euler equations. Quirk also adds a catalogue of situations where the Flux Vector Splitting (FVS) Riemann solvers are deficient, serving to increase the awareness of the CFD community to their limitations. Ensuring the positivity property for scalars, which is critical for calculating chemical species or rarefaction flows, is not necessarily guaranteed by these upwind schemes. These situations as stated by Quirk [104], include the inaccurate viscous layer solutions by the FVS and the so called "carbuncle shock" by the Flux Difference Solvers (FDS). Both the Flux Vector Splitting (FVS) and Flux Difference Solvers (FDS) schemes address the convection and pressure fluxes but do not treat the viscous and thermal conduction terms in an upwind manner [113]. The comprehensive work of Yee, [86], is highly recommended. This presents a large class of high resolution explicit and implicit shock capturing methods with applications to steady state and transient, perfect gases, equilibrium real gases and non-equilibrium flows.

These TVD upwind schemes have undoubtedly become the main spatial discretization technique adopted in codes targeted at Hypersonic flows [10], [114]–[116]. Yet, dissatisfaction with existing schemes exists in many situations, as they may lack robustness, accuracy, or efficiency. Since difficulties appear in the simplest of problems, their implications should deserve some serious attention insofar as developing better alternative methods. TVD upwind methods have been tested, developed and validated in 1D and then implemented for structured 2D grids. This has allowed the progress of the TVD schemes to go relatively unchecked because they have not been widely applied to Hypersonic vehicles with curved surfaces where unstructured grids are far easier to apply.

3.4.3 Characteristics of Hyperbolic Solutions

Before detailing the broad number of Hypersonic research papers where construction of high-order shock capturing methods is needed, some very useful and required concepts must be introduced. These concepts are indeed properties of the true solution to scalar conservation laws which means that it is reasonable to impose them on the numerical solution as well. Phenomena which are Hyperbolic in character or are governed by systems of Hyperbolic partial differential equations (such as the Euler equations), have limited or no physical dissipation. In such cases the solution is

characterized by the propagation of waves with little or no loss in amplitude. Recently the construction of effective numerical schemes for such problems relies on concepts such as monotonicity, monotonicity preserving methods, Total variation diminishing (TVD), local extremum diminishing (LED), total variation bounded (TVB) and essentially non-oscillatory (ENO) methods.

These concepts are based upon non-oscillatory properties of the true solution to a scalar conservation law, and it is reasonable that they may be imposed upon the numerical solution to a full system of equations. Comprehensive definitions of these concepts may be found in the research by Hirsch [87]. A converged numerical solution obtained with a conservative high-resolution scheme is expected to be physically correct, provided that the first order scheme as mentioned by Sweby [117] is employed in its construction and satisfies the entropy condition. It must be noted that none of these properties alone, with the exception of monotonicity, ensures that the entropy condition is satisfied. In addition, a general trend which is encountered when the scheme moves from monotone towards non-oscillatory is that higher-order accuracy is achieved at the expense of introducing a larger stencil of points, more complexity, less versatility and less flexibility in the computational implementation. These features, connected with memory and CPU requirements, should be carefully considered if a fair comparison is to be made between the different classes of methods [50].

3.5 Recent Hypersonic Research (2004-2010)

Several advanced shock capturing studies have been reviewed including central differencing methods with switched artificial viscosity, flux vector splitting and flux difference splitting methods. The order of the Hypersonic research papers are in chronological order to give a flavour of where the research community are now focusing their attention:

3.5.1 Zoby and Thompson [118]

In 2004, Zoby and Thompson, conducted a two pronged approach to modelling a Hypersonic CAVs configuration, otherwise known as a Waverider. The Euler equations were solved over the CAVs configuration using an solver known as Langley Aerothermodynamic Upwind Relaxation Algorithm (LAURA) devised by Olynick et al [119]. This was then followed with a boundary layer solver where the thermal field was computed using the results of LAURA. One of the purposes of this PhD project is to compute the thermal and flow field in a coupled fashion, rather than employing two separate solvers, circumnavigating much complexity in code writing.

3.5.2 Greenshields et al, [120]

Greenshields et al, [120], develops and discusses the implementation of a CFD tool for the simulation of high speed flows. It comprised a finite volume (FV) discretisation, using a non-staggered central scheme for co-located variables prescribed on a mesh of polyhedral cells that can possess an arbitrary number of faces. Greenshields et al, [120], describes the scheme in detail, and in particular explaining the choice of variables whose face interpolation was limited. The solution of the momentum and the energy transport equations - in the Navier Stokes equations - used an operator splitting approach; first of all an explicit predictor equation for the convection of conserved variables is solved, and then an implicit corrector equation is utilized for the diffusion of primitive variables. The solver was validated against four sets of data; (1) an analytical solution of the one dimensional shock tube case; (2) a numerical solution of two dimensional, transient, Supersonic flow over a forward facing step; (3) interferogram density measurements of a Supersonic jet from a circular nozzle; (4) pressure and heat transfer measurements in a Hypersonic flow over a 25°-55 biconic. The results indicated that the employed central-upwind scheme developed by Kurganov et al, [121], is competitive with the best methods published such as piecewise Parabolic methods coined by Collella

& Woodward , [122], and the Roe solver with van Leer limiting methods [30], and that it is inherently simple and well suited to a co-located, polyhedral FV framework.

The KNP method offers clear improvements in accuracy over its predecessor the Kurganov and Tadmor method [123]. Greenshields recommended as best practice to interpolate only ρ, u and T in the f+ and f- directions using the van Leer limiter, and derive other face interpolated scalars from these 3 primitive variable fields. For more details review Greenshields et al, [120].

3.5.3 Cheuret and Steelant [124]

For this study the Supersonic combustion experimental facility (ITLR) in ESTEC was used to investigate the transpiration cooling efficiency of carbon/carbide (C/C) porous materials. The tested sample had a porosity of 16.1% i.e. ε=16.1% and was exposed to Supersonic M=2.1 flow conditions at moderate total temperature levels of 450K for the main flow. The surface temperatures of the C/C material were measured with thermocouples and infrared thermography.

This experimental data was used to validate the user- subroutines within ESA modified commercial CFD code CFD-ACE+ for accurately computing the scientific phenomena of transpiration cooling mechanisms within porous materials. These modified sub-routines were based on the work by Cheuret et al. [116]. The method followed a strongly coupled approach and accounts also for the mass and momentum transport in the porous medium. The discretisation scheme in the user-subroutines were adapted locally in order to account for the discontinuities occuring at the interface. For this study Cheuret and Steelant, [124], utilized a Spalarat-Allmaras turbulence model [125] applied within the pressure based solver along with a second ordered upwind discretisation technique in combination with a min-mod limiter within CFD-ACE+. This commercial code CFD-ACE+ is based on the research by [126]. The transport through the porous medium was accepted to account for the reduced passage and volume by introducing the porosity value into the mass, momentum and energy equation by including customized flux corrections at the interface handling the discontinuity in the flow variables in the interface between the porous and main flow zone.

For this research the CFD results were compared to the ITLR experimental results from the simulating transpiration cooling applied to porous medium composite materials. It was observed when analysing the results that when computing the wall temperature of the porous sample, deviations are still observed. The deviation appeared due to the insufficient modelling of the walls 3D-thermal boundary conditions in the 2D computations. A full discussion and conclusion of the results can be found in Cheuret and Steelant, [124].

3.5.4 Azevedo and Korzenowski, [10]

The Azevedo and Korzenowski, [10], work compared five different spatial discretisation algorithm's for cold gas Hypersonic flow simulations. The application of interest is the cold gas flow through a typical Hypersonic inlet. The algorithm's presented were applied to the solution of Supersonic and Hypersonic inlet flows. The inlet entrance conditions were varied from M_∞=4 up to M_∞=16. Results for different entrance Mach numbers and Mesh topologies were discussed in order to assess the comparative performance of the various spatial discretisation schemes. An inviscid formulation was used and the fluid was treated as a perfect gas. Although Azevedo and Korzenowski, [10], noted that that for actual flight condition simulations, real gas effects would have to be taken into account, flow-fields were simulated using the 2-D Euler equations, discretised in a cell-centered FV procedure on unstructured triangular meshes. The algorithm's studied included a central difference-type scheme [127], and 1st- van Leer [128] and 2nd- order Liou and Shuen [85] flux vector splitting schemes. The methods were then implemented in an edge-based, unstructured grid procedure which allows for adaptive mesh refinement based on flow property gradients. This adaptive mesh refinement strategy

in [10] and seeks to refine the mesh in parallel with the flow field computations. The consideration of very high Mach number flows has the objective of testing the behaviour of the different algorithm's in the presence of strong shocks.

Details of the unstructured grid implementation of the algorithm's were presented together with a discussion of the data structure and of the adaptive refinement strategy are presented in [10].

3.5.5 Haoui [129]

The aim of the research work by Haoui [129] was to analyse high temperature flows around an axisymmetric blunt body, and taking into account chemical and vibrational non-equilibrium state for air mixture species. For this purpose, a FV methodology was employed to determine the Supersonic flow parameters around the axi-symmetric blunt body. This allowed the capture of a shock wave before a blunt body which was placed in a Supersonic free stream. The numerical technique uses the flux vector splitting of Van Leer, [111]. Here, adequate time stepping parameters, along with the Lewy et al, [24], coefficient and mesh size level were selected to ensure numerical convergence, sought with an order of 10^{-8}.

The numerical simulation of Haoui, around blunt bodies at high temperatures provided satisfactory results from a numerical and a physical point of view. With high degree of accuracy requirements, computational convergence was achieved and the physical phenomena considered were visible after the detached shock wave and around the blunt body. The choice of the kinetic model was interesting. The model with 17 reactions proved to be more realistic since it considered all the possible collisions between molecules and atoms of the mixture of air. However, it is more complex in computations and implementation than the perfect gas modelling.

3.6 Computational Challenge and Strategy

The default pressure correction algorithm in the host code PHYSICA becomes unstable at Hypersonic speeds when there are strong non-linearities in the pressure and the velocity fields such as localized regions around shocks. The aim of the project is to embed a flow solver that can capture the Hyperbolic character and the strong non-linearities for velocity and pressure, the strong coupling between the enthalpy, density and velocity in the boundary layer, and the complex geometries involved for aerodynamic Hypersonic vehicles and finally the high storage and CPU time involved in practical simulations. A 1% error was sought in the initial benchmarks, therefore there is a requirement for the scheme to be both 2^{nd} order accurate and robust enough to handle shocks. The dearth of results concerning Hypersonic flow simulations using unstructured meshes as mentioned in research by Lyra & Morgan [130] and Greenshields et al, [120] has stimulated this present work.

3.6.1 The Characteristic Based Split Algorithm

For the reasons stated above it will be somewhat of a challenge to develop and implement a 2^{nd} ordered upwind scheme with unstructured grids. Obviously, applying 2^{nd} ordered upwind schemes to unstructured multidimensional problems will incur an overhead in computing the upwind direction and the 2^{nd} upwind neighbour or the donor cell. However, it is necessary to utilize unstructured grids instead of structured grids because of their relative flexibility, potentially using an unlimited number of distorted elements detail around the air-skin surface interface that can model the pertinent physics - the viscous and thermal interaction - over Hypersonic vehicles.

The Characteristic Based Split (CBS) scheme is a potentially attractive candidate scheme that is viewed as utilitarian enough to allow the solution of a number of flow regimes as seen in the research

[131]–[134]. The scheme is utilitarian enough to be applied to those flow regimes in this research - Hypersonic, Trans-Sonic and Subsonic speeds. The application of shock capturing viscosities to the CBS algorithm has already proven to be a success when solving Supersonic flows, in the research by Nithiarasu et al. [134], in the finite element context.

It will prove informative to detail the origins of the CBS algorithm. As already referred to in section 2.3 over the last three decades various types of upwind algorithm's for fluid dynamics have been developed. As Greenshields et al, [120], states that some of these are implicit methods and are not capable of computations without Riemann solvers, Jacobian evaluation and characteristic decomposition. This means that in practice they are more complex than CD methods when applied to a polyhedral framework, and computationally more expensive per time step. These 2^{nd} order accurate upwind methods are also difficult to employ as a unified approach to both compressible and incompressible flow problems. As a fix to the problems, Zienkiewicz and Codina, [47], developed a finite element version of the Lax Wendroff family followed by the original CBS method which was introduced as a fully explicit solution procedure by Nithiarasu et al. [134], later extended to a semi implicit form for incompressible problems [135]. Research on the applied need for shock capturing viscosities for Supersonic flows [134] showed that the scheme is utilitarian enough to be applied to the different flow regimes at Hypersonic, Trans-Sonic and Subsonic speeds . The CBS scheme was also extended to solve problems in other fields such as porous media flow as seen in Massarotti, Nithiarasu, & Zienkiewicz, [136]. This extension to porous media flow is another potential benefit for this research considering the novel application is to model porous - transpiration cooled - components in a Hypersonic environment.

For the reasons discussed above the decision was made to use the 2^{nd} order spatially accurate CBS method, and transform it from a finite element context to a finite volume algorithm. This decision was made because it was concluded that the CBS algorithm provided the appropriate versatility and spatial accuracy for the final novel application - solving thermo-viscous interactions over unstructured grids. The drawback, however, is that central differencing methods tend to be dispersive in the proximity of discontinuities and prone to instability at high convective speeds. Therefore, a more robust artificial viscosity term was developed by Jameson et al, [105], and was used in this work to replace the previous artificial viscosity terms used in the original Finite Element work of Nithiarasu and Codina, [131], which was deemed wanting in terms of stability.

3.7 Concluding Remarks

The route finally chosen by the author for the target application was a 2^{nd} ordered central difference method (CDM) with a non-linear artificial viscous term over an unstructured grid for the reasons stated in Section 3.6 . In conclusion the CBS method was chosen on the basis of the following considerations:

1. Relative ease in understanding the numerical method, and does not have to evaluate the Jacobian, the local Riemann solution and the upwind direction, as is the case for flux vector splitting and flux difference splitting [120].
2. Utilitarian enough to be applied to the different flow regimes Hypersonic, Trans-Sonic and Subsonic speeds [131].
3. As opposed to the 2^{nd} ordered upwind scheme that often needs 3 grid points to determine face values, this is problematic when flow is not aligned with grid lines.
4. Central differencing alternatively only requires 2 grid points, upstream and downstream of the face, meaning that they are easily extendable to utilize unstructured finite volumes.

5. The CBS algorithm has already been applied to porous media flows with success, [136], an important requirement for this research - see novel problem in Section 1.1.
6. Keeping the same interpolation methods for the convection and diffusion terms was thought to be more physically rigorous than using upwind methods on only the convection terms.
7. As mentioned by Liou, [137], CDM are superior to upwind methods when applied to additional physical models such as turbulence and chemical reactions.

A further caveat is the requirement for the code to accurately capture Subsonic incompressible flows i.e. the Blasius benchmark, see Chapter 7. Incompressible flows are modelled because the industrial sponsors were concerned to ensure the solver can work through the flow regimes from Subsonic to Trans-Sonic and then to Hypersonic speeds. As mentioned previously using density based schemes (DBS) for incompressible problems are problematic, as in this instance the density will be constant throughout the flow domain. A fix or relationship is needed to re-write the continuity equation in terms of pressure, and this is done according to the standard scheme as seen in Chapter 7. This fix with the CBS algorithm has already been applied to incompressible flows with success [47], [96], [138]; hence, an important issue for this research is already addressed. Another consideration for the solver is the accurate handling of porous flows, see novel problem in section 1.1. Fortunately the CBS algorithm has also already been applied to porous media flows with success [136].

4. INVISCID 1-D FLOW SIMULATIONS

4.1 Introduction

The purpose of this chapter will be to illustrate two key capabilities of the CBS algorithm:- first in accurately capturing purely Supersonic compressible flow within an enclosed domain, and secondly capturing a normal shock wave within the enclosed domain. These capabilities will enable the final goal of this research which is to create a Hypersonic simulation tool. To demonstrate the above capabilities two different flow problems with known analytical solutions have been chosen.

Many problems in engineering and science are governed by conservation laws expressed in terms of Hyperbolic partial differential equations, such as the system of Euler equations Hirsch [18]. This particular class of partial differential equations presents some properties which must be well understood before attempting to develop numerical techniques. The reliability of a solution computed using a numerical technique is directly related to the capacity of the mathematical model representing the physical behaviour of the problem as mentioned by Hirsch [18]. Assuming that an appropriate numerical technique is in hand, there are two requirements which must be fulfilled in order to obtain reliable results. The first requirement is to adequately represent the geometry of the computational domain with a discrete grid. This task requires the development of a suitable mesh generator, as well as connecting the discretisation with the steady state solution. This must be done in order to capture the changes in parts of the domain where the physical quantities are changing rapidly, because as suggested by Versteeg and Malalasekera, [17] it is inefficient to construct a fine mesh everywhere. The second requirement is the design of a technique that will allow an assessment of the error in the solution for various computational grids. This is known as a grid independent assessment. This grid independent assessment is achieved through careful investigation of benchmarks with known analytical data and is carried out on the FV Characteristic Based Split (CBS) algorithm in this chapter.

In the following sections, a detailed description is given of the numerical formulations employed, and with special attention to the finite difference approach. From section 4.4 to the end of section 4.7 the 1-D inviscid benchmark examples of this thesis will be introduced. In section 4.5 the CBS algorithm is coupled with artificial viscosity terms (AVT) developed by MacCormack [29]. In a CFD solution for Supersonic flows, to obtain shock features free from odd even order decoupling, it is essential to use some form of artificial dissipation, an approach favored by [29], [60], [105], [134]. The following chapter will also introduce some suggested AVT refinements by Jameson, Schmidt & Turkel's [105]. In section 4.7.2 and section 4.9.1 the performance of the resulting algorithm, the CBS algorithm coupled with Jameson, Schmidt & Turkel's AVT, is assessed by comparing the numerical solution with the analytical results for the de Laval nozzle. It is important to keep in mind throughout this chapter that the industrial sponsors considered a CFD solution to be sufficiently accurate if it is within 1% of the analytical solution. A full review of this analytical solution will also be given in this chapter.

4.2 Isentropic Quasi-1D Nozzle Flow

Subsonic air flow within the convergent section of a nozzle accelerates to purely Supersonic flow within the divergent section of the nozzle, and is the first benchmark case presented in this chapter. This nozzle is popularly known as the de Laval nozzle and its premise is to accelerate Subsonic gas

flow at the nozzle inlet to Supersonic speeds at the outlet. This is possible through the asymmetrical physical phenomenon which has been highlighted by Anderson, [15], page 285.

> When the [de Laval] nozzle's area decreases in the nozzle's principal direction the flow speed increases, the maximum speed is limited by the minimum throat area. If the speed at the throat attains Trans-Sonic speeds the dependent relationship between the nozzle area and flow speed is reversed. Hence, at the divergent section [after the throat], as the nozzle area increases again, the flow accelerates to Supersonic speeds.

According to Flack, [13], de Laval nozzle's have been developed, used and optimised in rocket engines such as the space shuttle afterburners and speeds of up to Mach 13 have been recorded at sea level. The optimal operating mode for de Laval afterburners is when the jet pressure at the outlet equals the ambient pressure of the atmosphere. During shuttle takeoff as the rocket ascends, the ambient pressure changes with flight altitude. If the pressure of the air leaving the jet nozzle is approximately 2.5 times lower than the ambient pressure, flow separation occurs and the air leaving the jet can mechanically damage the nozzle [13]. If this flow separation occurs it could cause catastrophic results.

Optimisation of rocket design is therefore required for safety and efficiency which has resulted in extensive numerical work on the subject of the de Laval nozzle. If the air flow is assumed to be isentropic (fully reversible), and the flow is assumed to occur along a straight line from the inlet to the exit i.e. a quasi 1-dimensional (1D) flow, then the de Laval nozzle is approximated by a closed form analytical solution. Although the de Laval nozzle is assumed to be a 1D nozzle in Anderson [15] and in this chapter, it is in reality a multidimensional problem. Conversely the 3D flow assumption has been made and developed in the research of Vandromme & Saouab [139], instead of the 1D assumption. However this research is trying to construct a simplified engineering model of the flow which will make it easier to solve.

The numerical results from the computed experiment of the highly compressible air flow within the de Laval nozzle generated in this work and reported here, have been compared against the analytical results described by Anderson, [15]. This has been done in order to demonstrate that the Characteristics Based Split algorithm formulation has the basic capability to handle flows across a wide range of Mach numbers, which is one of the key tasks this research has to address. A novel comparison between MacCormack's Predictor-Corrector algorithm and the CBS procedure is also presented to show that the CBS algorithm is indeed competitive in terms of accuracy and efficiency when compared to other CFD algorithm's. The conservation laws for the quasi 1D nozzle are presented below. For the full derivation consult Anderson, [15], page 288. This is followed by the derivation and application of the Characteristic Based Split time marching procedure for the quasi-1D de Laval nozzle.

4.3 Theoretical Background

The three dimensional Euler equations can be applied to scientific problems where viscous effects can be assumed to be negligible. The equations and variables are documented in Section 2.6. The assumption made for this benchmark is that flow variables across the nozzle's cross section are uniform. This assumption means that integral forms for the Euler equations are applied to infinitesimal slices along the nozzle length, and such problems are called Quasi-1-Dimensional. Obviously, in reality, the real flow in the nozzle is three dimensional, but the main purpose of this phase of the work is to formulate and then compare geometrically simplified models using the CBS approach with analytical solutions to assess the formers' numerical performance. The following

equations as presented below are extracted from Anderson's, [15], work on the de Laval nozzle, and are suitable for the unsteady quasi-1-Dimensional flows.

Continuity equation:

$$\frac{\partial(\rho A)}{\partial t}+\frac{\partial(\rho A V)}{\partial x}=0 \tag{4.1}$$

Momentum equation:

$$\rho\frac{\partial V}{\partial t}+\rho V\frac{\partial V}{\partial x}=-R\left(\rho\frac{\partial T}{\partial x}+T\frac{\partial \rho}{\partial x}\right) \tag{4.2}$$

Energy equation:

$$\rho C_V\frac{\partial T}{\partial t}+\rho V C_V\frac{\partial T}{\partial x}=-\rho RT\left(\frac{\partial V}{\partial x}+V\frac{\partial(\ln A)}{\partial x}\right) \tag{4.3}$$

Where
ρ - density
C_V - coefficient of thermal expansion
γ - ratio of coefficient of expansion
V - velocity in principal direction
A - Area
T - Temperature
R - universal gas constant

Anderson, [15], states that for nozzle flow studies, the flow field variables are frequently expressed in terms of non-dimensional variables, where the flow variables are relative to reference values. The non-dimensional variables P/P_∞, ρ/ρ_∞ and T/T_∞ vary between 0 and 1 in the analytical solution to the de Laval nozzle, which is an aesthetic advantage when presenting the results, allowing the modeller to easily display all flow variables on a single plot.

For the sake of comparison purposes this chapter will follow Anderson's, [15], work on the de Laval nozzle and use non-dimensional variables. Where L is the full length of the nozzle and ∞ denotes the reference values.

$$T'=\frac{T}{T_\infty} \qquad x'=\frac{x}{L} \qquad t'=\frac{t}{L/c_\infty}$$

$$\rho'=\frac{\rho}{\rho_\infty} \qquad c_\infty=\sqrt{T_\infty R\gamma} \qquad V'=\frac{V}{c_\infty}$$

$$P'=\frac{P}{\rho_\infty RT_\infty}$$

V' non-dimensional velocity in the principal direction in this case the principal direction is the x direction. Finally the local area is divided by the throat area A* defining a reference dimensional area.

$$A'=\frac{A}{A^*} \tag{4.4}$$

Anderson re-wrote the equations (4.1)-(4.3) in non-dimensionalised form to get a better understanding of the coupling between the changing nozzle area and the primitive variables.

$$\frac{\partial\rho'}{\partial t'}=-\rho'\frac{\partial V'}{\partial x'}-\rho' V'\frac{\partial(\ln A')}{\partial x'}-V'\frac{\partial\rho'}{\partial x'} \tag{4.5}$$

$$\frac{\partial V'}{\partial t'} = -V'\frac{\partial V'}{\partial x'} - \frac{1}{\gamma}\left(\frac{\partial T'}{\partial x'} + \frac{T'}{\rho'}\frac{\partial \rho'}{\partial x'}\right) \tag{4.6}$$

$$\frac{\partial T'}{\partial t'} = -V'\frac{\partial T'}{\partial x'} - (\gamma - 1)T'\left(\frac{\partial V'}{\partial x'} + V'\frac{\partial (\ln A')}{\partial x'}\right) \tag{4.7}$$

Where ρ' -Non-dimensional density P'- Non-dimensional pressure
T'- Non-dimensional temperature V'- Non-dimensional velocity
t' – Non-dimensional time x'- Non-dimensional distance

4.4 Benchmark Examples

In the following section a full review of the computational procedure aimed at solving the Subsonic to Supersonic de Laval nozzle is made, involving the geometrical profile of the nozzle, the nozzle's boundary conditions, the initial conditions required for the computational procedure and finally the analytical solution; for a more comprehensive review of these issues review Anderson [9] and [15].

Due to the practical impossibility to test the Characteristic Based Split algorithm for every scientific benchmark and physical problem, only the most important issues are addressed in this chapter. It must be stated that some of the results which will be presented here were obtained during the early stages of this research and performed before some improvements were introduced later on. In this way, they do not represent the best possible results, but rather a typical performance that can be expected from this algorithm.

4.4.1 Transition Subsonic to Supersonic Nozzle: Study

To obtain a base knowledge of Supersonic problems the available literature of CFD for aerospace applications were reviewed, such as [15], [17], [20], [84]. The Supersonic de Laval nozzle case was taken from Anderson's , [15], study on computational fluid dynamics with applications. For this research the motivation to study this problem was because the Supersonic case has a closed analytical solution that can be used to evaluate the accuracy and stability of CBS algorithm's, as well as being able to identify the limitations of the CBS algorithm when used to model Supersonic compressible flows. MacCormack's predictor-corrector algorithm which is used to compute the flow field in this Supersonic de Laval nozzle case in Anderson [15], uses 31 equally spaced grid points along the length of the nozzle to capture the flow successfully. To compare closely with [15], the CBS calculations are also run over 31 equally spaced grid points.

4.4.2 Subsonic to Supersonic Nozzle: Boundary Conditions

The boundary conditions also taken from Anderson [15], and have been set out in Table 4-1, note that they are non-dimensional values.

Table 4-1 Boundary conditions Inlet & Outlet.

	Inlet Conditions	Outlet Conditions
Supersonic de Laval Nozzle	$\rho' = 1$ $T' = 1$ $(V')_1 = 2(V')_2 - (V')_3$	$(\rho')_{N_{max}} = 2(\rho')_{N_{max}-1} - (\rho')_{N_{max}-2}$ $(V')_{N_{max}} = 2(V')_{N_{max}-1} - (V')_{N_{max}-2}$ $(T')_{N_{max}} = 2(T')_{N_{max}-1} - (T')_{N_{max}-2}$ Nmax= total number of nodes in domain

4.4.3 Subsonic to Supersonic Nozzle: Initial Conditions

To start the iterative calculations, we must stipulate initial conditions for ρ' , T' and V' for time=0 as a function x. In theory these can be arbitrary according to Anderson, [15], however, in practice there are two reasons why one would want to choose the initial conditions intelligently. Firstly efficiency in generating results, the closer the initial conditions are to the final answer, the faster the time marching procedure will converge and secondly and most importantly, enhancing the stability of the calculations. If the initial conditions are too far from the analytical results, the initial psuedo time wise gradients will be very large causing instability. From solving the two benchmarks in this chapter it has been the author's experience that the biggest gradients occur at early parts of the pseudo time stepping procedure. This can cause the procedure to become unstable and diverge. Therefore, in choosing the initial conditions the user is required to use any information or knowledge about the flow problem. For this present problem Anderson, [15], asserts that ρ and T decrease and V increases as the flow expands through the divergent section of the nozzle (after the throat). Hence Anderson, [15], chooses initial conditions that behave in the same fashion. For simplicity he assumes linear variations of these flow variables, as a function of nozzle length, x. This research will use exactly the same functions as seen in [15], because a close comparison between MacCormack [29] Predictor-

Corrector algorithm and the CBS procedure is required. This comparison is needed to assess the performance the CBS procedure relative to another compressible CFD algorithm.

$$\rho' = 1 - 0.3146x \tag{4.8}$$

$$T' = 1 - 0.2314x \tag{4.9}$$

$$V' = (0.1 - 1.09x)T^{1/2} \tag{4.10}$$

Where $0 \leq x \leq 3$

4.4.4 Subsonic to Supersonic Nozzle: Analytical Solution

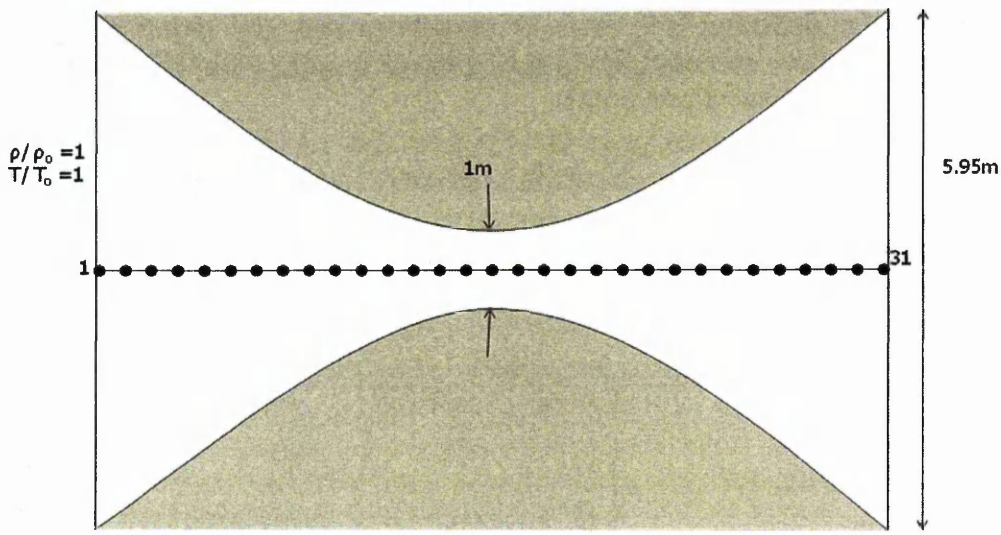

Figure 4:1– Longitudinal view through de Laval nozzle.

The first nozzle modelled has a convergent divergent geometry as seen in Figure 4:1.

$$\frac{A(x)}{A^*} = \frac{1}{M^2}\left[\frac{2}{1-\gamma}\left(1 + \frac{1-\gamma}{2}M^2\right)\right]^{\frac{\gamma+1}{\gamma-1}} \tag{4.11}$$

A* - A_t - the throat area which induces a sonic speed, $1\,m^2$.
A(x) - the area of the nozzle is a function of x, the length along the nozzle.

The relationship between area and length along the nozzle, x is given by this relationship.

$$A(x) = 1 + 2.2(x - 1.5)^2 \tag{4.12}$$

where x- is the distance in meters from the inlet along the length of the nozzle.

Equation (4.11) is an important relationship; it is called the *area- Mach number relation,* and it contains a striking result. Turned "inside out", equation (4.11) gives M=f(A/A*); which means mathematically that the Mach value, M, at any location in the duct is a function of the ratio of the local duct area over the throat area. Anderson [9] mentions that an important feature of de Laval nozzle's is that, A, must be greater than A*, and the case where A<A* is ***not possible*** in an isentropic flow. Also, (4.11) interestingly yields two solutions for M at a given A/A*, a Subsonic M value and a Supersonic M value. The value of M at each location depends on the pressure at the inlet and the exit of the nozzle. For the following de Laval nozzle case, Subsonic M values are associated with points in the convergent section and Supersonic M are associated with points in the divergent section.

To determine the Mach number at each discrete grid point, i, this research re-arranged equation (4.11) by subtracting both sides by A/A* and solves for M using an implicit iterative approach.

$$0 = \frac{1}{M^2}\left[\frac{2}{1-\gamma}\left(1+\frac{1-\gamma}{2}M^2\right)\right]^{\frac{\gamma+1}{\gamma-1}} - \frac{A}{A^*} \tag{4.13}$$

A simple root finding method was used to determine the value of M at each station, i , and this root finding method was the fzero function taken from the functions section in MATLAB R2008a Inc, [140]. The fzero command algorithm, was developed by T. Dekker, and can be found in the work by Brent [141]. It uses a combination of bisection, secant, and inverse quadratic interpolation methods.

The flow properties through the nozzle are a function of the local area ratio A/A* and are obtained using the following sequential steps:

1) For a specified station location, x, we can calculate the local area, A/A*=f(x) from (4.12). From this value we can solve (4.13) using the fzero function in MATLAB R2008a Inc, [140]. This will yield two values, a Supersonic Mach value and a Subsonic Mach value. The Subsonic Mach corresponds with the convergent section of the nozzle X<1.5m. The Supersonic Mach corresponds to the divergent section. The Mach distribution through the complete nozzle is thus obtained and is thus sketched in Figure 4:2.
2) Once the Mach number distribution is known, then the corresponding variation of pressure, density and temperature can be obtained from Anderson, [15]. The distribution of P/P_∞ are also sketched in Figure 4:2.

$$\frac{P}{P_\infty} = \left(1+\frac{\gamma-1}{2}M^2\right)^{-\gamma/(\gamma-1)} \tag{4.14}$$

$$\frac{\rho}{\rho_\infty} = \left(1+\frac{\gamma-1}{2}M^2\right)^{-\gamma/(\gamma-1)} \tag{4.15}$$

$$\frac{T}{T_\infty} = \left(1+\frac{\gamma-1}{2}M^2\right)^{-1} \tag{4.16}$$

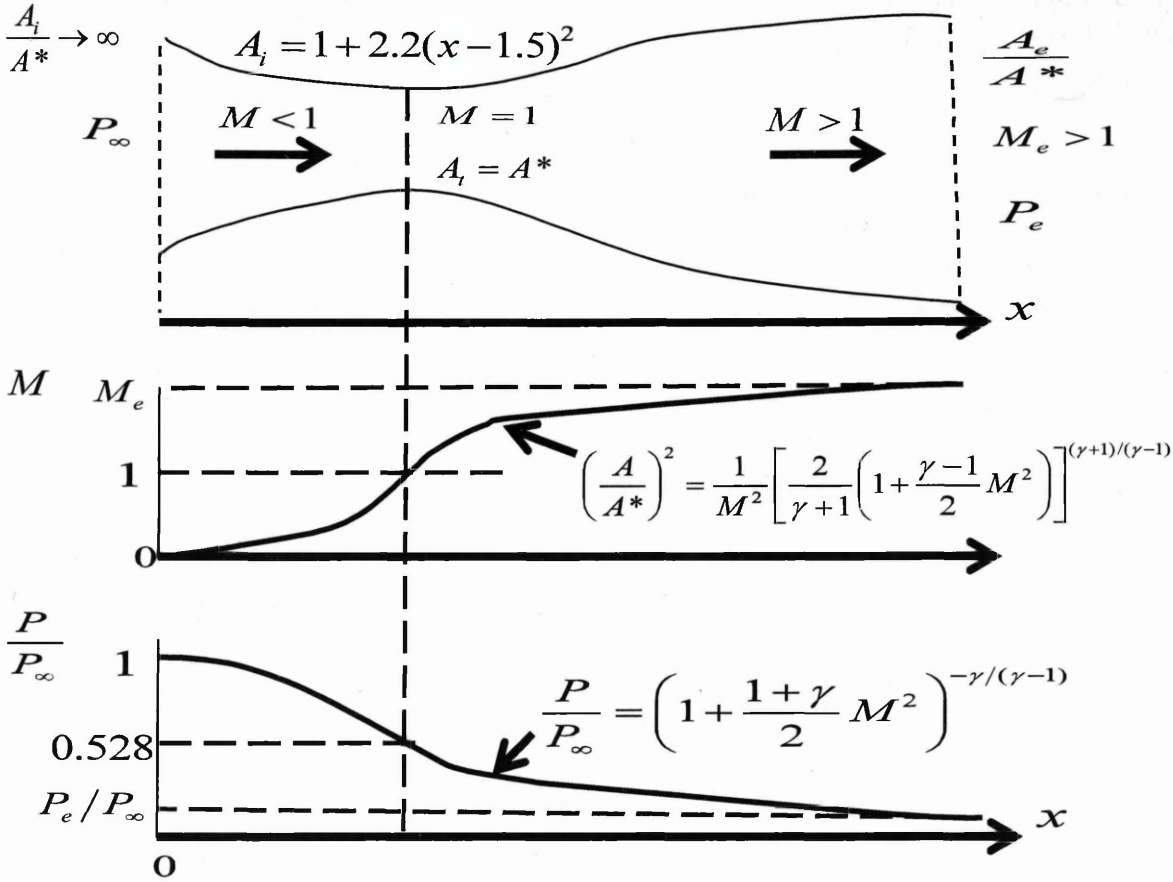

Figure 4:2-Diagram of de Laval nozzle as used in rocket engines to create exhaust gas Supersonic velocity from Beychok [142] and the observable relationship between the Mach speed and non-dimensional pressure.

In Figure 4:2 it is possible to observe that the Mach number monotonically increases from near 0 at the inlet to M=1 at the throat and to the Supersonic value M_e at the exit. The non-dimensional pressure, however, decreases from 1 at the inlet to $0.528P_\infty$ at the throat and to the lower value of P_e/P_∞ at the exit. Again we re-emphasize that the distribution of M and hence, P/P_∞ through the nozzle depends on the local area ratio. This is the key to the analysis of isentropic, quasi-one dimensional nozzle flows as mentioned by Anderson [9].

Table 4-2 Area for the Supersonic Nozzle cases.

	Area	Analytical Solution
Supersonic de Laval nozzle	$A(x) = 1 + 2.2(x-1.5)^2$ Where $0 \le x \le 3$	$\frac{A(x)}{A^*} = \frac{1}{M^2}\left[\frac{2}{1-\gamma}\left(1+\frac{1-\gamma}{2}M^2\right)\right]^{\frac{\gamma+1}{\gamma-1}}$ Where A* is $1\,m^2$, the area of the throat

As already mentioned in chapter 2 the major challenge when solving the Euler equations for Supersonic compressible speeds is capturing the non-linearities and the Hyperbolic character of the equations. What follows are not the best possible results, but what can be typically expected from the algorithm. MacCormack's artificial viscous term, S, as seen in Anderson [15], was brought into the discretised solution to damp out the decoupling, enabling a stable solution for this problem.

4.5 Non-Conservation Equations: The FD/FV CBS Approach

The next step in constructing an approximation to the problem is to define the solution domain or the length of the nozzle. Anderson [15], assumed that the 1D computational domain as seen in **Figure 4:3** is vertically positioned in the center of the throat. 13 nodes are used in Figure 4:3 for presentation reasons, however, in the actual problem 31 nodes, equidistant apart and spanning the length of the nozzle, are used to discretise the domain. The first point is 1 and the last point is N_{max}; in this case N_{max}=31. The 31 nodes can be broken up into two groups: the internal nodes and the two boundary nodes.

As seen in Figure 4:3 point i is simply an arbitrary grid point, with points i-1 and i+1 denoting its adjacent points. The CBS technique used in this thesis is an explicit method.

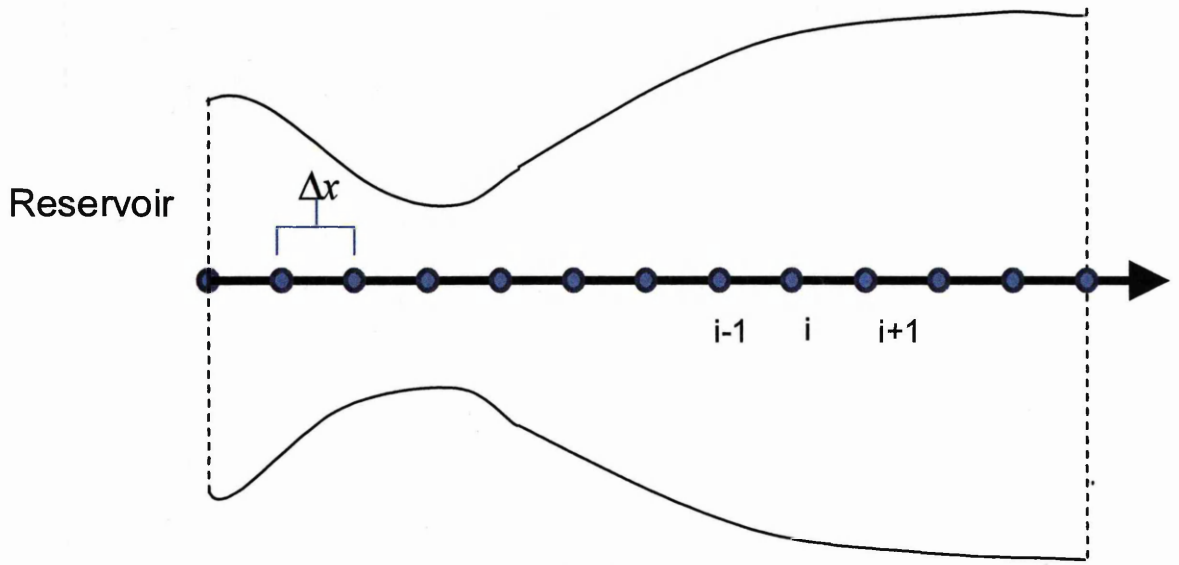

Figure 4:3 Grid point distribution along the nozzle.

The sequential computational procedure for the CBS finite difference algorithm can be done in a number of ways but for this research the following general procedure was agreed upon after numerical experimentation.

Each step described below is applied to all the interior nodes in a sweep of the grid. After this sweep the boundary conditions as seen in step 6 are computed. Then the sequential computational iterative procedure is repeated by going to step 1. The CBS method was implemented in MATLAB R2008a and the simulations run within a dual core laptop with 2046MB of RAM to solve the non-conservation system of equations, where the geometry of the nozzle and the boundary conditions are given below for the Supersonic nozzle.

1) Calculate the local time step. Where C is the Courant number and depending on the problem is usually < 0.5

$$\Delta t_i^n = C\frac{\Delta x'}{V_i^n + |c_i^n|} \qquad (4.17)$$

Where the superscript n equals the current iterative level

2) Compute the intermediate momentum equation sweeping through the interior nodes from i=2,3,4...., N_{max} -1

$$\left(V'^{*}\right)_i^n = \left(V'\right)_i^n - \Delta t'_i \left(V'\right)_i^n \left(\frac{\partial V'}{\partial x'}\right)_i^n + \frac{\Delta t'^2_i}{2}\left(V'\right)_i^n \frac{\partial}{\partial x'}\left(\left(V'\right)_i^n \left(\frac{\partial V'}{\partial x'}\right)_i^n\right) \tag{4.18}$$

3) Correct the momentum values using the corrected momentum equation sweeping through the interior nodes from i=2,3,4...., N_{max} -1

$$\left(V'\right)_i^{n+1} = \left(V'^{*}\right)_i^n - \Delta t'_i \left[\begin{array}{l} \Delta t'_i \frac{1}{\gamma}\left\{\left(\frac{\partial T'}{\partial x'}\right)_i^n + \frac{T'^n_i}{\rho'^n_i}\left(\frac{\partial \rho'}{\partial x'}\right)_i^n\right\} \\ + \frac{\Delta t'_i}{2} V'^n_i \frac{\partial}{\partial x'}\left(\frac{1}{\gamma}\left\{\left(\frac{\partial T'}{\partial x'}\right)_i^n + \frac{T'^n_i}{\rho'^n_i}\left(\frac{\partial \rho'}{\partial x'}\right)_i^n\right\}\right) \end{array}\right] \tag{4.19}$$

Where the superscript n+1 equals the next iterative level

4) Calculate the density from the continuity equation using the momentum values from step 3) sweeping through the interior nodes from i=2,3,4...., N_{max} -1

$$\rho'^{n+1}_i = \rho'^n_i - \Delta t'\left(\rho'^n_i \left(\frac{\partial V'^{n+1}}{\partial x'}\right)_i + \rho'^n_i V'^{n+1}_i \left(\frac{\partial (\ln A')}{\partial x'}\right)_i + V'^{n+1}_i \left(\frac{\partial \rho'^n}{\partial x'}\right)_i\right) \tag{4.20}$$

5) Compute the temperature from sweeping through i=2,3,4...., N_{max} -1

$$\left(T'\right)_i^{n+1} = \left(T'\right)_i^n - \Delta t'_i \left(\begin{array}{l} V'^n_i \left(\frac{\partial T'}{\partial x}\right)_i^n + (1-\gamma) T'^n_i \left(\frac{\partial V'}{\partial x}\right)_i^n + V'^n_i \left(\frac{\partial (\ln A')}{\partial x'}\right)_i \\ \frac{\Delta t'_i}{2} V'^n_i \frac{\partial}{\partial x'}\left\{V'^n_i \left(\frac{\partial T'}{\partial x}\right)_i^n + (1-\gamma) T'^n_i \left(\frac{\partial V'}{\partial x'}\right)_i^n + V'^n_i \left(\frac{\partial (\ln A')}{\partial x'}\right)_i\right\} \end{array}\right) \tag{4.21}$$

6) Calculate the non-dimensional pressure and speed of sound at the interior nodes from i=2,3,4....,N_{max}-1

$$\left(P'\right)_i^{n+1} = \left(T'\right)_i^{n+1}\left(\rho'\right)_i^{n+1}$$

$$\left(c'\right)_i^{n+1} = \sqrt{\left(T'\right)_i^{n+1}}$$

7) Compute the outlet values using linear extrapolation.

$$\left(\rho'\right)_{N_{max}}^{n+1} = 2\left(\rho'\right)_{N_{max}-1}^{n+1} - \left(\rho'\right)_{N_{max}-2}^{n+1}$$

$$\left(V'\right)_{N_{max}}^{n+1} = 2\left(V'\right)_{N_{max}-1}^{n+1} - \left(V'\right)_{N_{max}-2}^{n+1}$$

$$\left(T'\right)_{N_{max}}^{n+1} = 2\left(T'\right)_{N_{max}-1}^{n+1} - \left(T'\right)_{N_{max}-2}^{n+1}$$

Extrapolate the velocity at the inlet and fix density and temperature.

$$\rho' = 1$$

$$T' = 1$$

$$\left(V'\right)_1 = 2\left(V'\right)_2 - \left(V'\right)_3$$

8) Check convergence to steady state values by sensing whether the relative error is less than the agreed tolerance of 10^{-5} or the number of iteration/sweeps is below the maximum

iteration/sweeps, I_{Max}, stipulated by the user, this value was set initially to 95,000 iterations.

$$\rho_{error}^{n+1} = \sum_{i=1}^{N_{max}} \frac{\left(\rho_i^{n+1} - \rho_i^n\right)}{\left(\Delta t_i^n \times \left(c^2\right)_i^n\right)} \qquad (4.22)$$

9) If convergence has been achieved exit the procedure and display results otherwise begin computational sweep by going back to step 1.

Quotients

Linear interpolation in terms of the neighbouring nodal values is adopted for the face fluxes. For (4.18),(4.21) and (4.20) the derivative terms can be calculated by substitution of the following discrete terms.

Let

$$\frac{\partial V^n}{\partial x_i} = \frac{V_{i+1/2}^n - V_{i-1/2}^n}{\Delta x} \quad \text{where} \quad V_{i+1/2}^n = \frac{(V_{i+1}^n + V_i^n)}{2} \quad \text{and} \quad V_{i-1/2}^n = \frac{(V_i^n + V_{i-1}^n)}{2}$$

Meaning

$$\therefore \frac{\partial V^n}{\partial x_i} = \frac{V_{i+1}^n - V_{i-1}^n}{2\Delta x} \qquad (4.23)$$

The higher order derivatives in (4.18)-(4.21) are calculated in a similar manner where

Let

$$\frac{\partial}{\partial x}\left(\frac{\partial V}{\partial x}\right)_i^n = \left(\frac{\partial V/\partial x_{i+1/2} - \partial V/\partial x_{i-1/2}}{\Delta x}\right)^n$$

And

$$\left(\frac{\partial V}{\partial x}\right)_{i+1/2}^n = \left(\frac{V_{i+1} - V_i}{\Delta x}\right)^n \text{ and } \left(\frac{\partial V}{\partial x}\right)_{i-1/2}^n = \left(\frac{V_i - V_{i-1}}{\Delta x}\right)^n$$

Meaning

$$\therefore \frac{\partial}{\partial x}\left(\frac{\partial V}{\partial x}\right)_i^n = \left(\frac{V_{i+1} - 2V_i + V_{i-1}}{\Delta x^2}\right)^n$$

Calculation of Local Time Step

The use of implicit approaches to represent the time discretisation might be attractive, but due to the scale of problems normally faced in CFD, iterative approaches are preferred. These iterative approaches will be of particular importance when the extension of these methods to the solution of large scale 3D problems is envisaged.

The governing system of equations (4.1)- (4.3) are Hyperbolic with time, and the magnitude of Δt that can be used in the above equations can be obtained from the simple stability analysis for linear problems. The simple stability analysis of a *linear* Hyperbolic equation carried out by Lewy, Courant, & Friedrichs (1928) for an explicit numerical solution gives the result that C<1. Yet, the present compressible Supersonic flow is governed by *nonlinear* partial differential equations. In this case the exact stability criterion for a linear equation can only be viewed as general guidance for the present

nonlinear problem, but as indicated by Anderson [15], it turns out to be a reasonable guide to *nonlinear* problems.

General Remarks

1) Contrary to the advice of researchers Nithiarasu and Codina, [131] splitting the momentum equation into two parts is not required and the CBS algorithm appears to derive its stability from both the higher order temporal terms and the local time stepping for the following benchmarks in this chapter.

2) For stable pressure at the nozzle exit the mass flow, $\dot{m}'$, at each node should remain constant throughout the domain. For the following benchmarks the $\dot{m}'$ is plotted along the length of the nozzle and compared to the analytical result, the $\dot{m}'$ at the throat.

$$\left(\dot{m}'\right)_i^n = \left(\rho' V' \mathrm{A}'\right)_i^n \tag{4.24}$$

3) MacCormack's 2nd ordered artificial viscous term (AVT) was also coupled with the CBS algorithm where it was used as an explicit stabilizing source term. The stabilization of the CBS algorithm by the addition of this numerical source term is necessary to extend the stability region of the scheme. Unreasonable results with respect to the analytical solution and even divergence is encountered when the CBS algorithm is not coupled with any artificial viscosity terms.

4.5.1 MacCormack and Jameson, Schmidt and Turkel

The following section displays the numerical results for the nozzle referred to in Table 4-2. The stabilization of the central differencing CBS scheme is enhanced by the adoption of artificial viscosity terms (AVT). One of the AVT is taken from MacCormack [29] scheme and the other one is taken from Jameson, Schmidt & Turkel's [105]. A comparison is made relative to the analytical solution in order to assess the most accurate and stable AVT term for coupling with CBS algorithm. The experience proved to be useful when extending the algorithm to the multidimensional benchmarks that will follow in the next chapters, and which will also give an indication that the CBS algorithm can capture the final novel application - modelling transpiration cooling through porous media in Hypersonic flows.

4.5.2 MacCormack's Artificial Viscosity Term

The following technical discussion on MacCormack's artificial viscosity term (AVT) should not be confused with MacCormack [29] Predictor-Corrector iterative algorithm which is not used in this research. By augmenting the CBS steps with MacCormack's AVT this research is trying to suppress decoupling which can lead to divergence. Hence, the explicit CBS continuity equation (4.20) becomes.

$$\rho_i'^{n+1} = \rho_i'^{n} - \Delta t' \left(\rho_i'^{n} \left(\frac{\partial V'}{\partial x'} \right)_i^n + \rho_i'^{n} V_i'^{n+1} \left(\frac{\partial (\ln A')}{\partial x'} \right)_i + V_i'^{n+1} \left(\frac{\partial \rho'}{\partial x'} \right)_i^n \right) - \left(S_1\right)_i^n \tag{4.25}$$

This form of artificial viscosity is taken from Anderson [15], and is equivalent to adding a 4th ordered differential term. Here,

$$\left(S_1\right)_i^n = \left[\frac{C_x \left| (P')_{i+1}^n - 2(P')_i^n + (P')_{i-1}^n \right|}{(P')_{i+1}^n - 2(P')_i^n + (P')_{i-1}^n} \left\{ (\rho')_{i+1}^n - 2(\rho')_i^n + (\rho')_{i-1}^n \right\} \right] \tag{4.26}$$

where C_x is the user defined weighting parameter. The greater this C_x value the more dissipation is applied to areas of the domain that contain numerical gradients. This C_x term appears in the three expressions for $(S_1)_i^n, (S_2)_i^n$ and $(S_3)_i^n$. The intermediate momentum equation just like the continuity equation above has an artificial viscous term added, with the same rationale in mind to stabilize the quantities solved.

$$(V'^*)_i^n = (V')_i^n - \Delta t'_i (V')_i^n \left(\frac{\partial V'}{\partial x'}\right)_i^n + \frac{\Delta t'^2_i}{2}(V')_i^n \frac{\partial}{\partial x'}\left((V')_i^n \left(\frac{\partial V'}{\partial x'}\right)_i^n\right) - (S_2)_i^n \quad (4.27)$$

where $(S_2^n)_i$ is calculated in a similar fashion to (4.26) where the ρ terms in the {} brackets are changed to V terms:

$$(S_2)_i^n = \left[\frac{C_x \left|(P')_{i+1}^n - 2(P')_i^n + (P')_{i-1}^n\right|}{(P')_{i+1}^n + 2(P')_i^n + (P')_{i-1}^n}\left\{(V')_{i+1}^n - 2(V')_i^n + (V')_{i-1}^n\right\}\right] \quad (4.28)$$

where the explicit CBS energy equation is re-written from (4.21) to

$$(T')_i^{n+1} = (T')_i^n - \Delta t'_i \left(\begin{array}{l} V_i^m \left(\frac{\partial T'}{\partial x}\right)_i^n + (1-\gamma) T_i^m \left(\frac{\partial V'}{\partial x}\right)_i^n + V_i^m \left(\frac{\partial (\ln A')}{\partial x'}\right)_i \\ \frac{\Delta t'_i}{2} V_i^m \frac{\partial}{\partial x'}\left\{V_i^m \left(\frac{\partial T'}{\partial x}\right)_i^n + (1-\gamma) T_i^m \left(\frac{\partial V'}{\partial x'}\right)_i^n + V_i^m \left(\frac{\partial (\ln A')}{\partial x'}\right)_i\right\} \end{array}\right) - (S_3)_i^n \quad (4.29)$$

where the artificial term is calculated in a similar fashion to (4.26) and (4.28)

$$(S_3)_i^n = \left[\frac{C_x \left|(P')_{i+1}^n - 2(P')_i^n + (P')_{i-1}^n\right|}{(P')_{i+1}^n + 2(P')_i^n + (P')_{i-1}^n}\left\{(T')_{i+1}^n - 2(T')_i^n + (T')_{i-1}^n\right\}\right] \quad (4.30)$$

C_x is the user defined weighting parameter. A recommended value by Anderson [15], for this parameter is 0.2 although a certain level of experimentation is needed on a case by case basis, for optimizing the accuracy of and the speed of generating a numerical solution.

4.6 Benchmark Example 1: Subsonic to Supersonic Nozzle Results

The CBS method was implemented into the MATLAB R2008a program and the simulations run within a dual core laptop with 2046MB of RAM to solve the non-conservation variables, ρ', T' and V'. The CBS finite difference code solves the primitive variables along the grid points as seen in Figure 4:1. The relative error for density, equation (4.22), is an indication of how the numerical solution progresses through time and is the summation of the errors at every node. Similar equations have been used to obtain the relative error for V' and T', where ρ' in (4.22) is replaced by V' or T' respectively. These three errors V', T' and ρ' have been plotted in Figure 4:4 against the number of iterations. The solution has not dropped to the prescribed tolerance, which is most likely due to how the artificial viscosity introduces numerical dissipation (errors) that damp out numerical oscillations in the solution.

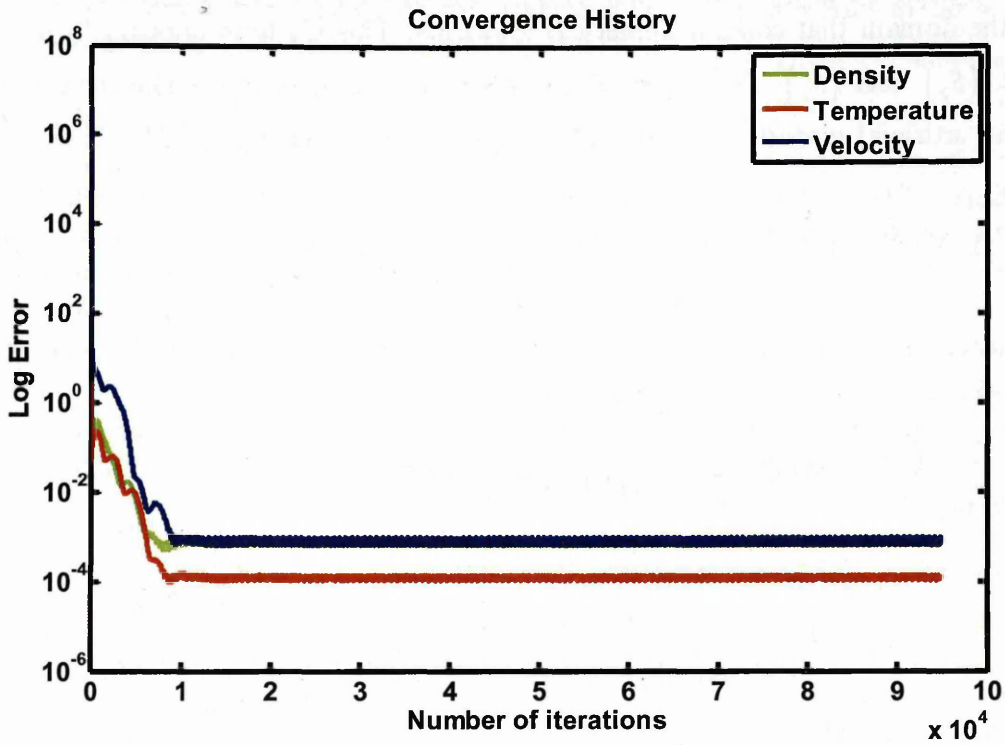

Figure 4:4-Convergence History for density, temperature and velocity for the Characteristic Based Split scheme applied to the non-conservation equations.

The number of iterations needed for a relative error of 10^{-3} is approximately 95,000. At this point the steady state solution has been achieved for all practical purposes and the calculation can be stopped. This termination of the calculation can be done automatically in the code by a test calculation, sensing when the changes in the primitive variables between each iteration becomes smaller than the prescribed tolerance. As recommended by Lyra, [7], the 2nd order numerical viscosity term damps 2nd ordered modes, helping the stability behaviour of the algorithm, but it is not enough to damp the non-linear effects which introduce errors. Ultimately the residual cannot always drop beyond a certain level as seen in Figure 4:4. It must be mentioned that as well as the AVT the convergence behaviour was also found to depend strongly on the value of Courant number, C.

During comparative calculations of the simulations, it became apparent that the CBS calculation is highly dependent on the extra temporal terms in the intermediate momentum and enthalpy equations. Appropriate time relaxation was employed to minimize the time derivatives in the early stages of the computations by employing the Courant number C of 0.095 and a AVT dissipation weighting as seen in (4.26), (4.28) and (4.30) of C_x=0.1.

As mentioned the relative errors of density, velocity and temperature of the order of 10^{-3} as calculated by equation (4.22), is an adequate relative error for CFD, and because the relative errors prove to be a valued indicator of whether a CFD solution has fallen to the steady state solution, it is possible to say that the solution has converged to a steady state.

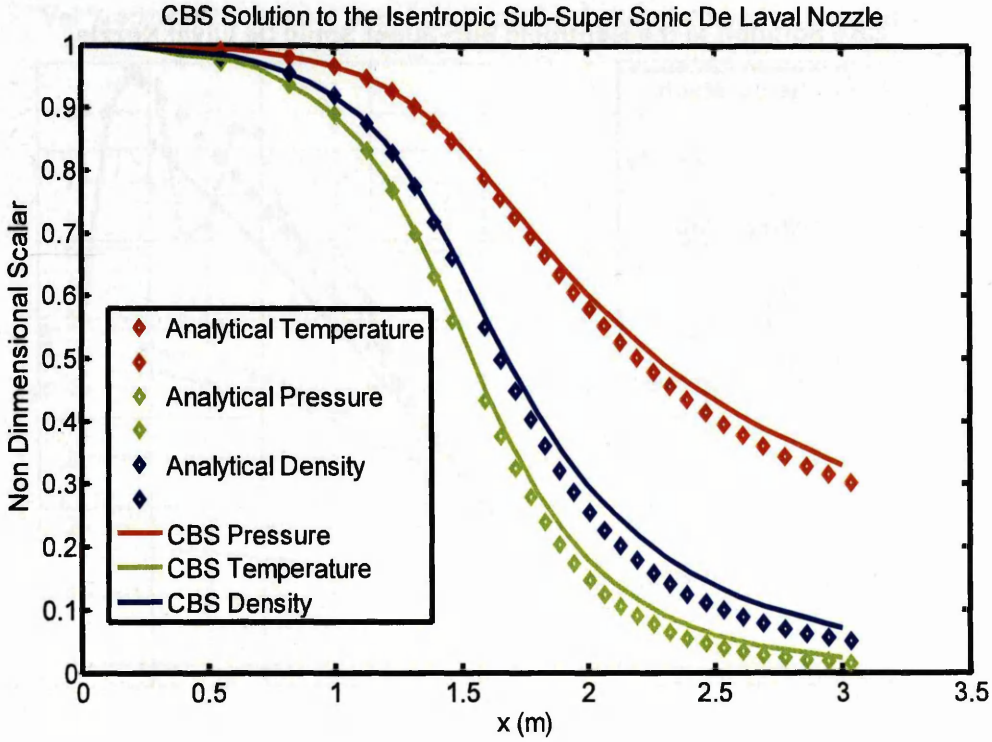

Figure 4:5 - Physical properties of air in a sub to Supersonic de Laval nozzle, comparing the CBS numerical results solving the non-conservation equations (full line-) with the analytical solution (◊).

As mentioned earlier, CFD solutions should display two properties of a discretisation technique; efficiency in generating a solution and accuracy of the solution in relation to the analytical solution. The theoretical results for ρ', T' and P' as calculated by (4.14)-(4.16) are shown in Figure 4:5 and are shown by the diamond shaped markers. The CBS solution being the full lines, the ρ, P and T are normalized so they can be displayed on the same plot. The vertical axis is labeled with "non-dimensional scalar" and the horizontal axis label with the "x(m)" length along the nozzle from the inlet in meters. Figure 4:5 shows that the ρ', T' and P' solution as calculated by the CBS algorithm, and is not in agreement with the analytical solution even though the algorithm has converged to relative density errors of the order of 10^{-5}. Particularly inadequate along the divergent section (X>1.5m) and at the outlet (X=3m) of the nozzle are the profiles for ρ', T' and P' are they all over-estimated.

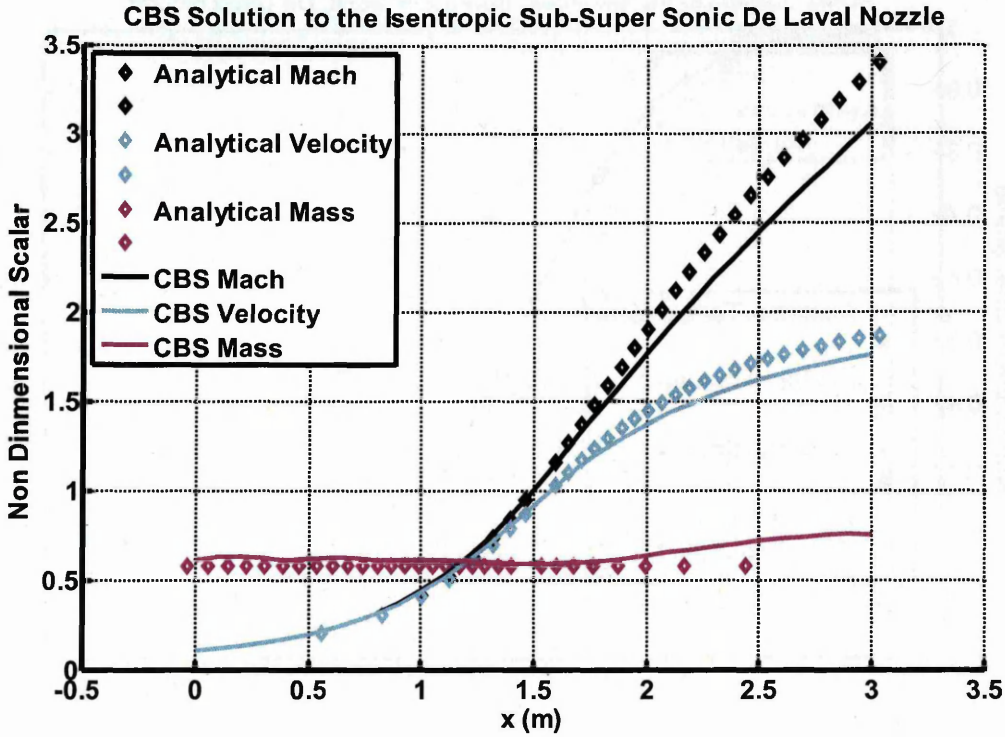

Figure 4:6- Physical properties of air in a sub to Supersonic de Laval nozzle, comparing the CBS numerical results solving the non-conservation equations (full line-) with the analytical solution (◊).

The Mach speed, normalized velocity and normalized mass flow as calculated by the CBS algorithm (4.25)-(4.22) are displayed in Figure 4:6. As presented throughout this chapter the theoretical results are given by the diamond shapes and the full lines are the CBS steady state solution. Like Figure 4:5 shows that the solution as calculated by the CBS algorithm, is not in agreement with the analytical solution even though the solution has converged to relative errors of the order of 10^{-5}. Particularly inadequate are the estimates of the velocity and Mach number after the throat where they are both underestimated.

4.6.1 Accuracy with Respect to the Analytical Solution

As mentioned previously CFD solutions should display accuracy with respect to the analytical solution. An important parameter used to gauge the accuracy of the final converged solution with respect to the analytical solution is the absolute error. The industrial sponsors typically require a numerical solution to be within 1% of the analytical solution at each grid point. As calculated below:

$$V_{i,abserror} = \frac{\left| V_i^{Steady,st} - V_{i,analytical} \right|}{V_{i,analytical}} \times 100 \qquad (4.31)$$

Where $V_{i,analytical}$ is the analytical value of velocity at node i and $V_i^{Steady,St}$ is the velocity at node i for a converged, numerical steady state CBS solution.

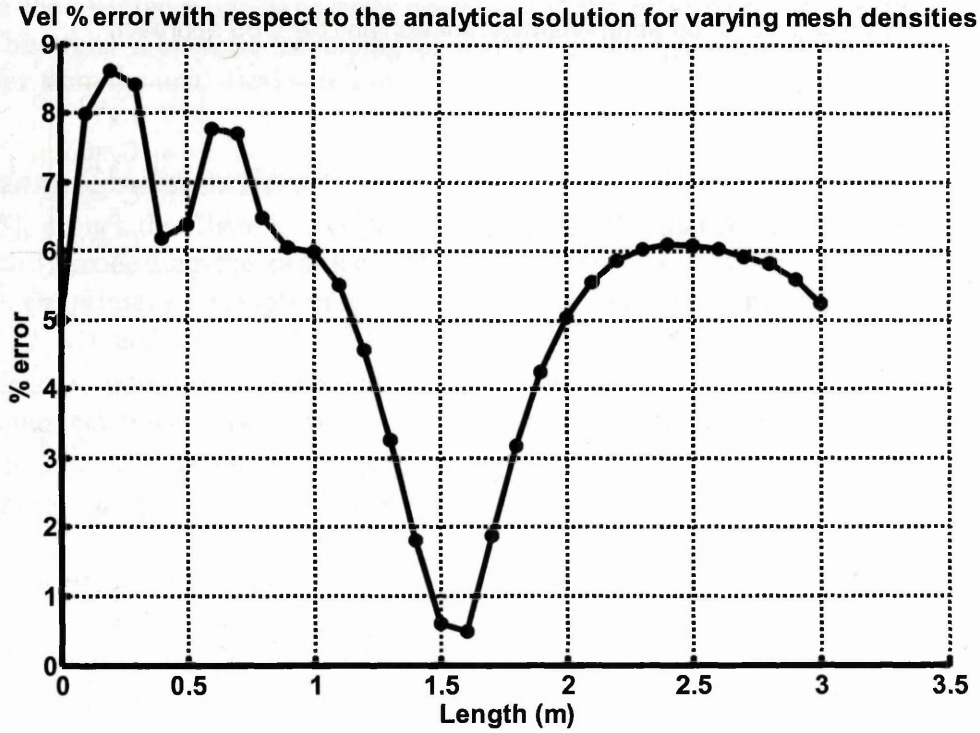

Figure 4:7 – Percentage error between the analytical solution and the CBS solution when solving the non-conservation equations coupled with MacCormack's AVT with C_x of 0.1

Figure 4:7 shows that the CBS solution along with a C_x value of 0.1 is not accurate enough at capturing the property fields. The percentage error depicted in Figure 4:7 shows that the absolute error is some way above the specified 1%. The percentage error at the inlet is above 5%, an unreasonable error, reducing to approx 1% at the throat (X=1.5m) and then increasing again to approx 5 % at the nozzle outlet.

To decide on the amount of artificial viscosity that should be used to remedy this problem with accuracy, four more computational runs were conducted with varying amounts of artificial viscosity. For four different values of C_x specifically C_x = {0.1, 0.2, 0.3, 0.4} the percentage error between the analytical solution and the converged CBS numerical solution was analysed.

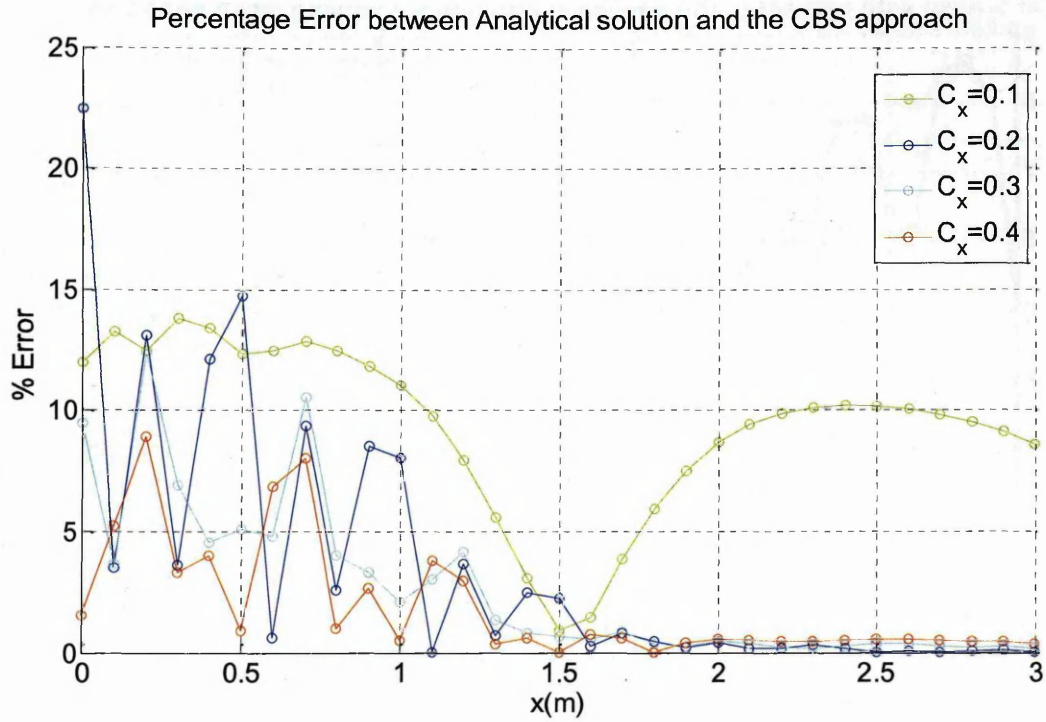

Figure 4:8 – Percentage error between the analytical solution and the Characteristic Based Split scheme applied to the non-conservation equations where C_x of 0.1.

To gauge the accuracy of the CBS approach with respect to the analytical solution of the velocity field at each of the C_x values the following average absolute error was calculated and compared for each of the converged solutions.

$$\hat{V}_{abserror} = \frac{1}{N_{max}} \sum_{i}^{N_{max}} V_{i,abserror} \qquad (4.32)$$

Where N_{max}=total number of nodes

$V_{i,abserr}$=error between the analytical velocity and the CBS solution's velocity

Table 4-3 below summarizes the effect of increasing the value of C_x in equations (4.26), (4.28) and (4.30). Stated in words the value of C_x=0.4 gives the lowest average percentage error and when C_x=0.1 the final solution gives the highest average percentage error of the four scenarios investigated.

Table 4-3-Table showing the effect of C_x in (4.26), (4.28) and (4.30) on the average absolute error in (4.32).

Number of Sweeps	C_x	Average absolute error In equation (4.32)
95600	0.1	9.340%
95600	0.2	3.586%
95600	0.3	2.651%
95600	0.4	1.876%

To summarize the average percentage error decreases as the value of C_x is increased for this nozzle benchmark. This trend is because increasing C_x damps out those numerical errors that make the CBS algorithm differ from the analytical solution.

Inlet Boundary Condition Error

Anderson, [15], argues that there is a built in error at the inlet that the modeller has to acquiesce to when numerically modelling this problem. As seen in Table 4-4, the first grid point where x=0 and the A=5.95m^2, the primary assumption is density, pressure and temperature are at reference values of, $\rho/\rho_\infty = 1$, $T/T_\infty = 1$ and $P/P_\infty = 1$. This is only mathematically possible if M=0 and V=0 at this inlet node, a counter-intuitive situation since in reality, to allow a finite mass flow through the nozzle a finite Mach number must exist at x=0. Thus the steady state CBS numerical value for V/V_∞ at the inlet node gives a percentage error of 1.54%, as can be seen in Table 4-4. This error has been ignored by Anderson [15], and for comparison purposes will be ignored in this research.

Table 4-4—Density ratio and velocity ratio distribution through the nozzle for a C_x value of 0.4.

x/L	A/A*	CBS ρ/ρ_∞	Analytical ρ/ρ_∞	% err ρ/ρ_∞	CBS V/V_∞	Analytical V/V_∞	% err V/V_∞
0.000	5.950	1.000	0.995	0.503	0.098	0.096	1.546
0.100	5.312	1.006	0.994	1.245	0.110	0.116	5.233
0.200	4.718	1.003	0.992	1.145	0.124	0.135	8.910
0.300	4.168	0.993	0.990	0.277	0.140	0.144	3.299
0.400	3.662	0.981	0.987	0.601	0.160	0.153	4.021
0.500	3.200	0.981	0.983	0.176	0.184	0.183	0.933
0.600	2.782	0.991	0.978	1.378	0.213	0.228	6.887
0.700	2.408	0.986	0.970	1.672	0.247	0.267	8.053
0.800	2.078	0.958	0.958	0.027	0.291	0.294	1.029
0.900	1.792	0.930	0.942	1.239	0.343	0.334	2.694
1.000	1.550	0.919	0.920	0.110	0.406	0.408	0.499
1.100	1.352	0.902	0.888	1.544	0.482	0.501	3.800
1.200	1.198	0.856	0.844	1.411	0.572	0.589	3.002
1.300	1.088	0.786	0.787	0.149	0.676	0.678	0.389
1.400	1.022	0.710	0.716	0.851	0.790	0.786	0.617
1.500	1.000	0.633	0.634	0.164	0.913	0.913	0.001
1.600	1.022	0.550	0.547	0.601	1.036	1.044	0.776
1.700	1.088	0.465	0.461	0.835	1.154	1.161	0.593
1.800	1.198	0.385	0.382	0.842	1.263	1.264	0.022
1.900	1.352	0.317	0.315	0.700	1.361	1.355	0.424
2.000	1.550	0.262	0.258	1.516	1.446	1.438	0.561
2.100	1.792	0.218	0.213	2.147	1.519	1.512	0.495
2.200	2.078	0.182	0.176	3.265	1.583	1.575	0.450
2.300	2.408	0.153	0.147	3.802	1.637	1.629	0.464
2.400	2.782	0.129	0.124	3.898	1.683	1.674	0.531
2.500	3.200	0.110	0.105	4.446	1.724	1.714	0.570
2.600	3.662	0.094	0.090	4.556	1.759	1.749	0.564
2.700	4.168	0.082	0.078	4.717	1.789	1.780	0.498
2.800	4.718	0.071	0.068	4.452	1.816	1.808	0.454
2.900	5.312	0.063	0.059	6.644	1.840	1.831	0.484
3.000	5.950	0.055	0.052	5.410	1.861	1.854	0.373

4.6.2 MacCormack's AVT: Results - C_x=0.4

The following results were run using a Courant number of 0.095 and a C_x value of 0.4. To decide on the amount of artificial viscosity that should be used to remedy this problem with accuracy. Four different values of C_x specifically C_x = {0.1, 0.2, 0.3, 0.4} were run where the percentage error between the analytical solution and the converged CBS numerical solution was analysed, leading to the conclusion that the closest approximation to the analytical solution occured when C_x=0.4. The resultant figures are displayed below.

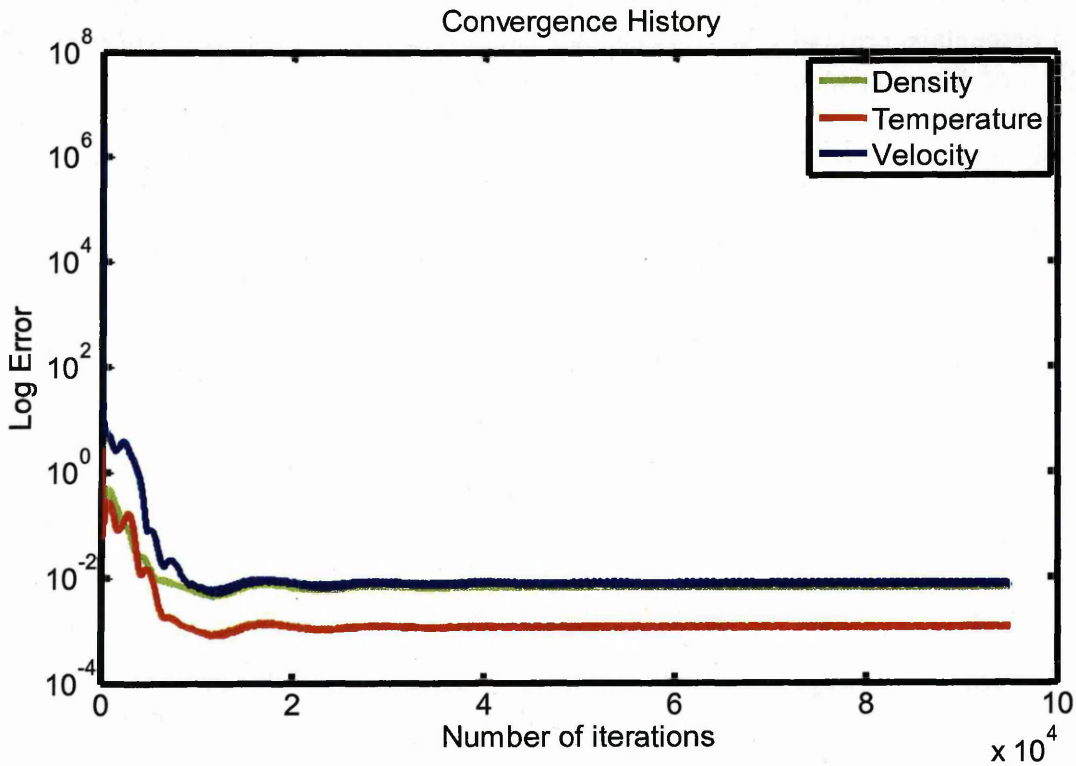

Figure 4:9-Convergence History for density, temperature and velocity for the CBS scheme when solving the non-conservation equations for Cx=0.4.

The number of sweeps needed to obtain relative error of density 10^{-2} is approximately 5,000. After another 90,000 sweeps the relative error has not increased or decreased in magnitude. At this point the steady state solution has been achieved and the calculation can be stopped. Increasing the value of C_x from 0.1 to 0.4 means that the final relative errors for C_x=0.4 cannot reduce to those relative values for C_x=0.1, which is 10^{-3}.

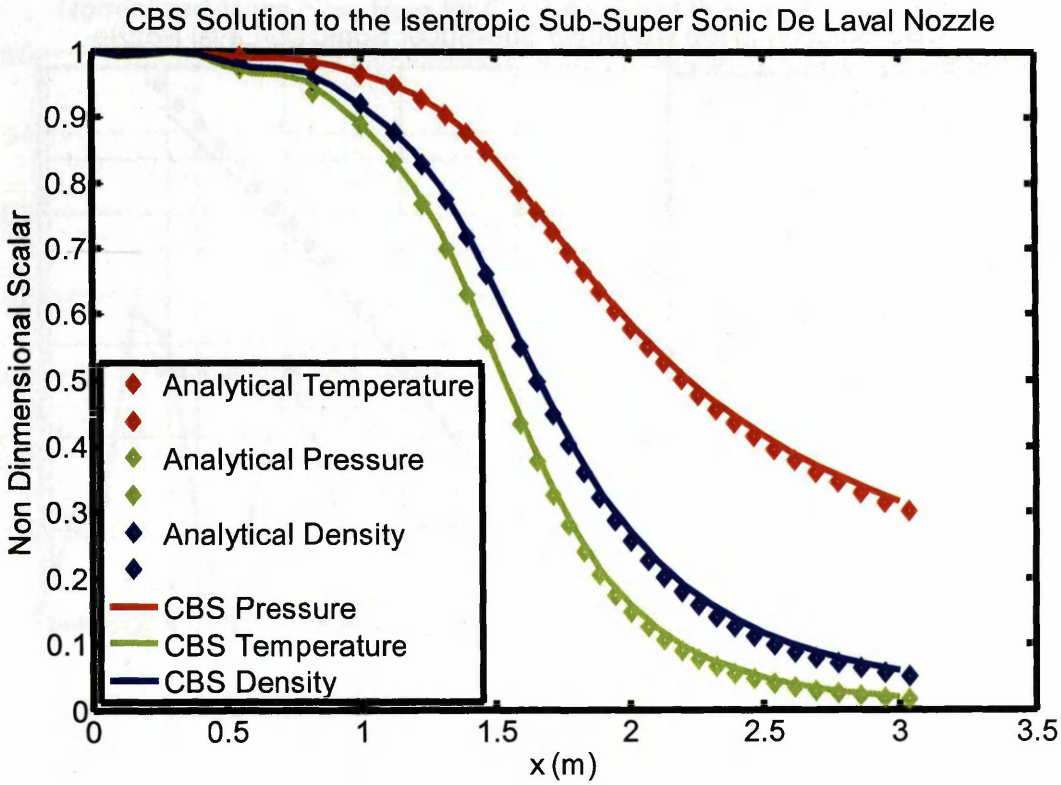

Figure 4:10 – T', P' and ρ' of air in a sub to Supersonic de Laval nozzle, comparing the CBS numerical results when solving the non-conservation equations (full line-) with the analytical solution (◊) for C_x=0.4.

The numerical profile for T', P' and ρ' using C_x=0.4, is superior in terms of accuracy with respect to the analytical solution when compared with the case of C_x =0.1 as seen in Figure 4:5. Oscillations at the inlet are present in the C_x =0.4 case but have been greatly reduced. The major result though is that after approximately 1m from the inlet the numerical solution shows excellent agreement with the analytical solution.

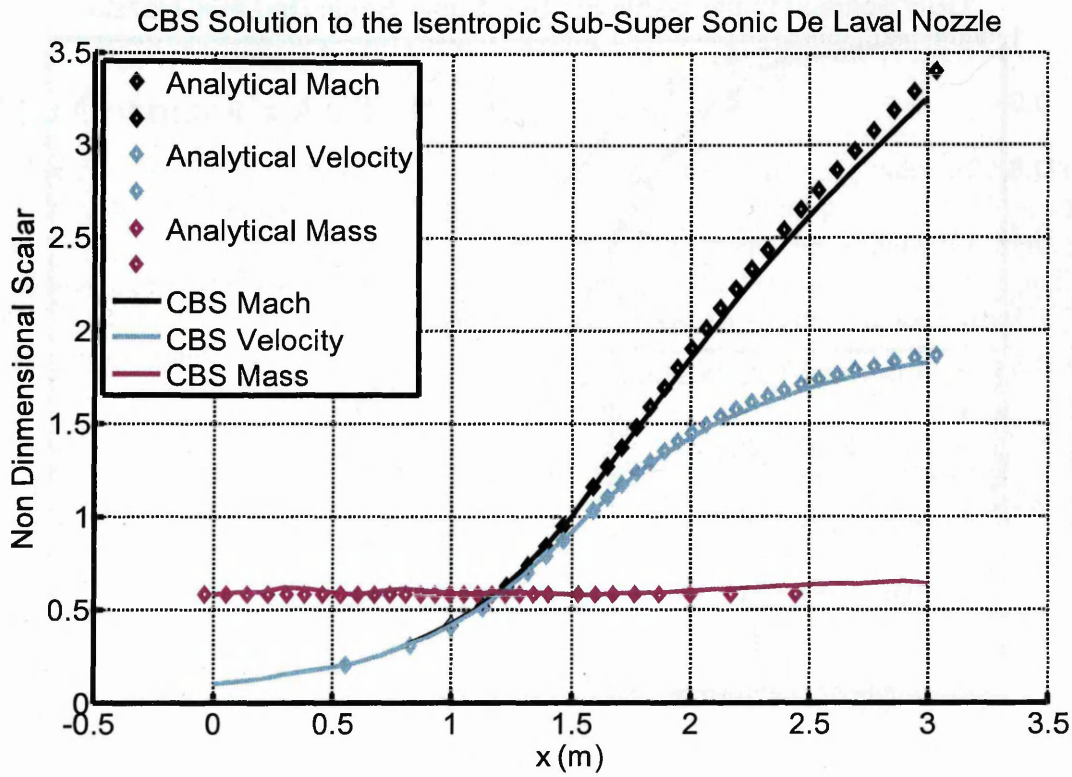

Figure 4:11 – V', M and $\dot{m}'$ of air in a sub to Supersonic de Laval nozzle, comparing the CBS numerical results when solving the non-conservation equations (full line-) with the analytical solution (◊).

When compared with the case of C_x =0.1 seen in Figure 4:6 the converged numerical profile for V', M and $\dot{m}'$ for C_x=0.4 as seen Figure 4:11, is superior in terms of accuracy. As seen in Figure 4:11 oscillations for $\dot{m}'$ at the inlet are present in this case of C_x =0.4, but have been greatly reduced when compared to the C_x =0.1 case - Figure 4:6. The major result though is that after approximately 1m to the nozzle exit the numerical solution shows excellent agreement with the analytical solution.

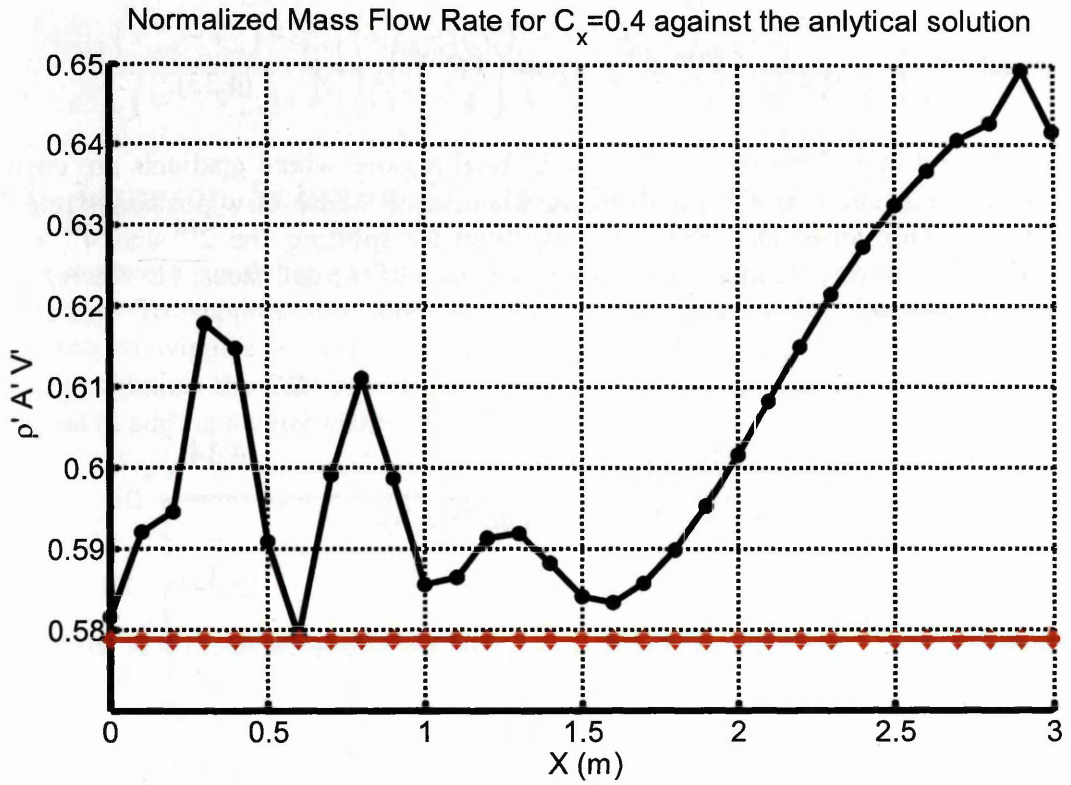

Figure 4:12 – $\dot{m}'$ of air in a sub to Supersonic de Laval nozzle, comparing the CBS numerical results when solving the non-conservation equations (full line-) with the analytical solution (◊).

The $\dot{m}'$ flow as computed from the CBS non-conservation form of the Euler equations is observed as the black line in Figure 4:12. The analytical solution is represented by the red line. It seems that MacCormack's artificial viscous term reacts to small scale oscillations and thus introduces dissipation that leads to source terms for mass flow. MacCormack's 2nd order numerical viscosity damps 4th order modes helping the stability of the algorithm, but it is not always enough to damp the higher order modes introduced by the limiting procedure.

4.7 Jameson, Schmidt & Turkel's AVT: Background

The next step in this case study is to employ Jameson, Schmidt & Turkel's artificial viscosity term (AVT) in the place of MacCormack's AVT in an attempt to drive down the absolute error as seen in Figure 4:8 to less than 1%. This is done because MacCormack's AVT is Δx^2 ordered even when no changes of the flow variables occur. However according to Jameson and Mavriplis [60], the Jameson, Schmidt and Turkel's AVT is of the order Δx^4 in smooth regions of the flow, preserving the second order accuracy of the numerical scheme employed i.e. the CBS algorithm.

4.7.1 Numerical Derivation

The energy equation, the intermediate momentum equation and the continuity equation are all coupled with an artificial viscous term (AVT) for the continuity equation.

$$\rho_i'^{m+1} = \rho_i'^{m} - \Delta t' \left(\rho_i'^{m} \left(\frac{\partial V'}{\partial x'} \right)_i^n + \rho_i'^{m} V_i'^{m+1} \left(\frac{\partial (\ln A')}{\partial x'} \right)_i + V_i'^{m+1} \left(\frac{\partial \rho'}{\partial x'} \right)_i^n \right) - (D)_i^n \quad (4.33)$$

The 2nd ordered artificial dissipation term is activated in local regions where gradients are changing rapidly such as shock waves and the 4th ordered term is activated where flow possesses relatively smooth property fields. This term, D_i , above is calculated by splitting the 2nd and 4th ordered derivatives into two 1st order and 3rd ordered derivatives, on each of the cell faces, i.e. the i+1/2 face and the i-1/2 face, respectively.

$$D_i^n = D_{i+1/2}^n - D_{i-1/2}^n$$

Let

$$D_{i+1/2}^n = \left(\varepsilon_{i+1/2}^{(2)} \left(\rho_{i+1}^n - \rho_i^n \right) - \varepsilon_{i+1/2}^{(4)} \left(\rho_{i+2}^n - 3\rho_{i+1}^n + 3\rho_i^n - \rho_{i-2}^n \right) \right) \quad (4.34)$$

where $\varepsilon_{i+1/2}^{(2)}$ is called the 2nd order weighting value. This is defined by

$$\varepsilon_{i+1/2}^{(2)} = k^{(2)} \max(\nu_i, \nu_{i+1}) \quad (4.35)$$

where ν_i is the pressure sensor "switch" and is always positive providing the domain is not in a vacuum. These are defined by

$$\nu_i = \frac{\left| P'_{i+1} - 2P'_i + P'_{i-1} \right|}{\left| P'_{i+1} \right| + \left| 2P'_i \right| + \left| P'_{i-1} \right|} \quad (4.36)$$

And

$$\varepsilon_{i+1/2}^{(4)} = \max(0, (k^{(4)} - \varepsilon_{i+1/2}^{(2)})) \quad (4.37)$$

If $\varepsilon_{i+1/2}^{(2)}$ is greater than $k^{(4)}$ then the $\varepsilon_{i+1/2}^{(4)}$ value is zero. In inviscid regions of the flow, the term, $\varepsilon_{i+1/2}^{(4)}$, should damps out higher order oscillations. The weighting parameters recommended by Jameson, Schmidt & Turkel's [105] for Supersonic applications are:

$$k^{(2)} = 0.25, k^{(4)} = 0.004$$

However a parametric study should be carried out, to empirically test, the values that best capture the case investigated, relative to the analytical solution. The full form of the artificial viscosity at node i may then be expressed as [105]. So for the CBS continuity equation D_i^n becomes.

$$D_i^n = \begin{pmatrix} \varepsilon_{i+1/2}^{(2)} \left(\rho_{i+1}'^{m} - \rho_i'^{m} \right) - \varepsilon_{i+1/2}^{(4)} \left(\rho_{i+2}'^{m} - 3\rho_{i+1}'^{m} + 3\rho_i'^{m} - \rho_{i-1}'^{m} \right) \\ -\varepsilon_{i-1/2}^{(2)} \left(\rho_i'^{m} - \rho_{i-1}'^{m} \right) + \varepsilon_{i-1/2}^{(4)} \left(\rho_{i+1}'^{m} - 3\rho_i'^{m} + 3\rho_{i-1}'^{m} - \rho_{i-2}'^{m} \right) \end{pmatrix} \quad (4.38)$$

The dissipative terms for the remaining equations are obtained by replacing ρ' by V' and T' respectively. For example D_i^n for the intermediate momentum equation becomes:

$$D_i^n = \begin{pmatrix} \varepsilon_{i+1/2}^{(2)} \left(V_{i+1}'^{m} - V_i'^{m} \right) - \varepsilon_{i+1/2}^{(4)} \left(V_{i+2}'^{m} - 3(V')_{i+1}^n + 3(V')_i^n - V_{i-1}'^{m} \right) \\ -\varepsilon_{i-1/2}^{(2)} \left(V_i'^{m} - V_{i-1}'^{m} \right) + \varepsilon_{i-1/2}^{(4)} \left(V_{i+1}'^{m} - 3(V')_i^n + 3(V')_{i-1}^n - V_{i-2}'^{m} \right) \end{pmatrix} \quad (4.39)$$

Note: The equation above has been slightly adjusted to allow 3rd ordered derivative to be calculated on node 30 i.e. using the following equation for node 30.

$$D_i^n = \begin{pmatrix} \varepsilon_{i+1/2}^{(2)}\left(V_{i+1}^n - V_i^n\right) - \varepsilon_{i+1/2}^{(4)}\left(V_{i+1}^n - 3(V')_i^n + 3(V')_{i-1}^n - V_{i-2}^n\right) \\ -\varepsilon_{i-1/2}^{(2)}\left(V_i^n - V_{i-1}^n\right) + \varepsilon_{i-1/2}^{(4)}\left(V_{i+1}^n - 3(V')_i^n + 3(V')_{i-1}^n - V_{i-2}^n\right) \end{pmatrix} \quad (4.40)$$

4.7.2 Jameson, Schmidt & Turkel's AVT: Results

Simulations were run using a safety factor of 0.095 and $k^{(2)}$ values and $k^{(4)}$ values of 0.25, 0.004 respectively. To suppress the tendency for odd and even point decoupling, and to prevent the appearance of wiggles in regions containing severe pressure gradients a second form of artificial viscosity augments the CBS algorithm. This is taken from Jameson, Schmidt & Turkel [105], and is equivalent to adding a combination of 2^{nd} and 4^{th} order terms.

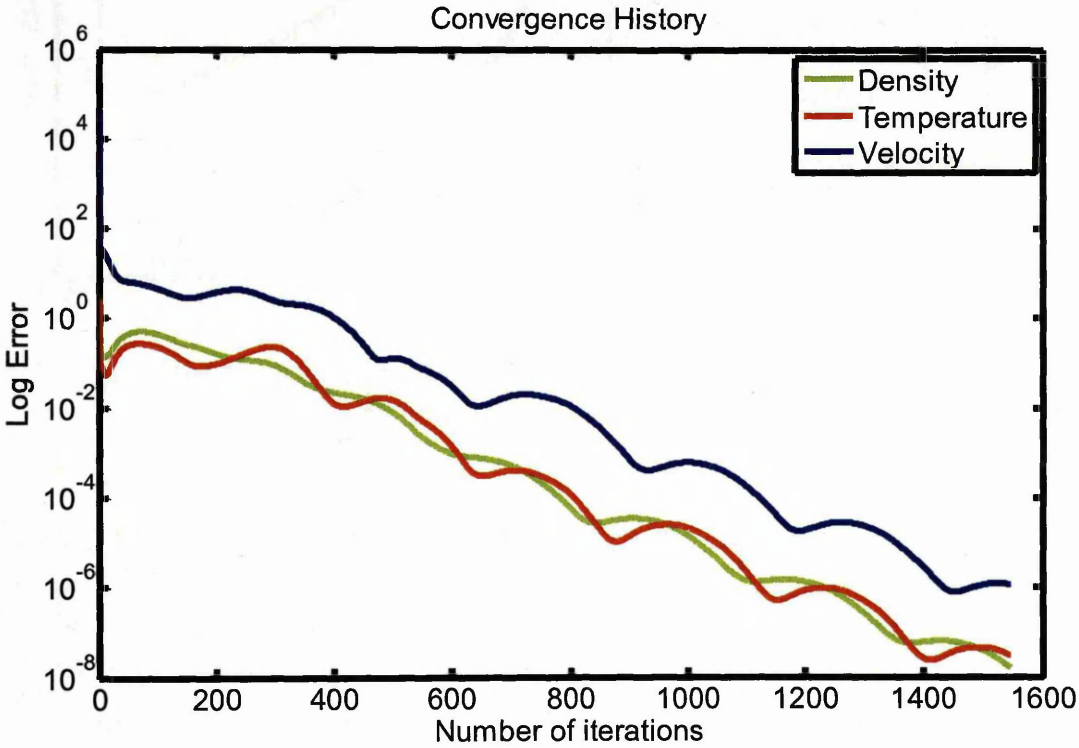

Figure 4:13-Convergence History for density, temperature and velocity for the Characteristic Based Split scheme.

Even with 31 discrete solution points the number of sweeps needed for convergence to a relative error of 10^{-6} is approximately 1,500. At this point the steady state solution has been achieved and the calculation can be stopped. Figure **4:13** shows that the numerical solution has converged rapidly when compared to Figure 4:4, and nearly dropping to machine zero which is due to Jameson, Schmidt & Turkel's AVT introducing a switch between 2^{nd} and 4^{th} ordered terms depending on the property fields. The 4^{th} ordered term leads to information being spread more rapidly which leads to less solver iteration required for steady state convergence, yet this occurs at a cost of increased computational time per iteration because of the subsequent lines of code.

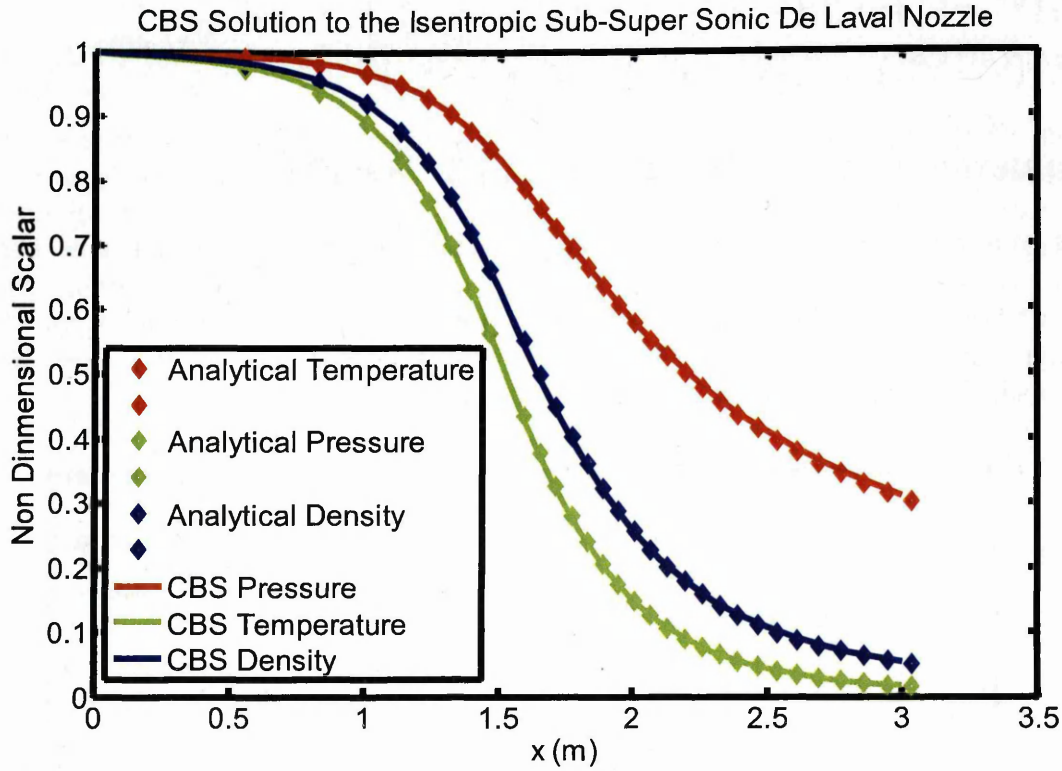

Figure 4:14 - Physical properties of air in a sub to Supersonic de Laval nozzle, comparing the CBS numerical results (full line-) with the analytical solution (◊).

The T', P' and ρ' as calculated by the CBS formulation, are presented in Figure 4:14. The theoretical results are given by the diamonds and the full lines are the CBS solution. These values are also normalized with the reference values for aesthetic reasons when plotting the results. The CBS finite difference code coupled with Jameson, Schmidt & Turkel's AVT solves the primitive variables. The CBS algorithm is successful in accurately identifying the monotonically decreasing property fields throughout the enclosed domain. In summary, Figure 4:14 shows that the CBS solution is in excellent agreement with the analytical solution, another promising indication of the capability of the CBS approach for the final application.

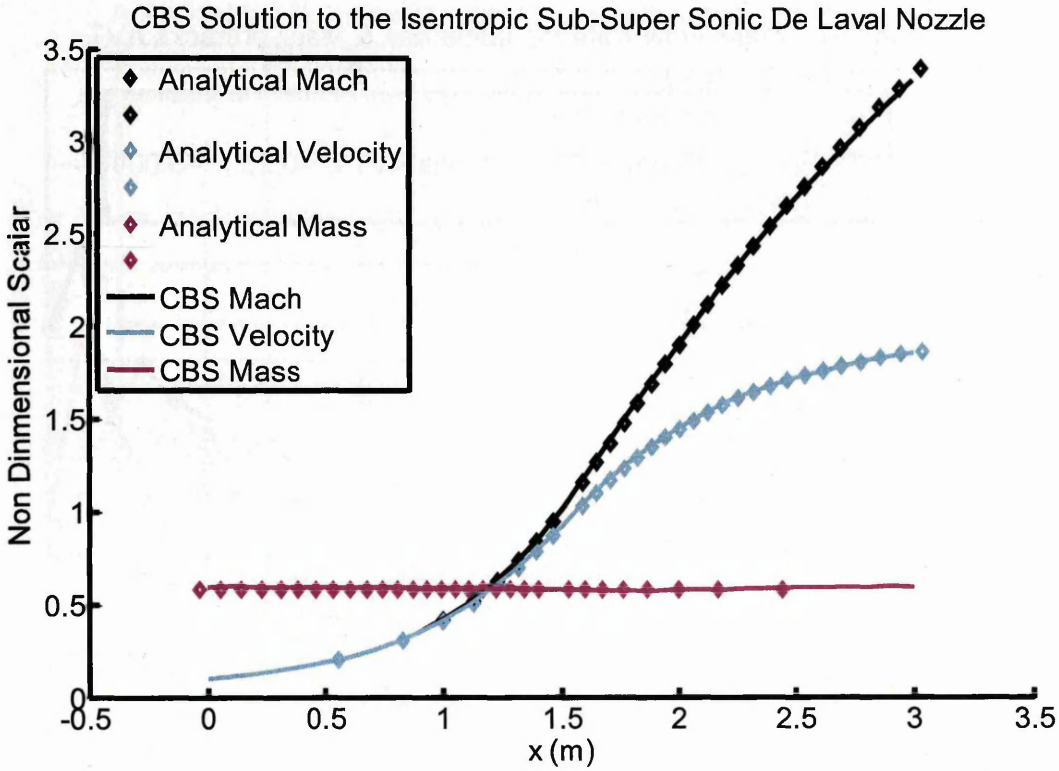

Figure 4:15 - Physical properties of air in a sub to Supersonic de Laval nozzle, comparing the CBS numerical results (full line- -) with the analytical solution (◊).

The V', M and $\dot{m}'$ as calculated by the CBS formulation to the non-conservation governing equations, presented in Figure 4:15. The theoretical results are given by the diamonds and the full lines the CBS solution. These values are normalized with the reference values so they can be displayed on the same plot. The CBS finite difference code coupled with Jameson, Schmidt & Turkel's AVT, solves the primitive variables Figure 4:15 shows that the CBS solution is in excellent agreement with the analytical solution, a promising indication of the capability of the CBS approach for the final application; solving 2D Hypersonic compressible flow over transpiration cooled components.

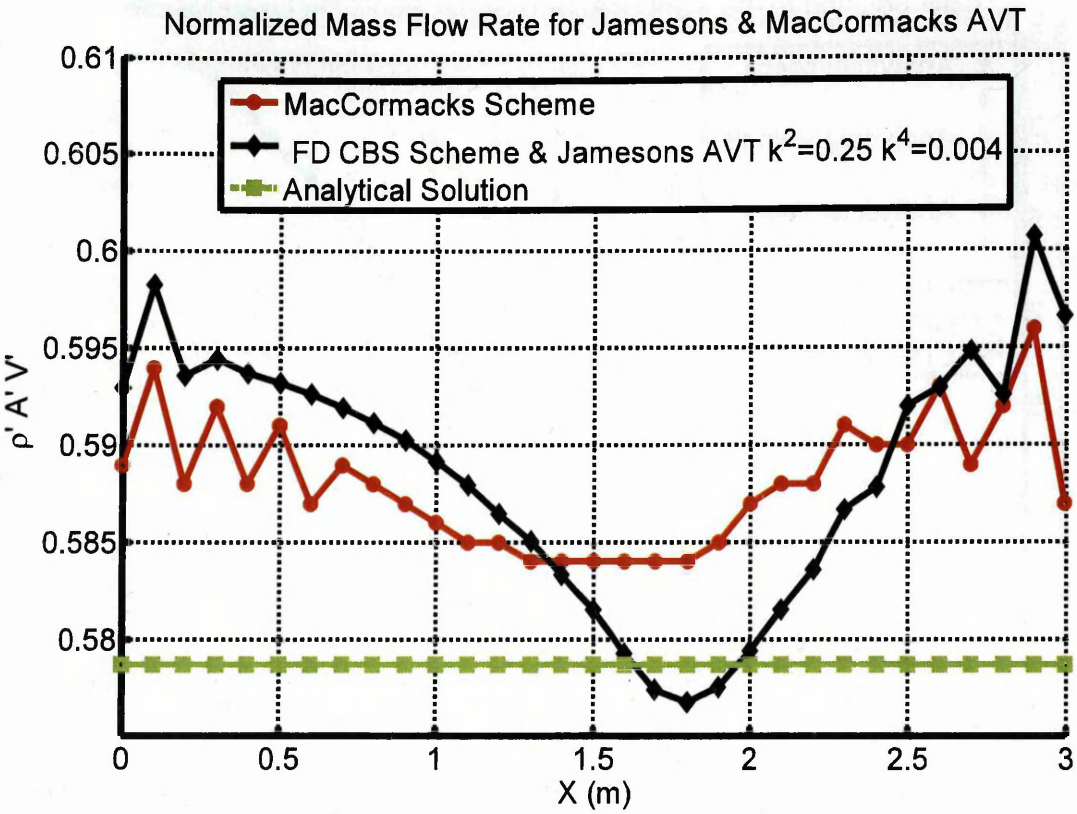

Figure 4:16 Mass flow Variations (magnified) for the CBS and MacCormack's scheme where the analytical solution is the green trend-line.

The $\dot{m}'$ as computed from the CBS non-conservation form of the Euler equations is observed as the full green line in Figure 4:16, whereas the red line is the MacCormack's predictor corrector solution. The analytical solution is represented by the blue line along the length of the nozzle. Both the CBS and MacCormack's profiles have a sizeable variation from the constant analytical non-dimensional value of 0.579, with some spurious oscillations observed at both the inlet and outlet. On a practical basis when the $\dot{m}'$ profile is plotted on the same scale as seen in Figure 4:14 these variations are not apparent and the mass flow appears constant. It seems that Jameson, Schmidt & Turkel's [105] artificial viscous terms react to small scale oscillations and thus introduces too much dissipation that leads to source terms for mass flow.

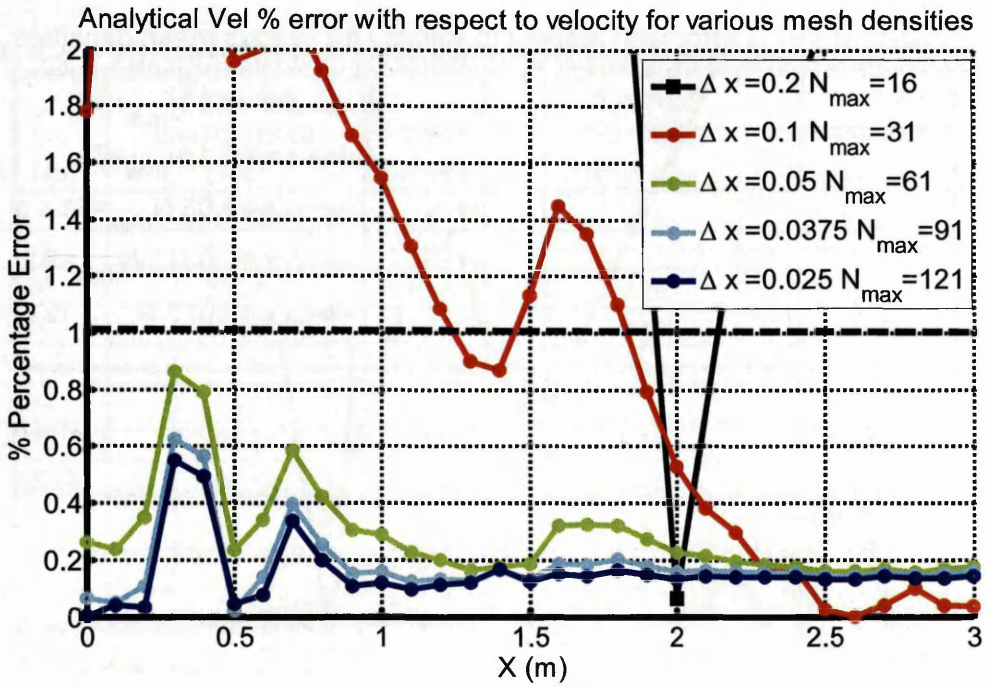

Figure 4:17 – Percentage error between the analytical normalized velocity value the CBS scheme and the MacCormack's predictor corrector scheme.

Figure 4:17 shows that the CBS algorithm after 1524 iterations with a $k^{(2)}= 0.25$ and $k^{(4)} =0.004$ succeeds as being accurate enough at capturing the simplified flow through most of the nozzle. The percentage error depicted in Figure 4:17 shows that the absolute error is below 1% after 1m of the nozzle inlet. The percentage error at the inlet shows that it is approx 1.1%, reducing to approx 1% by (X=1m). As mentioned earlier CFD solutions should display two ingredients of a discretisation technique; efficiency in generating a solution and accuracy of the solution with respect to the analytical solution. A consistency study was conducted to see if the numerical solution can converge onto the analytical solution further. Therefore to decide on the number of grid points or elements that should be applied to this problem, five more computational runs were conducted with incremental increases in the number of grid points in the solution domain. The percentage error with respect to the analytical solution was tracked and compared with five different grids.

4.7.3 Grid Independence

The matter of grid independence is a serious consideration in CFD and this section will seek to address, grid independence for this benchmark case. According to Anderson [15], if a first CFD grid is too coarse then the solution will not be an accurate enough approximation to the analytical solution. Therefore finer grids need to be employed in order to resolve the property fields with respect to the analytical solution and also to check that the numerical solution is not a function of the number of grid points - an untenable result. Various runs using different grid density will be done to establish grid independence.

The numbers of nodes were approximately doubled from 16 to 31 to 61 to 91 to 121. After convergence the percentage error with respect to the analytical velocity field at the same 31 stations i.e. 0m- 0.1m- 0.2m- 0.3m- 0.4m.....3.1m was tracked. The response for a CFD technique after each increase in the grid density should be a reduction in the absolute error until grid independence where no reduction in the absolute error is practically observed.

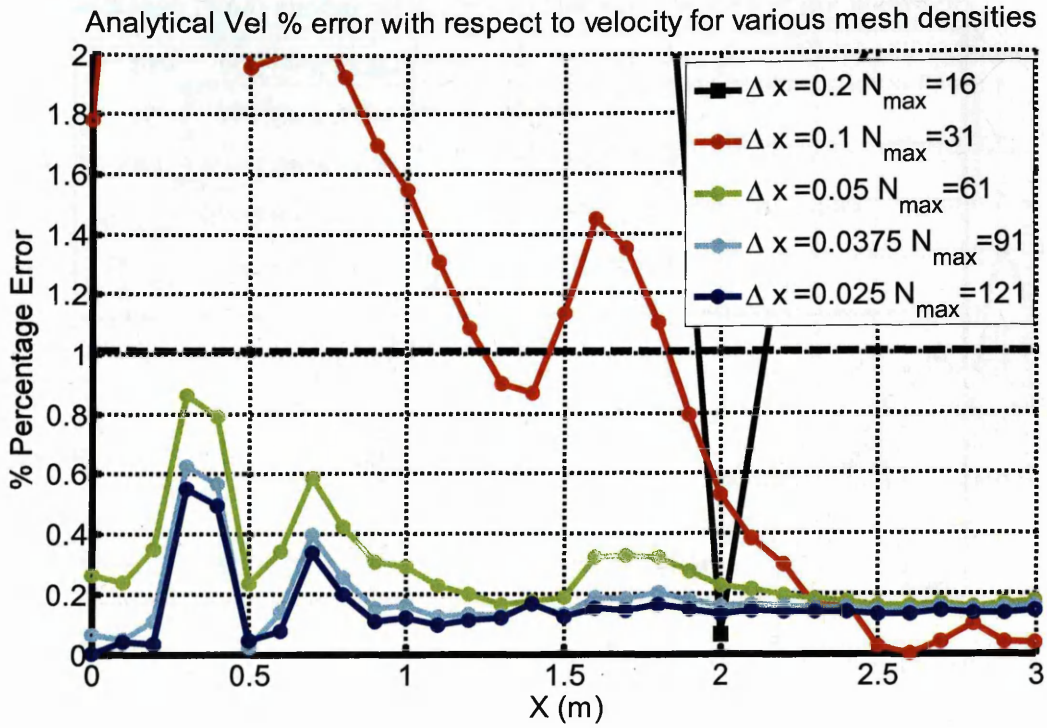

Figure 4:18 – Grid independence plot: Each line represents a steady state solution to the flow field when varying the number of grid points (legend).

Figure 4:18 shows the absolute errors for steady state solutions for various mesh densities. The steady state solution were obtained with a $k^{(2)}= 0.25$ and $k^{(4)} =0.004$ and a C number of 0.095. The finer grids of 61 nodes and above are accurate enough at capturing the flow through the nozzle. The percentage error for 61 nodes shows that the absolute error is below 1% (the green line) for the entire domain. As the grid density increases to 91 and 121 nodes the percentage error decreases, proof that the CBS procedure is grid independent.

Table 4-5 – The table displays the convergence behaviour to steady state for each grid.

Nodes	Δx (m)	Time for convergence (sec)	Number of Sweeps	Average absolute error (%)	Percentage decrease in absolute error	Memory used MB
16	0.2	22.92	6712	2.50	N/A	452.31
31	0.1	11.69	1555	0.56	1.95	452.57
61	0.05	22.20	3171	0.15	0.39	454.63
91	0.0325	85.06	4808	0.12	0.03	456.77
121	0.025	116.42	6488	0.10	0.00	461.23
151	0.02	195.57	8769	0.10	0.00	469.15
241	0.0125	720.14	14267	0.10	0.00	565.23
481	0.00613	5749.92	29032	0.10	0.00	584.23

The major trend from Table 4-5, is as Δx, the grid spacing decreases the subsequent error as calculated from equation (4.32) with respect to the analytical velocity decreases. Figure 4:19 verifies that the CBS scheme is consistent, which means that as the grid spacing is reduced between grid points, the numerical solution approaches the analytical solution.

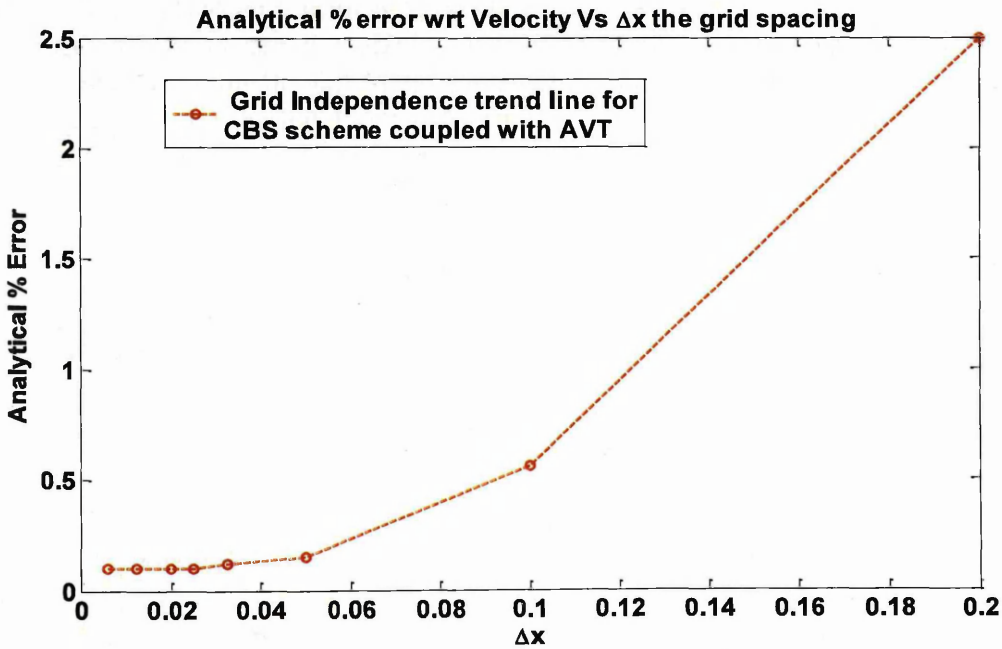

Figure 4:19- Grid independence study showing the relationship between the grid spacing and the average % analytical error.

4.8 Benchmark Example 2: Choked Nozzle

The second benchmark illustrates the application of shock capturing for the CBS algorithm. To evaluate this capability a flow problem with a known analytical solution is solved. Understanding shock capturing for 1-D Hyperbolic problems is the main attraction for tackling this case. It is essential that a working methodology is established for shock capturing so that multidimensional Hyperbolic problems are solved, such as the final application - modelling transpiration cooling through porous media in Hypersonic flows.

For Choked flow in a nozzle, a stationary normal shock wave is present in the divergent section of the nozzle. This will occur, for instance, in a convergent-divergent channel when the pressure differences between the inlet and the outlet of the nozzle are significantly large. The flow is accelerated to sonic speed in the throat and further accelerated in the divergent section to Supersonic velocities. The Supersonic region is terminated by a strong shock which brings the flow down to Subsonic velocities before the nozzle's outlet.

Anderson, [15], argues that the non conservation form of the governing equations are inadequate at modeling normal shocks. Therefore the conservation variables - (ρ, ρV, ρE) - are used in place of the primitive variables - (ρ, V, T). To solve these variables, (ρ, ρV, ρE) at the nodal points, this section will examine the conservation form of the equations. The conservation form of the governing equations has been written in MATLAB R2008a, where the geometry of the nozzle is that shown in Figure 4:1 and the area and boundary conditions are given in the following Section.

4.8.1 Theoretical Background: The Conservation Equations

As mentioned a shock wave is present within the solution domain for Choked nozzle flows, which make, the non-conservation quasi-1D Euler equations (4.18)-(4.21) inappropriate when capturing shock fronts. Anderson [15], also observes that *"the conservation form simply does a better job of conserving mass"*, which means that the conservation form yields a better mass flow distribution throughout the solution domain. It is important to stress that this chapter is comparing the performance of the CBS method in conservative form for the Choked nozzle problem with Anderson's [15] solver, and therefore the conservation form of the equations are now solved in place of the primitive variables.

4.8.2 The Finite Difference Conservation Approach

From the conservation equations - the 3D Euler system of equations - can be manipulated into the following form for quasi 1-D nozzle flows. The governing equations are taken from the work of Anderson ([15], page 336) on Choked nozzle flows and is repeated below.

The 1-D nozzle continuity equation in conservation form is:

$$\frac{\partial(\rho' A')}{\partial t'}+\frac{\partial(\rho' A' V')}{\partial x'}=0 \qquad (4.41)$$

The 1-D nozzle momentum equation in conservation form is:

$$\frac{\partial(\rho' A' \mathrm{V}')}{\partial t'}+\frac{\partial(\rho' A' V'^2+(1/\gamma)\mathrm{P}'\mathrm{A}')}{\partial x'}=\frac{1}{\gamma}P\frac{\partial A'}{\partial x'} \qquad (4.42)$$

The 1-D nozzle energy equation in conservation form is:

$$\frac{\partial\left[\rho' A'\left(T'/(\gamma-1)+\gamma/2(V'^2)\right)\right]}{\partial t'}+\frac{\partial\left[\rho' A' V'\left(T'/(\gamma-1)+\gamma/2(V'^2)\right)+P' A' V'\right]}{\partial x'}=0 \qquad (4.43)$$

Re-writing the above equations in terms of the conservation vectors U_1, U_2 and U_3 and the flux vectors F_1,F_2 and F_3 as demonstrated by Anderson [15], yields.

Equation (4.41) can be written as.

$$\frac{\partial U_1}{\partial t'} = -\frac{\partial F_1}{\partial x'} \tag{4.44}$$

Equation (4.42) can be written as.

$$\frac{\partial U_2}{\partial t'} = -\frac{\partial F_2}{\partial x'} + J \tag{4.45}$$

Where

$$J = \frac{1}{\gamma} P' \frac{\partial (A')}{\partial x'} \tag{4.46}$$

And finally equation (4.43) becomes

$$\frac{\partial U_3}{\partial t'} = -\frac{\partial F_3}{\partial x'} \tag{4.47}$$

Where

$$U_1 = \rho' A' \tag{4.48}$$

$$U_2 = \rho' A' V' \tag{4.49}$$

$$U_3 = \rho' A' \left(\frac{T'}{\gamma - 1} + \frac{\gamma}{2} V'^2 \right) \tag{4.50}$$

$$F_1 = \rho' A' V' \tag{4.51}$$

$$F_2 = \rho' A' V'^2 + \frac{A' P'}{\gamma} \tag{4.52}$$

$$F_3 = \rho' A' V' \left(\frac{T'}{\gamma - 1} + \frac{\gamma}{2} V'^2 \right) + P' A' V' \tag{4.53}$$

4.8.3 Computational Procedure for the Conservation Equations

By re-writing the governing conservation equations above for quasi 1-D flow they can be implemented into the framework of the CBS algorithm, where the non-dimensional notation ' is now dropped for writing the equations. For every step described below each step is applied to all the interior nodes in a sweep of the grid or otherwise known as an iteration. After this the boundary conditions as seen in step 6 are computed. Then the sequential computational procedure is repeated by going to step 1). This CBS method to solve the conservation system of equations was implemented in MATLAB R2008a and the simulations run within dual core laptop with 2046MB of RAM:

1) Calculate the local time step from (4.17) Where C is the Courant number and depending on the problem is usually C< 0.5
2) Calculate the derivatives for all flux variables $\left(\partial F_1/\partial x\right)_i^n, \left(\partial F_2/\partial x\right)_i^n$ and $\left(\partial F_3/\partial x\right)_i^n$ and J at all the interior nodes from i=2 to i=30 and

$$J_i^n = \frac{1}{\gamma}(P)_i^n \frac{\ln(A)_{i+1} - \ln(A)_{i-1}}{2\Delta x} \tag{4.54}$$

3) The intermediate momentum variable U_2^* is computed from i=2,3,4.....N_{max}-1

$$\left(U_2^*\right)_i = \left(U_2\right)_i^n - \Delta t_i \left(\frac{\partial F_2}{\partial x}\right)_i^n + \frac{\Delta t_i^{\,2}}{2} V_i^n \left(\frac{\partial^2 F_2}{\partial x^2}\right)_i^n \tag{4.55}$$

4) The corrected momentum variable, U_2 is computed from i=2,3,4.....N_{max}-1

$$\left(U_2\right)_i^{n+1} = \left(U_2^*\right)_i + \Delta t_i \, (J)_i^n - \frac{\Delta t_i^2}{2} V_i^n \left(\frac{\partial J}{\partial x}\right)_i^n \tag{4.56}$$

5) The inviscid flux variable, F_1 is evaluated at the next iterative level (n+1)

$$\left(F_1\right)_i^{n+1} = \left(U_2\right)_i^{n+1} \tag{4.57}$$

6) The inviscid flux variable, F_1^{n+1} is differenced to evaluate the conservation variable U_1

$$\left(U_1\right)_i^{n+1} = \left(U_1\right)_i^n - \Delta t_i \left(\frac{\partial F_1}{\partial x}\right)_i^{n+1} \tag{4.58}$$

7) The conservation variable U_3 , is solved from i=2,3,4.....N_{max}-1 to completing the system of equations

$$\left(U_3\right)_i^{n+1} = \left(U_3\right)_i^n - \Delta t \left(\frac{\partial F_3}{\partial x}\right)_i^n + \frac{\Delta t_i^2}{2} V_i^n \left(\frac{\partial^2 F_3}{\partial x^2}\right)_i^n \tag{4.59}$$

8) Decouple the primitive variables -including the pressure- from the conservation variables and calculate the flux variables from conservation variables

$$\left(\rho\right)_i^{n+1} = \left(U_1\right)_i^{n+1} / A_i \tag{4.60}$$

$$\left(V\right)_i^{n+1} = \left(U_2\right)_i^{n+1} / \rho_i^{n+1} A_i \tag{4.61}$$

$$\left(T\right)_i^{n+1} = (\gamma - 1)\left(\frac{1}{\left(\rho^{n+1} A\right)_i}\left(U_3\right)_i^{n+1} - \frac{\gamma}{2}\left\{\left(V\right)_i^{n+1}\right\}^2\right) \tag{4.62}$$

$$\left(F_1\right)_i^{n+1} = \left(U_2\right)_i^{n+1} \tag{4.63}$$

$$\left(F_2\right)_i^{n+1} = \frac{\left\{\left(U_2\right)_i^{n+1}\right\}^2}{\left(U_1\right)_i^{n+1}} + \frac{\left(AP\right)_i^{n+1}}{\gamma} \tag{4.64}$$

$$\left(F_3\right)_i^{n+1} = \left(\frac{U_2}{U_1}\right)_i^{n+1} \left(U_3\right)_i^{n+1} + \left(P\right)_i^{n+1} \left(\frac{\left(U_2\right)_i^{n+1}}{\left(\rho\right)_i^{n+1}}\right) \tag{4.65}$$

9) Check convergence using (4.22) by sensing whether the relative error is below the agreed tolerance of 10^{-6} or the number of sweeps is below the maximum sweep number stipulated by the user I_{Max}. Sum the relative density error from i=1,2,3,4.....N_{max}.

10) If convergence has been achieved exit the procedure and display results otherwise begin computational sweep as described by going back to step 1)

General Remarks

1) Artificial viscous terms were deemed to be necessary to extend the stability region of the CBS algorithm.
2) Jameson, Schmidt & Turkel's 2nd and 4th ordered artificial viscous term (AVT) was also coupled with the CBS algorithm where it was used as an explicit stabilizing source term. Unreasonable results with respect to the analytical solution and even divergence is encountered when the CBS algorithm is not coupled with any artificial viscosity terms.
3) The main difference from the non-conservation sequential procedure seen in section 4.3.1 to this sequential procedure seen in section 4.7.3 is that the conservation variables U_1, U_2 and U_3 and the flux vectors F_1, F_2 and F_3 are approximated on cell faces, and finally decoupled at the nodes after an iterative step.

4.8.4 Choked de Laval Nozzle: Analytical Solution

Consider how the mass flow through the convergent divergent nozzle seen in Figure 4:1 changes as the exit pressure, P_e, ***decreases***, initially the flow velocity in the throat ***increases***, meaning the mass flow ***increases***. The mass flow $\dot{m}$, is experimentally measured at the throat by $\dot{m} = \rho_t V_t A_t$, but as Anderson [9] states that as the exit pressure, P_e, decreases, V_t will increase and ρ_t decrease. But the ***percentage increase*** in V_t is much greater than the ***percentage decrease*** in ρ_t. As a result, $\dot{m}$ increases, as sketched in Figure 4:20. When $P=P_{e,3}$ sonic flow is achieved at the throat meaning that the mass flow is calculated using sonic values for V and ρ i.e. $\dot{m} = \rho_t V_t A_t = \rho^* V^* A^*$. Anderson [9] states that if P_e is further reduced below $P_{e,3}$ then interestingly the conditions at the throat remain unchanged. The mass flow rate, remains constant as P_e reduces below $P_{e,3}$. Thus the isentropic flow assumption, mans the Mach number at the throat ***cannot exceed 1***. In words as P_e is reduced below $P_{e,3}$, M will remain equal to 1 at the throat. This relationship has been illustrated in Figure 4:20.

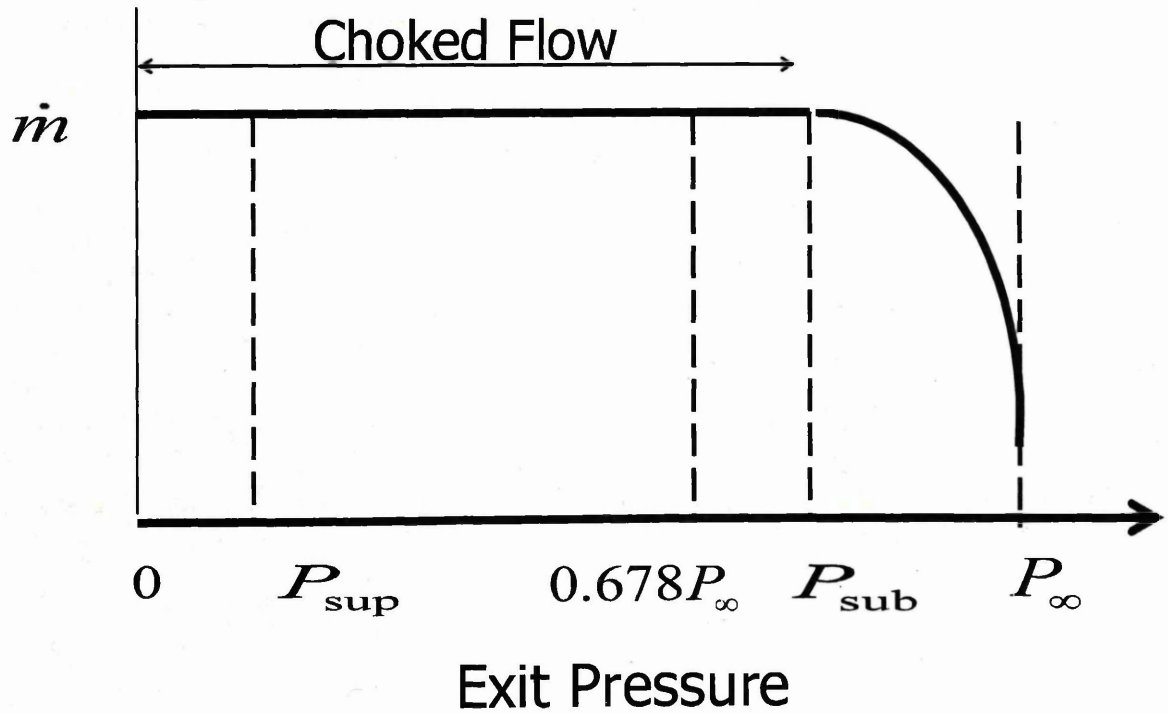

Figure 4:20 Variation of mass flow, $\dot{m}$, against exit pressure: illustration of Choked flow taken from Anderson [9].

In a sense the flow at the throat as well as the flow upstream of the throat becomes "frozen". Once the flow becomes sonic at the throat, the characteristics cannot work their way upstream of the throat. Hence the flow in the convergent section of the nozzle no longer communicates with the exit pressure and has no way of knowing that the exit pressure continues to decrease to below P_{sub}. As a result this situation is denoted Choked flow.

The analytical solution to this Choked de Laval nozzle is illustrated in Figure 4:21, this analytical solution will be further described now. The gas velocity in the divergent section of the nozzle in Figure 24 is purely Supersonic and isentropic from the throat to slightly upstream of the shock. Through the normal shock wave the flow goes from Supersonic to Subsonic velocities and furthermore the flow's entropy has increased. Therefore the assumption of isentropic flow in this small region of the nozzle has been violated. Downstream of the shock, Subsonic gas flow is maintained to the exit and isentropic flow is recovered in this nozzle section x>2.1m. Anderson [15], states that an exit pressure ratio between the free-stream pressure and the outlet is 0.6784, to occasion a shock wave, at a location of 2.1m from the nozzle's entrance. Where the Mach numbers pre/post-shock and the pressure ratio's are taken from page 266 [15], as follows:

$$M_1 = 2.07$$

$$M_2 = 0.566$$

$$\frac{P_2}{P_1} = 4.83$$

Here the subscript 1 indicates pre shock values and the subscript 2 indicates post shock values.
To determine the upstream Mach number at the shock location 2.1m, equation (4.66) was solved to determine the value of M at each station, i: for M, using a simple root finding method. This root finding method was the fzero function taken from the functions section in MATLAB R2008a Inc, [140]. The fzero command algorithm, was introduced by Dekker and it utilizes a combination of bisection, secant, and inverse quadratic interpolation methods.

$$0 = \frac{1}{M^2}\left[\frac{2}{1-\gamma}\left(1+\frac{1-\gamma}{2}M^2\right)\right]^{\frac{\gamma+1}{\gamma-1}} - \frac{A}{A^*} \qquad (4.66)$$

Down stream of the shock, x>2.1, A* =1 in equation (4.66) is replaced by $A_2^* > A^*$. The same root finding method, with a different denominator value for the second term on the right hand side of the equation, is applied to calculate M at each station, i.

$$0 = \frac{1}{M^2}\left[\frac{2}{1-\gamma}\left(1+\frac{1-\gamma}{2}M^2\right)\right]^{\frac{\gamma+1}{\gamma-1}} - \frac{A}{A_2^*} \qquad (4.67)$$

After evaluating M then it is then possible to calculate the ρ' P' , and T' profile along the nozzle from (4.14), (4.15) and (4.16):

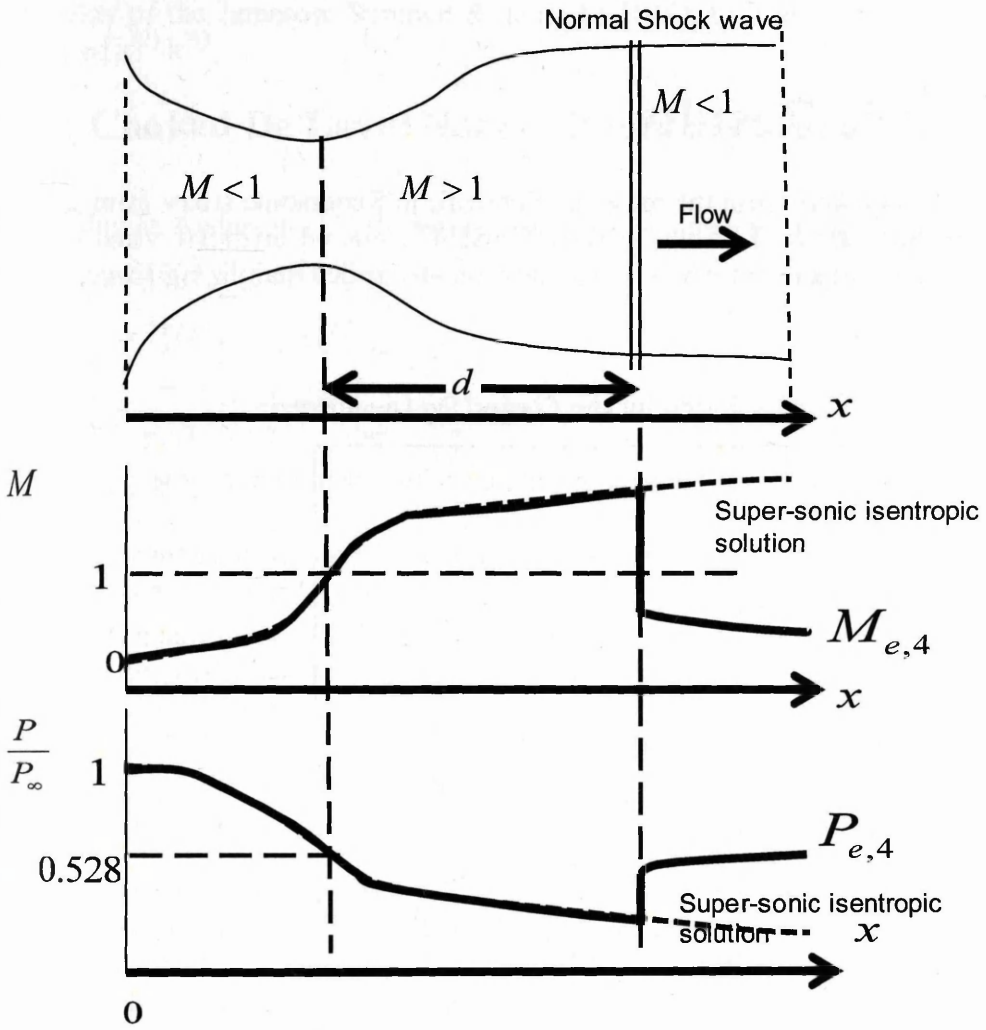

Figure 4:21-Supersonic nozzle flow with a normal shock inside the nozzle taken from Anderson [9].

As seen in Figure 4:21 above the shock introduces a discontinuous jump in the ρ', V', P' and T' fields flow variables Such a discontinuous change always has the potential to introduce oscillations into the numerical solution, oscillations which according to Jameson et al.[105] are virtually eliminated by introducing some explicit form of artificial viscosity. It is the experience of the author that the addition of Jameson, Schmidt & Turkel's [105] Artificial Viscosity Terms (AVT) to the scheme stabilizes Supersonic problems containing shocks. Moreover in smooth regions of the flow, the scheme is not sufficiently dissipative unless the fourth differences are included, with the result that calculations will generally not converge to a completely steady state. It is mentioned in Jameson, Schmidt & Turkel's [105] that after they have reached an almost steady state, oscillations of very low amplitude continue indefinitely. These appear to be induced by reflections from the boundaries of the computational domain.

4.9 Choked Nozzle Results

The CFL safety factor, C, has been kept from the previous Subsonic to Supersonic study from section 4.5.2 at C=0.095. Jameson, Schmidt & Turkel's [105] 2nd and 4th ordered artificial viscous term (AVT) was coupled with the CBS algorithm where it was used as an explicit stabilizing source term, and will be used here.

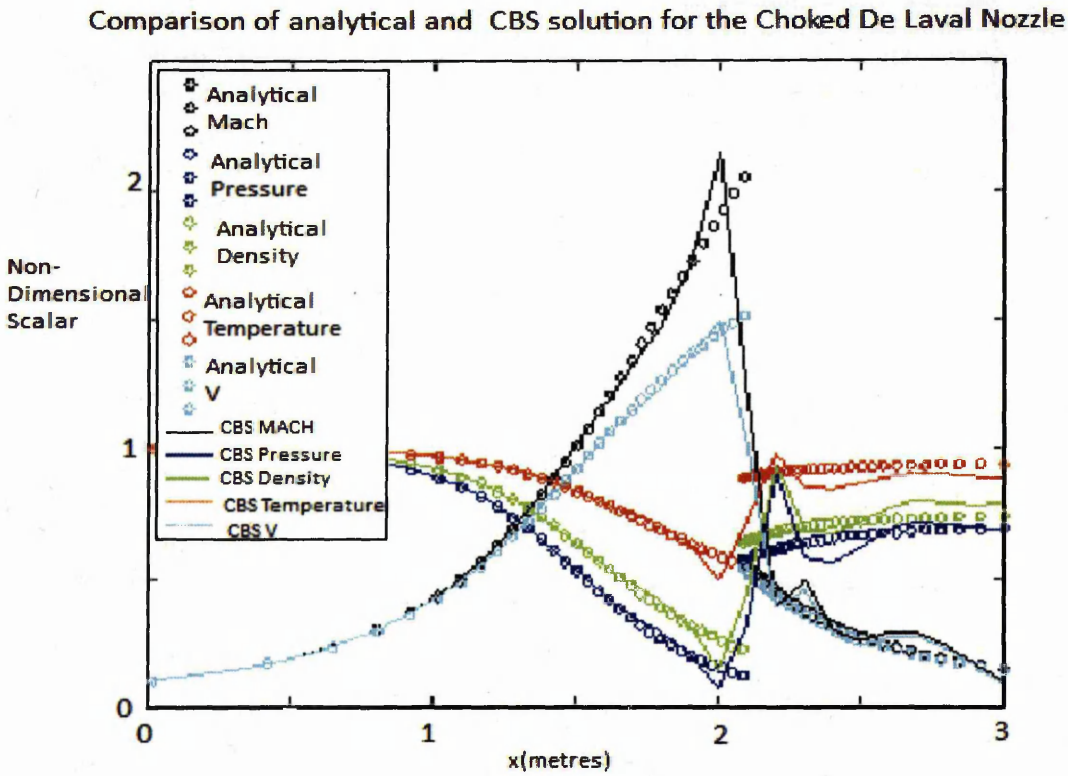

Figure 4:22-The Mach, P, ρ, T and V profiles of air in a Choked de Laval nozzle, comparing the CBS techniques numerical results (solid line -) with the analytical solution (○) Artificial viscosity has not been tuned.

The red, blue, green and light blue lines in Figure 4:22 show the first attempted converged solution using the CBS algorithm for the conservation equations given in (4.54)-(4.65). The CBS algorithm successfully captures the physical behavior at a distance before the shock location is reached (x<1.7m). However as exhibited in Figure 4:22 the T', ρ' and P' profiles display undershoots pre shock and overshoots post shock. Conversely in Figure 4:22, the Mach number and V' displays overshoots pre shock and undershoots post shock, which means failure to identify the actual analytical values in proximity of the shock.

The solution of this problem should display two requirements of a discretisation technique; firstly efficiency of generating the solution and secondly accuracy of the converged CBS solution with respect to the analytical solution. This will require a solution where the tuned Jameson, Schmidt & Turkel's [105] AVT supplies enough dissipation to damp out those undershoots and overshoots as seen in Figure 4:22, but not enough to irrevocably change the nature of the physical flow. Thus it was decided that a parametric study should be carried out. A parametric study intended to discern the

capability of the Jameson, Schmidt & Turkel's [105] AVT at capturing shocks when using different values of $k^{(2)}$ $k^{(4)}$.

4.9.1 Choked De Laval Nozzle: Boundary Conditions

According to Anderson [15] the boundary conditions may be prescribed as

$$(U_1)_{N_{max}} = 2(U_1)_{N_{max}-1} - (U_1)_{N_{max}-2} \quad (4.68)$$

$$(U_2)_{N_{max}} = 2(U_2)_{N_{max}-1} - (U_2)_{N_{max}-2} \quad (4.69)$$

$$(U_3)_{N_{max}} = \frac{P'}{\gamma - 1} A' + \frac{\gamma}{2}(U_2)_{N_{max}} V'_{N_{max}} \quad (4.70)$$

where N_{max} is the total number of the nodes in the computational domain

For the nozzle seen in Figure 4:1, shows an arbitrary pressure value at the nozzle outlet of between P'=0.02 and P'=0.92. Anderson ([15], page 358) uses a pressure value of 0.6784. Anderson ([15], page 358) manipulated the algebra so that this exit pressure ratio of 0.6784 is couched into the conservation variables, U_3, as seen above in the boundary conditions (4.68), (4.69) and (4.70). To compare with his results the same is done here.

Jameson, Schmidt & Turkel's Artificial Viscosity Terms

There is a need to prevent the appearance of for odd and even point decoupling in regions containing severe pressure gradients for instance in the neighbourhood of shock waves, by using a second form of artificial viscosity terms (AVT) to augment the CBS algorithm. Jameson, Schmidt & Turkel's [105] AVT is equivalent to adding a 2nd and 4th order term. The energy equation, the intermediate momentum equation and finally the continuity equation are all augmented with an artificial viscous term:

$$\left(U_1\right)_i^{n+1} = \left(U_1\right)_i^n - \Delta t_i \left(\frac{\partial F_1}{\partial x}\right)_i^{n+1} - D_i^n \quad (4.71)$$

Let

$$D_i^n = D_{i+1/2}^n - D_{i-1/2}^n$$

For the continuity equation $D_{i+1/2}^n$ becomes

$$D_{i+1/2}^n = \left(\varepsilon_{i+1/2}^{(2)}\left(U_{1i+1}^n - U_{1i,j}^n\right) - \varepsilon_{i+1/2}^{(4)}\left(U_{1i+2}^n - 3U_{1i+1}^n + 3U_{1i}^n - U_{1i-2}^n\right)\right) \quad (4.72)$$

where $\varepsilon_{i+1/2}^{(2)}$ is called the 2nd order weighting value. This is defined by

$$\varepsilon_{i+1/2}^{(2)} = k^{(2)} \max(\nu_i, \nu_{i+1})$$

where ν_i is the pressure sensor "switch" and is always positive providing the domain is not in a vacuum.

$$\nu_i = \frac{\left|P'_{i+1} - 2P'_i + P'_{i-1}\right|}{\left|P'_{i+1}\right| + \left|2P'_i\right| + \left|P'_{i-1}\right|}$$

And

$$\varepsilon_{i+1/2}^{(4)} = \max(0, (k^{(4)} - \varepsilon_{i+1/2}^{(2)}))$$

The weighting parameters for Supersonic applications as recommended by Jameson, Schmidt & Turkel's [105] are,

$$k^{(2)} = 0.25, k^{(4)} = 0.004$$

However a parametric study should be carried out, to empirically test, the values that best capture the case investigated, relative to the analytical solution. The full form of the artificial viscosity at node i may then be expressed as [105]:

$$D_i^n = \begin{pmatrix} \varepsilon_{i+1/2}^{(2)}\left((U_1)_{i+1}^n - (U_1)_i^n\right) - \varepsilon_{i+1/2}^{(4)}\left((U_1)_{i+2}^n - 3(U_1)_{i+1}^n + 3(U_1)_i^n - (U_1)_{i-1}^n\right) \\ -\varepsilon_{i-1/2}^{(2)}\left((U_1)_i^n - (U_1)_{i-1}^n\right) + \varepsilon_{i-1/2}^{(4)}\left((U_1)_{i+1}^n - 3(U_1)_i^n + 3(U_1)_{i-1}^n - (U_1)_{i-2}^n\right) \end{pmatrix} \quad (4.73)$$

U_1 in equation (4.72) is replaced by U_2 and U_3 in equation (4.74) and equation (4.75) respectively.

$$\left(U_2^*\right)_i = \left(U_2\right)_i^n - \Delta t_i \left(\frac{\partial F_2}{\partial x}\right)_i^n + \frac{\Delta t_i^{\,2}}{2} V_i^n \left(\frac{\partial^2 F_2}{\partial x^2}\right)_i^n - D_i^n \quad (4.74)$$

$$\left(U_3\right)_i^{n+1} = \left(U_3\right)_i^n - \Delta t \left(\frac{\partial F_3}{\partial x}\right)_i^n + \frac{\Delta t_i^2}{2} V_i^n \left(\frac{\partial^2 F_3}{\partial x^2}\right)_i^n - D_i^n \quad (4.75)$$

It has been found that in smooth regions of the flow, the scheme is not sufficiently dissipative unless the fourth differences are included, with the results that calculations will generally not converge to a completely steady state. After they have generally reached an almost steady state, oscillations of very low amplitude continue indefinitely. In near shock waves it has been found that the fourth differences tend to induce overshoots, and therefore they are switched off by sensing when the term $(\varepsilon^{(2)}\text{-}k^{(4)})$ is less than zero in equation (4.37).

4.9.2 Parametric Study: Jameson, Schmidt & Turkel's AVT

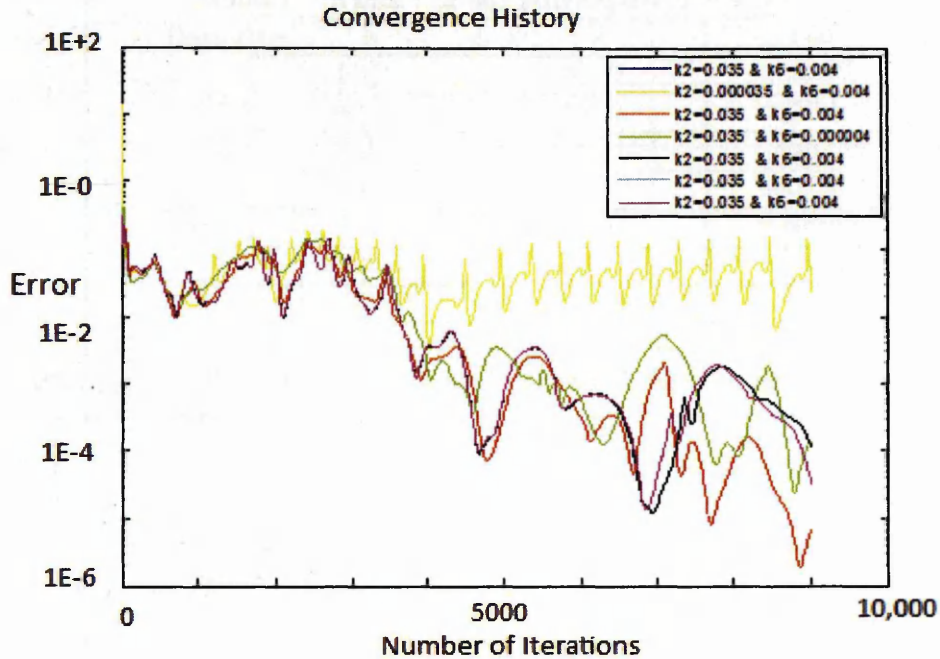

Figure 4:23 The convergence histories between various artificial viscosities for the CBS scheme.

Convergence is verified using the relative density error calculation seen in equation and plotted in Figure 4:23 against number of iterations. All simulations have been terminated after 9000 sweeps because it was deemed enough sweeps for gauging steady state conditions or displaying divergence of the 7 different solutions in Figure 4:23, only one of the seven simulations did not reach a relative density of 10^{-3}. This curve has $k^{(2)}$ =0.000035 and $k^{(4)}$=0.004. This was because the small values of $k^{(2)}$ and thus $\varepsilon_{i+1/2}^{(2)}$ are not enough to damp those non-linearities in the numerical solution.

Table 4-6 states $k^{(2)}$ and $k^{(4)}$ values for each simulation with the line color relating to the CBS solutions in Figure 4:24 and Figure 4:23. To discern the trends when changing $k^{(2)}$ and $k^{(4)}$ the following values were decided upon. For the first series of runs the $k^{(4)}$ value was decreased to ascertain the effect this had on the accuracy of solution against the analytical solution.

Table 4-6-**Displaying the $k^{(2)}$ and $k^{(4)}$ values.**

Color	$k^{(2)}$	$k^{(4)}$
Black	0.035	0.04
Dark Blue	0.035	0.004
Orange	0.000035	0.004
Light Blue	0.0035	0.004
Purple	0.035	0.004
Red	0.035	0.0004
Green	0.035	0.00004

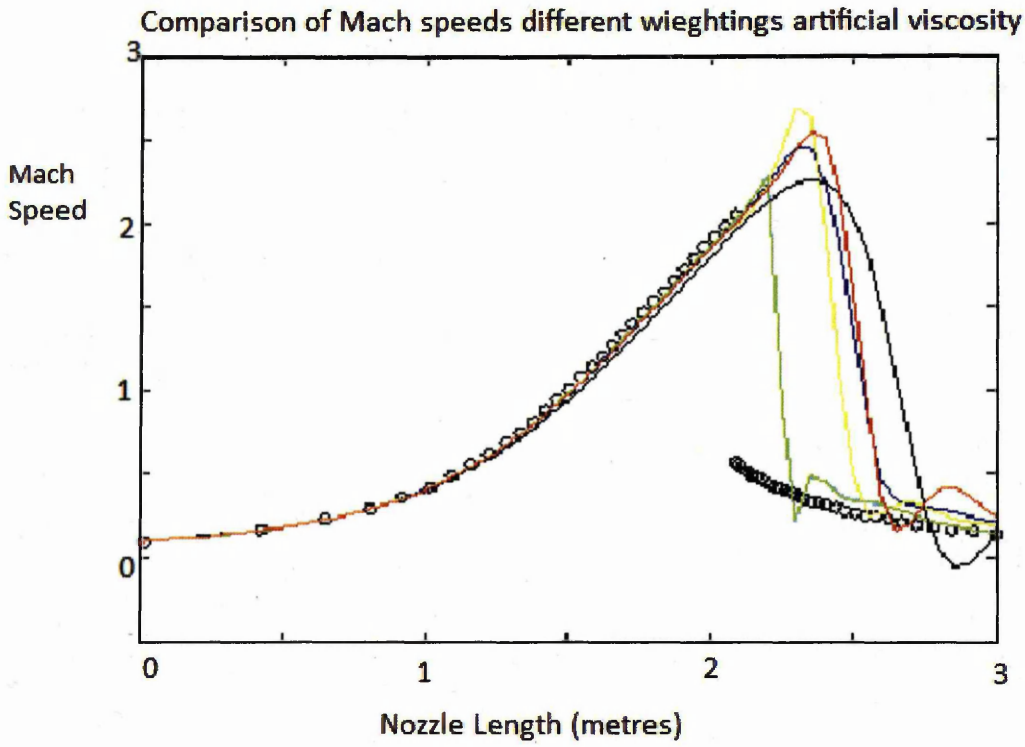

Figure 4:24-Comparison between the analytical Mach profile (○) and several results using Jameson, Schmidt & Turkel's artificial viscosities (solid line-) the key can be found in Table 4-6.

As can be seen in Figure 4:24 the Mach speed along the length of the nozzle is plotted for each of the seven different $k^{(4)}$ values. The seven different curves are plotted together with the analytical solution so their accuracy can be inferred. The green curve has a $k^{(2)}$ of 0.035 and $k^{(4)}$ of 0.00004 and possesses the greatest semblance to the analytical solution. Thus smaller values for $k^{(4)}$ produce more comparable results with respect to the analytical solution. Using large values of $k^{(4)}$ leads to smearing and large undershoots meaning failure of the scheme when capturing the location of the shock, and a failure at identifying the Mach number post shock. As stated by Anderson ([15], page 363) this is analogous to the effect that an actual increase in physical viscosity μ would have on the Mach profile.

In order to show that Jameson, Schmidt & Turkel's [105] AVT with further investigation can accurately capture the analytical solution, shock location and stabilize the solution at the same time, more solutions with different values of $k^{(2)}$ were collected where the $k^{(4)}$ fixed term to 0.004.

Table 4-7- **Displaying the $k^{(2)}$ and $k^{(4)}$ values**

Color	$k^{(2)}$	$k^{(4)}$
Dark Blue	0.002	0.004
Orange	0.004	0.004
Red	0.012	0.004
Green	0.016	0.004
Black	0.0014	0.004
Light Blue	0.00095	0.004
Purple	0.00075	0.004

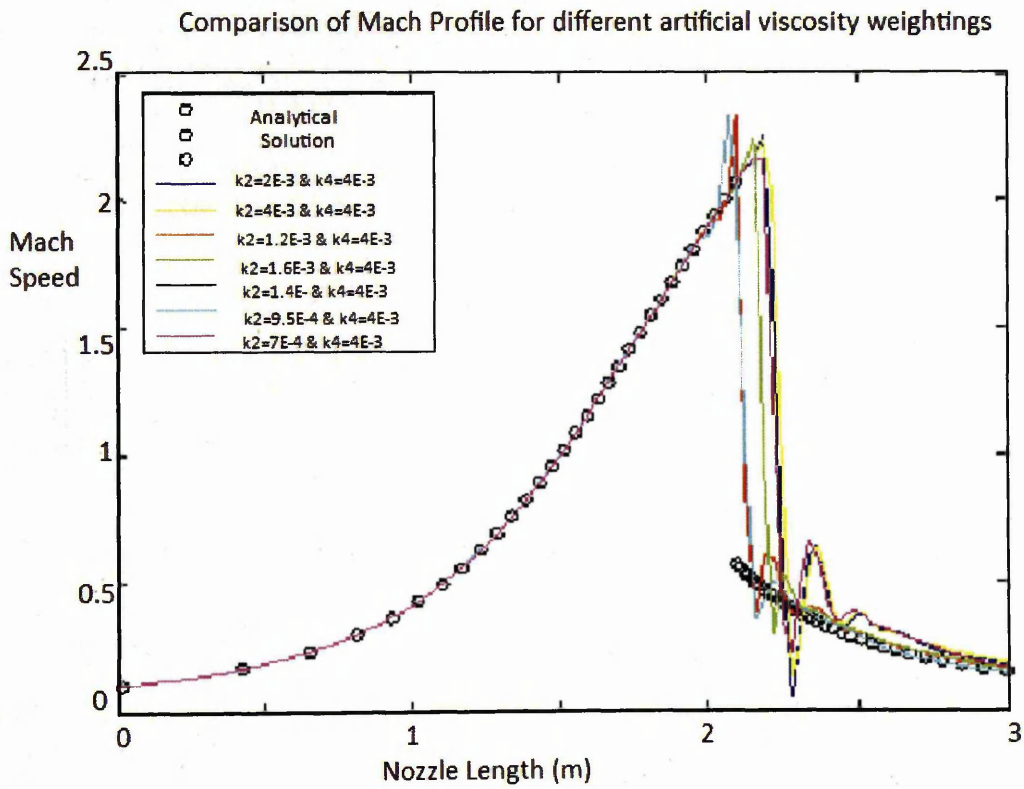

Figure 4:25- Second comparison between the analytical Mach profile (○) and different artificial viscosities for the CBS scheme (solid line-).

Figure 4**:25** is encouraging and demonstrates the importance of a low $k^{(2)}$ term for a good representation of the discontinuity and a post shock flow free from large undershoots/overshoots. The light blue curve where k^2=0.00095 k^4=0.004 gives the most accurate result of all the solutions seen in Figure 4**:25**. For the shock seen in Figure 4**:25**, the light blue curve is not as smeared as those other curves seen in Figure 4**:25**. Therefore a small value for $k^{(2)}$ is required to capture the large gradients in the flux variables of the shock.

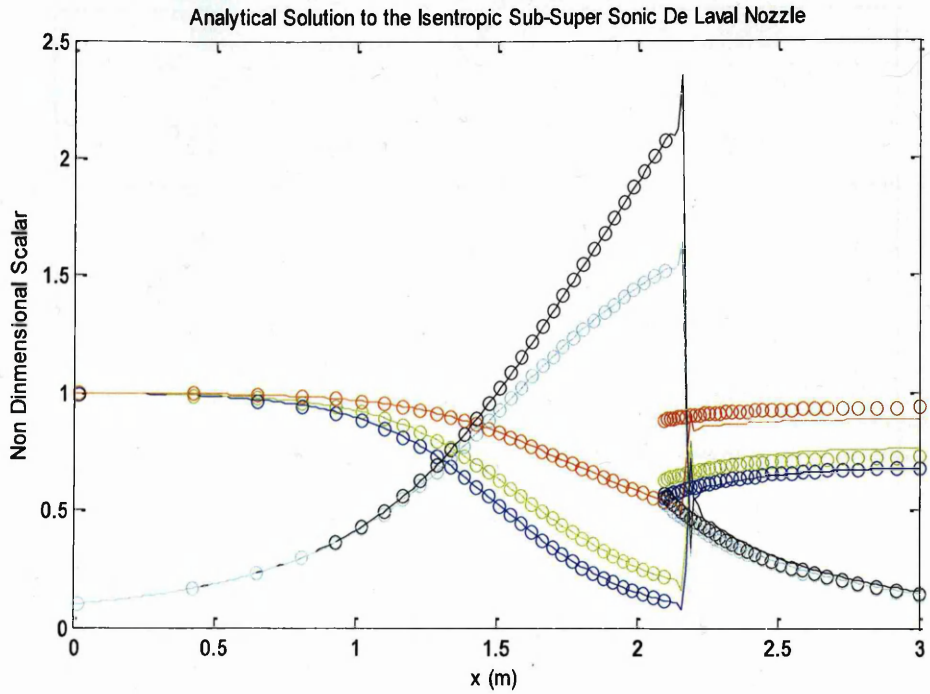

Figure 4:26- Mach profile of air in a Choked de Laval nozzle, comparing the numerical results obtained with the optimised artificial viscosity (solid line -) and the analytical solution (○) where $k^{(2)}$ =0.016 and $k^{(4)}$=0.004.

The use of Jameson, Schmidt & Turkel's 2nd and 4th ordered AV terms with the values of $k^{(2)}$ =0.016 and $k^{(4)}$=0.004 respectively helped to stabilize the case seen in Figure 4:26. This demonstrates that through experimenting with the values of $k^{(2)}$ and $k^{(4)}$, the CBS algorithm can be remedied, to handle discontinuities in the flow field. A major drain on time in the solution process is manually tuning these constants as it is not an exact science. A CBS solver that can automatically apply the effective amount of viscosity and time relaxation depending on the flow problem represents the ultimate shock capturing method in CFD. However, Figure 4:26 shows the combination of the 2nd ordered accurate explicit CBS algorithm and the artificial viscosity presented by Jameson, Schmidt & Turkel's [105] yields a flexible and robust code for the solution of the Choked nozzle as presented in Figure 4**:25**.

4.10 Concluding Remarks

This chapter on 1-D inviscid flow simulations has demonstrated the development of a 2nd ordered explicit algorithm for simplified Supersonic compressible inviscid flows using a 1D finite difference formulation. In the above work a simple explicit, one stage time integration was adopted. Because this chapter seeks to compare the CBS results with MacCormack's Predictor-Corrector scheme in (Anderson, [15] page 283) which also uses the simple explicit time integration.

4.10.1 CBS Algorithm Achievements

The Characteristic Based Split algorithm utilizes the finite difference framework instead of the original finite element integral approach as described by Nithiarasu and Codina, [131], for the Characteristic Based Split (CBS) algorithm. This demonstrates the versatility of the CBS approach to the finite difference formulation and, more importantly for this research the finite volume framework. Simply stated for multi dimensions the finite volume formulation is an extension of the finite difference approach. During these simulations it became apparent that the Characteristic Based Split

(CBS) calculations are highly dependent on the extra temporal terms and by extension the CFL number in the momentum and enthalpy equations. It has been argued by Nithiarasu and Codina, [131], that either too small or too large values for the CFL number can cause instability and divergence, requiring careful experimentation on an individual case basis. This can be demonstrated by the unacceptable errors of the purely Supersonic flow in a divergent nozzle as seen in Figure 4:15 and Figure 4:14. The substitution of Jameson, Schmidt & Turkel's [105] AVT, was required to obtain an acceptable solution in terms of absolute error. The grid independence study showed, as the grid is refined the numerical solution approaches the analytical solution satisfying the essential consistency property of a numerical technique.

4.10.2 Capturing the Sub to Supersonic De Laval Nozzle

The algorithm captures air flow from the inlet at approximately 34 m/s (Mach= 0.098) at a density of 1.2 kg/m^3, to the outlet where the air possess a velocity of 647m/s (Mach= 3.36) at a density of 0.0630 kg/m^3. This means a 95% compressibility ratio is handled when using the CBS algorithm with Jameson, Schmidt & Turkel's [105] AVT. This is a promising indication that the CBS algorithm can deal with the Supersonic compressible flows for the final novel application- transpiration cooling through porous media at Hypersonic speeds. The major results of this benchmark are that first of all the decreasing grid spacing occasions a closer approximation to the analytical solution and secondly that Jameson, Schmidt & Turkel's [105] AVT facilitates the stability of the algorithm for the Supersonic de Laval nozzle calculations.

4.10.3 Capturing the Choked De Laval Nozzle

The use of the conservation variables for the flux terms instead of the primitive variables is recommended by Anderson, [15] for shock capturing in the chocked nozzle case and was also followed in this chapter for comparison purposes. To suppress the tendency for odd and even point decoupling, and to prevent the appearance of wiggles in regions containing severe pressure gradients in the neighbourhood of shock, waves a second form of artificial viscosity which augments the CBS algorithm was introduced. The substitution of Jameson, Schmidt & Turkel's 2nd and 4th ordered blend into the discrete approach yielded an acceptable solution in terms of absolute error with respect to the analytical solution. Although numerical experimentation is required to optimize the shock capturing approach, Jameson, Schmidt & Turkel's [105] AVT performed robustly for this benchmark. Furthermore the experience gained here in using the artificial viscous term will prove invaluable when extending the algorithm to the 2-dimensional benchmarks that will follow in the next chapters.

Given the success reported here, the CBS algorithm coupled with Jameson, Schmidt & Turkel's AVT to 2-dimensions, using the finite volume integral framework, will be implemented in the following chapters of this thesis.

5. 2-DIMENSIONAL NUMERICAL IMPLEMENTATION

5.1 Introduction

As seen in Chapter 4, the 1-D analysis is insightful and helpful to understand many properties of the CBS algorithm and the shock capturing scheme as well as to give an insight into the behaviour and performance of this scheme for more elaborate problems. However, careful investigation of 2-dimensional performance is unavoidable for any scientific conclusion on behalf of the solver, either in terms of accuracy, robustness or computational efficiency. Therefore, this chapter will look at the extension of the 1-D computational implementation to 2-dimensions. It has to be kept in mind that the dearth of results concerning Hypersonic flow simulations involving unstructured meshes has stimulated the present research. Some of the major difficulties which have to be overcome when attempting the numerical solution of the Hypersonic 2-dimensional Hyperbolic PDEs are: the non-linear nature of the flow; the complex geometries involved in industrial applications; and the high storage and CPU time involved in practical solutions as stated by Lyra, [7].

A 2-dimensional fluid solver targeted at Hypersonic compressible flows will be integrated into the host software platform, PHYSICA for this research project. Current partitioning tools for parallel computing and meshing routines have previously been encoded as spelled out in PHYSICA beginners guide and have previously been tested on a number of industrial problems as seen in the literature [1], [38], [68]. A brief discussion of the current solver within PHYSICA and its drawbacks, sets out the reasons to eliminate this current solver for this research problem.

5.2 PHYSICA - Multi Physics Software

The software toolkit PHYSICA solver strategy utilises three dimensional unstructured finite volume meshes of any arbitrary mix of element shapes from tetrahedral to hexahedral elements [143]. PHYSICA simulates fluid flow, coupled with heat transfer, solid stress and electro- magnetic fields in a parallel fashion. The software design which has a coherent structure is applied to the full range of continuum physics operating scalably on high performance clusters [1].

The default algorithm in PHYSICA is a derivative of the Semi-Implicit Momentum-Pressure coupled with the corrected momentum equation (SIMPLEC), which is a pressure based algorithm developed in 1972 by Spalding & Patankar, [32]. The algorithm in PHYSICA has been extended to unstructured meshes and is essentially a cell centered co-located version of the SIMPLEC scheme [41]. The logic is to update the pressure from a residual calculated in the continuity equation. After testing and validating the SIMPLEC algorithm it was reasoned that for optimal performance the solution should be heavily weighted to the pressure correction step and the momentum equation, and should be comparatively damped [38]. The flow diagram of the SIMPLE algorithm is given in the Appendices.

In previous research, PHYSICA has been applied to simulate metal casting in [2], [144], metal forging in [69], mineral deposition applications in [145] and bio medical applications in Carswell et al, [146] . As a consequence of the mentioned research, partitioning and meshing tools are already embedded in PHYSICA. All that is required for the current project is to develop a fluid flow solver to

simulate highly compressible air flows for Hypersonic applications. As stated previously SIMPLEC is pressure based, and modifications have been made to accommodate large levels of compression [38]. Although the simplifying assumptions that are applied to pressure based schemes become insufficient for the highly compressible flows to be modelled. Mainly, because the assumption for the artificial relationship as seen in Chapter 2 cannot be used. Also, solving the conservation quantities, the mass flux, enthalpy and density across a shock front will hopefully be continuous instead of solving the alternative primitive variables across a shock front which can be proved to be discontinuous (Anderson, [15], page 283).

Going forward with the algorithm integration, a property compromise between the accuracy, stability and flexibility of the CFD technique needs to be struck. Therefore, the density based schemes as developed by Chorin were employed and it was deemed sensible to employ a density based method for compressible flows with a standard scheme option for incompressible flows. The density based method was chosen over a pressure based method, however considerable foresight and science is still necessary to complete a successful computation.

1. Grid selection - the choice of grid, whether it be a structured grid or an unstructured grid, is crucial to the performance of a numerical method. Plain square meshes are only appropriate for certain cases. Grids should be finer in regions in high gradients in the solution variables. Poor quality grids can result in instability or failure to converge [15].
2. In unsteady flows, the gradients can move; hence the grids need ideally to be changeable or adaptive. See the references [7], [43].
3. Leonard [147], sates that when the free stream Reynolds number reaches turbulent values the computational approach requires a turbulence model such as [148] and [149].

The solution of Hyperbolic problems varies considerably in space and time, exhibiting for instance, initial transients where highly oscillatory components of the solution are rapidly decaying. Therefore, efficient computational methods, for this class of problems require the use of mesh spacing and time-steps which are variable, ideally in space and time.

5.3 CBS Algorithm – A Family of Finite Element Compressible Schemes

As a remedy to the numerical challenges encountered by the upwind algorithm's Zienkiewicz and Codina [47], developed a finite element version of the Lax Wendroff family. These methods were formulated to explicitly solve the Navier-Stokes equations. Unfortunately, in spite of this the instability which occurred due to the pressure term in the momentum equation, otherwise known as the LBB condition, persisted.

Pressure stabilization can be achieved by utilizing different interpolation functions for pressure and velocity. To maintain equal order interpolation, which is attractive for mixed convection-diffusion problems, a fix was sought that would reduce the pressure instability. This fix was achieved by splitting the momentum equation, into two stages: an intermediate momentum step, and a corrected momentum step, at every pseudo time level, as well as utilizing a second ordered pressure derivative which acts to smooth the pressure field. This was originally coined as the operator split method by Chorin (1967). For transient problems the classical fractional step methods are known to introduce a first ordered time error in pressure, which can be eliminated by suitable pressure stabilization Malan, Lewis, & Nithiarasu, [150]. For a steady state problem, however, a fractional step method is viewed to be the best compromise between speed of convergence and accuracy [131]. The stability of the CBS scheme stems from employing higher ordered terms akin to those terms seen in the classical Taylor series expansion and secondly splitting the momentum equation into two equations using the Chorin type split. Owing to the reasons cited above, the CBS method was stated to be stable in Nithiarasu and Codina, [131], for the Trans-Sonic flow past an aerofoil [88] and the Hypersonic viscous flow past a double ellipsoid.

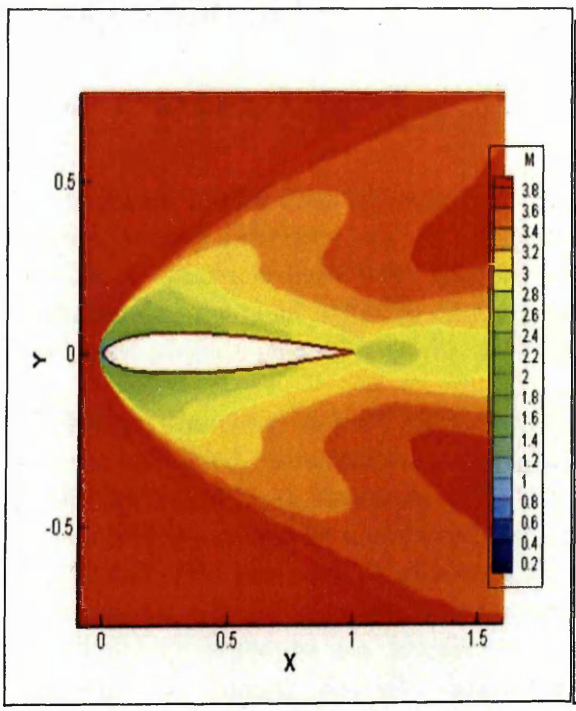

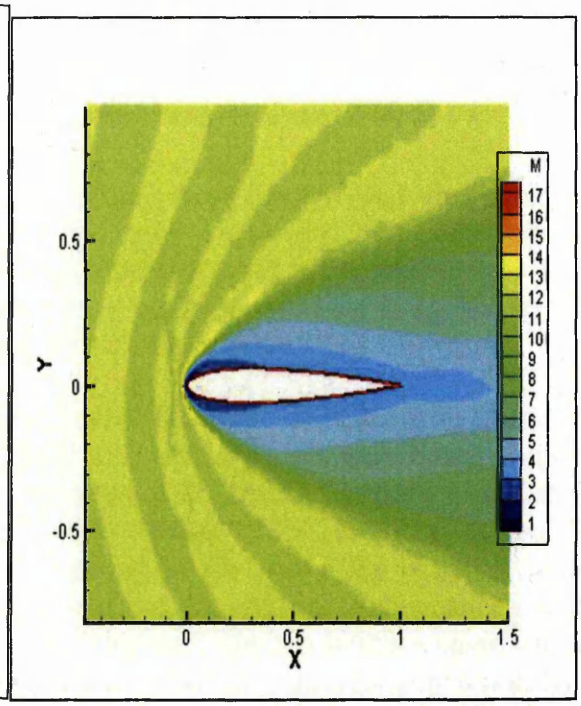

Figure 5-1 CBS velocity contour plot at Mach 4 Figure 5-2 CBS velocity contour plot at Mach 20.

As can be seen in Figure 5-1 and Figure 5-2 the finite element CBS algorithm is stable for inviscid flowsranging from Mach 4 and Mach 20 [151]. An important requirement for modelling-Hypersonic flows affecting the operation Cruise Air-breathing Vehicles (CAVs).

5.3.1 Higher Order Truncation Term

The following technical notes illustrate the Characteristic Based Split (CBS) algorithm's format and stability. The supposed stability is derived from the introduction of a Taylor series expansion of the convection terms in the Navier Stokes equations. In order to better understand the CBS, Figure 5-3 below illustrates how in one dimension the characteristics propagate in the x-t plane if a constant characteristic speed and zero diffusion is considered.

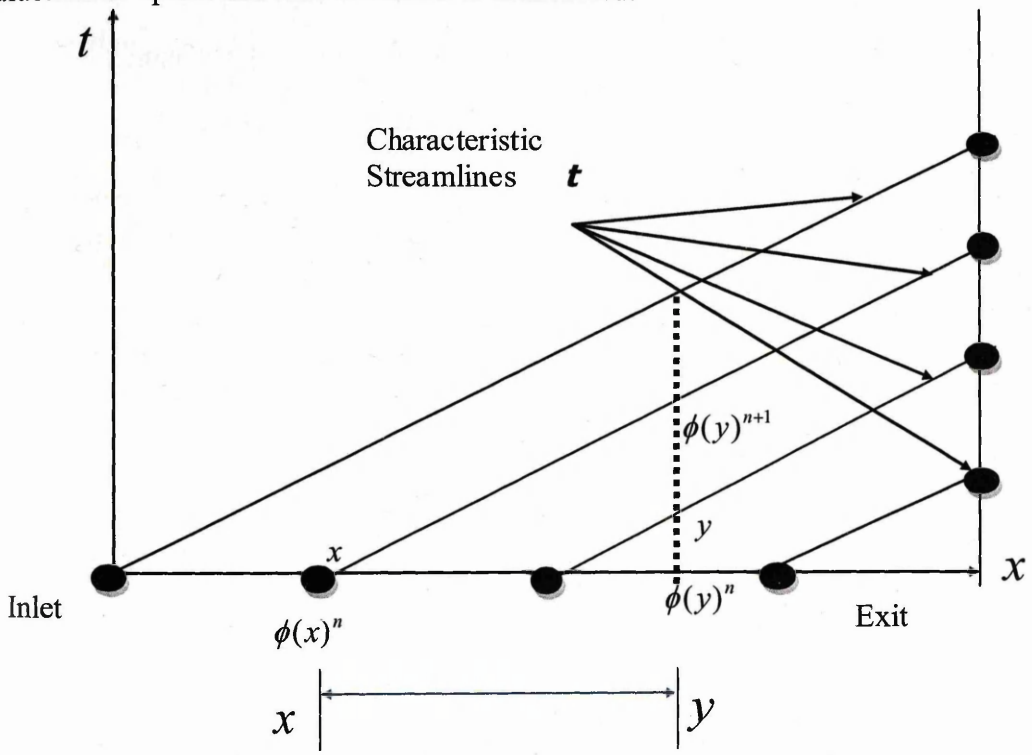

Figure 5-3:

Linear convection problem. Characteristics.

For different particles on a common characteristic streamline Zienkiewicz & Codina, [47] that the particles share the same scalar properties or in notation:

$$\phi(y)^{n+1} = \phi(x)^n \tag{5.76}$$

Where $\phi(y)^{n+1}$ is downstream of $\phi(x)^n$ but share the same domain of dependence given by the characteristic black line in Figure 5-3. This statement illustrates the well-known fact that the scalar variable ϕ along a characteristic irrespective of the time level are the same [18]. This is the fundamental feature of the characteristic approach to computing flows and is taken forward by Nithiarasu, Zienkiewicz, Codina, Vazquez, & Ortiz, [152] and Zienkiewicz & Codina, [47] to develop the CBS scheme.

Taking the discretised form of the convection equation (5.76) it is possible to state that:

$$\frac{\phi(y)^{n+1} - \phi(x)^n}{\Delta t} = 0 \tag{5.77}$$

When using the local Taylor series expansion for the scalar variable $\phi(x)$ one gets:

$$\phi(x)^n = \phi(y)^n - (y-x)\frac{\partial \phi(y)^n}{\partial x} + \frac{(y-x)^2}{2}\frac{\partial^2 \phi(y)^n}{\partial x^2} + O((y-x)^3) \qquad (5.78)$$

By replacing (y-x) in (5.78), in terms of the time step Δt and the average velocity $\bar{u}$ of the characteristic, one gets:

$$(y-x) = \bar{u}\Delta t \qquad (5.79)$$

Substituting (5.79) into equation (5.78) we obtain.

$$\phi(x)^n = \phi(y)^n - \bar{u}\Delta t\frac{\partial \phi(y)^n}{\partial x} + \frac{\bar{u}^2\Delta t^2}{2}\frac{\partial^2 \phi(y)^n}{\partial x^2} + O(\Delta t^3) \qquad (5.80)$$

Using the relationship seen in (5.76) and re-arranging the above equation (5.80), we state

$$\frac{d\phi}{dt}(x',t) \Rightarrow \frac{\phi(y)^{n+1} - \phi(y)^n}{\Delta t} = -\bar{u}\frac{\partial \phi(y)^n}{\partial x} + \frac{\bar{u}^2\Delta t}{2}\frac{\partial^2 \phi(y)^n}{\partial x^2} + O(\Delta t^2) \qquad (5.81)$$

Equation (5.76) to equation (5.81) assumes a constant characteristic speed $\bar{u}$ throughout the computational domain. Importantly for the CBS approach, equation (5.81) is the non-conservation form of the convection equation for the scalar variable ϕ and is suitable for flow with a divergence-free approximation i.e. incompressible flows. For compressible divergent flows a modified derivation for the convection equation, is required with additional assumptions for the characteristic speed $\bar{u}$. This should be kept in mind when reading on. Figure 5-4 below, illustrates that the characteristic propagation for non-linear convection.

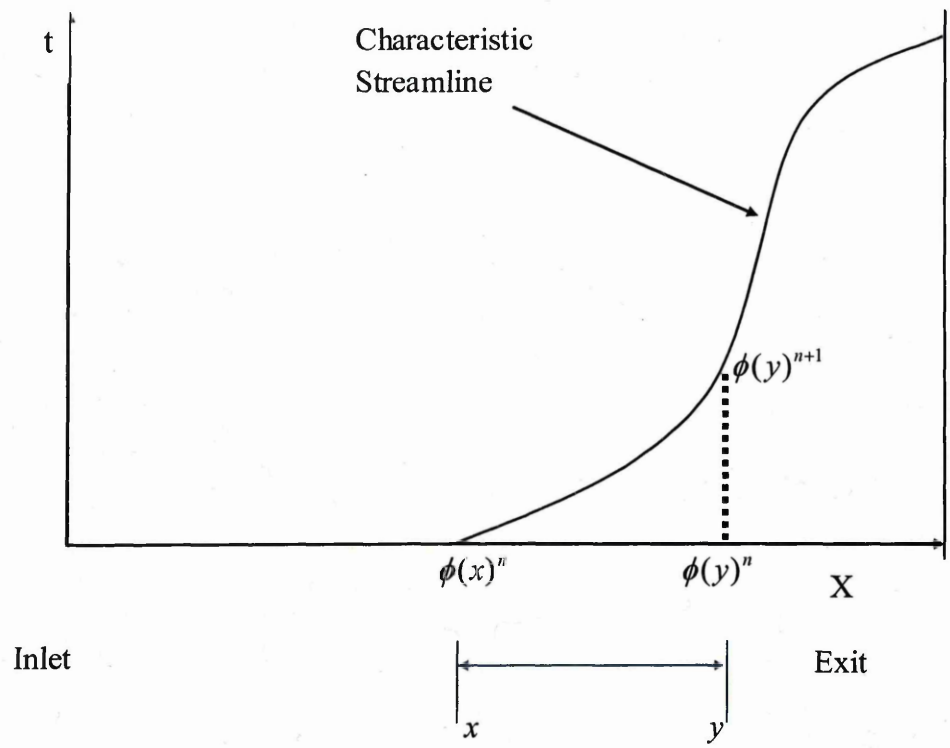

Figure 5-4 : Non-linear convection problem. One characteristic and a scalar variable at different levels.

For compressible flows the characteristic speed and the convection terms in the Navier-Stokes equations, are non-linear in space. To apply an equation with the same format as equation (5.81) to

non-linear speeds, compressible Navier Stokes equations. Where ϕ in equation (5.81) is replaced by $u\phi(y)$. An approximation for $u\phi(x)$ using the Taylor series expansion is stated below as:

$$u\phi(x)^n = u\phi(y)^n - (y-x)\frac{\partial(u\phi(y))^n}{\partial x} + \frac{(y-x)^2}{2}\frac{\partial^2(u\phi(y))^n}{\partial x^2} + O((y-x)^3) \qquad (5.82)$$

Where

$$(y-x) = \bar{u}\Delta t \qquad (5.83)$$

Substituting equation (5.83) into (5.82) and one garners:

$$\frac{\phi(y)^{n+1} - \phi(y)^n}{\Delta t} = \begin{pmatrix} -\frac{\partial}{\partial x}(u\phi(y))^n + \frac{\Delta t}{2}u\frac{\partial}{\partial x}\left[\frac{\partial}{\partial x}(u\phi(y))\right]^n + \\ \frac{\Delta t^2}{6}u^2\frac{\partial^2}{\partial x^2}\left[\frac{\partial}{\partial x}(u\phi(y))\right]^n + O(\Delta t^3) \end{pmatrix} \qquad (5.84)$$

Equation (5.84) is the scalar convection equation that will be the template for the CBS approach. Before we apply this method to the Navier-Stokes equations, the following points need to be considered.

Point 1

Although equation (5.84) is third order time accurate, it is seldom possible to achieve this accuracy using unstructured grids as establishing third order derivatives becomes difficult. After removing the 3rd ordered temporal terms from (5.84) one can obtain the following discrete equation that ultimately relates the next temporal value with 1st and 2nd ordered spatial derivatives.

$$\frac{\phi(x)_i^{(n+1)} - \phi(x)_i^n}{\Delta t} = -\frac{\partial}{\partial x}(u\phi(x))^n + \frac{\partial}{\partial x}(k\frac{\partial\phi(x)}{\partial x}) + \frac{\Delta t}{2}u\frac{\partial}{\partial x}\left(\frac{\partial}{\partial x}(u\phi(x))^n - \frac{\partial}{\partial x}(k\frac{\partial\phi(x)}{\partial x})\right) \qquad (5.85)$$

Point 2

The convected variable whether it be ρ, ρu, ρv or ρE becomes the characteristic variable and the speed at which it is convected becomes the characteristic speed.

Point 3

When the time step $\Delta t = 0$ the LHS of equation (5.84) the next time level is approximately equal to the 1st ordered term on the RHS. As the time step $\Delta t > 0$ the 2nd and 3rd ordered terms in equation (5.84) have a greater role in calculating the next iterative level on the LHS, as long as the average velocity, $\bar{u}$ is sufficiently large. Therefore a dichotomy exists between large enough Δt values for spatial accuracy to be realized but not large enough to cause instability as the CFL condition dictates.

Point 4

Equation (5.84) ignores the effect of the pressure term, seen in the momentum equation.

5.3.2 Fully Explicit Pseudo Time Integration

The use of implicit approaches for time discretisation might be attractive, but due to the scale of problems normally faced in CFD, explicit iterative approaches are preferred because they are much easier to implement for large scale 3D complex problems [131]. The Navier Stokes equations, eq (2.39)-(2.40), are Hyperbolic with time, and the magnitude of Δt that can be used in the above equations can be obtained from the simple stability analysis for linear problems. The simple stability analysis of a *linear* Hyperbolic equation carried out by Lewy, Courant, & Friedrichs [24], for an explicit numerical solution gives the result that C<1. Yet, the present compressible Supersonic flow is governed by *nonlinear* partial differential equations. In this case the exact stability criterion for a

linear equation can only be viewed as general guidance for the present nonlinear problem, but as mentioned by [18], it turns out to be a good guide to *nonlinear* problems.

The sequential computational iterative procedure is repeated. Because of their easy and efficient parallelization the fully explicit schemes have been employed as the default method [132].

5.4 The CBS Algorithm – Original Finite Element Scheme

As seen in Nithiarasu and Codina, [131], the sequential relationships in the CBS finite element algorithm are set out to solve the system of partial differential equations governing fluid mechanics. Each equation is applied to every node in a sweep of the grid before the code enters the next equation. After the final equation the boundary conditions are applied.

The sequential computational procedure for the CBS finite element algorithm can be done in a number of ways but the following general procedure was taken from the work of Nithiarasu and Codina, [131]. The following equations introduce 2nd order accurate convection stabilizing terms, which are weighted by the coefficient mainly in the intermediate momentum, corrected momentum and enthalpy equation. However the finite element formulation for the CBS method was not implemented in this thesis to solve the system of equations. Instead the CBS method is formulated within the favored finite volume framework. A novel development for the finite element CBS approach. For a comprehensive review of the finite element CBS scheme see [47], [131], [152], [153]. The finite element (FE) CBS formulation is presented here, because it is the best guide, there is, to construct a novel finite volume method.

The FE CBS scheme incorporates local pseudo time stepping, and in a local time stepping approach different time steps are used at different nodes. Then the physical fields are accelerated to a steady state solution. According to Nithiarasu and Codina, [131], using globally minimum time steps, the calculations to steady state takes a much longer time than the local time stepping procedure. The local time step is given by the following equation: where C is the Courant number and depending on the problem is usually $C < 0.5$.

$$\Delta t_{ele}^{n} = C\left(\frac{h_{ele}}{c+\sqrt{(u_i u_i)}}\right)_{iele}^{n} \qquad (5.86)$$

where the superscript n equals the current iterative level
the subscript ele denotes an element
h-characteristic element length (m)
u-velocity (m/s)
Δt-local time step value (s)
c-speed of sound (m/s)

Pseudo local time stepping is adopted for both compressible and incompressible flow calculations. It acts like a iterative scheme advancing but only advances the solution to convergence i.e. at the final pseudo time level steady state has been achieved. Local pseudo time stepping slows down computations in problematic areas and accelerates the calculations elsewhere in the domain. It is necessary to use an appropriate characteristic element length, h_e, in (5.86) the following relationship for three dimensional cases recommended by Nithiarasu and Codina, [131]:

$$h_i = \sum_{f=1,TOTFIC} \min\left(\frac{3\Delta V}{\Delta A_f}\right)_{ele} \tag{5.87}$$

Similarly for two dimensions the element size according to [131] is calculated from:

$$h_i = \sum_{f=1,TOTFIC} \min\left(\frac{2\Delta A}{\Delta L_f}\right)_{ele} \tag{5.88}$$

Where ΔA is the total area of the 2D element

The second step in the FE CBS method, is the removal the pressure term from the momentum equation, and augment with higher order temporal term to calculate an intermediate velocity:

$$\rho u_i^* = \rho u_i^n - \Delta t\left(\frac{\partial}{\partial x_j}\left(\rho u_j u_i\right) - \frac{\partial \tau_{ij}}{\partial x_j} + \frac{\Delta t}{2} u_k \frac{\partial}{\partial x}\left(\frac{\partial}{\partial x_j}\left(\rho u_j u_i\right) - \frac{\partial \tau_{ij}}{\partial x_j}\right)\right)^n \tag{5.89}$$

where u*-intermediate velocity (m/s)
u_i-velocity component (m/s)
Δt-local time step value(s)
ρ-density (kg/m^3)
τ_{ij}-is the deviatoric stress component (N/m^2) given by eq (2.27)
i,j,k-[x,y,z]

The FE CBS Continuity equation is the next step: To compute the pressure field using the mass fluxes calculated from the intermediate equation (5.89).

$$\frac{1}{\left(c^n\right)^2}\left(P^{n+1} - P^n\right) = -\Delta t\left(\theta_1 \frac{\partial\left(\rho u_j\right)^*}{\partial x_j} - (1-\theta_1)\frac{\partial\left(\rho u_j\right)^n}{\partial x_j} + \frac{\Delta t}{2} u_k \frac{\partial}{\partial x_k}\left(\frac{\partial P^n}{\partial x_j}\right)\right) \tag{5.90}$$

where the superscript n+1 denotes the next iterative level
P-static pressure (N/m^2)
θ_1-Stabilisation weighting parameter $0.5 \le \theta_1 \le 1$
For this research the best choice was found to be $\theta_1 = 1$

The third step is to correct the momentum equation by adding the pressure terms omitted in (5.89).

$$\left(\rho u\right)_i^{n+1} = \rho u_i^* - \Delta t\left(\frac{\partial P^{n+\theta_2}}{\partial x_i} - \frac{\Delta t}{2} u_k \frac{\partial}{\partial x_k}\left(\frac{\partial P^n}{\partial x_i}\right)\right) \tag{5.91}$$

Where θ_2-implicit/explicit weighting parameter $0 \le \theta_2 \le 1$ ($\theta_2 = 0$ for fully explicit scheme and $\theta_2 > 0$ for semi implicit scheme)

As a fourth step the semi-discrete energy equation is stated as:

$$\left(\rho E\right)^{n+1} = \left(\rho E\right)^n + \Delta t\left(\begin{array}{l} -\frac{\partial\left(\rho E u_j\right)}{\partial x_j} + \frac{\partial}{\partial x_j} k\left(\frac{\partial T}{\partial x_j}\right) - \frac{\partial\left(P u_j\right)}{\partial x_j} + \frac{\partial\left(u_j \tau_{ji}\right)}{\partial x_j} \\ + \frac{\Delta t}{2} u_k \frac{\partial}{\partial x_k}\left(-\frac{\partial\left(\rho E u_j\right)}{\partial x_j} + \frac{\partial}{\partial x_j} k\left(\frac{\partial T}{\partial x_j}\right) - \frac{\partial\left(P u_j\right)}{\partial x_j} + \frac{\partial\left(u_j \tau_{ji}\right)}{\partial x_j}\right) \end{array}\right)^n \tag{5.92}$$

where E-specific energy (kg m^2/s^2).
k-coefficient of thermal diffusion (W/(m K)).
T- absolute temperature (K).

and the total specific energy, E, is defined as: eq (2.33) from this relationship the temperature can be inferred. To close the equation set, calculate the density, by using the ideal gas law.

$$(\rho)^{n+1} = P^{n+1} / (T^{n+1} R) \qquad (5.93)$$

where R is the universal gas constant (287 J/(kg K) for air).

Additional scalar variables from appropriate governing equations are calculated such as the wave speed as seen in (2.36).

Finally the solver should check convergence to steady state values by sensing whether the relative error is less than the agreed tolerance of 10^{-5} or the number of iteration is below the maximum iteration, I_{Max}, stipulated by the user.

General Remarks

To obtain stable solutions at all Mach numbers three additional strategies are required:

1. The addition of artificial viscosity for inviscid and viscous problems at Supersonic and Hypersonic speeds. MacCormack's 2nd ordered artificial viscous term (AVT) was coupled (Chapter 4) with the CBS algorithm where it was used as an explicit stabilizing source term. Unreasonable results with respect to the analytical solution and even divergence is encountered when the CBS algorithm is not coupled with any artificial viscosity terms.
2. An empirical relationship between the viscosity and temperature is needed for compressible problems: Sutherlands law, eq (2.34) is used in this research.
3. A set of well posed boundary conditions that can distinguish the different fluid applications.

5.5 The CBS algorithm - In a Novel Finite Volume Context

The aim was to embed a candidate algorithm in a finite volume framework to tackle the research problem seen in section 1.1. The finite volume approach was utilize because it is relatively easier to extend from 2D to 3D geometries, whereas finite difference cannot and finite element needs basis functions for face values which can be computationally expensive [7]. The second reason is that the finite volume method, when mathematically integrated can be thought of locally to conserve mass, momentum and enthalpy at each control volume. Whereas the finite element approach as already stated in Chapter 1, does not guarantee local conservation of mass, momentum and enthalpy. In addition the existing host code PHYSICA has been a finite volume code since its inception [1] where geometric and parallel decomposition subroutines are ready to be used straight away.

The design of finite volume approaches in multidimensions, is accomplished for an arbitrary discretisation, and by considering the propagation of information locally in the direction normal to the cell faces. The key step for the finite volume method is the integration of the governing equations over a three dimensional control volume (CV) using Gauss's divergence principle [16]:

$$\rho u_i^* = \rho u_i^n - \frac{\Delta t}{\Delta V}\left(\begin{array}{l}\int_{CV} div\left(\rho u_j u_i\right) dV - \int_{CV}\left(\frac{\partial \tau_{ji}}{\partial x_j}\right) dV \\ +\frac{\Delta t}{2} u_k \int_{CV} div\left(grad\left(\rho u_j u_i\right)\right) dV\end{array}\right) \quad (5.94)$$

Where the subscript CV- control volume

ΔV- volume of cell (m^3)

A_f- is the area of the volumes face (m^2)

Gauss's divergence principle for a vector field u_j acting on a volume states that:

$$\int_{CV} div\left(u_j\right) dV = \int_{Area} n_j \bullet u_j dA \quad (5.95)$$

Here

$$n_j = [n_x, n_y, n_z] \quad (5.96)$$

where n_x denotes the component, in direction x, of the unit outward normal vector to surface dA. The physical interpretation of $n_j \bullet u_j$ is the component of a vector, u_j, in the direction normal n_j, to the surface element dA.

Applying Gauss's divergence theorem, (5.95) to the intermediate momentum equation (5.94).

$$\rho u_i^* = \rho u_i^n - \frac{\Delta t}{\Delta V}\left(\begin{array}{l}\sum_{f=1,TOTFIC}\left(\left(\rho u_i u_j\right) \bullet n_j A\right)_f - \sum_{f=1,TOTFIC}\left(\frac{\partial \tau_{ji}}{\partial x_j} \bullet n_j A\right)_f \\ +\frac{\Delta t}{2} u_k \sum_{f=1,TOTFIC}\left(div\left(\rho u_i u_j\right) \bullet n_j A\right)_f\end{array}\right)^n \quad (5.97)$$

Where the summation $\sum$ is done over the total number of faces belonging to the control volume. By applying (5.95), Gauss's divergence theorem to the corrected momentum equation, the continuity equation and the enthalpy equation in a similar fashion to the intermediate momentum equation one obtains the sequential finite volume CBS scheme is obtained in Section 5.5.1.

5.5.1 The Sequential Finite Volume CBS Scheme

Each step described below is applied to all the interior nodes in a sweep of the computational grid. After this sweep the boundary conditions are computed. Then the sequential computational procedure is repeated by going back to step 1. The CBS method was implemented in the computing language FORTRAN and the simulations run within Swansea University's cluster to solve the Navier Stokes system of equations.

1. The CBS scheme incorporates local pseudo time stepping. The pseudo time step is given by the following equation: where C is the Courant number and depending on the problem is usually < 0.5.

$$\Delta t_{CV}^n = C \frac{h_{CV}}{c_{CV}^n + \sqrt{u_i u_i}^n_{CV}} \quad (5.98)$$

It is necessary to use an appropriate control volume length, h_e, for the local time computation (5.98) where Nithiarasu and Codina, [131], recommend the following relations for three dimension cases:

$$h_{CV} = \sum_{f=1}^{TOTFIC} \min\left(\frac{\Delta V}{A_f}\right) \quad (5.99)$$

And in the two dimensional

$$h_{CV} = \sum_{f=1}^{TOTFIC} \min\left(\frac{\Delta A}{L_f}\right) \tag{5.100}$$

Where L_f is the length of the face

2. Finite Volume (FV) Intermediate Momentum Step

$$\rho u_i^* = \rho u_i^n - \frac{\Delta t}{\Delta V}\left(\begin{array}{l}\sum_{f=1,TOTFIC}\left(\left(\rho u_i u_j\right)\bullet n_j A\right)_f - \sum_{f=1,TOTFIC}\left(\frac{\partial \tau_{ji}}{\partial x_j}\bullet n_j A\right)_f \\ +\frac{\Delta t}{2}u_k \sum_{f=1,TOTFIC}\left(div\left(\rho u_i u_j\right)\bullet n_j A\right)_f\end{array}\right)^n \tag{5.101}$$

3. FV corrected momentum Step

$$\rho u_i^{n+1} = \rho u_i^* - \frac{\Delta t}{\Delta V}\left(\sum_{f=1,TOTFIC} P_f \bullet n_i A_f - \frac{\Delta t}{2}u_k \sum_{f=1,TOTFIC}\frac{\partial P}{\partial x_i}\bullet n_i A_f\right) \tag{5.102}$$

4. The Continuity step is solved using the momentum values from (5.102) at the n+1 "time" level

$$\rho_{CV}^{n+1} = \rho_{CV}^n - \frac{\Delta t}{\Delta V}\left(\sum_{f=1,TOTFIC}\left(\rho u_j \bullet n_j A\right)_f\right)^{n+1} \tag{5.103}$$

5. Enthalpy Step

$$\left(\rho E\right)_{CV}^{n+1} = \left(\rho E\right)_{CV}^n + \frac{\Delta t}{\Delta V}\left(\begin{array}{l}-\sum_{f=1,TOTFIC}\left(\left(\rho E u_j\right)\bullet n_j A\right)_f + \sum_{f=1,TOTFIC}\left(k\left(\frac{\partial T}{\partial x_j}\right)\bullet n_j A\right)_f \\ -\sum_{f=1,TOTFIC}\left(\left(P u_j\right)\bullet n_j A\right)_f + \sum_{f=1,TOTFIC}\left(\frac{\partial\left(u_j \tau_{jl}\right)}{\partial x_j}\bullet n_j A\right)_f \\ +\frac{\Delta t}{2}u_k\left(\sum_{f=1,TOFIC}\left(\frac{\partial\left(\rho E u_j\right)}{\partial x_j}\bullet n_j A\right)_f + \sum_{f=1,TOTFIC}\left(\frac{\partial\left(u_j P\right)}{\partial x_j}\bullet n_j A\right)_f\right)\end{array}\right)^n \tag{5.104}$$

Temperature is inferred from Enthalpy equation by using the following identity:

$$T_{CV}^{n+1} = \frac{1}{C_V}\left\{\frac{\left(\rho E\right)_{CV}^{n+1}}{\rho_{CV}^{n+1}} - \frac{\left(u_{CV}^{n+1}\right)^2 + \left(v_{CV}^{n+1}\right)^2}{2}\right\} \tag{5.105}$$

6. To close the equation set the Ideal Gas Law, Sutherlands Law and the Prandtl Law are used as seen below.

$$k_{CV} = \frac{\mu_{CV} C_p}{\Pr} \tag{5.106}$$

The Prandtl number in [82], which is assumed constant for ideal gases at moderate temperature where Pr is 0.74.

Thereby for air at standard conditions the thermal conductivity parameter is.

$$k_{CV} = \frac{1.789\times10^{-5}\times1005}{0.74}$$

$$k_{CV} = 0.024297 W/m^{\circ}K$$

General Remarks

To obtain smooth solutions at all Mach numbers some additional techniques are required:

1. The above steps introduce 2nd order convection stabilizing terms mainly in the intermediate momentum equation (5.101) and the enthalpy equation (5.104).
2. These higher order temporal terms are a function of the local time step. The time step is part of the stabilization process. These temporal terms should lie as close as possible to the stability limit.
3. The addition of artificial viscosity is required for inviscid and viscous problems at Supersonic and Hypersonic speeds.
4. Typically a CFD solver needs to have a "kick" out mechanism.

5.5.2 Convergence Criteria for Compressible Problems

This kick out mechanism usually tracks the residual between successive iterations and compares it with a pre-defined tolerance. The steady state requirement for compressible problems is calculated as follows:

$$\varepsilon^{n}_{Rel} = \frac{1}{NUMCV}\sqrt{\left[\frac{\sum_{cv=1}^{NUMCV}\left(\frac{\left|\rho^{n+1}_{CV}-\rho^{n}_{CV}\right|}{\Delta t_{CV}/(L/u_{\infty})}\right)^{2}}{\sum_{CV=1}^{NUMELE}\left(\rho^{n+1}_{CV}\right)^{2}}\right]} \qquad (5.107)$$

Where L is the characteristic length of the case investigated, i.e. an aerofoil length or the length of a de Laval nozzle, u_∞ is the free-stream velocity. The above equation is non-dimensionalized using a characteristic time scale of (L/u_∞). The tolerance is reduced to 10^{-5}, which in short means a steady state solution. For all intent and purposes is achieved when the velocity residual is less than 10^{-5}.

For the CBS solutions to the compressible benchmark cases investigated, the results are validated with the associated analytical solutions, [84], [154], [155] where a tolerance of 1% between these analytical values and the computed CBS result are deemed accurate enough for CFD solvers applied to CAVs Hypersonic vehicles i.e. $\varepsilon^{n}_{abs} < 1\%$.

$$\varepsilon^{n}_{abs} = 100\frac{1}{NUMCV}\left[\sum_{CV=1}^{NUMCV}\left(\frac{\left|\rho^{n+1}_{CV}-\rho^{analytical}_{CV}\right|}{\rho^{analytical}_{CV}}\right)\right] \qquad (5.108)$$

This comparison is carried out here because the industrial sponsor, requested that the final CFD scheme should be tested against a number of compressible and incompressible benchmarks with theoretical results.

The explicit compressible CBS solution of the fully incompressible fluid dynamics equations is not possible [131]. Thus in order to compute incompressible flows where only the pressure and velocity change within the flow field, the CBS algorithm needed to be re-cast in the same fashion as the standard scheme to solve the pressure. This standard scheme is summarized by below and can be seen in [156], [157].

5.6 Solving Incompressible Flows using the AC CBS algorithm

From the research carried out by Nithiarasu and Codina, [131], it is noted that tackling the fully incompressible fluid dynamics equations using the copressible CBS scheme is not possible, unless an artificial compressibility method is employed. This is accomplished by utilizing a relationship between the changes in pressure relative to the change in density, and by assuming constant entropy for an ideal gas we obtain.

$$\frac{\partial P}{\partial \rho} = c^2 = \frac{\gamma P}{\rho} \tag{5.109}$$

The compressible CBS procedure calculates the local pseudo time step (5.98). However, for incompressible flows the compressible wave speed c, and compared to u_i is extremely large. This means that the pressure and velocity field end up numerically stiff, which imposes severe time step restrictions on the computations. To remedy this problem one can introduce the local artificial parameter β that depends on the local speed and local Reynolds number at each control volume. Then using relationship (5.109) and the continuity equation yields.

$$\frac{\partial \rho}{\partial t} = \frac{\partial (\rho u_i)}{\partial x_i} \Rightarrow \frac{\partial \rho}{\partial t} = \frac{\partial \rho}{\partial P}\frac{\partial P}{\partial t} \Rightarrow \frac{1}{c^2}\frac{\partial P}{\partial t} = \frac{1}{\beta^2}\frac{\partial P}{\partial t} \tag{5.110}$$

Where β is the artificial wave speed. According to Malan et al. [150] for incompressible flows this parameter is calculated as:

$$\beta_{CV}^n = \max\left(\varepsilon_\beta, \sqrt{u_i u_i}, \frac{2\mu_\infty}{\rho_\infty h_{CV}}\right) \tag{5.111}$$

As stated by Nithiarasu and Codina, [131], ε_β is set to 0.5 for incompressible benchmarks which enforces an even weighting between adjacent control volumes.

$$\Delta t_{CV}^n = \min\left(\left(\Delta t_{CV}^n\right)_{conv}, \left(\Delta t_{CV}^n\right)_{diff}\right) \tag{5.112}$$

where the convection pseudo time step for incompressible flow is analogous to the compressible time step

$$\left(\Delta t_{CV}^n\right)_{conv} = \frac{h_{CV}}{\beta_{CV} + \sqrt{u_i u_i}} \tag{5.113}$$

And the diffusion time step as presented by Malan et al. [150] is given by:

$$\left(\Delta t_{CV}^n\right)_{diff} = \frac{\rho_\infty \{h_{CV}\}^2}{2\mu_\infty} \tag{5.114}$$

The pressure is computed for incompressible applications, the continuity equation (5.103) is replaced with the equation below (5.115) for the (AC CBS) procedure.

$$P_{CV}^{n+1} = P_{CV}^n - \left(\beta_{CV}^n\right)^2 \frac{\Delta t}{\Delta V}\left(\sum_{f=1,TOTFIC}\left(\rho u_j \bullet n_j A\right)_f\right)^{n+1} \tag{5.115}$$

Finally the enthalpy equation (5.104) is dropped completely from the computational loop because incompressible flows benchmarks are assumed to be isothermal.

5.6.1 The Sequential Artificial Compressibility CBS Scheme

The precedent artificial compressible characteristic based split (AC CBS) procedure described performed well for incompressible flow over a flat plate, Subsonic flow through porous media and pipe flow. Other variants of this procedure were evaluated for these benchmarks but not to the same degree of success as this precedent method. Each step described below is applied to all the interior nodes in a sweep of the grid. After this sweep the boundary conditions are computed. Then the sequential computational iterative procedure is repeated by going to step 1. The AC CBS method was implemented in the computing language FORTRAN and the simulations run within the cluster to solve the Navier Stokes system of equations.

1. According to Malan et al. [150], for incompressible flows the artificial wave speed is calculated as seen in (5.111).

2. The CBS scheme incorporates local pseudo time stepping. The pseudo time step is given by the following equation: where C is the Courant number and depending on the problem is usually < 0.5 The convection time step is analogous to the compressible time step and the diffusion time step as calculated by Malan et al. [150]:

$$\Delta t_{CV}^{n} = \min\left(\left(\Delta t_{CV}^{n}\right)_{conv}, \left(\Delta t_{CV}^{n}\right)_{diff}\right) \tag{5.116}$$

$$\left(\Delta t_{CV}^{n}\right)_{conv} = C\frac{h_{CV}}{\beta_{CV} + \sqrt{u_i u_i}} \tag{5.117}$$

$$\left(\Delta t_{CV}^{n}\right)_{diff} = C\frac{\rho_{\infty}\left\{h_{CV}\right\}^{2}}{2\mu_{\infty}}$$

3. Intermediate Momentum

$$\rho u_i^{*} = \rho u_i^{n} - \frac{\Delta t}{\Delta V}\left(\begin{array}{l}\sum_{f=1,TOTFIC}\left(\left(\rho u_i u_j\right)\bullet n_j A\right)_f - \sum_{f=1,TOTFIC}\left(\frac{\partial \tau_{ji}}{\partial x_j}\bullet n_j A\right)_f \\ +\frac{\Delta t}{2}u_k \sum_{f=1,TOTFIC}\left(div\left(\rho u_i u_j\right)\bullet n_j A\right)_f\end{array}\right)^{n} \tag{5.118}$$

4. Corrected Momentum

$$\rho u_i^{n+1} = \rho u_i^{*} - \frac{\Delta t}{\Delta V}\left(\sum_{f=1,TOTFIC} P_f \bullet n_j A_f - \frac{\Delta t}{2}u_k \sum_{f=1,TOTFIC}\frac{\partial P}{\partial x_j}\bullet n_j A_f\right) \tag{5.119}$$

5. The Continuity Equation is solved using the momentum values from (5.119) at the n+1 "time" level as seen in (5.115)

$$P_{CV}^{n+1} = P_{CV}^{n} - \left(\beta_{CV}^{n}\right)^{2}\frac{\Delta t}{\Delta V}\left(\sum_{f=1,TOTFIC}\left(\rho u_i \bullet n_i A\right)_f\right)^{n+1} \tag{5.120}$$

6 Check convergence to steady state values by sensing whether the relative error is less than the agreed tolerance of 10^{-5} or the number of iteration/sweeps is below the maximum iteration/sweeps, I_{Max}, stipulated by the user. This value was set initially to 95,000 iterations.

7. If convergence has been achieved exit the procedure and display results otherwise begin computational sweep by going back to step 1.

5.6.2 Convergence Criterion for Incompressible Flows

As argued in section 5.4.2 the CFD solver needs to have a "kick" out mechanism when the algorithm has converged to a stable solution. The steady state requirement for incompressible problems is

calculated in a similar fashion to the compressible problems. Where ε^n_{Rel} is the velocity relative error and is calculated by:

$$\varepsilon^n_{Rel} = \frac{1}{NUMCV}\sqrt{\left[\frac{\sum_{CV=1}^{NUMCV}\left(\frac{\left|u^{n+1}_{CV}-u^{n}_{CV}\right|}{\Delta t_{CV}(L/u_\infty)}\right)^2}{\sum_{CV=1}^{NUMCV}\left(u^{n+1}_{CV}\right)^2}\right]} \tag{5.121}$$

The tolerance is set to 10^{-5}. In the following benchmark cases the CBS solution is compared with their associated analytical solutions in [84], [154], [155] where a tolerance of 1% between the analytical values and the computed CBS result are deemed accurate enough for CFD solvers applied to CAVs Hypersonic vehicles.

$$\varepsilon^n_{abs} = 100\frac{1}{NUMELE}\left[\sum_{CV=1}^{NUMELE}\left(\frac{\left|u^{n+1}_{CV}-u^{analytical}_{CV}\right|}{u^{analytical}_{CV}}\right)\right] \tag{5.122}$$

5.7 Transient Flow

When transient effects are so substantial that the steady state CBS procedure seen in Section 5.5.1 will not converge, this situation requires the mathematical consideration of real time intervals. One example is the unsteady eddy flows behind a circular cylinder as seen in Sampaio, Lyra, Morgan, & Wetherill [158].

Only steady state benchmarks were modelled in this research because of the availability of analytical solutions for comparison and hardened validation. No transient benchmarks were tackled in this research, therefore the reader is directed to the available literature. For further details on the dual time step procedure the interested reader should refer to the available literature [159]–[161].

5.8 Concluding Remarks

This chapter describes the numerical implementation of a 2nd ordered explicit algorithm to 2-dimensions on general unstructured meshes. As already mentioned, some of the major difficulties which have to be overcome when attempting the numerical solution of the 2-dimensional Hyperbolic PDEs are: the non-linear nature of the flow; the complex geometries involved in industrial applications; and the high storage and CPU time involved in practical solutions [7]. The fact that non-linear Hyperbolic equations such as the Euler system of equations admit spurious solutions, is in general a result of ignoring some physical effects in the determination of the model, such as the viscous effects. Although viscous effects may be negligible throughout most of the flow, near discontinuities the effect is always strong, and the apparent discontinuities are in reality thin regions with very steep gradients [7]. Some conditions as stated by Hirsch [18], and Le-Veque, [73], must be imposed in order to pick up the correct physical solution and to guarantee uniqueness. For fluid dynamic problems the second law of thermodynamics, which states that the entropy should increase, is invoked and turns out to be a sufficient condition to determine a physically correct and unique solution Hirsch, [18]. This condition is normally referred to as the entropy condition.

In addition to this entropy condition other important requirements of the proposed CFD algorithm adopted in this thesis include:

1. The use of the finite volume method as the basis for spatial discretisation. Simply stated for multi dimensions, the finite volume formulation is an extension of the finite difference approach.
2. A central differencing technique that does not rely on the determination of the upwind direction or Jacobian evaluation removing much complexity in understanding and code writing.
3. The adaptation of an explicit local time stepping approach for steady state problems.
4. The chosen algorithm can handle unstructured elements, an important features for non-linear configurations, such as the geometry of Hypersonic CAVs.
5. The use of techniques to capture shocks by using artificial viscous terms that guarantee an increase in entropy for CFD solutions.
6. 2^{nd} order spatial accuracy that improves the likelihood that the scheme will satisfy the specification from industrial sponsors that the CFD algorithm should be as accurate, relative to the analytical solution as possible.

Improvements in accuracy, efficiency and robustness of a CFD technique represents an important challenge that has to be overcome before present algorithm's for unstructured grids can be applied to industrial applications. Another important and challenging issue refers to the exploitation of the available parallel computer configuration.

It is well known that the treatment of the boundary conditions is an important step with associated costs on the performance in terms of accuracy, stability and convergence of the algorithm. Further study centered upon this subject must be undertaken with the hope to improve some characteristics of the present formulations. The benchmark studies and results presented in chapter 6,7,8,9 and 10 were performed in 2D, and although the systemic implementation of the CBS algorithm has been carried out in 3D a careful study of popular CFD 3D benchmarks needs to be carried out. This represents an important task to be pursed in the future.

6 COMPRESSIBLE INVISCID 2D FLOW ANALYSIS

6.1 Introduction

The development of numerical techniques for the simulation of Hypersonic viscous flows is an area of current practical importance, due to the interest being shown by the aerospace industry in the development of aerodynamically efficient Supersonic and Hypersonic vehicles. As stated by Hirschel and Weiland [5], the simulation of the Hypersonic regimes of interest represents a formidable challenge to any flow solver due to the highly non-linear nature of the interactions. Although our ultimate goal is to simulate numerically the full system of Navier-Stokes equations, the importance of accurately modeling the inviscid flow cannot be overstated. The success of viscous computations at high speed is dependent on how well the scheme succeeds in dealing with the inviscid convection dominated character of the flow.

Some major difficulties which have to be overcome when attempting the numerical solution of the 2-dimensional compressible Euler equations are: the non-linear nature and hyperbolic character of the equations; the complex geometries involved for Hypersonic vehicles which tend to be curved for heat dissipation reasons; and the high storage and CPU time involved in practical simulations. The one dimensional problem in Chapter 4 is of limited use, as it does not provide a strong enough test for evaluating the solvers ability at controlling oscillations propagating in 2-dimensions. Therefore two dimension Supersonic problems generally provide a better test of shock capturing capability than one dimensional problems, where propagation of disturbances can freely travel in the transverse direction transporting spurious oscillations in the process according to Greenshields et al [120]. We therefore devote much attention to develop strategies to damp out these undesirable oscillations by using artificial viscosity.

The large elapsed time necessary to produce structured grids for extremely complex configurations and the difficult control on the quality of the elements represents major disadvantages when employing the structured grid approach. Therefore CFD practitioners have devoted much effort to the development and use of unstructured mesh based finite volume or finite element procedures for compressible Euler equations. These efforts have been driven by the promise of generating rapidly a sufficiently high quality mesh for complex geometries [7]. Unfortunately, the unstructured approach is accompanied by some well-known drawbacks. The major concerns are the accuracy and efficiency of generating steady results in terms of CPU time and storage requirements. These will be of particular importance when the extension to the solver of large 3-D problems is envisaged.

In the following sections, a detailed description is given of the numerical formulations employed, with special attention focused on the finite volume approach to the Characteristic Based Split algorithm with artificial viscosity terms presented by MacCormack [29] with improvements suggested by Jameson's 2^{nd} and 4^{th} ordered blend. The performance of the resulting algorithm is assessed by comparing the discrete solution with the inviscid flow over a Supersonic 2D wedge. It must be emphasized that the generic use of the term n-order scheme refers to the order of the scheme in the smooth region of the solution.

As mentioned previously, the additional operational count involved in the computation using higher-resolution upwind procedures, including the promise of extra difficulties and complexities which

need be faced extending upwind schemes for implementation on multidimensional unstructured grids, make it less attractive in the present research than central differencing procedures. Therefore high resolution, central differencing, shock capturing will be employed as the candidate numerical scheme in the remainder of this research work.

6.2 The Euler Equations

The Euler equations as described in Chapter 2 describe flows where viscosity, thermal conduction and diffusion are ignored and are called inviscid flows. These flows are non-linear, multidimensional and are assumed to be laminar for all flow speeds. As mentioned previously, interest in solving the Euler equations in the aerospace sector began for applications where viscous effects are deemed to be negligible.

The three dimensional Euler equations apply to scientific problems where viscous effects can be assumed to be negligible The set of the Euler equations is closed with the addition of the perfect gas model, this equation and the various variables are detailed in Chapter 2: Mathematical Basis.

While we adopt the Euler equations in the knowledge that they are not an accurate representation of the physical reality, it will allow us to compare the candidate scheme with some closed form analytical solutions.

6.2.1 The FV Approach for the Euler Equations

The candidate density based scheme used here is based on the Characteristic Based Split (CBS) algorithm which has been originally developed by Nithiarasu P, Codina R, [131], in a finite element context. Other research focused on extending the CBS scheme for a variety of fluid applications such as visco-elastic problems and incompressible flow problems [136], [138]. In Nithiarasu P, Codina R, [131], the finite element CBS algorithm was shown to be stable for a number of regimes, ranging from incompressible to Hypersonic flows.

The Characteristic Based Split algorithm enhances the stability of a central differencing approach for the convection flux terms by adding extra temporal terms to the governing equations. For a more comprehensive study of the numerical stability, the dual time stepping methodology and the limitations of the algorithm for finite elements the reader is referred to Nithiarasu P, Codina R, [131].

The CBS algorithm as previously mentioned can be applied as either an explicit or an implicit procedure; see Massarotti, Arpino, Lewis, & Nithiarasu, [132], for a comparison on accuracy and efficiency of these approaches. So far in this research the CBS scheme has been applied as an explicit technique that, ultimately, for extension to unstructured grids has the advantage of negating the need for matrix solvers. Whereby for larger 3D problems we can circumvent solving large matrices, which will hopefully avoid the large overheads in CPU time and memory storage.

Application of the Finite Volume (FV) method begins by expressing the differential equations we wish to solve as an integral within a generic cell volume V, which is assumed fixed in space in this research. Divergence and gradient terms are then converted to integrals over the cell surface A, using a generalized form of Gauss's theorem. The integration requires fluxes at cell faces. For unstructured polyhedral with an arbitrary number of faces, the intended meshing technique for this project, it is desirable that the interpolation to a given face is between owner and neighbor cells only, otherwise it becomes excessively complex according to Greenshields et al [120]. The second ordered CBS algorithm can permit this and is described as a central differencing procedure rather than the higher

order up-winding processes of "reconstruction" , "evolution" or "projection". There is, therefore, no need for any polynomial functions.

For unstructured grids in general there is no alignment of the mesh with the co-ordinate system and the number of neighboring cells can vary from cell to cell [120]. The only statement that can be made about the cell connectivity is that a cell face is either internal and intersects two cells only or comprises part of an external boundary and belongs to a single cell only. In presenting the numerical scheme, we must dispense with notations based on nodal values 'j' and 'k' or points of a compass [120].

6.2.2 The FV Approach on Unstructured Grids

The inviscid CBS method in 1D as seen in Chapter 3 has a convective and a diffusive like term. The convective and the diffusive terms are first and second ordered respectively. From hand calculations of initial computations, the second ordered terms are used as a correction to decrease the magnitude of the first ordered terms. These second order terms were originally computed by linear interpolation of centroid values of the 2^{nd} ordered Laplacian differential; ultimately, this implies a large stencil. This original method was thought to become problematic around the shock fronts as it does not adequately capture the large gradients that are needed to clip the convective terms.

Therefore we propose in this research to obtain a more accurate local approximation for these 2^{nd} ordered diffusion-like terms:

1. I propose that the same method is used to determine the diffusion contribution for a non-orthogonal face.
2. I propose the calculation of a more concise local value for the Cartesian derivatives on the cell faces.

However the use of these two strategies demands the stipulation of the primitive variables on control volume corners alternatively known as the cell vertices. This was done through linear interpolation from the 4 adjacent centroid values because of ease of computation. These early simulations confirmed that such a small stenciled approximation, instead of large stencils for the second ordered terms, is important for accurately resolving the shock however the CBS scheme still seems to be susceptible to instability around the stagnation point at the leading edge.

6.2.2.1 *Cross Diffusion Terms*

When using unstructured grids it becomes possible to accurately fit a mesh to any solution region without the use of cell blockages [17]. In addition, attractive features can be placed in the mesh to aid the solution procedure, for example a polar region can be positioned near an inflow as surmised in Versteeg & Malalasekera, [17] where there is a rotational component to the fluid velocity. However there is an associated cost as fitting meshes to complex boundaries can frequently lead to mesh skewness. There are two major types of mesh skewness firstly non-orthogonality, the definition of which will be given in the following section, and secondly elements which are not convex. Whereby neighbouring elements possess bounding faces which intersect each other.

The process of generating a mesh should not in general allow elements, possessing intersecting faces which are not convex. A good mesh tool will reduce the level of mesh skewness but for highly complex geometries there will always be some degree of skewness in the generated mesh [143]. To accurately model the transfer of conserved quantities through a region where there is mesh skewness requires corrections to be made to the numerical discretisation of the conservation equations. To simplify these corrections the skewness of a mesh is split into a number of contributing components.

These two types of skewness will from now on be denoted as non-orthogonality, which affects the diffusion terms only, and non-conjunctionality which affects the interpolated convection face values only.

6.2.2.2 *Non-Orthogonality*

What follows is a detailed examination of the form the diffusion flux should take for unstructured grids. The following technical notes could apply to 2D elements such as triangles and quadrilatrals or 3D elements such as tetrahedral through to hexahedral elements.

In unstructured grids the lines connecting two centroids P and A are not necessarily parallel to the face unit normal n_j, as shown in Figure 6-1 this is widely known as non-orthogonality Versteeg & Malalasekera, [17].

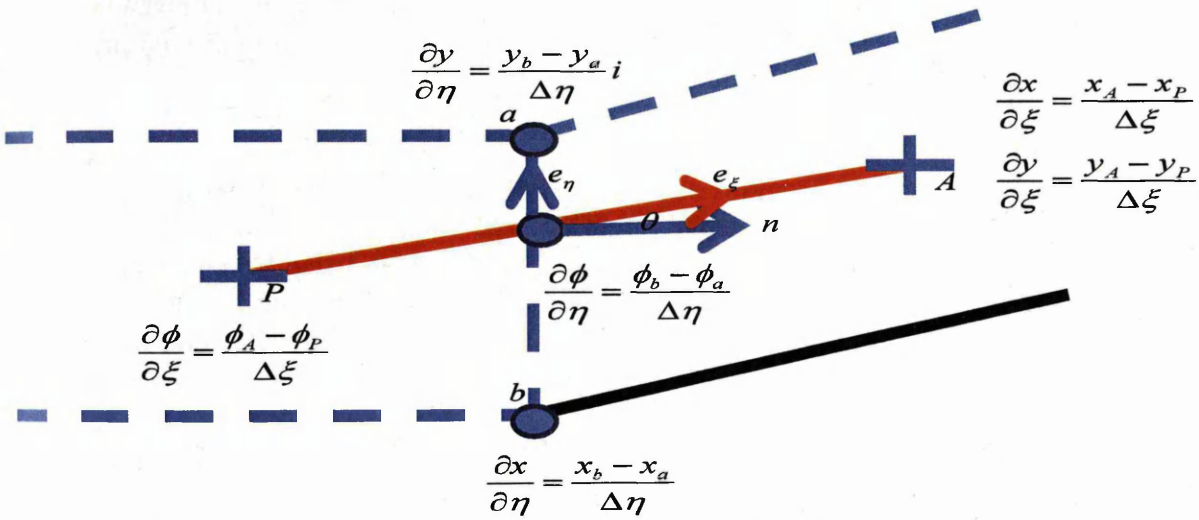

Figure 6-1 Unstructured grid with terms that will aid in the computation of the non-orthogonal diffusion term.

For the CBS algorithm procedure will need to compute a number of diffusion terms around each cell face, these scalars are conventionally represented by ϕ, which takes many values.

$$\phi = (\rho uu, \rho uv, \rho vv, P, \rho uE, \rho vE, uP, vP) \tag{6.1}$$

From Figure 6-1 the computed variables $\partial\phi/\partial\xi$ and $\partial\phi/\partial\eta$ in terms of x and y are to be re-cast to compute the Cartesian derivative using the product rule as summarized in [17]:

$$\frac{\partial \phi}{\partial \xi} = \frac{\partial \phi}{\partial x}\frac{\partial x}{\partial \xi} + \frac{\partial \phi}{\partial y}\frac{\partial y}{\partial \xi} \tag{6.2}$$

$$\frac{\partial \phi}{\partial \eta} = \frac{\partial \phi}{\partial x}\frac{\partial x}{\partial \eta} + \frac{\partial \phi}{\partial y}\frac{\partial y}{\partial \eta} \tag{6.3}$$

Rearranging (6.3) and (6.2) an expression for the Cartesian derivative in the principal directions x,y is obtained which represent the diffusion terms:

$$\frac{\partial \phi}{\partial y} = \frac{1}{J}\left(-\frac{\partial \phi}{\partial \xi}\frac{\partial x}{\partial \eta} + \frac{\partial \phi}{\partial \eta}\frac{\partial x}{\partial \xi}\right) \tag{6.4}$$

$$\frac{\partial \phi}{\partial x} = \frac{1}{J}\left(\frac{\partial \phi}{\partial \xi}\frac{\partial y}{\partial \eta} - \frac{\partial \phi}{\partial \eta}\frac{\partial y}{\partial \xi}\right) \tag{6.5}$$

where

$$J = \left(\frac{\partial x}{\partial \xi}\frac{\partial y}{\partial \eta} - \frac{\partial x}{\partial \eta}\frac{\partial y}{\partial \xi}\right) \tag{6.6}$$

Using the quantities in Figure 6-1 we have everything needed to calculate (6.4), (6.5) and (6.6). This procedure was used to represent the artificial viscosity terms as seen in (6.20) later in this chapter. Here a small stenciled approximation is preferable especially around non-linear regions of pressure such as shocks and stagnation points.

The derivation of the Cartesian derivatives above in (6.4) and (6.5) were in two dimensions only because we are primarily concerned with the development of robust algorithms for 2D benchmarks, however it is worth asking the question - what happens in three dimensions? Within the appendices we set out the procedure to calculate these Cartesian derivatives in three dimensions. As mentioned when employing unstructured grids the calculation of the Cartesian gradients is needed in the governing equations. Scalars and vector values need to be computed on the vertices of the control volume. These vertex values are calculated using linear interpolation from the neighboring cells much like face interpolation, i.e. for quadrilateral elements the vertex values will have a contribution from all the control volumes containing the vertex point. These small stenciled gradients are required in the artificial viscosity terms that follow further on this chapter.

6.2.2.3 *Non-Conjunctionality*

For central differencing methods it becomes essential to calculate values for the convection fluxes and pressure, on the faces. This quantity should be an average value for the whole of the face and should be found at the face centroid. The estimation of the face value is achieved through interpolation, in most cases using distance weighting, along the lines connecting the centroids of the elements either side of the face as discussed by Croft, [143]. The key axiom of central differencing schemes is that the variables change linearly between two cells[7].

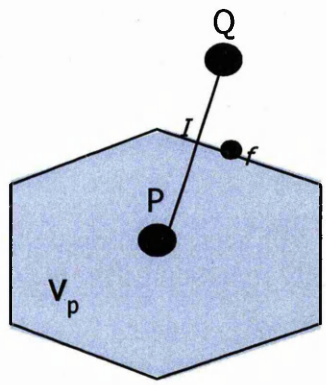

Figure 6-2 Shows a case where the face intersection point,I, of the line connecting adjacent cells does not coincide with the centre of the face.

Figure 6-2 displays the information for non-conjunctional skewness which occurs when the line connecting the centroids P and Q either side of a face, does not pass through the midpoint of the face, point f. The non-conjunctionality correction terms employ an interpolated value at the intersection point, point I, and use additional gradients of the scalar quantity, ϕ, at the face to obtain a more accurate estimate for the face centre.

$$\phi_f = \phi_I + \underline{d}_{If}\left[\frac{\partial \phi}{\partial x_j}\right]_f \qquad (6.7)$$

[7] Although the CBS algorithm is a central differencing scheme it uses higher order terms to correct the magnitude of the face values so they are <u>not</u> exactly like other central differencing methods

where $\underline{d}_{If}$ is the distance vector from the intersection point, I, to the face centre, f. Problems arise in the evaluation of the gradients of ϕ at the face, as seen in (6.7) as the calculation of the gradients require prior knowledge of the face values for ϕ

$$\frac{\partial \phi}{\partial x} = \frac{1}{V} \sum_f A_f n_x \left(\phi_I + \sum_j \left[\frac{\partial \phi}{\partial x_j} \right]_f \left(d_{If} \right)_j \right) \tag{6.8}$$

$[d \phi /dx]_f$ was previously calculated by the subroutines in PHYSICA by linear interpolation of the two adjacent element values either side of the face as documented by Croft, [143]. This dependence can be resolved by transforming (6.8) and the similar equations for the y and z gradients into a 3 by 3 matrix equation for the unknown element gradients. Unfortunately, the solution of this equation would require the inversion of a matrix which would be computationally expensive for very large meshes. Therefore, an improved alternative method is employed in which the previous iteration's gradients are stored and these values are used on the right hand side of (6.8). Moreover this correction is not applied to any of the gradient terms as the most commonly used assumptions in [143] is that quantities vary linearly between points so gradients of gradients would be zero leading to no correction.

The following benchmarks will initially utilize orthogonal quadrilateral meshes before extension to unstructured triangular non-orthogonal meshes. As a consequence the numerical discretization on non-orthogonal triangular meshes described above, will be employed to compute the compressible flow over a 2D wedge, proving the versatility of the FV CBS algorithm.

6.3 Inviscid 2D Supersonic Wedge Benchmark

To obtain a base knowledge of multidimensional Supersonic problems, the Supersonic wedge was recommended by the industrial sponsors at ESA, because this is an application with practical importance to the design of Hypersonic vehicles as it represents sufficiently well the leading edge of a fuselage. The accurate capture of an oblique shock/discontinuity at an angle to the mesh makes this problem challenging in terms of stability. Three wedge geometries were tackled where close agreement was sought with the analytical results. Investigation into inviscid flows was done to enable an understanding of the effects that the extended form of artificial viscosity and mesh resolution has on obtaining stable solutions. For example the errors involved should reduce with the increase of the order of the scheme and the refinement of the mesh.

The Supersonic inviscid wedge case was then reviewed and followed from Anderson, [84]. The motivation to study this problem here was because this Supersonic case has a simplified closed analytical solution that can be used to evaluate the accuracy of the candidate CBS algorithm, it is also able to identify the limitations of the CBS algorithm when used to model multidimensional flows.

Due to the practical impossibility of testing the algorithm for every scientific benchmark and physical problem, only the most important benchmarks are addressed in this study. Moreover it must be stated that some of the results which will be presented here were obtained during the early stages of this research before some improvements were introduced later. In this way, they do not represent the best possible results, but rather a typical performance that can be expected from this algorithm.

6.3.1 Boundary Conditions

This study into inviscid flows also enabled an understanding of the effects that the 2D boundary conditions have on obtaining stable solutions. The boundary conditions can be put into 4 categories for the 2D Supersonic wedge; Free-stream boundaries, Solid wall boundaries, Symmetric boundaries and Outlet boundaries, and these are represented in Figure 6-3 below.

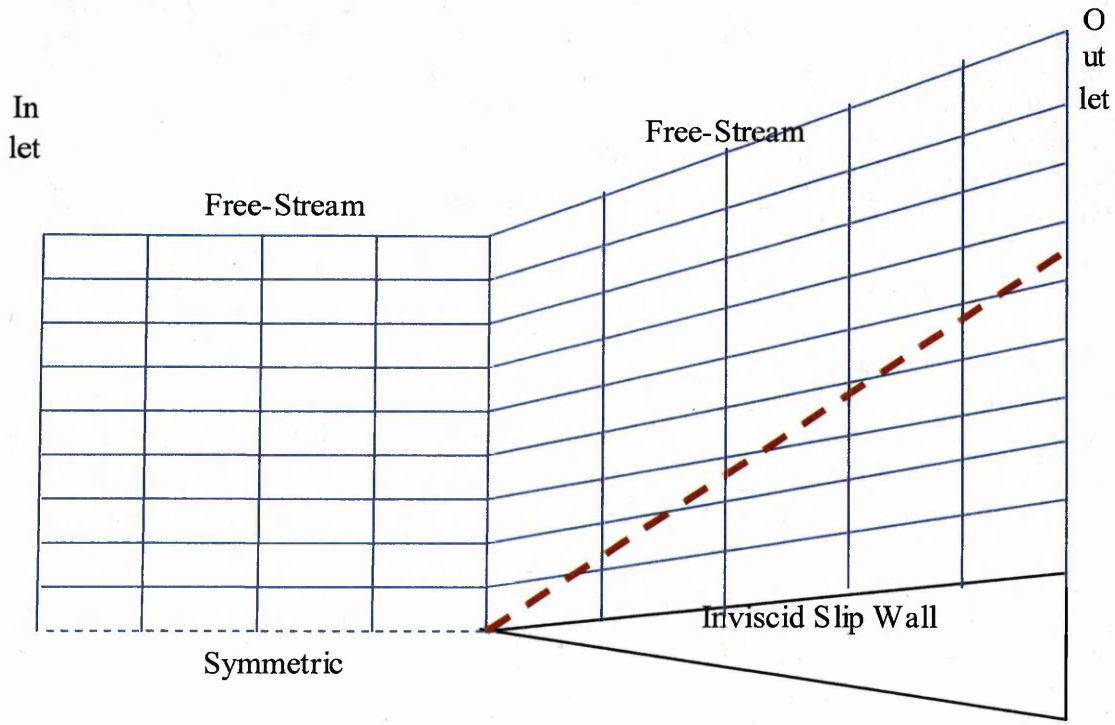

Figure 6-3 **Boundary Conditions for 2D Supersonic wedge.**

6.3.1.1 *Free-Stream*

The free-stream boundaries as seen on the inlet and top of the domain represented in Figure 6-3 are otherwise known as a Dirichlet boundary condition, where the velocity and scalar values are fixed to the respective free-stream values. For example the first wedge problem uses the following parameters.

$M_\infty = 2$

$\rho_\infty = 1.2 \frac{kg}{m^3}$

$T_\infty = 300K$

and $P_\infty = \rho_\infty R T_\infty$

6.3.1.2 *Outlet*

After preliminary simulations with a Neumann boundary condition it was found for the wedge, that the 2nd ordered extrapolation of the solved variables is required and, this extrapolation is preferable for rapid convergence:

$$\frac{\partial^2 (\rho u)}{\partial n^2} = 0$$

$$\frac{((\rho u)_{I+1}-(\rho u)_I)}{\Delta n_{I+1/2}}=\frac{((\rho u)_I-(\rho u)_{I-1})}{\Delta n_{I-1/2}}$$

where $\Delta n_{i+1/2}=\Delta n_{i+1/2}=\Delta n$ implies that the distance connecting adjacent cells is approximately equal. Then it can be shown after re-arrangement that:

$$(\rho u)_{I+1}=2(\rho u)_I-(\rho u)_{I-1}$$

6.3.1.3 *Symmetric Plane*

The default approach for symmetric planes are a Neumann condition i.e. the first ordered extrapolation for the scalar variables and normal velocity at the boundary are assumed to be zero, however, since the tangential velocity on the boundary is zero, this is analogous to a slip wall parallel to the flow. It is worth mentioning that this strategy is only used to model problems where symmetrical profiles are predicted, scientifically, such as slow laminar flow, through symmetric pipes or ducts.

$$\frac{\partial\phi}{\partial n}=0$$

where $\phi=(\mathrm{T},\mathrm{P},\rho,u)$ and $\mathrm{v}_f=0$

$$T_f=T_{CV}$$

$$\rho_f=\rho_{CV}$$

$$P_f=P_{CV}$$

$$u_f=u_{CV}$$

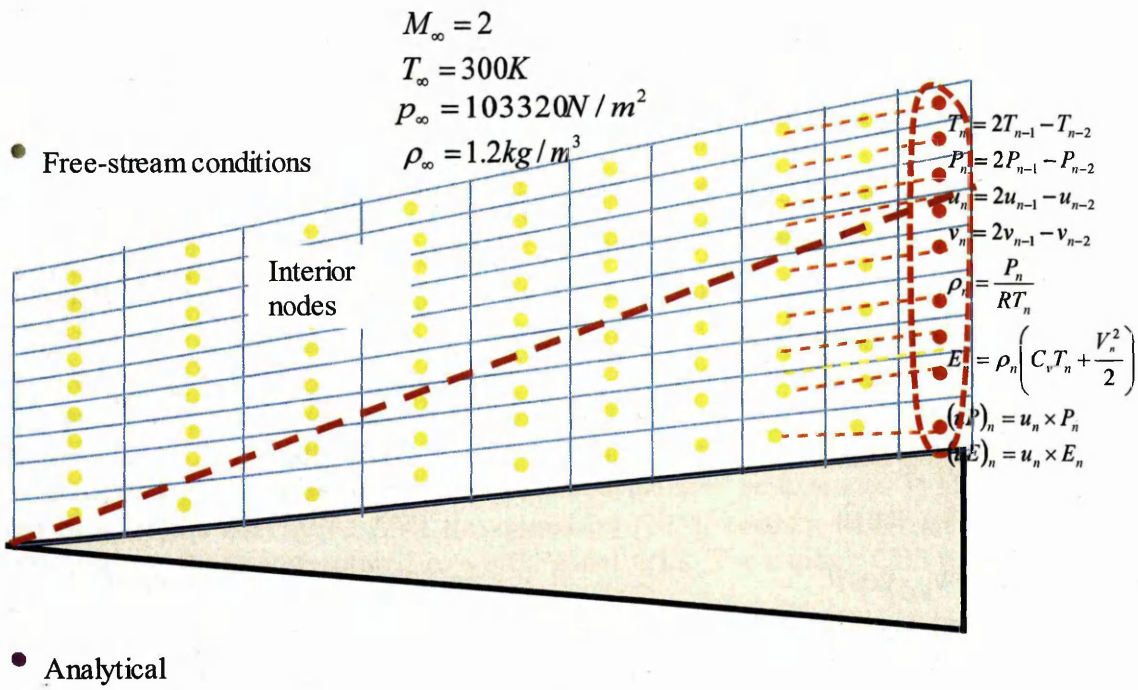

Figure 6-4 **Boundary Conditions for 2D Supersonic wedge.**

6.3.1.4 *Inviscid Slip Walls*

Firstly it is worth mentioning that the problem of slip walls is limited to inviscid flows and is replaced by non-slip walls for viscous problems. Initially we developed and tested the slip wall using the Prandtl Meyer function used in Anderson, [84], and presented in the appendices. However during

the initial simulations, disruptive numerical oscillations at the leading edge occurred resulting in divergence of the solution. Therefore a remedy was sought using the popular ghost cell approach as covered in [73], [162], [163].

Ghost Cell Approach

For the following runs, the Prandtl Meyer Wave was replaced with the Ghost cell approach. For the first benchmark of a Mach 2 inviscid Wedge the solution converged to the analytical solution, an encouraging indication that the coupling of the ghost cell approach and the FV CBS approach is compatible with the inviscid slip walls. The Ghost cell approach can be reviewed in [73], [162], [163] and is summarized below.

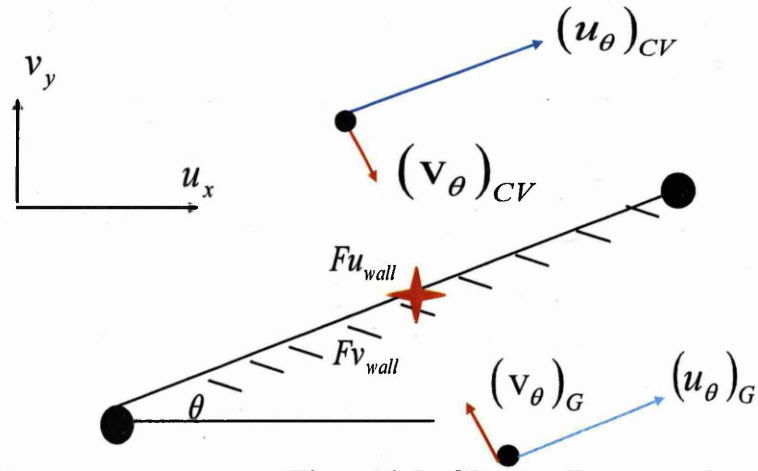

Figure 6-5: **Ghost cell approach.**

where u_θ is the velocity parallel to the wedge surface and v_θ is the velocity normal to the wedge surface. Moreover for this approach $(u_\theta)_G = (u_\theta)_{CV}$ and $(v_\theta)_G = -(v_\theta)_{CV}$ finally the scalar variables at the ghost cell should be equal to the adjacent cell $(\phi_\theta)_G = (\phi_\theta)_{CV}$ where the scalars are given by $\phi = (T, p, \rho)$.

$$u_{\theta,G} = u_{x,G}\cos\theta + v_{y,G}\sin\theta \tag{6.9}$$

$$v_{\theta,G} = -u_{x,G}\sin\theta + v_{yG}\cos\theta \tag{6.10}$$

$$u_{x,G} = u_{\theta,G}\cos\theta - v_{\theta,G}\sin\theta \tag{6.11}$$

$$v_{y,G} = u_{\theta,G}\sin\theta + v_{\theta,G}\cos\theta \tag{6.12}$$

where Fu is the velocity on the face of the control volume that straddles the slip wall.

$$u_{f,wall} = 0.5(u_{x,G} + u_{x,CV}) \tag{6.13}$$

$$v_{f,wall} = 0.5(v_{y,G} + v_{y,CV}) \tag{6.14}$$

6.3.2 Initial Conditions

As stated in Chapter 4 to start the iterative calculations, we must stipulate initial conditions for ρ, T and V for time=0. As previously stated if the initial conditions are too far from the analytical results, the initial pseudo time gradients will be very large causing instability. The user is therefore required to use any information or knowledge about the flow problem. For this present problem T and P increase and ρ and V decrease across the shock front. However for simplicity we assume a constant value of the flow variables, T, P, ρ and V, throughout the solution domain.

6.3.3 Procedure for Analytical Solution

The analytical solution was taken from relationships found on page 135 of Anderson, [84], which were initially derived by Rankine, [164], and applied to the wedge seen in Figure 6-4. The main assumption is of a perfect gas with no chemical reactions. To determine the shock angle the equation below is solved implicitly.

$$\sin^6\beta_w - \left[\frac{M_\infty^2+2}{M_\infty^2}+\sin^2\theta\right]\sin^4\beta_w + \left(\frac{2M_\infty^2+1}{M_\infty^4}+\left[\frac{(\gamma+1)^2}{4}+\frac{(\gamma+1)^2}{M_\infty^2}\right]\sin^2\theta\right)\sin^2\beta_w+\frac{\cos^2\theta}{M_\infty^4}=0 \tag{6.15}$$

where θ is the wedge's half angle, β_w is the shock angle as measured against the horizontal line and M_∞ is the free-stream Mach number. A secant root finding method was used to determine the value of β_w. This root finding method, is the simple subroutine program oblshk written by [165] from the publically accessible NASA website [166]. The program oblshk, uses a, secant root finding method with the initial guess coming from approximate relations. It then evaluates a theta-beta-Mach relation from the wedge half angle, θ , and the parameters such as the Mach number, T, ρ and P after the shock wave.

6.3.4 MacCormack's AVT

The following technical discussion on MacCormack's artificial viscosity term (AVT) should not be confused with the predictor-corrector explicit 2D finite difference scheme derived by MacCormack [29]. By augmenting the CBS steps with MacCormack's AVT we try to suppress decoupling which can lead to divergence. The stabilization of the CBS algorithm by the addition of this numerical source term is necessary if the stability region of the scheme is to be extended [131]. This is initially implemented because the alternative AVT developed by [105], needs a larger stencil and is overly complex when applying it to unstructured non-orthogonal grids. The explicit CBS continuity equation is as follows:

$$\rho_{CV}^{n+1}=\rho_{CV}^{n}-\frac{\Delta t}{\Delta V}\left(\sum_{f=1,\textit{TOTFIC}}\left(\rho u_i \bullet n_i A\right)_f\right)^{n+1}+(S_1)_{CV}^{n} \tag{6.16}$$

where TOTFIC is total number of faces in cell.

$$(S_1)^t_{I,J} = \begin{bmatrix} \dfrac{C_x\left|(P)^t_{I+1,J} - 2(P)^t_{I,J} + (P)^t_{I-1,J}\right|}{\left|P^t_{I+1,J}\right| + \left|2(P)^t_{I,J}\right| + \left|(P)^t_{I-1,J}\right|}\left\{(\rho)^t_{I+1,J} - 2(\rho)^t_{I,J} + (\rho)^t_{I-1,J}\right\} + \\ \dfrac{C_y\left|(P)^t_{I,J+1} - 2(P)^t_{I,J} + (P)^t_{I,J-1}\right|}{\left|(P)^t_{I,J+1}\right| + \left|2(P)^t_{I,J}\right| + \left|(P)^t_{I,J-1}\right|}\left\{(\rho)^t_{I,J+1} - 2(\rho)^t_{I,J} + (\rho)^t_{I,J-1}\right\} \end{bmatrix} \qquad (6.17)$$

This form of artificial viscosity is in the original finite difference formulation taken from Anderson, [84], and is equivalent to adding a 4th ordered differential term where C_x and C_y is the user defined weighting parameter. A recommended value by Anderson for C_x and C_y is 0.2 although a certain level of experimentation is needed on a case by case basis, for optimizing the accuracy of and the speed of generating a numerical solution. The greater this $(S_1)^n_{CV}$ value the more dissipation is applied to areas of the domain that contain large numerical gradients. The intermediate momentum equation, just like the continuity equation above, has an artificial viscous term added, with the same rationale in mind to stabilize the velocity field. Thus, C_x and C_y appears in the three terms $(S_1)^n_{CV}$, $(S_2)^n_{CV}$ and $(S_3)^n_{CV}$. However for unstructured un-orthogonal grids the artificial viscous term in (6.17) is modified in this research to deal with mesh skewness:

$$(S_1)^n_{CV} = \begin{bmatrix} \dfrac{C_x\left|\sum_{f=1,TOTFIC} n_x \dfrac{\partial P}{\partial \bar{x}_f}\right|}{\sum_{f=1,TOTFIC}\left|n_x\right|\left(P_{adj} + P_{CV}\right)}\left\{\sum_{f=1,TOTFIC} n_x \dfrac{\partial \rho}{\partial \bar{x}_f}\right\}_{CV} + \\ \dfrac{C_y\left|\sum_{f=1,TOTFIC} n_y \dfrac{\partial P}{\partial \bar{y}_f}\right|}{\sum_{f=1,TOTFIC}\left|n_y\right|\left(P_{adj} + P_{CV}\right)}\left\{\sum_{f=1,TOTFIC} n_y \dfrac{\partial \rho}{\partial \bar{y}_f}\right\}_{CV} \end{bmatrix} \qquad (6.18)$$

where $\bar{x}_f$ is the non-dimensional area (unity) which implies that the geometric values such as the face area and control volume do not directly affect the magnitude of the S term. Hence, the $\left(S_2^n\right)_i$ and $\left(S_3^n\right)_i$ terms are calculated in a similar fashion to (6.18) where the ρ terms in the brackets, {}, are changed to ρu and ρE terms .

6.4 Sequential FV Inviscid CBS procedure

The sequential computational procedure for the CBS finite volume inviscid algorithm can be done in a number of ways but for this research the following general procedure was pursued after numerical experimentation. Each step described below is applied to all the interior nodes in a sweep of the grid. After this sweep the boundary conditions as seen in step 6 are computed. Then the sequential computational procedure otherwise known as an iteration is repeated by going to step 1. The CBS method was implemented in the scientific/engineering computer language FORTRAN 95 and the simulations run within the high performance cluster in Swansea University to solve the system of equations, where the mesh of the geometry of each of the domains is given.

1. The CBS scheme incorporates local pseudo time stepping. The pseudo time step is given by the following equation: where C is the Courant number and depending on the problem is usually < 0.5.

$$\Delta t^n_{CV} = C\frac{h_{CV}}{c^n_{CV} + \sqrt{(u_i u_i)^n_{CV}}} \tag{6.19}$$

2. The numerical dissipation is calculated from (6.20)

$$(S_1)^n_{CV} = \begin{bmatrix} \dfrac{C_x\left|\sum_{f=1,TOTFIC} n_x \dfrac{\partial P}{\partial x_f}\right|}{\sum_{f=1,TOTFIC}|n_x|\left(P_{adj}+P_{CV}\right)}\left(\sum_{f=1,TOTFIC} n_x \dfrac{\partial\{\rho\}}{\partial x_f}\right)_{CV} + \\ \dfrac{C_y\left|\sum_{f=1,TOTFIC} n_y \dfrac{\partial P}{\partial y_f}\right|}{\sum_{f=1,TOTFIC}|n_y|\left(P_{adj}+P_{CV}\right)}\left(\sum_{f=1,TOTFIC} n_y \dfrac{\partial\{\rho\}}{\partial y_f}\right)_{CV} \end{bmatrix} \tag{6.20}$$

3. Intermediate Momentum step

$$\rho u_i^* = \rho u_i^n - \frac{\Delta t}{\Delta V}\left(\begin{array}{l}\sum_{f=1,TOTFIC}\left((\rho u_i u_j)\bullet n_j A\right)_f - \\ +\dfrac{\Delta t}{2}u_k\sum_{f=1,TOTFIC}\left(div\left(\rho u_i u_j\right)\bullet n_j A\right)_f\end{array}\right)^n + \left(S^n_{CV}\right)_2 \tag{6.21}$$

where u_i - intermediate velocity component in the i direction (m/s)

$\sum_{f=1,TOTFIC}$ denotes a summation over cell faces

4. Finite volume Corrected Momentum Step

$$\rho u_i^{n+1} = \rho u_i^* - \frac{\Delta t}{\Delta V}\left(\sum_{f=1,TOTFIC} P_f \bullet n_j A_f - \sum_{f=1,TOTFIC}\frac{\partial P}{\partial x_j}\bullet n_j A_f\right) \tag{6.22}$$

5. The Continuity Equation is solved using the momentum values from (6.22) at the n+1 "time" level.

$$\rho_{CV}^{n+1} = \rho_{CV}^{n} - \frac{\Delta t}{\Delta V}\left(\sum_{f=1,\textbf{TOTFIC}} \left(\rho u_j \bullet n_j A\right)_f\right)^{n+1} + \left(S_{CV}^{n}\right)_1 \tag{6.23}$$

6. Enthalpy Equation

$$\left(\rho E\right)_{CV}^{n+1} = \left(\rho E\right)_{CV}^{n} + \frac{\Delta t}{\Delta V}\left(\begin{array}{l} -\sum_{f=1,TOTFIC}\left(\left(\rho E u_j\right)\bullet n_j A\right)_f - \sum_{f=1,TOTFIC}\left(\left(P u_j\right)\bullet n_j A\right)_f + \\ +\frac{\Delta t}{2}u_k\left(\sum_{f=1,TOTFIC}\left(\frac{\partial\left(\rho E u_j\right)}{\partial x_j}\bullet n_j A\right)_f + \sum_{f=1,TOTFIC}\left(\frac{\partial\left(u_j P\right)}{\partial x_j}\bullet n_j A\right)_f\right) \end{array}\right)^{n} + \left(S_{CV}^{n}\right)_3 \tag{6.24}$$

To close the equation set the Ideal Gas Law, Sutherlands Law and the Prandtl Law are used. The Prandtl number, which is assumed constant for ideal gases at moderate temperature [82] where Pr is 0.74.

7. Compute the outlet values using linear extrapolation.

$$\left(\rho\right)_{N_{\max},J}^{n+1} = 2\left(\rho\right)_{N_{\max}-1,J}^{n+1} - \left(\rho\right)_{N_{\max}-2,J}^{n+1} \tag{6.25}$$

$$\left(\rho u\right)_{N_{\max},J}^{n+1} = 2\left(\rho u\right)_{N_{\max}-1,J}^{n+1} - \left(\rho u\right)_{N_{\max}-2,J}^{n+1} \tag{6.26}$$

$$\left(\mathrm{T}\right)_{N_{\max},J}^{n+1} = 2\left(\mathrm{T}\right)_{N_{\max}-1,J}^{n+1} - \left(\mathrm{T}\right)_{N_{\max}-2,J}^{n+1} \tag{6.27}$$

$$\left(\rho \mathrm{v}\right)_{N_{\max},J}^{n+1} = 2\left(\rho \mathrm{v}\right)_{N_{\max}-1,J}^{n+1} - \left(\rho \mathrm{v}\right)_{N_{\max}-2,J}^{n+1} \tag{6.28}$$

and at the inlet and fix the velocity, density and temperature.

$$\begin{aligned} M_\infty &= \{2,3,9\} \\ \rho_\infty &= 1.2\frac{kg}{m^3} \\ T_\infty &= 300K \end{aligned} \tag{6.29}$$

8. Check convergence to steady state values by sensing whether the relative error is less than the agreed tolerance of 10^{-5} or the number of iteration/sweeps is below the maximum iteration/sweeps, I_{Max}, stipulated by the user, this value was set initially to I_{Max} =95,000 iterations.

9. If convergence has been achieved exit the procedure and display results otherwise re-start the computational sweep by going back to step 1.

Quotients

Linear interpolation in terms of the neighbouring nodal values is adopted for the face fluxes. For the two momentum equations, intermediate and corrected momentum the derivative terms can be calculated by careful substitution of the following discrete terms.

Let $U = \rho u$ and $V = \rho v$

$$\left(\frac{\partial U}{\partial x}\right)^{n}_{I+1} = \sum_{k=1}^{k_{max}} n_x A_k U_k \quad \text{Where} \quad U^n_k = \frac{(U^n_{I+1} + U^n_I)}{2}$$

General Remarks

The CBS scheme has been derived as either fully explicit or semi implicit scheme. The implicit time integration does not require severe time limitations as with fully explicit schemes. However this comes at a cost with a direct or indirect matrix solver being employed. The CBS algorithm in this chapter was employed as a fully explicit time integration because of this reason. However this results in a severe restriction in the time step which is remedied when using the local finite wave speed and the Courant number stopping the pressure field from diverging from the true pressure field. [8]

In the present study we are principally concerned with the spatial accuracy of the schemes under investigation. Therefore, the time derivatives in the equations are discretized by a simple Euler explicit scheme rather than more elaborate methods, such as higher order Runge-Kutta time integration. There is however, no difficulty in incorporating such methods for time integration into specific further research.

6.5 Mach 2 Inviscid Wedge Study

As stated previously the motivation to study this problem was because the Supersonic 2D wedge case has a closed form analytical solution that can be used to evaluate the accuracy and stability of CBS algorithms. It is also able to identify the limitations of the CBS algorithm when modelling Supersonic compressible flows. When large Mach numbers (Mach>5) applications are modelled, numerical oscillations in proximity of the shock propagating in the transverse direction are strongly damped by the flow, resulting in errors being pushed out from the solution domain. However at transonic or low Supersonic speeds (Mach<2) the oscillations are more likely to build up causing instability [120]. Therefore this benchmark at Mach 2 represents an important challenge for the CFD solver chosen. Moreover, the main challenge for the numerical procedure in this case is the resolution of the discontinuity at the leading edge. Prediction of the discontinuity is extremely sensitive to dissipation of the numerical scheme; the more dissipation, the thicker the shock meaning an un-physical solution. However too little dissipation leads to spurious oscillations in the solution causing instability or divergence.

6.5.1 Analytical Solution

The analytical solution for this benchmark is obtained using an iterative approach in the subroutine taken from Slater, [165], where the input is the free-stream conditions and the 2D wedge's geometrical parameters, where L is the length of the wedge β is the shock half angle, θ is the wedges half angle and ∞ denotes the reference values.

[8] Using the local pseudo time stepping scheme does not capture the transient nature of the flow.

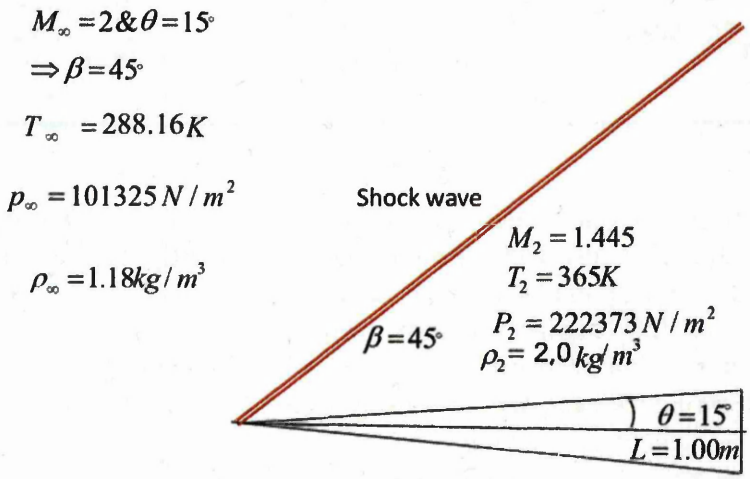

Figure 6-6 Schematic of the Supersonic Mach 2 15° Wedge with primitive variables post shock.

The oblique shock wave evolves from its leading edge as shown in Figure 6-6. The computational domain should be high enough so that the shock does not exit the domain at the top and instead exits the domain at the right outlet boundary. Meaning that the flow variables as seen in Section 6.3.1.2 can be extrapolated at the right hand boundary and a free-stream boundary will be applied to the top boundary.

Table 6-1- Grid and flow parameters for Mach 2 Wedge.

Mach 2 Wedge	M_∞[-]	ρ_∞[kg/m^3]	T_∞[K]	θ[-]	N_x	N_y	N_t
	2	1.18	300	15°	76	62	4712

6.5.2 Solver Results

During hand calculations of the following simulations it became apparent that the CBS calculation is highly dependent on the higher order terms in the intermediate momentum and enthalpy equations. Divergence is encountered for the numerical formulation when the Courant number >0.1, therefore a value of 0.05 was employed for all the cases in this chapter. When the steady state solution is reached the termination of the calculation can be done automatically in the code by a test calculation, sensing when the changes in the flow variables between each iteration becomes smaller than a prescribed tolerance.

As mentioned the relative errors of density, velocity and temperature of the order of 10^{-5}, is an adequate relative error for CFD, and because the relative errors prove to be a useful indicator of whether a CFD solution has fallen to the steady state solution. The following fixed mesh was employed with a fixed mesh spacing so that the effect of increasing the artificial viscosity can be ascertained. This is done by increasing the artificial viscosity term by substituting different values of C_x & C_y of 0.1,0.2,0.4 and 0.6.

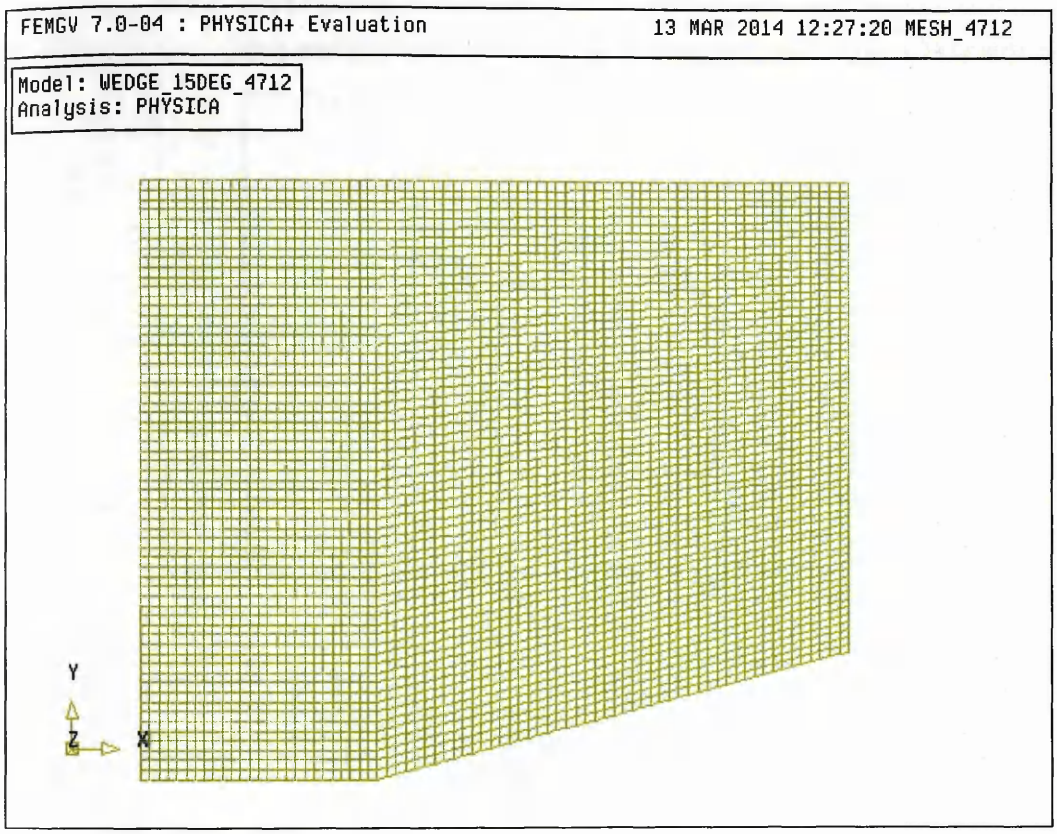

Figure 6-7- Mesh1, Containing 4712 quadrilateral elements that was used to capture Figure 6-6.

6.5.2.1 *Artificial Viscosity Parametric Study*

As Lyra, [7], states the 2nd order numerical viscosity term damps 2nd ordered modes, helping the stability behaviour of the algorithm, but it is not enough to damp the numerical errors introduced by the limiting procedure. Ultimately the residual cannot always drop below a certain level. The convergence behaviour was also found to depend strongly on the value of Courant number, C. The initial results were obtained using MacCormack's AV term, where C_x and C_y in equation (6.20) was tuned for the investigated benchmark. Where $C_x = C_y = [0.1, 0.2, 0.4, 0.8]$. This form of artificial viscosity is taken from Anderson, [84], and is equivalent to adding a 4th ordered differential term. The stabilization of the CBS algorithm by the addition of this numerical source term is necessary to extend the stability region of the scheme for this problem.

The Mach speed is plotted for each of the C_x and C_y values seen above for all control volumes adjacent to the bottom boundary. Starting at the inlet (X=0m) and running through to the trailing edge (X=1.5m). For comparison purposes the Mach components are plotted against the analytical results.

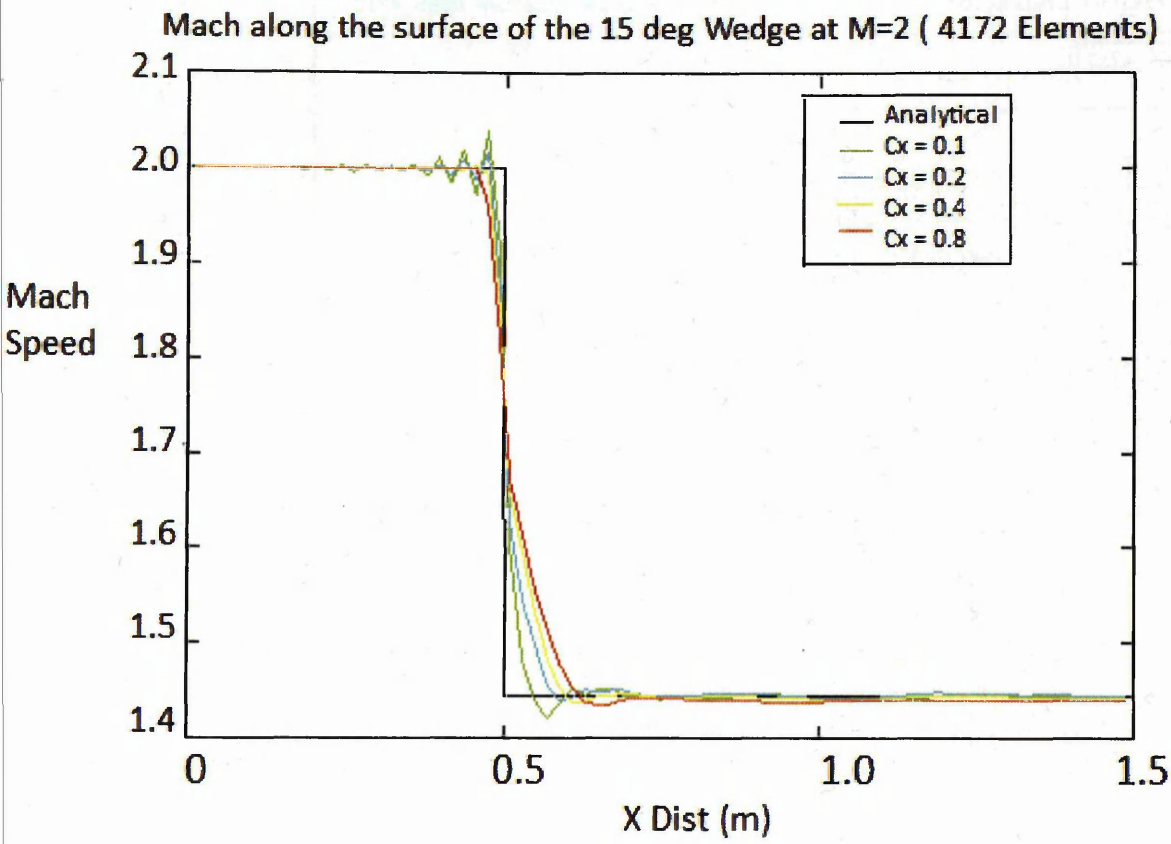

Figure 6-8- Quantifying the effect that the value for C_x & C_y has on the converged Mach profile for the Supersonic wedge depicted in Figure 6-6.

The purpose of this plot is to evaluate how increasing the value of C_x effects the CBS's ability to resolve the discontinuity. The vertical axis is labelled with "Mach number" and the horizontal axis label with "x(m)", the length along the wedge from the inlet in metres. The main trend displayed in Figure 6-8 is that as C_x and C_y is increased, oscillations are damped, however, the shock becomes smeared causing a converged un-physical solution; something of a drawback. The Mach speed as calculated in the CBS solver using C_x and C_y values as seen in the key i.e. 0.1, 0.2, 0.4 and 0.8 are shown in Figure 6-8. This is compared against the analytical solution as seen as the full back line.

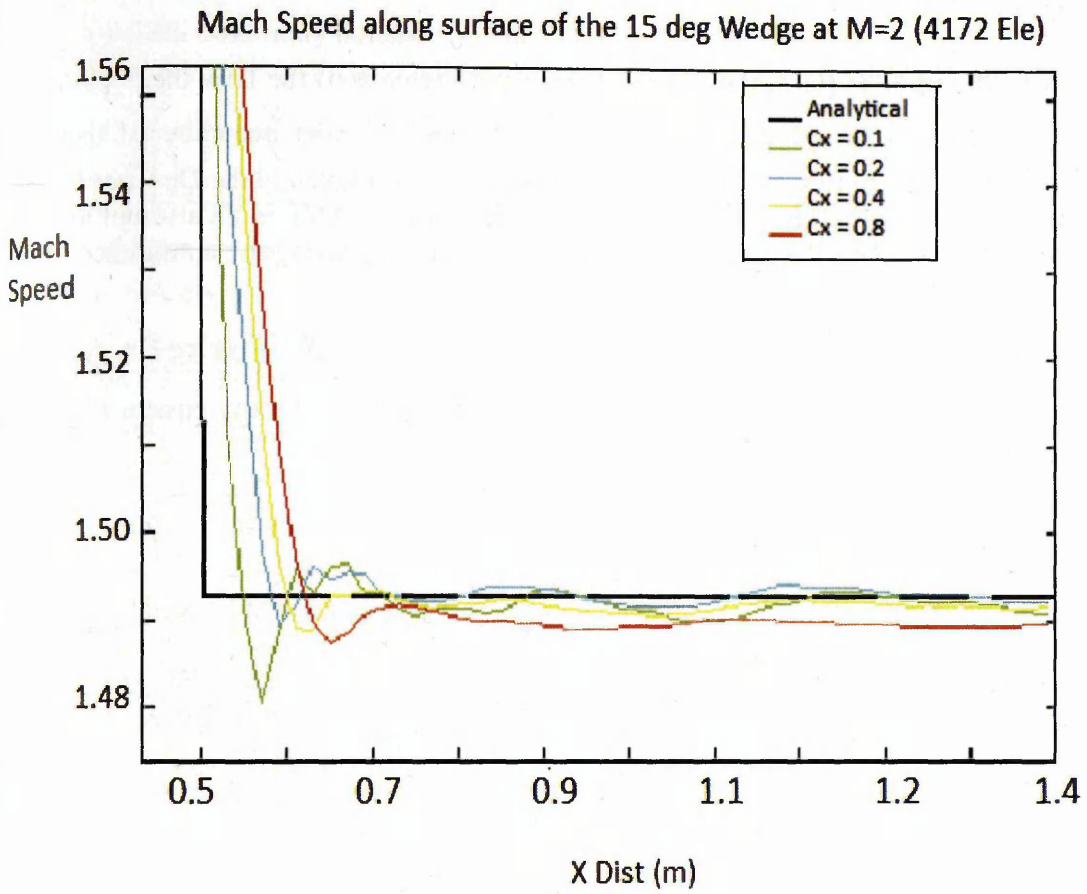

Figure 6-9- Quantifying the effect that the value for C_x & C_y has on the converged Mach profile for the Supersonic wedge depicted in Figure 6-6 magnified for the post shock profile.

Figure 6-9 is a magnified plot of Figure 6-8. This shows conclusively that the Mach number solution as calculated by the CBS algorithm, is not in perfect agreement with the analytical solution even though the algorithm has converged to relative density errors of the order of 10^{-5} with the 4 different C_x and C_y parameter values. Particularly inadequate are the large undershoots after the shock at (X=1 m), because the Mach numbers are all under-estimated. A CFD solution should display accuracy of the solution in relation to analytical/experimental results. Even with large values of C_x and C_y the solution seen in Figure 6-9 seems to be lacking in accuracy in relation to the analytical solution. Therefore the challenge as the next set of results will show, is to determine the adequate type of artificial viscosity which should be large enough to damp instabilities and, at the same time, be small enough to avoid the destruction of flow features such as the discontinuity.

6.6 Jameson, Schmidt & Turkel's AVT

Just like the collaboration between the Finite Volume CBS algorithm and JST AVT in the 1-D results in Chapter 4, MacCormacks AVT in this chapter was replaced with the JST AVT that importantly has a fourth ordered term that is activated in the inviscid region of the flow.

The mono-artificial viscosity term (AVT) devised by MacCormack [29] and displayed in Figure 6-8 and Figure 6-9 is easier to implement for non-orthogonal unstructured grids notably because this is a $\partial^2(U)$ ordered term whereas Jameson, Schmidt & Turkel's artificial viscosity term (JST AVT) has an additional, $\partial^4(U)$ term.

According Jameson & Mavriplis in [60] , the JST AVT in smooth regions of the flow the $\partial^4(U)$ term is activated and the $\partial^2(U)$ is turned off, which ensures the second order accuracy of the CBS scheme. Therefore the next step in this case study, just like the approach taken in the De-Laval study, was to employ a modified form of JST AVT in place of MacCormack's AVT in an attempt to drive down the absolute error to less than 1% from the analytical solution, increasing the confidence of the accuracy of the CFD results.

6.6.1 Numerical Implementation of Jameson, Schmit & Turkel's AVT

Now the energy equation, the intermediate momentum equation and the continuity equation will all be coupled with an JST AVT.

$$\rho_{CV}^{n+1} = \rho_{CV}^{n} - \frac{\Delta t}{\Delta V}\left(\sum_{f=1,TOTFIC}\left(\rho u_j \bullet n_j A\right)_f\right)^{n+1} + (D_1)_{CV}^{n} \tag{6.30}$$

The term, $D_{I,J}$ & D_{CV}, are interchangeable. This term, D_{CV}, in (6.30) is calculated by splitting the 2nd and 4th ordered derivatives into two 1st order and 3rd ordered derivatives, on each of the cell faces. The 2nd ordered artificial dissipation term is activated in regions where gradients are changing rapidly such as shock waves and the 4th ordered term is activated where flow regions have relatively smooth property fields.

$$D_{I,J}^{n} = k_{I,J}^{(2)}\partial^2(U) + k_{I,J}^{(4)}\partial^4(U) \tag{6.31}$$

$$D\rho = D_x\rho - D_y\rho$$

$$D_x\rho_I^n = D_{I+1/2,J}^n - D_{I-1/2,J}^n$$

Hence

$$D_y\rho_I^n = D_{I,J+1/2}^n - D_{I,J-1/2}^n$$

Let

$$D_{I+1/2,J}^n = \left(\varepsilon_{I+1/2,J}^{(2)}\left(\rho_{I+1,J}^n - \rho_{I,J}^n\right) - \varepsilon_{I+1/2,J}^{(4)}\left(\rho_{I+2,J}^n - 3\rho_{I+1,J}^n + 3\rho_{I,J}^n - \rho_{I-1,J}^n\right)\right) \tag{6.32}$$

where $\varepsilon_{i+1/2}^{(2)}$ is called the 2nd order weighting value.

$$\varepsilon_{I+1/2}^{(2)} = k^{(2)}\max(\nu_I, \nu_{I+1})_J \tag{6.33}$$

where ν_x is the pressure sensor "switch" and is always positive providing the domain is not in a vacuum Jameson, Schmidt & Turkel's [105].

$$\nu_x = \left(\frac{\left|P_{I+1}^n - 2P_I^n + P_{I-1}^n\right|}{\left|P_{I+1}^n\right| + \left|2P_I^n\right| + \left|P_{I-1}^n\right|}\right)_J \tag{6.34}$$

$$\varepsilon_{I+1/2}^{(4)} = \max(0, (k^{(4)} - \varepsilon_{I+1/2}^{(2)}))_J \tag{6.35}$$

If $\varepsilon_{I+1/2}^{(2)}$ is greater than $k^{(4)}$ then the $\varepsilon_{I+1/2}^{(4)}$ value is zero meaning in inviscid regions of the flow the term $\varepsilon_{I+1/2}^{(4)}$ damps out higher order oscillations. The weighting parameters that are recommended by Jameson, Schmidt & Turkel's [105] for Supersonic applications are:

$$k^{(2)} = 0.25, k^{(4)} = 0.004$$

So for the CBS continuity equation D_x^n becomes.

$$D_x(\rho)_{I,J}^n = \begin{pmatrix} \varepsilon_{I+1/2}^{(2)}\left(\rho_{I+1}^n - \rho_I^n\right) - \varepsilon_{I+1/2}^{(4)}\left(\rho_{I+2}^n - 3\rho_{I+1}^n + 3\rho_I^n - \rho_{I-1}^n\right) \\ -\varepsilon_{I-1/2}^{(2)}\left(\rho_I^n - \rho_{I-1}^n\right) + \varepsilon_{I-1/2}^{(4)}\left(\rho_{I+1}^n - 3\rho_I^n + 3\rho_{I-1}^n - \rho_{I-2}^n\right) \end{pmatrix}_J \tag{6.36}$$

The dissipative terms for the remaining equations are obtained by replacing ρ with ρu, ρv and ρE respectively.

The above strategy for constructing 2nd and 4th ordered terms for the x-direction is repeated for the y direction. i.e. D_y^n for the continuity equation will be:

$$D_y(\rho)_{I,J}^n = \begin{pmatrix} \varepsilon_{I,J+1/2}^{(2)}\left(\rho_{I,J+1}^n - \rho_{I,J}^n\right) - \varepsilon_{I,J+1/2}^{(4)}\left(\rho_{I,J+2}^n - 3\rho_{I,J+1}^n + 3\rho_{I,J}^n - \rho_{I,J-1}^n\right) \\ -\varepsilon_{I,J-1/2}^{(2)}\left(\rho_{I,J}^n - \rho_{I,J-1}^n\right) + \varepsilon_{I,J-1/2}^{(4)}\left(\rho_{I,J+1}^n - 3\rho_{I,J}^n + 3\rho_{I,J-1}^n - \rho_{I,J-2}^n\right) \end{pmatrix} \tag{6.37}$$

where ν_y is the pressure sensor "switch" in the y-direction and is always positive Jameson, Schmidt & Turkel's [105].

$$\nu_y = \frac{\left|P_{I,J+1}^n - 2P_{I,J}^n + P_{I,J-1}^n\right|}{\left|P_{I,J+1}^n\right| + \left|2P_{I,J}^n\right| + \left|P_{I,J-1}^n\right|}$$

$$\varepsilon_{I,J+1/2}^{(2)} = k^{(2)} \max(\nu_{I,J}, \nu_{I,J+1})$$

$$\varepsilon_{I,J+1/2}^{(4)} = \max(0, (k^{(4)} - \varepsilon_{I,J+1/2}^{(2)}))$$

The above procedure is sufficient for orthogonal and structured grids. To extend this method to unstructured grids the following method is employed.

6.6.2 Extension to Unstructured grid

For an unstructured non-orthogonal grids there are artificial viscous terms in (6.32) which are modified in this research to deal with mesh skewness (6.31). As discussed earlier this term, $D_{I,J}$, above is calculated by splitting the 2nd and 4th ordered derivatives into two 1st order and 3rd ordered derivatives, on each of the cell faces like so.

$$D(\rho)_{I,J}^n = D_x\rho - D_y\rho \tag{6.38}$$

So for the contribution from the gradients in the x-direction the equation becomes:

$$(D_x)_{I,J}^n = \frac{1}{TOTFIC} \sum_{f=1,TOTFIC} (D_x)_f n_x \tag{6.39}$$

where $\sum_{f=1,TOTFIC}$ denotes a summation over the total number of faces in a cell.

$$(D_x)_f^n = \left(\varepsilon_f^{(2)}(n_x)_f\left(\rho_{I+1}^n - \rho_I^n\right) - \varepsilon_f^{(4)}(n_x)_f\left(\rho_{I+2}^n - 3\rho_{I+1}^n + 3\rho_I^n - \rho_{I-1}^n\right)\right)_J$$

where $\varepsilon_f^{(2)}$ is called the 2nd order weighting value, and is calculated using.

$$(\varepsilon_x)_f^{(2)} = k^{(2)} \max((\nu_x)_I, (\nu_x)_{I+1})_J \tag{6.40}$$

where ν_x is the pressure sensor "switch".

$$(\nu_x)^n_{I,J} = \left[\frac{\left| \sum_{f=1,TOTFIC} n_x \frac{\partial P}{\partial \bar{x}_f} \right|}{\sum_{f=1,TOTFIC} |n_x| (P_{I+1} + P_I)} \right]_j$$

Where $\bar{x}$ is unity and n_x is the, x component of the normal vector.

$$(\varepsilon_x)^{(4)}_f = \max(0, (k^{(4)} - (\varepsilon_x)^{(2)}_f)) \qquad (6.41)$$

For orthogonal meshes, if the $\varepsilon^{(2)}_f$ is greater than $k^{(4)}$ then $\varepsilon^{(4)}_f$ is zero. This means in inviscid regions of the flow the term $\varepsilon^{(4)}_{I+1/2}$ damps out higher order oscillations. The weighting parameters recommended by Jameson, Schmidt & Turkel's [105] are:

$$k^{(2)} = 0.25, k^{(4)} = 0.004$$

An equivalent procedure is adopted for the y-contributions to the above numerical formulation for the artificial viscosity term is implemented into the PHYSICA source codes for unstructured grids.

After initial runs were done on a coarse 4712 mesh, it was realized that unless a non-zero value for $k^{(4)}$ is used, the CBS calculations are unstable and soon diverge. An improvement to the solution quality was sought by conducting a parametric study for the JST AVT, instead of the mono second ordered artificial viscosity. Four different values for $k^{(2)}$ were employed.

$$k^{(2)} = [0.1, 0.15, 0.25, 0.35]$$

$$k^{(4)} = 0.004$$

6.6.3 Jameson, Schmit & Turkel's AVT Results

The following runs were conducted for the wedge depicted in Figure 6-6 where the Courant number equals 0.05 and where $k^{(4)}$ equals 0.004 for all the four differing values of $k^{(2)}$. These results for the Mach number and pressure were taken over the surface of the wedge when the density error was less than the stipulated tolerance of 10^{-5}.

Table 6-2-Legend for Figure 6-10.

Color	$k^{(2)}$	$k^{(4)}$
Green	0.1	0.004
Dark Blue	0.15	0.004
Light Blue	0.25	0.004
Red	0.35	0.004
Black	Analytical	Analytical

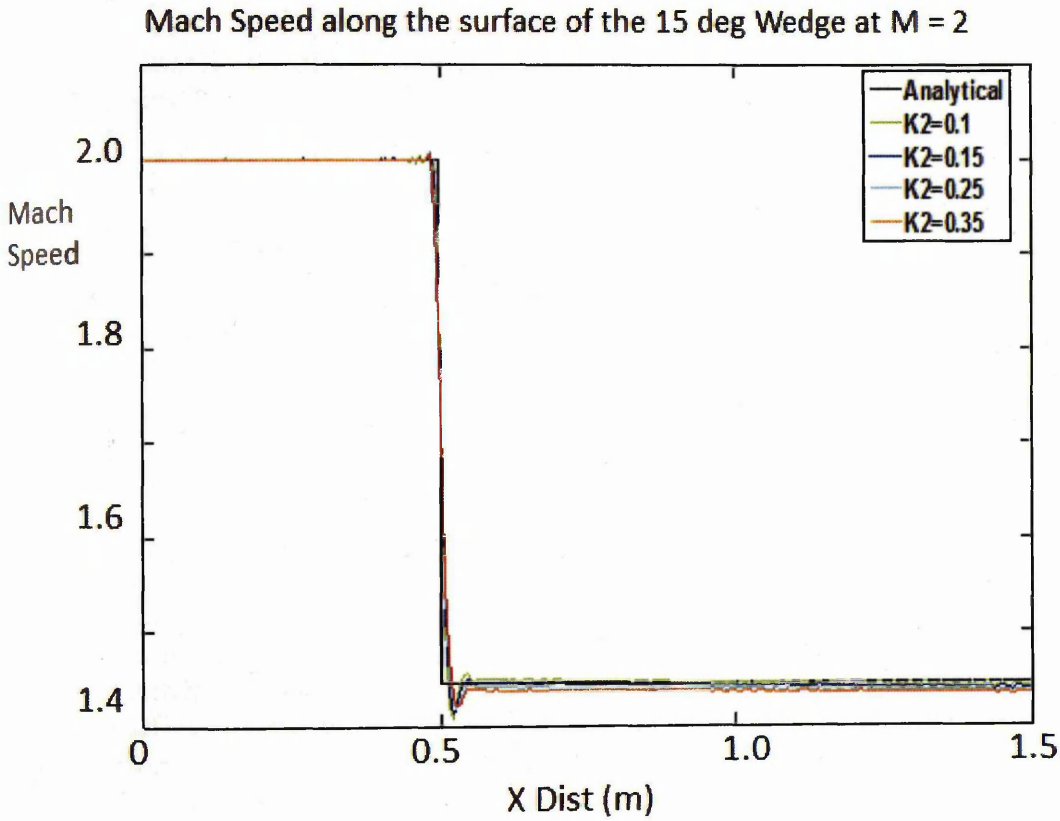

Figure 6-10 - Quantifying the effect that the value for $k^{(2)}$ has on the converged profile for the Supersonic wedge depicted in Figure 6-6.

The Mach number as calculated by the CBS formulation to the conservation governing equations, as presented in equations (6.21)-(6.24) is given by the coloured lines and the analytical profile for the Mach speed over the surface of the wedge as calculated by the subroutine presented by [165] is shown in Figure 6-10 as the full back line. The vertical axis is labelled with "Mach number" and the horizontal axis is labelled with "x(m)" and the length from the inlet is measured in metres. The legend identifies the values of $k^{(2)}$ used in this JST AVT parametric study.

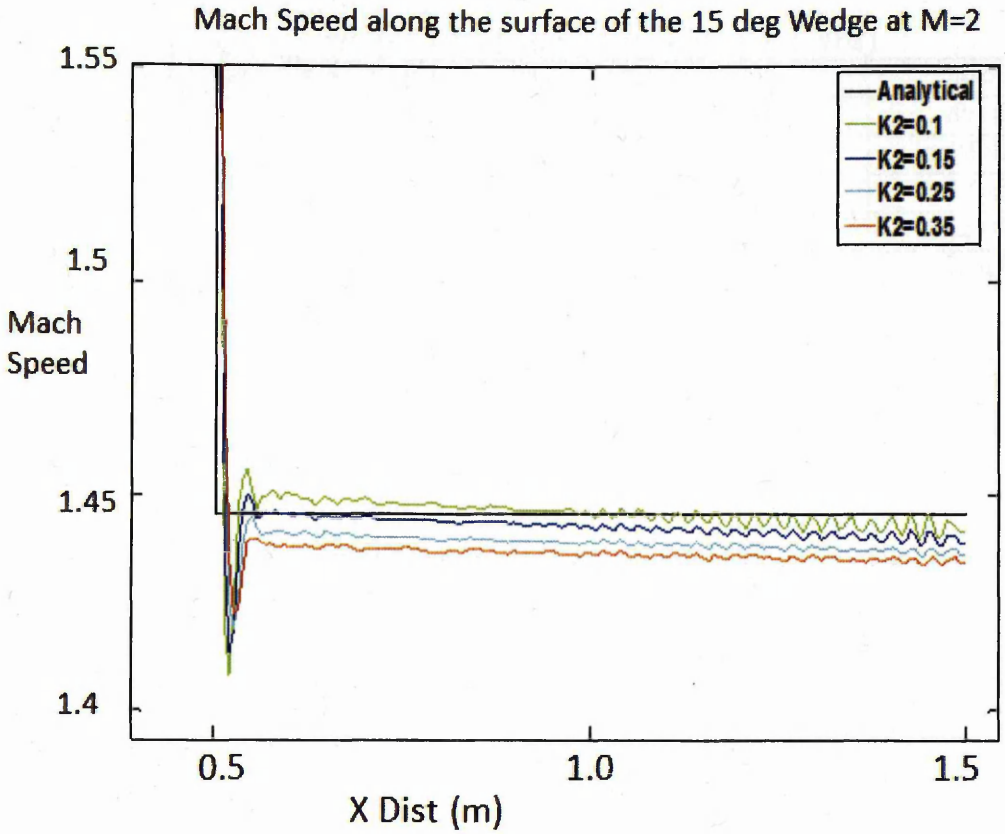

Figure 6-11 - Quantifying the effect that the value for $k^{(2)}$ has on the converged profile for the Supersonic wedge depicted in Figure 6-6, magnified for the post shock profile.

Figure 6-11 above is a magnified plot of Figure 6-10. This shows conclusively that the Mach number solution as calculated by the CBS algorithm, is not in perfect agreement with the analytical solution even though the algorithm has converged to relative density errors of the order of 10^{-5}. The analytical solution as calculated by (6.15) is displayed as the full black line. The differing CBS solutions are given by the legend.

The CBS results are compared against the associated analytical solution, taken from [165]. As highlighted earlier, according to industrial sponsors a tolerance of 1% between these analytical values and the computed CBS result are deemed accurate enough for CFD solvers applied to Hypersonic vehicles.

$$\varepsilon_{abs}^{n} = 100 \frac{1}{NUMELE} \left[\sum_{ele=1}^{NUMELE} \left(\frac{\left| M_{ele}^{n+1} - M_{ele}^{analytical} \right|}{M_{ele}^{analytical}} \right) \right] \qquad (6.42)$$

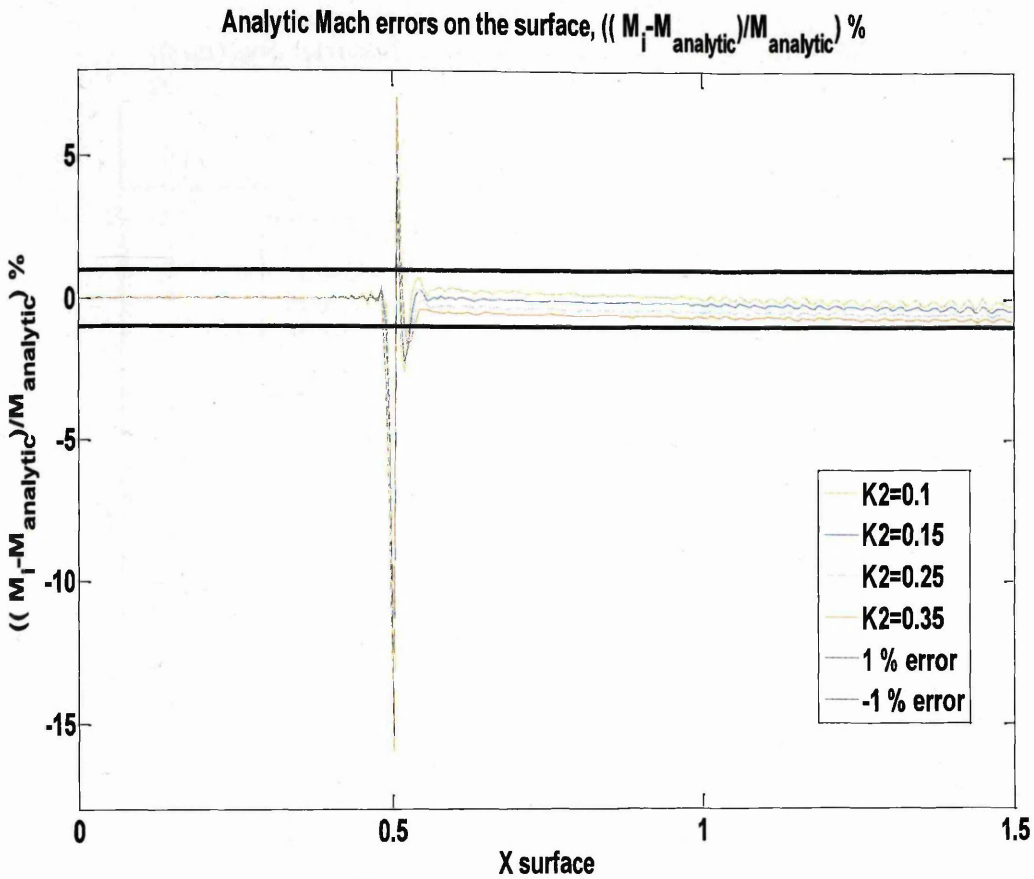

Figure 6-12-Quantifying the effect that the value for $k^{(2)}$ has on the percentage error for the Supersonic wedge depicted in Figure 6-6.

Figure 6-12 shows the absolute errors for the Mach number as calculated by (6.42) for the mesh seen in Figure 6-7. The steady state solutions for all runs were obtained with a fixed value for $k^{(4)}$ of 0.004, a Courant number of 0.05 and with differing $k^{(2)}$ values seen in Table 6-2 (0.1,0.15,0.25,0.35). Apart from the leading edge region the CBS scheme is accurate enough at capturing the Mach number along the surface of the wedge. The percentage error shows that the average absolute error is between the ±1% tolerance.

An important quantity used throughout the analysis of aerodynamic shapes is the coefficient of pressure, where the coefficient of pressure is defined as.

$$C_p = \frac{P_{ele} - P_\infty}{0.5\rho_\infty u_\infty^2} \qquad (6.43)$$

where P is the pressure and the subscript ∞ is the free-stream conditions and ele is the element.

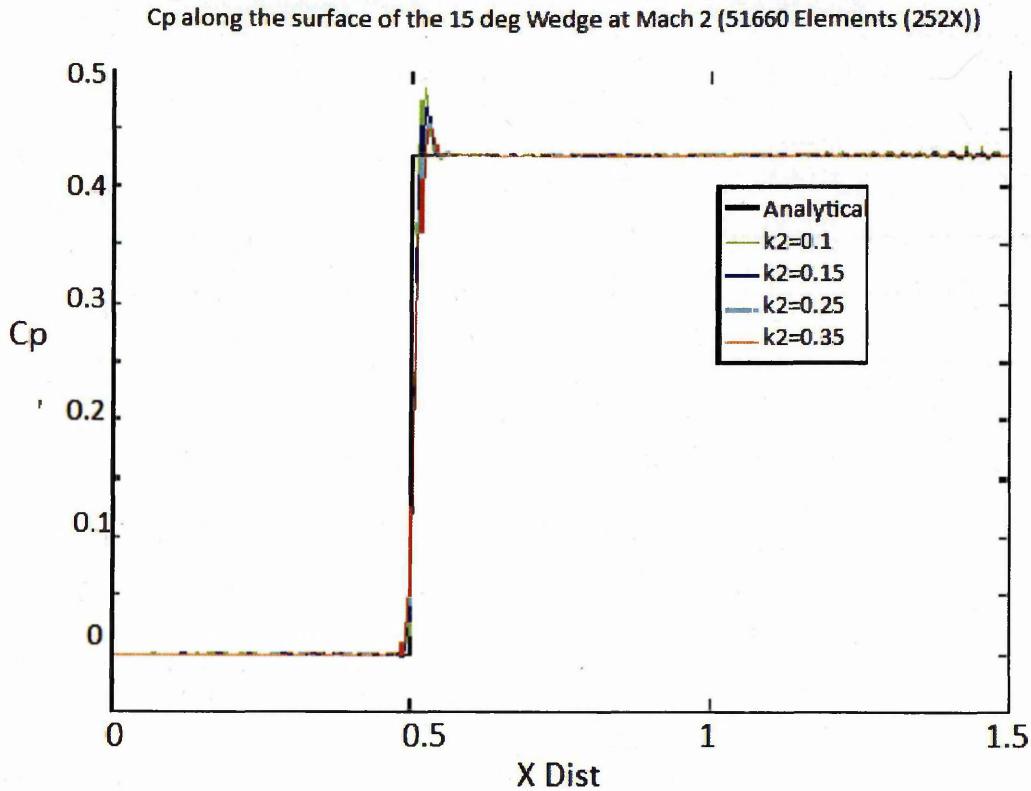

Figure 6-13- The effect that the value for $k^{(2)}$ has on the converged profile for the Supersonic wedge depicted in Figure 6-6.

The CBS solution for the coefficient of pressure as calculated by the computational procedure is shown in Section 6.4. The analytical solution is plotted as the full back line. The purpose of this plot is to show how the different values of $k^{(2)}$ effect the final solution. From observing Figure 6-13 above it can be seen that a small $k^{(2)}$ value leads to large overshoots post shock (X>0.5m).

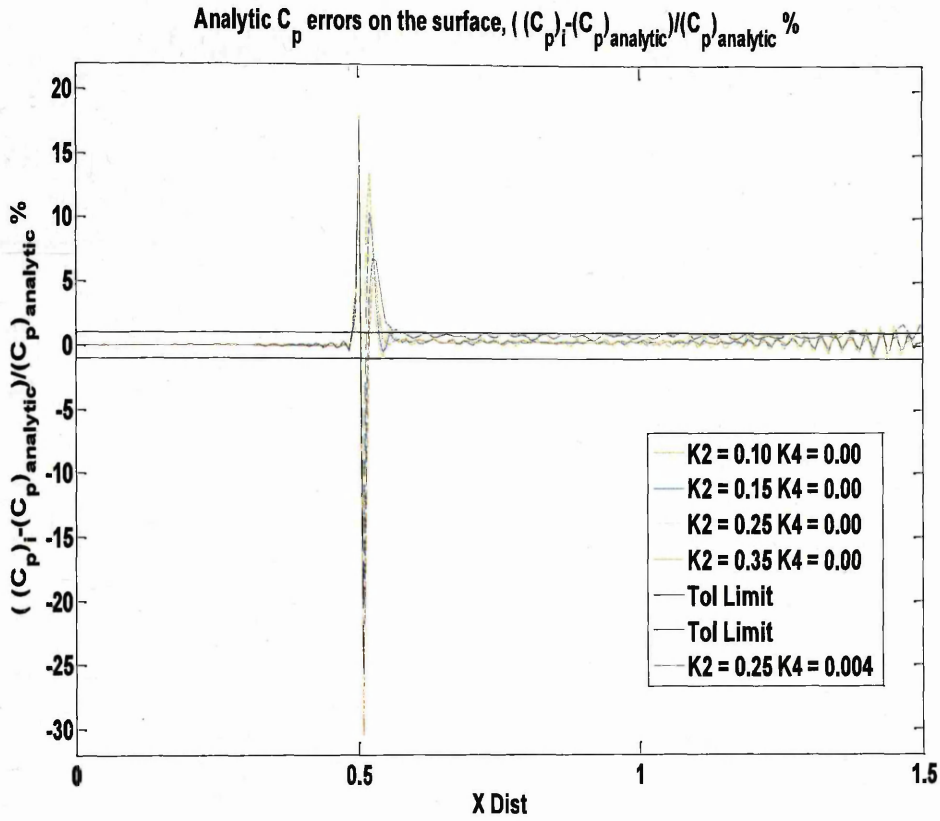

Figure 6-14- Quantify the effect that the value for $k^{(2)}$ has on the converged profile for the Supersonic wedge depicted in Figure 6-6.

Figure 6-14 shows the absolute errors for the steady state C_p solution along the XX plane as seen in Figure 6-7. The steady state solutions were obtained with $k^{(2)}$=(0.1,0.15,0.25,0.35) and all runs were done using a fixed value for $k^{(4)}$ =0.004 and a Courant number of 0.05. Apart from the leading edge region, the CBS scheme is accurate enough at capturing the flow along the surface of the wedge because the percentage error is within the ±1% tolerance.

This shows that the CBS solution is in excellent agreement with the analytical solution, a promising indication of the capability of the CBS approach for the final application; solving 2D Hypersonic compressible flow over transpiration cooled components.

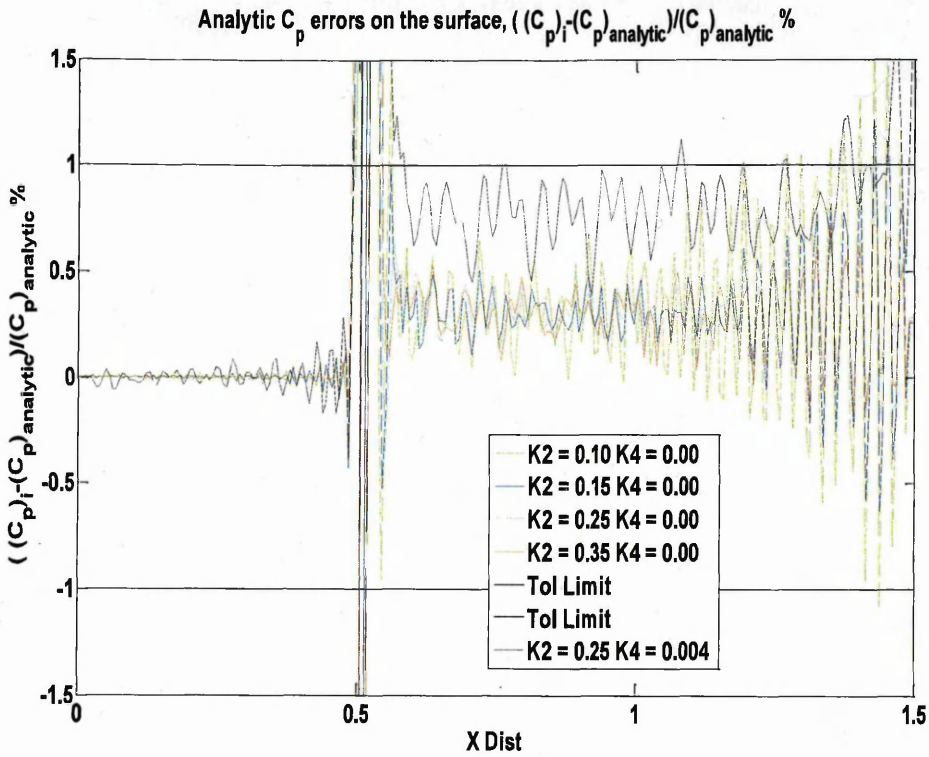

Figure 6-15 - Quantifying the effect that the value for $k^{(2)}$ has on the converged profile for the Supersonic wedge depicted in Figure 6-6.

Figure 6-15 shows the absolute percentage error at each control volume along the surface of the wedge. The black straight lines indicate a tolerance of 1%. For the coefficient of pressure the errors are well within these limits for all five of the $k^{(2)}$ values used- excluding the leading edge. For the collaboration of the CBS and Jameson's AV scheme, the one feature that is of importance is the large under shoot at the leading edge.

6.7 Mach 3 Inviscid Wedge Study

As stated earlier motivation to study this problem was because the Supersonic inviscid wedge case has a closed analytical solution. This can be used to evaluate the accuracy and stability of the CBS algorithm, as well as being able to identify the limitations of the CBS algorithm when used to model Supersonic compressible flows. Here the CBS algorithm and the analytical solution is also compared to the FLUENT study (which is available on the web) by Cornell, [167]. This novel comparison between FLUENT and the CBS procedure is done to highlight that the CBS algorithm is indeed competitive in terms of accuracy and efficiency when compared to other CFD procedures.

6.7.1 Mach 3 Wedge Analytical Solution

For the sake of comparison purposes the boundary conditions will follow the Cornell, [167], work on the 2D Supersonic wedge. As described in Section 6.3.3 the analytical solution for this research is obtained using an iterative approach from the subroutine taken from Slater, [165].

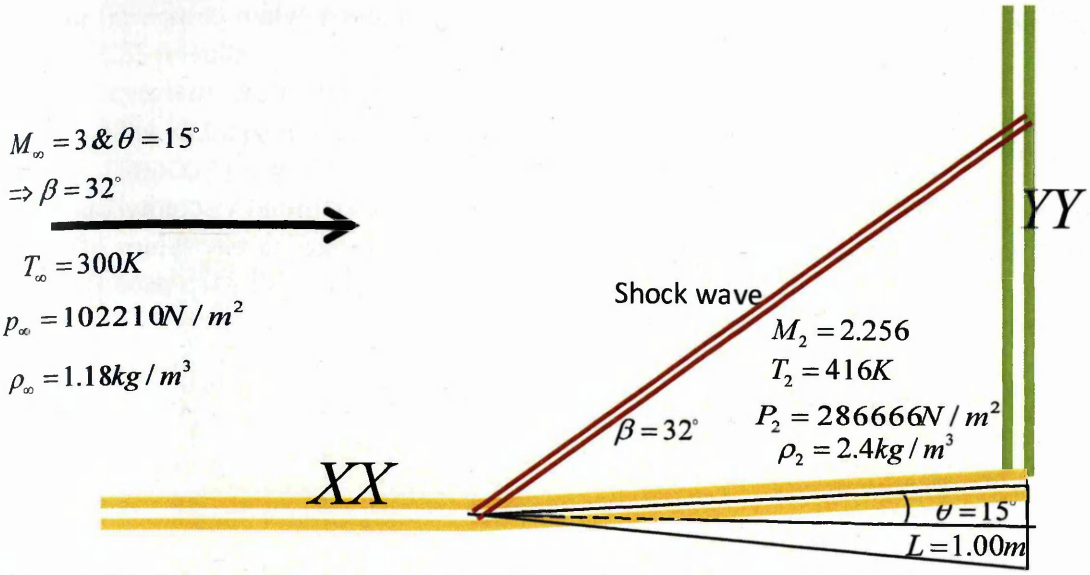

Figure 6-16: **Schematic of the Mach 3 Wedge with the plane XX and YY.**

Where the input is the free-stream values and the wedge geometrical parameters, where L is the length of the wedge and ∞ denotes the reference values.

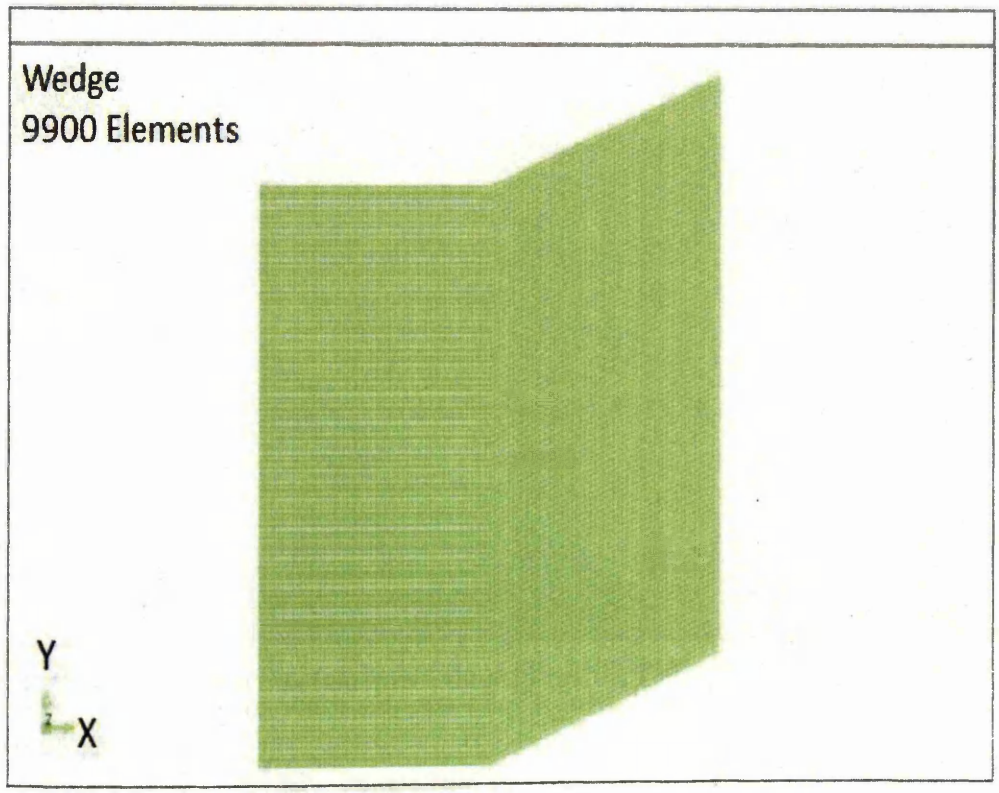

Figure 6-17: Structured grid for the wedge depicted in Figure 6-16.

As stated earlier the motivation to study this problem was because the Supersonic inviscid wedge case has a closed analytical solution, which is used to evaluate the accuracy of the CBS algorithm, as well as being able to identify the limitations of the CBS algorithm. Here the CBS algorithm and the analytical solution is also compared to the FLUENT study (which is available on the web) by Cornell, [167]. This novel comparison between FLUENT and the CBS procedure is done to highlight that the

CBS algorithm is indeed competitive in terms of accuracy and efficiency when compared to other CFD procedures.

6.7.2 Mach 3 Wedge Solver Results

The third wedge was modelled to gain a better insight into the effect the artificial viscosity has on the solution of a more challenging discontinuity and free-stream velocity, moreover the values of C_x and C_y in equation (6.20) were varied to gain an insight into the effect that the artificial viscosity has on stabilizing the algorithm and its effect on the accuracy of the final solution.

Table 6-3- Grid and flow parameters for the FLUENT comparsion Study.

Mach 3 Wedge	M_∞[-]	ρ_∞[kg/m^3]	T_∞[K]	θ[-]	Nx	Ny	Nt
	3	1.18	300	15°	100	99	9900

Where Nx is number cells in the x direction.
Ny is number the cells in the y direction.
Nt is total number the cells.

6.7.2.1 *FLUENT Comparison*

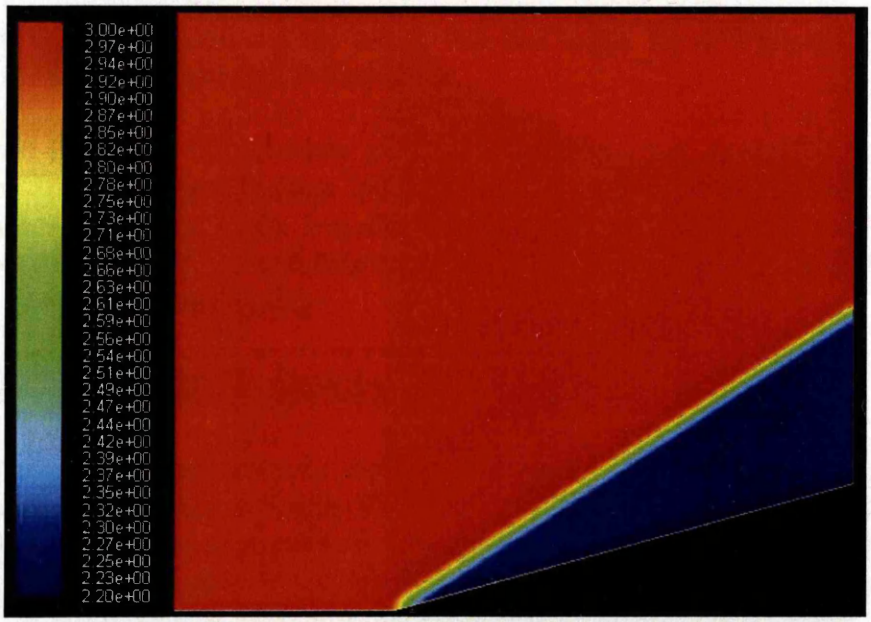

Figure 6-18: Mach contours for FLUENT Solver (15000 elements) at modelling the Mach number for a 15° wedge at Mach 3.

Figure 6-18 shows the Mach contours as calculated by FLUENT and taken from Cornell, [167], for the solution domain for the Mach 3 wedge, as seen in Figure 6-16. As can be seen, the discontinuity occurs across a few elements - which is an important feature of an accurate and robust CFD procedure. In addition the Mach speed is below 3 throughout the flow domain and does not display oscillations within the solution domain, another important feature of a reliable and robust code.

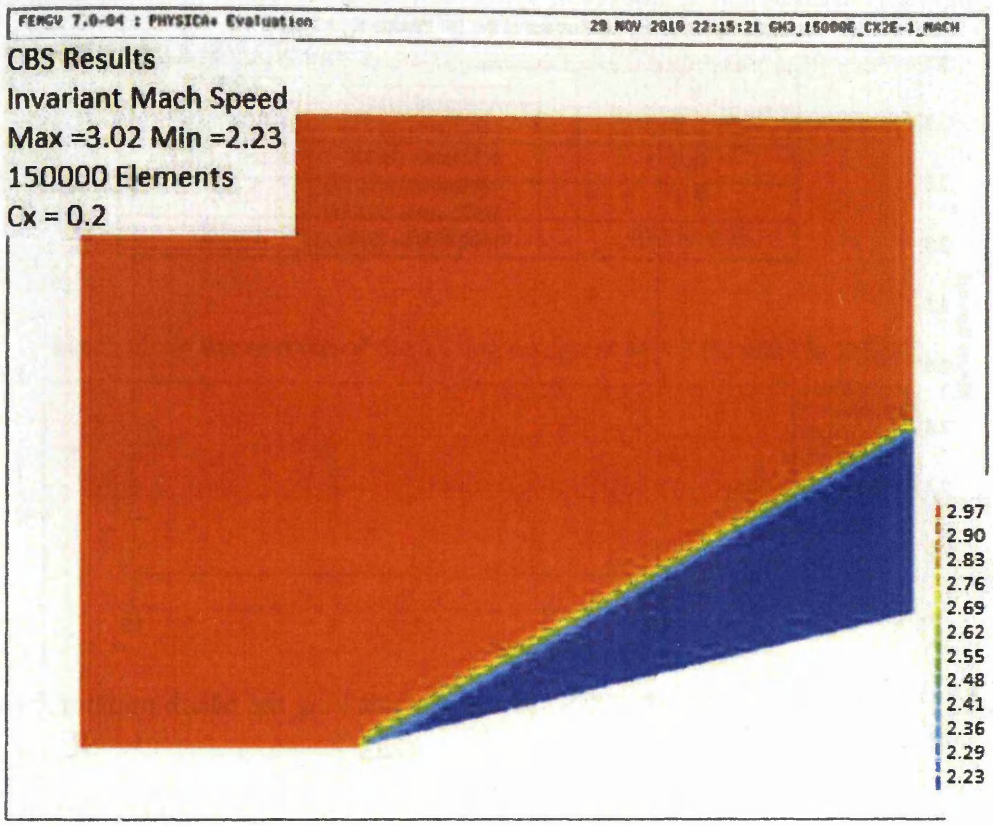

Figure 6-19: Mach contours for the CBS solver (15000 elements) at modelling the Mach number for a 15° wedge at Mach 3.

Figure 6-19 shows the Mach contours as calculated by the CBS algorithm for the solution domain for a Mach 3 wedge as seen in Figure 6-16. As can be seen in Figure 6-19 the discontinuity occurs across a few elements just like Figure 6-18. The CBS solution, like that of the FLUENT solution, shows features of a robust solver. The Mach speed is below 3.02 throughout most of the flow domain - in this case the boundedness criteria is satisfied. This boundedness is an indication that the CBS solution is a reliable solver.

6.7.2.2 Mesh Sensitivity Study

The matter of grid independence is a serious consideration in CFD and this Section will seek to address, grid independence for this benchmark case. Finer grids need to be employed in order to resolve the property fields and to check that the numerical solution is not a function of the number of grid points - an untenable result. The steady state solutions were obtained with a C_x=0.2 and a Courant number of 0.05. Runs were stopped after a tolerance of 10^{-5} were reached or alternatively, after 30,000 iterations.

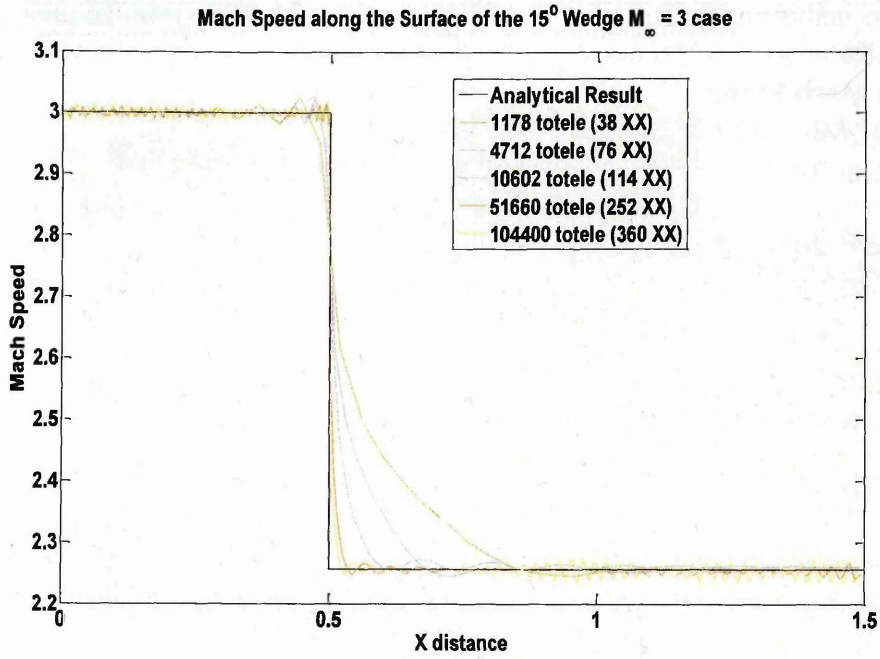

Figure 6-20: Mesh sensitivity for the CBS solvers at modelling the Mach number for a 15° wedge at Mach 3.

The analytical solution as calculated by Slater's [165], Fortran subroutine is displayed as the full black line and the Mach speed as calculated by the CBS formulation for different mesh densities is displayed in the key. The x axis "X distance" is in meters.

Figure 6-20 shows as the grid density increases from 1178, 4712, 10602, 51660 and 104,400 elements the shock starts to become resolved. However numerical oscillations build up after successive refinements, for example, the profile for 104,400 elements displays spurious oscillations building up after the discontinuity. This means one of these issues arises when solving this 2-D problem.

1. The artificial viscosity (C_x =0.2) is not large enough to damp the numerical oscillations,
2. The 2D CBS scheme is a function of the grid density
3. The boundary conditions are ill posed and the oscillations only shows up on refined meshes.

To ascertain that the oscillations are in fact not a function of the number of elements, more simulations were carried out on the 516,600 mesh to test whether the C_x values are large enough to damp out the numerical oscillations.

6.7.2.3 *Artificial Viscosity Parametric study*

As stated by Azevedo & Korzenowski, [10], schemes based on central differencing possess symmetry with respect to a change in sign, for the Jacobian matrix eigenvalues, meaning the discretization does not distinguish between upstream or downstream influences. In such cases these schemes do not consider physical properties of the flow equations in the discretized formulation and this generates oscillations in the proximity of the discontinuity which have to be damped by the addition of artificial dissipation terms Azevedo & Korzenowski, [10]. The challenge, as this parametric study will show, is to determine the adequate amount of artificial viscosity which should be large enough to damp instabilities and at the same time, small enough to avoid the destruction of flow features such as the discontinuity.

Table 6-4-Legend for Figure 6-21.

Color	C_x	C_y
Green	0.2	0.2
Light Blue	0.6	0.6
Red	1.5	1.5
Black	Analytical	Analytical

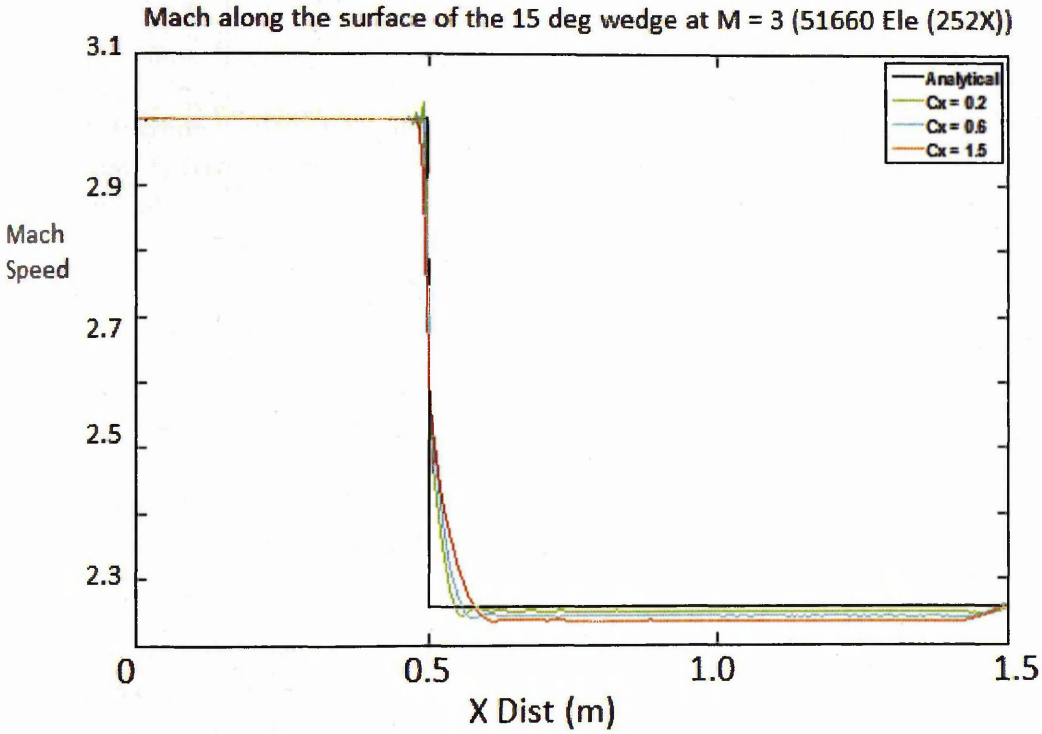

Figure 6-21-Mach Speed along the XX plane as represented in Figure 6-16 for different values of the artificial viscosity tuning factor C_x (legend) against the analytical solution (black).

Figure 6-21 shows that the CBS approach with large values of C_x >0.2 produces impressive solutions that are generally accurate without the appearance of noise. Meaning at large values of C_x oscillations pre shock are successfully damped however the accuracy is degraded post shock. On the flip side, if the value for C_x is too small then accuracy of the solution is assured post shock but oscillations are encountered in the proximity of the shock. Therefore to resolve the shock accurately a judicious amount of artificial viscosity should be introduced. In Figure 6-21 the best fit between the analytical and the CBS results occurred when C_x 0.2.

From Figure 6-21, the CBS algorithm is shown to be sufficient at modelling the Supersonic Mach 3 inviscid wedge. The profiles above were obtained after coupling the MacCormack's 2^{nd} ordered differential artificial viscosity with CBS algorithm. By altering the value for C_x as seen in equation (6.20), we are aiming to obtain a final Mach profile within a defined absolute tolerance of 1% of the analytical solution. Solutions for the Mach 3 case at a mesh density of 100,000 elements show perturbations along the surface of the wedge. For the case of the 50,000 mesh, we can see that an increase in the value of C_x alters the Mach speed post shock.

6.8 Mach 9 Wedge Study

The following higher speed benchmark was investigated because the targeted speed for the Hypersonic CAVs is intended to be Mach 9. Therefore the algorithm should be tested against this velocity regime along with the shock and associated temperature increase. As discussed previously to suppress the tendency for odd and even point decoupling, and to prevent the appearance of wiggles in regions containing severe pressure gradients a form of artificial viscosity augments the CBS algorithm.

6.8.1 Mach 9 Wedge Analytical Solution

As described the analytical solution for this research is obtained using an iterative approach from the subroutine taken from [165], where the input is the free-stream values and the wedge geometrical parameters. For the case of a 15° wedge with a free-stream Mach number of 9 then the post Mach number and shock angle is.

$M_\infty = 9$ $\qquad$ $M_2 = 5.036$

$\beta = 15^\circ$ $\qquad$ $\alpha = 20^\circ$

$\rho_\infty = 1.2 kg/m^3$ $\qquad$ $\rho_2 = 4.762 kg/m^3$

$T_\infty = 300K$ $\qquad$ $T_2 = 848.94K$

Here the subscript ∞ indicates pre shock values and the subscript 2 indicates post shock values. Where α=shock angle.

6.8.2 Mach 9 Wedge Solver Results

The following results were generated with a Courant number of 0.05 and a $k^{(2)}$ value of 0.25 and a $k^{(4)}$ value of 0.004 as well as the following grid parameters. All the cases as seen in Table 6-3 converged to a steady solution for a tolerance of 10^{-5} where the final Mach profile is compared against the analytical solution.

Table 6-5- Grid and flow parameters.

M_∞[-]	ρ_∞[kg/m^3]	T_∞[K]	θ[-]	Nx	Ny	Nt
5	1.18	300	15°	100	99	9900
7	1.18	300	15°	100	99	9900
9	1.18	300	15°	100	99	9900

Where Nx is the number of elements in the x direction
Ny is the number of elements in the y direction
Nt is the total number of elements

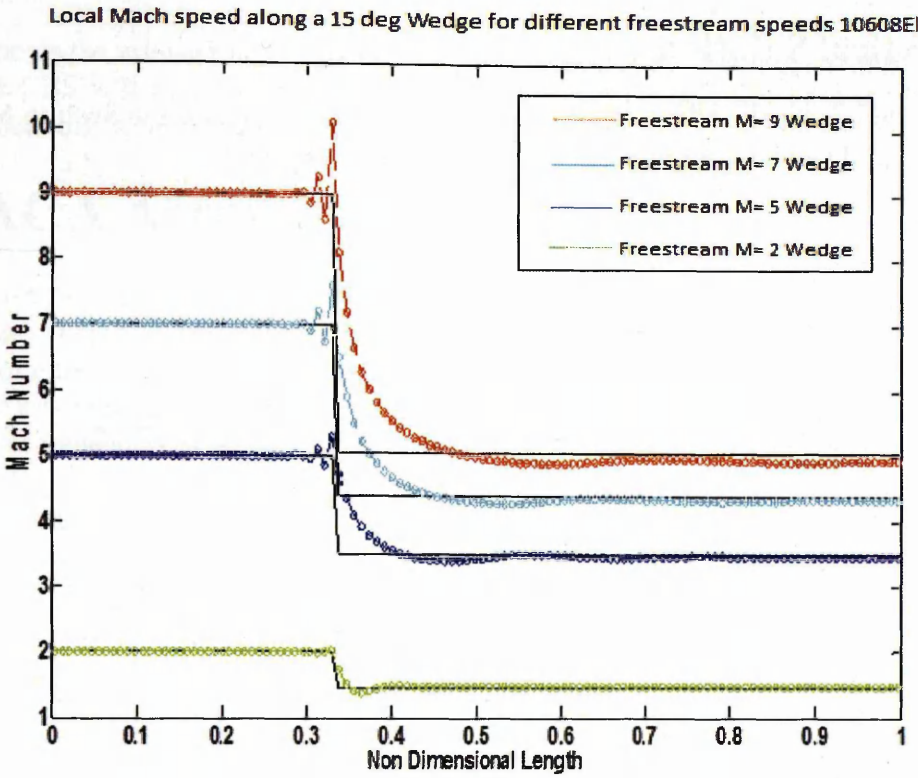

Figure 6-22 - Different Mach speeds (legend) for the 15° wedge depicted in Figure 6-6 against the analytical solution (black).

The Mach 9 simulations converge impressively to within the specified relative error tolerance. A very promising indication that the CBS algorithm can deal sufficiently with the shocks appearing at Hypersonic compressible flows of the final novel application- transpiration cooling through porous media at Hypersonic speeds. Increasing the free-stream velocity produces larger numerical oscillations that propagate and travel upstream These oscillations can be damped down by increasing the value of $k^{(4)}$. Overshoots and undershoots, post and pre shock, can be damped down by increasing the value of $k^{(2)}$. Six nodes are required in proximity of the discontinuity to yield stable results for the Supersonic inviscid wedge.

In the next Section we examine and develop the solver further through tests on unstructured non-orthogonal grids by adopting triangle elements - an important extension for the final objective as seen in the research objective, Chapter 1.1.

6.9 Unstructured Mesh Benchmark Study

This case gives an insight into the versatility of the CBS algorithm .i.e. these results will provide information on how the CBS scheme performs on non-orthogonal unstructured grids. The face values and Cartesian derivatives were re-cast as seen in Section 6.2.2.1 to accommodate mesh skewness.

Unstructured triangular elements were used to model the Supersonic Wedge. Empowering the code to handle unstructured grids was the next endeavor to establish a CFD strategy that can successfully capture compressible flow affecting single stage to orbit vehicles. This required evaluation of the non-orthogonal and non-conjunctional terms in Section 6.2.2.1.

6.9.1 Analytical Solution

The analytical solution for the 15° can be obtained using the procedure seen in Section 6.3.3. The values for ρ, P and M can be seen in Section 6.5.1 and is repeated here.

$M_\infty = 2$ $\quad$ $M_2 = 1.445$

$\beta = 15°$ $\quad$ $\alpha = 54°$

$\rho_\infty = 1.2 kg/m^3$ $\quad$ $\rho_2 = 2.05 kg/m^3$

$T_\infty = 300K$ $\quad$ $T_2 = 365K$

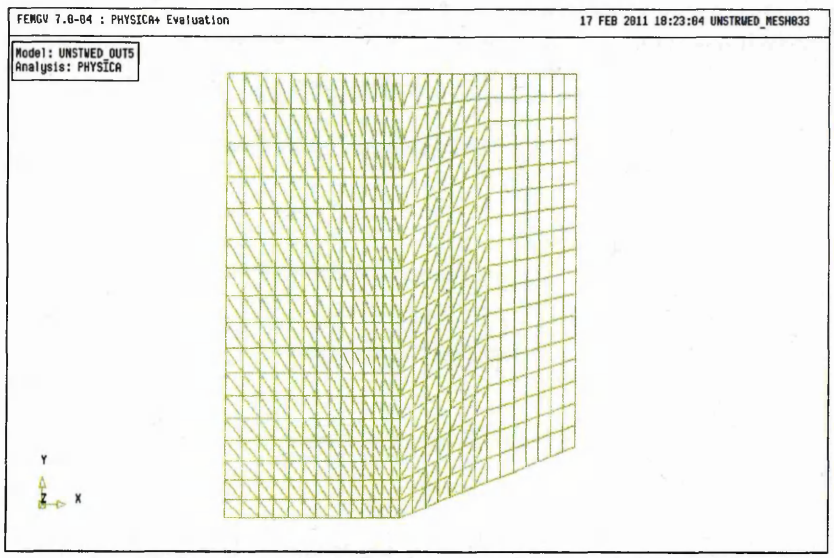

Figure 6-23- Unstructured grid for the wedge depicted in Figure 6-16.

6.9.2 Solver Results

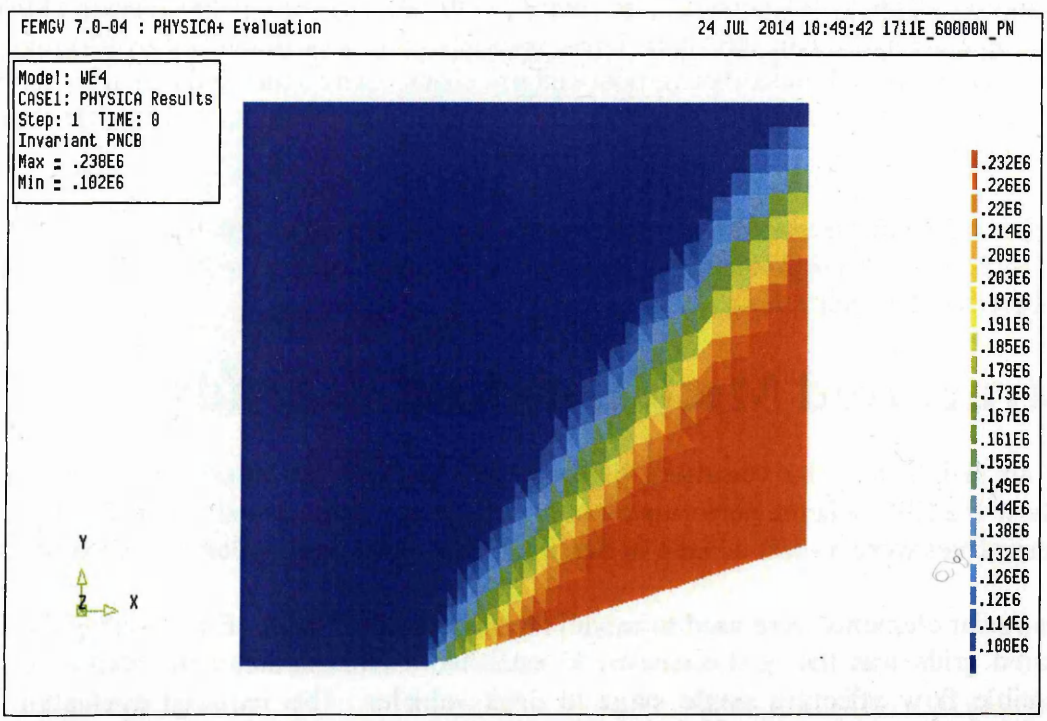

Figure 6-24 - Pressure for the wedge depicted in Figure 6-23 using unstructured elements.

Figure 6-24 shows the inviscid flow over an unstructured grid is sufficiently modelled using the CBS algorithm. The CBS will be required to employ unstructured meshes for those applications at ESA where the applications have non-linear geometries.

6.10 NACA Aerofoil

Inviscid flow over a NACA aerofoil is the next multidimensional benchmark tackled in this Chapter. The problem is covered extensively in the literature for example in AGARD 13 [88] and has also been solved using the finite element version of the CBS algorithm by Nithiarasu P, Codina R, [131]. Along with the extensive experimental data for this Supersonic problem the technical appeal for this research is the non-linear geometry of this case when compared to the 2-D wedge.

In addition to these reasons, a mesh sensitivity study is now conducted with the objective of determining a realistic solution to the problem. By refining the mesh and modelling the NACA aerofoil we can show that the algorithm displays mesh independence after progressive increments of mesh refinement an essential requirement - for a reliable CFD solver.

6.10.1 Boundary Conditions

The Supersonic NACA0012 aerofoil tackled had a chord length of 1m and its geometrical coordinates can be taken from the web resource AIAA, [168]. The far-field boundaries, i.e. the top and inlet according to Nithiarasu P, Codina R, [131] should be 25 chord lengths (25m) away from the leading edge.

Unfortunately for this research this was not practical as the number of elements and hence geometrical information superseded the memory allocation limit for serial runs. Therefore new grids were constructed where the inlet was placed 4m before the leading edge and the top boundary was situated 10.5m above the centre line and likewise the bottom boundary was placed 10.5 m below the centre line.

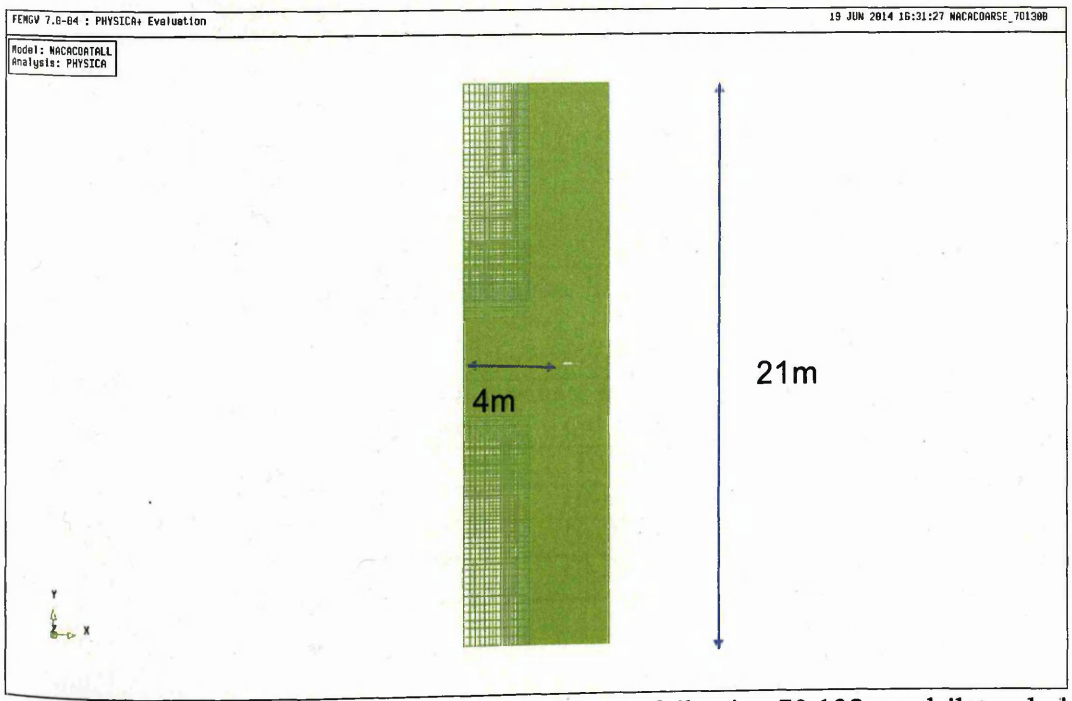

Figure 6-25- Structured grid for the NACA0012 aerofoil using 70,132 quadrilateral elements.

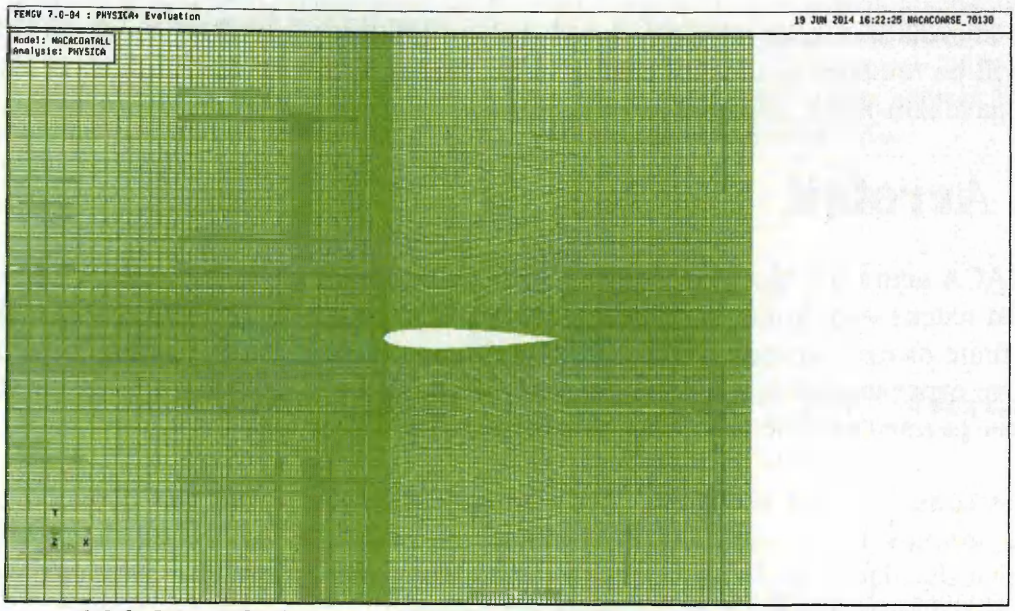

Figure 6-26- Magnified image of the structured grid for the NACA0012 aerofoil at the leading edge for 70,132 elements.

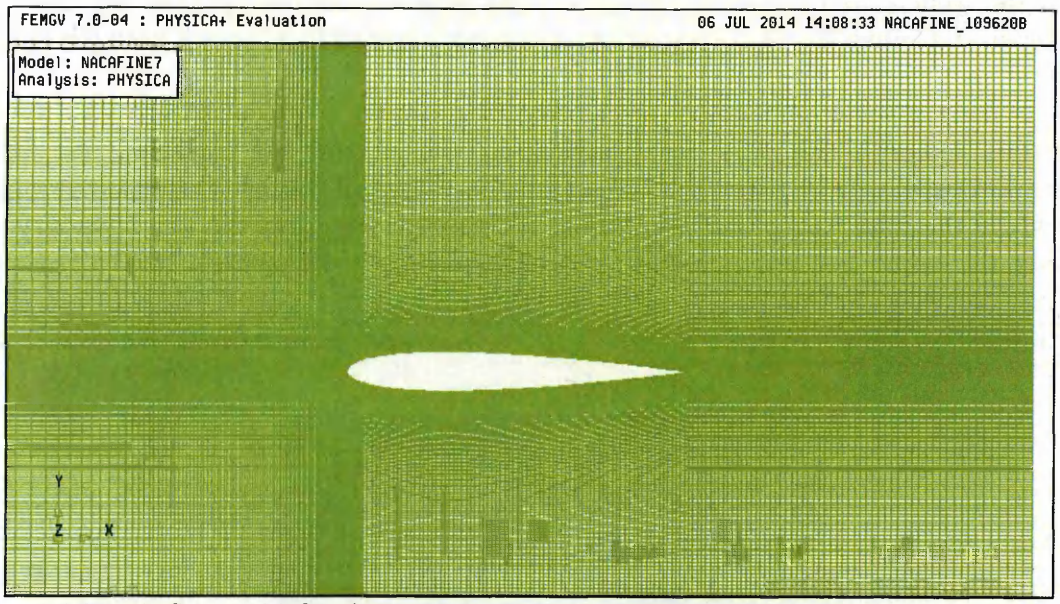

Figure 6-27- A finer grid for the NACA0012 aerofoil using 109,620 elements.

Table 6-6- Grid for the NACA aerofoil mesh sensitivity study.

Mach Number	**Number Of Elements**	Nx	Ny	Δx at leading edge (m)	Δy at leading edge (m)
1.2	40,582	394	103	7.7E-03	7.94E-03
1.2	70,132	178	394	7.18E-03	1.59E-02
1.2	141,120	252	560	4.53E-03	8.76E-03
1.2	156,150	347	450	1.85E-03	4.72E-03

6.10.2 Solver Results for NACA0012

Computations were run using the FV CBS algorithm coupled with MacCormack's AVT. The Courant number was set to 0.01 and a C_x and C_y value were both set to 0.2 for the AVT tuning parameter. The free-stream Mach number is set to 1.2 and the angle of attack set to 0°. The aim of this study is two-fold; firstly the stability of the algorithm over non-linear geometry and secondly to show mesh independence for this challenging 2D inviscid problem.

The contour plot above displays the Mach distribution for the case seen in row 1 of Table 6-6. The Mach distribution exhibits no decoupling. This is another promising indication that the CBS algorithm coupled with MacCormacks AVT is an adequate strategy for modelling Supersonic problems, especially when considering that the 40,582 element mesh is the coarsest grid used to model the problem as seen in Table 6-6.

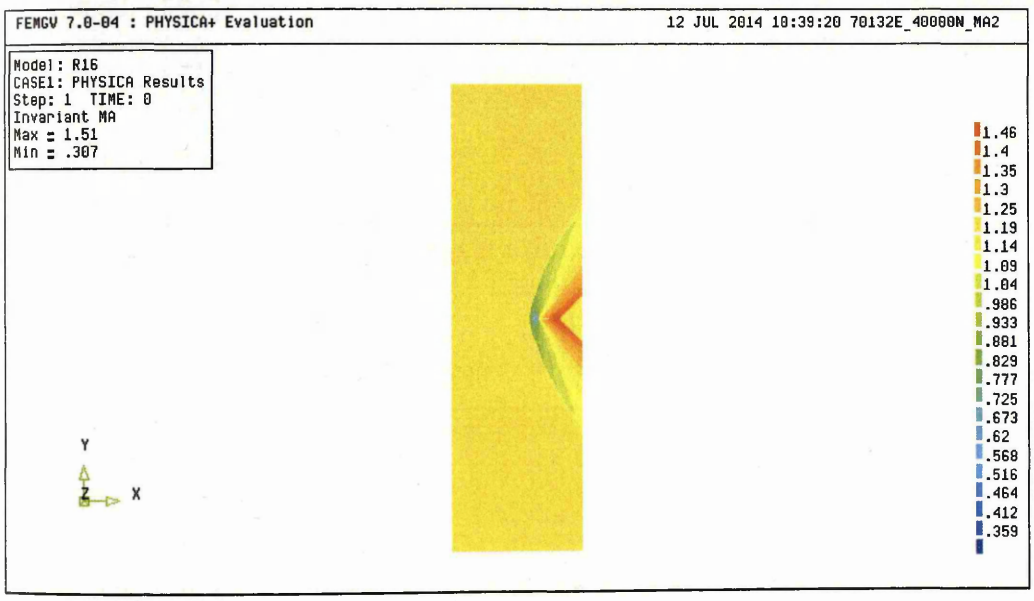

Figure 6-28- Mach contours for the NACA0012 aerofoil at a Mach number of 1.2 using 70,132 elements.

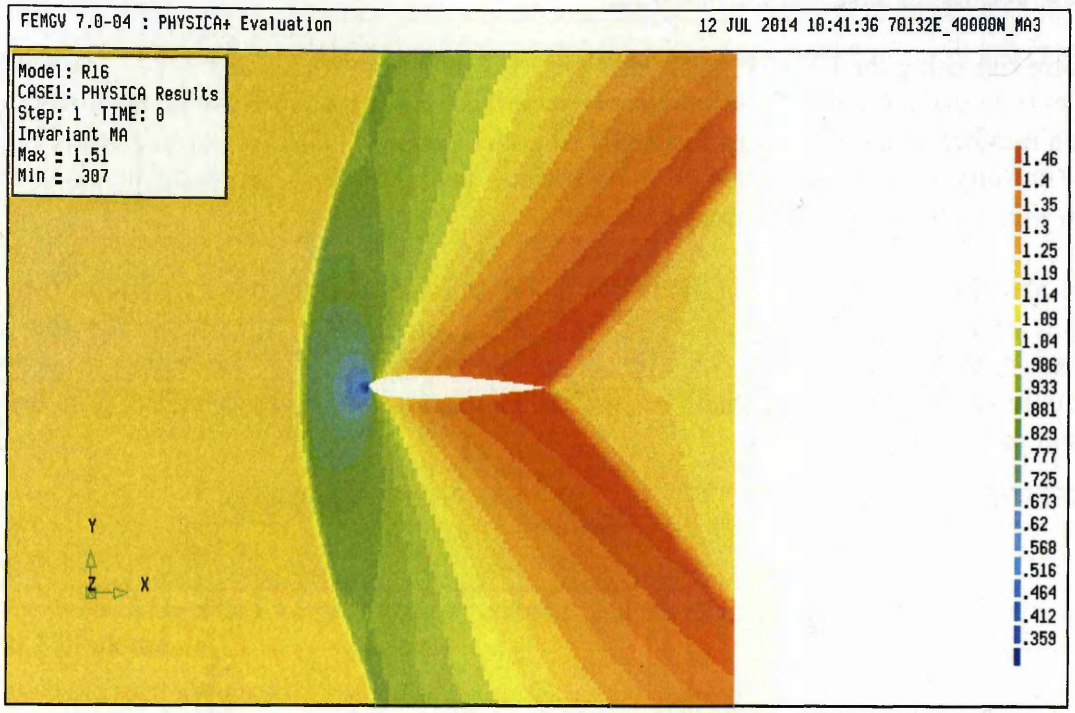

Figure 6-29- Mach contours for the NACA0012 aerofoil magnified at the leading edge for 70,132 elements.

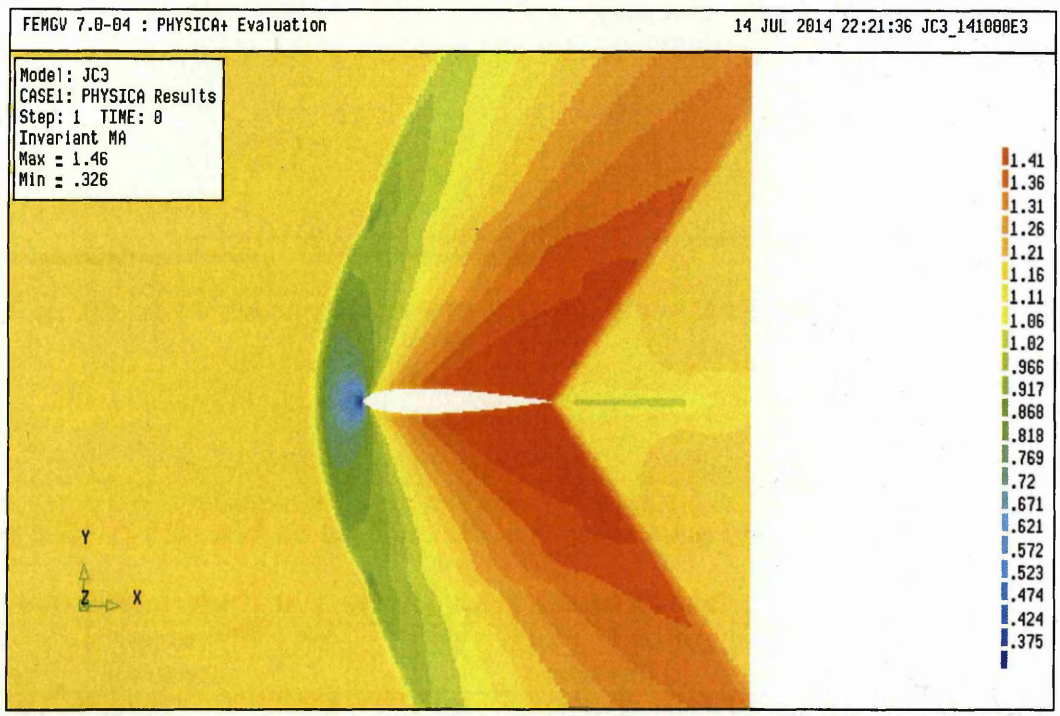

Figure 6-30- Mach contours for the NACA0012 aerofoil magnified at the leading edge for 141,000 elements.

Figure 6-29- Mach contours for the NACA0012 aerofoil magnified at the leading edge for 70,132 elements. Likewise

Figure 6-30- Mach contours for the NACA0012 aerofoil magnified at the leading edge for 141,000 elements.

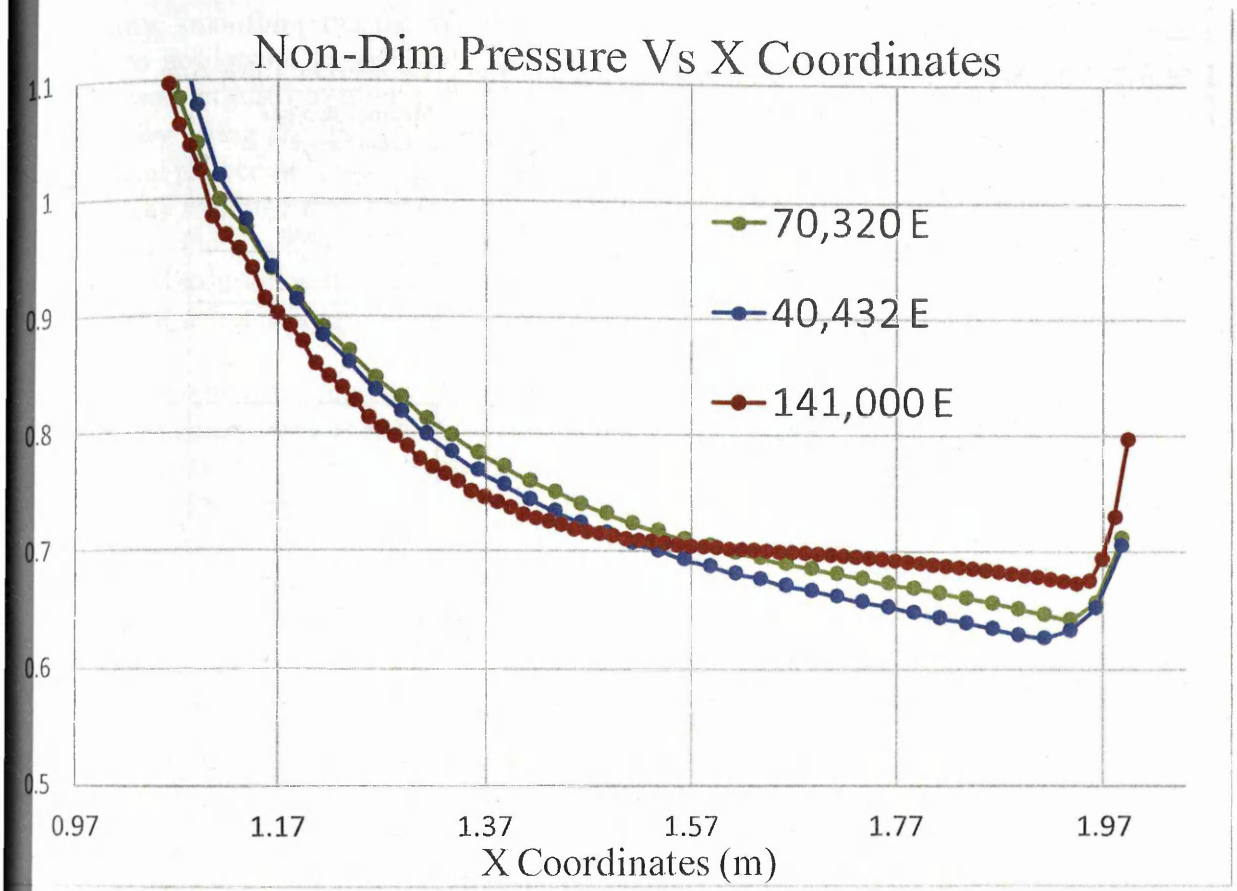

Figure 6-31- Pressure along the top surface of the NACA0012 aerofoil .

The non-dimensional pressure P/P_{∞} along the top surface of NACA0012 aerofoil for the meshes seen in Table 6-6 and the different mesh densities is displayed in the key. The x axis "X distance" is in meters. The y axis "Y distance" is the non-dimensional pressure which is relative to the free-stream pressure.

Since there is no analytical result for this case, the analytical error cannot be ascertained. Figure 6-31 shows as the grid density increases from 40,582 elements 70,132 elements, to 141,120 elements, the numerical profile starts to become resolved.

Table 6-7- Memory and Run time parameters for each of the grids seen in Table 6-6.

Number Of Elements	Iterations	ρ err	Run Time hh:mm:ss	Run Time per solution point	Memory Requirements	Memory Req per solution point
40,582	40000	5.88E-007	12:22:48	1.08 sec per node	663512kb	1.10kb per node
70,132	40000	1.916E-006	22:33:30	1.15 sec per node	722660kb	10.30 kb per node
141,000	40000	1.22E-006	35:28:37	0.90 sec per node	1294920kb	9.18 kb per node
156,150	40000	4.785E-6	44:32:37	1.027 sec per node	1591944kb	10.2047 kb per node
213,000	Failed Out of Memory		Failed Out of Memory		Failed Out of Memory	

Table 6-7 dispays important parameters for the run time and memory requirements for each of the grids. Notice that the run time and memory requirement per solution point is approximately the same for each of the grids employed. Exactly what you would expect to observe.

6.11 Concluding Remarks

This chapter on inviscid flow simulations has demonstrated the development of a 2nd order explicit algorithm for Supersonic compressible flows using a 2D Finite Volume formulation. In the present chapter a validation of 4 different benchmarks is carried out: the Mach 2, the Mach 3 and the Mach 9 wedges were modelled using structured grids. And further validation on the Mach 2 wedge using an unstructured grid with triangular elements over the wedge. The final benchmark was NACA0012 aerofoil using 3 further structured grids.

The CBS scheme was implemented in a finite volume formulation as opposed to the finite difference framework seen in Chapter 4 or the initial finite element approach as published by Nithiarasu P, Codina R, [131], for the Characteristic Based Split (CBS) algorithm. The solution of flow over 2D wedges was carried out where the inlet speed was varied from Mach 2 to Mach 9. An inviscid formulation was used and the fluid was treated as a perfect gas. Clearly, as opposed to the inviscid assumptions for actual flight conditions, viscous interactions coupled with thermal conduction interactions and real gas effects would have to be taken into account. In this chapter however the consideration of Supersonic flows simply has the objective of testing the behavior of the candidate scheme in the presence of strong 2D shocks. The analytical solution as given by the implicit procedure in [165] was used to evaluate the accuracy of the CBS solution.

6.11.1 Summary of CBS Algorithm for 2D Structured Grids

At large Mach numbers in multidimensions the CBS algorithm requires artificial viscosity. Two forms are available in the software tool depending on the CFD programmer's requirements. The first being, MacCormack's, [29], mono 2nd ordered term and the second being Jameson, Schmidt & Turkel's [105] AVT. MacCormack's artificial viscosity is designed to control the calculations by a magnitude equivalent to a fourth order term in the truncation error and the effect is to increase the

viscosity, smoothing out the discontinuities for Supersonic flow. Although MacCormack's AVT is easier to implement for non-orthogonal grids, the substitution of Jameson, Schmidt & Turkel's [105] AVT, was required to obtain an acceptable solution in terms of absolute error for the Mach 2 case. Hence by using the JST AVT the solution converged to the analytical solution as given by the analytical procedure in [165].The inclusion of $k^{(4)}$ produces more accurate results with respect to the analytical solution than those with no $k^{(4)}$ values. However the inclusion of too much artificial viscosity, for example, high values of $k^{(4)}$, in an attempt to improve stability, can denegrate the numerical solution with respect to smeared shocks. From this researcher's perspective the stabilty of a numerical solution is preferable to unstable solutions.

The candidate solution was applied to another challenging case. The solution for the Mach 3 case; firstly the contours in Figure 6-19 show that the shock is resolved over a few elements, a feature of a reliable CFD solver. Secondly the Mach speed is below 3, the free-stream value, throughout the flow domain, showing that in this case the boundedness criteria is satisfied. Boundedness is another important indication that the CBS algorithm is a reliable solver.

The CBS algorithm was then also applied to enable solutions on the more pertinent problem for its final use, involving Mach speeds of 9 successfully. This speed is envisaged as the operating velocity for the Hypersonic cruise air-breathing vehicles (CAVs). However further validation is required to reduce the overshoots pre-shock as seen in Figure 6-22.

6.11.2 Extension to 2D Unstructured Grids

To enhance the versatility and flexibility of the CBS algorithm, the finite volume formulation for 2D orthogonal quadrilateral grids used in Section 6.5, was extended to handle polyhedral 2D triangular elements as seen in Section 6.2.2. This extension in theory can in general be applied to any 2D elements with any number of faces.

Figure 6-24 indicate that it is possible to obtain stable converged solutions with the CBS algorithm, for the Supersonic flows. However, these solutions will most certainly have small numerical oscillations.

6.11.3 Extension to NACA aerofoil

The FV CBS algorithm was extended to solve Supersonic flow over a NACA0012 aerofoil and test stability and mesh independence. Since there is no analytical result for this case, the absolute error cannot be ascertained and hence grid independence investigated. Figure 6-31 shows as the grid density increases from 40,582 elements to 70,132 elements, to 141,120 elements, and to 156,150 elements the numerical shock starts to become resolved i.e. the pressure profile does not change substantially.

7 INCOMPRESSIBLE FLOW SIMULATIONS

7.1 Introduction

The objective of this chapter is to apply the proposed algorithm to the 2-D Subsonic scientific benchmark of external incompressible laminar flow over a flat plate. The reason for tackling this Subsonic benchmark is as follows. Firstly, according to recent research into Hypersonic flow solvers by Azevedo & Korzenowski, [10], when building a CFD solver to model air-borne vehicles-

> *"It [modelling incompressible flows] is a necessary step in order to construct a robust code to deal with the complete environment encountered in actual flight"*

Secondly, research into transpiration cooling applications by ESTEC researcher Steelant, [169], points out that the CFD code should allow the possibility of keeping laminar Subsonic flow in the porous media and having compressible Supersonic turbulent flow in the main flow. In this chapter, the assessment of incompressible flow benchmark in terms of accuracy and efficiency is carried out. Accuracy and efficiency are viewed as important features of a robust CFD solver. Therefore the assessment of the quality of results is based on the errors with respect to the theoretical solution throughout the computational domain.

The theoretical, Blasius solution, for the Subsonic boundary layer over a flat plate has been shown to be very close to experimental data collected by Liepmann and Roshko in [82]. Hence, according to industrial supervisors at ESTEC the Blasius solution represents a substantial and fundamental viscous benchmark for any CFD code

Before presenting the solution of incompressible flow over a flat plate, an overview of laminar and turbulent flow is provided. For the flow solver these two flow characters have differing stability issues that the reader needs to be aware of.

7.2 Laminar, Transition and Turbulent Flow

In experiments on fluid systems by Reynolds, [170], it is observed that at values below the so called critical Reynolds number, Re_{crit}, the flow is smooth and adjacent layers of fluid slide past each other in an orderly fashion. This regime is called laminar flow. As measured by Okamura, Wazzan, & Smith, [171], experimental studies show that the laminar boundary layer has a $Re < 9.1x10^5$ with transition occurring at this Re_{crit} value $9.1x10^5$. At Reynolds numbers above Re_{crit} a complicated series of events takes place which eventually leads to a radical changes in the flow character. In this state the flow behavior becomes random and chaotic. Even with constant steady imposed boundary conditions the motion becomes intrinsically unsteady and is called turbulent flow. This regime is illustrated in the diagram below.

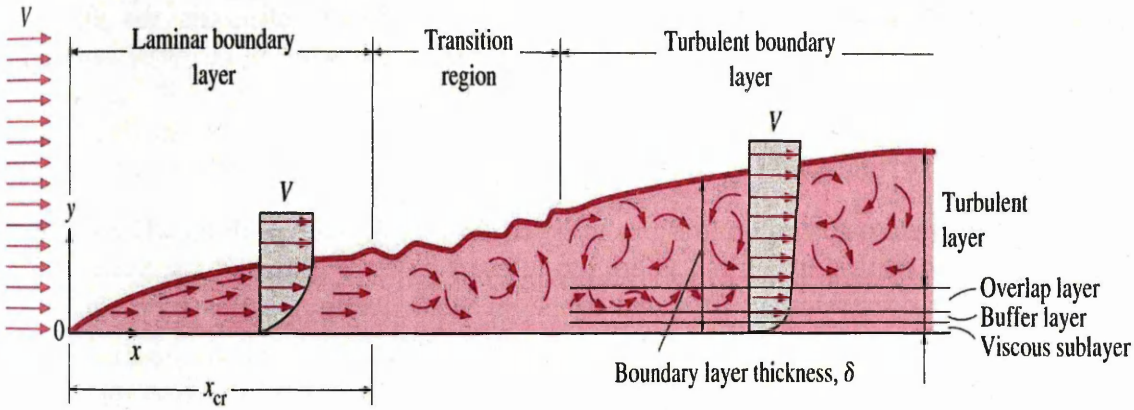

Figure 7-1 Evolution of a viscous boundary layer from laminar to turbulent flow.

As seen in Figure 7-1 above, the fully turbulent boundary layer on the right as measured by experimental studies [154] is shown to occur at $Re>3x10^6$. Prediction of turbulence is one of the fundamental problems of computational fluid dynamics [33]. In contrast to laminar flow, turbulence develops as an instability which is irregular, sporadic and intermittent. Because of the random and chaotic nature of the turbulence phenomena it is customary to work with time averaged forms of the governing equations. Turbulence models provide additional turbulent forces that are a result of random eddy fluctuations. The most popular being the Reynolds averaged model which provides information about the overall mean flow properties as used by the researchers Vandromme & Saouab, [139]. This does not simulate the detail of the turbulent motion, only the effect of turbulence on the mean flow behavior. According to [17] The random nature of turbulent flow precludes an economical description of the motion of fluid particles because of the associated small time and length scales [17]. Even in flows where the mean velocities and pressures vary in one or two space dimensions, turbulent flow always possesses a three dimensional spatial character [17]. The main reason for modelling laminar flow in this chapter is its relative simplicity when constructing a numerical scheme and the theoretical comparison when compared to turbulent flow.

7.3 The Navier-Stokes Equations for Incompressible Flows

As we have seen in Chapter 2 the Navier-Stokes equations describe combined viscous-convection flow problems which are non-linear and multidimensional and, at larger Reynolds numbers solutions contain turbulent flow structures [17], [18], [80]. As mentioned previously to model them numerically requires a considerable amount of effort to capture the localised physics and alleviate the numerical instabilities.

The Navier-Stokes equations are obtained by simultaneously taking the Euler equations as solved in Chapter 6 and adding a 2nd order diffusion term. The 2nd order diffusion term has the effect of distributing the physical properties, velocity and temperature, along gradients in all directions. The Navier-Stokes equations may be repeated from Chapter 2 as follows:

$$\frac{\partial \mathbf{U}}{\partial t}+\frac{\partial \mathbf{F}^j}{\partial x_j}=\frac{\partial \mathbf{G}^j}{\partial x_j} \text{ for i=1,...N}_d \tag{7.1}$$

where N_d indicates the number of spatial dimensions to be considered in each problem, **U** represents the vector of conservative variables and **F** and **G** are the relevant inviscid flux and the viscous flux terms, respectively. The two dimensional isothermal counterpart of equation (7.1) can be simplified to:

$$\mathbf{U}=\begin{bmatrix}\rho\\ \rho u_1\\ \rho u_2\end{bmatrix}\mathbf{F}^j=\begin{bmatrix}\rho u_j\\ \rho u_1u_j+P\delta_{1j}\\ \rho u_2u_j+P\delta_{2j}\end{bmatrix}\mathbf{G}^j=\begin{bmatrix}0\\ \tau_{1j}\\ \tau_{2j}\end{bmatrix} \tag{7.2}$$

where the variables and units are seen in Chapter 2.
Importantly for viscous flows though.

$$\tau_{ij}=\mu\left(\frac{\partial u_i}{\partial x_j}+\frac{\partial u_j}{\partial x_i}\right)-\frac{2}{3}\mu\frac{\partial u_k}{\partial x_k}\delta_{ij} \tag{7.3}$$

where μ - dynamic viscosity (kg/(m s))
the Kronecker delta term as we have seen is determined by.

$$\delta_{ij}=\begin{cases}0 & i\neq j\\ 1 & i=j\end{cases}\mapsto \tag{7.4}$$

Equations (7.1)-(7.2) are valid for any Newtonian incompressible fluid. A flow is incompressible for low speeds, for air, that is, Mach<0.3 although the effect of compressibility may appear at Mach numbers, as low as 0.1, in localized regions, depending on pressure and density changes. As such the flow is conventionally assumed to be incompressible on the macroscopic scale [20].

If flow is compressible the continuity equation may be used as a transport equation for density and the enthalpy equation as a transport equation for temperature. The pressure may then be obtained from the perfect gas law $P=f(\rho,T)$. If flow is incompressible, a challenge arises in how then to resolve the pressure. Although pressure gradients appear in each of the momentum equations, there are no pressure terms in the continuity equation meaning there are more unknowns than equations. Therefore to tackle this challenge, pressure is linked to the velocity through an artificial relationship

in the continuity equation, because if the correct pressure field is applied to the momentum equations the resulting velocity field will satisfy the continuity equation.

To employ the pressure based method, AC CBS scheme, the modifications from [150] will be discussed now. The pressure based methods solve the primitive variables (P,**u**,T) at the solution points [20]. For future reference primitive variables as can be shown by Anderson [15], are not suited to compressible problems with discontinuities present, computing the compressible flow through a choked nozzle. Therefore the pressure based AC CBS algorithm is only applied to these incompressible flows.

7.3.1 Pressure Based Formulation for Continuity equation

In Massarotti, Zienkiewicz, & Nithiarasu, [138], the solution of incompressible flow problems was initially obtained by using the semi-implicit version of the AC CBS scheme, with the necessity of solving a set of simultaneous algebraic equations. However interest is gathering momentum in fully explicit techniques as stated by Monti & Pezella, [172], because of easy and efficient parallelization for viscous 3D problems in the aerospace and aeronautical community. The following numerical detail outlines how the CBS formulation is modified for incompressible flows, which couples pressure and velocity in the continuity equation. Malan, Lewis, & Nithiarasu, [173], it should be noted:

1. Fully explicit schemes applied to convective flows need to possess sufficient stability producing a diagonally dominant system of equations. This is usually achieved by using small time steps or by refining the mesh small length scales [131].
2. When equal order interpolation functions are used for both the velocity and pressure terms for incompressible flow solvers, this can cause "checker-boarding" in the pressure field according to research in Harlow and Welch, [26], compromising the accuracy of the solution.

These two instabilities are not to be confused with the instability caused by turbulence present at large Reynolds Numbers as stated by [174]. As mentioned above, at incompressible speeds the pressure based schemes make theoretical assumptions that allow a solution to a flow problem to be attempted. However when the free-stream speed becomes compressible (Mach>0.3) these assumptions, such as $\partial\rho / \partial p = 0$, need to be re-assessed.

7.3.2 Modify utilizing a Pressure Based Formulation

The density based (DB) formulation for the CBS technique is in general applicable to compressible flow. Generally these schemes solve the conservation variables (ρ, $\rho\mathbf{u}$, ρE) instead of those quantities solved by pressure correction methods (P,**u**,T) at the solution points [17]. The down side for density based schemes are they cannot be easily applied to solve incompressible flows as the density remains constant [150]. Therefore a derived link between the continuity equation and pressure needs to be established such as the one developed in [150]. For incompressible problems these modified algorithms, such as the FV AC CBS scheme developed in this chapter, hinge on this artificial relation between pressure and density through a pressure-density derivative in the continuity equation:

$$\frac{\partial \rho}{\partial P}\frac{\partial P}{\partial t} = \frac{\partial \rho u}{\partial x} + \frac{\partial \rho v}{\partial y} \tag{7.5}$$

$$\frac{1}{\beta^2}\frac{\partial P}{\partial t} = \frac{\partial \rho u}{\partial x} + \frac{\partial \rho v}{\partial y} \tag{7.6}$$

Where (7.7)

$$\beta = \max\left(\varepsilon_\beta, \sqrt{u_i u_i}, \frac{2\mu}{\rho\{\min(\Delta x, \Delta y)\}} \right)$$

ε_β is set to 0.5 for incompressible benchmarks which enforces an even weighting between adjacent control volumes. The differential equation, above is substituted for the density continuity equation as seen in (7.2) in the following formulation.

7.3.3 The Sequential Artificial Compressibility CBS Scheme

The Finite Element Artificial Compressible Characteristic Based Split (AC CBS) procedure performed well for the incompressible problem, flow within a lid driven cavity, seen in Malan et al [96]. Now the Finite Volume AC CBS is implemented and applied to flow over a flat plate. Other variants of this procedure were evaluated for this benchmark but did not have the same success as this method. Each step described below is applied to all the interior nodes in a sweep of the grid. After this sweep the boundary conditions are computed. Then the sequential computational iterative procedure is repeated by going back to step 1. The AC CBS method was implemented in FORTRAN within the PHYSICA code framework and simulations were then run on the cluster to solve the Navier-Stokes system of equations.

1. According to Malan et al [173] for incompressible flows the artificial wave speed is calculated as from (7.7) where ε_β is set to 0.5 for incompressible benchmarks.

2. The CBS scheme incorporates local pseudo time stepping. The pseudo time step is given by the following equation: where C is the courant number and depending on the problem is usually < 0.5 The convection time step is analogous to the compressible time step and the diffusion time step as calculated by Malan et al, [150]:

$$\Delta t^n_{CV} = \min\left(\left(\Delta t^n_{CV}\right)_{conv}, \left(\Delta t^n_{CV}\right)_{diff} \right) \tag{7.8}$$

$$\left(\Delta t^n_{CV}\right)_{conv} = C \frac{h_{CV}}{\beta_{CV} + \sqrt{u_i u_i}} \tag{7.9}$$

$$\left(\Delta t^n_{CV}\right)_{diff} = C \frac{\rho_\infty \{h_{CV}\}^2}{2\mu_\infty} \tag{7.10}$$

3. Intermediate Momentum

$$\rho u_i^* = \rho u_i^n - \frac{\Delta t}{\Delta V} \left(\begin{array}{l} \sum_{f=1,TOTFIC} \left(\left(\rho u_i u_j\right) \bullet n_j A \right)_f - \sum_{f=1,TOTFIC} \left(\tau_{ij} \bullet n_j A \right)_f \\ + \frac{\Delta t}{2} u_k \sum_{f=1,TOTFIC} \left(div\left(\rho u_i u_j\right) \bullet n_j A \right)_f \end{array} \right)^n \tag{7.11}$$

Where n_j is the unit normal vector in the j direction

for example if i=x

$$\tau_{xj} \bullet \underline{n} = \tau_{xx} \bullet n_x + \tau_{xy} \bullet n_y$$

$$\tau_{xj} \bullet \underline{n} = \left[\mu\left(2\frac{\partial u_x}{\partial x} \right) - \frac{2}{3}\mu \frac{\partial u_x}{\partial x} \right]_f \bullet \left(n_x\right)_f + \left[\mu\left(\frac{\partial u_x}{\partial y} + \frac{\partial u_y}{\partial x} \right) \right] \bullet \left(n_y\right)_f$$

6. Corrected Momentum

$$\rho u_i^{n+1} = \rho u_i^* - \frac{\Delta t}{\Delta V}\left(\sum_{f=1,TOTFIC} P_f \bullet n_i A_f - \frac{\Delta t}{2} u_k \sum_{f=1,TOTFIC} \frac{\partial P}{\partial x_i} \bullet n_i A_f \right) \quad (7.12)$$

7. The Continuity Equation is solved using the momentum values from (7.12) at the n+1 "time" level.

$$P_{CV}^{n+1} = P_{CV}^n - \left(\beta_{CV}^n\right)^2 \frac{\Delta t}{\Delta V}\left(\sum_{f=1,TOTFIC} \left(\rho u_j \bullet n_j A\right)_f \right)^{n+1} \quad (7.13)$$

8. Check convergence to steady state values by sensing whether the relative error is less than the agreed tolerance of 10^{-5} or the number of iteration/sweeps is below the maximum iteration/sweeps, I_{Max}, stipulated by the user. This value was set initially to 95,000 iterations. The steady state error for incompressible problems is calculated as:

$$\varepsilon_{Rel}^n = \frac{1}{NUMELE} \sqrt{\left[\frac{\sum_{CV=1}^{NUMELE} \left(\frac{\left| u_{CV}^{n+1} - u_{CV}^n \right|}{\Delta t_{CV} (L/u_\infty)} \right)^2}{\sum_{CV=1}^{NUMELE} \left(u_{CV}^{n+1} \right)^2} \right]} \quad (7.14)$$

9. If convergence has been achieved exit the procedure and display results otherwise begin computational sweep by going back to step 1.

Remarks:

The artificial wave speed calculation utilized by Massarotti et al, [132], equation (7.17), is given below. This value was not dimensionally consistent.

$$\beta = \max\left(\varepsilon_\beta, \sqrt{u_i u_i}, \frac{2}{h_{CV}\,\mathrm{Re}_x} \right) \quad (7.15)$$

$$\Delta t = \min\left(\Delta t_{conv}, \Delta t_{diff} \right) \quad (7.16)$$

$$\Delta t_{diff} = \frac{h_{CV}^2\,\mathrm{Re}_x}{2} \quad (7.17)$$

$$\mathrm{Re}_x = \frac{\rho_\infty u_{CV} \Delta x_{CV}}{\mu_\infty} \quad (7.18)$$

Therefore this procedure (7.14)-(7.17) was successfully replaced with equations (7.9), (7.7) and (7.10) as set out by Nithiarasu P, Codina R in [131].

7.4 0.01m Flat Plate

Initially for this benchmark a decision was made to model a preliminary 1cm plate, before modelling the 1m long benchmark case. This was done to keep the local Peclet number low so that a solution can be attained without a need for uneconomically large grids. Once satisfactory results could be attained then the 1m plate and hence larger Reynolds numbers were attempted. The local Peclet number is denoted as:

$$(Pe_x)_I = \frac{(\rho u)_I}{\mu / \Delta x_{I,I+1}} \tag{7.19}$$

where the sub script I indicates a control volume, I+1 is the adjacent control volume and $\Delta x_{I,I+1}$ is the distance from I to I+1.Where the non-dimensional Peclet number is a measure of the relative strength of convection relative to diffusion. According to Patankar, [36], for central differencing schemes, for a stable computation, then the Peclet number should be less than 2. The cell Peclet number can be reduced primarily by reducing the grid size $\Delta x_{I,I+1}$.

7.4.1 Boundary Conditions

A 1cm flat plate is initially used to test the AC CBS algorithm capability for solving incompressible flows. A schematic of the domain is shown in Figure 7-2. This problem is an external flow problem, providing the boundaries are far enough from the region of the physical interactions. The initial domain is 1.2cm long spanning a flat plate of 1.0cm and it extends 0.2cm upstream of the leading edge. The height of the domain was initially set as 0.5cm.

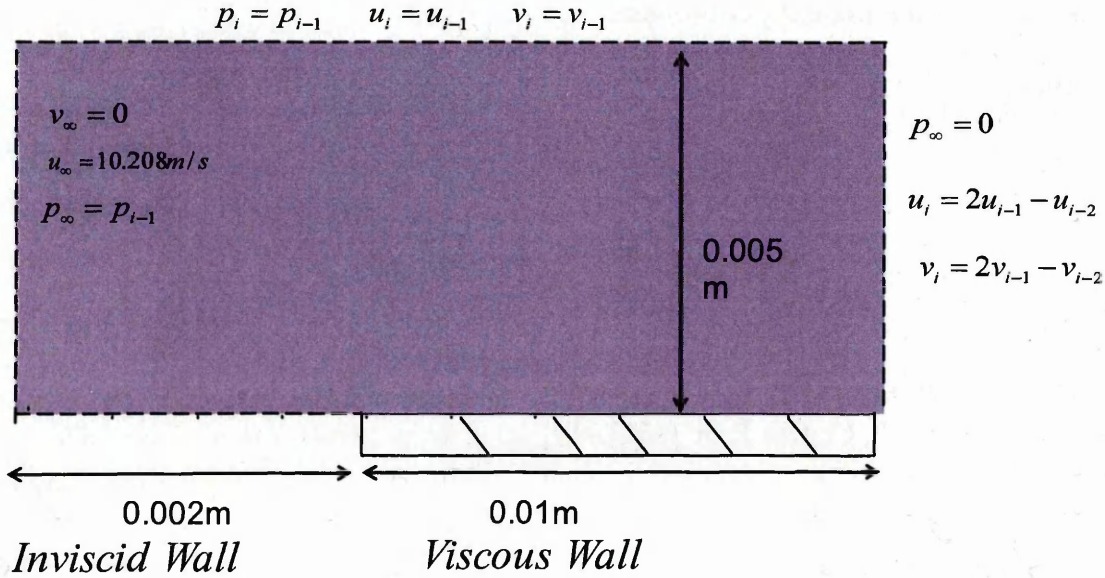

Figure 7-2- Specification for the 0.01m plate.

As seen in Figure 7-2, the boundary conditions are also labelled as the wall. The left most boundary is the inlet and differs from the Supersonic inlet seen in the 2D Supersonic wedge example; here the pressure floats and is extrapolated from the cells downstream. Thereby the pressure on the inlet boundary is calculated as part of the solution for external Subsonic flow problems.

The top boundary is either fixed to the free-stream velocity values with a pressure extrapolated from the cells below – note, this should only be applied when the top is far enough from the flat plate, however in our case, u, v and P are extrapolated from within the solution domain. The physical values on the outlet were initially extrapolated, using 1st ordered extrapolation values, and this gave rise to instability and divergence. Therefore boundary values were extrapolated using the 2nd ordered formulation, which gave rise to stable results.

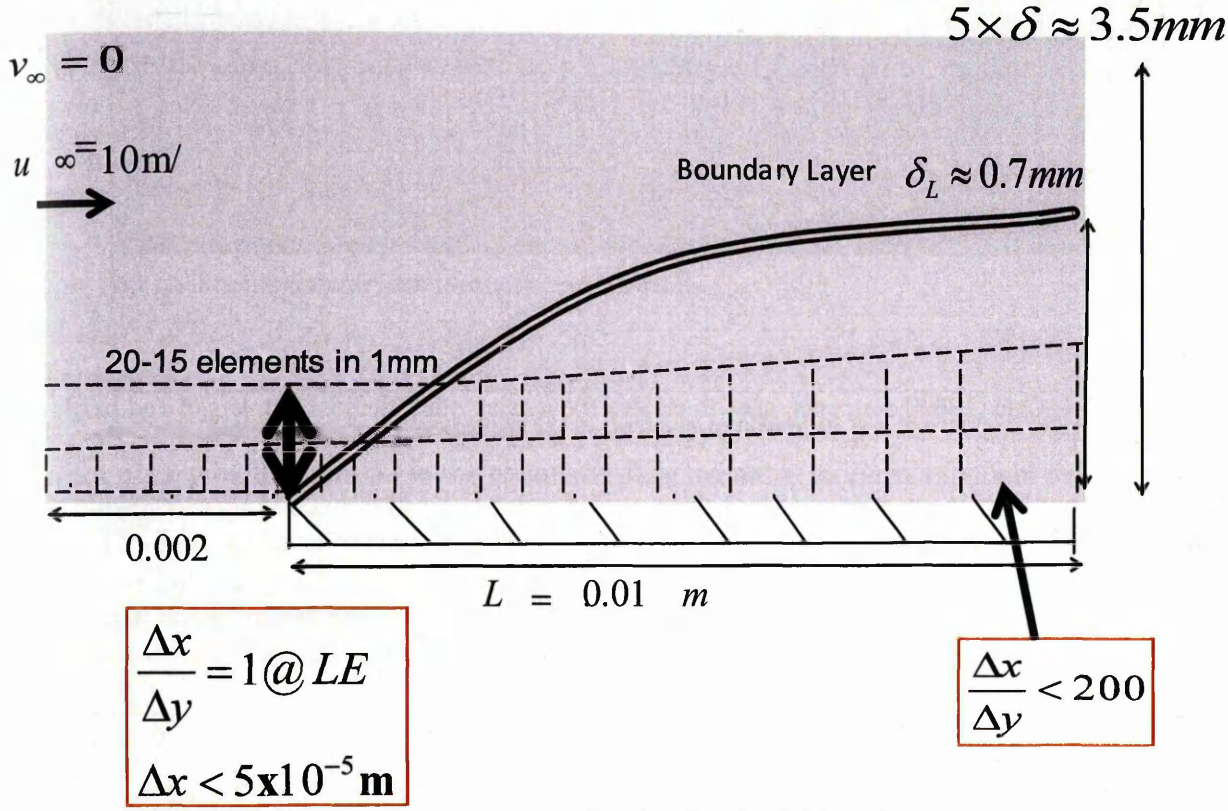

Figure 7-3- Specification for the 0.01m plate.

To obtain grid resolution in the boundary layer region and reducing the aspect ratio for cells at the trailing edge to less than 200. The guidelines for mesh construction can be seen in Figure 7-3. For neighbouring elements, we stretched the grid from the leading edge in the x and y direction utilizing a growth factor of less than 1.05 in the y direction and 1.1 in the x direction. This growth factor was enforced using the power law in the FEMGV mesh construction tool as seen in Figure 7-4.

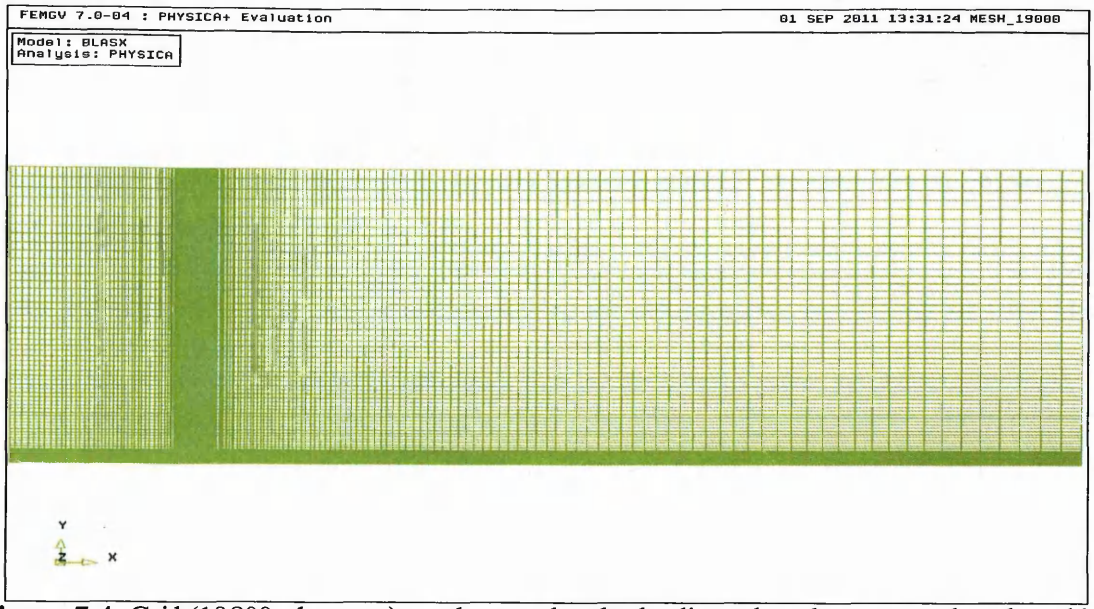

Figure 7-4–Grid (19800 elements) used to resolve the leading edge element to a length and height of $2.3x10^{-6}$m.

The first set of simulations were done to test the required mesh resolution needed by employing a grid independence study. This was done to capture the realistic pressure field over a flat plate. The size of the leading edge was found to effect the final pressure profile over the flat plate for steady state conditions. A grid independence study was carried out on 6 separate meshes. Each mesh has a different leading edge size as seen in Table 7-1.

Table 7-1-Grid parameters for mesh sensitivity study.

	Nx	Ny	Nt	LE Dx (10^{-6}m)	LE Dy (10^{-6}m)
Mesh 1	165	110	24000	30.00	42.00
Mesh 2	210	120	30000	20.00	30.80
Mesh 3	270	100	36000	1.33	1.82
Mesh 4	140	120	26000	9.35	1.63
Mesh 5	200	160	47000	7.9	8.97
Mesh 6	220	90	19800	2.5	2.88

where Nx is the number of cells in the x direction.
Ny is the number of cells in the y direction.
Nt is the total number of cells.

7.4.2 Wall Coefficients

The distribution of the pressure coefficient, heat transfer and skin friction are normally required during hardened validation of the CFD solver against theoretical solutions according to Lyra, [7]. Where the wall pressure is directly obtained using the flow variables and the ideal gas law. The heat flux at the wall q_w and the wall shear stress τ_w are obtained respectively, from.

$$q_w = \frac{\partial T}{\partial \mathbf{n}_w} \tag{7.20}$$

And

$$\tau_w = t_y n_x - t_x n_y \tag{7.21}$$

Here, t_x and t_y denotes the surface tractions evaluated as-

$$t_x = \tau_{xx} n_x + \tau_{xy} n_y$$

$$t_y = \tau_{yx} n_x + \tau_{yy} n_y$$

Where the shear stress tensor components τ_{ij} is defined in Chapter 2.

For a flat plate which is parallel to the oncoming flow the stress tensor component reduces to.

$$\tau_w = \mu_w \left(\frac{\partial u_x}{\partial y} \right)_w \tag{7.22}$$

To compare the steady state CFD results with the experimental and numerical data the coefficient of pressure, coefficient of heat transfer and skin friction C_p, C_H and C_f are defined by.

$$C_P = \frac{P_w}{0.5 \rho_\infty u_\infty^2} \tag{7.23}$$

$$C_H = \frac{q_w}{\rho_\infty u_\infty \left[H_\infty - H_w \right]} \tag{7.24}$$

$$C_f = \frac{\tau_w}{0.5 \rho_\infty u_\infty^2} \tag{7.25}$$

Where the subscripts w and ∞ refer to the wall and free stream values respectively.

7.4.3 Analytical Solution

The drag on a flat plate is either due to friction created by laminar, transitional, and turbulent boundary layers according to White, [154]. When validating the FV AC CBS scheme the comparison is made with the coefficient of friction, C_f, for laminar flow between the theoretical result and the numerical solution.

The Blasius approach to solving the boundary layer was to transform the partial differential Navier-Stokes equation into ordinary differential equations that yield to series expansion. Thus the theoretical result is simply a function of the x distance The resultant drag on a flat plate from laminar flow is theoretically approximated by the equation in (White, [154] p.235) and seen below (7.26). This result is otherwise known as the Blasius solution.

$$C_{f,x} = \frac{0.664}{Re_x^{\frac{1}{2}}} \tag{7.26}$$

Because the Blasius solution to the boundary layer over a flat plate has been shown to be very close to experimental data collected in Liepmann & Roshko, [82] this boundary layer flow is therefore a cornerstone for this CFD solver.

7.4.4 Simulation Results

When the steady state solution is reached the termination of the calculation can be done automatically in the code by a test calculation, sensing when the changes in the flow variables between each iteration becomes smaller than the prescribed tolerance.

As mentioned the relative errors of density of the order of 10^{-5}, is an adequate relative error tolerance for compressible flow problems. For incompressible flows the relative errors are done with respect to the velocity as seen in (7.14). Appropriate time relaxation was employed to minimize the time derivatives in the early stages of the computations by employing the Courant number, C, of 0.01. So that the effect of mesh resolution on the final accuracy of the CBS scheme can be ascertained the following meshes in Table 7-1 were employed.

Mesh Sensitivity Study

Problems with convergence were encountered for the incompressible flow over a 1cm flat plate, in this case the convergence criteria or tolerances was reduced to 10^{-3}. For solutions reaching this tolerance the resultant pressure profiles were compared along the bottom grid line of Figure 7-3. The challenge for this case is to obtain grid independence for the pressure field.

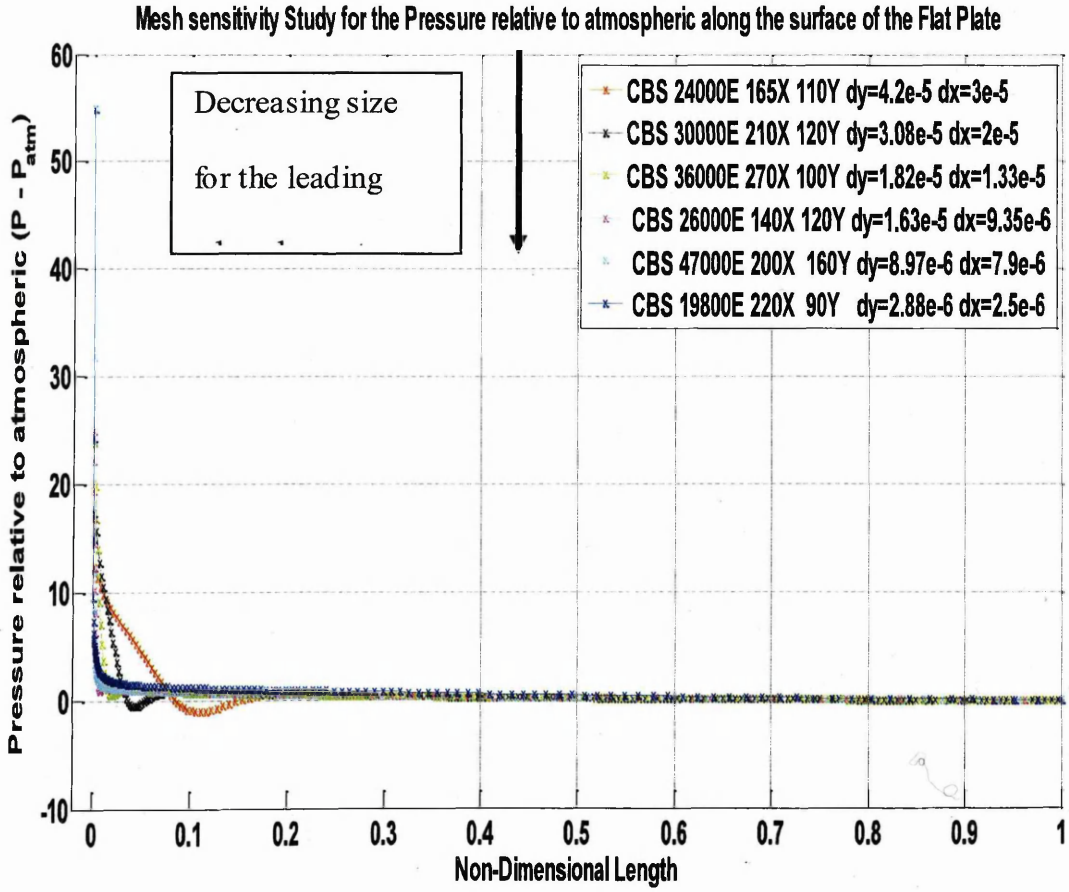

Figure 7-5– Comparison of pressure along the surface of the plate for different grids that have increased resolution at the leading edge.

The relative pressure along the flat plate is shown in Figure 7-5 for the 6 meshes seen in Table 7-1. For external flows, the 2-D flat plate problem, the pressure profile should exhibit positive relative pressure along the length of the plate, with no negative values. This positive pressure profile is an indication that the numerical results are physically reliable. Conversely, for mesh 1-4, when the relative pressure is negative, it implies a sink for mass[9]. A mass sink on the surface of the plate is an unrealistic and incoherent situation for this chosen benchmark problem.

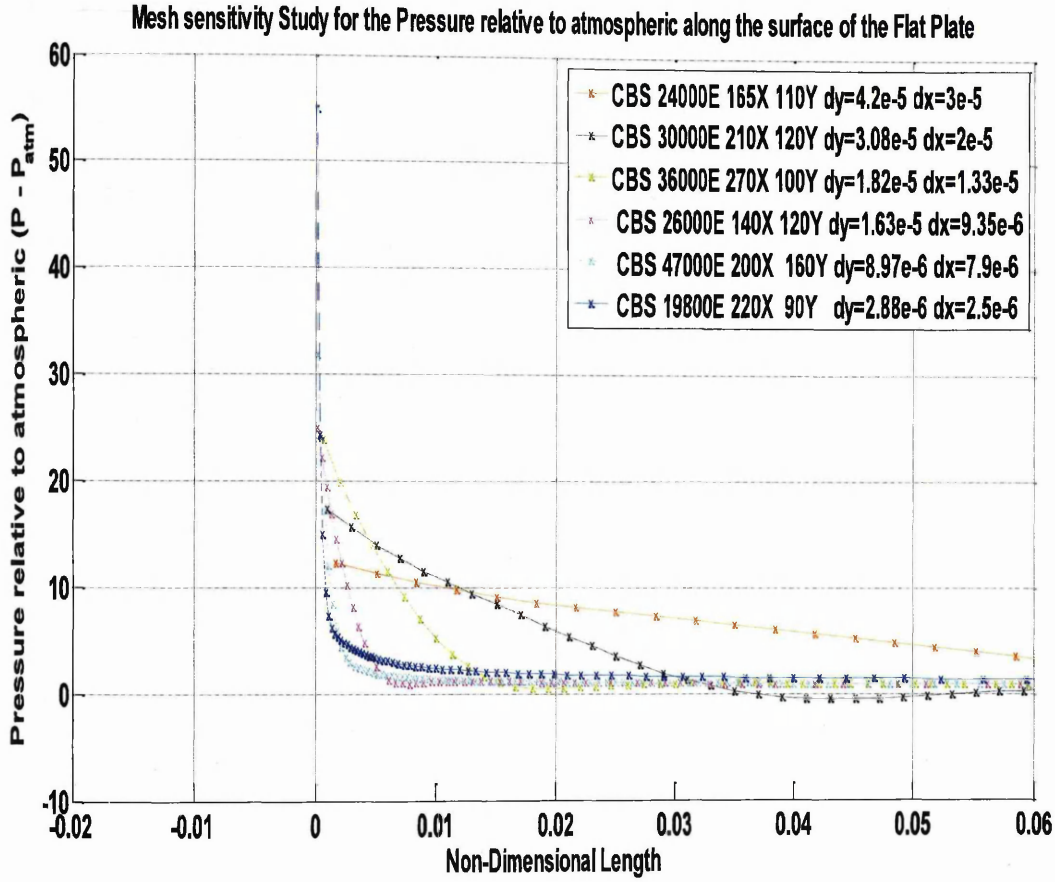

Figure 7-6– Comparison of pressure along the surface of the plate for different mesh densities. Each refinement means a decrease of the leading edge size.

Figure 7-6 shows the relative pressure along the leading edge of the flat plate for the 6 meshes described in Table 7-1. The successive solutions on finer grids should show grid independent as the mesh is refined, as seen in mesh 5 and mesh 6. The plot shows that the 6th mesh in Table 7-1 displays purely positive relative pressures. Ensuring the results are physically correct. Therefore for the remainder of this research this 6th mesh the 19800 mesh was employed for the simulations.

For the results above, the CBS code requires a resolution of 2.3 x 10^{-6} m at the leading edge, however according to supervisors at ESA competitive CFD codes require a resolution of only 5x10^{-5}m. The next set of results were done to measure the accuracy of the AC CBS relative to the analytical solution mentioned in Section 7.4.3. The accuracy was quantified using the equation for the final AC CBS C_f values. All the results below were computed with the 6th mesh in Table 7-1 the 19800 mesh.

[9] Since velocity goes from relative high to relative low pressure in incompressible problems.

Table 7-2- Grid and flow parameters for the next set of simulation results.

1cm Flat Plate	u_∞[m/s]	ρ_∞[kg/m^3]	μ_∞[kg/(ms)]	Re[-]	Nx	Ny	Nt
	10.208	1.225	1.789×10^{5}	7.0×10^{3}	190	220	19800

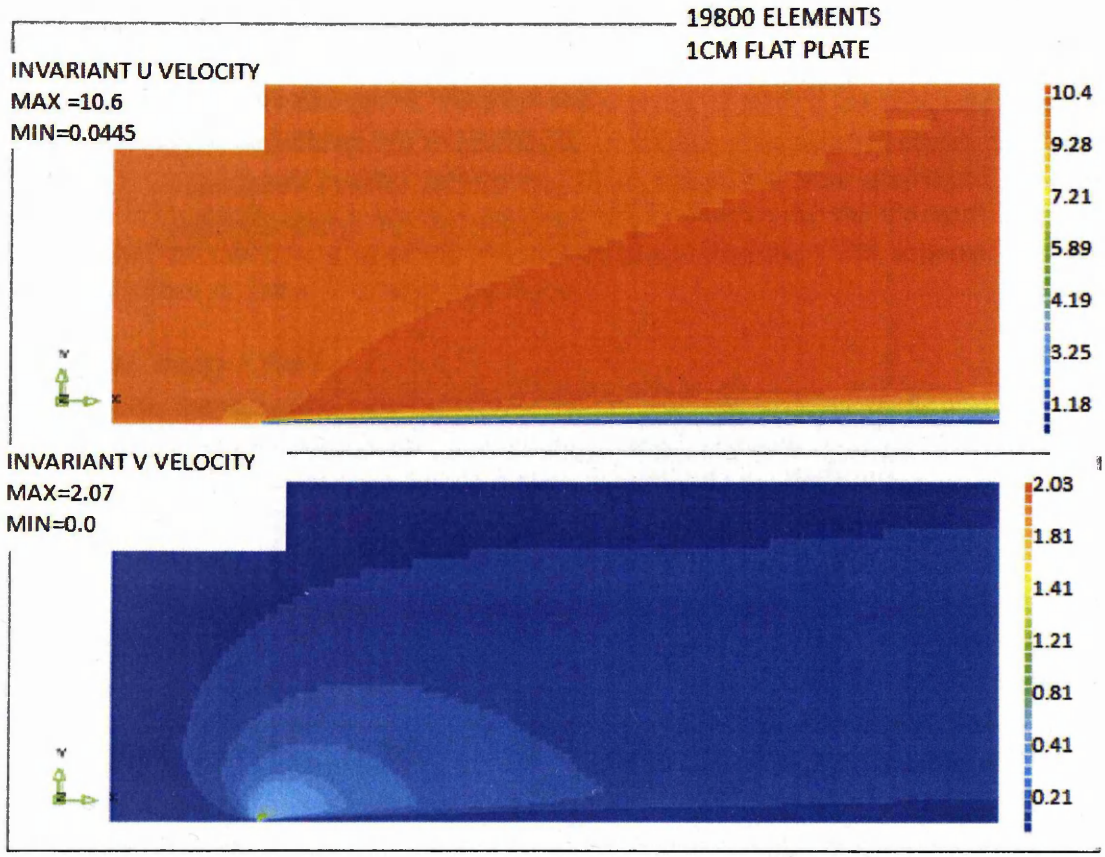

Figure 7-7- Velocity contours from the AC CBS solver for the 19800 element mesh.

UNCB in the left hand corner of the scalar contours (Top plot) shown in Figure 7-7 denotes the velocity in the x direction and VNCB denotes (Bottom plot) the velocity component in the y direction. These components are calculated at the solution points, the centroids of the mesh as seen in Figure 7-4. The top contour plot has a large range for these contours (0-10.5 m/s) where the change of x velocity occurs predominately through the boundary layer. In contrast, the bottom plot, where the localized region of contours occurs around the leading edge, has a smaller range for the contours (0-2.07 m/s).

Accuracy relative to analytical solution

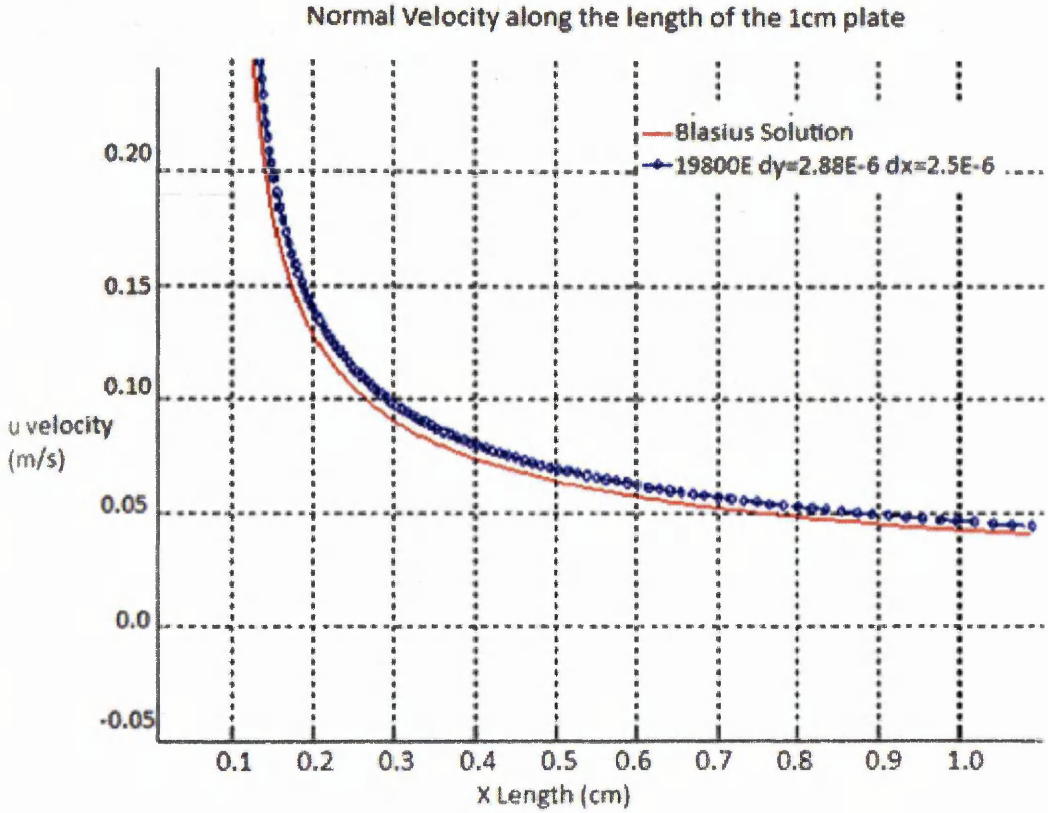

Figure 7-8–Coefficient of friction (C_f) values along the surface of the plate for the 19800 element grid which resolves the leading edge x-length $2x10^{-6}$m.The numerical solution is compared with the Blasius solution (red line).

In Figure 7-8, the laminar skin friction curve obtained with the FV AC CBS algorithm and the 19800 mesh is in *reasonably* good agreement with the theoretical curve provided in Section 7.4.3. and displayed as the red curve. However as previously mentioned industrial sponsors ESTEC require an accuracy of less than 1% error between the C_f value predicted by theory and the C_f value calculated through the CBS scheme. The next plot displays the absolute errors along the flat plate.

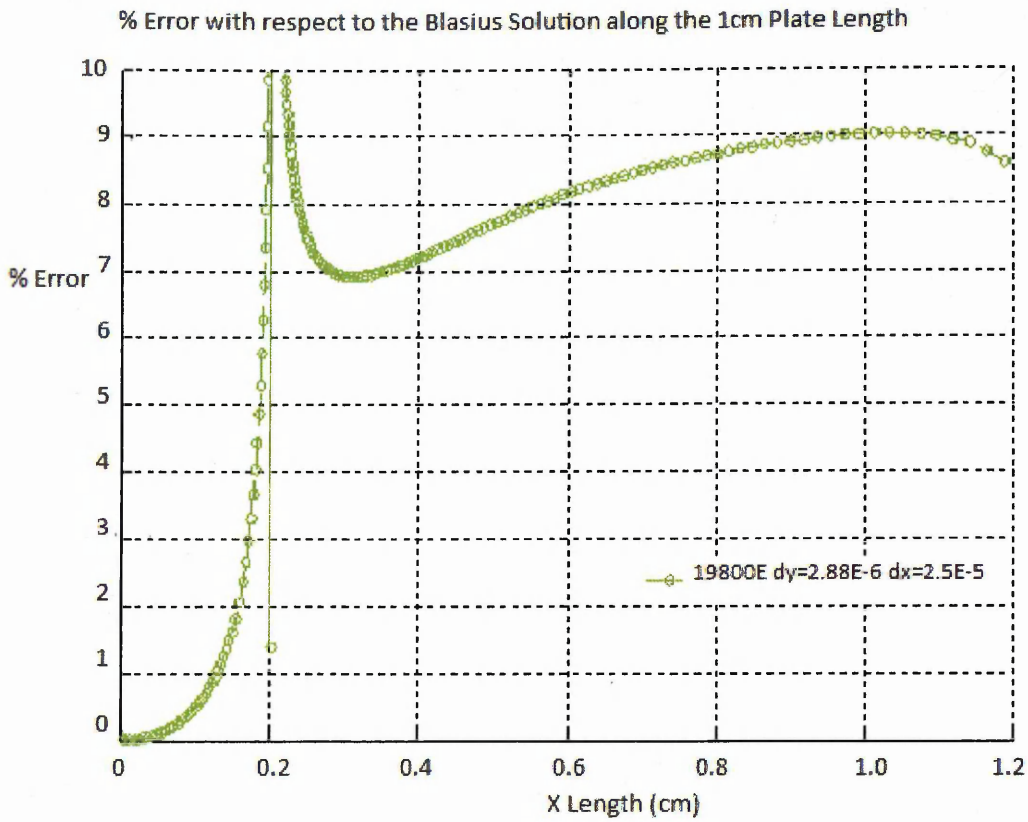

Figure 7-9–Absolute percentage error for the C_f values along the surface of the plate as solved over the mesh seen in Figure 7-4.

Figure 7-9 displays the percentage error between the numerical solution and the theoretical result for C_f. The recommended average percentage error should be below 1% as recommended by ESTEC. The average percentage error is calculated and is seen below for the 19800 mesh using the AC CBS scheme as:

$$\varepsilon_{abs,err} = \frac{1}{ELEXX} \sum_{N=1,ELEXX} \left(\left(\frac{C_{f,Blas} - C_{f,CBS}}{C_{f,Blas}} \right) \times 100 \right) \tag{7.27}$$

$$\varepsilon_{abs,err} = 8\%$$

Where ELEXX number of elements on the surface of the plate.

7.5 Extension to 1.00m Flat Plate

By building blocks onto the 19800 element mesh seen in Figure 7-4 we obtained what would be a satisfactory grid for the 1 meter plate. However initial simulations showed that the AC CBS algorithm was unstable at modelling the viscous Subsonic boundary layer; for a free stream Reynolds number of 7×10^5. A number of strategies were employed to stabilize the algorithm, however, none were as effective as increasing the viscosity, an indication that the instability is due to turbulent eddies.

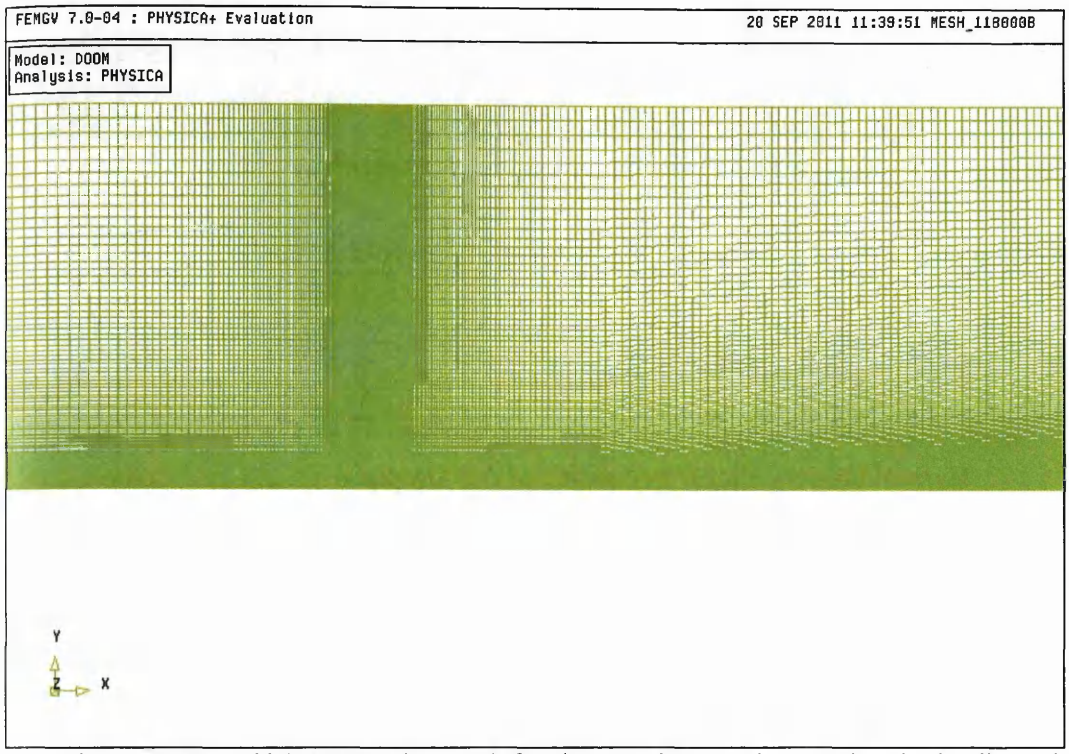

Figure 7-10–Grid (118000 elements) for the 1m plate used to resolve the leading edge element to a length and height of $2.3\text{x}10^{-5}$m.

The aspect ratio at the inlet and the outlet were tracked because if they are , as anything greater than 200, according to the industrial sponsors, is potentially de-stabilising.

Table 7-3- Grid and flow parameters for the 1m flat plate.

1m Flat Plate	u_∞[m/s]	ρ_∞[kg/m^3]	μ_∞[kg/(ms)]	Re[-]	Nx	Ny	Nt
	10.208	1.18	1.789×10^5	7.0×10^5	590	200	118000

In order to clarify that the algorithm's inability to stabilize the current problem was due to high Reynolds number, we created an enlarged copy of the 19800 mesh as seen in Figure 7-4 (x100 the length in the x direction & x100 the height in the y direction and by utilising an identical Reynolds number as the 0.01m case). In order to get identical Reynolds numbers for both the 0.01m and 1m plate a larger kinematic viscosity was substituted into the 1m plate in place of the viscosity for air.

$$\mu_{new} = \frac{1.225\times10.208\times1}{7\times10^3} = 1.789\times10^3\left[kg/(ms)\right]$$

$$\text{Re} = \frac{\rho u l}{\mu_{new}} = 7\times10^3$$

The above kinematic viscosity is x100 greater than the 1cm plate case. The schematic domain is analogous to Figure 7-2. However the domain is 1.2m long, here, spanning a flat plate of 1.0m and it extends 0.2m upstream of the leading edge. The height of the domain was initially set as 0.5m instead of 0.005m.

To verify that the viscous AC CBS algorithm stability is independent of the domain size but more than likely dependent on the Reynolds number, then we make the following conjecture. *"If the AC CBS solver has an intrinsic flaw at modelling larger domains then the final velocity profile should be different to the 0.01m case."* Then the following results must converge to steady state and the results must be in close agreement with the C_f values for the 1cm case as seen in Figure 7-8.

The aspect ratio for the grids employed at the inlet and the outlet needs to be assessed; anything greater than 200, according to the industrial sponsors is potentially de-stabilising. Therefore the mesh for the 1cm flat plate in Figure 7-4 was re-created but instead with a length of 1m and a height of 0.5m so that the leading edge element has a height and length of 2.3×10^{-4}m.

Table 7-4- Grid and flow parameters for the next set of simulation results.

1m Flat Plate	u_∞[m/s]	ρ_∞[kg/m^3]	μ_∞[kg/(ms)]	Re_x[-]	Nx	Ny	Nt
	10.208	1.225	1.789×10^3	7.0×10^3	190	220	19800

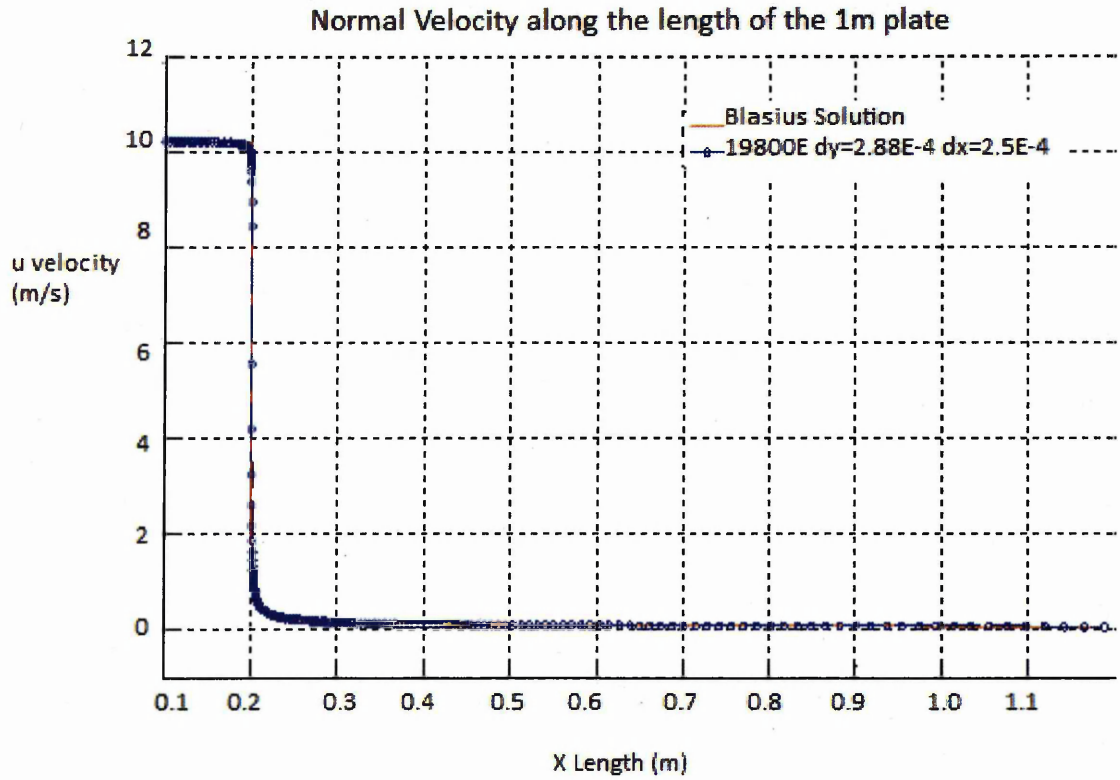

Figure 7-11– Velocity along the surface of the plate for the 19800 element grid with the leading edge element set to a length $2.3\text{x}10^{-4}$m. The AC CBS results (blue circle) are plotted against the Blasius solution (red solid line).

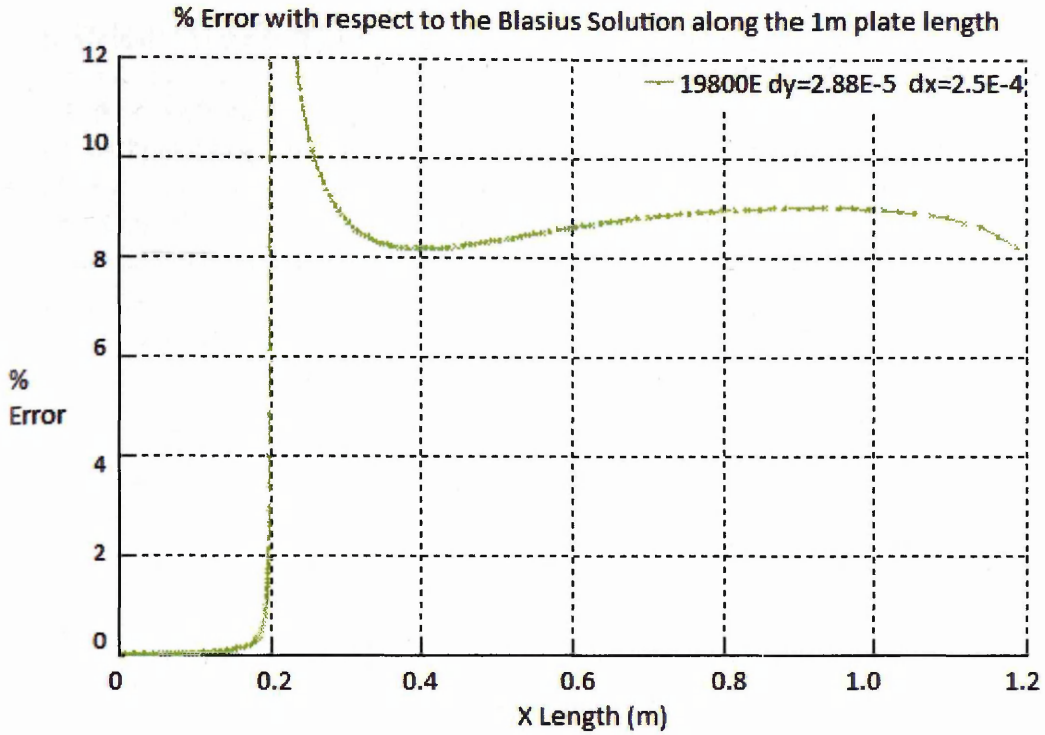

Figure 7-12. Illustrates percentage error for the coefficient of friction for the 19800 element grid with the leading edge element set to a length $2.3\text{x}10^{-4}$m. The CBS results (green circle).

The AC CBS algorithm has shown that it is restricted to stable solutions for problems with a free-stream Reynolds numbers (Re)< $7\text{x}10^5$. However for Re= 7.0×10^3 the AC CBS solution converged to a steady state solution.

$$\varepsilon_{abs,err} = \frac{1}{ELEXX}\sum_{N=1,ELEXX}\left(\left(\frac{C_{f,Blas}-C_{f,CBS}}{C_{f,Blas}}\right)\times 100\right) \tag{7.28}$$

$$\varepsilon_{abs,err} = 8\%$$

Where ELEXX is the total number of elements adjacent to the flat plate.

Unsurprisingly the average percentage error (8%) for the 1m plate as calculated by (7.28) is approximately the same as the value seen in the first benchmark study; the 1cm flat plate case. Since the average percentage error (8%) is well above the acceptable value of 1% further work was carried out on driving down the error to below the 1% tolerance. These efforts included a study into enlarging the domain, because this will allow us to quantify the effect that the distance between the flow inlet and the leading edge (LE) has on the final solution.

Before we can remedy the CBS FV scheme so that it can capture reliable results with respect to the analytical solution we first need to understand the reason for the insufficient accuracy that the external flow problem is displaying.

7.5.1 Boundary Conditions

To deduce the underlying reasons for the insufficient accuracy, a literature search into the flat plate problem flagged up studies by Hirsch, [175] and Vaughn, [176].

Back in 1984 Hirsch studied the effect that the proximity of the far field boundaries has on the flat plate solution. Hirsch, [175], concluded that the correct placement of boundaries was required to gain an accurate answer for the numerical scheme favoured in Hirsch, [175]. In addition, if free-stream boundary conditions were applied to the top boundary and extrapolation is applied to the exit boundary Hirsch's algorithm converged to the analytical solution. Hirsch showed that the inlet should be 49.5 plate lengths away from the leading edge and the top of the domain should be 50 plate lengths above the plate surface. I propose to try the following amedments and investigate the effect it has on the final solution.

I. For the 1st set of results obtained by the FV AC CBS approach a 1st ordered extrapolation was applied to the top boundary, which allowing mass and enthalpy to leave the domain.
II. For the 2nd set of simulations, I applied free-stream velocities, $v_{top}=0$, to the top boundary akin to the boundary conditions in Hirsch, [175] meaning no mass will enter/exit the domain through the top boundary.

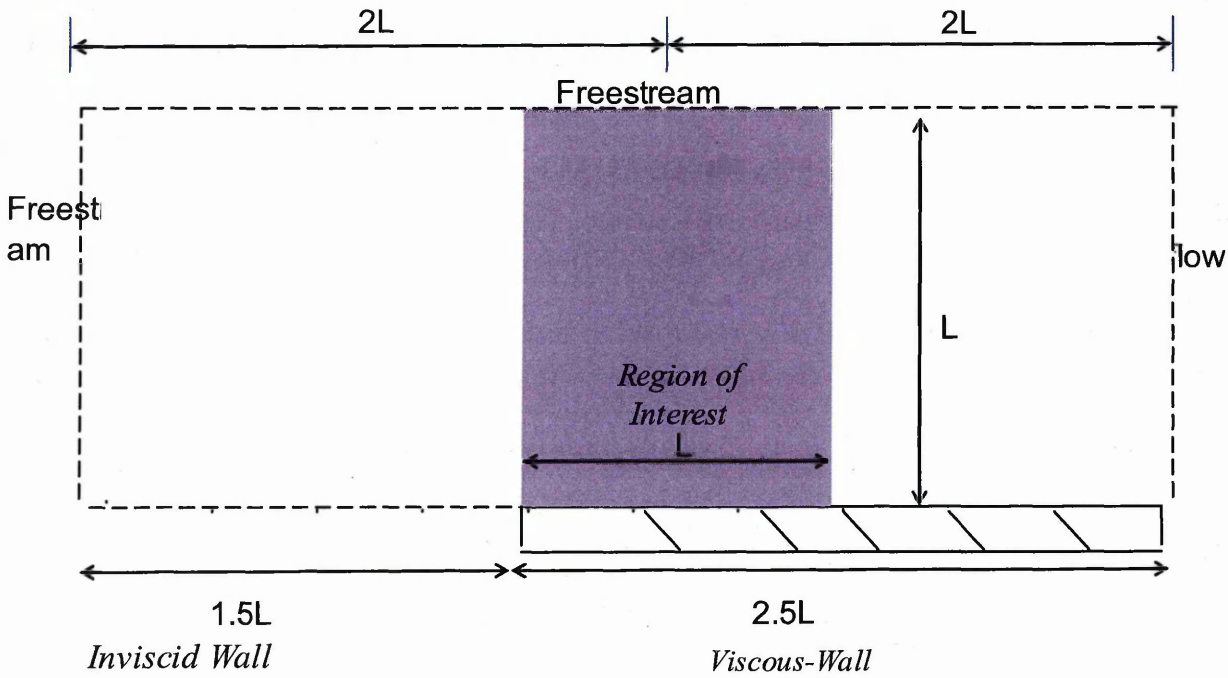

Figure 7-13-Domain for the 1m plate as set out by [176].

The location of the domain boundaries to the region of interest was stipulated in a more recent study by Vaughn, [176] as follows. The inlet to the leading edge should be a distance of 1.5 times the plate length and the top domain boundary should be 1 plate length above the region of interest. Vaughn, [176], obtained accurate results for the flat plate problem after conducting numerical experiments using different domain sizes. His final agreed domain size is illustrated in Figure 7-13. This shortening of the domain size, when compared to Hirsch's domain size, was most likely down to the more reliable numerical algorithm used by Vaughn, [176], at solving the incompressible flow problem.

Thus these two strategies were employed to stabilize the algorithm and to obtain accurate solutions. Namely

1. Move the inlet away from the leading edge.
2. Fix the top boundary to the free-stream velocities.

7.5.2 Simulation Results

To distil the effect that the distance from the inlet to the leading edge has on the accuracy of the final solution, the same grid used over the region of interest, i.e. the surface of the plate was repeated from Figure 7-4.

Domain Enlargement X Direction

The "inviscid wall'' as seen in Figure 7-14, was lengthened incrementally. In addition the different grids have the inlet element aspect ratio (AR=dx/dy) fixed to those seen in the 1cm mesh meaning AR < 200-

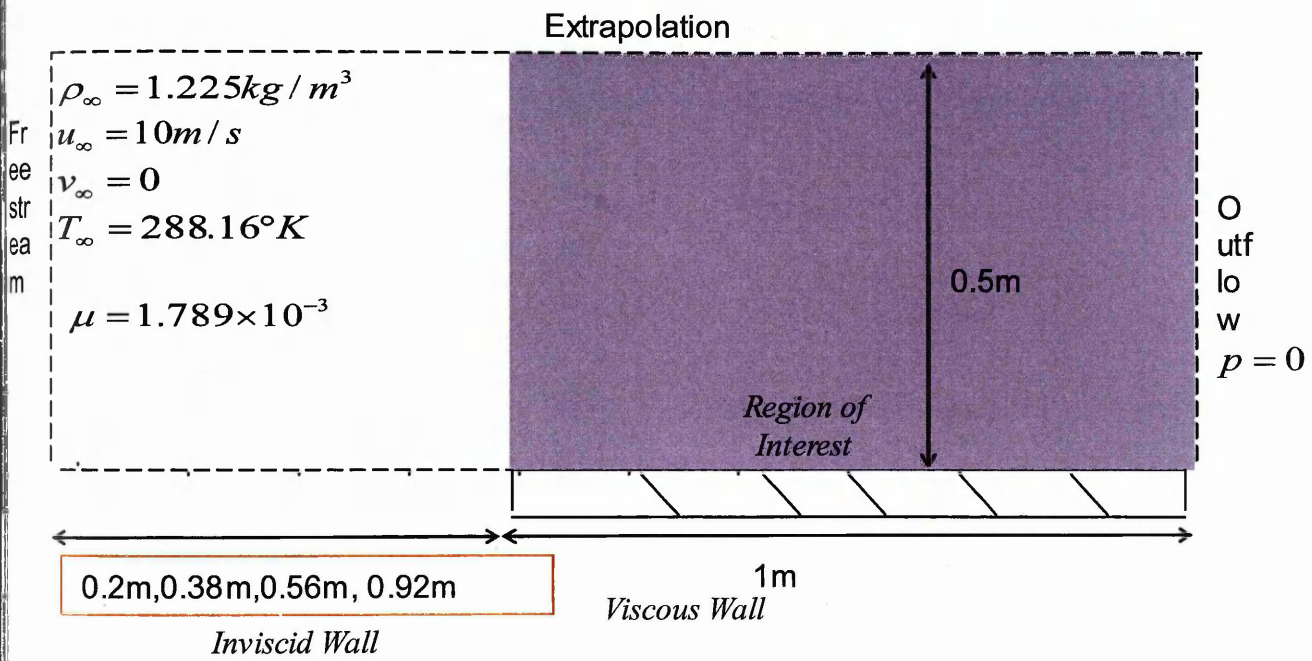

Figure 7-14-Specifications for the 1 m plate with varying LE to inlet lengths.

The next strategy as described above is to increase the upstream distance from the leading edge to the inlet boundary. The effect of increasing this distance on final solution was then studied by using 4 different meshes as noted below. Below is one of these new grids as seen in **Figure 7-15**:

Table 7-5-Grid parameters for inlet sensitivity study

	LE Length (m)
Mesh 1	0.2
Mesh 2	0.38
Mesh 3	0.56
Mesh 4	0.92

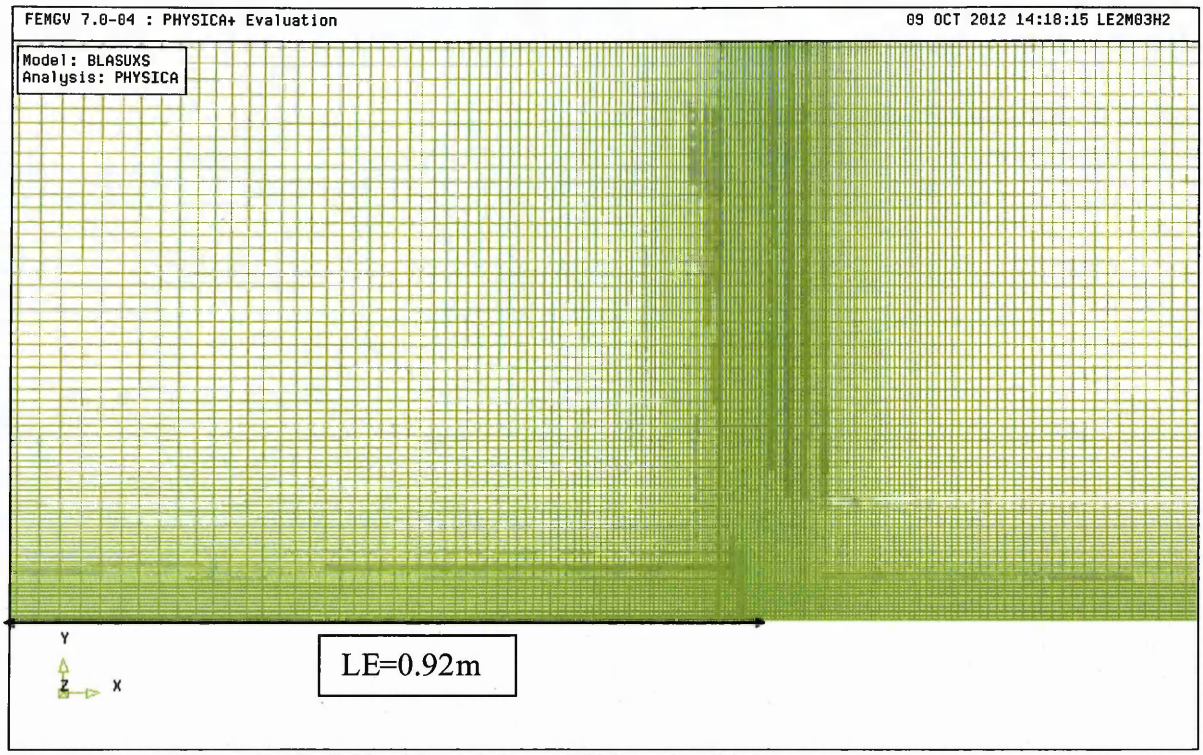

Figure 7-15-Grid with an inlet to LE length of 1.0m.

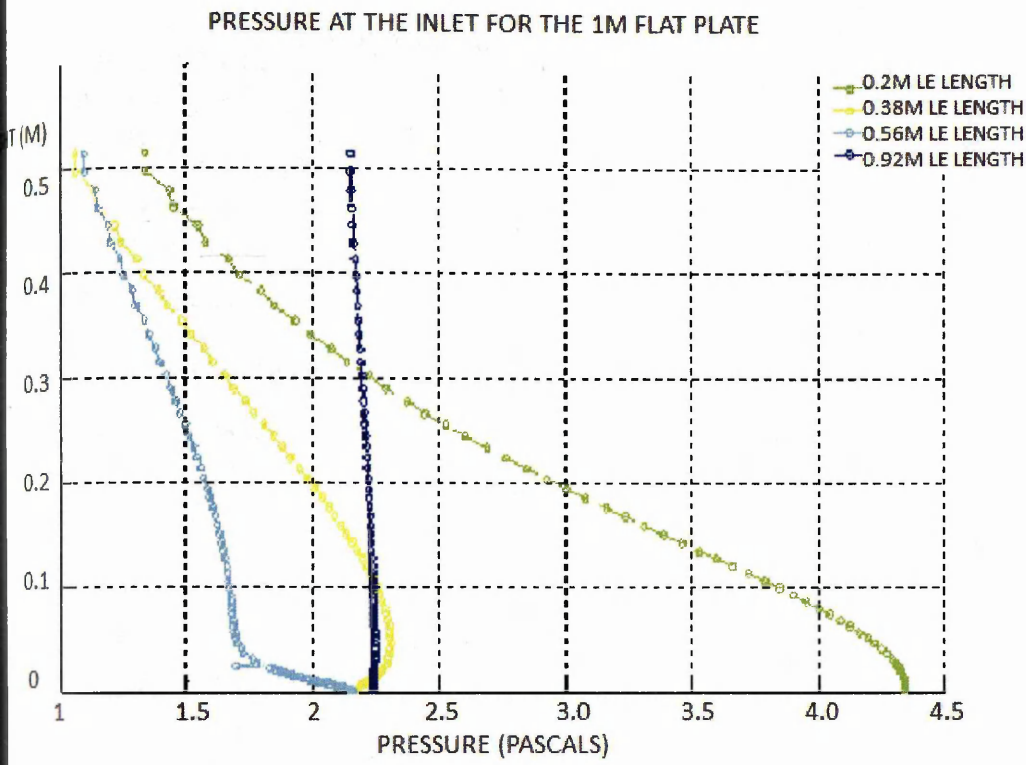

Figure 7-16-Pressure at the inlet in the y direction for the different LE lengths.

For meshes harbouring leading edge (LE) lengths of 0.2m up to 0.56m the above Figure , Figure 7-16, displays a negative pressure gradient in the y direction: green, blue & yellow lines. A positive v velocity, with a non-negligible magnitude, is produced from this negative pressure gradient. This is not consistent and not coherent with the stipulated inlet condition of zero v velocity at the inlet. At inlet to LE lengths of 0.92m the pressure profile is relatively straight. This is the inlet profile that is consistent with the stipulated boundary condition of zero v velocity. Going forward, meshes will have to contain LE lengths of 0.92m or more.

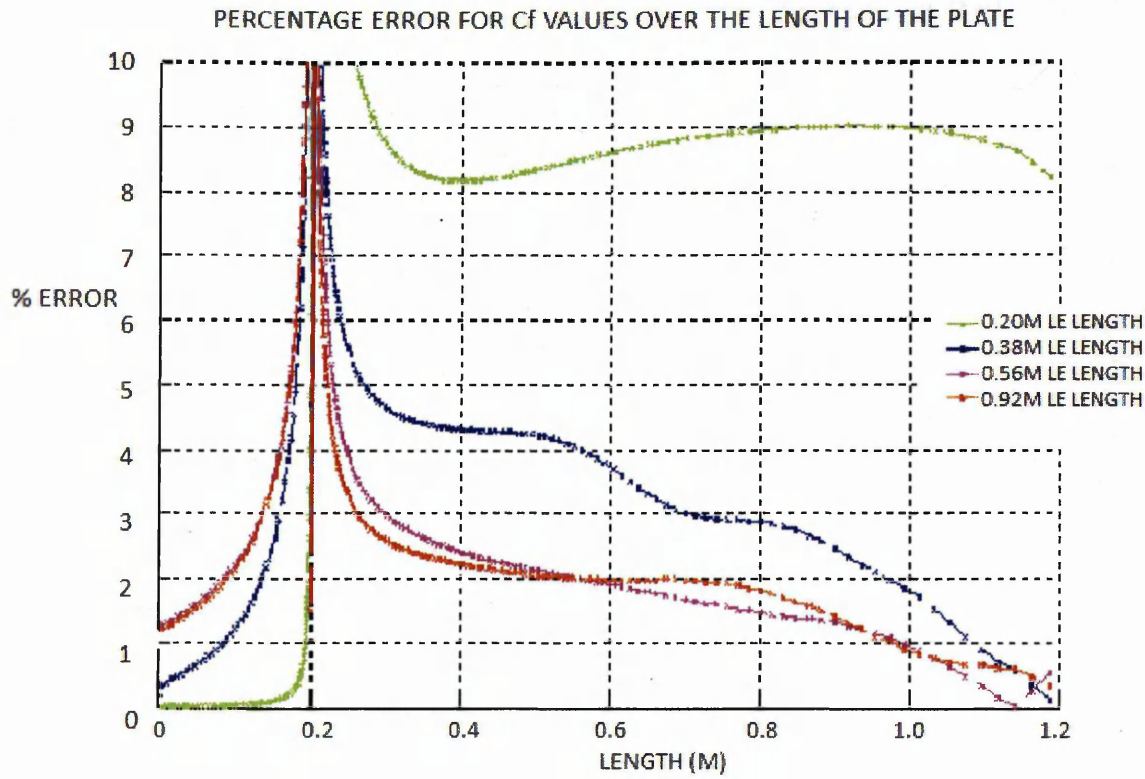

Figure 7-17–Percentage error for the C_f for different grids where the distance from the inlet to the leading edge is given by the legend.

As the spatial length between the leading edge (LE) and the inlet increases from 0.2m to 1.7m, the final velocity field, approaches the analytical Blasius solution as seen in equation (7.26). Where a minimum average error of 1.88% is obtained with the 0.92m LE length. The boundary placement plays a fundamental role in obtaining an accurate CFD solution. Futhermore as the length between the leading edge and the inlet increases from 1.7m to 2.0m the CBS solution does not improve its accuracy.

Since the average percentage error (1.88%) is still above the acceptable level of 1% further work was carried out on driving down the error namely assigning the top boundary, free stream values (zero mass transfer across the top boundary).

In Figure 7-18 below, the top boundary value is fixed to the free stream v velocity (zero mass transfer). By fixing the top boundary to the free-stream values we can now infer the effect that this has on the v-velocity field at the downstream boundary.

Table 7-6- Grid and flow parameters for the next set of simulation results.

1m Flat Plate	u_∞[m/s]	ρ_∞[kg/m^3]	μ_∞[kg/(ms)]	Re [-]	LE[m]	H[m]	Top Boundary
	10.208	1.225	1.789×10^{3}	7.0×10^{3}	1.5	0.5	Fixed Free-stream

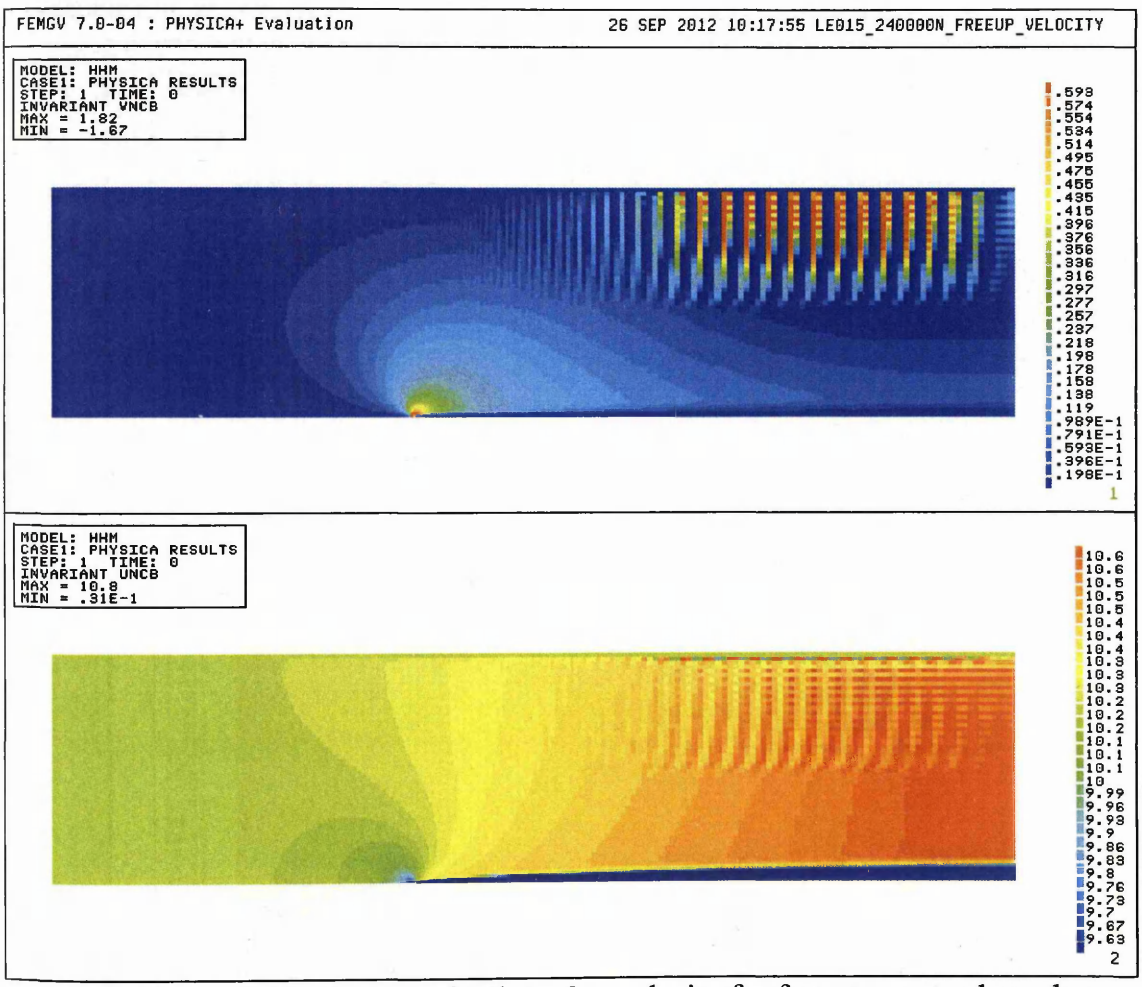

Figure 7-18: Contours for the u & v velocity for free-stream top boundary.

UNCB in the scalar contours shown in Figure 7-18 denotes the velocity in the x direction and VNCB denotes the velocity component in the y direction. It can be inferred from the above figures, that the top boundary (y=0.5m) is not far enough from the surface of the plate to successfully apply the zero mass transfer condition across the top boundary.

The v velocity plot shows unrealistic oscillations. Figure 7-18 displays beyond doubt that applying the free stream velocity values produces decoupling even though the solution converges to errors of the region of 10^{-3}. Meaning the top boundary is either too close to the boundary layer or that another boundary condition needs to be applied to the top boundary instead.

Table 7-7- Grid and flow parameters for the next set of simulation results.

1m Flat Plate	u_∞[m/s]	ρ_∞[kg/m^3]	μ_∞[kg/(ms)]	Re [-]	LE[m]	H[m]	Top Boundary
	10.208	1.225	1.789×10^{3}	7.0×10^{3}	1.5	0.5	2nd Interpolation

In the figure below the top boundary value is allowed to float with the interior values. This was done as a control to demonstrate which is the most appropriate or consistent boundary condition for the top boundary to obtain an accurate CFD solution. Simulations were carried out where the top boundary of the grid had both 1st ordered interpolation and 2nd ordered interpolations applied. No noticeable difference was observed.

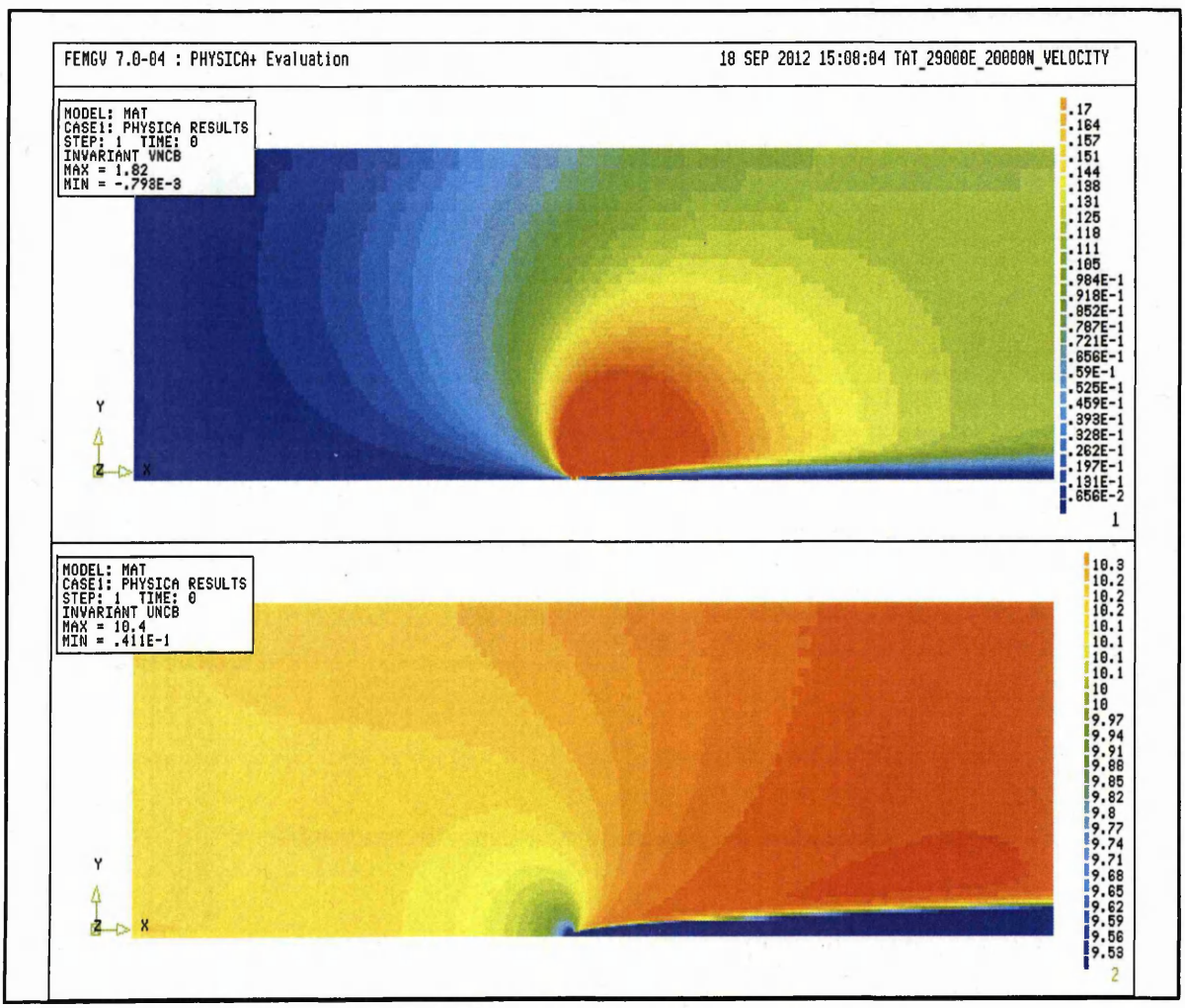

Figure 7-19: Contours for the u & v velocity for case 2.

Figure 7-19 shows the result of the 2nd ordered interpolation i.e. $\phi_{I,J} = (2\phi_{I,J-1}) - \phi_{I,J-2}$ boundary condition. From Figure 7-19 it was inferred that the top boundary is still not far enough from the flat plate (viscous region) to apply the interpolation condition. Therefore the next simulations will be on grids that have been constructed specifically with an enlarged domain in the y direction.

Domain Enlargement in Y direction

In a final attempt to reduce the analytical error to below 1% from 1.88% the next strategy was to experiment further with the placement of the domain's boundary. For the next simulations the height of the domain was fixed and the length upstream of the leading edge to the inlet boundary, otherwise known as the LE length, was varied.

Table 7-8- Grid and flow parameters for the enlarged domain.

1m Flat Plate	u_∞[m/s]	ρ_∞[kg/m^3]	μ_∞[kg/(ms)]	Re [-]	LE[m]	H[m]	Top Boundary
	10.208	1.225	1.789×10^{3}	7.0×10^{3}	2.0	8.0	Fixed Free-stream

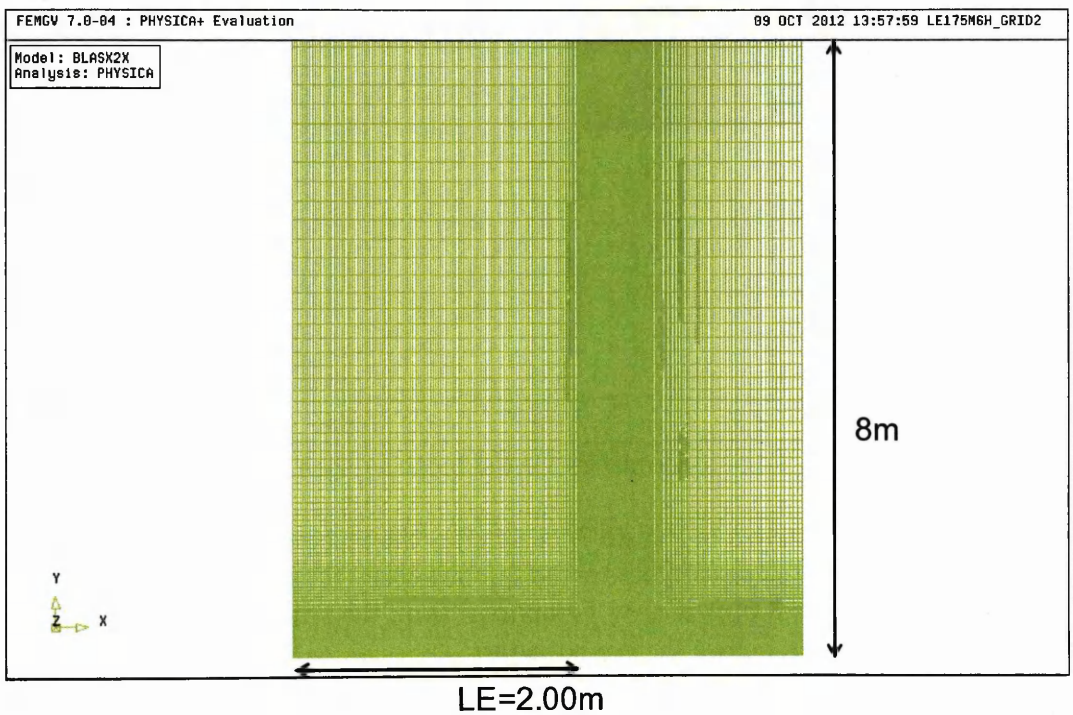

Figure 7-20:Mesh with domain enlarged in the Y direction

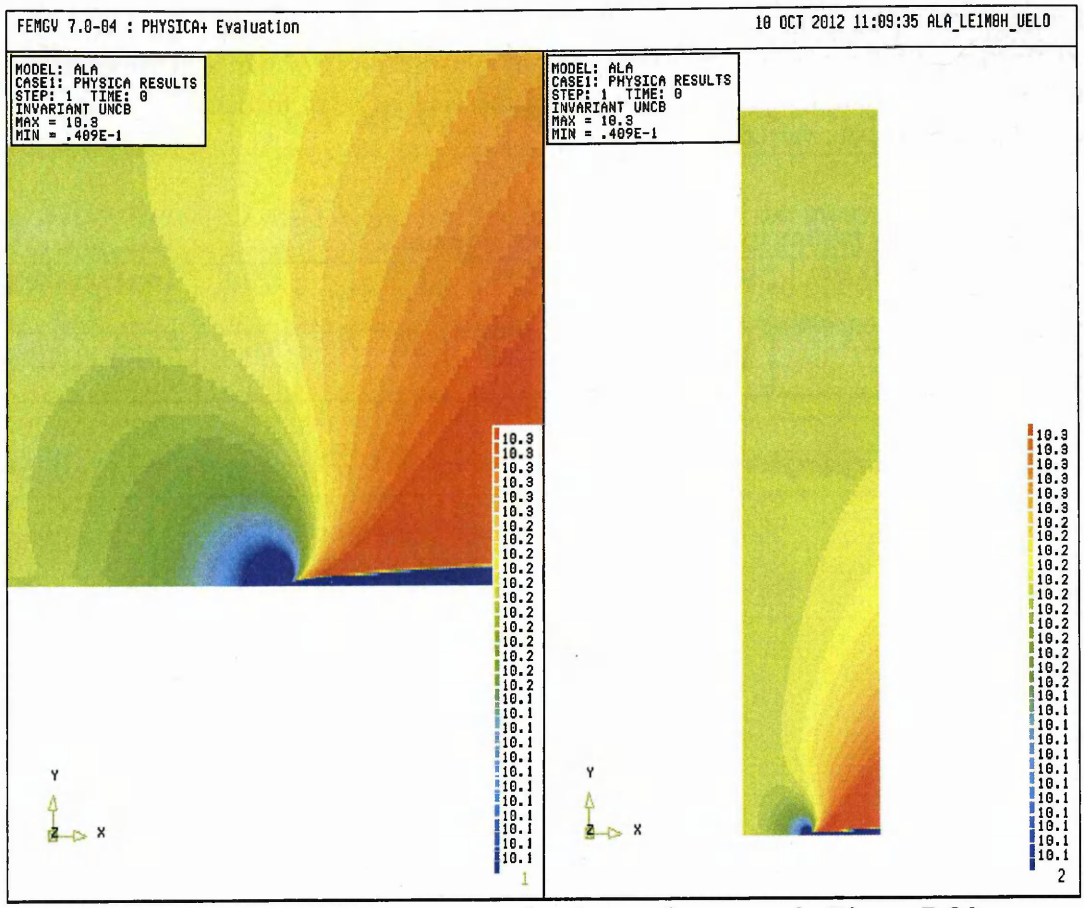

Figure 7-21: Velocity contours for the mesh as seen in Figure 7-20.

UNCB in the scalar contours shown in Figure 7-21 denotes the velocity in the x direction. Because all contours occur or interactions occur well below the top boundary it can argued from the above Figure 7-21 that the top boundary (Y=8.0m) is now far enough from the surface of the plate to successfully apply the free stream conditions across the top boundary.

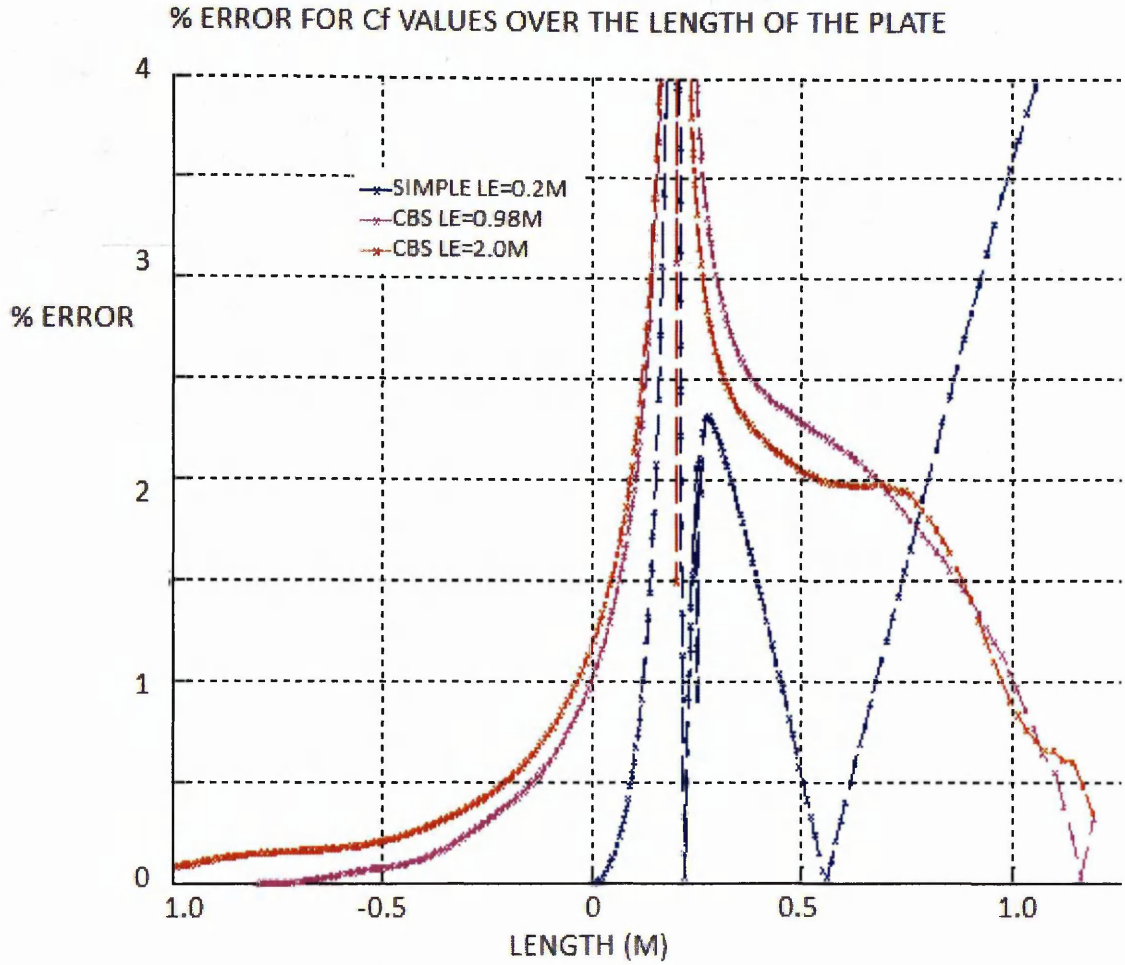

Figure 7-22– Percentage error for the coefficient of friction for different grids where the distance from the inlet to the leading edge is changing (see legend) & the height is fixed to 8m.

In Figure 7-22 the two meshes mentioned have their absolute C_f error's plotted together, red and pink. Where the pink line corresponds to the 0.98m leading edge (LE) meshed domain and the red line to the 2m LE length meshed domain as seen in Figure 7-20. According to Hirsch, [175], as the length between the leading edge and the inlet increases from 1m to 2m the CFD solver should improve its accuracy relative to the Blasius solution. Frustratingly the result is that the average error value of 2.05%.

This is as far as the boundary placement study was taken because no more gain in accuracy is produced when increasing the domain size. Although the 1% tolerance was not satisfied, the Artificial Compressibility CBS FV algorithm's performance needs to put into context. The final planned problem to be modelled is a compressible Supersonic flow problem not an incompressible Subsonic problem. Incompressible problems are solved with the AC CBS FV algorithm whereas compressible problems are solved using the CBS FV algorithm, which does not utilize the relationships seen in Section 7.3.2. The density based CBS algorithm is primarily a compressible fluid solver designed to handle discontinuities with extensions to porous media [136].

7.6 Concluding Remarks

The candidate CFD code should allow the possibility of keeping a laminar Subsonic flow in the porous media as mentioned by [169], [177] and [178]. Therefore 2D simulations of viscous Subsonic flow over a flat plate have been performed to verify that the CBS scheme can correctly reproduce a laminar boundary layer. Only steady state solutions were sought throughout the incompressible study because of the dearth of theoretical solutions to transient incompressible fluid problems. Target errors of 1% between the analytical solution and the AC CBS algorithms results were expected by industrial sponsors. Only computational domains which were significantly larger than the domain suggested by ESA, gave satisfactory results. As highlighted by Hirsch, [175], and verified above, the flow field boundaries' proximity to the region of interest needs to be investigated prior to solving each viscous Subsonic problem.

7.6.1 Summary of the AC CBS algorithm for incompressible flow

Relative to the analytical solution for viscous incompressible Subsonic flow the accuracy with respect to the analytical solution is slightly above 1%. The accuracy of the results were extremely dependent on specific features of the domain such as the resolution at the leading edge and, the aspect ratios of elements at the trailing edge and inlet. In addition so that the formation of the boundary layer can be accurately captured, a leading edge element length, Δx, should be of the oreder of $2.3\times10^{-6}m$. And all aspect ratios should be less than 200 when possible.

In addition to these specifications, a check on the dimensions in the original pseudo time step by Massarotti et al, [132] , and the artificial wave speed calculation showed that it was not dimensionally consistent, which was believed to have caused instability for early simulations of the 1cm flat plate. Therefore equation (7.17) was replaced with equation (7.10) with comparative success.

For a free stream Reynolds number of $7x10^5$ initial simulations, for a 1m plate, using the CBS algorithm, were unstable and diverged. A number of strategies were employed to stabilize the algorithm however none were ultimately effective enough at obtaining stable results for such high Reynolds numbers. Hence a turbulence model will be required to compute high Reynolds number flows but this is beyond the scope of the laminar flow simulations analysed here.

In order to clarify that the algorithm's inability to stabilize the current problem was due to high Reynolds number, we created a 1m copy of the 19800 mesh from the 1cm case as seen in Figure 7-4. In order to get identical Reynolds numbers for the 0.01m and 1m plate a larger kinematic viscosity was substituted in place of the viscosity for air. This unsurprisingly resulted in stable solutions however not the accuracy that the industrial supervisors permit. Then a number of strategies were employed to enhance the accuracy of solutions however none were as effective as moving the boundaries away from the leading edge. As computed by equation (7.27) the most accurate result was seen in Figure 7-17, with a LE length of 1.7m, where the Blasius and AC CBS differed by 1.88%.

It is the researcher's view that errors between the AC CBS simulations and Blasius's solution arise because of limitations, in the founding assumptions used in the Blasius approximation. The Navier-Stokes Equations reduce to the following equations for the limiting case of incompressible Subsonic flow at a large distance from the leading edge:

$$\frac{\partial(\rho v)}{\partial y}+\frac{\partial(\rho u)}{\partial x}=0 \tag{7.29}$$

$$\frac{\partial(\rho uv)}{\partial y}+\frac{\partial(\rho uu)}{\partial x}=\mu\frac{\partial^2 u}{\partial y^2} \tag{7.30}$$

The limitations of the Blasius Prediction include the fact that there are no pressure terms in equations (7.29)-(7.30). The assumptions may be valid at suitably large x distances from the leading edge but the assumption breaks down in proximitry of the leading edge location.

As we have seen in this chapter the pressure based algorithm, the AC CBS is stable at low Reynolds numbers, but it is not permitted by ESTEC because the errors are above the minimum it requires for a CFD solution. However the density based CBS scheme employed for the inviscid compressible Supersonic flows, for 1-D and 2-D inviscid problems, were reliable enough therefore it will be employed with caution for the final application of computing Supersonic high temperature components utilizing transpiration cooling.

8 NAVIER-STOKES SOLUTION FOR 2-D COMPRESSIBLE SUPERSONIC FLOW

8.1 Introduction

This chapter evaluates the reliability of the resulting solutions for the Navier-Stokes equations when using the finite volume (FV) CBS technique for the flow over a Supersonic flat plate. As already seen, impressive results with respect to accuracy and reliability, for the Euler equations, involving 1-D and 2-D geometries have been made in this thesis. In addition, stable and realistic solutions in terms of absolute errors to the analytical solution for incompressible boundary layers<10%, even when accuracy issues are fed in from ill-posed boundary conditions, have been obtained. In particular, the CFD results generated are physically realistic.

Due to the dearth of credible analytical and experimental results for Hypersonic viscous problems as mentioned by Hirschel & Weiland, [5], there is a limited number of CFD studies targeted at Hypersonic benchmarks. The major challenge according to Lyra, [7], for building a Hypersonic simulation tool is the development of a robust Supersonic flow solver, which can be applied to unstructured as well as structured grids. This chapter seeks to address the problem of developing a stable and reliable numerical scheme in order to capture the pertinent physics for compressible laminar flows only. Therefore studies into grid independence, boundary layer separation and compressible turbulence have not been investigated in this chapter.

Viscous flow over a Supersonic flat plate was benchmarked against the crude theoretical approximation, the Supersonic Temperature reference solution presented by Driest, [179]. It is crude, because it makes the simplifying assumption that pressure remains constant through the Supersonic compressible boundary layer [179]. In the sense that only a very thin region close to the solid wall is viscous, the benchmark problem in this chapter is assumed to be inviscid dominated, i.e. governed by the inviscid character of the Navier-Stokes equations. The numerical procedure adopted for the compressible Navier-Stokes simulations are built using the scheme developed in the 2D inviscid chapter with the inclusion of additional viscous terms in the momentum and enthalpy equations. Those viscous terms in the Navier-Stokes equations are numerically discretised in the same manner as the convection terms, by central differencing.

8.2 Supersonic Benchmark Case

As the Reynolds number in the next example is $< 10^5$ and because the Knudsen number $Kn \ll 1$ for the maximum speed, the Mach 4 case, the continuum model is assumed to valid and is applied with success.

In this chapter we extend the impressive Compressible Euler FV CBS solver that captured inviscid flow over a wedge in Chapter 6 to the problem of viscous flow over a Supersonic Flat Plate. Modelling the hyperbolic character of Supersonic inviscid flow is made possible by utilizing some form of numerical dissipation that allows the scheme to stabilize the non-linearities. However, the inherent numerical dissipation of viscous flows means that the numerical dissipation for the solution of the Supersonic flat plate, could possibly be overestimated, especially in proximity of the boundary layer as mentioned by Lyra, [7].

The following viscous benchmark problems all have the same plate length of 10 micrometers to restrict the Reynolds number but differ in terms of the free-stream velocity. This was done to test the CBS algorithm's Mach speed range. In addition, to the range of speed investigated, two opposing thermal boundary conditions at the flat wall, are also studied. These two cases are.

1. The constant isothermal cold wall case.
2. The adiabatic boundary condition.

The constant cold wall case represents the simplest and most stable boundary condition of the two. The adiabatic wall condition represents the next step for a more computationally involved and unstable condition, since the wall has to come into thermal equilibrium with the adjacent fluid layer.

This point is already mentioned but should be repeated to fully bring home the point that, the next benchmark problem is a 10 μm flat plate. It was scrutinized because it ensures small free stream Reynolds numbers, which ultimately means that the code can compute high speed problems without transition to turbulence, which otherwise cause solution instability - a major challenge. In addition smaller running times are experienced and hence more efficient data harvesting.

Table 8-1- Benchmark cases computed and now displayed in this Chapter: Navier-Stoke solution for 2-D compressible flow.

Benchmark	Mach Speed	Length[m]	Cold Wall/Adiabatic Boundary Condition
Case 1	2	$1x10^{-5}$	Cold Wall
Case 2	1.5	$1x10^{-5}$	Cold Wall
Case 3	4	$1x10^{-5}$	Cold Wall
Case 4	4	$1x10^{-5}$	Adiabatic

8.2.1 Boundary Conditions

The 10 μm flat plate was simulated due to its stability, and it makes a good introductory problem that highlights the issues for a stable solution to the more difficult problems that have much higher Reynolds numbers. The successful modeling of the Supersonic boundary layer over a flat plate is a

substantial and fundamental benchmark for any CFD code, considering that the reference temperature method is a simple and credible comparison for a compressible flow over a flat plate.

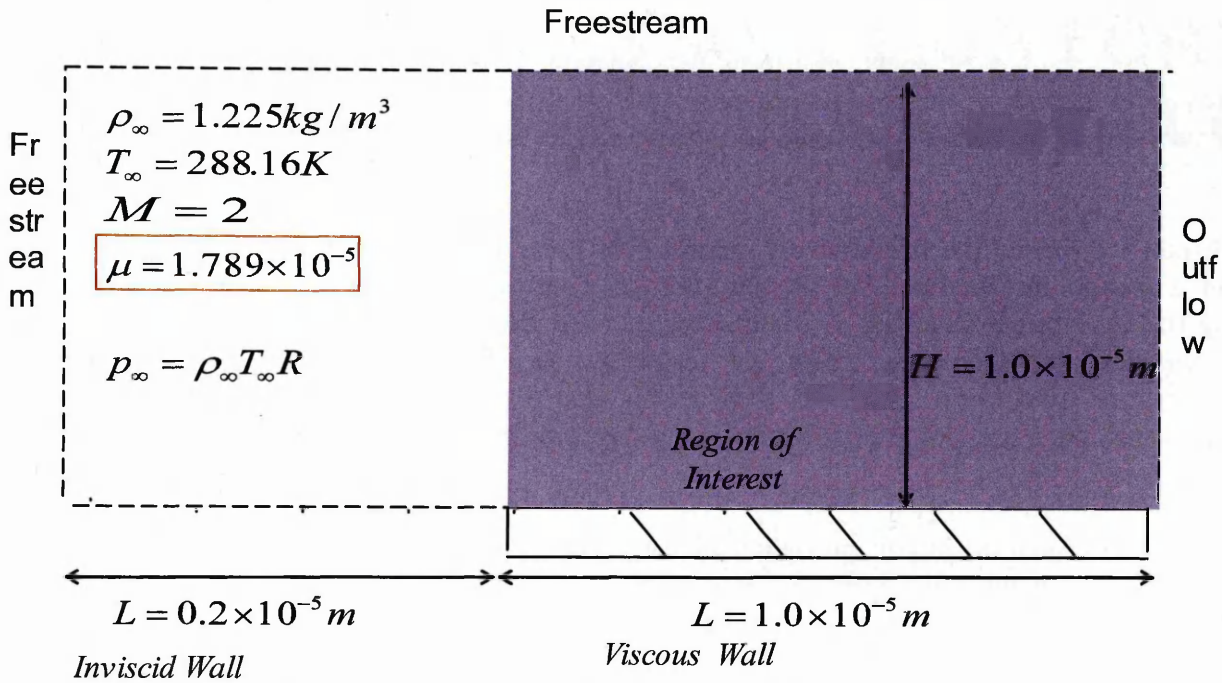

Figure 8-1: Specifications for the domain to the Supersonic 10μm plate as seen in [15].

A schematic of the domain is shown in Figure 8-1. This problem represents an external flow problem providing the boundaries are far enough from the region of the physical interactions. The initial domain is 1.2 x 10^{-5} m long spanning a flat plate of 1.0 x 10^{-5} m and it extends 0.2x10^{-5}m upstream of the leading edge. The height of the domain was initially set as 1.0x10^{-5}m. Free-stream values are stipulated for all cells at the west and the top boundary. The inlet boundary are open outflow boundaries and were extrapolated using the 2nd ordered formulation, which importantly gave rise to stable results.

8.2.2 Wall Coefficients

According to Lyra, [7] as seen in Section 7.4.2 the distribution of the coefficient of pressure, heat transfer and skin friction are required during the stage of validation of the Navier-Stokes solution algorithm or during the use of the algorithm for aerodynamic design. To compare the steady state CFD results with the experimental and numerical data the pressure heat transfer and skin friction coefficients C_p, C_H and C_f are defined by (7.22), (7.23) and (7.24) :

8.2.3 Analytical Solution

The reference temperature method is taken from Schlichting, [155], and is an approximate engineering method for predicting skin friction and heat transfer for laminar compressible flow over a flat plate. The idea was first proposed by Rubesin and Johnson [180], and was modified by Eckert, [181], to include a reference enthalpy. The reference temperature method is an approximate solution, because in most practical cases the assumptions are crude simplifications of the actual reality. Assumptions, such as the constant pressure through the boundary layer [155], therefore this point should be kept in mind when evaluating the accuracy of the final converged CBS solution. However, due to its simplicity, along with reasonable accuracy, it is useful for CFD design purposes, as it gives a crude ball park answer for the skin friction and the heat coefficient. It is founded in the idea of utilizing formulas akin to the Blasius solution for incompressible boundary layers seen in [154] and Chapter 7, but with amended temperature, density and dynamic viscosity values. Futhermore the

physical properties are numerically approximated at the temperatures inside the compressible boundary layer and adjacent to the wall surface. For laminar compressible flow the temperature is:

$$T^* = T_\infty \left(0.5 + 0.39 M_\infty^2 + 0.5 \frac{T_{AW}}{T_\infty} \right) \tag{1.1}$$

Where the subscript AW means adiabatic wall so T_{AW} is the adiabatic wall temperature
And M_∞ is the free-stream Mach number .

$$C_f^* = \frac{0.664}{\sqrt{\mathrm{Re}_x^*}} = \frac{\tau_w}{1/2 \rho^* u_\infty^2} \tag{1.2}$$

Where ρ^* is the reference density calculated from-

$$\rho^* = \frac{P_\infty R}{T^*} \tag{1.3}$$

And $\mathrm{Re}_x^* = \dfrac{\rho^* u_\infty L}{\mu^*}$

And the heat coefficient is calculated from.

$$C_H^* = \frac{0.332}{\sqrt{\mathrm{Re}_x^*}} (\mathrm{Pr}^*)^{(-2/3)} = \frac{q_w}{\rho^* u_\infty C_p (T_{AW} - T_w)} \tag{1.4}$$

Where the Reference Prandtl number for a compressible boundary layer is-

$$\mathrm{Pr}^* = \frac{\mu^* C_p}{k} \tag{1.5}$$

Where k is the thermal conductivity of air at a reference value of T_∞.
And μ is calculated from Sutherlands law at T*.
For the compressible flat plate case from Driest, [179].

$$\xi = \rho_\infty \mu_\infty u_\infty x \tag{1.6}$$

$$\eta = \frac{u_\infty}{\sqrt{2\xi}} \int_0^y \rho dy \tag{1.7}$$

When Pr=1 : i.e the ratio of the gases' kinematic viscosity to thermal diffusivity is unity therefore-

$$h_{AW} = C_P T_{AW} = h_\infty + \frac{u_\infty^2}{2} \tag{1.8}$$

When Pr<1 therefore

$$h_{AW} = h_\infty + r \frac{u_\infty^2}{2} \tag{1.9}$$

Where r is the recovery factor given by $r = \sqrt{\mathrm{Pr}}$

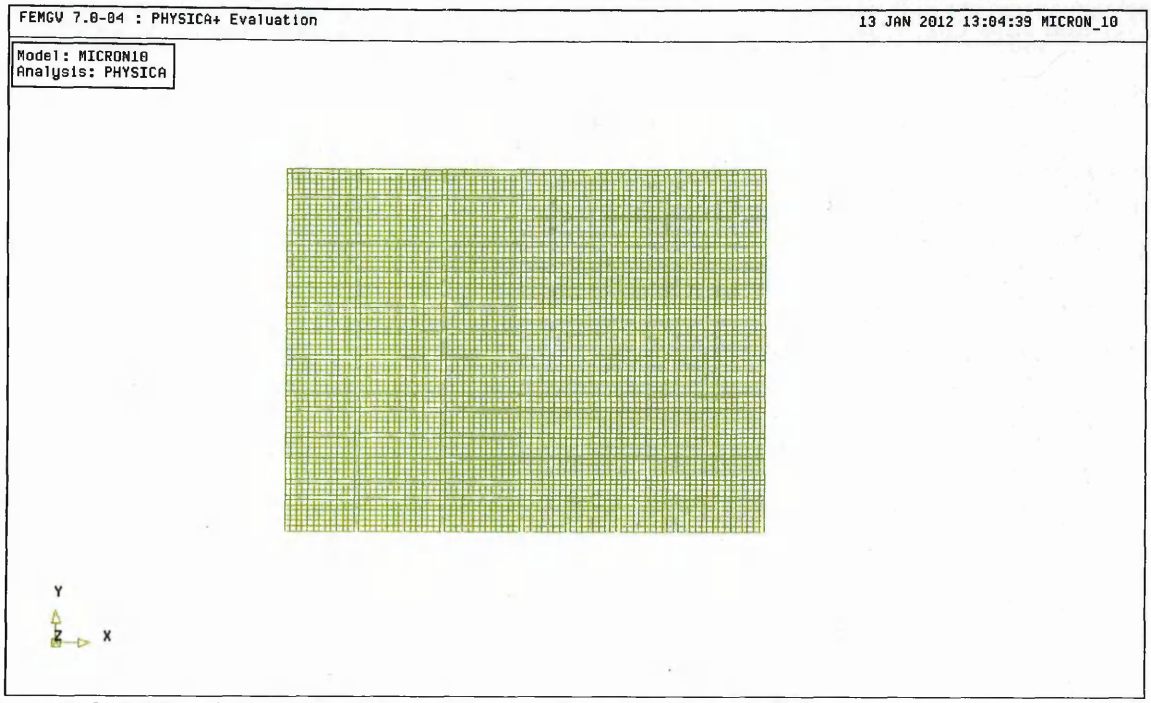

Figure 8-2: 9880 element mesh used to model the 10 micron flat plate Mach 2 case.

The following table contains the flow parameters for the next set of simulations. Notice that the Reynolds number is well within the laminar regime, and this is because we are primarily concerned with the capability of the algorithm to compute compressible laminar boundary layers. Where stability requirements and accuracy of the results are investigated. The small grid sizes also means convergence is achieved in a relatively small number of iterations.

Table 8-2- Grid and flow parameters for the next set of simulation results.

Length [m]	M_∞[-]	ρ_∞[kg/m^3]	μ_∞[kg/(ms)]	Re [-]	Nx	Ny	Nt
10^{-5}	2	1.225	1.789×10^{-5}	$4.60\text{x}10^2$	100	98	9800
10^{-5}	1.5	1.225	1.789×10^{-5}	$3.45\ \text{x}10^2$	100	98	9800
10^{-5}	4	1.225	1.789×10^{-5}	$9.20\text{x}10^2$	100	98	9800

8.4 Sequential FV CBS Procedure

The central differencing CBS technique was embedded within the PHYSICA code framework and simulations were then run to solve the Navier-Stokes system of equations. The PHYSICA environment allows the implementation of the dissipation terms into the enthalpy equation for this problem. The mesh for the domain is given before each solution. The sequential computational procedure for the CBS finite volume algorithm can be done in a number of ways, but for this research, the following general procedure was pursued after numerical experimentation. Each step described below is applied to all the cells in a sweep of the grid. After this sweep the boundary conditions as seen in step 7 are computed. Then the sequential computational procedure, otherwise known as an iteration is either exited or repeated after calculating the residual error and comparing to the agreed tolerance.

1. The CBS scheme incorporates local pseudo time stepping. The pseudo time step is given by the following equation: where C is the courant number and depending on the problem is usually < 0.5.

$$\Delta t_{CV}^{n} = C\frac{h_{CV}}{c_{CV}^{n} + \left|\mathbf{u}_{CV}^{n}\right|} \tag{1.10}$$

2. The numerical dissipation is calculated from-

$$\left(S_1\right)_{CV}^{n} = \begin{bmatrix} \dfrac{C_x\left|\sum_{f=1,TOTFIC} n_x \dfrac{\partial P}{\partial \bar{x}_f}\right|}{\sum_{f=1,TOTFIC}\left|n_x\right|\left(P_{adj}+P_{CV}\right)}\left(\sum_{f=1,TOTFIC} n_x \dfrac{\partial\{\rho\}}{\partial \bar{x}_f}\right)_{CV} + \\ \dfrac{C_y\left|\sum_{f=1,TOTFIC} n_y \dfrac{\partial P}{\partial \bar{y}_f}\right|}{\sum_{f=1,TOTFIC}\left|n_y\right|\left(P_{adj}+P_{CV}\right)}\left(\sum_{f=1,TOTFIC} n_y \dfrac{\partial\{\rho\}}{\partial \bar{y}_f}\right)_{CV} \end{bmatrix}$$

3. Compute the Intermediate Momentum field

$$\rho u_j^{*} = \rho u_j^{n} - \frac{\Delta t}{\Delta V}\left(\begin{array}{l} \sum_{f=1,TOTFIC}\left(\left(\rho u_i u_j\right)\bullet n_j A\right)_f - \sum_{f=1,TOTFIC}\left(\tau_{ji}\bullet n_j A\right)_f \\ +\dfrac{\Delta t}{2}u_k \sum_{f=1,TOTFIC}\left(div\left(\rho u_i u_j\right)\bullet n_j A\right)_f \end{array}\right)^{n} + \left(S_1^{n}\right)_{CV} \tag{1.11}$$

where $\sum_{f=1,TOTFIC}$ denotes a summation over cell faces

4. Compute the corrected momentum field-

$$\rho u_i^{n+1} = \rho u_i^{*} - \frac{\Delta t}{\Delta V}\left(\sum_{f=1,TOTFIC} P_f \bullet n_i A_f - \frac{\Delta t}{2}u_k \sum_{f=1,TOTFIC}\frac{\partial P}{\partial x_i}\bullet n_i A_f\right) \tag{1.12}$$

5. The Continuity Equation is solved using the momentum values from the n+1 "time" level-

$$\rho_{CV}^{n+1} = \rho_{CV}^{n} - \frac{\Delta t}{\Delta V}\left(\sum_{f=1,\mathit{TOTFIC}} \left(\rho u_i \bullet n_i A\right)_f \right)^{n+1} + \left(S_2^n\right)_{CV} \tag{1.13}$$

6. Compute the specific Enthalpy field

$$(\rho E)_{CV}^{n+1} = (\rho E)_{CV}^{n} + \frac{\Delta t}{\Delta V}\left(\begin{array}{l} - \sum_{f=1,\mathit{TOTFIC}} \left((\rho E u_j) \bullet n_j A \right)_f + \sum_{f=1,\mathit{TOTFIC}} \left(k \left(\frac{\partial T}{\partial x_j} \right) \bullet n_j A \right)_f \\ - \sum_{f=1,\mathit{TOTFIC}} \left((P u_j) \bullet n_j A \right)_f + \sum_{f=1,\mathit{TOTFIC}} \left(\frac{\partial \left(u_j \tau_{ji}\right)}{\partial x_j} \bullet n_j A \right)_f \\ + \frac{\Delta t}{2} u_k \left(\sum_{f=1,\mathit{TOTFIC}} \left(\frac{\partial \left(\rho E u_j\right)}{\partial x_j} \bullet n_j A \right)_f + \sum_{f=1,\mathit{TOTFIC}} \left(\frac{\partial \left(u_j P\right)}{\partial x_j} \bullet n_j A \right)_f \right) \end{array} \right)^{n} + \left(S_3^n\right)_{CV} \tag{1.14}$$

Temperature is inferred from Enthalpy: To close the equation set for the Navier Stokes equations the Ideal Gas Law, Sutherlands Law and the Prandtl Law. The Prandtl number, which is assumed constant for ideal gases at moderate temperature [82] where Pr is 0.74.

Compute the outlet values using linear extrapolation.

$$\frac{\partial \rho}{\partial x}^{n+1}_{N_{\max},J} = \frac{\partial \rho}{\partial x}^{n+1}_{N_{\max}-1,J}$$

$$\frac{\partial \rho u}{\partial x}^{n+1}_{N_{\max},J} = \frac{\partial \rho u}{\partial x}^{n+1}_{N_{\max}-1,J}$$

$$\frac{\partial \rho E}{\partial x}^{n+1}_{N_{\max},J} = \frac{\partial \rho E}{\partial x}^{n+1}_{N_{\max}-1,J}$$

Which for a orthogonal structured grid becomes:

$$(\rho)_{N_{\max},J}^{n+1} = 2(\rho)_{N_{\max}-1,J}^{n+1} - (\rho)_{N_{\max}-2,J}^{n+1}$$

$$(\rho u)_{N_{\max},J}^{n+1} = 2(\rho u)_{N_{\max}-1,J}^{n+1} - (\rho u)_{N_{\max}-2,J}^{n+1}$$

$$(\rho E)_{N_{\max},J}^{n+1} = 2(\rho E)_{N_{\max}-1,J}^{n+1} - (\rho E)_{N_{\max}-2,J}^{n+1}$$

Where N_{max} is the cell column adjacent to the outlet boundary and at the inlet and fix the velocity, density and temperature.

$$M_\infty = \{1.5, 2, 4\}$$

$$\rho_\infty = 1.2 \frac{kg}{m^3}$$

$$T_\infty = 300K$$

7. Check convergence to steady state values by sensing whether the relative error is less than the agreed tolerance of 10^{-5} or alternatively the number of iteration/sweeps is below the maximum iteration/sweeps, I_{Max}, stipulated by the

user, this value was set initially to I_{Max} =95,000 iterations.

$$\varepsilon_{Rel}^{n} = \frac{1}{NUMELE}\sqrt{\left[\frac{\sum_{CV=1}^{NUMELE}\left(\frac{\left|\rho_{CV}^{n+1}-\rho_{CV}^{n}\right|}{\Delta t_{CV}/(L/u_{\infty})}\right)^{2}}{\sum_{CV=1}^{NUMELE}\left(\rho_{CV}^{n+1}\right)^{2}}\right]} \qquad (1.15)$$

8. If convergence has been achieved exit the procedure and display results otherwise re-start the computational sweep by going back to step 1.

General Remarks

1. Solid wall boundary faces

At the flat plate, all the velocity components are set to zero. In addition, constant cold wall or adiabatic wall boundary conditions can be set. For the cold wall temperature plate at the face straddling the wall, the temperature is set to the prescribed value - to the free-stream values. However at an adiabatic wall, the condition of zero temperature gradient is weakly imposed through the discretisation of the energy equation.

2. Initial conditions

The initial conditions for this problem; all quantities were set to their respective free-stream values and then computations were conducted with the biggest gradients occurring in the region of interest.

The 1st case chosen consists of a free-stream Mach speed of 2, a density of 1.225 kg/m^3 and a temperature of 288.16K. The Reynolds number based on the size of the plate is 460. The local Prandtl number is assumed to be constant and equal to 0.74. The viscosity is a function of temperature and is calculated at the solution points using Sutherland law.

8.3 Simulation Results

A validation test for any algorithm for Supersonic flow is the comparison of the compressible laminar boundary layer development on a flat plate with the predicted solution from [155]. This comparison will hopefully indicate if there is excessive artificial dissipation in the numerical scheme.

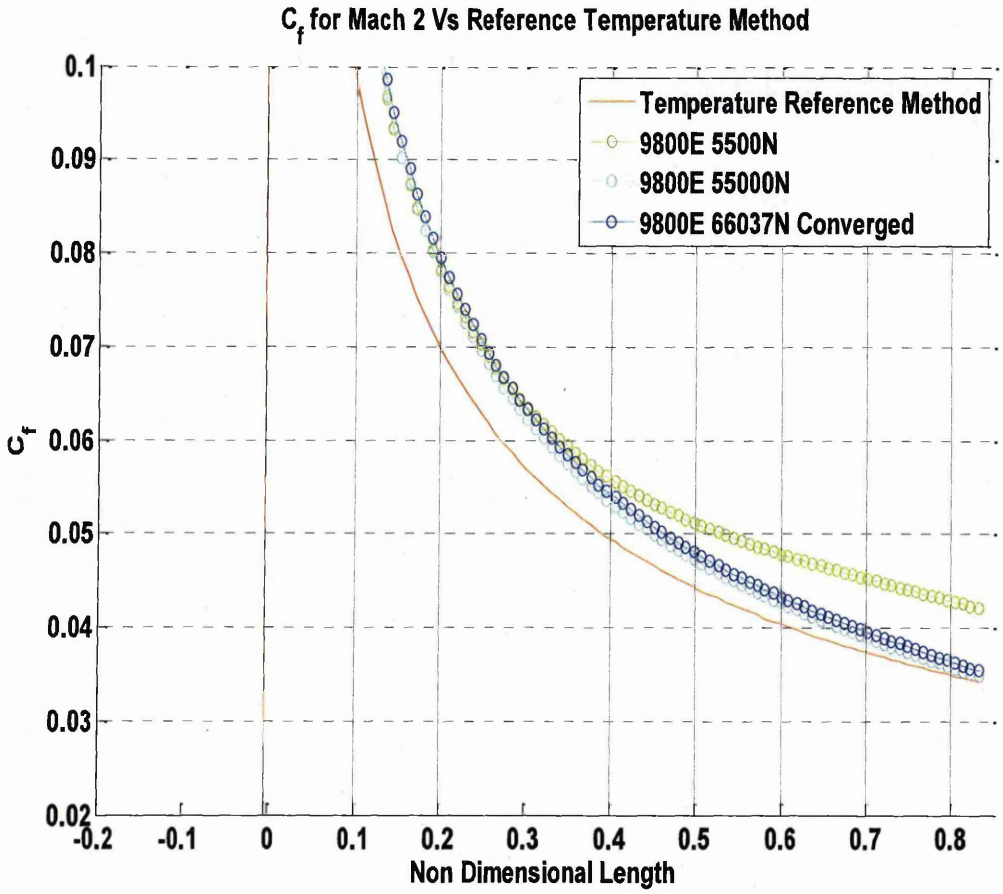

Figure 8-3- C^*_f values along the surface of the plate for the 9880 element grid.

The predicted skin friction coefficient from the CBS algorithm at different stages in the computations is compared with the approximate solution given by the temperature reference approximation solution (red line) in Figure 8-3. The three stages are 5,500 iterations (green circles), 55,000 iterations (light blue circles) and convergence at approximately 66,037N iterations (blue circles). Apart from the computed C_f value at the leading edge the final steady state shows good agreement with the temperature reference method.

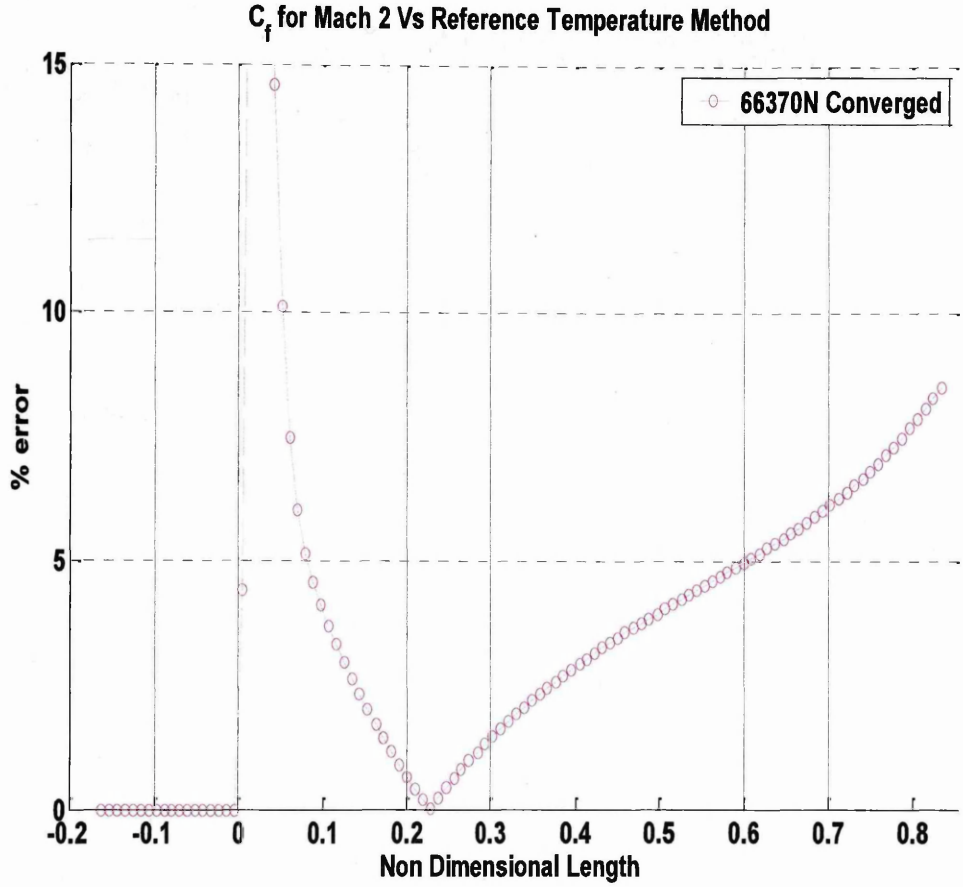

Figure 8-4– Percentage error for the C_f values along the surface of the plate,

The CBS algorithm calculated the C_f values along the surface of the plate for the 9880 element grid seen in Figure 8-4 which resolves the leading edge length 1.11×10^{7}m. The percentage error between the skin friction coefficient and the predicted value from the temperature reference method is approximately 6.8%.

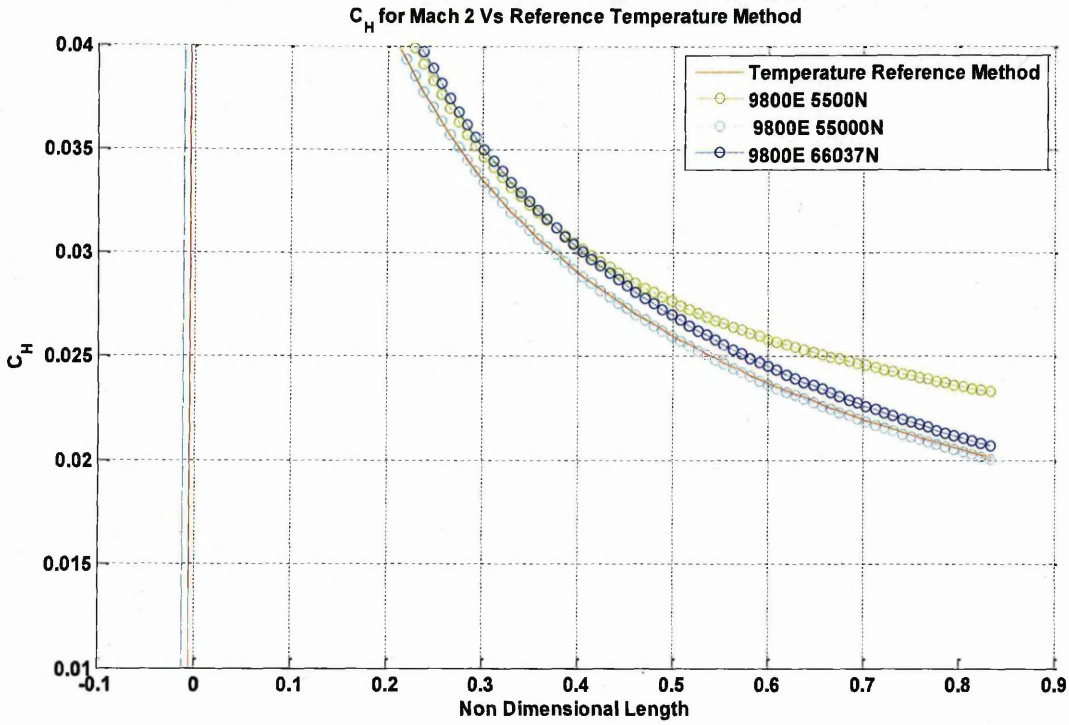

Figure 8-5–C^*_H values along the surface of the plate for the 9880 element grid which resolves the leading edge length 1.11×10^{-7} m.

Because it would be informative to see how the solution progresses relative to the analytical solution, Figure 8-5 displays the coefficient of heat as computed for the CBS algorithm for 3 different stages of the solution. The coefficient of heat is compared with the Temperature reference approximation (red line).

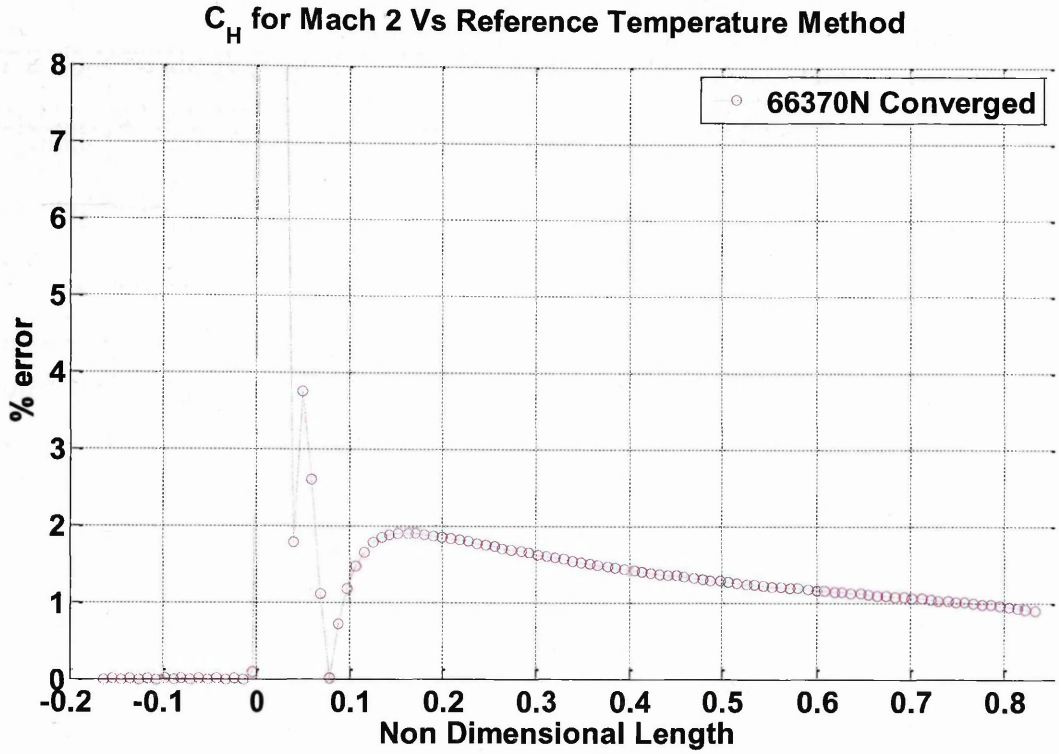

Figure 8-6–Percentage error for the C^*_H values along the surface of the plate for the 9880 element grid which resolves the leading edge length 1.11×10^{-7} m.

To mathematically evaluate the CBS algorithm we use the percentage error parameter defined below.

$$\varepsilon_{abs,err} = \frac{1}{ELEXX} \sum_{N=1,ELEXX} \left(\left(\frac{C_{H,TRM} - C_{H,CBS}}{C_{H,TRM}} \right) \times 100 \right) \tag{1.16}$$

$$\varepsilon_{abs,err} = 2.04\%$$

The CBS results for the 9800 grid, can be summarized for Supersonic compressible flow over a 10 μm flat plate as; The percentage error for C_H is below 2% as seen in Figure 8-6.

Care however needs to be taken in relying too heavily on the temperature reference method, which is an approximate solution. Fundamentally, it cannot be assumed to be absolutely accurate, because its founding assumptions are not consistent with the full reality of compressible high speed flows [155].

The CBS algorithm was applied to two more free-stream Mach numbers to gauge its versatility and stability at modelling the full Supersonic regime. The following plot presents the converged temperature field at the trailing edge ($X=1.2 \times 10^{-5}$ m) through the entire height of the outlet.

Table 8-3- Grid and Flow parameters for the higher speed simulation.

	Boundary Condition	Length [m]	M_∞[-]	ρ_∞[kg/m^3]	μ_∞[kg/(ms)]	Nx	Ny	Nt
Case 2	Cold Wall	10^{-5}	1.5	1.225	1.789×10^{-5}	110	90	9880
Case 3	Cold Wall	10^{-5}	4	1.225	1.789×10^{-5}	110	90	9880

In Figure 8-7 the non-dimensional temperature versus the boundary layer height, η, is plotted for the three cases where the η is employed so the three curves can fit on the same plot. This value is taken from [155], and is calculated from (1.7).

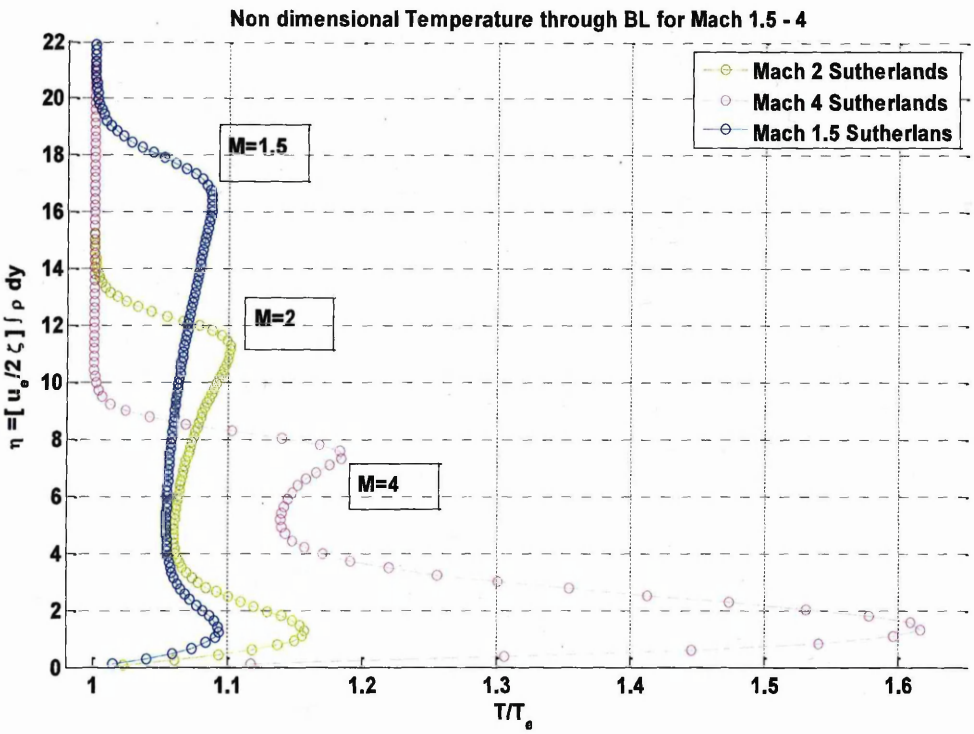

Figure 8-7–Non-dimensional temperature against the (non-dimensional) boundary layer height at the trailing edge of the flat plate case as seen in Figure 8-1.

The above plot mathematically displays the effect that both the thermal interactions inside the boundary layer and the thermal effect that the shock has, on the temperature field at the trailing edge. The rise in temperature near the plate surface is due to strong viscous effects and is most pronounced in the Mach 4 case and least pronounced in the Mach 1.5 case. In addition to this boundary layer heating, another phenomena is dispayed. For example, for the Mach 4 profile, the step rise in temperature at $\eta \approx 8$ is because of the gas flow, which is heating up across the shock wave. Similarly for the Mach 1.5 profile when $\eta \approx 17$ the heat jumps across the shock. Because the planned final problem is concerned with the modelling of heat performance of porous components more research is needed to ascertain the CBS algorithm's capability at modelling different thermal boundary condition scenrios .

8.3.1 Study of the Different Thermal boundary conditions

Table 8-4-Grid and flow parameters for high speed calculations.

	Boundary Condition	Length [m]	M_∞[-]	ρ_∞[kg/m^3]	μ_∞[kg/(ms)]	Nx	Ny	Nt
Case 4	Cold Wall	10^{-5}	4	1.225	1.789×10^{-5}	110	90	9880
Case 5	Adiabatic	10^{-5}	4	1.225	1.789×10^{-5}	110	90	9880

where Nx is the number of cells in the x direction.
Ny is the number of cells in the y direction.
Nt is the total number of cells.

Case 4: Cold wall $T_w=T_\infty$

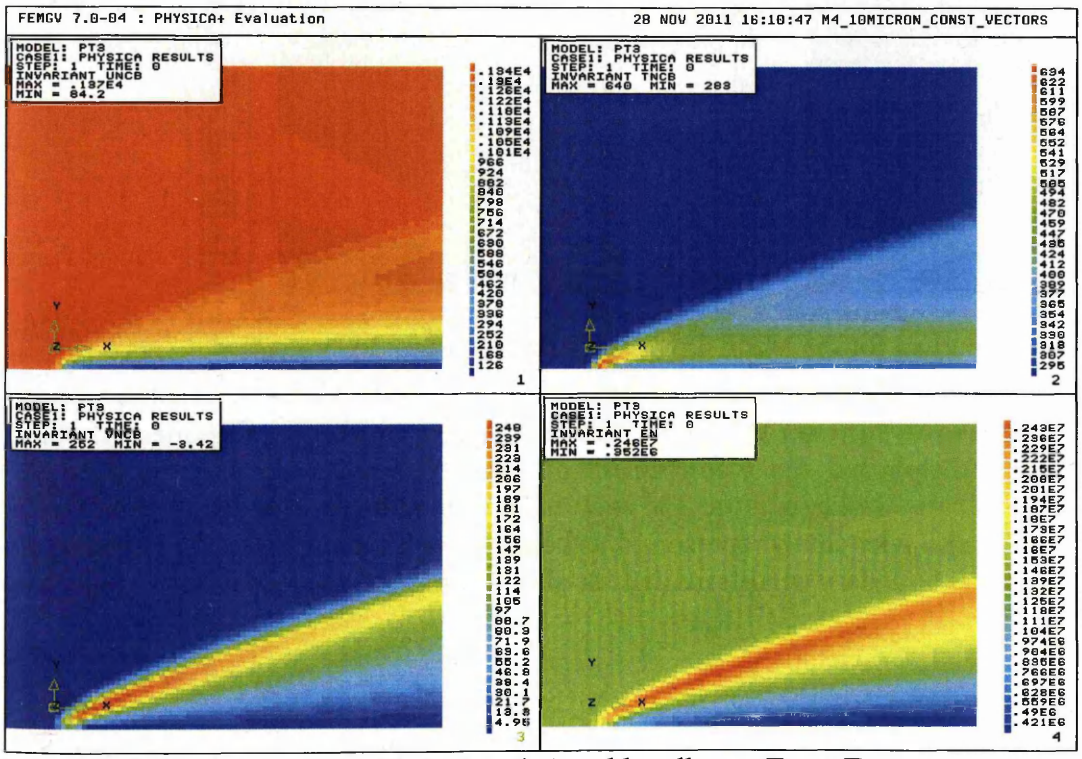

Figure 8-8: Velocity contours for the Mach 4, cold wall case $T_{wall}=T_\infty$.

The four contour plots above, going from top left in a clockwise fashion, are the x- component of velocity, the temperature, the enthalpy and the y-component of velocity. The steady state solution is for boundary case 4 i.e. constant wall temperature at the free-stream value. The contours are smooth and is an indication, of a stable algorithm. The shock is also adequately represented as being several cells across. The boundary layer is also represented as being three cells above the wall.

Case 5: Adiabatic Wall $(\partial T/\partial n)_w = 0$

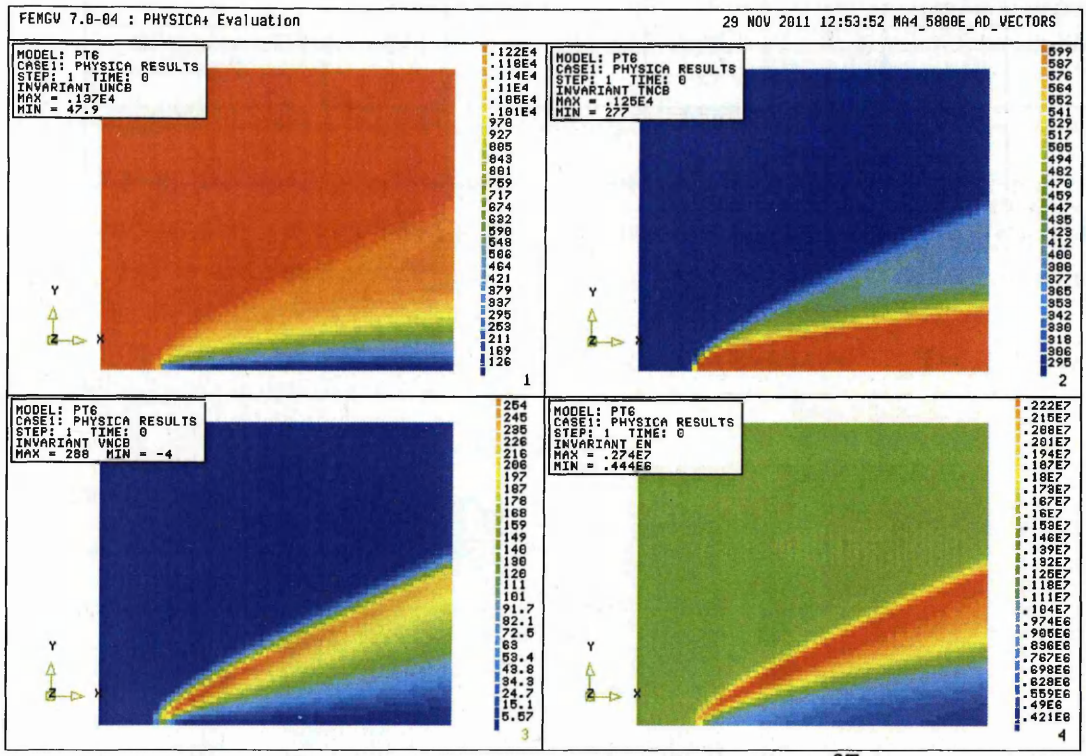

Figure 8-9: Velocity contours for the Mach 4,the adiabatic case ($\frac{\partial T}{\partial n} = 0$).

The four contour plots above from top left, in a clockwise fashion are the x- component of velocity, the temperature, the enthalpy and the y-component of velocity. The steady state solution is for boundary case 5 i.e. adiabatic wall condition. The contours are smooth and is an indication of a stable algorithm. The shock is also adequately represented as being several cells across. The boundary layer is much larger than case 4 boundary conditions and the shock possesses a larger oblique angle, as you would expect.

8.3.2 Comparison of CBS against MacCormack's Predictor Corrector Algorithm

The following CFD results are a comparison of the FV CBS algorithm against the profiles copied from Anderson, [4, page 469]. These profiles were computed with MacCormack's Finite Difference Predictor Corrector Algorithm [29] which was not implemented in this research. Only the plots generated with this technique were used to compare with the resultant profiles from the FV CBS algorithm. This comparison was pursued because we need to determine if the CBS algorithm performs to the same accuracy of other CFD codes.

In addition, because the temperature reference method is limited to a small amount of detail specifically at the plate surface, meaning no comparison can be made in proximity of the shock and in particular for the next case where oblique shock exits the domain. The relatively low free stream Reynolds numbers means achieving a converged solution for the compressible velocities with the Navier-Stokes equations is an essential and encouraging milestone for the scheme when considering the final benchmark problem. For the following simulations C_x =0.2.

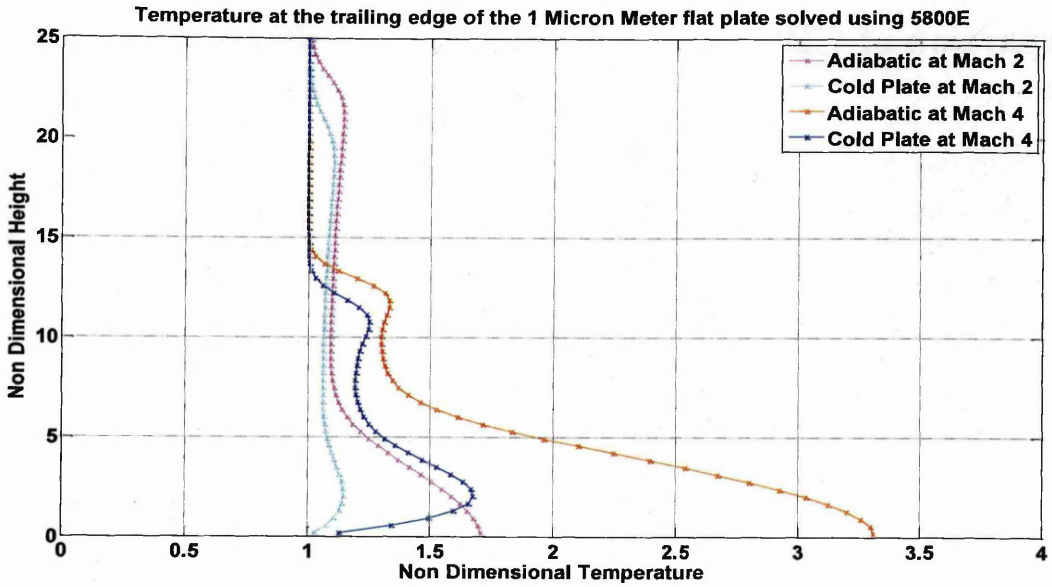

Figure 8-10: Temperature profile through the Boundary layer at the trailing edge for the cold wall and adiabatic cases at Mach 2 & 4 using the CBS algorithm.

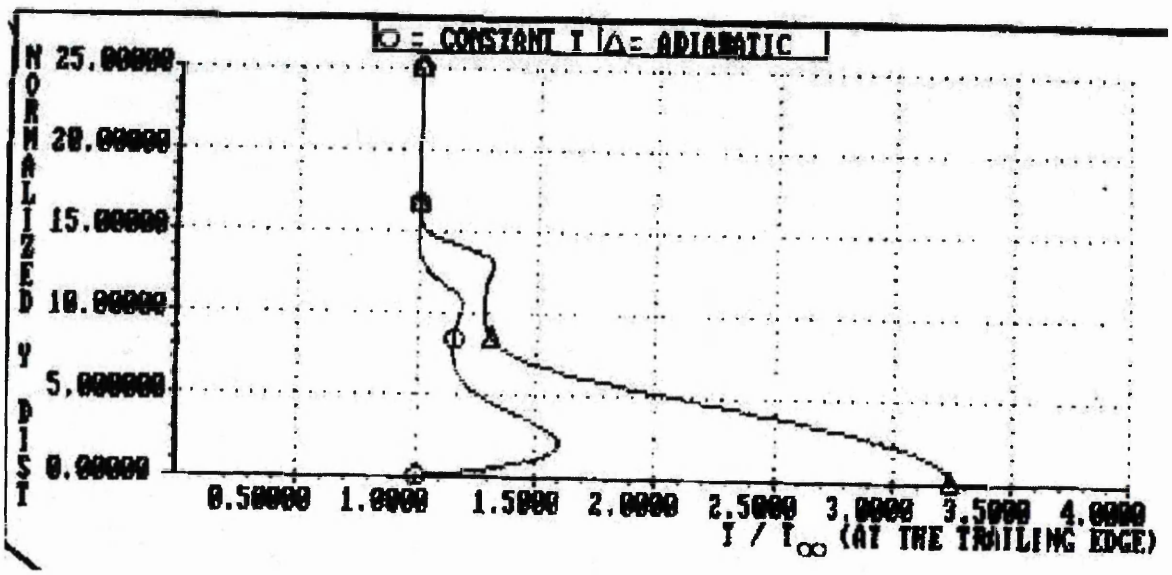

Figure 8-11: Temperature profile through the Boundary layer for the cold wall and adiabatic cases at Mach 2 & 4 using the MacCormack's algorithm.

The two figures Figure 8-10 and Figure 8-11 above display the non-dimensional temperature profile through the outlet at the trailing edge, 0 H -25 H. Figure 8-10 shows the FV CBS results for the Mach 4 Cold wall case and the Mach 4 Adiabatic case. As seen in Figure 8-11 this is taken from Anderson, [4, page 469] and is garnered through MacCormack's scheme [29]. The close likeness between the two figures is a promising indicator that the CBS algorithm is a viable compressible flow solver.

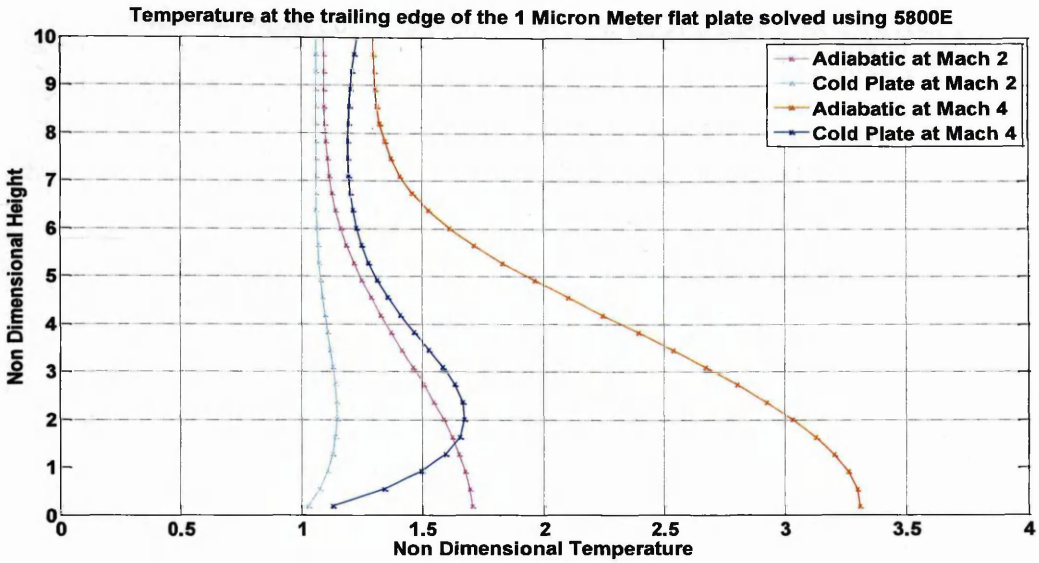

Figure 8-12: Temperature profile through the Boundary layer at the trailing edge for the cold wall and adiabatic cases at Mach 2 & 4 using the CBS algorithm.

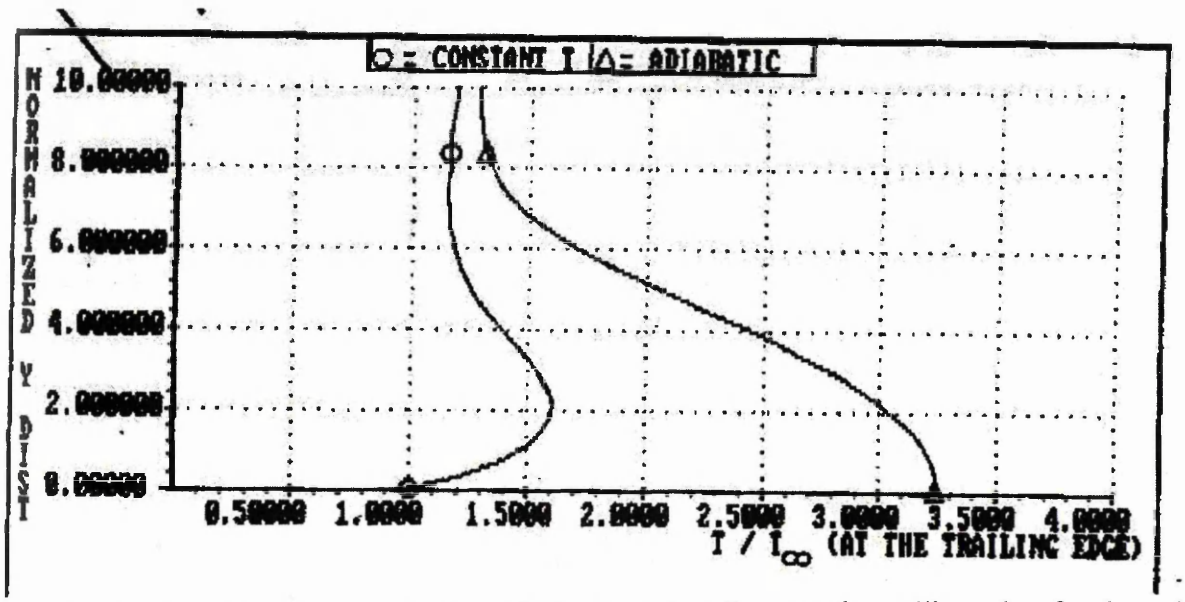

Figure 8-13: Temperature profile through the Boundary layer at the trailing edge for the cold wall and adiabatic cases at Mach 2 & 4 using the MacCormack's algorithm

The two figures Figure 8-12 and Figure 8-13 above display the non-dimensional temperature profile through the boundary layer at the trailing edge. Figure 8-12 shows the FV CBS results for the Mach 4 Cold wall case and the Mach 4 Adiabatic case. Both cases employed a 5880 mesh to discretise the domain. As seen in Figure 8-13 this is taken from Anderson, [4, page 469] and is garnered through MacCormack's scheme [29]. The close likeness between the two figures is another promising indicator that the CBS algorithm is a viable compressible flow solver.

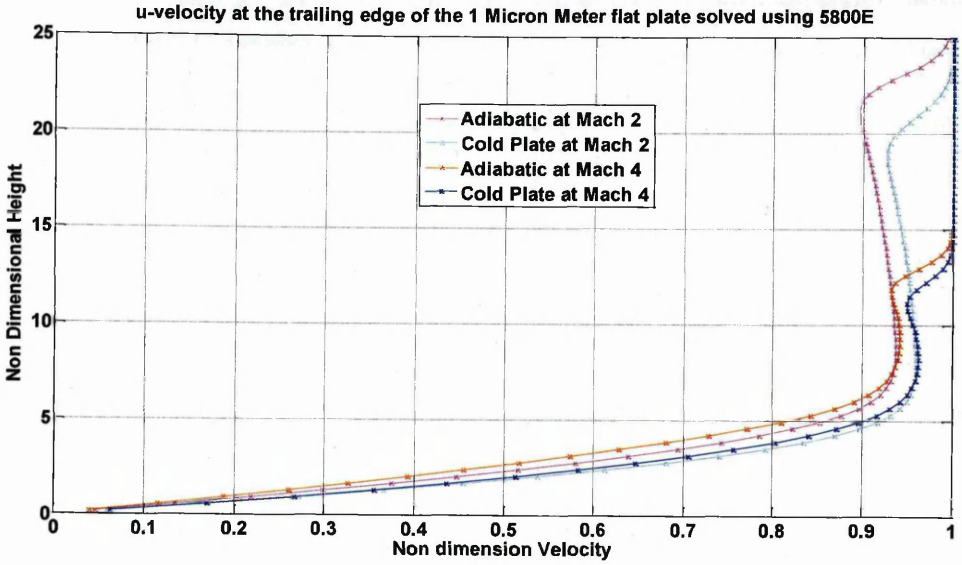

Figure 8-14: Velocity profile through the Boundary layer at the trailing edge for the cold wall and adiabatic cases at Mach 2 & 4 using the CBS algorithm.

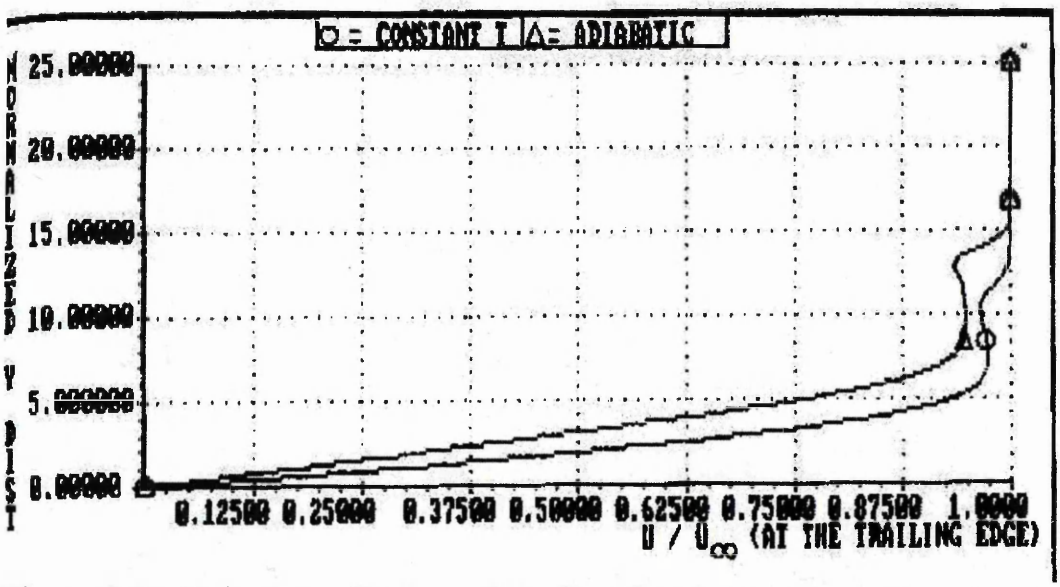

Figure 8-15: Velocity profile through the Boundary layer at the trailing edge for the cold wall and adiabatic cases at Mach 2 & 4 using the Anderson's MacCormack's algorithm.

The two figures Figure 8-14 and Figure 8-15 above display the non-dimensional velocity profile through the outlet at the trailing edge. Figure 8-14 shows the FV CBS results for the Mach 4 cold wall case and the Mach 4 adiabatic case. Both cases employed a 5880 mesh to discretise the domain. As seen in Figure 8-15 this is taken from Anderson, [4, page 469] and is garnered through MacCormack's scheme [29].

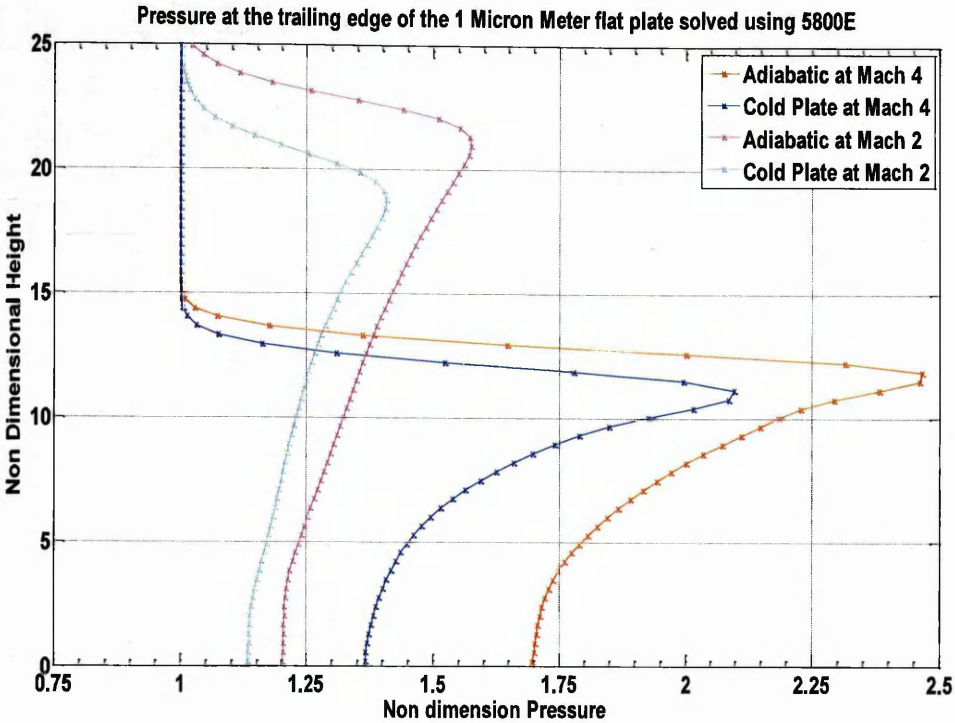

Figure 8-16: Pressure profile through the Boundary layer at the trailing edge for the cold wall and adiabatic cases i.e. for Mach 2 & 4 using the CBS algorithm.

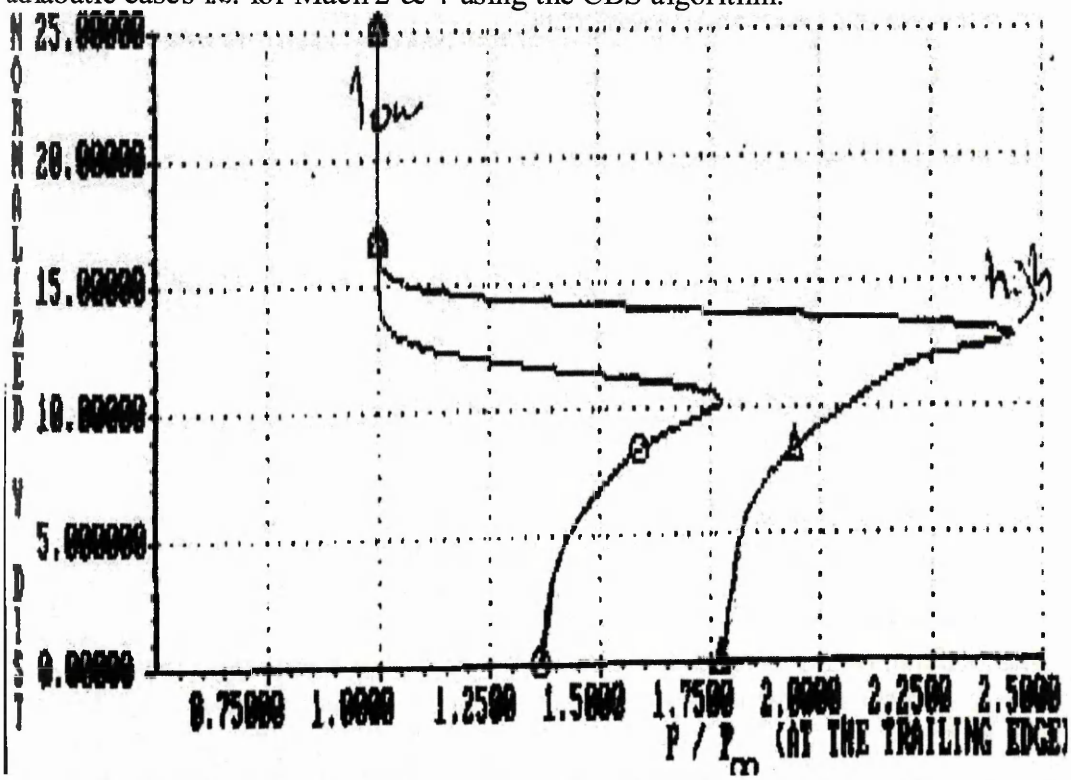

Figure 8-17: Pressure profile through the Boundary layer at the trailing edge for the cold wall and adiabatic cases i.e. for Mach 2 & 4 using MacCormack's algorithm.

The two figures Figure 8-15 and Figure 8-17 above display the non-dimensional pressure profile through the outlet at the trailing edge. Figure 8-15 shows the FV CBS results for the Mach 4 Cold wall case and the Mach 4 Adiabatic case. Both cases employed a 5880 mesh to discretise the domain.

As seen in Figure 8-17 and Figure 8-15 this is taken from [15], and is garnered through MacCormack's scheme.

To summarize, the temperature, pressure and velocity field profiles through the trailing edge of the domain compared favourably with the profiles garnered with MacCormack's predictor corrector scheme [29] as seen in Anderson, [4, page 469]. These encouraging results, modelling Supersonic compressible viscous flows, cannot be over-emphasized especially considering the instability issues exhibited for the Subsonic case over a flat plate.

8.4 Concluding Remarks

This chapter has looked at the methodology to gain a numerical solutions to compressible Supersonic viscous flow, where a comparison with the predicted skin friction and coefficient of heat from the temperature reference method and the FV CBS scheme is made. The temperature reference method is an approximate prediction as presented in Schlichting, [155]. This prediction makes crude simplifying assumptions such as zero pressure gradient, through the boundary layer [155], and therefore this point should be kept in mind when evaluating the accuracy of the converged numerical solution.

8.4.1 CBS against the Temperature Reference Method

The explicit FV CBS algorithm was successfully stable and converged to a steady state solution for the 1st benchmark, the Mach 2, constant cold wall, 10μm flat plate. The small domain for the 10μm flat plate means relatively small grid sizes. Where structured orthogonal grids can be employed (9800 elements) mitigating the need for careful mesh construction. This also has a (beneficial) effect on the simulation CPU time needed and the amount of time needed to harvest plots from the numerical outputs.

Skin friction values for this benchmark were computed using cells adjacent to the no-slip wall. These C_f values were compared with the predicted values from the temperature reference method. The C_f percentage error was less than 10% and the C_H value was less than 2% therefore considering the drawbacks of the temperature reference method then the CBS algorithm could be argued to produce viable results. Upon evaluation the C_H and C_f values from the CBS algorithm were in agreement with the predicted solution, and in particular towards the trailing edge where the simplifying assumptions are realized.

8.4.2 CBS against MacCormack's Predictor Corrector algorithm

The next set of simulations were carried out at a higher Mach number, Mach 4, for two different thermal boundary conditions; i.e. the cold wall case and the adiabatic wall case. The MacCormack [29], finite difference predictor corrector algorithm profiles which were copied from Anderson, [4, page 469], are used as a comparison. The figures in Anderson show physical quantities through the outlet, which unlike the temperature reference method encompasses the shock wave as well as the boundary layer. Therefore the various profiles at stations through the outlet edge from Anderson, [4], could be argued to be just as informative as the temperature reference method when assessing the performance of the numerical scheme. Another cogent reason as to why this comparison was conducted was the Anderson study contains pressure and density profiles as well as velocity and temperature through the outlet.

The FV CBS algorithm again reached steady state convergence for the two boundary condition cases. As expected from the discussion into this problem by Anderson, [4, page 470], the solution for the cold wall case is realized in fewer iterations that the adiabatic case. The CBS profiles are in excellent

agreement with the MacCormack finite difference predictor corrector algorithm [29] profiles, which are copied from [4]. Close comparison of the location of the shock and the maximum temperature through the boundary layer is realized as seen in Section 8.3.2. This example demonstrates the applicability of the FV CBS method for high speed viscous flow which could be argued to be a simplification of the transpiration cooling at Hypersonic speed problem.

9 POROUS MEDIA FLOW SIMULATIONS

9.1 Introduction

The operating speed of the Hypersonic cruise air-breathing vehicles (CAVs) will mean that the external air flow after passing through strong compressible shock waves and losing momentum to the no slip surface will heat up the localized air to high temperatures as seen in Chapter 8. Ultimately the CAVs of interest will certainly employ porous components with transpiration cooling applied to where high localized heat fluxes exist according to the scientific literature on Hypersonic applications [116], [124], [177], [182], [183].

With the availability of lightweight ceramic matrix composites (CMC) increasing as state of the art manufacturing techniques are refined [184], whereby research is needed for scientific validation, before utilizing such components. Promising ceramic matrix composite (CMC) materials include to date, carbon/carbon (C/C) or silicon carbide infiltrated carbon/carbon (C/C SiC). Transpiration cooling using CMC represents a promising strategy for both combustion-chamber engine cooling and external leading edge cooling according to the researchers Kelly [185] and Song, Choi, & Scotti [186]. For instance the CAVs leading edges such as the nose will be porous, permitting mass transfer from the porous material to the boundary layer. When coolant flows through the porous component, a uniform coolant film forms over the surface and thickens the boundary layer, resulting in reduced thermal gradients meaning the heat-flux, $q_w = k_w(T_i - T_w)/\Delta y$ strongly decreases with increased transpiration coolant blowing [71]. In addition the internal heat transfer within the porous wall plays a significant role in the cooling efficiency [187]. Modelling transpiration cooling applications requires a software tool that can simulate physical interactions throughout the flow regimes from incompressible to compressible as mentioned by Azevedo & Korzenowski [10]. In order to compute fluid flow through porous components, relevant papers were surveyed for an appropriate mathematical model to capture the effect of porous components. One such mathematical model is a derivative of the original Ergun source term as presented in Pantelis & Ritchie, [188] which is based on the term derived by Ergun, [189]. The derivative Ergun source term by Pantelis & Ritchie, [188] was employed for the incompressible flow problem with some amendments for the convection terms that account for the reduced passage suggested by Cheuret & Steelant, [124].

Compressible porous flow problems to date have no known analytical solution so the reliability of the CBS FV algorithm cannot be gauged. However Subsonic incompressible flow through a porous medium has an analytical solution allowing such an assessment of the CBS FV algorithm. Therefore a comparative study of the AC CBS formulation with the incompressible porous flow result is performed, where error assessment is achieved, by comparing with the analytical solution. In addition the methodology required for gaining a stable solution for incompressible flow will be both insightful and comparable to the methodology needed for stable compressible calculations through porous components.

In this chapter, we are addressing only the problem of flow solver development not a mesh sensitivity study and we present procedures for the implementation of flow algorithms which can be employed successfully for the simulation of porous flow. The porous media possess macroscopic fibres that restrict the free-stream gas filtering across. Where ε is the solid volume fraction, a property of porous

media. Where ε=0 for a continuum and ε=1 for an impermeable solid. In addition the pressure head decreases as the fluid filters through the porous media. To mathematically capture this physical pressure loss a source term is augmented to the Navier-Stokes equations. Modelling Subsonic flow through a porous structure can be simplified by assuming incompressible and isothermal flow. For this case, the absolute velocity jumps in magnitude instantaneously at the gas-porous structural interface. This discontinuous velocity jump is conceptually similar to the changes in velocity across an expansion shock. To capture this increase in velocity requires a mathematical model that treats the porous media as part of the continuum. This means the mathematical model solves the velocity, enthalpy, density and pressure throughout the solution domain even for those cells that contain the porous media.

In the following sections, a detailed description is given of the numerical formulations employed, with special attention focused on the finite volume approach to flow through a porous media.

9.1.1 Ergun Source Term

Amendments are made to the governing equations, which mathematically model the effect that the stationary porous structure has on the pressure and the velocity of the flow. For example the convective flux is treated differently depending on whether the cell straddles the porous bed or the free stream. Within the porous media the absolute velocity of the gas increases to satisfy mass flow for an incompressible porous problem.

The transport through the porous medium is therefore adapted to account for the reduced passage by introducing the solid volume fraction value, ε, into the momentum, continuity and energy equation. When the solid volume fraction, ε=0, in the main channel, the effect of the Ergun source term is ignored. The first strategy was to multiply the convection terms by the available area for flow due to the reduced passage which is multiplied by $(1-\varepsilon)^{2/3}$. This mathmatically means that the convection fluxes will conserve mass and momentum for porous media problems.

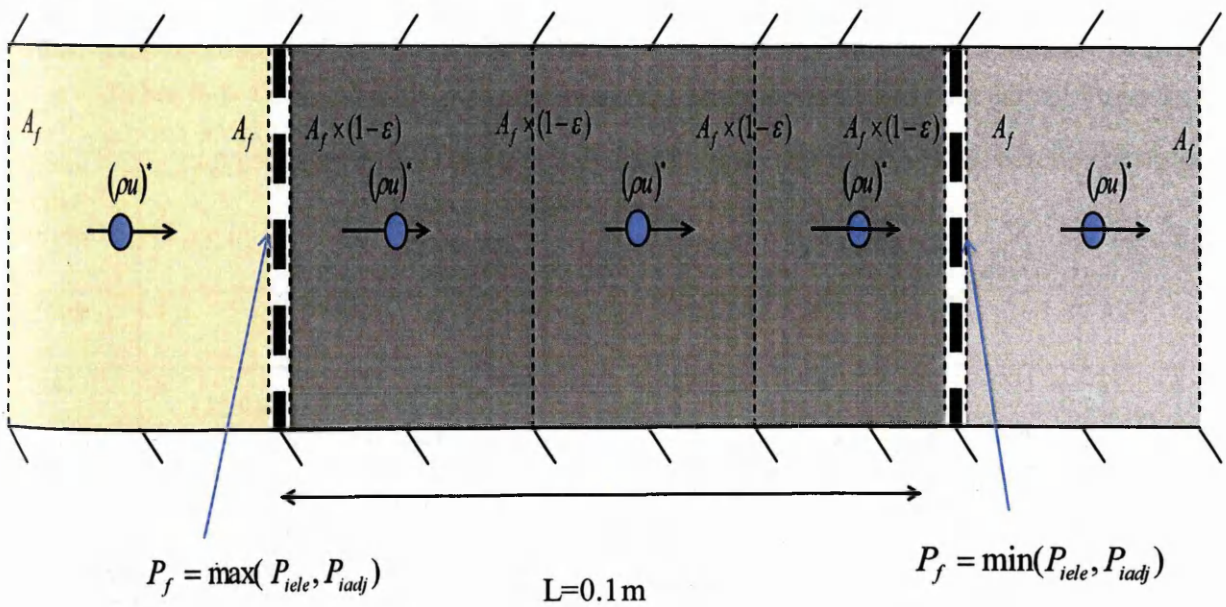

Figure 9-1- Spatial grid of porous medium with the interstitial velocity.

Figure 9-1 shows a schematic of the spatial discretization of a 1-D porous media problem. The numerical discretization of the convection terms needs to be amended for the faces straddling gas porous structure the interface. Near the interface of the porous wall and the main flow, the solid

volume fraction, ε, changes sharply from its porous value to the free stream value. The gas porous structure interface for this approach should be located on the interface between two adjacent cells because this interface leads to sharp changes in the local velocity values and the pressure gradients [116]. For example the intermediate FV CBS momentum can be written in the following form

$$\rho u_i^* = \rho u_i^n - \frac{\Delta t}{(1-\varepsilon)\Delta V}\left(\sum_{f=1,TOTFIC} \left((\rho u_i u_j)\right) \bullet n_j A_f (1-\varepsilon)^{2/3} - \sum_{f=1,TOTFIC} \left(\tau_{ij} \bullet n_j A\right)_f (1-\varepsilon)^{2/3} \right)^n \quad (9.17)$$

Where ε- solid volume fraction (1 for impermeable solid material and 0 for fluid continua)

When macroscopic fluid packets filter through a porous structure pressure head is lost due to friction. For porous media flow, the pressure drop along the length of the porous bed has been empirically tested and is accounted for by a derivative of Ergun's law as seen in Pantelis & Ritchie, [188].

$$\nabla P_{ERG} = -\frac{\left(1.75\rho^2 |\mathbf{u}| \varepsilon T_b\right)}{273 d_p (1-\varepsilon)^3 \rho_\infty} u_n \quad (9.18)$$

Where d_p is the mean diameter of porous particles.
T_b is the temperature of the porous bed.
u_n is the real velocity of gas or fluid through the bed.
ρ_∞ is the density of the free-stream gas.

Adding this source term to the corrected momentum equation results in:

$$\rho u_i^{n+1} = \rho u_i^* - \frac{\Delta t}{\Delta V_{Pass}}\left(\nabla P^n + \frac{\left(1.75\left(\rho^n\right)^2 |\mathbf{u}^n| \varepsilon T_b^n\right)}{273 d_p (1-\varepsilon)^3 \rho_\infty} u_i^n \right) \quad (9.19)$$

Where ΔV_{Pass} is the volume available for the fluid continuum therefore $\Delta V_{Pass} = \Delta V_{CV}(1-\varepsilon)$ where ΔV_{CV} is the total volume of the control volume porous and continuum structure included and, finally $A_{Pass} = A_{CV}(1-\varepsilon)^{2/3}$, is the area available for fluid continuum.

For incompressible flows the continuity equation for the AC CBS algorithm reduces to-

$$P^{n+1} = P^n - \beta^2 \frac{\Delta t}{\Delta V_{Pass}}\left(\sum_{f=1,TOTFIC} \rho u_j \bullet n_j A_f (1-\varepsilon)^{2/3} + u_k \frac{\Delta t}{2} \sum_{f=1,TOTFIC} \frac{\partial P}{\partial x_j}_f \bullet n_j A_f \right) \quad (9.20)$$

Where

$$\beta_{CV}^n = \max\left(\varepsilon_\beta, \sqrt{u_i u_i}, \frac{2\mu_\infty}{\rho_\infty h_{CV}} \right) \quad (9.21)$$

ε_β is set to 0.5 for incompressible benchmarks

Benchmark Problems

This chapter focusses on flows within porous media akin to the transpiration cooling applications of interest to industrial sponsors ESA. Where the FV CBS algorithm is applied following an incremental increase in the benchmark model complexity.

1. Incompressible Subsonic Laminar flow within a porous medium.
2. Compressible Subsonic Laminar flow within a porous medium.

Initially the Navier-Stokes equations were then implemented in a sequential Artificial Compressibility (AC) CBS procedure and used to solve the preliminary problem. However the strategy described was deemed wanting in terms of stability when applied to the porous benchmark fluid flows. It was deemed necessary by myself to introduce an amended AC CBS implicit strategy for incompressible porous problems. The following approach is the result of my own research and represent a novel approach for AC CBS algorithm when modelling incompressible porous flows.

9.2 Subsonic Incompressible Porous Flow

To investigateSubsonic incompressible porous flow, we made a comparative study between the analytical solution and the solution obtained using the numerical AC CBS scheme. The problem entails Subsonic incompressible gas which flows onto a perpendicular to a porous media otherwise known as plug flow. The challenge of this benchmark lies in capturing the pressure drop across the medium and resolving the discontinuous jump of velocity across the porous gas interface. Of the many mathematical models available the empirically tested Ergun source term as presented by Pantelis & Ritchie, [188], is chosen here to capture the effect of the porous medium. The analytical solution is used to allow direct comparison so that the FV AC CBS algorithm can be validated. As before a percentage error tolerance of more than 1% between the AC CBS solution and the analytical solution is deemed unacceptable.

9.2.1 Boundary Conditions

To evaluate the numerical performance of the FV CBS algorithm coupled with the Ergun source term, two problems involving Subsonic incompressible flow through a porous medium are considered. These examples involve simple geometries, which means that structured quadrilaterals can be used. A high free stream viscosity was employed reducing the free stream Reynolds number because this study is concerned with developing a successful strategy for laminar gas flow on porous media, before extending the strategy for higher Reynolds number, at a later stage. The following table summarizes the flow parameters, for the next two sets of simulations.

Table 9-1- Grid and flow parameters for the a small porous length of 0.0001 m and a larger porous length of 0.1 m.

Porous Media Length [m]	u_∞[m/s]	ρ_∞[kg/m^3]	μ_∞[kg/(ms)]	Re [-]	Nx	Ny	Nt
0.001m	8	1.225	1.789	0.00547792	56	2	112
0.1m	8	1.225	1.789	0.547792	56	2	112

Where Nx is the number of control volumes in the x-direction.
Ny is the number of control volumes in the y-direction.
Nt is the total number of control volumes.

Case 1: Porous Length, PL = 0.001m

The 1st case investigated using a small porous length meaning the maximum pressure, P_{in}, will be small compared to the reference pressure. The algorithm was successful at modelling relatively small pressure rises. The schematic diagram, Figure 9-2, illustrates the incompressible porous benchmark problem.

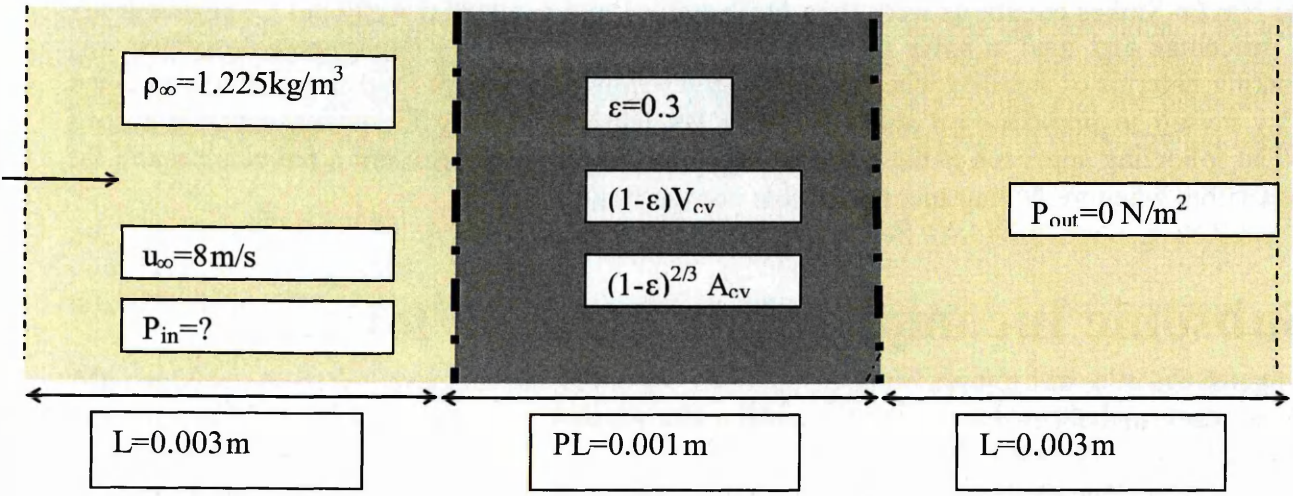

Figure 9-2 Schematic of Porous Flow (where green indicates the porous media).

Case 2: Porous Length, PL = 0.1m

For the 2nd case investigated, the above problem is repeated but where all x and y lengths are approximately x100 larger. This means that the maximum pressure, P_{in}, will be increased by a factor of 100 compared with case 1.

9.2.2 Analytical Solution

The analytical solutions for the two cases above are attractive because they can be calculated in a straight foward manner. By substituting the above values from Table 9-1 into the Ergun source term, equation (9.18), and integrating over the porous length, PL, we can work out the pressure drop through the porous medium by substituting the values d_p=0.003m and T_b=288.16K.

For an isothermal and incompressible flow with a porous length of 0.001m the analytical solution is now presented.

$$\nabla P = -\frac{\left(1.75\rho^2 |\mathbf{u}|(1-\varepsilon)T_b\right)}{273 d_p \varepsilon^3 \rho_\infty} u_n$$

$$\nabla P = -\frac{\left(1.75\times 1.225^2 \times \left|\frac{8}{0.7}\right|(0.3)288.16\right)}{273\times 0.003\times 0.7^3 \times 1.225}\left(\frac{8}{0.7}\right)$$

$$\nabla P = 86165.85 N/m^3$$

Where $P_2 = 0.0 N/m^2$ as seen in Figure 9.3.

Then the pressure at the inlet, P_1, is obtained by substituting P_2 and PL :

$$\frac{P_1 - P_2}{PL} = 86165.85$$

$$\Rightarrow P_1 = 86165.85\times 0.001$$

$$P_1 = 86.165 N/m^2$$

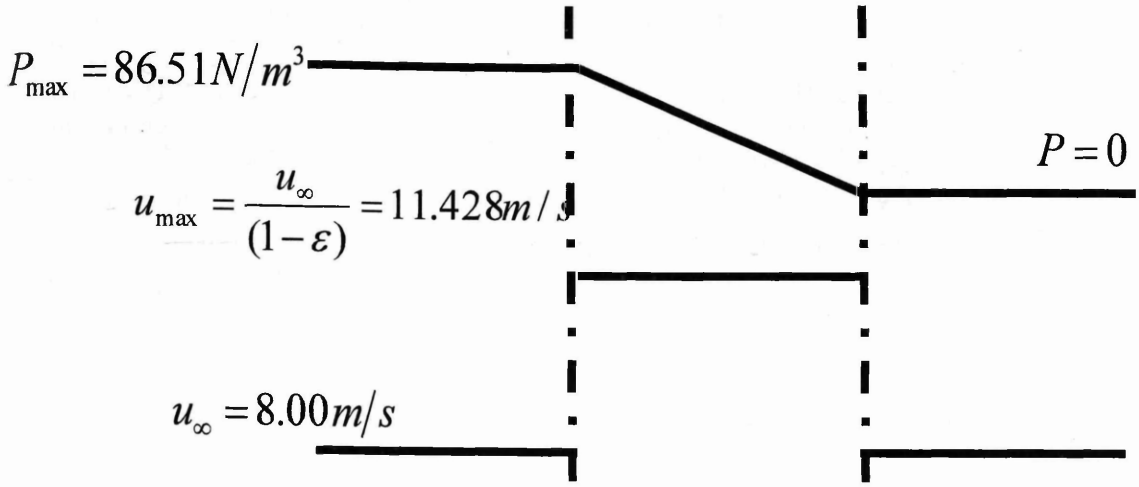

Figure 9-3 Velocity & Pressure profile through the porous media.

For the 2nd case, the porous length (PL), is increased to 0.1m. Therefore replacing PL with 0.1m instead of 0.001m the analytical solution is obtained in a similar fashion,

Case 2 Porous Length, PL = 0.1m

$\nabla P = 86165.85N/m^3$

$P_2 = 0.0N/m^2$

$\Rightarrow P_1 = 86165.85 \times 0.1$

$P_1 = 8616.5N/m^2$

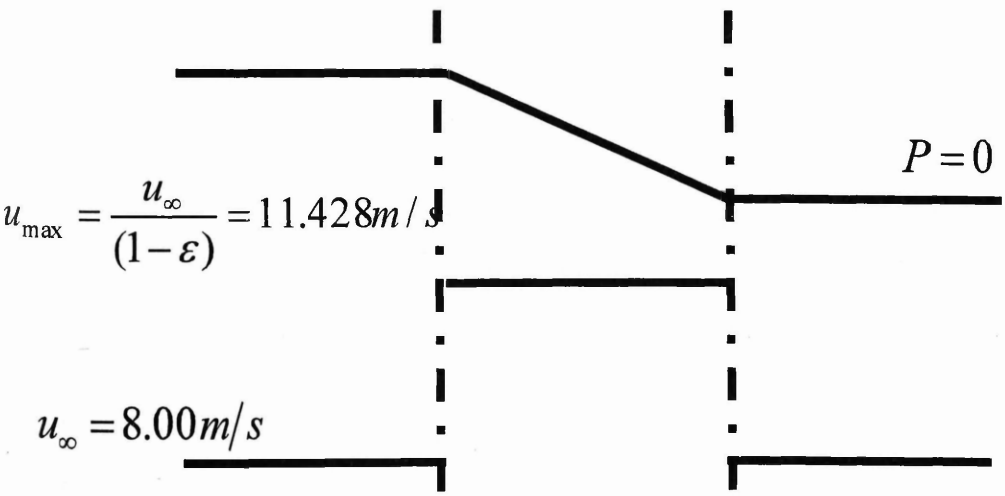

Figure 9-4: Velocity & Pressure profile through the porous medium.

9.2.3 Mesh

To calculate the incompressible, isothermal Subsonic flow through porous media, a preliminary AC CBS sequential procedure was applied to the above case without efficiency. The reason for not displaying it in the main body of the thesis was because the author wishes to present only those computational procedures which are stable and efficient for a wide class of problems making the thesis as concise as possible.

9.2.4 Solver Results

To stabilize the computations for the PL=0.001m case the Courant number was set to 0.0005. To put this into context a Courant number of 0.05 is used for incompressible flow over a supersonic flat plate. The initial conditions were set to the free-stream conditions seen in table 1. The following velocity and pressure profile for the 1st case were plotted after 3000, 6000 and 12000 iterations respectively. After 12,000 iterations the relative error as seen in equation (9.19), reached the tolerance of 10^{-5}.

Case 1 LP=0.001m

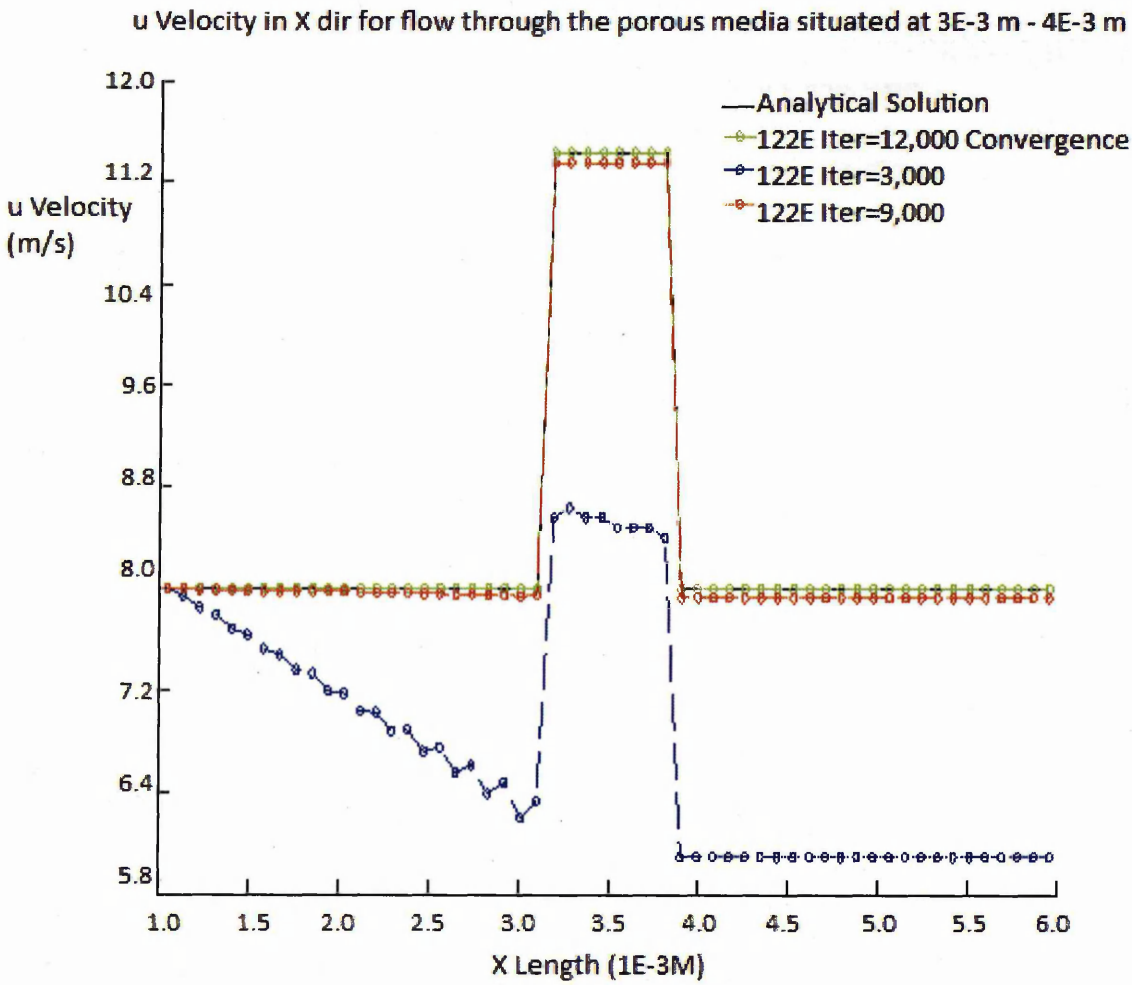

Figure 9-5 Velocity profile through the porous medium.

As seen in Figure 9-5 the computed velocity profiles for 30,000, 60,000 and 120,000 iterations are shown as the blue, red and green lines respectively. The analytical solution is given by the full black line. The y axis is the free-stream velocity is 8m/s. The x axis is dimensional length. After 12,000 the velocity profile as computed by the FV AC CBS algorithm converges onto the analytical velocity profile as seen in Figure 9-3. The above figure demonstrates that the velocity profile through porous media (PL=0.001m) can be accurately captured using the FV AC CBS scheme. However the effect of using such small Courant numbers means an uneconomical amount of iterations are needed to even for the coarse grid.

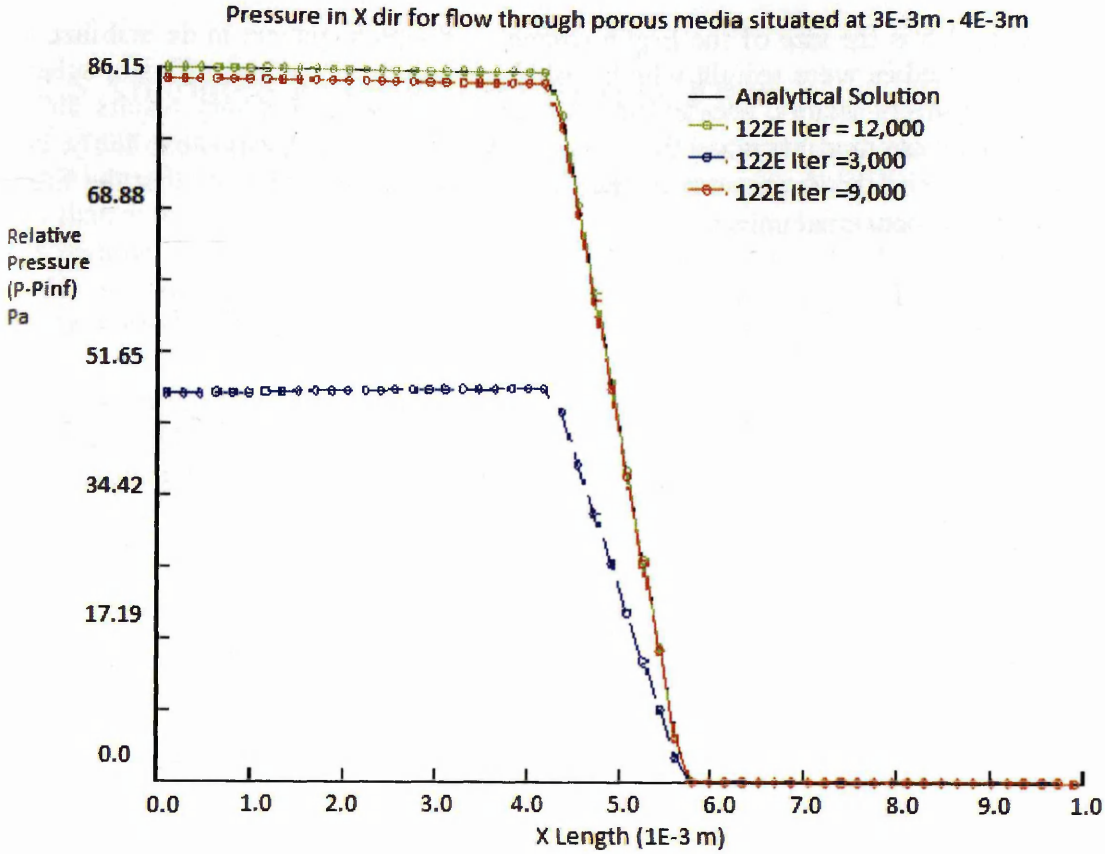

Figure 9-6: Pressure profile through the porous medium where the porous length, L_p = 0.001m.

As seen in Figure 9-6 the computed pressure profiles for 30,000, 60,000 and 120,000 iterations are shown as the blue, red and green lines respectively. The y axis is dimensional pressure relative to the free-stream value. The x axis is dimensional length. The above figure, just like Figure 9-5 demonstrates that the velocity profile through porous media (PL=0.001m) can be accurately captured using the AC CBS scheme as seen in equation (9.17)-(9.21).

To summarize the CBS results for incompressible porous flow through a porous medium of length 0.001m: The CBS scheme converges to the analytical solution for the PL = 0.001m case. However with the small Courant number of 0.0005, the number of iterations needed to obtain the analytical solution is 120,000 iterations, an un-economical number. In terms of u the Ergun source term is a quadratic (u^2). This term will become significant at small values of u (< 1m/s) however when u>1 the magnitude of the source term increases above 1m/s to the power 2.

To Summarize:

- The incompressible CBS scheme is capable of modelling porous media of 0.0001m.
- Convergence and stability are reliant on extremely small Courant numbers.

Case 2 PL=0.1m

As the size of the domain seen in Figure 9-2 is increased by a factor of 100, convergence cannot be achieved with the stability criterion used for Case 1. A major problem during the solution of the

problem as seen in Figure 9-5 is the size of the Ergun source term which appears to de-stabilize the computations. Therefore remedies were sought which would produce a robust and efficient scheme that allows relatively large safety factors, accelerating convergence. The preliminary results for the incompressible porous flow were unstable when the Ergun source term was calculated explicitly. Due to concerns about the stability of the Ergun source term, a dimensional check showed that the Ergun source term had the correct dimensional units.

$$\frac{\left(1.75\rho^2|\mathbf{u}|(1-\varepsilon)T_b\right)}{273d_p\varepsilon^3\rho_\infty}u_n=\left(\frac{kg}{m^3}\right)\left(\frac{m}{s}\right)\frac{1}{s}\frac{K}{K}\left(\frac{m^3}{kg}\right)\left(\frac{m}{s}\right) \tag{9.22}$$

$$\frac{\left(1.75\rho^2|\mathbf{u}|(1-\varepsilon)T_b\right)}{273d_p\varepsilon^3\rho_\infty}u_n=\left(\frac{N}{m^2}\right)/m \tag{9.23}$$

$$\rho u_i^{n+1}=\rho u_i^*-\frac{\Delta t}{\Delta V_{Pass}}\left(\sum_{f=1,TOTFIC}P_f\bullet n_i A_f(1-\varepsilon)^{2/3}+\frac{\left(1.75\left(\rho^n\right)^2|\mathbf{u}^n|(1-\varepsilon)T_b^n\right)}{273d_p\varepsilon^3\rho_\infty}u_i^n\Delta V_{Pass}\right) \tag{9.24}$$

$$\left(\frac{kg}{m^3}\right)\left(\frac{m}{s}\right)=\left(\frac{kg}{m^3}\right)\left(\frac{m}{s}\right)-\left(\frac{s}{m^3}\right)\left(\frac{N}{m^2}m^2+\frac{kg}{m^2}\frac{1}{s^2}m^3\right)$$
$$\therefore=\left(\frac{kg}{m^3}\right)\left(\frac{m}{s}\right)-\left[\left(\frac{kg}{m^3}\right)\left(\frac{m}{s}\right)+\left(\frac{kg}{m^3}\right)\left(\frac{m}{s}\right)\right] \tag{9.25}$$

The incompressible CBS scheme is not capable of modelling porous media lengths of the order of 0.1m. So the following approach is the result of my own research and represent a novel approach for AC CBS algorithm when modelling incompressible porous flows.

9.2.5 Amended Approach for Porous Flow

The Ergun source term is de-stabilizing the AC-CBS scheme because the residual on the right hand side of equation (9.24) becomes excessively large, meaning potentially the value of ρu^{n+1} could be less than zero an unphysical and unstable result. Various strategies were reviewed that would decrease this residual including employing an implicit form of the FV AC CBS which will demand iterative matrix solver routines, however the associated drawback with this iterative matrix solver is the additional need for additional computer codes that could potentially introduce human error.

Instead of utilizing the implicit form of the FV AC CBS scheme for this research I propose a simple revision to the AC CBS scheme that promotes stability. The following amendments were made after hand calculations of the AC CBS sequential method;

1. The overall scheme gained stability when the 1st ordered convection term in the intermediate momentum was neglected for the following computations.
2. Secondly treating the Ergun contribution on the right hand side of equation (9.24) as an implicit source term rather, meaning no implicit system matrix needs to be solved. The corrected equation is now solved with the use of the generic quadratic root formula. This correction when applied, means the final residual value for $u^{n+1} - u^n$ in equation (9.24) will be smaller than for a explicit treatment (9.9).

$$\rho u_x^{n+1} = \rho u_x^* - \frac{\Delta t}{\Delta V_{Pass}}\left(\sum_{f=1,TOTFIC} P_f \bullet n_x A_f (1-\varepsilon)^{2/3} + \frac{\left(1.75(\rho^n)^2 \sqrt{u_x u_x}^{n+1} \varepsilon T_b^n\right)}{273 d_p (1-\varepsilon)^3 \rho_\infty} u_x^{n+1} \Delta V_{Pass} \right) \tag{9.9}$$

If we subtract both sides of equation (9.9) by the following term.

$$-\frac{\Delta t}{\Delta V_{Pass}}\left(\frac{\left(1.75\rho^2 \sqrt{u_x u_x}^{n+1} \varepsilon T_b\right)}{273 d_p (1-\varepsilon)^3 \rho_\infty} u_x^{n+1} \Delta V_{Pass} \right) \tag{9.10}$$

Equation (9.9) after re-arrangement becomes a quadratic equation in terms of the variable u^{n+1}.

$$\Delta t \left\{ \frac{\left(1.75\rho^2 \varepsilon T_b\right)}{273 d_p (1-\varepsilon)^3 \rho_\infty} \right\}^n \left(u_x^{n+1}\right)^2 + \rho u_i^{n+1} - \left\{ \rho u_x^* + \frac{\Delta t}{\Delta V_{Pass}} \left(\sum P_f \bullet n_x A_f (1-\varepsilon)^{2/3} \right) \right\}^n = 0 \tag{9.11}$$

The positive root of the quadratic formula is now used as seen below. Where b,a and c are obtained from equation (9.11).

$$\mathbf{b} = \rho^n$$

$$\mathbf{a} = \Delta t \left\{ \frac{\left(1.75\rho^2 \varepsilon T_b\right)}{273 d_p (1-\varepsilon)^3 \rho_\infty} \right\}^n \tag{9.12}$$

$$\mathbf{c} = -\rho u_x^* + \frac{\Delta t}{\Delta V_{Pass}} \left(\sum P_f^n \bullet n_x (1-\varepsilon)^{2/3} A_f \right)$$

3. Thirdly because the two major steps outlined above stabilize by reducing the residual, an additional step will be required to speed up the computations to convergence. An amplification factor was brought into the amended continuity equation motivated by the need to speed up to

convergence. This amplification factor, AF_{pres}, was optimised with success, for the incompressible porous problem, where the AF_{pres} value was set to 100.

$$P^{n+1} = P^n - AF_{Pres}\beta^2 \frac{\Delta t}{\Delta V_{Pass}} \left(\sum_{f=1,TOTFIC} \rho u_j \bullet n_j A_f (1-\varepsilon)^{2/3} + u_k \frac{\Delta t}{2} \sum_{f=1,TOTFIC} \frac{\partial P}{\partial x_j}_f \bullet n_j A_f \right) \quad (9.13)$$

where $AF_{Pres} = 100$ and β_{CV}^n is calculated from (9.21).

9.3 The Sequential AC CBS Scheme for Porous Flow

Each step in the boxed area below is applied to all the interior nodes in a sweep of the grid. After this sweep the boundary conditions are computed. Then the sequential computational iterative procedure is repeated by going to step 1. The AC CBS method was implemented in FORTRAN within the PHYSICA code framework and simulations were then run on the cluster to solve the porous medium problem seen in Figure 9-4.

1. According to Malan et al [150] for incompressible flows the artificial wave speed is calculated from (9.21).

2. The CBS scheme incorporates local pseudo time stepping. The pseudo time step is given by the following equation: where C is the Courant number and depending on the problem is usually < 0.5 The convection time step is analogous to the compressible time step and the diffusion time step as calculated by Malan et al [150]:

$$\Delta t_{CV}^n = \min\left(\left(\Delta t_{CV}^n\right)_{conv}, \left(\Delta t_{CV}^n\right)_{diff} \right) \quad (9.14)$$

$$\left(\Delta t_{CV}^n\right)_{conv} = C \frac{h_{CV}}{\beta_{CV} + \sqrt{u_i u_i}} \quad (9.15)$$

$$\left(\Delta t_{CV}^n\right)_{diff} = C \frac{\rho_\infty \{h_{CV}\}^2}{2\mu_\infty} \quad (9.16)$$

3. Intermediate Momentum step ignoring the convection terms

$$\rho u_i^* = \rho u_i^n - \frac{\Delta t}{\Delta V_{Pass}} \left(\begin{array}{l} 0 - \sum_{i=1,TOTFIC} \left(\tau_{ij} \bullet n_j A\right)_f (1-\varepsilon)^{2/3} \\ + \frac{\Delta t}{2} u_k \sum_{i=1,TOTFIC} div\left(\rho u_i u_j\right) \bullet n_j A_f (1-\varepsilon)^{2/3} \end{array} \right) \quad (9.17)$$

4. Corrected Momentum step

$$\Delta t \left\{ \frac{\left(1.75\rho^2 \varepsilon T_b\right)}{273 d_p (1-\varepsilon)^3 \rho_\infty} \right\}^n \left(u_i^{n+1}\right)^2 + \rho u_i^{n+1} - \left\{ \rho u_i^* + \frac{\Delta t}{\Delta V_{Pass}} \left(\sum P_f \bullet n_j A_f (1-\varepsilon)^{2/3} \right) \right\}^n = 0 \quad (9.18)$$

The quadratic formula, in terms of u_i^{n+1} is now employed where b,a and c are obtained from equation (9.18).

5. The Continuity Equation (9.13) is solved using the momentum values from at the n+1 "time" level from equation (9.18) where $AF_{Pres} = 100$.

6. Check convergence to steady state values by sensing whether the relative error is less than the agreed tolerance of 10^{-5} or the number of iteration/sweeps is below the maximum iteration/sweeps, I_{Max}, stipulated by the user. This value was set initially to 95,000 iterations. The steady state requirement for incompressible problems is calculated as:

$$\varepsilon_{Rel}^{n} = \frac{1}{NUMELE}\sqrt{\left[\frac{\sum_{CV=1}^{NUMELE}\left(\frac{\left|u_{CV}^{n+1}-u_{CV}^{n}\right|}{\Delta t_{CV}(L/u_{\infty})}\right)^{2}}{\sum_{CV=1}^{NUMELE}\left(u_{CV}^{n+1}\right)^{2}}\right]} \qquad (9.19)$$

7. If convergence has been achieved exit the procedure and display results otherwise begin computational sweep by going back to step 1.

General Remarks

By employing these novel amendments in the AC CBS FV algorithm for porous medium flows, stability and accuracy relative to the analytical solution were regained for this challenging benchmark.

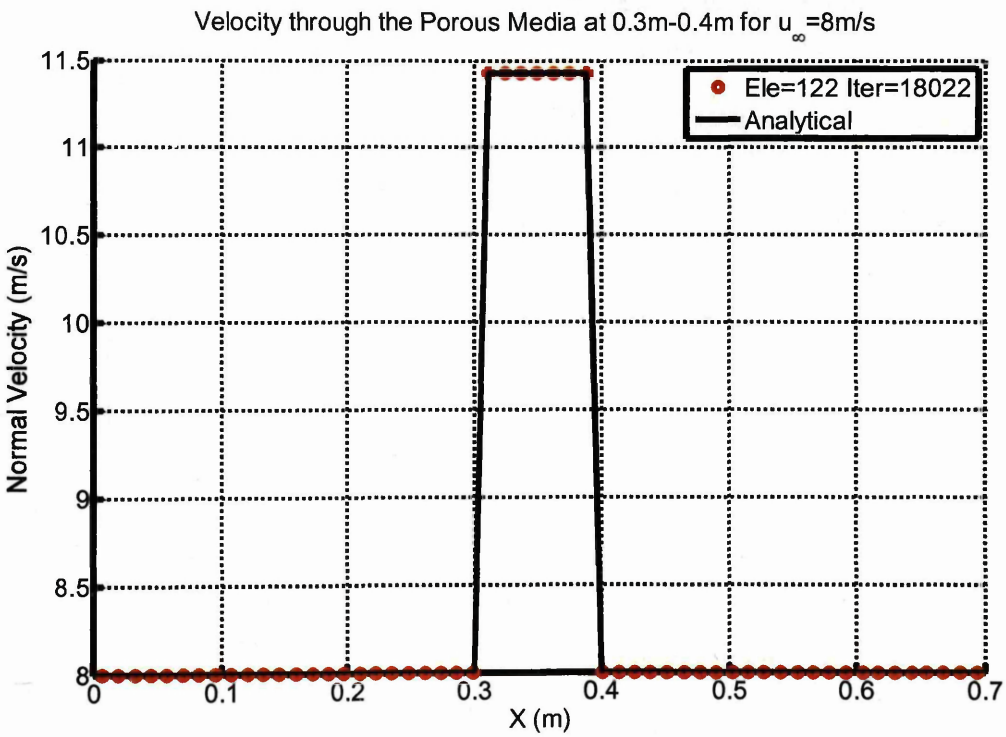

Figure 9-7- Normal velocity profile through the porous medium.

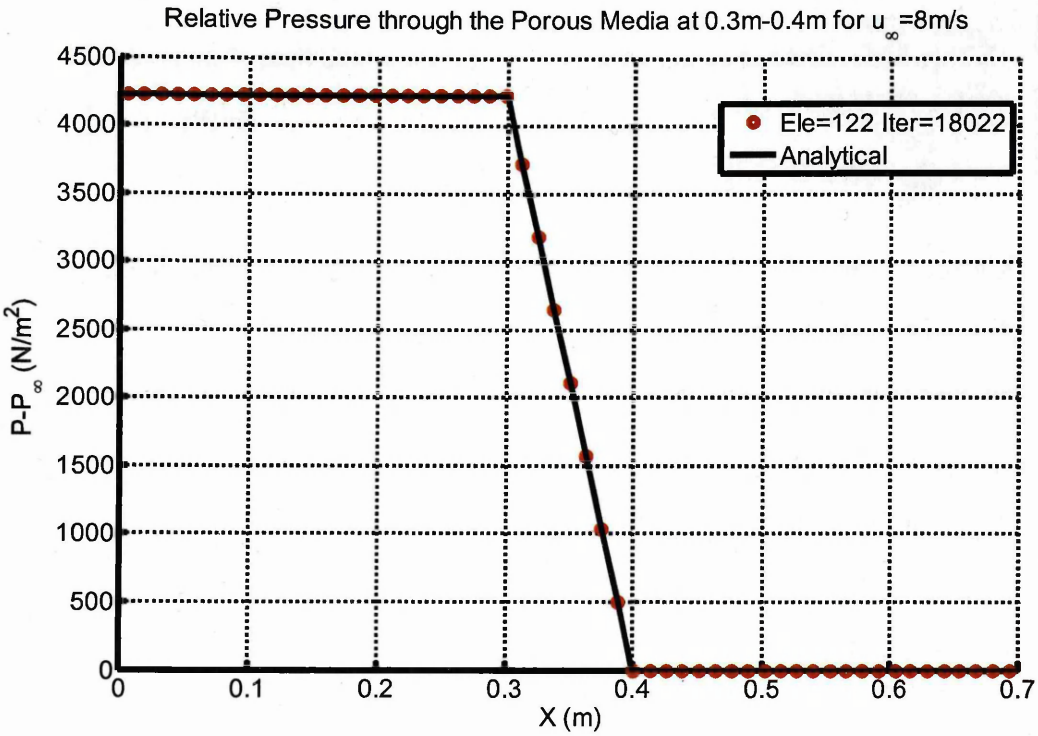

Figure 9-8- Pressure profile through the porous medium.

The range of free-stream velocities was increased so that the stability of the amended AC CBS could be gauged and verified before going onto compressible problems.

Table 9-2- Flow parameters for the higher speeds applied to incompressible porous flow.

Porous Media Length [m]	u_∞[m/s]	ρ_∞[kg/m^3]	μ_∞[kg/(ms)]	Re [-]	Nx	Ny	Nt
0.1	0.05	1.225	1.789	0.003423	56	2	112
0.1	8	1.225	1.789	0.0547792	56	2	112
0.1	20	1.225	1.789	0.136948	56	2	112
0.1	90	1.225	1.789	6.16266	56	2	112

Where Nx is the number of elements in the x direction.
Ny is the number of elements in the y direction.
Nt is the total number of elements in total.

9.3.1 Solver Results

The number of control volumes used to mesh the domain was 112. The inlet speed was initially set at 0.05m/s. After the convergence criterion was satisfied for a speed of 0.05m/s the inlet speed was changed to 8m/s, 20m/s and 90m/s and modelled. The following results show the velocity and pressure profile, as well as this, displayed in the legend, are the number of iterations required for convergence.

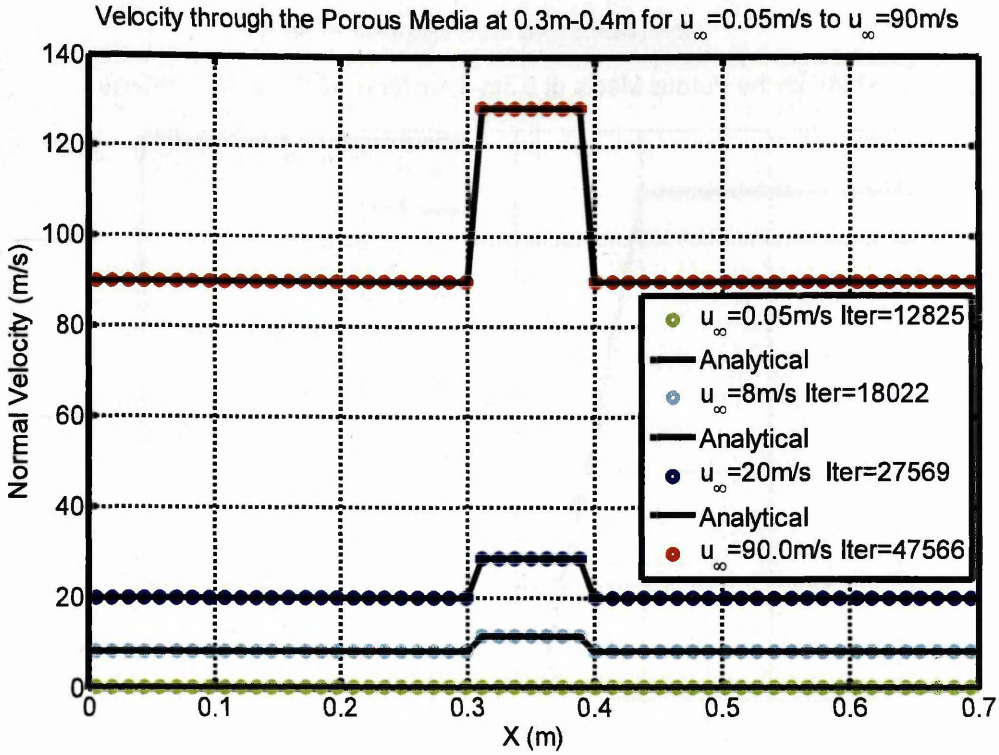

Figure 9-9- Normal velocity profile through the porous medium.

As seen in Figure 9-9 the computed velocity profiles for a free stream of 0.05m/s, 8m/s, 20m/s and 90m/s through a porous medium of 0.1m is both stable and accurate The y axis is dimensional velocity measured in m/s. The x axis is dimensional length. The above figure demonstrates that the velocity profile through the porous medium (PL=0.001m) can be accurately captured using AC CBS scheme in Section 9.3. Moreover the new sequential AC CBS as seen in Section 9.3 is more successful at capturing porous media than the wholly explicit approach equation (9.17) - (9.19).

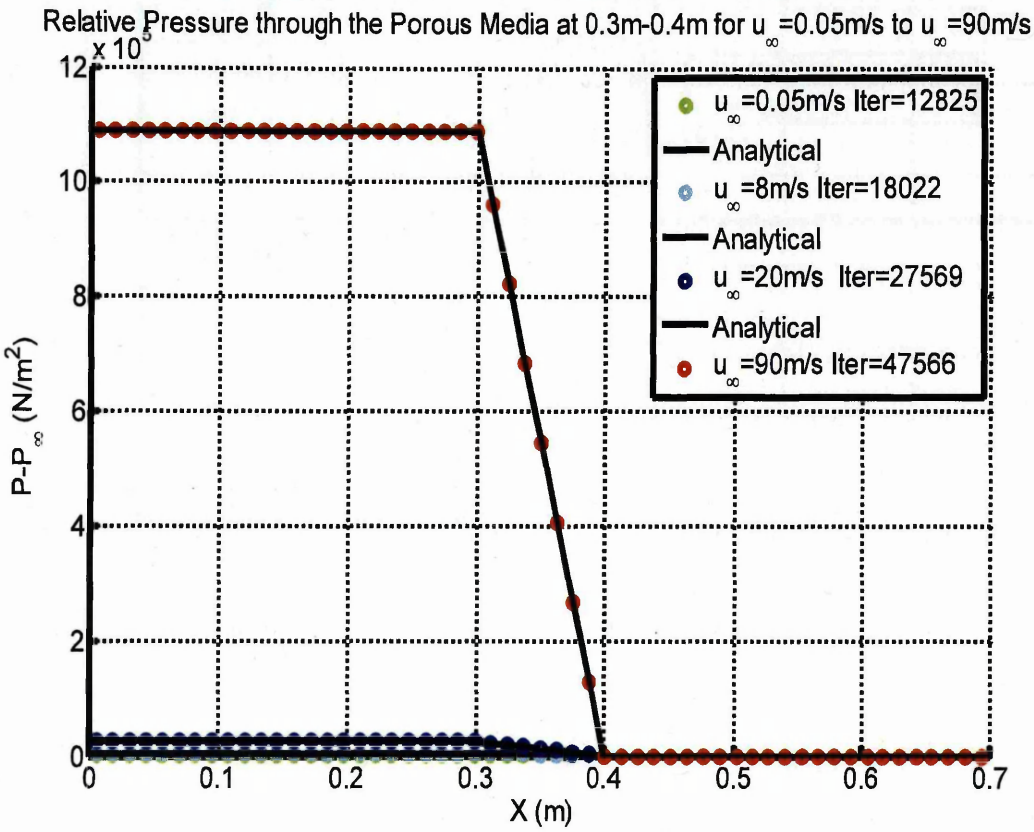

Figure 9-10: Pressure profile through the porous medium.

As seen in Figure 9-10 the computed pressure profile for 0.05m/s, 8m/s, 20m/s and 90m/s through a porous medium of 0.1m is stable and accurate. The y axis is dimensional pressure measured in N/m^2. The x axis is dimensional length. The above figure demonstrates that the pressure profile through porous media (PL=0.1m) can be accurately captured using AC CBS scheme as seen in equation Section 9.3.

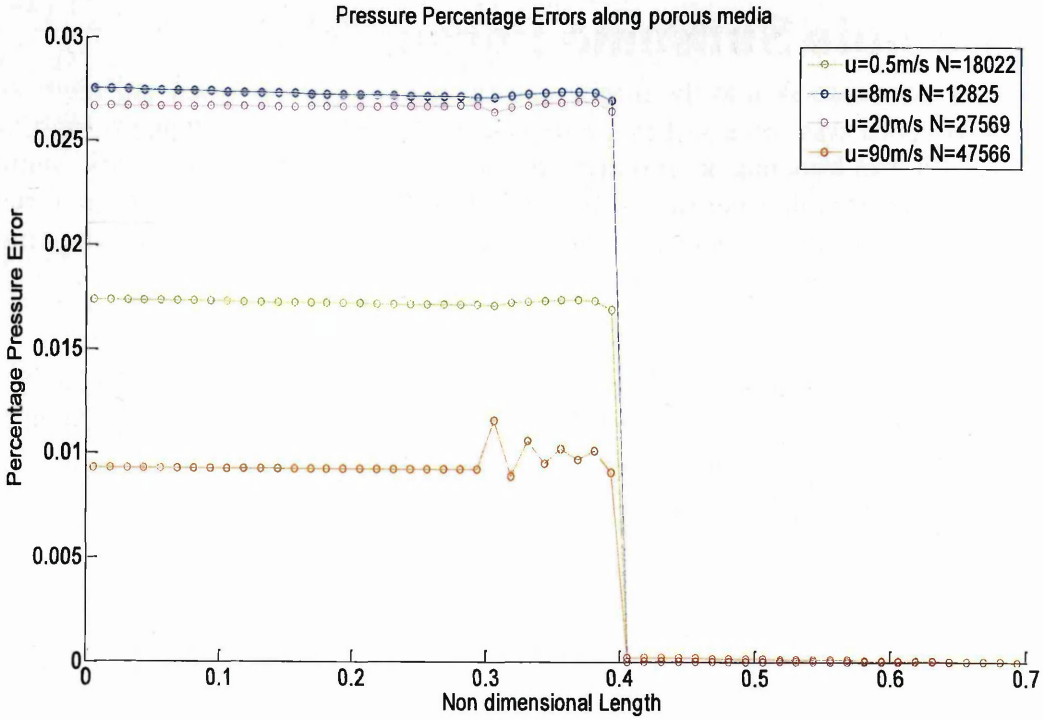

Figure 9-11: Percentage errors for the pressure through the domain.

As seen in Figure 9-11 the computed percentage error relative to the analytical pressure profile for the simulations set out in Table 9-2 i.e.u_∞ 0.05m/s, 8m/s, 20m/s and 90m/s are presented. The y axis is percentage error. The x axis is dimensional length. Most importantly for this revised approach all percentage errors in Figure 9-11 are below the 1% expected for a reliable CFD code. To summarize the CFD results for this problem;

- The results are encouraging as they prove that the amended AC CBS scheme can compute incompressible porous flows.
- The revised AC CBS algorithm works for inlet speeds ranging from 0.5m/s- 90m/s.
- The 1% tolerance has been satisfied for speeds of 0.5m/s up to 90m/s.
- By increasing the role that the continuity equation plays in the computation i.e. by favourably weighting the continuity equation (9.13), the more stable the FV AC CBS algorithm becomes. Alternatively if the momentum equation (9.18) becomes favourably weighted, this results in solution instability and divergence.
- The number of iterations required for convergence with 112 elements is approximately 12,000 iterations. As the intended case studies that will be tackled will have meshes with up to 100,000 control volumes this method is deemed to be uneconomical however it is still a marked improvement in terms of stability than the fully explicit method.

9.4 Compressible Subsonic Porous Flow

A compressible porous flow case akin to the incompressible porous flow specified in Figure 9-2 was studied where the flow speed was increased to a compressible speed of Mach=0.567 or u_∞=200m/s. Before going on to tackle this benchmark, appropriate studies were reviewed for a stable simulation tool including those on compressible porous flows [124], [169], [178], [182]. Within these research publications it was evident that the numerics for the pressure source term differs from the empirical tested Ergun, [189], source term used by Pantelis & Ritchie, [188].

Even though the different source terms in the mentioned publications are comparable. They all use an additional term proportional to the velocity, u. In order to make progress with this case the approach used by F Cheuret & Steelant, [124], is utilized as it is the most recent.

$$\nabla P = -\frac{(1-\varepsilon)\mu}{\kappa} u - \frac{(1-\varepsilon)^2 C_F \rho}{\sqrt{\kappa}} |u| u \tag{9.20}$$

Where C_F is the Forchiemer coefficient
for the carbon/carbon sample in [124] the κ is the permeability variable is 3.87E-13 m^2.

For this research however only the second ordered term as seen in (9.20) have been utilized, mainly because at high speeds (high u and low μ) the contribution of the second ordered term will dominate the rhs of (9.20). i.e.

$$\frac{(1-\varepsilon)^2 C_F \rho}{\sqrt{\kappa}} |u| u \gg \frac{(1-\varepsilon)\mu}{\kappa} u \tag{9.21}$$

Therefore for the numerical investigations to follow, the effect of this 1st ordered term was ignored for the following high speeds (high u and low μ) modelled. This means that the pressure loss through a porous sample was simplified to:

$$\nabla P = -\frac{(1-\varepsilon)^2 C_F \rho}{\sqrt{\kappa}} |u_n| u_n \tag{9.22}$$

Along with the lessons learnt from the previous benchmark, 1D incompressible, isothermal porous flow, careful study and evaluation of the approach recommended by the Cheuret & Steelant, [124], publication was carried out.

9.4.1 Numerical Formulation for Compressible Porous Flow

The following formulation again treats the porous medium in similar fashion to the full fluid continuum. This is also done by solving the Navier-Stokes equations inside and outside the porous medium. The first challenge for this compressible non-isothermal benchmark is trying to capture the changing temperature through the porous media. To do this we need to amend the CBS scheme utilizing the following numerics. The pressure source term in (9.22) needs to be calculated implicitly not explicitly. It is displayed below in semi discrete form. By substituting equation (9.23) in place of the explicit Ergun source term seen in equation (9.3) we obtain.

$$\rho u_i^{n+1} = \rho u_i^* - \frac{\Delta t}{\Delta V}\left(\sum P_f \bullet \mathrm{n}_i A_f (1-\varepsilon)^{2/3} + \frac{(1-\varepsilon)^2 C_F \left(\rho_{CV}^{n+1}\right)^2}{\rho_{CV}^n \sqrt{\kappa}} \left|\mathbf{u}^{n+1}\right| u^{n+1} \Delta V \right) \tag{9.24}$$

$$\Delta t \frac{(1-\varepsilon)^2 C_F}{\rho_{CV}^n \sqrt{\kappa}} \left(\rho u_{CV}^{n+1}\right)^2 + \rho u_{CV}^{n+1} - \left\{ \rho u_{CV}^* - \frac{\Delta t}{\Delta V} \left(\sum P_f \bullet \mathrm{n}_i A_f (1-\varepsilon)^{2/3} \right) \right\} = 0 \qquad (9.25)$$

$$\rho u_i^{n+1} = \frac{-b + \sqrt{b^2 - 4ac}}{2a}$$

$$b = 1$$

$$a = \frac{(1-\varepsilon)^2 C_F}{\rho_{CV}^n \sqrt{\kappa}} \Delta t$$

$$c = -\rho u_i^* + \frac{\Delta t}{\Delta V} \left(\sum P_f \bullet \mathrm{n}_i A_f (1-\varepsilon)^{2/3} \right)$$

The next challenge for this case is trying to capture the discontinuity across the porous-gas interface. The velocity changes instantaneously for the incompressible porous case, therefore it is assumed that the density and temperature change instantaneously for the compressible case also [124]. According to Cheuret & Steelant [124], the transient properties ρ_f, u_f and T_f are mathmatically captured using the following numerics.

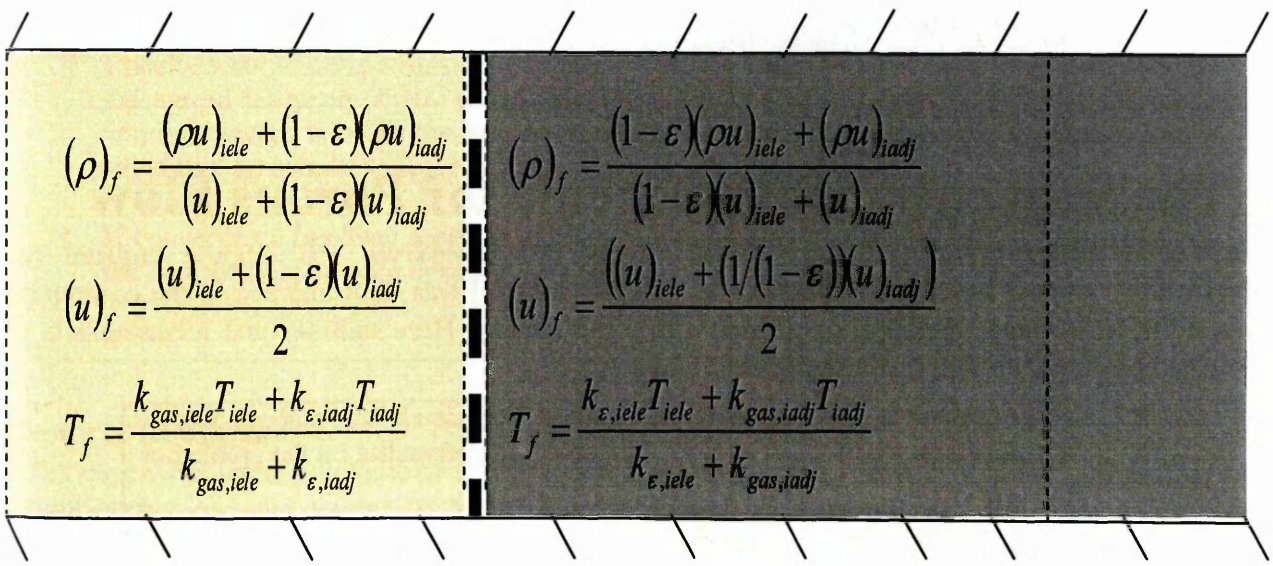

Figure 9-12: The physical quantities for non-isothermal porous flow need to be handled carefully. Where the following terms have been lifted from Cheuret & Steelant, [124].

Next the thermal conductivity term, k, is treated as a lump sum value, by weighting the coolant and the solid conductivity values. This is a consequence of Cheuret & Steelant, [124] the assumption of thermal equilibrium between the coolant and porous structure. Basically the interstitial heat conduction value, k_{int}, is treated by weighting the gases' and solids' thermal conductivity values as seen in Cheuret & Steelant, [124]. Where the thermal conductivity, k_{int} is calculated as a weighted value from the equation below.

$$k_{\text{int}} = -2k_{CC/Sic} + \frac{1}{\frac{(1-\varepsilon)}{2k_{CC/Sic} + k_{eff}} + \frac{\varepsilon}{k_{CC/Sic}}} \qquad (9.26)$$

$$k_{eff} = k_{lam} + k_{turb}$$

$$k_{turb} = \frac{\mu_{turb} C_p}{\mathrm{Pr}_{turb}}$$

For this research the turbulent effects were neglected for the thermal conductivity i.e. $k_{eff} = k_{lam}$ where $k_{lam} = 0.025\mathrm{W}/mK$ and $k_{CC/Sic} = 40\mathrm{W}/mK$.

Where the enthalpy equations in semi-discrete form is given by:

$$\rho E_{CV}^{n+1} = \rho E_{CV}^{n} - \frac{\Delta t}{\Delta V}\left(\begin{array}{l} \sum_{f=1,TOTFIC} \left(\rho u_j E\right)_f \bullet n_j A_f (1-\varepsilon)^{2/3} + \frac{\partial P}{\partial t} \\ - \sum_{f=1,TOTFIC} \left(u_j \tau_{ij}\right)_f \bullet n_j A_f (1-\varepsilon)^{2/3} - \sum_{f=1,TOTFIC} k_{\mathrm{int}} \left(\frac{\partial T}{\partial x_j}\right)_f \bullet n_j A_f \end{array} \right) \tag{9.27}$$

Where the enthalpy on the porous-gas interface, was given an upwind procedure, switching the value depending on the direction of the gas flow.

$$\rho E_f = \begin{cases} \rho E_{gas} & = u_f > 0 \\ \rho E_{por} & = u_f < 0 \end{cases}$$

Where the face f is seen as the broken black line in Figure 9-12.

9.5 The Sequential CBS Scheme for Porous Flow

The use of a compressible sequential CBS scheme was employed that should capture the compressibility and non-isothermal effects. The FV CBS method was implemented in the computing language FORTRAN and the simulations run within the cluster. Here stability and robustness is of paramount importance for this challenging benchmark.

1. The CBS scheme incorporates local pseudo time stepping. The pseudo time step is given by the following equation: where C is the Courant number and depending on the problem is usually < 0.5.

$$\Delta t_{CV}^{n} = C \frac{h_{CV}}{c_{CV}^{n} + \sqrt{\left(u_i u_i\right)_{CV}^{n}}} \tag{9.28}$$

2. Intermediate Momentum

$$\rho u_i^{*} = \rho u_i^{n} - \frac{\Delta t}{\Delta V_{Pass}}\left(\begin{array}{l} 0 - \sum_{i=1,TOTFIC} \left(\tau_{ij} \bullet n_j A\right)_f (1-\varepsilon)^{2/3} \\ + \frac{\Delta t}{2} u_k \sum_{i=1,TOTFIC} div\left(\rho u_i u_j\right) \bullet n_j A_f (1-\varepsilon)^{2/3} \end{array} \right) \tag{9.29}$$

3. Corrected Momentum

$$\frac{\left(1.75(1-\varepsilon)T_b\right)}{273 d_p \varepsilon^3 \rho_\infty} \Delta t \left(\rho u_i^{n+1}\right)^2 + \rho u_i^{n+1} - \left\{ \rho u_i^{*} - \frac{\Delta t}{\Delta V_{Pass}} \left(\sum P_f \bullet \mathrm{n}_i A_f (1-\varepsilon)^{2/3} \right) \right\} = 0 \tag{9.30}$$

Where b,a and c are obtained from the equation (9.30).

4. The Continuity Equation is solved using the momentum values at the n+1 "time" level

$$\rho^{n+1} = \rho^n - AF_{\text{Pres}} \frac{\Delta t}{\Delta V} \left(\sum_{f=1,TOTFIC} \rho u_j \bullet n_j A_f (1-\varepsilon)^{2/3} + u_k \frac{\Delta t}{2} \sum_{f=1,TOTFIC} \frac{\partial P}{\partial x_j}_f \bullet n_j A_f \right) \quad (9.31)$$

5. Enthalpy Equation

$$\rho E^{n+1} = \rho E^n - \frac{\Delta t}{\Delta V} \left(\begin{array}{l} \sum_{f=1,TOTFIC} \left(\rho u_j E\right)_f \bullet n_j A_f (1-\varepsilon)^{2/3} + \frac{\partial P}{\partial t} \\ - \sum_{f=1,TOTFIC} \left(u_j \tau_{ij}\right)_f \bullet n_j A_f (1-\varepsilon)^{2/3} - \sum_{f=1,TOTFIC} k_{\text{int}} \left(\frac{\partial T}{\partial x_j}\right)_f \bullet n_j A_f \\ + \frac{\Delta t}{2} u_k (1-\varepsilon)^{2/3} \left(\sum_{f=1,TOTFIC} \left(\frac{\partial \left(\rho E u_j\right)}{\partial x_j} \bullet n_j A \right)_f + \sum_{f=1,TOTFIC} \left(\frac{\partial \left(u_j P\right)}{\partial x_j} \bullet n_j A \right)_f \right) \end{array} \right) \quad (9.32)$$

The k_{int} value seen in the conduction term is calculated by using a weighted value as seen in (9.26) where For this research the turbulent effects were neglected for the thermal conductivity i.e. $k_{eff} = k_{lam}$ where $k_{lam} = 0.025W/m-K$ and $k_{CC/Sic} = 40W/m-K$

6. To close the equation set the Ideal Gas Law, Sutherlands Law and the Prandtl Law are used. The Prandtl number, Pr, which is assumed constant for ideal gases at moderate temperature is 0.74 [82].

7. Check convergence to steady state values by sensing whether the relative error is less than the agreed tolerance of 10^{-5} using equation (9.19) in terms of density. or the number of iteration/sweeps is below the maximum iteration/sweeps, I_{Max}, stipulated by the user, this value was set initially to I_{Max} =95,000 iterations.

8. If convergence has been achieved exit the procedure and display results otherwise re-start the computational sweep by going back to step 1.

General Remarks

After extensive hand calculations it was found that the equation given by [124] was inconsistent for neighbouring element values of temperature and thermal conductivity. By using euqation (9.33) below instead of (9.26) with an amended equation seen below and derived in the appendices.

$$k_{\text{int}} = k_{CC/Sic} - \frac{1}{\frac{(1-\varepsilon)}{k_{CC/Sic} - k_{eff}} + \frac{\varepsilon}{k_{CC/Sic}}} \quad (9.33)$$

Equation (9.33) is now physically consistent with adjacent temperature values. We are concerned primarily with getting a stable solution to this challenging problem therefore reliability relative to accuracy for this case is a secondary consideration.

9.5.1 Boundary Condition

Since there are no known closed form solutions for pressure and velocity for compressible porous flows that we can employ to evaluate the Finite Volume CBS secheme we thereby carry on the theme of plug flow as seen in Section 9.2. A comparison between the FV CBS scheme numerical solution and a constant mass flow throughout the domain of , $\rho_\infty u_\infty = 245kg/m^2 s$, is conducted. Whereby extending the speed from the incompressible problem in Section 9.2 to 200m/s.

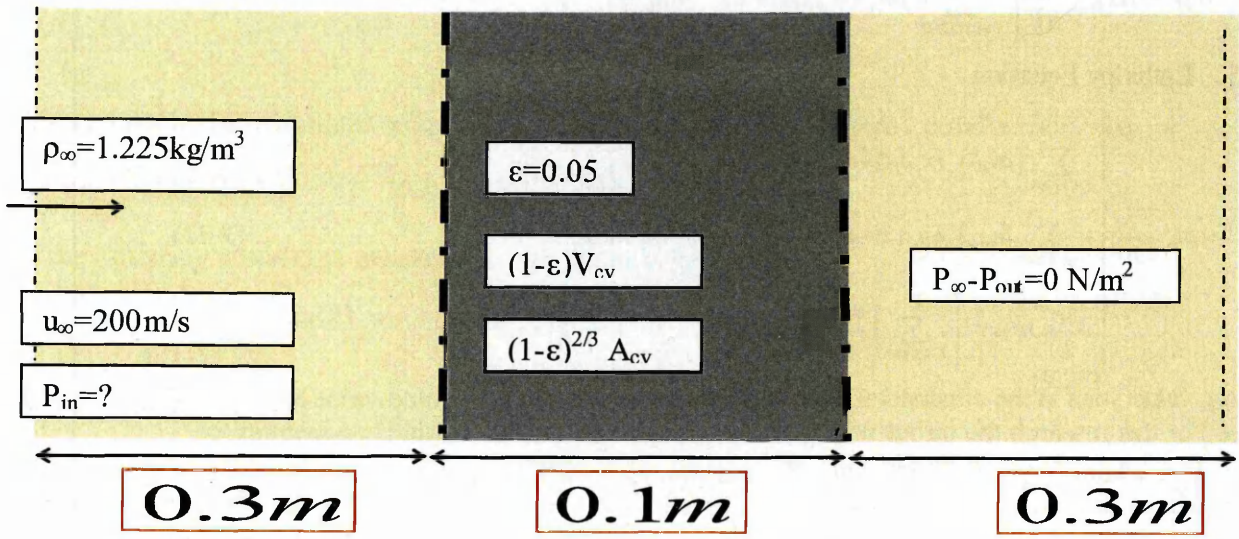

Figure 9-13: Schematic of compressible porous flow.

Table 9-3-Parameters for Compressible flow through a porous medium where the porous medium is treated as part of the fluid continuum.

Porous Media Length [m]	u_∞[m/s]	ρ_∞[kg/m^3]	μ_∞[kg/(ms)]	Re [-]	Nx	Ny	Nt
0.1	200	1.225	1.789	13.6905	56	2	112

Where Nx is the number of control volumes in the x-direction.
Ny is the number of control volumes in the y-direction.
Nt is the total number of control volumes.

9.5.2 Analytical Solution

A final solution with a constant mass flow, $\rho_\infty u_\infty = 245 kg/m^2 s$, throughout the domain was accepted as a realistic solution. We are primarily concerned with getting a stable solution to this challenging problem therefore reliability relative to the analytical solution for this benchmark case is a secondary consideration.

9.5.3 Solver Results

Unfortunately this strategy was unstable and eventually lead to divergence. Although impressive flow computations were carried out for incompressible porous flow benchmarks with a similar FV AC CBS method, however the FV CBS scheme cannot be said to be stable for compressible porous flow problems. Various amendments to the sequential CBS scheme were carried out but with limited success.

After hand calculation on the compressible porous medium flow the decision was made to treat the porous medium as a boundary condition like the strategy employed in Langener et al, [177]. Using this strategy for porous media models was in general more stable but at the expense of applicability for all conceivable application scenarios. The boundary condition approach as seen in Langener et al. [177], can only be applied to the case where coolant is forced through the porous medium and

perpendicular to the main gas flow. Therefore the compressible benchmark seen in Figure 9-4 was neglected over the new benchmark discussed in the next chapter.

9.6 Concluding Remarks

This chapter presents a working 2nd ordered explicit algorithm for incompressible, viscous, isothermal porous flow that is robust and reliable, essential requirements for CFD software tools. The chapter then goes on to present, an as of yet unsuccessful algorithm for compressible, non-isothermal porous flows. To mitigate the effect that the boundary conditions and domain size has on the algorithm both problems were in the Subsonic regime.

9.6.1 Summary of AC CBS Algorithm for Incompressible Porous flow

The explicit AC CBS algorithm which was applied to computing the boundary layer flow over a Subsonic plate as seen in Chapter 7 was initially applied with an explicit Ergun, [189], source term without success to the incompressible porous flow benchmark. For incompressible porous media flow, the pressure drop along the length of the porous bed has been tested empirically and is accounted by a derivative of Ergun's law as presented in Pantelis & Ritchie, [188].

A high free stream viscosity was employed in this chapter reducing the free stream Reynolds number because this study is mainly concerned with developing a stable strategy for laminar gas flow on porous media before extending the strategy for high Reynolds number, turbulent gas flows on porous media. The FV CBS scheme was able to handle problems that were up until recently unstable, after novel modifications to the FV CBS algorithm, which are 1) computing the Ergun term implicitly made to the code as seen in equation (9.11), and 2) neglecting the 1st ordered convection terms in the intermediate momentum equation (9.17). This modified procedure could handle speeds from 0.05m/s to 90 m/s. Now further research is needed to check the maximum speed that can be modelled. After the incompressible isothermal porous flow was modelled then the next milestone was to capture compressible, non-adiabatic flow within a porous medium using the modifications from Cheuret et al, [116], and the numerics that allowed stable incompressible porous flow computations.

9.6.2 CBS Algorithm Instability for Compressible Porous Flow

After extensive experimentation and amendments it was apparent that for the case seen in Figure 9-13 the CBS algorithm as seen in (9.28)- (9.32) is unstable and eventually leads to divergence. For all the amended variants of the FV CBS algorithm tested the algorithms did not achieve stability. Therefore other more recent publications for transpiration cooling effecting Supersonic applications were reviewed for successful strategies such as the boundary condition approach developed by Kays, Crawford, & Weigand [71], and favoured by Langener et al, [177]. The approach developed by Kays, Crawford, & Weigand [71], in the recent research into transpiration cooling for Hypersonic applications was utilized and is presented in Chapter 10.

10. NOVEL APPLICATION HYPERSONIC FLOW SIMULATIONS WITH POROUS BOUNDARIES

10.1. Introduction

This final chapter will look at Hypersonic wind tunnel experiments published in Langener et al [177], and compare their measurements with the computational results using a modified working FV CBS based computational model for porous media. The modified CBS method is coupled with the Kays et al [71], porous boundary method to allow this comparison. This fully explicit CBS technique is embedded within the modular framework of PHYSICA.

The cooling efficiency of Carbon/Carbon (C/C) material with randomly orientated fibres and porosities ($\varepsilon=V_{void}/V$) of 10.7% and 11.0% was experimentally assessed. Using the test facility available at the institute of Aerospace Thermodynamics (ITLR) at the University of Stuttgart, it is possible to model operational modes of a RAMJET and SCRAMJET combustor at flight Mach numbers 2-6, at an altitude of 32km. In the hot gas experiments with C/C as the transpiration-cooled CMC material, total temperatures up to $T_{t,g}=1060K$ at a main flow Mach number of M=2.1 were set at moderate total pressure levels of $P_{t,g}=0.3Mpa$. During the experiments, the steady state surface temperature was measured with thermocouples and an infrared camera system.

Kays et al. [71], developed a numerical approach for modelling the thermal performance of transpiration cooled boundaries by accounting for the fluid viscosity with respect to the through flow pressure and temperature change. Their computational model showed good agreement with the experimental data for different thermal loads and coolants within the Langener et al [177], investigation and will be used here.

10.1.1 Transpiration Cooling

For design purposes of future Hypersonic Cruise air-breathing vehicle (CAVs) geometries, numerical tools have to be available to evaluate external layouts of such CAVs as well as the transpiration - cooled components as discussed by Cheuret & Steelant, [124]. Therefore, available tools have to be extended and models capable of simulating thermal behaviour and momentum loss in porous structures have to be developed. The features of the co-located CBS FV scheme, as discussed by Nithiarasu P & Codina R [131], are its reliability at modelling Supersonic inviscid flows and its flexibility on unstructured grids. In addition to these fundamental properties, which is an additional advantage, the CBS algorithm in its Finite Element version allows porous flow extensions as studied by [136].

Although numerous high-ordered upwind schemes have been developed by the CFD community such as [85], [86], [114], [115], [128], [137] the inconvenience involved in their implementation is magnified when complex unstructured grids and 3-D extensions are envisaged. These deficiencies have motivated the development of this research to identify and develop a central differencing like scheme for Hypersonic high-temperature flow coupled with porous media flow.

A derivative of the Ergun Source term through porous media as seen in Pantelis & Ritchie, [188], was implemented into the sequential procedure and has since been successfully benchmarked against incompressible iso-thermal flow. When compressible non-isothermal flow through porous media is tackled using the Ergun Source term coupled with careful amendments for compressibility and non-isothermal effects at the interface, this results in instability.

Thus a recently studied modified approach was taken from Langener et al, [177], which treats the porous component and the coolant injection as a boundary condition. This means that the two sets of equations are used to model the porous flow,. The Navier-Stokes equations are used to capture the flow in the main channel and the second set of equations captures the coolants flow from its porous inlet to the surface of the porous membrane, which is described by Kays et al, [71]. The approach follows a 1-D heat balance approach with semi-empirical assumptions, and for the heat transfer coefficients it also takes into consideration the changing viscosity and pressure loss characteristics for the injected coolant. For a more in-depth analysis of this approach review [1], and [2].

10.1.2 Porous Boundary Condition Approach

This chapter documents the comparison of the FV CBS algorithm coupled with the porous model described by Kays et al. [71], against the wind tunnel experiments described in [177]. Hopefully close agreement between the FV CBS algorithm results and the experimental data in Langener et al, [177], will emerge, and this is the focus of the final benchmark.

The CFD tool in Langener et al, [177], was the commercial pressure based solver CFD-ACE+ which employs a second order upwind discretization in combination with a Min-Mod limiter (see Cheuret & Steelant, [124]). For porous computations this CFD tool is coupled with Kays et al. [71], showed good agreement with the experimental data in [177] for different thermal loads and varying fluid-type coolants.

Before going on to present the numerics of the Kays et al, [71], porous boundary condition approach an overview of the Hypersonic wind tunnel experiment is presented to familiarize the reader with the physics and the salient mathematical modelling issues involved. A basic schematic of the wind tunnel is presented below.

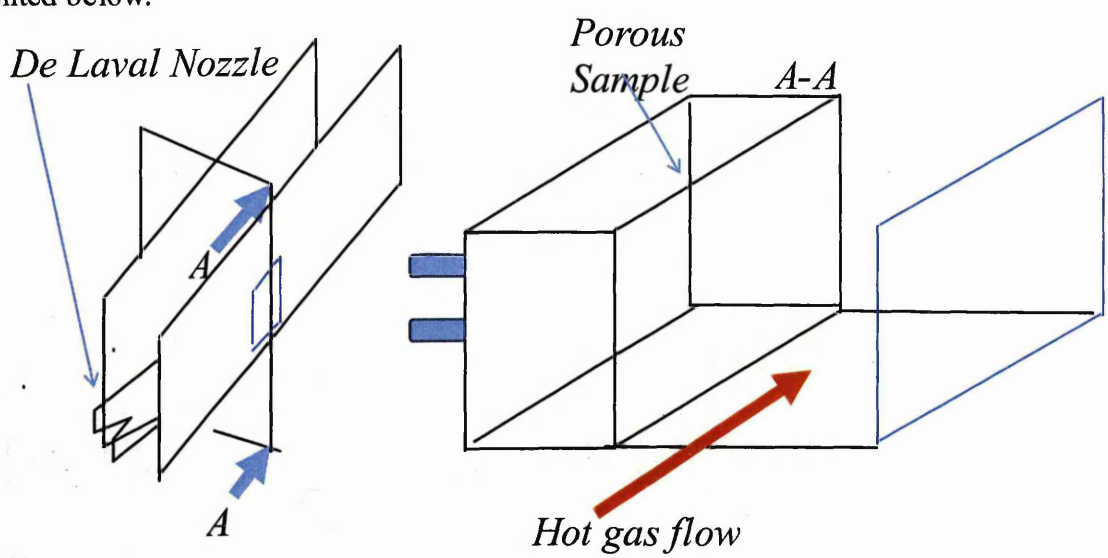

Figure 10-1 Longitudinal view of the Experimental setup in Langener et al, [177].

Figure 10-1 shows a view, specifically in the longitudinal direction of the high speed wind tunnel. To experimentally quantify the cooling efficiency of the porous components before the gas enters the nozzle inlet, heating filaments are used to heat the gas up to a maximum temperature of 1060K and a total pressure level of 0.3 MPa. The main De-Laval nozzle accelerates hot air to a Mach number of Mach=2.1. Embedded within the walls of the wind tunnel is a CMC-SiC sample with a porosity of 11%. Within the porous sample are 4 thermocouples. As a control run the sample's cooling efficiency is assessed without coolant blowing using the 4 thermocouples to measure the heat load.

As a back up to the thermocouple data, infrared thermography was used to obtain a 2-D surface temperature map of the porous material. A Mitsubishi IR M700 thermal imager (wavelength range of 1.2-5.9mm) was used and the data were recorded by the IRBIS 3.0 software by Infratec, Gmbh. The resolution of the camera was 720x480 pixels/mm for this setup. Within the setup, unknown optical quantities appear such as the object's emissivity, reflected radiation, and the temperature of the optical path. Therefore the IR data were calibrated *in situ* using the thermocouple data for the whole set of coolant mass mass-flow rates (F=0 to F_{max}) to cover the relevant temperature range.

A 2-D schematic of the Y cross section of the sample and the hot gas chamber is shown below in Figure 10-2.

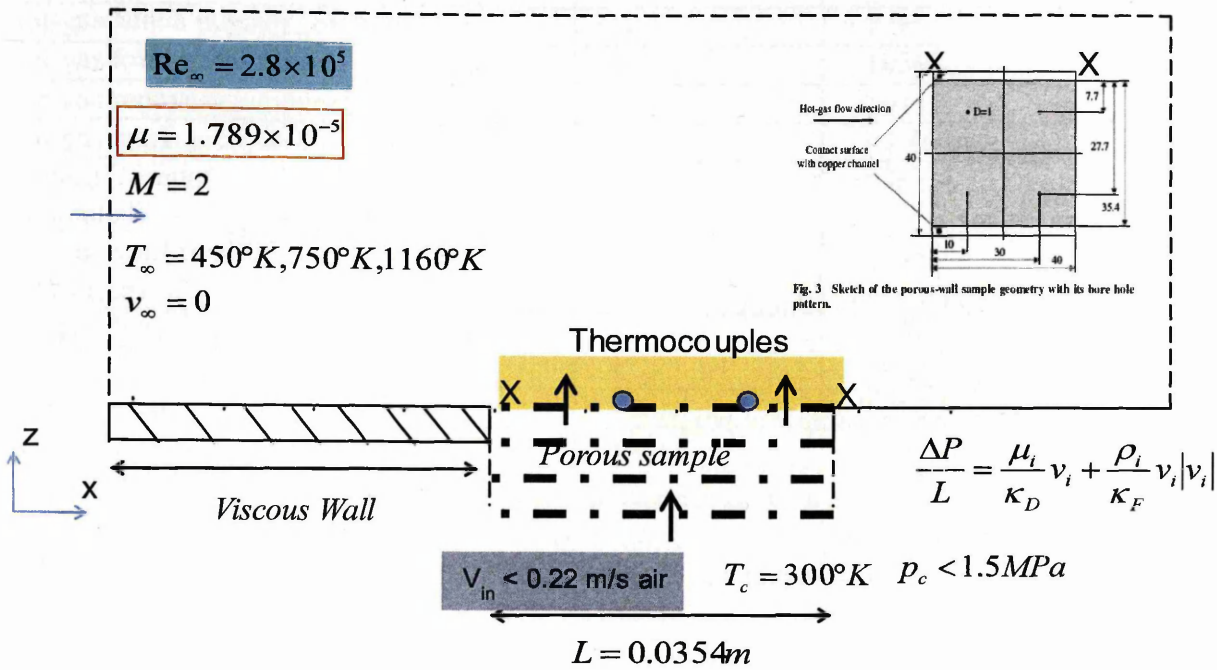

Figure 10-2: ITLR Supersonic combustion and hot gas flow experimental set up.

Pressure at the coolant inlet (plenum) is varied for the main battery of tests. By changing the pressure at the plenum we can study how the coolant's velocity effects the cooling efficiency of the porous CMC component. The velocity of the coolant was measured with a thermal mass controller where a maximum velocity at the coolant inlet was restricted to a $v_{in} < 0.22$m/s for air. Point temperature values are measured using the four thermocouples and the surface temperature distribution is taken with an infrared camera system where sapphire windows are embedded within the wind tunnel allowing optical access.

The second battery of tests carried out in Langener et al, [177], quantified another relationship, that is, the effect that different coolants have on the cooling efficiency. Again measurements are done using the four thermocouples and the infrared camera system, where three different coolants were employed: gaseous air, argon and helium. The insight that this experiment provides is an important and informative example for developing adequate mathematical models to predict heat flux to the porous wall. The mathematical models will then be evaluated by applying them to the modelling of Hypersonic CAVS transpiration cooled components.

10.1.3 Numerical Formulation for the Porous Boundary Condition

The approach favored by Langener et al, [177], which was originally developed by Kays et al, [71], captures an important relationship. The mass flow is constant through the porous media however the coolant's viscosity, density and temperature change over the porous media sample. The mathematical approach and the empirical relationships used are listed below. Firstly an extended Darcy-Forcheimer equation is derived assuming thermal equilibrium within the sample for a one dimensional situation. The non-dimensional energy equation is given by:

$$\frac{d\vartheta}{dX} = \frac{1}{C_{col}} \frac{d^2\vartheta}{dX^2} \tag{10.1}$$

$$\vartheta = \left(\frac{T_i - T_{col}}{T_w - T_{col}} \right) \tag{10.2}$$

$$X = \left(\frac{x}{L} \right) \tag{10.3}$$

$$C_{col} = \left(\frac{\rho_{col} C_p v_{col,in} L}{k_{col}} \right) \tag{10.4}$$

v_{in}- Velocity in the tangential direction (m/s)
L- sample thickness (m)
k_{col}- thermal conductivity (W/m K).
i- is the i location inside the porous sample at height x

At the hot gas side (X=1) of the porous wall section, a constant temperature (ϑ=1) is used, which can be measured. The coolant side (X=0) is assumed to be a coolant inlet temperature (ϑ=1), leading to the solution as devised by Kays et al, [71].

$$\vartheta = \frac{e^{C_{col}X} - 1}{e^{C_{col}} - 1} \tag{10.5}$$

These investigated experiments and the future applications justify a first hypothesis, where the flow velocities and the relevant coolant properties yield a cooling parameter C_{col} which is relatively small ($0 < C_{col} < 1.51$). This important point means that the temperature distribution within the CMC wall for simplicity can be approximated by a linear function. Where;

$$T_{col,i} = T_{col,in} + (T_w - T_{col,in}) \frac{x}{L} = T_{col,in} + b \frac{x}{L} \tag{10.6}$$

Table 10-1-Properties of the investigated samples from Langener et al, [177].

	L (m)	ε (%)	K_D (m^2)	K_F (m)	ρ(kg/m^3)	C_p(J/kg K)	k (W/m K)
Sample 1	10 x10^{-3}	11	9.07x10^{-14}	1.72x10^{-8}	1400	1300	14
Sample 2	5 x10^{-3}	10.7	6.18x10^{-14}	3.88x10^{-8}	1400	1300	14

Table 10-2- Parameters for modified Kays et al, [71] model with heat conduction.

Name	Symbol	Value
Hot-gas Mach number (measured)	M	2.06
Hot-gas total temperature (measured)	$T_{t,g}$	1039K
Hot-gas recovery temperature	$T_{r,g}$	1011K
Hot-gas static pressure (measured)	$P_{s,g}$	0.346 bar
Stanton number without blowing (estimated)	$St_{g,o}$	0.0034
Porous- wall temperature without blowing (measured)	$T_{w,0}$	644K
Cooper Temperature (measured)	T_{cu}	317K
Specific heat capacity hot-gas	C_p	1024 J/(kg K)
Specific heat capacity coolant: air	$C_{p,col}$	1010 J/(kg K)
Specific heat capacity coolant: Ar	$C_{p,col}$	525 J/(kg K)
Specific heat capacity coolant: He	$C_{p,col}$	5193 J/(kg K)
Coolant temperature (measured) f(F)	T_{col}	309 K
Hot-gas bulk velocity	u_g	979 K
Hot-gas density	ρ_g	0.210 kg/m^3
Reynolds number	Re_d	269737
Prandtl number	Pr	0.686

By incorporating the general power law, equation (10.6) is used to locally determine the local coolant viscosity for:

$$\mu_{i,col} = \mu_\infty \left(\frac{T_{i,col}}{T_\infty} \right)^{0.7} = \mu_\infty \left(\frac{T_{in,col} + b(x/L)}{T_\infty} \right)^{0.7} \tag{10.7}$$

where b- temperature difference of coolant between the two sides of the porous sample

T_{in} -temperature of coolant at the plenum inlet

$$\frac{P_{in,col}^2 - P_{out,col}^2}{2P_{in,col}L} = \left\{ \begin{array}{l} \dfrac{\mu_{in,col}}{K_D} \mathrm{v}_{in,col} \dfrac{1}{\frac{b}{2}(n+2)} \left[\left(1 + \dfrac{b}{T_{in,col}} \right)^{n+2} - 1 \right] \\ + \dfrac{\rho_{in,col}}{K_F} \mathrm{v}_{in,col}^2 \left(1 + \dfrac{b}{2T_{in,col}} \right) \end{array} \right\} \tag{10.8}$$

$$0 = \left\{ \frac{\rho_{in,col}}{K_F} \left(1 + \frac{b}{2T_{in,col}} \right) \mathrm{v}_{in,col}^2 + \frac{\mu_{in,col}}{K_D} \frac{1}{\frac{b}{2}(n+2)} \left[\left(1 + \frac{b}{T_{in,col}} \right)^{n+2} - 1 \right] \mathrm{v}_{in,col} - \frac{P_{in,col}^2 - P_{out,col}^2}{2P_{in,col}L} \right\} \tag{10.9}$$

All the parameters in equation (10.9) except one $v_{in,col}$ are obtained from Table 10-2 . The pressure at the coolant wall outlet is captured at the boundary node using the computational scheme in the hot channel. Then $v_{in,col}$ is obtained from the quadratic equation, an average value for $v_{in,col}$ from all cells on the porous boundary is the next step.

$$\mathrm{v}_{in,col} = \frac{1}{VBOUND} \sum_{f=1,VBOUND} \left(\mathrm{v}_{in,col} \right)_f \tag{10.10}$$

This average inlet coolant velocity , $v_{in,col}$, value for, v_{in}, is assumed by the author as a global value and is flowing out of the plenum into the porous membrane where VBOUND is the number of control volumes, that have a face on the porous boundary. Note that VBOUND varies for different grid resolutions.

$$F_{Blow} = \frac{\rho_{col}\hat{v}_{in,col}}{\rho_{\infty}u_{\infty}} \tag{10.11}$$

Except for $v_{in,col}$, all parameters on the right hand side of equation (10.11) can be obtained from Table 10-2. To compensate for the lateral heat conduction appearing in the experimental setup the Kays et al, [71], model sets up a simplified heat balance, using the following formula:

$$h_{g,0}\left(T_g - T_w\right) = \rho_{col} v_{in} C_{p,col}\left(T_w - T_{col}\right) + B(T_w - T_{cu}) \tag{10.12}$$

where T_{cu} is the temperature of the water cooled cooper pipes (317K)
$T_{w,0}$ is the temperature across the sample without blowing (663.63K)
h_g is the heat transfer coefficient.

The 1st, 2nd and 3rd terms denote the convective heat transfer, internal cooling and the heat conduction losses respectively. Here the coefficient B accounts for the thermal resistance from the porous surface to water cooled cooper parts at steady state. Thus B can be determined from a heat balance of the uncooled case where heat is laterally conducted onto the cooper pipes [177]: From equation (10.12) the 1st term on the right hand side can be ignored leading to the following reduction.

$$B = \frac{h_{g,0}\left(T_{r,g} - T_{w,0}\right)}{\left(T_{w,0} - T_{cu}\right)} \tag{10.13}$$

where $h_{g,0} = \frac{k_{g,0}}{\Delta y}$

Using (10.12) and (10.13) one can derive an expression for the expected wall temperature T_w in the case of transpiration cooling.

$$T_{w,f} = \left[\frac{aT_{cu} + T_g + \frac{h_{g,0}}{h_g}T_{cu}\frac{T_g - T_{w,0}}{T_{w,0} - T_{cu}}}{a + 1 + \frac{h_{g,0}}{h_g}\frac{T_g - T_{w,0}}{T_{w,0} - T_{cu}}}\right]_f \tag{10.14}$$

Compared with the uncooled case (no blowing), the effect of the blowing ratio F_{Blow} on the cooling efficiency is studied in Langener et al, [177].The term a, is an empirical parameter describing the change in heat transfer toward the cooled wall according to Kays et al, [71].

$$a = F_{Blow} \times \left(\frac{C_{p,col}}{C_p}\right) \times \left(\frac{1}{St_g}\right) \tag{10.15}$$

$$St_g = \left(\frac{B_H}{e^{B_H} - 1}\right) \times St_{g,0} \tag{10.16}$$

where $St_{g,0}$ equals 0.0034 and $C_{p,col}$ equals 1010.

$$B_H = F_{Blow}\left(\frac{C_{p,col}}{C_p}\right)^{0.6} \tag{10.17}$$

$$h_{g,0}=0.0034\rho_{\infty}u_{\infty}C_P \qquad (10.18)$$

where Pr equals 0.74 and μ is the dynamic viscosity obtained from equation (10.7). Then the gases density at each -*control volume*- face on the porous boundary is defined with the cell pressure and the face temperature from the equation below.

$$\rho_{w,f}=\left(\frac{P_{CV}}{T_{w,f}R}\right)$$

After the local density is calculated the velocity of the coolant which is blowing out of the porous surface into the main gas chamber is calculated below.

$$v_{w,f}=\frac{\rho_{col}\hat{v}_{in}}{\rho_{w,f}} \qquad (10.19)$$

where ρ_{col} equals 16.88 kg/m^3, $v_{w,f}$ calculated from (10.19) is a local value that depends on the density of the gas at the hot side of the porous wall. From this $v_{w,f}$ value, the convection fluxes and the viscous terms are computed for the use in the CBS formulation. For more information on this porous media boundary condition review Kays et al, [71].

10.1.4 Boundary Conditions

In this chapter the initial problem was modelled as seen in Figure 10-3. This was chosen because of its similarity to the final novel application and most importantly low Reynolds number. In conjunction with the Kays et al. [71] boundary condition, these small Reynolds numbers, ensure laminar flow, an appreciably simpler and more stable task to model.

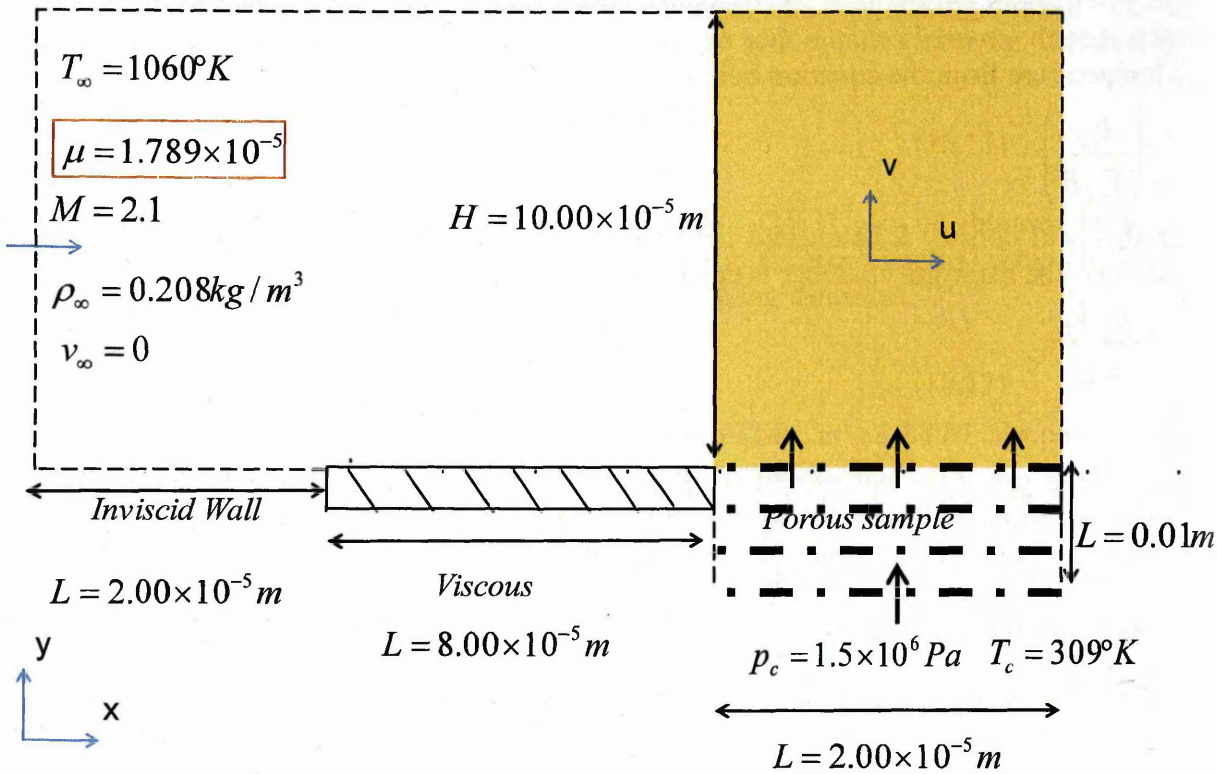

Figure 10-3: The first case study for transpiration cooling as devised by the author as a low Reynolds number compressible Supersonic flow benchmark.

The flat plate length is $8\text{x}10^{-6}$ m and the porous sample length is $2\text{x}10^{-6}$ m. The number of iterations before the coolant boundary condition was turned on was 7,000 iterations approximately, and after convergence for a $1\text{x}10^{-5}$ m flat plate the transpiration boundary condition was allowed to reach a steady state value for coolant velocity on for a further 7,000 iterations or divergence. Stability was sought firstly for the problem above, no requirement was set out for accuracy relative to the experimental data. Temperature contours were reviewed to assess that the final steady solution is free from decoupling and possesses smooth contours free from numerical noise. The advantage of this test case is the possibility to perform quick calculations that represent an important application: wall cooling for Hypersonic CAVs at the leading edge.

Table 10-3- Flow parameters for the main gas flow.

Total Length [m]	M_∞[-]	T_∞[K]	μ_∞[kg/(m s)]	ρ_∞[kg/(m^3)]	P_∞[bar]	Re [-]
1.2×10^{-5}	2.1	1060	1.789×10^{-5}	0.208	0.346	$4.60\text{x}10^2$

Table 10-4- Grid parameters for the computational domain.

Total Length [m]	Total Height [mm]	Nx	Ny	Nt
1.2×10^{-5}	2.1	100	58	5880

Table 10-5- Flow parameters for the coolant fluid

Porous Length [m]	Porous Thickness [mm]	T_{col} [K]	P_{col}[Pa]	μ_{col}[kg/ms]	$v_{in,col}$ (m/s)	ρ_{col}[kg/(m^3)]
0.8×10^{-5}	10	309	1.5×10^{6}	1.789×10^{-5}	1.2	12.7

10.2 The Sequential CBS Scheme for Compressible Porous Flow

The CBS based model was coupled with the Kays et al, [71], porous boundary condition, within the PHYSICA code framework and simulations were then run. The result of this is that the novel application is tackled. The sequential computational procedure for the CBS finite volume algorithm can be done in a number of ways, but here, the following general procedure after numerical experimentation was pursued. Each step described below is either applied to all the cells in a sweep of the grid or to the cells straddling the porous wall. After this sweep the boundary conditions as seen in step 6 are computed. Then the sequential computational procedure, otherwise known as an iteration is either exited or repeated after calculating the residual error and comparing them to the agreed tolerance.

1. The CBS scheme incorporates local pseudo time stepping.: Where C is the courant number and depending on the problem is usually < 0.5.

$$\Delta t_{CV}^{n} = C\frac{h_{CV}}{c_{CV}^{n} + \sqrt{\left(u_i u_i\right)_{CV}^{n}}} \tag{10.20}$$

2. The Kays et al, [71] boundary condition approach is used to calculate the velocity, pressure, temperature field on the surface of the flat plate at the start of the computational loop. Firstly $v_{in,col}$ is calculated at each control volume that possesses a face straddling the porous wall.

$$0 = \left\{\frac{\rho_{in,col}}{K_F}\left(1+\frac{b}{2T_{in,col}}\right)v_{in,col}^{2} + \frac{\mu_{in,col}}{K_D}\frac{1}{\frac{b}{2}(n+2)}\left[\left(1+\frac{b}{T_{in,col}}\right)^{n+2}-1\right]v_{in,col} - \frac{P_{in,col}^{2}-P_{out,col}^{2}}{2P_{in,col}L}\right\} \tag{10.21}$$

3. After computing v_{in} for all control volumes straddling the porous boundary. Where VBOUND equals total number of control volumes on the porous boundary. The average is taken.

$$v_{in,col} = \frac{1}{VBOUND}\sum_{f=1,VBOUND}\left(v_{in,col}\right)_f \tag{10.22}$$

This average inlet coolant velocity value, $v_{in,col}$, is a global value and is flowing out of the plenum into the porous membrane.

$$F_{Blow} = \frac{\rho_{col}\hat{v}_{in,col}}{\rho_{\infty}u_{\infty}}$$

4. The temperature on the porous-gas interface is calculated with blowing ratio.

$$T_{w,f} = \left[\frac{aT_{cu} + T_g + \frac{h_{g,0}}{h_g}T_{cu}\frac{T_g - T_{w,0}}{T_{w,0} - T_{cu}}}{a + 1 + \frac{h_{g,0}}{h_g}\frac{T_g - T_{w,0}}{T_{w,0} - T_{cu}}} \right] \tag{10.23}$$

And the rest of the variables seen are taken from Table 10-2

5. The density of the coolant-air mixture on the porous wall gridline is defined with the cell Pressure and the face temperature from equation (10.23).

$$\rho_{w,f} = \left(\frac{P_{CV}}{T_{w,f}R} \right) \tag{10.24}$$

The velocity of the coolant-air mixture that is blowing out of the porous surface into the main gas chamber is then calculated from the updated density.

$$F_{Blow} = \frac{\rho_{col}\hat{v}_{in,col}}{\rho_{\infty}u_{\infty}} \tag{10.25}$$

6. Intermediate Momentum

$$\rho u_i^{*} = \rho u_i^{n} - \frac{\Delta t}{\Delta V}\left(\begin{array}{l} \sum_{i=1,TOTFIC} \left(\rho u_i u_j\right) \bullet n_j A_f - \sum_{i=1,TOTFIC} \left(\tau_{ij} \bullet n_j A\right)_f \\ + \frac{\Delta t}{2} u_k \sum_{i=1,TOTFIC} div\left(\rho u_i u_j\right) \bullet n_j A_f \end{array} \right)$$

7. Corrected Momentum

$$\rho u_i^{n+1} = \rho u_i^{*} - \frac{\Delta t}{\Delta V}\left(\sum_{f=1,\mathbf{TOTFIC}} P_f \bullet n_j A_f - \frac{\Delta t}{2} u_k \sum_{f=1,\mathbf{TOTFIC}} \frac{\partial P}{\partial x_j} \bullet n_j A_f \right) \tag{10.26}$$

8. The Continuity Equation is solved using the momentum values from (10.26) at the n+1 "time" level.

$$\rho^{n+1} = \rho^{n} - \frac{\Delta t}{\Delta V}\left(\sum_{ifa=1,TOTFIC} \rho u_j \bullet n_j A_f \right) \tag{10.27}$$

9 Enthalpy Equation.

$$\rho E^{n+1} = \rho E^{n} - \frac{\Delta t}{\Delta V}\left(\begin{array}{l} \sum_{f=1,TOTFIC}\left(\rho u_i E\right)_f \bullet n_i A_f + \frac{\partial P}{\partial t} \\ - \sum_{f=1,TOTFIC}\left(u_i \tau_{ij}\right)_f \bullet n_i A_f - \sum_{f=1,TOTFIC} k_f \left(\frac{\partial T}{\partial x_i}\right)_f \bullet n_i A_f \\ + \frac{\Delta t}{2} u_k \left(\sum_{f=1,TOTFIC}\left(\frac{\partial\left(\rho E u_i\right)}{\partial x_j} \bullet n_j A\right)_f + \sum_{f=1,TOTFIC}\left(\frac{\partial\left(u_i P\right)}{\partial x_j} \bullet n_j A\right)_f \right) \end{array}\right) \quad (10.28)$$

Temperature is inferred from the enthalpy: To close the equation set the Ideal Gas Law and Sutherlands Law are solved. The Prandtl number, which is assumed constant for ideal gases at moderate temperature [82] where Pr is 0.74.

10 By sensing whether the relative error is less than the agreed tolerance of 10^{-5} check convergence to steady state values. Or alternatively if the number of iteration/sweeps is above the maximum iteration/sweeps, I_{Max}, stipulated by the user, I_{Max} =7,000 iterations.

$$\varepsilon_{Rel}^{n} = \frac{1}{NUMELE}\sqrt{\left[\frac{\sum_{CV=1}^{NUMELE}\left(\frac{\left|\rho_{CV}^{n+1} - \rho_{CV}^{n}\right|}{\Delta t_{CV} / (L/u_\infty)}\right)^2}{\sum_{CV=1}^{NUMELE}\left(\rho_{CV}^{n+1}\right)^2}\right]} \quad (10.29)$$

11 If convergence has been achieved exit the procedure and display results otherwise re-start the computational sweep by going back to step 1.

General Remarks

For system level design of the transpiration cooled components, the final approach should generate reliable predictions to the Hypersonic wind tunnel experiments. Initially, however, we are predominately concerned with a stable solution for compressible flow through porous media, which has been plagued by instability and divergence; review Chapter 9.

Initial Conditions

To reduce the initial transients for this method, which can cause instability and divergence, the initial conditions were set to the converged solution for a solid flat plate of L=1x10^{-5}m. The number of iterations before the coolant boundary condition was turned on was 7,000 approximately when convergence for a 1x10^{-5} m flat plate had been achieved. The boundary condition routines step 2-5, is switched on after convergence, for 7,000 more sweeps so that the transpiration boundary condition was allowed to reach steady state values. The solutionreaches steady state values specifically when v_{in} does not differ significantly from successive iterations.

As mentioned the approach presented by Cheuret & Steelant, [124] using a single set of equations to describe both bulk and porous flow for Compressible porous flow benchmark, resulted in instability and divergence as seen in chapter 9. Therefore the porous problem above was run to test the stability of the CBS algorithm when coupled with the approach favored by Kays et al, [71].

10.3 Simulation Results

The strategy was stable for Courant numbers of 0.05, an indication that the new boundary condition is a marked improvement in terms of stability from the approach advocated by Cheuret & Steelant, [124] as seen in chapter 9. Importantly the computations were stable and successfully converged to steady state values after the Kays et al, [71], porous boundary condition was turned on. The number of iterations required was 7,000 iterations once the sequential Kays et al, [71], porous boundary condition was activated. The resulting temperature contour maps are shown as proof of the final solution.

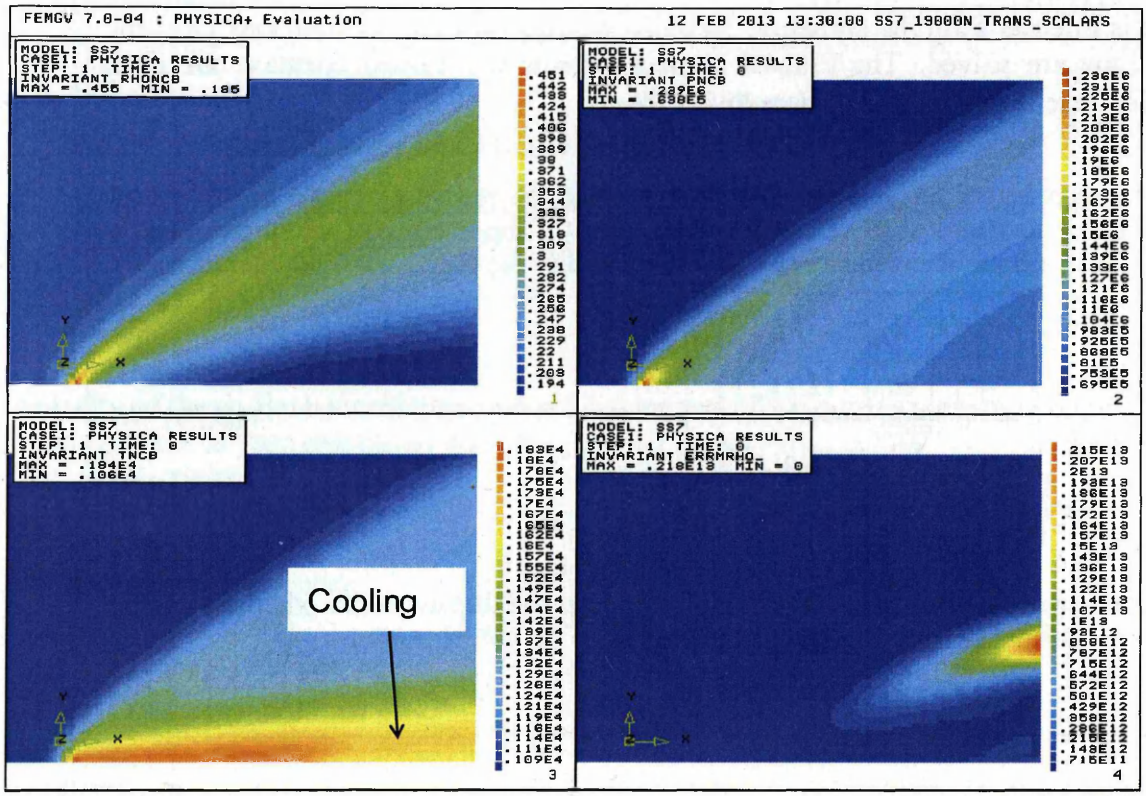

Figure 10-4: The scalar contours for the case shown in Figure 10-3 with transpiration cooling .

The four contour plots above, going from top left in a clockwise fashion, represent the density, the pressure, the enthalpy error over the flow domain and the temperature. The steady state solution is displayed when the porous wall condition is activated. The contours are smooth and this is an indication of a stable algorithm. The shock is also adequately represented as being several cells across. Notice the contour plot is smooth with banded color around the shock wave and the boundary layer without any decoupling, an essential ingredient for a reliable Hypersonic CFD tool.

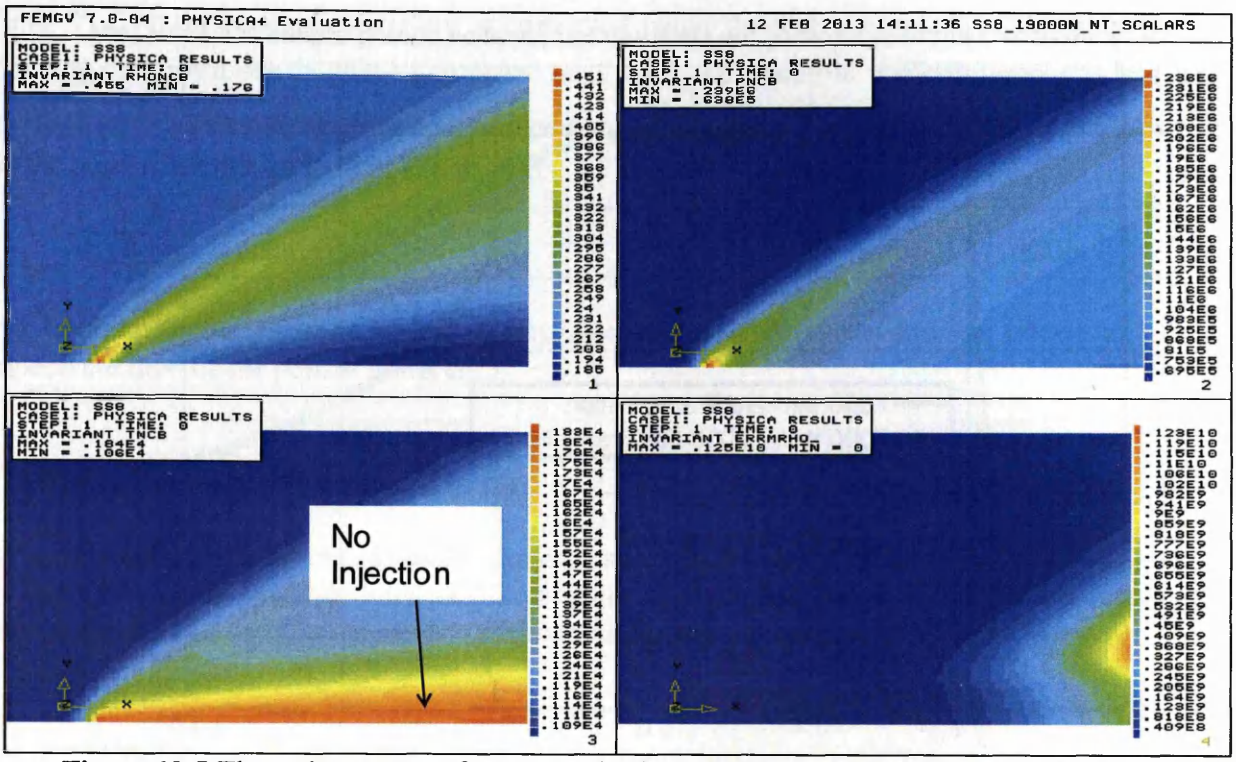

Figure 10-5 The scalar contours for case study shown in Figure 10-3 with no transpiration cooling.

The Figure above shows the four contour plots, going from top left in a clockwise fashion, the density, the pressure, the enthalpy error over the flow domain and the temperature

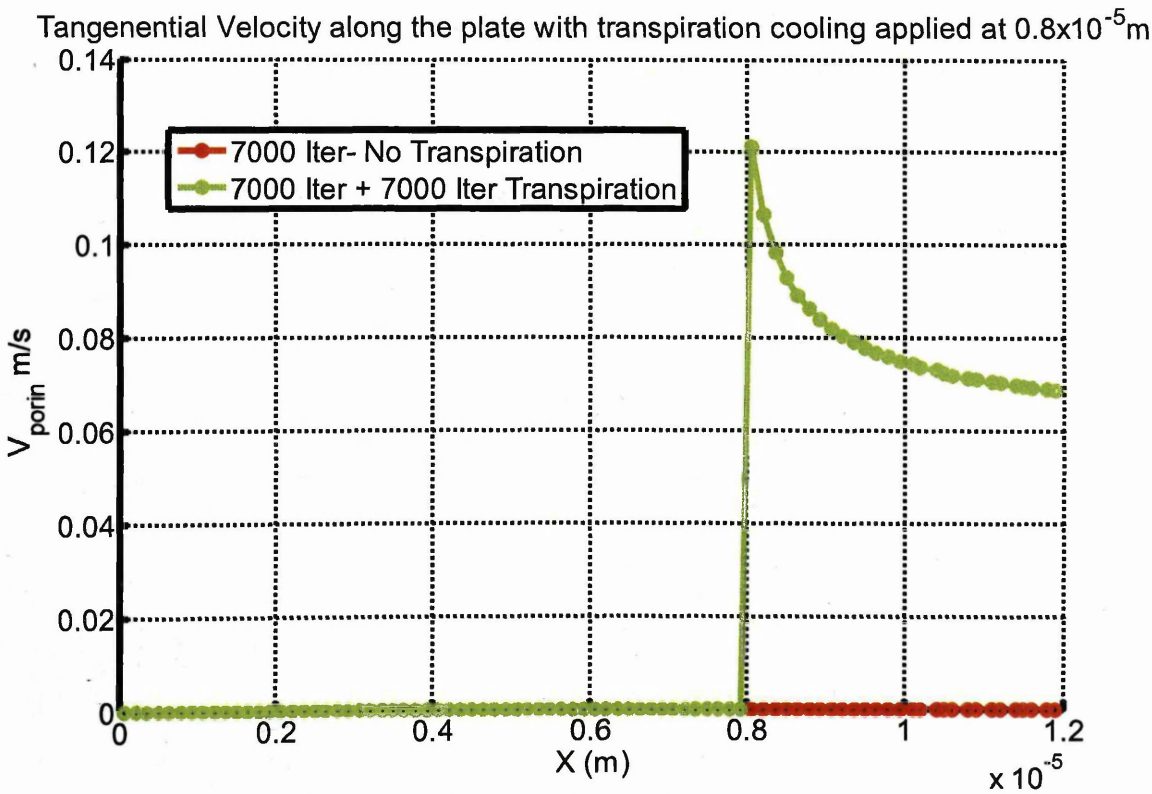

Figure 10-6 The tangential velocity for the cells straddling the wall over the porous media against the non transpiration cooling case.

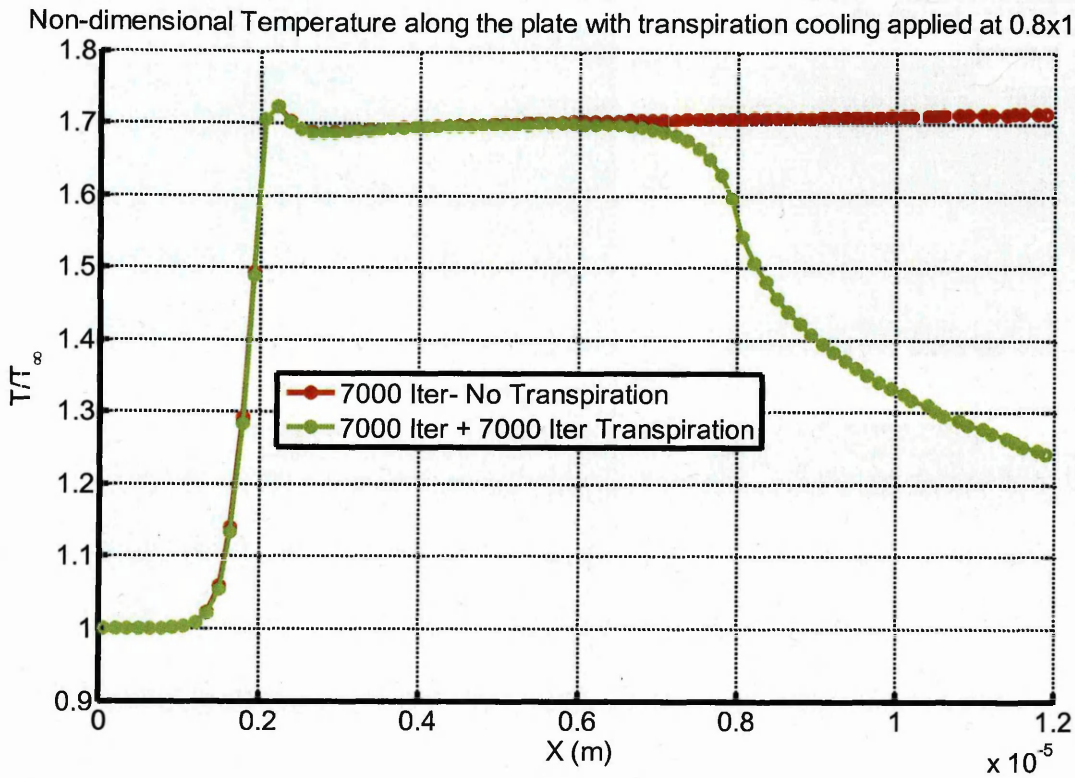

Figure 10-7 The temperature for the cells straddling the wall over the porous media against the non transpiration cooling case.

Figure 10- 6 and 10-7 show the v velocity and temperature respectively along the length of the domain, using the values from the cells straddling the most southern gridline. Further research is required to verify that the solution is realistic. Since there are no known analytical solutions to the case seen in Figure 10-3 the solved results will need to be compared against the experimental data from Langener et al, [177].

10.4 Modelling Langener's High Speed Wind-tunnel Experiment Novel Application

The goal of this second part is to validate the porous wall method developed by Kays et al, [71], and to couple this method to the FV CBS scheme by comparing computations with the experimental results seen in Langener et al, [177]. In varying free-stream conditions the cooling of the porous component is quantified. A non-dimensional cooling ratio is employed to describe the cooling efficiency of the transpiration cooled porous wall by Langener et al, [177]. In such a wind tunnel experiment it aims to reduce the influence of the lateral heat conduction effects and data interpretation by referring to the non-transpiration-cooled case. The efficacy of a porous component is quantified using the cooling efficiency ratio given by: It ranges from zero (no cooling) to unity (complete cooling). The wall temperature data was averaged from the four wall thermocouples.

$$\Theta_{Exper} = \frac{T_{W,F=0} - \overline{T}_{W,Exper}}{T_{W,F=0} - T_{CU}} \qquad (10.30)$$

Where Θ_{Exper} is the cooling efficiency as computed using the thermocouples in Langener et al, [177]. With this definition one is able to compare tests with, for example, different coolants and different sample materials. Here $\bar{T}_{W,Exper}$ is an average temperature value for the four thermocouples embedded into the porous sample as seen in Figure 10-2.

$$\bar{T}_{W,Exper} = \frac{\sum_{1\to4} T_f}{4} \tag{10.31}$$

As a back up to the thermocouple data, infrared thermography was used to obtain a 2-D surface temperature map of the porous material.

10.4.1Boundary Conditions

The next benchmark is similar to the earlier case study investigated in this chapter, which can be seen in Figure 10-3. However, the length of the porous medium and hence the domain is increased, so it matches the lengths seen in the wind tunnel experiment in Langener et al, [177].

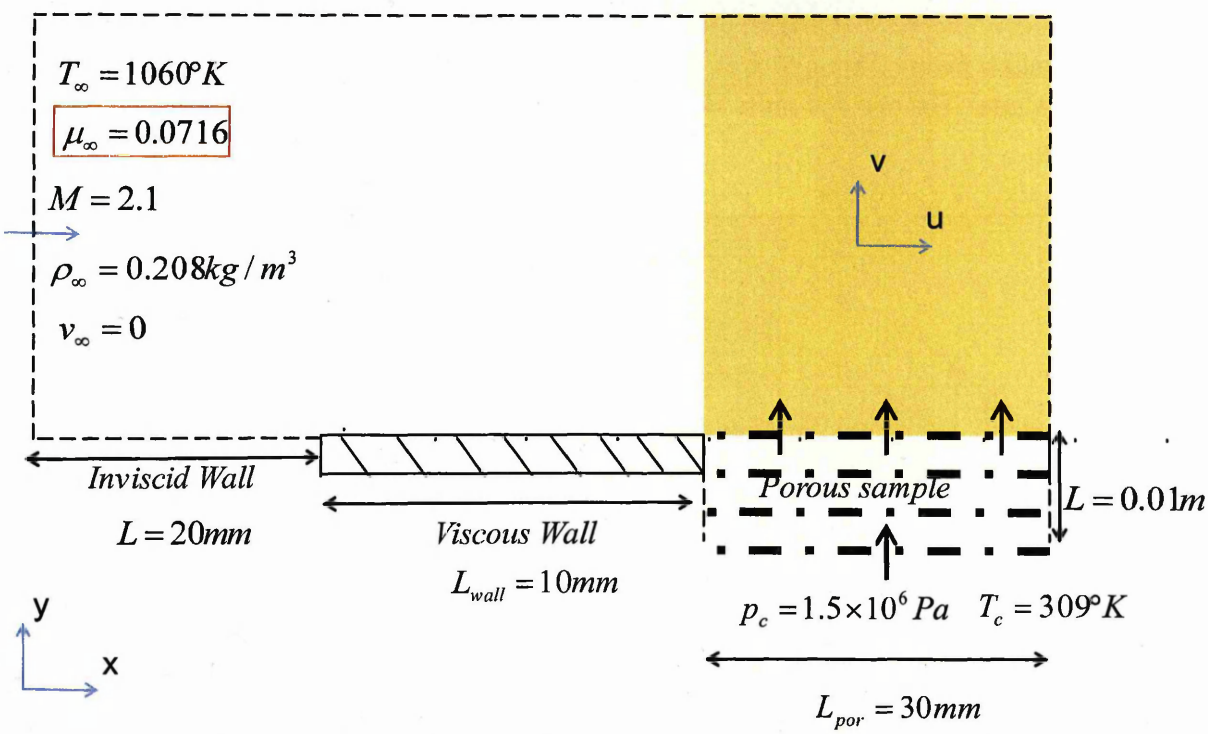

Figure 10-8: The second case study for transpiration cooling as devised by the author as a low Reynolds number compressible flow benchmark.

Firstly the free-stream viscosity was assumed to be $\mu = 0.0789(kg/(ms))$ which is done to keep the free-stream Reynolds number (Re) within the laminar regime because as mentioned before stability and hence convergence cannot be achieved with the FV CBS scheme for free-stream Re $>10^5$. Secondly all physical quantities for air in Table 10-6, except for the free-stream viscosity, are used. The flat plate is 10mm and the porous sample is 30mm.

Table 10-6- Grid and flow parameters for the main hot-gas.

Total Length [mm]	M_∞[-]	T_∞[K]	μ_∞[kg/(ms)]	P_∞[bar]	ρ_∞[kg/m^3]	Re [-]
60	2.1	1060	0.07019	0.346	0.208	$4.60\text{x}10^2$

Table 10-7- Flow parameters for the coolant.

Porous Length [mm]	Porous Thickness [mm]	T_{col}[K]	Range for P_c[Pa]	μ_{col} [kg/(ms)]	Range for $v_{in,col}$ (m/s)	ρ_{col}[kg/m^3]
30	10	309	1.0×10^5 - 1.5×10^6	0.07019	0.0097 to 1.2	16.9

10.4.2Comparative Wind Tunnel Results

The plots below are taken from Langener et al, [177]. Here, the cooling efficiency is plotted versus the coolant mass flow rate. The coolant mass flow rate is measured per cooled area.

$T_\infty = 1055K$

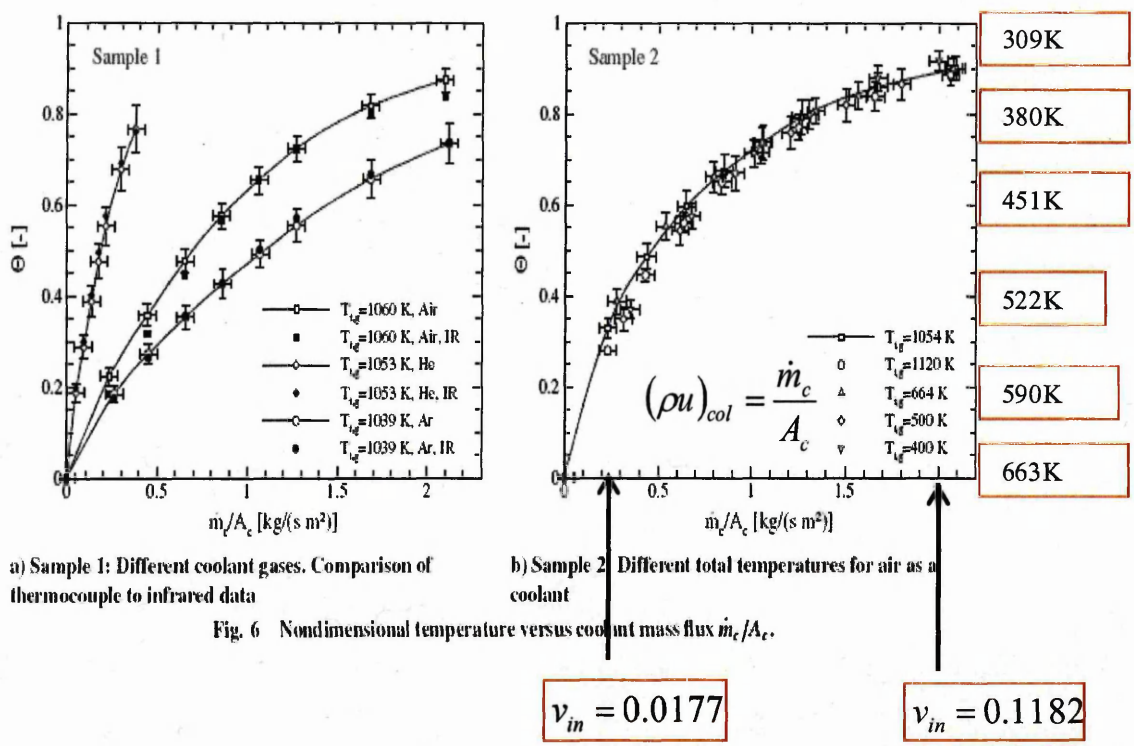

a) Sample 1: Different coolant gases. Comparison of thermocouple to infrared data

b) Sample 2: Different total temperatures for air as a coolant

Fig. 6 Nondimensional temperature versus coolant mass flux $\dot{m}_c/A_c$.

Figure 10-9 Numerical and experimental cooling efficiency vs. blowing ratio as taken from Langener, [177].

In the west graph in Figure 10-9 plot, the influence of the different coolants on the cooling efficiency is seen using sample 1. The parameters for sample 1 can be seen in Table 10-7. The impact of the gases' specific heat capacity is clear. With the same amount of coolant mass-flow rate, helium cools

the wall segment much better than air, whereas the cooling efficiency of argon is inferior to air and helium, due to its smaller specific heat capacity [177].

In the east plot in Figure 10-9 plot, the cooling efficiency of sample 2 is investigated at different hot gas total temperatures (inlet temperatures). Ranging from 400K up to 1120K, note that the non-dimensional temperature ratio, Θ, is independent from the hot gas total temperature at the same Mach number and coolant mass-flow rate.

10.4.3 Solver Results

The following two plots show the steady state temperature field as color contour plots. The two plots display the steady state values at two different blowing ratios where the blowing ratio ranges from 0.054%, $9x10^{-3}$m/s, and 0.12%, $2.35x10^{-1}$m/s , of the main gas flow rate.

10.4.3.1 *Computed Thermal Contour Plots*

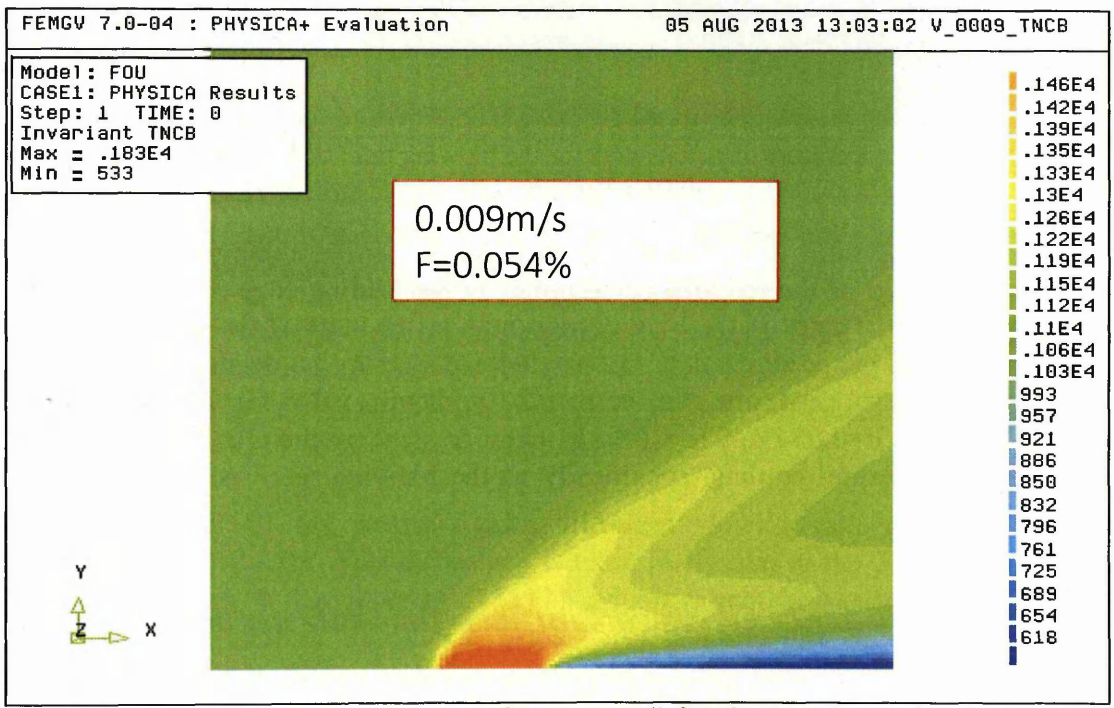

Figure 10-10 Surface temperature of porous wall for the blowing ratio of F_{Blow} =0.054 where the T_t=450k M=2.1.

When the blowing ratio is 0.054% the steady state profile exhibited is obtained after 1024 iterations. The start of the red area corresponds to the leading edge of the plate, whereas the end of the red area and the start of the blue corresponds to the start of the porous component. Importantly for this research the contour plots are banded and display no decoupling or numerical oscillations.

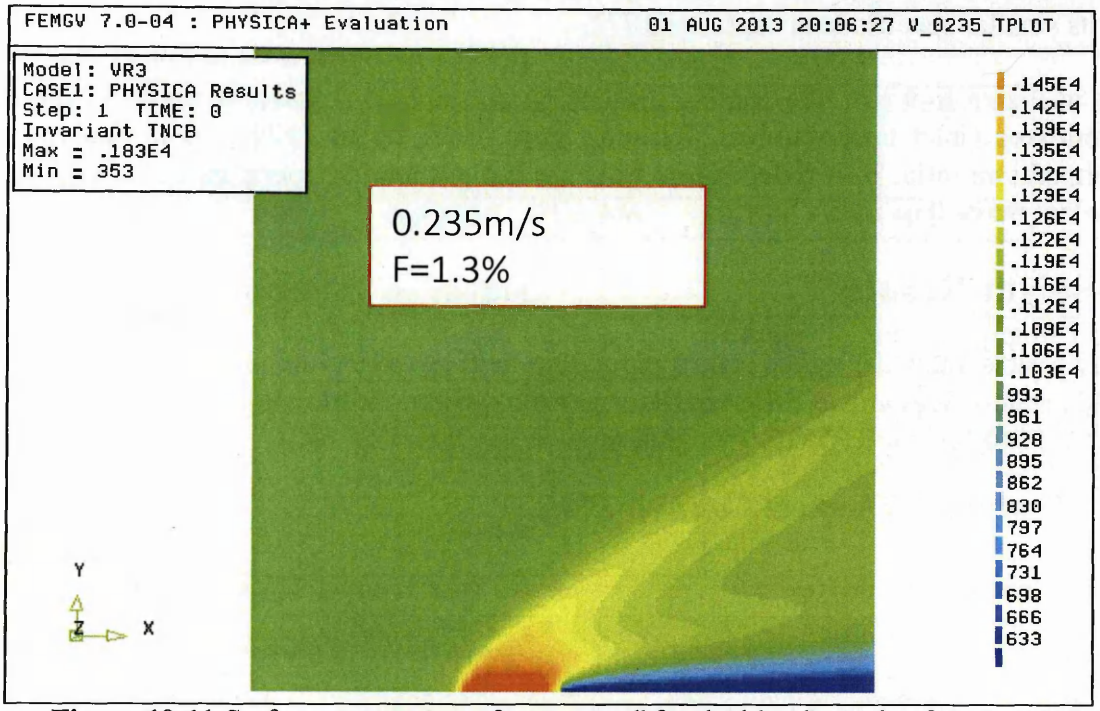

Figure 10-11 Surface temperature of porous wall for the blowing ratio of F_{Blow}=0.013 where the T_t=450k M=2.1.

For Figure 10-11 the blowing ratio is 1.3% and the steady state profile exhibited is obtained after 1460 iterations. Again the start of the red area corresponds to the leading edge of the plate, whereas the end of the red area and the start of the blue corresponds to the start of the porous component. Importantly for this research the contour plots are banded and display no decoupling or numerical oscillations. Comparing the two plots, one can see that the minimum value for temperature is 353K for F=1.3% and 533K for the F=0.054%. The CBS algorithm is showing the relationship between the coolant blowing ratio and thermal cooling, specifically as the blowing ratio increases transpiration cooling has a greater effect.

10.4.3.2 *Cooling efficiency versus coolant mass flow-rate per m²*

The following plot is generated, from the computed average wall temperature values. A total of twelve different simulations were done for 2 different blowing ratios and the average temperature after convergence was computed as seen below.

$$\bar{T}_{W,Com} = \frac{1}{VBOUND} \sum_{f=1,VBOUND} (T_w)_f \qquad (10.32)$$

where VBOUND is the total number of control volumes straddling the porous structure.

$$\Theta_{Com} = \frac{T_{W,F=0} - \bar{T}_{W,Com}}{T_{W,F=0} - T_{CU}} \qquad (10.33)$$

where Θ_{Com} is the cooling efficiency as computed using the numerical procedure developed in this thesis.

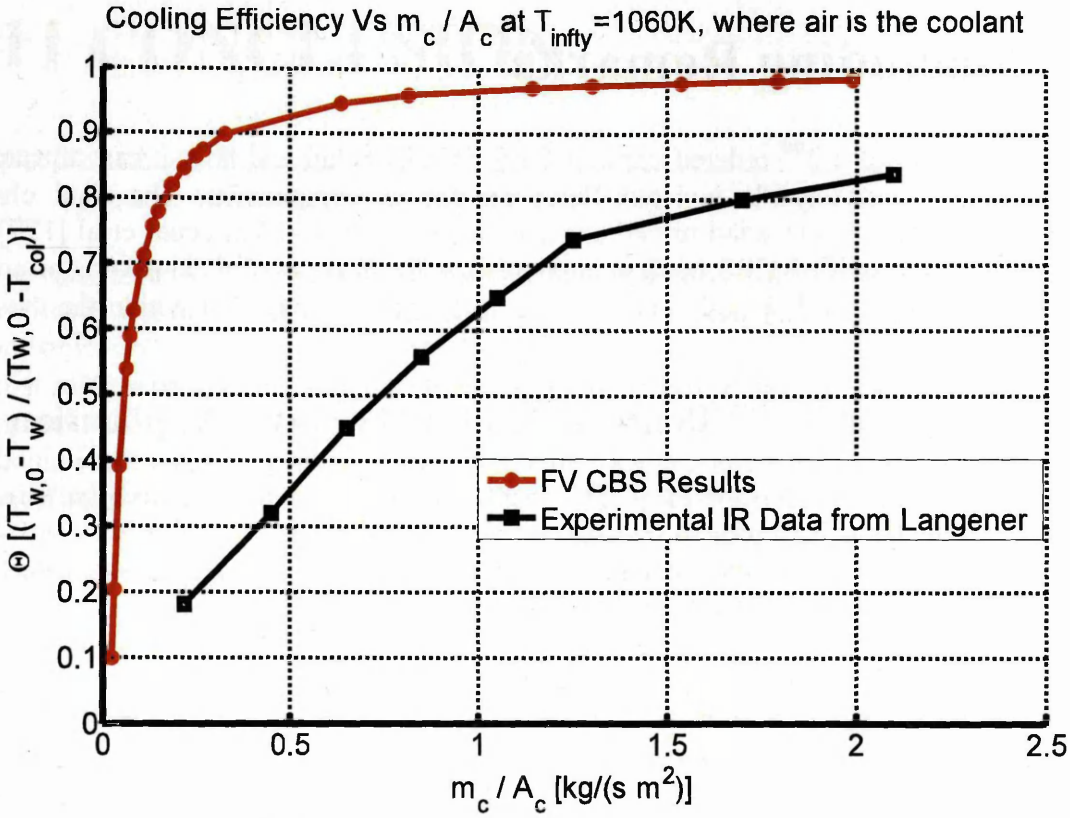

Figure 10-12 Comparing cooling efficiency vs. mass flow per unit area using the numerical and experimental procedures.

The comparison between the experimental results in Langener et al, [177], and the numerical solver developed during this thesis is shown in Figure 10-12. The physical relationship is in agreement, namely as the blowing ratio increases the cooling efficiency, Θ, increases. As Θ tends to 1 then the temperature on the porous component hot side approaches T_{col}.

The data points for Θ are plotted against different blowing ratio's, but are not completely in agreement with the IR data. This difference is most likely due to the 3D effects in the experimental procedure as covered in Langener et al [177], which cannot be accurately reproduced with Kay's boundary condition method. It could be argued that it might also be due to the artificial dynamic viscosity used in the simulations, which is employed for the requirement of stability.

10.5 Concluding Remarks

This chapter has demonstrated a 2nd ordered explicit CBS FV algorithm and how it can capture the behavior for Supersonic compressible inviscid flows on porous components. The final chapter utilized results from the Hypersonic wind tunnel experiments published in Langener et al [177], for comparison purposes. The modified CBS method is coupled with Kays et al. [71] porous boundary method to allow this comparison. This fully explicit CBS technique is embedded within the modular framework of PHYSICA.

10.5.1 Summary of the CBS algorithm for the Novel Application

The CBS algorithm is coupled with Kays et al. [71] porous boundary condition, and the resulting method is used to compute flow pertaining to the transpiration cooled experiments presented in [177]. The experimental test case was selected on the grounds of its close comparison to the final engineering application, and cooled components on Hypersonic CAVs.

To validate the numerical method used for designing CAVs, the numerical method has to show close agreement with the experimental data. The final numeric approach favored by Kays et al, [71], was stable and converged to a steady state solution. Ultimately this approach is more successful than the Cheuret & Steelant, [124], approach covered in Chapter 9. Also the implementation of the boundary condition method allowed us to generate different porous exit speeds by varying the plenum outlet pressure.

10.5.2 Comparison with Langener et al [177] Study

Figure 10-12 shows that this approach predicts the trend of blowing ratio versus cooling efficiency. Specifically that at high speeds and high temperature the heat load to the wall decreases with the transpiration blowing ratio. However differences in magnitude can be seen in Figure 10-12. This is most likely due to the artificial value we took for the dynamic viscosity of air. This was necessary to keep the flow laminar.

All problems were in the laminar regime where high Mach numbers are considered. This point is important, because the laminar regime can be modelled without the requirement of turbulence models. Turbulence and Turbulence models in themselves are worthy of a separate program of research. This would be extremely challenging considering the multi-disciplinary nature of turbulence effects, compressibility and transpiration cooling.

The developed method described by Kays et al, [71], and presented in this chapter can be used for non-adiabatic high temperature porous media set-ups, which are common in combustion chambers for aerospace propulsion and external transpiration cooling applications.

11 CONCLUSION

The development of numerical techniques for Hypersonic viscous flows is an area of current practical importance, which is due to the interest shown by the aerospace industry in the development of Hypersonic cruise air-breathing vehicles (CAVs). The simulation of the Hypersonic regimes of interest represents a formidable challenge to any flow solver, and can be attributed to the highly non-linear nature of the interactions which occur. The task of finding closed form solutions for mathematical models, which describe Hypersonic applications, proves to be fruitless in most applied engineering situations, and as a result, the computer simulation represents an attractive alternative for experiments that are difficult, dangerous or expensive to utilize as stated by Lyra, [7]. Alternatively CFD enables the possibility for analysis impossible in the laboratory. Experimentation still remains extremely important for engineering Hypersonic CAVs, however, with the advent of digital computers the trend for designing concept CAVs using numerical techniques is increasing. Some other difficulties which have to be faced when attempting the solution of the multidimensional Navier-Stokes equations is the complex geometries involved in industrial applications and the high CPU time involved in practical simulations. The large elapsed time necessary to produce structured grids for extremely complex configurations and the difficult control on the quality of the elements meant that unstructured grids were preferred in this thesis. Unstructured grid techniques are schemes that can be readily applied to unstructured, non-orthogonal grids, such as central differencing type schemes. And most Supersonic shock capturing techniques are those schemes that are based on orthogonal structured grids, such as 2^{nd} ordered upwind techniques. Lyra, [7], argues that through modifications and adjustments, many structured grid techniques can now be adopted for unstructured grids. Unfortunately they normally imply more complexity and less efficiency. Thus, unstructured grids were employed where applicable in this research to show the algorithms versatility when extension to modelling non-linear geometries are required.

This research has focused on applying a density based, explicit, collocated, central differencing finite volume algorithm to a number of benchmarks, favored by industrial supervisors, where the complexity of the benchmark's modelled, incrementally increases:

- 1-D Supersonic inviscid Flow
- 2-D Supersonic inviscid Flow
- 2-D Subsonic viscous Flow
- 2-D Supersonic viscous Flow
- Subsonic flow within a Porous Medium

Finally the goal of the research is modelling the novel engineering application:

- Subsonic flow within porous components coupled to Supersonic flow over these porous components

The chosen algorithm was assessed on its accuracy at capturing the pertinent physics of benchmark cases. The industrial sponsors stipulated an absolute error of less than 1% between the theoretical values and the codes results. The lack of transient (time dependent) benchmarks was a result of the dearth of theoretical solutions for transient fluid benchmarks when compared to those steady state theoretical solutions. In the event that transient effects need to be captured, the CBS algorithm, as

seen in Massarotti, Arpino, Lewis, & Nithiarasu, [132], can be easily extended to capture transient fluid applications.

Within each chapter of this thesis, relevant concluding remarks as well as recommendations for further work have been presented for each specific benchmark case. Therefore this thesis comes to an end with a summary of the achievements of this algorithm, the general stability issues when applying the algorithm and recommendations for extensions to each of the presented benchmarks

11.1 Summary of CFD Requirements

The list of requirements of a computational tool targeted at fluid dynamic problems coupled with heat transfer for Hypersonic applications as mentioned by Lyra, [7], are in this order of importance: reliability, robustness, efficiency and versatility. Both the effect of these four requirements on the success of a computational tool to deal with engineering applications and the amount of work required to improve any of these four requirements is enormous and cannot be overstated Lyra, [7]. However, the first requirement, reliability, was the major concern for the industrial sponsor, ESA. They need to scrutinize high temperatures encountered in the Hypersonic regime. The common features of the chosen numerical formulation applied to each of the benchmark cases include:

- The use of the finite volume method as the spatial discretisation in the numerics.
- Studies for each benchmark case that assess the accuracy of the final numerical solution.
- Improve the versatility of the algorithm by formulating the numerics so that it can easily handle unstructured, non-orthogonal grids.
- Data structures and code logic that is suitable for a large number of solution points.
- The adoption of numerical techniques such as artificial viscosity to extend the stability of the explicit approach for problems with inherent instability such as Oblique Shocks.
- Adopting pseudo local time stepping to control the stability of simulations especially around extrema, such as stagnation regions and discontinuities. .
- For slow convergence, for example in the case of incompressible flow through porous media as seen in Chapter 9, techniques to improve efficiency of the computations, such as an amplification factor, are employed
- Jamesons, Schmidt and Turkel's artificial dissipation is made up of 4^{th} and 2^{nd} ordered components. In invisicd regions of the flow, the 2^{nd} ordered components are equal to zero, meaning the 2^{nd} ordered accuracy of the CBS algorithm is recovered.
- The adoption of a number of tuneable free-parameters, such as the weighing factors for the artificial viscosity, helps to improve the stability of the final algorithm

In Chapter 4 the author emphasized the insight and importance of the 1D shock capturing Supersonic nozzle benchmark, on the development of the numerical scheme for multidimensions. For instance, the 1-D models represent a numerical laboratory, allowing the CFD user to acquaint himself with the features and issues of numerical computations and, in addition, to test, compare and perform an initial validation of numerical theory in 1-D, as stated by Lyra, [7]. An obvious point, is that a failure of a shock capturing numerical scheme, to model 1-D problems will typically mean further failure when modelling multidimensional shock problems. However the success of a 1-D model although promising does not guarantee success with the corresponding multidimensional shock problems. Therefore experimentation on the desired number of dimensions must be pursued for a comprehensive validation of the code. Issues such as well posed boundary conditions, multidimensional decoupling, and computational efficiency have limited meaning in 1-D computations. The numerical scheme described here in theory, are capable of solving a very wide

range of engineering problems and are extendible for the analyses of 3-D problems. The envisaged computer code for 3-D problems has features such as explicit time stepping which also make it easily extendible for implementation on parallel architecture.

11.1.1 Supersonic Inviscid Compressible Benchmark with Discontinuities

As seen in Chapter 4 the FV CBS algorithm was analysed against the 1D inviscid de Laval nozzle with excellent performance in terms of reliability and robustness. Two different cases were modelled; Supersonic and Choked nozzle. All computations displayed excellent performance in terms of stability and reliability. Hence the FV CBS algorithm was envisaged as the prime candidate scheme for the target benchmark problem, Hypersonic flow over transpiration cooled components.

The reliable and robust FV CBS algorithm for 1D inviscid problems was then extended for 2D problems; the Supersonic wedge benchmark. In contrast to the 1D inviscid study, greater experimentation of the user applied parameters in the artificial viscosity terms is required to meet the accuracy for a reliable computational tool. In addition to capture localized areas where physical interactions specific to the problem occur, such as the oblique shock over the wedge, the FV CBS algorithm, requires a fine grid to match accordingly to the localized areas of interest. The requirement for grids that capture shock waves is between 3-6 control volumes across the shock wave.

11.1.2 Subsonic Viscous Incompressible Benchmark

Further validation on various flow problems was carried out to assess the reliability of the chosen algorithm before applying the FV AC CBS algorithm to the targeted problem. The next benchmark test was the computation of a Subsonic viscous incompressible boundary layer over a flat plate. The motivating factor for modelling incompressible benchmarks was to show that the chosen numerical technique can work through the flow regimes in actual flight, potentially capturing laminar Subsonic flow as well as compressible Supersonic flow. Bad performance of compressible schemes is often experienced when they are directly applied to incompressible or very low Mach number problems [86]. Relevant modifications from research of Malan, Lewis, & Nithiarasu, [96], [150], [173]; and Nithiarasu, [160] that re-casts the density based CBS scheme as a pressure based solver were employed, they have also been presented in Chapter 7 for brevity.

However after implementing these modifications, the code became susceptible to numerical instability and divergence for free-steam Reynolds number (Re) > 6.86×10^4. It is my view that further work on turbulence models is required to allow reliable and robust computations around this Re number range. However for free-steam Reynolds number of < 6.86×10^4 results were stable, however accuracy issues arise due to errors relative to the theoretical prediction. Upon investigation on the meshes used to discretize the domain it was found that one factor affecting the accuracy of the solution, was the location of the inlet and top boundary to the region of viscous interactions.

The proximity of the free-stream domain boundaries to the region of interest significantly affected the accuracy of the final solution. i.e moving the inlet further upstream, resulted in greater accuracy in predicting, the C_f value over the flat plate. However, the associated gains when moving the boundaries did not drive the absolute error in the solution to below the tolerance of 1% and a minimum average error value of 1.88% persisted.

Alternative issues for an accurate prediction of the drag coefficient are the capturing of localized areas where physical interactions specific to viscous problems occur. For example, the FV CBS algorithm requires a fine grid to match accordingly with the flow-solid surface interface, where the

large velocity gradients play out. For example, the requirement for grids where the leading edge region of the flat plate was a dx length of 2.3×10^{-6}m or a ratio of $\frac{\mu}{\Delta x} = 7.7$.

11.1.3 Compressible Supersonic Problems

The next benchmark test was the computation of a Supersonic Compressible boundary layer over a flat plate. The motivating factor for modelling this benchmark, is that, the solver as already mentioned should capture compressible Supersonic and Hypersonic applications by Steelant, [169].

The explicit FV CBS algorithm was successfully stable and converged to a steady state solution for the 1st benchmark, the Mach 2, constant cold wall, 10μm flat plate. The small domain for the 10μm flat plate means relatively small grid sizes. Structured orthogonal grids can be employed (9800 elements) removing the need for careful mesh construction. This also has a (beneficial) effect on the simulation CPU time needed and the amount of time needed to harvest plots from the numerical outputs

Skin friction values, C_f, for this benchmark were computed using cells straddling the no-slip wall. These C_f values were compared with the predicted values from the temperature reference method. The C_f percentage error was less than 10% and the C_h value was less than 2%. Considering the drawbacks of the temperature reference method then the CBS algorithm could be argued to produce viable results. The C_h and C_f values from the CBS algorithm were in agreement in particular towards the trailing edge where the simplifying assumptions are realized.

Computations were also carried out on a higher Mach number, Mach 4, for two different wall thermal boundary conditions; the constant wall case and the adiabatic wall case. The MacCormack, [29], finite difference predictor corrector algorithm profiles which were copied from Anderson, [15], are used as a comparison. The figures in Anderson show physical quantities through the outlet, which unlike the temperature reference method encompasses the shock wave as well as the boundary layer. Therefore the various profiles at stations through the outlet edge from Anderson, [15], could be argued to be as informative than the temperature reference method when assessing the performance of the numerical scheme.
The CBS profiles are in excellent agreement with MacCormack, [29], finite difference predictor corrector algorithm profiles which were copied from Anderson, [15]. The final FV CBS solution for temperature and velocity and displayed close agreement with MacCormack's algorithm, [29], results, particularly for the location of the shock and the maximum temperature through the boundary layer.

11.1.4 Incompressible Subsonic Porous Problem

Due to time constraints the FV CBS scheme was then applied to a benchmark that involves Subsonic incompressible flow within a porous medium. The reason this was done was because it was seen as easier to understand issues relating to a successful porous media computation for incompressible problems, before more complicated problems, such as compressible flow over porous components were tackled. The source term used in Pantelis & Ritchie, [188], was initially employed because of how it replicates the effect of the porous medium. This term, as seen in Chapter 10, is proportional to the (local) velocity quadratic. The numerics of the FV CBS scheme went through a revision when applied to incompressible flow through porous media, as I propose that the source term should be re-cast from an explicit term as used by Pantelis & Ritchie, [188], to an implicit source term as used here. This revision brought about gains in stability and accuracy as the final solution was within the 1% absolute tolerance.

As encouraging as the incompressible results were for a reliable computational tool, for the target problem, modelling compressible flow through a porous medium was attempted next. The same geometry and porous medium parameters were used. However the free-stream velocity was set to a compressible speed of 200m/s (Mach=0.58).

The subsequent computations were characterized by instability and eventually diverged. Modifications to the approach were applied but with no avail. It was obvious that a new computational strategy needed to be employed as the continuum strategy produced an unstable problem.

11.1.5 Compressible Supersonic Flow over Subsonic Porous Components

Modelling Supersonic flow through porous media using the finite volume CBS algorithm was characterized by instability even with the implicit source term and the modifications presented by Cheuret & Steelant, [124]. The approach presented in Langener et al., [177], when implemented into the FV code resulted in stable computations for the non-isothermal, compressible flow within porous media. Langener et al., [177], modelled the porous media as a boundary condition and not part of the flow continuum.

There were many challenges and setbacks in this work but the research has succeeded in providing a knowledge base and a cautionary warning for modelling the different flow problems with the explicit finite volume CBS scheme.

The encouragement to write about the research work developed during my PhD in a self-contained thesis is a result of the help and advice I have received when working in the computational and civil engineering Centre at Swansea University. I hope that this thesis provides sufficient background information, and that the reader has sufficient information to implement the formulation. I also hope that the thesis will provide enough reasons to pursue the further studies, such as those seen in the Future Work section.

The explicit central differencing finite volume method implementation and its performance evaluation is best stated as Challenging. Due to the closely coupled nature of the equations, which prevents establishing where the numerical errors originate in the code, it is difficult to reason whether the instability are down to the unstable nature of the Navier-Stokes equations, (i.e. turbulence) or as a result of incompatibility with certain meshes. Another reason is that there may have been software errors in the code. It becomes a matter of experience and intuition to find the reasons for solution instability.

To summarize, the computational tools represent the initial accomplishment of this work, and the explanation for the reason behind the approach and the remedies for the instability issues represent the second and most important contribution of the present work. The necessity to concentrate a large number of points close to solid walls in order to resolve the boundary layer with sufficient accuracy, mainly at high Reynolds number, requires highly stretched elements. Apart from the big reduction on the allowable time-step, with severe implications on convergence towards a steady state solution using an explicit time integration, the viscous layer meshes very frequently lead to aspect ratios bigger than 1/200. Special attention needs to be exercised when constructing meshes for viscous problems.

Ultimately, no scheme in existence today can be seen as both reliable and robust enough for all flow scenarios. Definitely not for all speed regimes ranging from Subsonic through to Transonic through to Hypersonic speeds [5]. In order to make schemes accurate and robust, adjustable user parameters have to be tuned or different flux limiters need to be implemented. In scientific and engineering modelling this is par for the course according to Lyra, [7].

In the field of CFD, as pointed out by Lyra, [7], there are preferences when it comes to the analysis of fluid problems, and the performance of numerical schemes is not free from favoritism. After satisfying the requirement of reliability (accuracy relative to the analytical solution for the 1-D and 2-D benchmark problems) the CBS scheme was then utilized because of the motivating factors mooted in Chapter 1. Every mathematical model implies a perspective. An example is the search for what is an important relationship to capture, and these perspectives by their very nature have limitations, meaning they are not true in the absolute sense. A close comparison with rival or a number of rival of higher order upwind algorithms needs to be performed before we can say conclusively that the FV CBS algorithm is a relatively robust, efficient and versatile scheme.

11.2 Future Work

11.2.1 3D Modelling

The problems so far have been solved in 2D. The code has been devised in 3D and needs to be verified against 3D benchmark cases. Turbulence, as stated by White, [154], is one such 3D phenomenon. It must be noted that tackling ambitious simulations, such as complex 3-D viscous turbulent flows, coupled with real gas effects, chemical reactions, electro-magnetic effects, still represents a tremendous challenge for CFD users. Experiments of high standard level of accuracy must be provided so validation of any proposed scheme can commence. Some of these problems require a multi-disciplinary effort to be undertaken.

11.2.2 Turbulence Modelling

As presented by this Research and summarized in the conclusion, the CBS code is prone to instability at large Reynold Numbers $>6.56\text{x}10^5$, therefore the employment of an accurate turbulence model such as the $\kappa - \varepsilon$ model or the Baldwin Lomax model [149] is needed.

11.2.3 Implicit Solver

Devise an implicit version of the CBS method and apply it to the viscous flat plate benchmark to ascertain its performance relative to the explicit version. ESA have recommended that the 1m plate benchmark is revisited.

11.2.4 Real Gas Effects

Model the chemical and vibrational effects in the hot viscous layer at Hypersonic speeds by using the appropriate gas model as classified in the Literature Review Chapter.

11.2.5 Post Processor Developments

More versatile post processors need to be developed that can automatically display 2D plots, i.e. velocity versus height above surface, instead of manually copying values to MATLAB® and Excel® . This may make the process of evaluating the accuracy of the CFD tool easier.

References

[1] N. Croft, M. Cross, and K. Pericleous, "PHYSICA: A Multiphysics environment for complex flow processes," *Numer. Methods Laminar Turbul. FLow*, vol. 9, no. 2, pp. 1269–1280, 1995.

[2] A. J. Williams, T. N. Croft, and M. Cross, "Computational Modelling Of Metal Extrusion and Forging Processes," *J. Mater. Process. Technol,* vol. 125–126, pp. 573–582, 2002.

[3] A. Williams, T. N. Croft, and M. Cross, "A group based solution strategy for multi-physics simulations in parallel," *Appl. Mathmatical Model,* vol. 30, no. 7, pp. 656–674, 2006.

[4] J. J. Anderson, *Hypersonics and High Temperature Gas Dynamics*. New-York: McGraw-Hill, 2006.

[5] E. Hirschel and C. Weiland, *Selected Aerothermodynamic Design Problems of Hypersonic Vehicles*, 229th ed. Berlin: Springer, 2009.

[6] P. E. Ceruzzi, *In beyond the limits: flight enters the computer age*. MIT Press, 1989, p. 207.

[7] P. R. M. Lyra, "PhD Thesis. Unstructured Grid Adaptive Algorithms for Fluid Dynamics and Heat Conduction," Swansea University, 1994.

[8] R. P. Goff, "A History of Aerodynamics and its impact on Flying Machines," *Endeavour*, vol. 22. p. 133, 1998.

[9] J. J. Anderson, *Fundamentals of Aerodynamics*, 4th ed. McGraw-Hill, 2007, p. 630.

[10] J. Azevedo and H. Korzenowski, "An assessment of unstructured grid Finite Volume Schemes for cold gas Hypersonic flow calculations," *J. Aerosp. Technol. Manag,* vol. 1, no. 2, pp. 135–152, 2009.

[11] S. Succi, *The Lattice Boltzmann Equation for Fluid Dynamics and Beyond*, vol. 222. Oxford: Oxford Science Publication, 2001, pp. 145–197.

[12] D. Schaefer and D. Yuan, "A thermal Lattice Boltzmann Two-Phase Flow Model and its Application to Heat transfer Problems-Part 1. Theoretical Foundation," *J. Fluid Eng,* pp. 142–150, 2006.

[13] R. D. Flack, *Fundamentals of Jet Propulsion with Applications*. New York: Cambridge University Press, 2005.

[14] M. E. Gurtin, *An introduction to continuum mechanics*, 158th ed. Academic Press Limited, 1981.

[15] J. J. Anderson, *Computational Fluid Dynamics: The Basics with Applications*. 1995, p. 547.

[16] M. W. Versteeg H K, "Introduction to Computational Fluid Dynamics (The Finite Volume Method)," *Book*, 1995. [Online]. Available: http://www.scribd.com/doc/8650266/Versteeg-H-K-Malalasekera-W-Introduction-to-Computational-Fluid-Dynamics-the-Finite-Volume-Meth.

[17] H. K. Versteeg and W. Malalasekera, *Computational Fluid Dynamics: The Finite Volume Method*, vol. M. 2007, p. 503.

[18] C. Hirsch, *Numerical Computation of Internal and External Flows, Volume 1*. Chichester: John Wiley & Sons, 1988.

[19] J. J. Anderson, R. H. Pletcher, and J. C. Tannehill, *Computational Fluid Mechanics and Heat Transfer*. Hemisphere Publishing Corporation, 1984.

[20] T. J. Chung, *Computational Fluid Dynamics*, 2nd ed. Cambridge, UK: Cambridge University Press, 2002.

[21] P. D. Lax and R. D. Richtmyer, "Survey of the Stability of Linear Finite Difference Equations," *Commun. Pure Appl. Math,* vol. 9, no. 2, pp. 267–293, 1956.

[22] R. D. Richtmyer and K. Morton, *Difference Methods for Initial-Value Problems,*. New York: Wiley-Interscience, 1967.

[23] L. F. Richardson, "The approximate arithmetical solution by finite differences of physical problems involving differential equations, with an application to the stresses in a masonry dam," *Philos. Trans. R. Soc. A*, vol. 210, pp. 307–357, 1910.

[24] H. Lewy, R. Courant, and K. Friedrichs, "Uber die Partiellen Differenzengleichungen der Mathematischen Physik," *Mathematische Annalen*, vol. 100. pp. 32–74, 1928.

[25] F. H. Evans, Martha W. and Harlow, "The Particle-in-Cell Method for Hydrodynamic Calculations," 1957.

[26] F. H. Harlow and J. E. Welch, "Numerical Calculation of Time Dependent Viscous Incompressible Flow of Fluid with Free Surface," *Phys. Fluids*, vol. 8, pp. 2182–2189, 1965.

[27] S. K. Godunov, "A difference method for numerical calculation of discontinuous solutions of the equations of hydrodynamics," *Math. Sb,* vol. 47, no. 3, pp. 271–306, 1959.

[28] P. D. Lax and B. Wendroff, "Systems of Conservation Laws," *Commun. Pure Appl. Mathmatics*, vol. 13, no. 2, pp. 217–37, 1960.

[29] R. W. MacCormack, "The effect of viscosity in Hyper-velocity impact cratering," *AIAA*, vol. 69, p. 354, 1969.

[30] B. van Leer, "Towards the ultimate conservative difference scheme. II. Monotonicity and conservation combined in a second-order scheme," *J. Comput. Phys,* vol. 14, no. 4, pp. 361–370, 1974.

[31] H. McDonald, "The Computation of Transonic Flow through Two-Dimensional gas turbine cascades," *Tech. Rep,* vol. asme, pp. 71–89, 1971.

[32] D. . Spalding and S. . Patankar, "A calculation procedure for heat, mass and momentum transfer in three-dimensional parabolic flows," *International Journal of Heat and Mass Transfer*, vol. 15. pp. 1787–1806, 1972.

[33] D. McBride, "PhD Thesis. Vertex-Based Discretisation Methods for Thermo-Fluid Flow in a Finite Volume- Unstructured Mesh Contex," University of Greenwich London, 2003.

[34] L. S. Caretto, R. M. Curr, and D. B. Spalding, "Two Numerical Methods for Three-Dimensional Boundary Layers," *Comput. Methods Appl. Mech. Eng,* vol. 1, pp. 39–57, 1972.

[35] A. J. Chorin, "Numerical Solution of the Navier-Stokes Equations," *Math. Comput,* vol. 22, no. 104, pp. 745–762, 1968.

[36] S. V Patankar, *Numerical Heat Transfer and Fluid Flow*, vol. 8. Hemisphere Publishing Corporation, 1980, p. 197.

[37] G. D. Raithby, "skew upstream differencing schemes for problems involving fluid flow," *Comput. Methods Appl. Mech. Eng,* pp. 153–164, 1976.

[38] N. Croft, "PhD Thesis. Unstructured Mesh - Finite Volume Algorithms for Swirling, Turbulent, Reacting Flows," University of Greenwich London, 1998.

[39] D. Pan, C. H. Lu, and J. C. Cheng, "Incompressible flow solution on Unstructured Triangular Meshes," *Numer. Heat Transf,* vol. 26, no. 2, pp. 207–224, 1994.

[40] P. M.-Y. Chow, "A Control Volume unstructured Procedure for convection-diffusion solidification processes," University of Greenwich London, 1993.

[41] P. M.-Y. Chow, M. Cross, and K. Pericleous, "A Natural Extension of the Conventional Finite Volume Method into Polygonal Unstructured Meshes for CFD Applications," *Appl. Math. Model,* vol. 20, no. 2, pp. 170–183, 1996.

[42] S. R. Idelsohn and E. Onate, "Finite Volumes and Finite Elements: Two 'Good Friends,'" *Int. J. Numer. Methods Eng,* vol. 37, pp. 3323– 3341, 1994.

[43] O. Hassan, E. J. Probert, K. Morgan, and J. Peraire, "Mesh generation and adaptivity for the solution of compressible viscous high speed flows," *Int. J. Numer. Methods Eng,* vol. 38, no. 7, pp. 1123–1148, 1995.

[44] O. C. Zienkiewicz and Y. K. Cheung, "Finite Elements in the solution of Field problems," *Eng,* vol. 507–10, 1965.

[45] J. C. Heinrich, P. S. Huyakorn, O. C. Zienkiewicz, and A. R. Michell, "An upwind finite element scheme for two dimensional convective transport equations," *Int. J. Numer. methods Mech. Eng,* vol. 11, no. 1, pp. 131–44, 1977.

[46] J. Donea, "A Taylor–Galerkin method for convective transport problems," *Int. J. Numer. Methods Eng,* vol. 20, no. 1, pp. 101–119, 1984.

[47] O. C. Zienkiewicz and R. Codina, "A general algorithm for compressible and incompressible flow—Part I. the split, characteristic-based scheme," *Int. J. Numer. Methods Fluids*, vol. 20, no. 8, pp. 869–885, 1995.

[48] J. T. Oden, I. Babuska, and C. E. Baumann, "A discontinous hp finite element method for diffusion problems," *Comput. Math. with Appl,* vol. 37, no. 9, pp. 103–122, 1999.

[49] P. M. Gresho and R. L. Sani, *Incompressible Flow & the Finite Element Method - Advection-Diffusion & Isothermal Laminar Flow*. 1998.

[50] K. Morgan and P. R. M. Lyra, "A Review and Comparative Study of Upwind Based Schemes for Compressible flow Computation. Part I: 1-D higher Order Schemes," *Arch. Comput. Methods Eng,* vol. 7, no. 1, pp. 19–55, 2000.

[51] S. Whitaker, "Advances in Theory of Fluid Motion in Porous Media," *Ind. Eng. Chem,* vol. 61, pp. 14–28, 1969.

[52] W. J. Gordon and C. A. Hall, "Construction of curvilinear co-ordinate systems and applications to mesh generation," *Int. J. Numer. Methods Eng,* vol. 7, pp. 461–477, 1973.

[53] W. Shyy and T. Vu, "On the Adoption of Velocity Variable and Grid System for Fluid Flow Computation in Curvilinear Coordinates," *J. Comput. Phys,* vol. 92, pp. 82–105, 1991.

[54] I. Demirdžić and M. Perić, "Finite volume method for prediction of fluid flow in arbitrarily shaped domains with moving boundaries," *Int. J. Numer. Methods Fluids*, vol. 10, no. 7, pp. 771–790, 1990.

[55] V. Semin and I. Poliakov, "An introduction into the Method for Implementing Multi-Block Grids and/or Grid Refinement in PHOENICS," *PHOENICS J. Comput. Fluid Dyn. its Appl,* vol. 7, no. 2, pp. 34–57, 1994.

[56] S. L. Karman, J. P. Steinbrenner, and K. M. Kisielewski, "Analysis of the F-16 Flow field by a Block Grid Euler aproach," in *AGARD*, 1986, p. 412.

[57] Y. Burtschell and D. E. Zeitoun, "Shock/Shock and Shock/boundary layer interactions in an axisymmetric steady laminar flow," *Shock Waves*, vol. 12, no. 6, pp. 487–495, 2003.

[58] K. Powell and W. J. Coirier, "Solution Adaptive Cartesian Cell approach for viscous and inviscid flow," *AIAA J,* vol. 34, no. 5, pp. 938–945, 1996.

[59] W. J. Coirier and K. Powell, "Solution Adaptive Cartesian Cell approach for viscous and inviscid flow," *AIAA*, vol. 34, no. 5, pp. 938–945, 1996.

[60] A. Jameson and D. Mavriplis, "Finite Volume Solution of the Two-Dimensional Euler Equations on a Regular Triangular Mesh," *AIAA*, vol. 24, no. 4, pp. 611–618, 1985.

[61] L. Thomadakis, "Numerical Simulation of Viscous Incompressible Flows Using Pressure-Correction Method and Unstructured Meshes Grids," in *ECCOMAS '94 Conference*, 1994.

[62] T. Barth, "Numerical Aspects of Computing Viscous High Reynolds Number Flows on Unstructured Meshes," *AIAA*, vol. 91, pp. 07–21, 1991.

[63] J. Cabello, K. Morgan, and R. Lohner, "A comparison of Higher Order Schemes used in a Finite Volume Solver for Unstructured Grids," *AIAA*, vol. 94, pp. 22–93, 1994.

[64] O. Hassan, E. J. Probert, K. Morgan, and J. Peraire, "Line Relaxation Methods for the solution of 2D and 3D Compressible Viscous Flows using Unstructured Meshes," in *Recent Developments and Applications in Aeronautical CFD*, 1993.

[65] H. D. Simon and J. S. Kowalik, *Parallel Computational Fluid Dynamics: Implementation and Results*. Cambridge, Massachusetts: MIT, 1992.

[66] "nvidia-coe," 2010. [Online]. Available: http://www.sci.utah.edu/nvidia-coe.html.

[67] K. Morgan, N. P. Weatherill, O. Hassan, and J. Brookes, P. J, Said, R, Jones, "Parrallel framework for multidiscplinary aerospace engineering simulations using unstructured meshes," *Int. J. Numer. Methods Fluids*, vol. 31, no. 1, pp. 159–173, 1999.

[68] K. McManus, A. Williams, M. Cross, T. N. Croft, and C. Walshaw, "Assessing the parallel performance of multi-physics tools for modelling of solidification and melting processes," *Int. J. High Perform. Comput. Appl,* pp. 1–27, 2005.

[69] J. A. Lawrence, "Ph.D Thesis. Computational modelling of mold filling and related free surface flows in shape casting: An overview of the challenges involved," *Trans. Metall. Mater,* pp. 879–885, 2006.

[70] A. K. Slone, A. J. Williams, T. N. Croft, and M. Cross, "Dynamic fluid structure interaction in Parallel: a challenge for Scalability, in Parallel, Distributed and Grid Computing for Engineering," *Saxe-Coburg*, pp. 329–350, 2009.

[71] W. Kays, M. Crawford, and B. Weigand, *Convective Heat and Mass Transfer*, 4th ed. New York: McGraw-Hill, 2005.

[72] P. D. Lax, *Systems of Conservation Laws and Mathmatical Theory of Shock Waves*, 16th ed. Philadephia, 1973.

[73] R. Le-Veque, "Numerical Methods for Conservation Laws," *Birkkhauser Verlag Base*, 1990.

[74] P. R. M. Lyra and K. Morgan, "A review and comparative study of upwind biased schemes for compressible flow computation. Part III: Multidimensional extension on unstructured grids," *Arch. Comput. Methods Eng,* vol. 9, no. 3, pp. 207–256, 2002.

[75] R. Courant, E. Isaacon, and M. Rees, "On the Solution of Nonlinear Hyperbolic Differential Equations by Finite Difference," *Commun. Pure Appl. Mathmatics*, vol. 5, no. 3, pp. 243–255, 1952.

[76] J. B. Scaraborough, *Numerical Mathmatical Analysis*, 4th ed. Baltimore: John Hopkins Univeristy Press, 1958.

[77] P. J. Roache, *Computational Fluid Dynamics*. Albuquerque: Hermosa Publications, 1976.

[78] I. Currie, *Fundamental Mechanics of Fluids*. McGraw-Hill, 1974.

[79] J. C. Slattery, *Momentum, Energy and Mass Transfer in Continua*, 2nd ed. New York: Robert E. Krieger Publishing Company, 1981.

[80] A. J. M. Spencer, *Continuum Mechanics*, 1st ed. New York: Longman Scientific & Tecnical, 1980.

[81] I. S. Sokolnikoff, *Tensor Analysis: Theory and Applications to Geometry and Mechanics of Continua*. John Wiley & Sons, 1964.

[82] H. W. Liepmann and A. Roshko, *Elements of Gas-Dynamics*, 4th ed. New-York: John Wiley & Sons, 1957.

[83] C. Truesdell and W. Noll, "Encyclopedia of Physics- The Non-Linear Field Theories of Mechanics," *Springer-Verlag*, vol. volume III, 1965.

[84] J. J. Anderson, *Modern compressible flow with historical perspective*, vol. 4. 2003.

[85] M. Liou, B. van Leer, and J. S. Shuen, "Splitting of Inviscid Fluxes for Real Gases," *J. Comput. Phys,* vol. 87, pp. 1–24, 1990.

[86] H. Yee, "A class of high-resolution explicit and implicit shock capturing methods," *von Karman Inst. Fluid Dyn. Lect. Ser. 1989-04, 1989*, vol. NASA TM-10, 1989.

[87] C. Hirsch, *Numerical Computation of Internal and External Flows, Volume 2*. Chichester: John Wiley & Sons, 1990.

[88] T. H. Pullium and J. Barton, "Euler computations of AGARD working group 07, Airfoil test cases," *AIAA 23rd Aerosp. Sci. Meet,* 1986.

[89] P. Dutt, "Stable boundary conditions and difference shemes for Navier-Stokes Equations," *SIAM J. Numer. Anal,* vol. 25, no. 2, pp. 245–267, 1988.

[90] B. Gustafsson and A. Sundstrom, "Incompatability parabolic problems in fluid dynamics," *SIAM J. Numer. Anal,* vol. 35, no. 2, pp. 343–357, 1978.

[91] T. J. Poinsot and S. Lele, "Boundary Conditions for Direct Simulations of Compressible Viscous Flows," *J. Comput. Phys,* vol. 101, no. 104–129, 1992.

[92] Rudy and Strickwerda, "A Non-Reflecting Outflow Boundary Condition for Subsonic Navier-Stokes Calculation," *J. Comput. Phys,* vol. 36, pp. 55–70, 1980.

[93] C. Fletcher, *Computational Techniques for Fluid Dynamics*. Springer-Verlag, 1988.

[94] A. Chorin, "A numerical method for solving incompressible viscous flow problems," *J. Comput. Phys,* vol. 2, no. 1, pp. 12–26, 1967.

[95] P. Roe, "Characteristic-Based Schemes for the Euler Equations," *Annual Review of Fluid Mechanics*, vol. 18. pp. 337–365, 1986.

[96] A. G. Malan, R. W. Lewis, and P. Nithiarasu, "An improved unsteady, unstructured, artificial compressibility, finite volume scheme for viscous incompressible flows: Part I. Theory and implementation," *Int. J. Numer. Methods Eng,* vol. 54, no. 5, pp. 695–714, Jun. 2002.

[97] T. J. R. Hughes, "Multiscale phenomena: Green's functions, the Dirichlet-to-Neumann formulation, subgrid scale models, bubbles and the origins of stabilized methods," *Computer Methods in Applied Mechanics and Engineering*, vol. 127. pp. 387–401, 1995.

[98] G. Kuruvila and J. J. Anderson, "A Study of the Effects of Numerical Dissipation On the Calculation of Supersonic Separated Flow," *AIAA J,* 1985.

[99] G. D. Raithby, "A critical evaluation of upwind differencing formulation for differential expressions involving both first and secon order derivatives," *Int. J. Numer. methods Eng,* pp. 551–559, 1972.

[100] D. B. Spalding, "A Novel Finite -difference Formulation for Differential Expressions involving both First and Second Derivatives," *Int. J. Numer. Methods Eng,* vol. 551, no. 4, 1972.

[101] B. P. Leonard, "A stable and accurate convective modelling procedure based on quadratic upstream interpolation," *Comput. Methods Appl. Mech. Eng,* vol. 19, pp. 59–98, 1979.

[102] J. von Neumann and R. D. Richtmyer, "A Method for the Numerical Calculation of Hydrodynamic Shocks," *J. Appl. Phys,* vol. 21, pp. 232–237, 1950.

[103] J. P. Boris and D. L. Book, "Flux Corrected Transport I, SHASTA, A Fluid Transport Algorithm that Works," *J. Comput. Phys,* vol. 11, no. 1, pp. 38–69, 1973.

[104] J. J. Quirk, "A contribution to the great Riemann solver debate," *ICASE Rep,* pp. 92–64, 1992.

[105] A. Jameson, W. Schmidt, and E. Turkel, "Numerical solutions of the Euler equations by finite volume methods using Runge-Kutta time-stepping schemes," *AIAA Pap,* vol. 12, no. 59, pp. 1–19, 1981.

[106] E. Turkel, "Improving the accuracy of Central differencing schemes," Hampton, 1988.

[107] J. Peraire, J. Peiro, and K. Morgan, "Finite Element Multigrid solution of Euler Equations past installed aero-engines," *Comput. Mech,* vol. 11, pp. 431–455, 1993.

[108] R. . Swanson and E. Turkel, "On central-difference and upwind schemes," Hampton, 1990.

[109] J. B. Goodman and R. Le-Veque, "ICASE: Technical Report," Hampton, 1984.

[110] J. B. Goodman and R. Le-Veque, "On the accuracy of stable schemes for 2-D Scalar Conservation Laws," *Math. Comput,* vol. 25, p. 15:21, 1985.

[111] B. van Leer, "Flux-Vecor Splitting for the Euler Equations," *Notes Phys,* vol. 170, pp. 501–512, 1982.

[112] M. S. Liou and C. J. Steffen, "A new Flux Splitting Scheme," *J. Comput. Phys,* vol. 107, no. 1, pp. 23–39, 1993.

[113] M. Liou, "The Evolution of AUSM Schemes," *Def. Sci. J,* vol. 60, pp. 606–613, 2010.

[114] P. Roe, "A suvey of upwind differencing techniques," *Lect. notes Phys,* pp. 323–69, 1989.

[115] B. van Leer, "Towards the ultimate conservative difference scheme III. Upstream-centered finite-difference schemes for ideal compressible flow," *J. Comput. Phys,* vol. 23, no. 3, pp. 263–275, 1977.

[116] F. Cheuret, J. Steelant, M. Bouchez, and E. Dufour, "Performance of existing models for transpiration cooling," in *Space Propulsion 2008: 5th International Spacecraft Propulsion Conference & 2nd International Symposium on Propulsion for Space Transportation*, 2008, pp. 1–10.

[117] P. K. Sweby, "High Resolution Schemes Using Flux Limiters for Hyperbolic Conservation Laws," *SIAM Journal on Numerical Analysis*, vol. 21. pp. 995–1011, 1984.

[118] V. Zoby and R. Thompson, "Aeroheating Design Issues for Reusable Launch Vehicles -- A Perspective," *AIAA*, vol. 42, no. 1, pp. 1–5, 2004.

[119] D. R. Olynick, P. A. Gnoffo, K. J. Weilmuenster, H. H. Hamilton, and E. Venkatapathy, "Computational Aerothermodynamic Design Issues for Hypersonic Vehicles," *Journal of Spacecraft and Rockets*, vol. 36. pp. 21–43, 1999.

[120] C. J. Greenshields, H. G. Weller, L. Gasparini, and J. M. Reese, "Implementation of semi-discrete, non-staggered central schemes in a colocated, polyhedral, finite volume framework, for high-speed viscous flows," *Int. J. Numer. Methods Fluids*, vol. 63, no. 1, pp. 1–21, 2009.

[121] A. Kurganov and G. Petrova, "Central-upwind schemes on traingular grids for hyperbolic systems of conservation laws," *Numer. Methods Partial Differ. Equ,* vol. 21, no. 3, pp. 536–552, 2005.

[122] P. Colella and P. Woodward, "The piecwise parabolic method (PPM) for gas- dynamical simulations," *J. Comput. Phys,* vol. 54, pp. 174–204, 1984.

[123] A. Kurganov and E. Tadmor, "New High-Resolution Central Schemes for Nonlinear Conservation Laws and Convection-Diffusion Equations," *J. Comput. Phys,* vol. 160, pp. 241–282, 2000.

[124] F. Cheuret and J. Steelant, "CEAS-2009 Simulations On Transpiration Cooling For Supersonic Flow," in *CEAS 2009 Air and Space Conference edition:2*, 2009, pp. 1–11.

[125] P. R. Spalart and S. R. Allmaras, "A One-Equation Turbulence Model for Aerodynamic Flows," *AIAA*, vol. 92, pp. 04–39, 1992.

[126] T. Barth and D. C. Jespersen, "The Design and application of Upwind schemes on Unstructured Meshes," in *27th Aerospace Sciences Meeting and Exhibit*, 1989, vol. 89, pp. 03–66.

[127] D. Mavriplis, "Multigrid Solution of the Two-Dimensional Euler Equations On Unstructured," *AIAA J,* vol. 218, no. 2, pp. 213–221, 1988.

[128] B. van Leer, "Towards the ultimate conservative difference scheme. V. A second-order sequel to Godunov's method," *J. Comput. Phys,* vol. 32, no. 1, pp. 101–136, 1979.

[129] R. Haoui, "Finite Volume Analysis of a Supersonic Non-Equilibrium Flow around an Axisymmetric Blunt Body," *Int. J. Aeronaut. Sp. Sci,* vol. 11, no. 2, pp. 59–68, 2010.

[130] P. R. M. Lyra and K. Morgan, "A review and comparative study of upwind biased schemes for compressible flow computation. Part II: 1-D higher-order schemes," *Arch. Comput. Methods Eng,* vol. 7, no. 3, pp. 333–377, 2000.

[131] P. Nithiarasu, R. Codina, and O. C. Zienkiewicz, "The Characteristic Based Split Scheme- a unified approach to fluid dynamics," *Int. J. Numer. Methods Eng,* vol. 66, no. 10, pp. 1514–1546, 2006.

[132] N. Massarotti, F. Arpino, R. W. Lewis, and P. Nithiarasu, "Explicit and Semi-Implicit CBS procedures for incompressible viscous flows," *Int. J. Numer. Methods Eng,* vol. 66, no. 10, pp. 1618–1640, 2006.

[133] P. Nithiarasu and O. C. Zienkiewicz, "A Universal Algorithm for Fluid Dynamics. The Characteristic Based Split (CBS) procedure Some test on the stability and boundary conditions," *Arch. Mech,* vol. 52, pp. 857–887, 2000.

[134] P. Nithiarasu, O. C. Zienkiewicz, B. V. K. S. Sai, K. Morgan, R. Codina, and M. Vázquez, "Shock capturing viscosities for the general fluid mechanics algorithm," *Int. J. Numer. Methods Fluids*, vol. 28, no. 9, pp. 1325–1353, 1998.

[135] R. Codina, M. Vazquez, and O. C. Zienkiewicz, "A general algorithm for Compressible and Incompressible flows. Part III: the semi-implicit form," *Int. J. Numer. Methods Fluids*, vol. 27, no. 1–4, pp. 13–32, 1998.

[136] N. Massarotti, P. Nithiarasu, and O. C. Zienkiewicz, "Natural convection in porous medium-fluid interface problems-A finite element analysis by using the CBS procedure," *Int. J. Numer. Methods Heat Fluid flow*, vol. 11, no. 5, pp. 473–490, 2001.

[137] M. S. Liou, "Progress towards an Improved CFD Method: AUSM+," *AIAA*, vol. 36, no. 9, pp. 1610–1617, 1998.

[138] N. Massarotti, O. C. Zienkiewicz, and P. Nithiarasu, "Characteristic Based Split algorithm for Incompressible flow problems with heat transfer," *Int. J. Numer. methods Heat Fluid FLow*, vol. 8, no. 8, pp. 969–990, 1998.

[139] D. Vandromme and A. Saouab, "Implicit solution of Reynolds Averged Navier Stokes Equations for Supersonic Jets on Adaptive meshes," in *Computational Fluid Dynamics*, New-York, 1992, pp. 727–731.

[140] D.C. Sorensen, R. B. Lehoucq, C. Yang, and K. Maschhoff, "MATLAB Function Reference, Help Section,MathWorks Inc." 2008.

[141] R. Brent, *Algorithms for Minimization Without Derivatives*. New Jersey: Prentice-Hall, 1973, p. 195.

[142] M. Beychok, "De-Laval nozzle," 2010. [Online]. Available: http://en.citizendium.org/wiki/File:De_Laval_nozzle_2.png. [Accessed: 31-Feb-2014].

[143] N. Croft, "PHYSICA Theory Guide," in *Version 3.10*, 2007.

[144] A. J. Williams, N. T. Croft, and M. Cross, "Modelling of ingot development during the start up phase of direct casting," *Metall. Mater. Trans. B*, vol. 34, no. 5, pp. 727–734, 2003.

[145] M. Cross, D. McBride, and Gebhardt, "A Comprehensive Gold Oxide Heap Leach Model: Development And Validation," *Hydrometallurgy*, vol. 113, no. 114, pp. 98–108, 2012.

[146] D. Carswell, M. Cross, D. McBride, T. N. Croft, G. Foster, and A. K. Slone, "A CFD model for the prediction of haemolysis in micro axial left ventricular assist devices," *Appl. Math. Model,* vol. 37, no. 6, pp. 4199–4207, 2013.

[147] A. Leonard, "Energy cascade in large-eddy simulations of turbulent fluid flows," *Adv. Geophys. A*, vol. 18, pp. 237–248, 1974.

[148] P. R. Spalart and S. R. Allmaras, "A One-Equation Turbulence Model for Aerodynamic Flows," *Rech. Aerosp,* vol. 1, pp. 5–21, 1994.

[149] B. S. Baldwin and H. Lomax, "Thin Layer Approximation and Algebraic Model for Separated Turbulent Flows," *AIAA J,* vol. 2, pp. 78–257, 1978.

[150] A. G. Malan, R. W. Lewis, and P. Nithiarasu, "An improved unsteady, unstructured, artificial compressibility, finite volume scheme for viscous incompressible flows: Part I. Theory and implementation," *Int. J. Numer. Methods Eng,* vol. 54, no. 5, pp. 695–714, Jun. 2002.

[151] P. Nithiarasu, "Course Notes for Computational Fluid Dynamics :EG-360." Swansea Uiversity, Swansea, 2006.

[152] P. Nithiarasu, O. C. Zienkiewicz, R. Codina, M. Vazquez, and P. Ortiz, "The Characteristic Based Split Procedure: An efficient accurate algorithm for fluid problems," *Int. Numer. methods fluids*, vol. 31, no. 1, pp. 359–392, 1999.

[153] R. Codina, H. Coppola-Owen, P. Nithaiarsu, and C. B. Liu, "Numerical comparison of CBS and SGS as stabilization techniques for the Incompressible Navier–Stokes equations," *Eur. Congr. Compuatiational Methods Appl. Sci. Eng. ECCOMAS*, vol. 66, no. 10, pp. 24–28, 2004.

[154] F. M. White, *Viscous Fluid Flow*, 6th ed. New-York: McGraw-Hill, 1974.

[155] H. Schlichting, *Boundary Layer Theory*. New York: McGraw-Hill, 1979, p. 799.

[156] J. H. Ferziger and M. Perić, *Computational Methods for Fluid Dynamics*, vol. 3. 1999, p. xiv, 356 p.

[157] Y. Zhao and B. L. Zhang, "A higher-order characteristics upwind FV method for incompressible flow and heat transfer on unstructured grids," *Comput. Methods Appl. Mech. Eng,* vol. 190, no. 5–7, pp. 733–756, 2000.

[158] D. Sampaio, P. R. Lyra, K. Morgan, and N. P. Wetherill, "Petrov-Galerkin solutions of the incompressible Navier Stokes equation in primitive variables with adaptive re-meshing," *Comput. Methods Appl. Mech. Eng,* pp. 143–178, 1993.

[159] R. W. Lewis, P. Nitharasu, and K. N. Seetharamu, *Fundamentals of the Finite Element Method For Heat and Fluid*. New-York: Wiley-Interscience, 2004.

[160] P. Nithiarasu, "An efficient artificial compressibility (AC) scheme based on the characteristic based split (CBS) method for incompressible flows," *Int. J. Numer. Methods Eng,* vol. 56, no. 13, pp. 1815–1845, Apr. 2003.

[161] M. K. Nithiarasu P, Mathur J, Wetherill NP, "Three Dimensional Incompressible flow calculations using the Characteristic Based Split (CBS) scheme," *Int. J. Numer. methods fluids*, vol. 44, no. 11, pp. 1207–1229, 2004.

[162] A. Dadone and B. Grossman, "Surface Boundary Conditions for the Numerical Solution of the Euler Equations," *AIAA*, vol. 32, no. 2, pp. 285–293, 1994.

[163] A. Villa, L. Barbieri, and R. Malgesini, "Ghost cell boundary conditions for the Euler equations and their relationships with feedback control," *Commun. Appl. Ind. Math,* vol. 3, no. 1, p. 394, 2012.

[164] M. Rankine, "On the Thermodynamic Theory of Waves of Finite Longitudinal Disturbance," *Philos. Trans. R. Soc. London*, vol. 160, pp. 277–288, 1870.

[165] J. W. Slater, "oblique shock subroutine," 2010. [Online]. Available: http://www.grc.nasa.gov/WWW/wind/valid/wedge/oblshk.f.

[166] NASA, "National Program for orientated research in CFD," 2010. [Online]. Available: http://www.grc.nasa.gov/WWW/wind/.

[167] Cornell, "FLUENT study," 2013. [Online]. Available: https://confluence.cornell.edu/display/SIMULATION/ANSYS+WB+-+Supersonic+Flow+Over+a+Wedge+-+Problem+Specification.

[168] AIAA, "AIAA-NACA0012," 2014. [Online]. Available: https://info.aiaa.org/tac/ASG/FDTC/DG/BECAN_files_/Workshop_June_2010_Final_problem_Statements/Problem 1 -- Trailing Edge Noise/Workshop Airfoil Coordinates rev1.xls. [Accessed: 11-Jul-2014].

[169] J. Steelant, "ATLLAS: Aero-Thermal Loaded Material Investigations for High-Speed Vehicles," in *15th AIAA International Space Planes and Hypersonic Systems and Technologies Conference*, 2008, vol. 15, pp. 715–725.

[170] O. Reynolds, "An experimental investigation of the circumstances which determine whether the motion of water shall be direct or sinous, and of the law of resistance in parrallel channels," *Philos. Trans. R. Soc. A*, vol. 174, no. 0, pp. 935–982, 1883.

[171] T. Okamura, A. R. Wazzan, and A. M. O. Smith, "The stability of water flow over a heated and cooled flat plates," *J. Heat Transfer*, vol. 90, no. 1, pp. 109–114, 1968.

[172] R. Monti and G. Pezella, "A New Philosophy for the design of Re-Entry Vehicles," *Sp. Technol,* pp. 179–191, 2004.

[173] A. G. Malan, R. W. Lewis, and P. Nithiarasu, "An improved unsteady, unstructured, artificial compressibility, finite volume scheme for viscous incompressible flows: Part II. Application," *Int. J. Numer. Methods Eng,* vol. 54, no. 5, pp. 715–729, Jun. 2002.

[174] T. A. Zang and L. Kleiser, "Numerical Simulation of transition in wall bounded shear flows," *Annu. Rev. Fluid Mech,* vol. 23, pp. 495–537, 1991.

[175] C. Hirsch, *Numerical Computation of Internal and External Flows*. McGraw-Hill, 1984.

[176] M. E. Vaughn, "Guidelines for gridding simple flows- The flat plate in laminar flow," 2008.

[177] T. Langener, J. Von Wolfersdorf, and J. Steelant, "Experimental Investigations on Transpiration Cooling for Scramjet Applications Using Different Coolants," *AIAA J,* vol. 49, no. 7, pp. 1409–1419, Jul. 2011.

[178] F. Cheuret and J. Steelant, "ATLLAS: Performance of existing models for transpiration cooling," 2008.

[179] V. Driest, "The problem of aerodynamic heating," *Aeronaut. Eng. Rev,* pp. 26–41, 1956.

[180] M. W. Rubesin and H. A. Johnson, "A critcial review of skin friction and heat transfer solutions of the laminar boundary layer equations of a," *Trans. Am. Soc. Mech. Eng,* pp. 383–388, 1949.

[181] E. R. G. Eckert, "Engineering Relations for the heat transfer and frction in high-velocity laminar and turbulent boundary-layer flow over surfaces with constant pressure and temperature," *Trans. Am. Soc. Mech. Eng,* 1956.

[182] J. Steelant, "Achievements obtained on Aero-Thermal Loaded Materials for High-Speed Atmospheric Vehicles within ATLLAS," *16th AIAA/DLR/DGLR Int. Sp. Planes Hypersonic Syst. Technol. Conf. AIAA*, pp. 92407–92407, 2009.

[183] F. Cheuret and J. Steelant, "ATLLAS: Non-Reacting coolant flows with warm/hot air external flow-AST5-CT-2006-030729," 2010.

[184] B. Heidenreich, "Carbon Fibre Reinforced SiC Materials Based on Melt Infiltration," in *Proceedings of the 6th International Conferance On High temperature ceramic matrix composition*, 2007.

[185] H. Kelly and M. Blosser, "Active Cooling from the Sixties to NASP," Hampton, VA, 1994.

[186] K. Song, S. Choi, and S. Scotti, "Transpiration Cooling Experiment for Scramjet Engine Combustion Chamber by High Heat Fluxes," *J. Propuls. Power*, vol. 22, no. 1, pp. 96–102, 2006.

[187] M. R. Lecruyer and R. S. Colladay, "Influence of Porous-Wall Thermal Effectiveness on Boundary-Layer Heat Transfer," *NASA TN D*, vol. 6837, pp. 1–25, 1972.

[188] G. Pantelis and A. Ritchie, "Rate limiting factors in dump leaching of Pyritic Ores," *Appl. Math. Model,* vol. 16, no. 10, pp. 553–560, 1992.

[189] S. Ergun, "Fluid flow through packed columns," *Chem. Eng. Prog,* vol. 48, no. 2, pp. 89–94, 1952.

APPENDIX A

Gas Models and their Differentiation

3. Perfect gas model
    - According to Anderson [1] this model starts to break down at 800℃ = 1073.15℃K = $2.66T_\infty$ it is not applicable at temperatures of 2000K i.e 6 T_∞-$7T_\infty$
4. Frozen Gas Model
    - For a frozen flow the only way that approximately no changes can occur in the internal energy modes and the chemical composition, is to have approximately zero reaction rates, or infinitely long relaxation times. In reality, neither of the preceding flows actually exists
3. Equilibrium
    - Local equilibrium flow is assumed where the internal energy modes and the chemical composition of a fluid element moving along a streamline adjust instantly to the changing conditions and the flow is said to have infinitely fast reaction rates. For ball park solutions use Fay-Ridell equation [2] and Mollier diagrams [3]
4. Non Equilibrium
    - The extreme viscous dissipation within hypersonic boundary layers may be high enough to increase the vibrational energy internally within molecules and to cause dissociation within the gas mixture. In addition if transpiration cooling of a cryogenically cooled fluid occurs then chemical mixing will give rise to complex heterogenous reactions. In both scenarios this gives rise to chemically reacting boundary layers wetting the surface of the hypersonic vehicle[10]. When the gas temperatures are increased to high enough values, the gas behaves in a "non-ideal'' fashion. This renders a model that will solve 5 "stiff " ODEs using the five species model and a Schrödinger equation such as the model described in the research by Shanker (1994).

A real-gas model assumes that a gas is chemically reactive, but also assumes all chemical reactions have had time to complete and all components of the gas have the same temperature (this is called thermodynamic equilibrium). When air is compressed by a shock wave, it is superheated by compression and chemically dissociates. The distance from the shock wave to the stagnation point on the re-entry vehicle's leading edge is called shock wave stand-off. An approximate rule of thumb for shock wave standoff distance is 0.14 times the nose radius. One can estimate the time of travel for a gas molecule from the shock wave to the stagnation point by assuming a free-stream velocity of 7.8 km/s and a nose radius of 1 meter, i.e., time of travel is about 18 microseconds [5]. This is roughly the time required for shock wave initiated chemical dissociation to approach chemical equilibrium thus enabling an equilibrium model to be usable. For this case, most of the shock layer between the shock wave and stagnation point of an entry vehicle is chemically reacting and *not* in a state of equilibrium. The Fay-Riddell equations [2], are ordinary differential equations and they are employed when modelling the peak heat flux for chemical equilibrium. The time required for the shock layer gas to reach equilibrium is strongly dependent upon the shock layer's pressure. For example, in the case of the Galileo Probe's entry into Jupiter's atmosphere, the shock layer was mostly in equilibrium during peak heat flux due to the very high pressures experienced [5]. According to

[10] For extreme cases not only can the boundary layer be chemically reacting but the entire shock layer can be dominated by chemical interactions, such as re-entry of the Apollo capsule [6].

Anderson [6] such high temperature chemically reacting flows can have a considerable influence on lift, drag, and moments on a hypersonic vehicle. Such effects have been found to be important for estimating the amount of body flap deflection necessary to trim the space shuttle during high-speed re-entry.

A crude approximation for estimating re-entry temperature is to assume the air temperature in degrees-Kelvin to be equal to the entry speed in meters per second i.e. a space shuttle entering the atmosphere at 7.8 km/s would experience a peak shock layer temperature of 7800 K. This relationship can only occur at re-entry speeds, as the kinetic energy proportionally increases with the square of the velocity. At typical space shuttle re-entry temperatures, the air in the shock layer is ionized and dissociated [5].

1) The vibrational energy increases and this causes and this causes the specific heats C_p and C_v to become functions of temperature meaning that the ratio, $\gamma = C_p/C_v$, also becomes a function of temperature. For air, this effect becomes important above 800K.
2) As the gas temperature is increased above 800K, chemical reactions occur. For air at 1atm pressure, O_2 dissociation ($O_2 \rightarrow 2O$) begins at about 2000K, and all the molecular oxygen is essentially totally dissociated at 4000K. At this temperature N_2 dissociation ($N_2 \rightarrow 2N$) begins and is essentially totally dissociated at 9000K. Above a temperature of 9000K, ions are formed ($N \rightarrow N^+ + e^-$) and ($O \rightarrow O^+ + e^-$), and the gas becomes a partially ionizied plasma that has to be modelled using the Fay and Riddell equations [2].
3) If the shock layer temperatures are high enough the thermal radiation emitted by the gas itself can become important, giving rise to radiative fluxes to the surface called radiative heating. Radiative heat fluxes can become the main heating process i.e. for Apollo re-entry, radiative heat transfer was more than 30% of the total heating and for a space probe entering the atmosphere of Jupiter, the radiative heating will be more than 95% of the total heating [6].

Frozen, Equilibrium Non-Equilibrium Gas models

To differentiate if a gas flow is in thermodynamic and chemical equilibrium or alternatively whether the gas is in non-equilibrium conditions, scientists use equilibrium, non-equilibrium, frozen flow definitions. Let τ_f be the general time for a fluid element to traverse the domain $\tau_f \approx V_\infty / l$ where l is the characteristic length of the flow field and τ_c is the time it takes for the internal energy modes and chemical reactions to occur. The comparative length of the time between the chemical reactions and the transit time of each element define the state of the gas flow:

1) Local equilibrium flow is assumed where the internal energy modes and the chemical composition of a fluid element moving along a streamline adjust instantly to the changing conditions and the flow is said to have infinitely fast reaction rates.

$$\tau_f \gg \tau_c \tag{1.1}$$

2) Alternatively, for a frozen flow the only way that approximately no changes in the internal energy modes and the chemical composition can occur is to have approximately zero reaction rates, or infinitely long relaxation time. In reality, neither of the preceding flows actually exists.

$$\tau_f \ll \tau_c \tag{1.2}$$

3) For all other situations, especially for $\tau_f \approx \tau_c$, a non-equilibrium flow exists [6]

$$\tau_f \approx \tau_c \tag{1.3}$$

τ_c is also referred to as the chemistry time. If the chemistry has plenty of time to adjust while the fluid element moves through the flow field then the flow can be assumed to be in local equilibrium. Alternatively when the fluid element traverses through the flow field before any chemical changes can take place then the flow can be assumed to be frozen. If the opposite were true, we have non-equilibrium flow, which is markedly more difficult to analyse.

The extreme viscous dissipation within hypersonic boundary layers may be high enough to increase the vibrational energy internally within molecules and to cause dissociation within the gas mixture. In addition if transpiration cooling of a cryogenically cooled fluid occurs then chemical mixing will give rise to complex heterogenous reactions. In both scenarios this gives rise to chemically reacting boundary layers wetting the surface of the hypersonic vehicle[11]. When the gas temperature values are increased to high enough values, the gas behaves in a "non-ideal'' fashion.

[11] For extreme cases not only can the boundary layer be chemically reacting but the entire shock layer can be dominated by chemical interactions, such as re-entry of the Apollo capsule.

APPENDIX B

SIMPLE

As stated in the literature review, incompressible flows can be modelled using the pressure based schemes such as the SIMPLE type algorithms as presented by Patankar and Spalding [7]. The Semi implicit momentum pressure linked equation (SIMPLE) is used to stabilize the pressure field in the momentum equations by implicitly linking it to the continuity equation. It works by updating a pressure correction field in the momentum equation from intermediate velocities calculated in the continuity equation. These pressure correction terms are used to update both the pressure and velocity fields. Then from the continuity equation an intermediate velocity field is calculated. Then the intermediate velocity field is used to calculate the pressure correction field. Finally the pressure correction terms are used to update the pressure and velocity field. Hence from the updated pressure field, the process starts again, and continues until we have a converged solution for instance when the pressure correction terms approach zero.

Unfortunately, although generally stable the above procedure has difficulty converging on the steady state solution if the initial guess is far away from the true pressure field. Under relaxation is done to numerically 'dampen' the large pressure correction terms added to the pressure field as the divergence of the pressure field is the number one reason why the SIMPLE algorithm 'diverges'. When damping the large pressure field we simply multiply the pressure correction term by a value between 0 and 1.

The SIMPLE Revised or the SIMPLE Consistent algorithms have been developed to address such convergence issues, however a sequential breakdown of the SIMPLE algorithm is shown below

1) Set the guessed values of pressure and velocity.

$$p^* = p$$
$$u^* = u \qquad \text{(B1.4)}$$
$$\mathrm{v}^* = \mathrm{v}$$

2) Firstly compute guessed velocity fields using a guessed pressure field P^* and any source terms:

$$a_u u^*_{I,J} = \sum_{nb} a_{\mathrm{nb}} u^*_{\mathrm{nb}} + \nabla_x p^* + b_{I,J}$$
$$a_{\mathrm{v}} \mathrm{v}^*_{I,J} = \sum_{nb} a_{\mathrm{nb}} \mathrm{v}^*_{\mathrm{nb}} + \nabla_y p^* + b_{I,J} \qquad \text{(B1.5)}$$

3) Compute the corrected velocity field.

$$a_{I,J} p'_{\mathrm{I,J}} = \sum_{nb} a_{\mathrm{nb}} p'_{\mathrm{nb}} + b_{\mathrm{I,J}} \qquad \text{(B1.6)}$$

4) Calculate the actual pressure using the corrected pressure field, p', and using the guessed pressure, p^*:

$$p_{\mathrm{I,J}} = p'_{\mathrm{I,J}} + p^*_{\mathrm{I,J}} \qquad \text{(B1.7)}$$

5) Update the velocity with the corrected pressure field p'

$$u_{I,J} = u^*_{I,J} + d_{I,J}\left(\nabla_x p'\right)$$
$$v_{I,J} = v^*_{I,J} + d_{I,J}\left(\nabla_y p'\right) \quad \text{(B1.8)}$$

6) The scalar quantities are then computed using the following equation

$$a_{I,J}\Phi_{I,J} = \sum_{nb} a_{nb}\Phi_{nb} + b_{i,j} \quad \text{(B1.9)}$$

7) Check for convergence by calculating the residual

General Remarks

Equation (B1.6) leads to a linear equation with weak diagonal dominance. Once this equation has been solved and a pressure correction field obtained, the correct pressure field may be obtained using formula (B1.7). The SIMPLE approximations made tend to lead to an over-estimation of the pressure correction values, making the pressure-correction equation susceptible to divergence unless some under-relaxation is used during the iterative procedure.

The face velocity component and their related coefficients are interpolated from control volume nodal values. The control volume pressure gradient, which enters the momentum equations in (B1.5) and (B1.8) as a source term is evaluated as a sum of surface integrals over each face bounding the control volume,

$$\int_{cv} \nabla_{x_j} p dV = \sum_f A_f \left(n_j\right)_f p_f \quad \text{(1.10)}$$

Where p_f is interpolated from adjacent values.

APPENDIX C

3D Unstructured Jacobian

For 2D problems the evaluation of Jacobian terms necessary for the calculation of the viscous and thermal conduction terms were simple and easy to formulate. For 3D problems the evaluation of the Jacobian term will be not be so straight forward. Thereby the following corollary will show the numerical procedure to obtain these the 3D Jacobian.

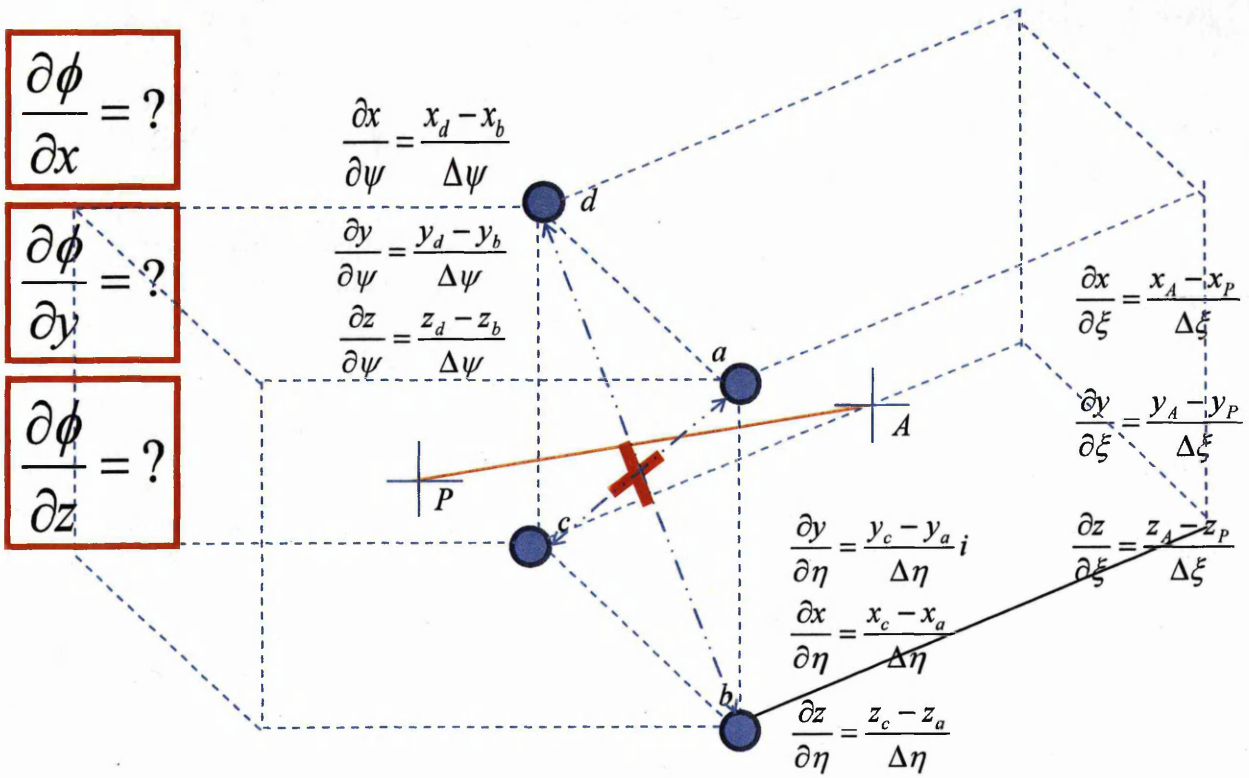

Figure 13 Unstructured grid with terms that will aid in the computation of the non-orthogonal diffusion term

$$\frac{\partial \phi}{\partial \xi} = \frac{\phi_A - \phi_P}{\Delta \xi} \qquad \text{(C1.11)}$$

$$\frac{\partial \phi}{\partial \eta} = \frac{\phi_c - \phi_a}{\Delta \eta} \qquad \text{(C1.12)}$$

For the artificial viscous terms $\phi = (\rho u, \rho v, \rho w, \rho E, \rho)$ seen in chapter 5.

$$\frac{\partial \phi}{\partial x} = \frac{1}{J}\left(\left(\frac{\partial y}{\partial \psi}\frac{\partial z}{\partial \eta} - \frac{\partial y}{\partial \eta}\frac{\partial z}{\partial \psi}\right)\frac{\partial \phi}{\partial \xi} - \left(\frac{\partial y}{\partial \psi}\frac{\partial z}{\partial \xi} - \frac{\partial y}{\partial \xi}\frac{\partial z}{\partial \psi}\right)\frac{\partial \phi}{\partial \eta} + \left(\frac{\partial y}{\partial \eta}\frac{\partial z}{\partial \xi} - \frac{\partial y}{\partial \xi}\frac{\partial z}{\partial \eta}\right)\frac{\partial \phi}{\partial \psi}\right) \qquad \text{(C1.13)}$$

$$\frac{\partial \phi}{\partial z} = \frac{1}{J}\left(\left(\frac{\partial x}{\partial \psi}\frac{\partial y}{\partial \eta} - \frac{\partial x}{\partial \eta}\frac{\partial y}{\partial \psi}\right)\frac{\partial \phi}{\partial \xi} - \left(\frac{\partial x}{\partial \psi}\frac{\partial y}{\partial \xi} - \frac{\partial x}{\partial \xi}\frac{\partial y}{\partial \psi}\right)\frac{\partial \phi}{\partial \eta} + \left(\frac{\partial x}{\partial \eta}\frac{\partial y}{\partial \xi} - \frac{\partial x}{\partial \xi}\frac{\partial y}{\partial \eta}\right)\frac{\partial \phi}{\partial \psi}\right) \quad \text{(C1.14)}$$

$$\frac{\partial \phi}{\partial z} = \frac{1}{J}\left(\left(\frac{\partial x}{\partial \psi}\frac{\partial y}{\partial \eta} - \frac{\partial x}{\partial \eta}\frac{\partial y}{\partial \psi}\right)\frac{\partial \phi}{\partial \xi} - \left(\frac{\partial x}{\partial \psi}\frac{\partial y}{\partial \xi} - \frac{\partial x}{\partial \xi}\frac{\partial y}{\partial \psi}\right)\frac{\partial \phi}{\partial \eta} + \left(\frac{\partial x}{\partial \eta}\frac{\partial y}{\partial \xi} - \frac{\partial x}{\partial \xi}\frac{\partial y}{\partial \eta}\right)\frac{\partial \phi}{\partial \psi}\right) \quad \text{(C1.15)}$$

$$J = \left(\frac{\partial x}{\partial \psi}\left(\frac{\partial y}{\partial \eta}\frac{\partial z}{\partial \xi} - \frac{\partial y}{\partial \xi}\frac{\partial z}{\partial \eta}\right) - \frac{\partial x}{\partial \eta}\left(\frac{\partial y}{\partial \psi}\frac{\partial z}{\partial \xi} - \frac{\partial y}{\partial \xi}\frac{\partial z}{\partial \psi}\right) + \frac{\partial x}{\partial \xi}\left(\frac{\partial y}{\partial \eta}\frac{\partial z}{\partial \psi} - \frac{\partial y}{\partial \psi}\frac{\partial z}{\partial \eta}\right)\right) \quad \text{(C1.16)}$$

Revisions to the Sequential CBS scheme for porous flow

Assuming as a scientific check that both the porous medium and the main gas domain have the same thermal conductivity $k_{CC/Sic} = k_{lam} = 0.025W/m-K$. Where the following values are plugged into equation (C1.17) to give the following results

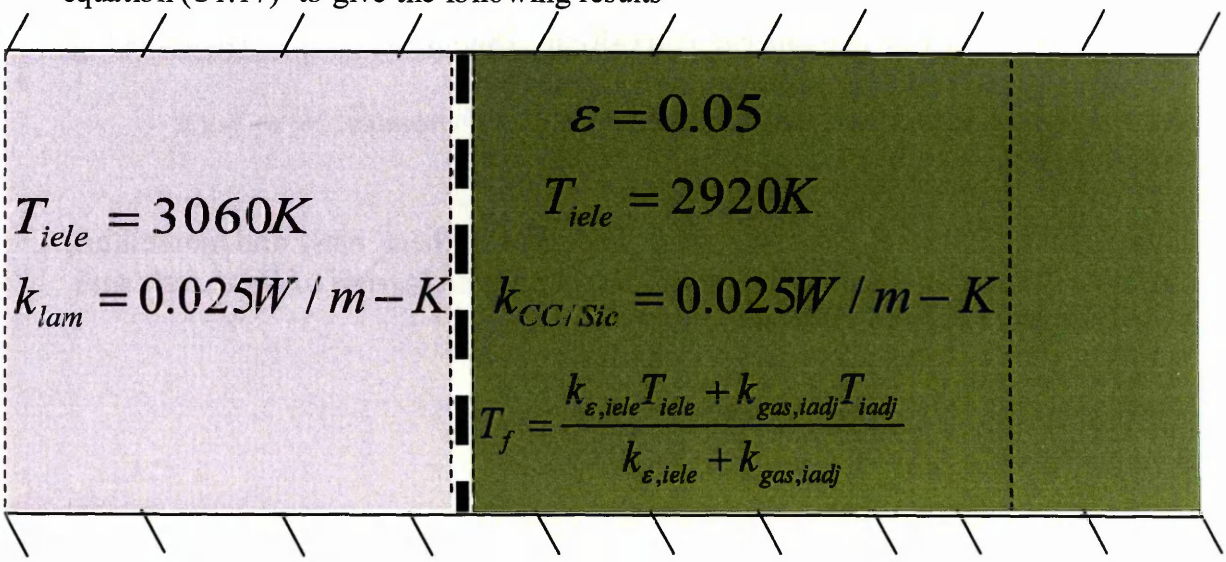

Figure 14: Density profile magnified through the porous medium which is situated between 6-6.5m

$$k_{\text{int}} = -2k_{CC/Sic} + \frac{1}{\frac{(1-\varepsilon)}{2k_{CC/Sic} + k_{eff}} + \frac{\varepsilon}{k_{CC/Sic}}} \quad \text{(C1.17)}$$

$k_{\text{int}} = 0.0184W/m-k$ X

$T_f = 3001K$ X

An amended version of equation (C1.17) was used to calculate the interface thermal conductivity.

$$k_{\text{int}} = k_{CC/Sic} - \frac{1}{\frac{(1-\varepsilon)}{k_{CC/Sic} - k_{eff}} + \frac{\varepsilon}{k_{CC/Sic}}} \quad \text{(C1.18)}$$

$k_{int} = 0.025W/m-k$ ✓

$T_f = 2990K$ ✓

Computations were made using (C1.17) instead of (C1.18). However this strategy lead to instability and eventually to divergence Even with large amounts of damping applied to the time step the solution was plagued with instability.

References

[1] J. J. Anderson, *Modern compressible flow with historical perspective*, vol. 4. 2003.

[2] J. A. Fay and F. R. Riddell, "Theory of Stagnation Point Heat Transfer in Dissociated Air," *J. Aeronaut. Sci.*, vol. 25, no. 2, pp. 73–85, 1958.

[3] K. Raiput, "Engineering Thermodynamics," *Infin. Sci. Ser. 3rd Ed.*, 2009.

[4] R. Shanker, *Principles of Quantum Mechanics*, 2nd ed. Springer, 1994.

[5] "Wikipedia- Atmospheric - Entry," 2013. [Online]. Available: http://en.wikipedia.org/wiki/Atmospheric_entry#Real_.28equilibrium.29_gas_model.

[6] J. J. Anderson, *Hyper-Sonics and High Temperature Gas Dynamics*. New-York: McGraw-Hill, 2006.

[7] D. . Spalding and S. . Patankar, "A calculation procedure for heat, mass and momentum transfer in three-dimensional parabolic flows," *International Journal of Heat and Mass Transfer*, vol. 15. pp. 1787–1806, 1972.